CONCEPTUAL DESIGN OF A HIGH ENERGY ASTRONOM` OBSERVATORY - VOLUME 1- PRELIMINARY ANALYSIS VOLUME 11 - APPENDICES

George C. Marshall Space Flight Center
Marshall Space Flight Center, Alabama

16 February 1970

Distributed ... 'to foster, serve
and promote the nation's
economic development
and technological
advancement.'

CLEARINGHOUSE
FOR FEDERAL SCIENTIFIC AND TECHNICAL INFORMATION

U.S. DEPARTMENT OF COMMERCE/National Bureau of Standards

This document has been approved for public release and sale.

$N10L-a$

NASA TECHNICAL
MEMORANDUM

NASA TM X-53976

N70-22901

(ACCESSION NUMBER)

753

(PAGES)

TMX-53976

(NASA CR OR TMX OR AD NUMBER)

N70-22923

(THRU)

/

(CODE)

31

(CATEGORY)

CONCEPTUAL DESIGN OF A HIGH ENERGY
ASTRONOMY OBSERVATORY
VOLUME I — PRELIMINARY ANALYSIS
VOLUME II — APPENDICES

By Program Development

February 16, 1970

NASA

George C. Marshall Space Flight Center
Marshall Space Flight Center, Alabama

Cat: 31

NASA

1. REPORT NO. ~~TM X-53976~~

2. GOVERNMENT ACCESSION NO.

3. RECIPIENT'S CATALOG NO.

4. TITLE AND SUBTITLE
Conceptual Design of a High Energy Astronomy Observatory
Volume I — Preliminary Analysis
Volume II — Appendices

5. REPORT DATE
February 16, 1970

6. PERFORMING ORGANIZATION CODE
PD-DO

7. AUTHOR(S)
Program Development

8. PERFORMING ORGANIZATION REPORT #

9. PERFORMING ORGANIZATION NAME AND ADDRESS
Preliminary Design Office
Program Development
Marshall Space Flight Center, Alabama 35812

10. WORK UNIT. NO.
188-41-01

11. CONTRACT OR GRANT NO.

12. SPONSORING AGENCY NAME AND ADDRESS

13. TYPE OF REPORT & PERIOD COVERED
Technical Memorandum

14. SPONSORING AGENCY CODE

15. SUPPLEMENTARY NOTES

16. ABSTRACT
  In response to a request from the Office of Space Science and Applications, a Phase A — Preliminary Analysis of a High Energy Astronomy Observatory was undertaken by the George C. Marshall Space Flight Center. Results of this study are reported in two volumes, Volume I containing the preliminary analysis and conceptual design of a baseline spacecraft and Volume II containing supporting technical data and discussion of mission and spacecraft alternatives..
  The High Energy Astronomy Observatory treated in this work is the first of four planned spacecraft in the High Energy Astronomy Observatory program, designated in this report as HEAO-A. The primary mission objective of the HEAO-A spacecraft is to completely survey the celestial sphere for high energy X-rays, gamma-rays, and cosmic-rays, with primary emphasis in the galactic belt region; the secondary mission objective is selective pointing at specific celestial targets.
  To ensure a comprehensive system analysis for feasibility assessment, a baseline mission and spacecraft was defined with a realistic, but hypothetical, experiment package. Total weight of the baseline spacecraft is approximately 19 000 pounds and launch is assumed from ETR on the Titan IIID launch vehicle in March 1974. The satellite is placed into a 200-n. mi. circular orbit with a 28.5-degree inclination; during the first month in orbit the slowly rotating satellite scans a region measuring ±8.5 degrees from the galactic plane; during the next 6 months the entire celestial sphere is scanned; and during the last 5 months of the first mission year the satellite employs a pointing mode for selected source investigations. Satellite design lifetime is 1-year minimum, with 2 years desired.

17. KEY WORDS
High Energy Astronomy Observatory
Scientific Satellite
High Energy Space Physics
Conceptual Satellite Design
Unmanned Spacecraft

18. DISTRIBUTION STATEMENT
STAR Announcement

Erich E. Goerner
Director, Preliminary Design Office

19. SECURITY CLASSIF. (of this report)
Unclassified

20. SECURITY CLASSIF. (of this page)
Unclassified

21. NO. OF PAGES
767

22. PRICE
$3.00

MSFC - Form 3292 (May 1969)

TABLE OF CONTENTS — VOLUME I

1. Observatories -- Design

I. T.
II. T; High ... observatory

TABLE OF CONTENTS — VOLUME II

Page

ACKNOWLEDGMENTS

Goddard Space Flight Center has contributed heavily in the identification and description of experiments which make up the reference payload. Also, GSFC has been of valuable assistance in the assessment of the expected capability of the STADAN network to handle the HEAO data flow.

The Physics and Astronomy Division of OSSA has worked closely with MSFC in establishing appropriate mission objectives and requirements and has provided the inputs on the high energy physics and astronomy background information presented in Appendix A.

Questions pertaining to the material contained in this report should be directed to the following MSFC personnel:

Total Phase A Study	Mr. C. Dailey PD-MP-S	453-3431
	Mr. J. Heyer PD-DO-DIR	453-4161
Experiments and Mission (Section II and Appendix A)	Mr. C. Dailey PD-MP-S	453-3431
Launch Vehicle (Section III and Appendix B)	Mr. R. Crawford PD-SA-V	453-0480
Orbit Selection and Operations (Section IV and Appendix C)	Mr. R. Hill PD-DO-PM	453-3938
Systems Integration and Alternate Configurations (Section V and Appendix D)	Mr. J. Butler PD-DO-SI	453-3068
Structure (Section VI and Appendix E)	Mr. C. Colley PD-DO-MS	453-4260
Thermal (Section VII and Appendix F)	Mr. C. Fritz PD-DO-MP	453-4197
RCS and Kick Stage (Section VIII and Appendix G)	Mr. B. Price PD-DO-MP	453-4196
Power (Section IX and Appendix H)	Mr. R. Boehme PD-DO-EP	453-5726

Communications and Data (Section X and Appendix I)	Mr. C. Hamilton PD-DO-EC	453-3667
Attitude Sensing and Control (Section XI and Appendix J)	Mr. D. Schultz PD-DO-ES	453-5730
Mission Operations (Section XII)	Mr. C. Casey PM-MO-A	453-3660
Program Support (Section XIII)	Mr. B. Guyton PD-PS-T	453-2630

In addition to the personnel listed above, the following MSFC personnel were principal contributors to the study:

Mr. L. Allen, PD-DO-SR
Mrs. F. Andrews, PD-DO-DIR
Mr. J. Beasley, PD-PS-E
Mr. D. Black, PD-DO-SL
Mr. J. Blumrich, PD-DO-SL
Mr. C. Darwin, PD-DO-SI
Mr. B. Davis, PD-DO-ES
Mr. S. Denton, DP-DO-MS
Mr. J. Fults, PD-DO-PF
Mr. O. Green, PD-DO-ES
Mr. H. Manning, PD-DO-ME
Mr. J. Peoples, PD-DO-SI
Mr. D. Perkinson, PD-DO-PF
Mr. R. Potter, PD-MP-S
Mr. J. Price, PD-DO-MP
Mr. N. Raley, PM-MO-A
Mr. R. Rood PD-DO-EP
Mr. J. Sanders, PD-DO-MP
Mr. O. Sparks, PD-DO-SR
Mr. G. Tovar, PD-DO-MS
Mr. A. Young, PD-DO-SI

SUMMARY

In response to a request from the Office of Space Science and Applications, a Phase A — Preliminary Analysis of a High Energy Astronomy Observatory was undertaken by the George C. Marshall Space Flight Center. Results of this study are reported in two volumes. Volume I contains the preliminary analysis and conceptual design of a baseline spacecraft and Volume II contains supporting technical data and discussion of mission and spacecraft alternatives.

The High Energy Astronomy Observatory treated in this work is the first of four planned spacecraft in the High Energy Astronomy Observatory program, designated HEAO-A. The HEAO-A primary mission objective is to perform a survey of the celestial sphere with primary emphasis on the galactic belt region. Secondary objective is pointing at specific celestial targets.

The launch vehicle selected is the Titan IIID, and launch is expected to be from ETR in March 1974. The mission lifetime requirement is 1 year, with 2 years desired. The orbit selected is a 200-n. mi., 28.5-degree inclination orbit. The STADAN network was selected as the ground tracking network.

The baseline experiment package is a hypothetical package of six experiments which are considered typical for the HEAO mission. The baseline spacecraft is 30 feet long, has an octagonal cross section of 105 inches maximum diameter, and weighs approximately 19 000 pounds, including 12 500 pounds of experiments. Maximum emphasis is placed on using existing hardware and techniques whenever possible. Power is supplied by a solar array and rechargeable battery system. In the celestial scan mode, the spacecraft rotates slowly about an axis (scan axis) perpendicular to the solar array; the experiments are mounted so that their viewing direction is perpendicular to the scan axis, and, hence, great circles of the celestial sphere are swept by the experiments while the solar arrays remain oriented toward the sun. In the galactic scan mode and pointing mode, the spacecraft scan axis is tilted off-sun, but this is limited by power availability from the solar array.

Experiment data and spacecraft housekeeping data are recorded on tape for subsequent playback to ground when the spacecraft is over a station. Two S-band links, one VHF beacon link and one command link, are provided for data transmission and communication with the spacecraft.

A combination of magnetic coils, RCS thrusters, and a flywheel are used to control the attitude of the spacecraft and stabilize it. The magnetic coils react with the earth's magnetic field to generate torques on the spacecraft for small attitude changes. The thrusters utilize hydrazine monopropellant to generate torques on the spacecraft for larger attitude changes.

The thermal control approach used is basically passive, consisting of coatings, insulation, and selective component locations and mounting techniques.

The structure is basically a dual-beam box truss concept, with aluminum skin covering the structure. An adapter is provided for mating the payload to the launch vehicle.

The Phase A — Preliminary Analysis has confirmed the feasibility of the HEAO-A baseline concept.

DEFINITION OF SYMBOLS

ACED	A. C. Electronics Division
ACS	Attitude control system
AFO	Announcement of Flight Opportunity
AGE	Aerospace ground equipment
APS	Auxiliary Propulsion System
ASCS	Attitude sensing and control system
AS&E	American Science and Engineering Company
ATM	Apollo Telescope Mount
ATS	Advanced Technology Satellites
BTL	Bell Telephone Laboratories
BW	Bandwidth
CBR	Charger-battery-regulator
CBRM	Charger battery regulator module
C/N	Carrier-to-noise ratio
CPU	Central processor unit
CsI(Na)	Sodium-doped cesium-iodide
EB	Experiments bottom (mounted nearer to bottom than center of HEAO)
EC	Experiments center (mounted near longitudinal center of HEAO)
EMC	Electromagnetic compatibility
ETR	Eastern Test Range

DEFINITION OF SYMBOLS (Continued)

FOV	Field-of-view
FPR	Flight performance reserve
GSE	Ground support equipment
GSFC	Goddard Space Flight Center
HEAO-A	High Energy Astronomy Observatory - Mission A
IGRA	Inner gimbal and rotor assembly
IGS	Inertial guidance system
IMG	Inertial measuring guidance unit
IMU	Inertial measurement unit
I/O	Input/output
IRIG	Interrange Instrumentation Group
ITL	Integrate-transfer-launch
kb/s	Kilobits per second
KSC	Kennedy Space Center
LASS	Lateral acceleration sensing system
LOS	Line-of-sight
M-87	A galaxy in Virgo A
MGC	Missile guidance computer
MSFC	Marshall Space Flight Center
MST	Mobile service tower

DEFINITION OF SYMBOLS (Continued)

NaI(Tℓ)	Thallium-doped sodium-iodide
NRL	Naval Research Laboratory
OAO	Orbital Astronomy Observatory
OSO	Orbital Scientific Observatory
OSSA	Office of Space Science and Applications
PAC	Programming and control unit
PAM	Pulse amplitude modulation
PCM/FM	Pulse code modulation/frequency modulation
PEP	Perpendicular to ecliptic plane
PLF	Payload fairing
PM	Photomultiplier
RAES	Radio Astronomy Explorer Satellite
RCS	Reaction Control System
RIME	Radio inertial measurement equipment
RMIS	Remote multiplexed instrumentation systems
RMU	Remote multiplex unit
ROM	Rough order of magnitude
ROU	Remote output units
SAMSO	Space and Missile Systems Organization, U. S. Air Force
SC	Signal conditioner

DEFINITION OF SYMBOLS (Concluded)

S/C	Spacecraft
SCOX-1	X-ray source of Scorpius
SMAB	Solid Motor Assembly Building
S/N	Signal-to-Noise Ratio
SRM	Solid rocket motor
STADAN	Space Tracking and Data Acquisition Network
TCU	Temperature control unit
TVC	Thrust vector control
UDMH	Unsymmetrical dimethylhydrazine
UPLF	Universal payload fairing
WECO	Western Electric Company
WTR	Western Test Range

SECTION I. INTRODUCTION

TABLE OF CONTENTS

CONCEPTUAL DESIGN OF A HIGH ENERGY ASTRONOMY OBSERVATORY

VOLUME I — PRELIMINARY ANALYSIS

SECTION I. INTRODUCTION

At the request of OSSA, the George C. Marshall Space Flight Center initiated a Phase A — Preliminary Analysis of the initial mission and satellite described in the High Energy Astronomy Observatory (HEAO) Project Plan. This analysis was accomplished by the Program Development organization at MSFC, with assistance from the Center's support contractor team; the results are reported in Volume I — Preliminary Analysis, and Volume II — Appendices.

The High Energy Astronomy Observatory (HEAO) project consists of several large automated spacecraft designed to transport scientific experiments into earth orbit and to serve as the base of operations for the experiments for a lifetime of one to two years. The primary objectives of the high-energy satellite program are to obtain high quality, high resolution data on cosmic-rays, gamma-rays, and X-rays. Data include information on the structure, spectra, polarization, and location of applicable sources. A corollary to the above is the visual identification from ground-based observatories of the stellar object emitting the high-energy radiations.

The objectives are to be accomplished by survey modes and pointing modes of spacecraft. The spacecraft concept and summary effort are as follows.

A. HEAO Spacecraft

1. Survey Class Spacecraft

● HEAO-A: The primary objective of HEAO-A, the initial mission, will be a complete survey of the celestial sphere to locate all sources of X-rays, gamma-rays, and cosmic-rays whose radiation falls

within the range of instrument sensitivities and spectral range. The secondary objective will be to study some of these sources in more detail by pointing the spacecraft for limited periods of time.

● HEAO-B: The overall configuration of the second mission is very similar to the first mission. The provision of improved pointing capability may, however, shift the emphasis from surveying the celestial sphere to pointing at selected targets.

2. Pointed Spacecraft. The HEAO-C and HEAO-D spacecraft will provide astronomers with a stable platform from which to conduct detailed studies of celestial sources. These missions will operate in an automated mode as will the initial survey missions; however, since HEAO-C and HEAO-D will be developed for flight during the middle 1970's when the Space Station and Shuttle are planned, it is a logical and desirable objective to have HEAO take maximum advantage of these facilities.

● HEAO-C: The first of the two pointed missions will be for several X-ray and gamma-ray experiments and will provide the first high resolution look at the X-ray stars. Candidate experiments include a nuclear emulsion spark chamber, Cerenkov detector, nuclear gamma-ray spectrometer, venetian blind telescope/spectrometer, and a small Wolter Type I X-ray telescope.

Stable pointing will be provided to a degree which is adequate for the heavy gamma-ray experiments. The lighter X-ray experiments will be mounted in a gimbal ring for fine stabilization.

The experiment package will weigh approximately 9000 pounds and the power requirements will be approximately 50 percent higher than HEAO-A and HEAO-B.

● HEAO-D: The second pointed mission will be a large grazing-incidence X-ray telescope facility with multiple experiments. The collecting area of this facility will be an order of magnitude or more increase from that provided in the precursor X-ray telescopes in HEAO-C. Potential experiments include a polarimeter, Bragg crystal spectrometer, channel plate multiplier imaging system, and a maximum sensitivity solid state detector.

Spacecraft stability needs are ±1 arc-min. Image stability will be further enhanced by an internal jitter removal system.

The experiment package will weigh approximately 6000 pounds.

B. Study Objective and Approach

The objective of the study reported in the following pages was to accomplish a Phase A — Preliminary Analysis of the initial survey class mission and spacecraft, HEAO-A. This has been achieved through conceptual spacecraft design and identification of promising alternatives, with emphasis on feasibility assessment of the overall project.

To accomplish conceptual spacecraft designs, a hypothetical experiment payload was assembled. This payload served to identify typical requirements for mass, volume, power, attitude control, structure, data handling, viewing constraints, and thermal environment. The actual flight payload will be selected by OSSA, and may differ from the one chosen as a reference; however, the conceptual designs which have evolved are expected to be responsive to the requirements of the officially selected payload.

Schedule and manpower constraints, coupled with the hypothetical nature of the experiment payload, dictated the adoption of a "baseline" conceptual spacecraft relatively early in the study to insure adequate concentration on a comprehensive feasibility assessment of the overall mission and spacecraft. Promising alternative spacecraft concepts were evolved and are compared, where appropriate, with the baseline concept and described more thoroughly in the Appendices. Detailed investigation, trade studies, optimization, and comparison of alternatives remain to be accomplished in a follow-on Phase B — Definition effort.

SECTION II. EXPERIMENTS AND MISSION DESCRIPTION

PRECEDING PAGE BLANK NOT FILMED.

TABLE OF CONTENTS

LIST OF ILLUSTRATIONS

LIST OF TABLES

SECTION II. EXPERIMENTS AND MISSION DESCRIPTION

Overall requirements for the HEAO-A mission evolved from discussions among MSFC, OSSA, and GSFC representatives and various scientists representative of the high-energy physics and astronomy disciplines. Definition of specific mission requirements began with the identification of a group of experiments that were representative of the types of experiments now being considered for the HEAO-A mission. Further discussions among these groups resulted in the development of general guidelines for use in preliminary design studies.

The group of experiments selected for this study, designated the "baseline experiment package," is described briefly in Paragraph A of this section. A more complete description of each experiment and related hardware is presented in Appendix A.

The baseline mission requirements and guidelines and the baseline mission profile are summarized in Paragraph B.

A. Baseline Experiment Package

A representative group of experiments was selected from a candidate list to establish overall mission operational requirements, develop conceptual spacecraft designs, and determine subsystem and system design requirements. The final payload will be selected by OSSA from the proposals submitted in response to an AFO not yet released. It may differ in some respects from the baseline experiment package chosen for this study; however, the conceptual designs developed by this study are expected to be responsive to the requirements of the experiment payload finally selected.

1. Baseline Experiment Package Summary. The group of six baseline experiments selected for this study are summarized in Table II-1. These experiments will measure the flux and spectra in the X-ray, gamma-ray, and cosmic-ray regions from 10^2 to 10^{15} ev. Since the basic experiment designs are determined primarily by the energy range (particles or photons) to be measured, the experiments are listed in the tables presented in this section and are discussed in Appendix A in the order of increasing energy measurements.

TABLE II-1. BASELINE EXPERIMENT PACKAGE SUMMARY

EXPERIMENT TITLE	MAJOR OBJECTIVES	MEASURABLE ENERGY RANGE	PRINCIPAL INSTRUMENTS
LARGE AREA X-RAY DETECTOR	DETECTION AND CLASSIFICATION OF X-RAY SOURCES ON THE CELESTIAL SPHERE	X-RAY FLUX INTENSITY FROM 10^2 TO 6×10^4 ev.	ARGON-XENON PROPORTIONAL COUNTER, NaI SCINTILLATION COUNTER
LOW-ENERGY GAMMA-RAY DETECTOR	GENERAL SKY SURVEY OF GAMMA PHOTONS WITH SPECTRAL ANALYSIS	GAMMA-RAY FLUX FROM 10^4 TO 5×10^5 ev	CsI SCINTILLATION DETECTOR
MEDIUM-ENERGY GAMMA-RAY DETECTOR	DETERMINE POSITION AND SPECTRUM OF POSSIBLE GAMMA-RAY SOURCES	GAMMA-RAY FLUX FROM 2×10^5 TO 10^7 ev	NaI SCINTILLATION DETECTOR
GAMMA-RAY TELESCOPE	DETERMINE EXTENT AND ORIGIN OF GAMMA RADIATION AND MEASUREMENT OF THE ENERGY SPECTRUM OF DISCRETE SOURCES.	GAMMA-RAY FLUX FROM 2.5×10^7 TO 10^{10} ev	PLASTIC SCINTILLATOR SPARK CHAMBERS, CERENKOV COUNTER, TOTAL ENERGY COUNTER
PRIMARY COSMIC RAY ELECTRON DETECTOR	DETAILED STUDY OF THE ENERGY SPECTRUM OF COSMIC-RAY ELECTRONS	ELECTRON ENERGIES FROM 5×10^8 TO 10^{12} ev	ELECTRON CALORIMETER USING TUNGSTEN, CERENKOV COUNTER
COSMIC-RAY CALORIMETER	STUDY OF COSMIC RADIATION HIGH ENERGY INTERACTION OF ENERGETIC PARTICLES WITH MATTER	CHARGE COMPOSITION FROM 10^{10} ev TO 10^{15} ev. ELECTRON SPECTRUM FROM 10^{10} TO 10^{14} ev ANISOTROPIC FLUX	SCINTILLATORS (PLASTIC) SPARK CHAMBERS. IRON, TUNGSTEN CALORIMETERS, CERENKOV COUNTER

2. **Baseline Experiments' Requirements and Restrictions.** A summary of the major requirements imposed on the spacecraft by the baseline experiment package is given in Table II-2. This table summarizes the weight, power, data rate, field of view, sizes, and attitude measurement accuracy required by each of the experiments.

A summary of the major restrictions imposed by the experiments on spacecraft materials and their location with respect to the experiments, and the restrictions imposed by the experiments during mission operations is given in Table II-3.

B. Mission Description

The HEAO-A mission will be accomplished with a large unmanned spacecraft which will transport a group of experiments into earth orbit and serve as an operations base for the experiments during the mission lifetime.

Because of time constraints in this study, it was deemed desirable to establish a baseline spacecraft concept and mission operations profile to serve as a design reference mission against which various design approaches could be compared. The baseline experiment package was reassessed and more fully defined and the general mission requirements and guidelines were expanded to establish the basis for the design reference mission. The baseline experiment package requirements were presented in Paragraph A above. The baseline mission requirements, guidelines, and mission profile are presented below.

1. **Baseline Mission Requirements.** The baseline mission requirements are defined in terms of primary and secondary objectives and preferred sequence of performance to aid in the analysis of spacecraft requirements. The secondary objectives have been identified as an attractive but more demanding mission in terms of overall requirements.

   a. Primary objective: A scan of the entire celestial sphere for X-rays, gamma-rays, and cosmic-rays, with emphasis on the galactic belt. An early scan entirely within the galactic belt is desired. The galactic belt of primary importance is 30 degrees wide. A scan of 15 degrees width is acceptable, but 30 degrees width is preferred. Because off-sun tilt of the spin axis will be required, power and control system trade studies may determine the approach to be used.

TABLE II-2. BASELINE EXPERIMENT PACKAGE REQUIREMENTS

EXPERIMENT	WEIGHT (LB)	POWER (W)		DATA RATE (KBITS/SEC)	FIELD OF VIEW (DEG)	DIMENSIONS	5 AMA (DEG)
		AVERAGE	PEAK				
LARGE AREA X-RAY DETECTOR-PART 1	2,000	100	100	3.0	1 x 4	6 BASIC MODULES 40 x 20 x 24 IN. 3 MODULATION COLLIMATORS 40 x 20 x 45 IN. 2 BRAGG SPECTROMETERS 40 x 50 x 12 IN.	± 0.25
PART 2	650	35	35	0.5	1 x 4	6 BASIC MODULES 40 x 20 x 24 IN.	
LOW-ENERGY GAMMA-RAY DETECTOR	350	10	15	1.0	4° CONE	11.25 IN. HEX. ACROSS FACE 10.62 IN. HEIGHT 1PM TUBES 5 IN. LONG 6 IN. FACE	± 0.1
MEDIUM ENERGY GAMMA-RAY DETECTOR	200	10	15	1.0	5° CONE	11 IN. DIAM. 21 IN. LONG	± 0.1
GAMMA-RAY TELESCOPE	2,500	40	40	2.5	45° CONE	2 24 IN. RAD DOME 3 50 IN. DIAM. 50 IN. LONG	± 0.2
PRIMARY COSMIC RAY ELECTRON DETECTOR	800	20	20	0.8	60° CONE	46 IN. DIAM. VIEW FACE 60 IN. H 50 IN. DIA	± 5
COSMIC-RAY CALORIMETER	6,000	50	50	8.0	60° CONE	4 48 IN. DIAMETER 100 IN. LONG	± 2
TOTAL	12,500	265	275	16.8			

NOTES:
1. FOUR PHOTOMULTIPLIER TUBES, SIZES OF EACH
2. TWO UNITS, SIZE OF EACH
3. TWO UNITS BACK TO BACK WILL BE FITTED TO SPACECRAFT DIAMETER
4. LENGTH WILL BE FITTED TO SPACECRAFT DIAMETER.
5. ATTITUDE MEASUREMENT ACCURACY

TABLE II-3. EXPERIMENT PACKAGE RESTRICTIONS IMPOSED ON SPACECRAFT

EXPERIMENT	RESTRICTIONS ON NEARBY MATERIAL	RESTRICTIONS ON EXPERIMENT OPERATION
LARGE AREA X-RAY DETECTOR	SINCE THORIUM CONTAMINATE THE BERYLLIUM USED IN THE COUNTERS, IT'S NEARBY USE IS PROHIBITED	NOT OPERATED IN SOUTH ATLANTIC ANOMALY SINCE EXTREME IONIZATION ENCOUNTERED THERE WILL DEGRADE COUNTER GAS
LOW-ENERGY GAMMA-RAY DETECTOR	NEARBY HEAVY MATERIAL SHOULD BE MINIMIZED. RADIATION LIMIT: 10^{-6} CURIE FROM CO ^{60}	NOT OPERATED IN SOUTH ATLANTIC ANOMALY - P. M. TUBES WILL BE DAMAGED BY FLUORESCENCE OF CsI
MEDIUM-ENERGY GAMMA-RAY DETECTOR	NO NEARBY CO^{60} CALIBRATION SOURCES PERMITTED	— — —
GAMMA-RAY TELESCOPE	$60°$ UNOBSTRUCTED CONE OF VIEW CLEAR OF HEAVY STRUCTURE IS DESIRED	— — —
PRIMARY COSMIC RAY ELECTRON DETECTOR	NO MORE THAN 0.5 gm/cm^2 OF MATERIAL PERMISSABLE IN THE $60°$ CONE OF VIEW	— — —
COSMIC RAY CALORIMETER	$90°$ UNOBSTRUCTED CONE OF VIEW CLEAR OF HEAVY STRUCTURE IS DESIRED	

b.   Secondary objective: Pointing at selected source targets for more detailed source analysis. Off-sun tilt of the spin axis is necessary to enhance target selection capability.

c.   Preferred sequence:

(1) Galactic scan (1 month).

(2) Celestial scan (6 months).

(3) Pointing mode (5 months).

(4) Repeat of first year (sequencing and time for each mode to be determined from first-year results).

d.   Maximum spacecraft spin rate of 1/10 revolution per minute.

e.   Experiment temperature limits from -10 degrees to +30 degrees centigrade.

f.   Minimum spacecraft orbital lifetime of 1 year (2 years desired).

g.   Spacecraft spin axis accuracy of ± 1.0 degree.

h.   Spacecraft attitude measurement accuracy of ± 0.1 degree.

i.   Maximum experiment data generation rate of 25 000 bits per second.

j.   Minimum interference from high background radiation of the South Atlantic Anomaly.

k.   Meteoroid protection for all critical components.

2. <u>Baseline Mission Guidelines.</u>

    a. Target launch date of March 1974.

    b. Experiment payload of 12 000 - 14 000 pounds.

    c. Launch vehicle:

        (1) Primary Titan IIID.

        (2) Secondary Titan IIIC.

    d. Due east launch from Eastern Test Range.

    e. Automated spacecraft in circular earth orbit.

    f. Orbital inclination of 28.5 degrees.

    g. Orbital altitude of 200 nautical miles.

    h. System design lifetime of 1-year minimum; 2 years desired.

    i. Maximum use of Space Tracking and Data Acquisition Network (STADAN).

    j. Modified Titan IIIC universal payload fairing with one 6-foot base section, five 5-foot modular sections, and one 9-foot nose section.

    k. Low cost and high reliability spacecraft design.

    l. Solar array electrical power source.

    m. Maximum use of existing flight-proven components.

3. <u>Baseline Mission Profile.</u> The HEAO-A baseline spacecraft, shown in Figure II-1, is designed to be launched on the Titan IIID launch vehicle. Launch is assumed from the Eastern Test Range in March 1974. A typical launch-to-orbit profile for the Titan IIID is depicted in Figure II-2.

    After injection into a 28.5-degree-inclination, 200-nautical-mile circular orbit, the spacecraft is separated, stabilized, and prepared for scientific data acquisition. Figure II-3 shows a typical sequence of major events for the first year of the baseline mission. The in-orbit preoperational
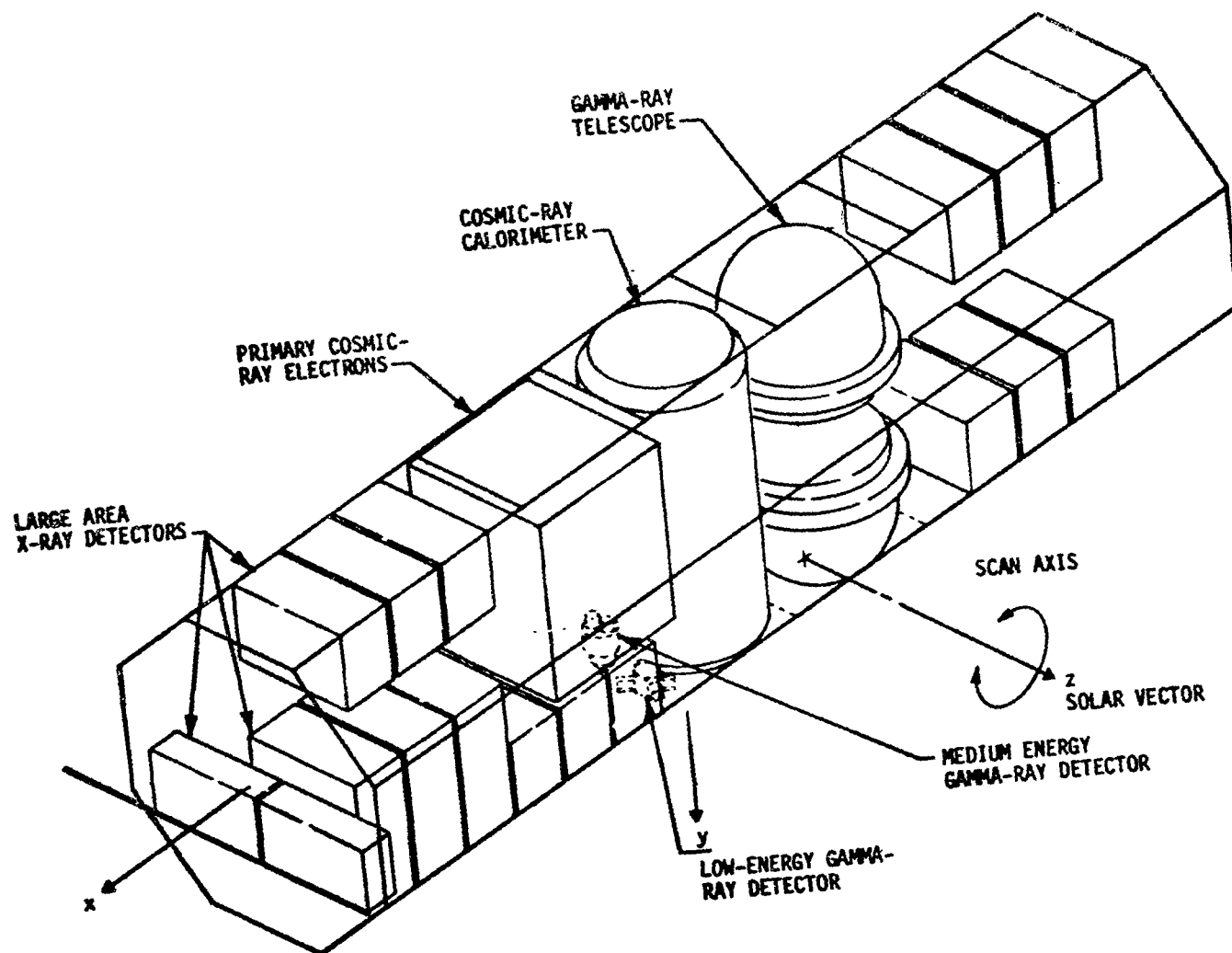
Figure II-1. Baseline conceptual spacecraft with reference payload.

ORBIT ALTITUDE

SECQUENCE OF EVENTS (ORBIT ALTITUDE 200 N. MI.)

1 START SOLID ROCKET MOTORS AND LIFT OFF

2 CORE STAGE 1 IGNITION

3 SOLID ROCKET MOTORS JETTISIONED

4 CORE STAGE 1 STAGED AND CORE STAGE 2
  IGNITION

5 SHROUD JETTISIONED

6 CORE STAGE 2 SHUTDOWN, STAGED, AND
  PAYLOAD INJECTED INTO ORBIT
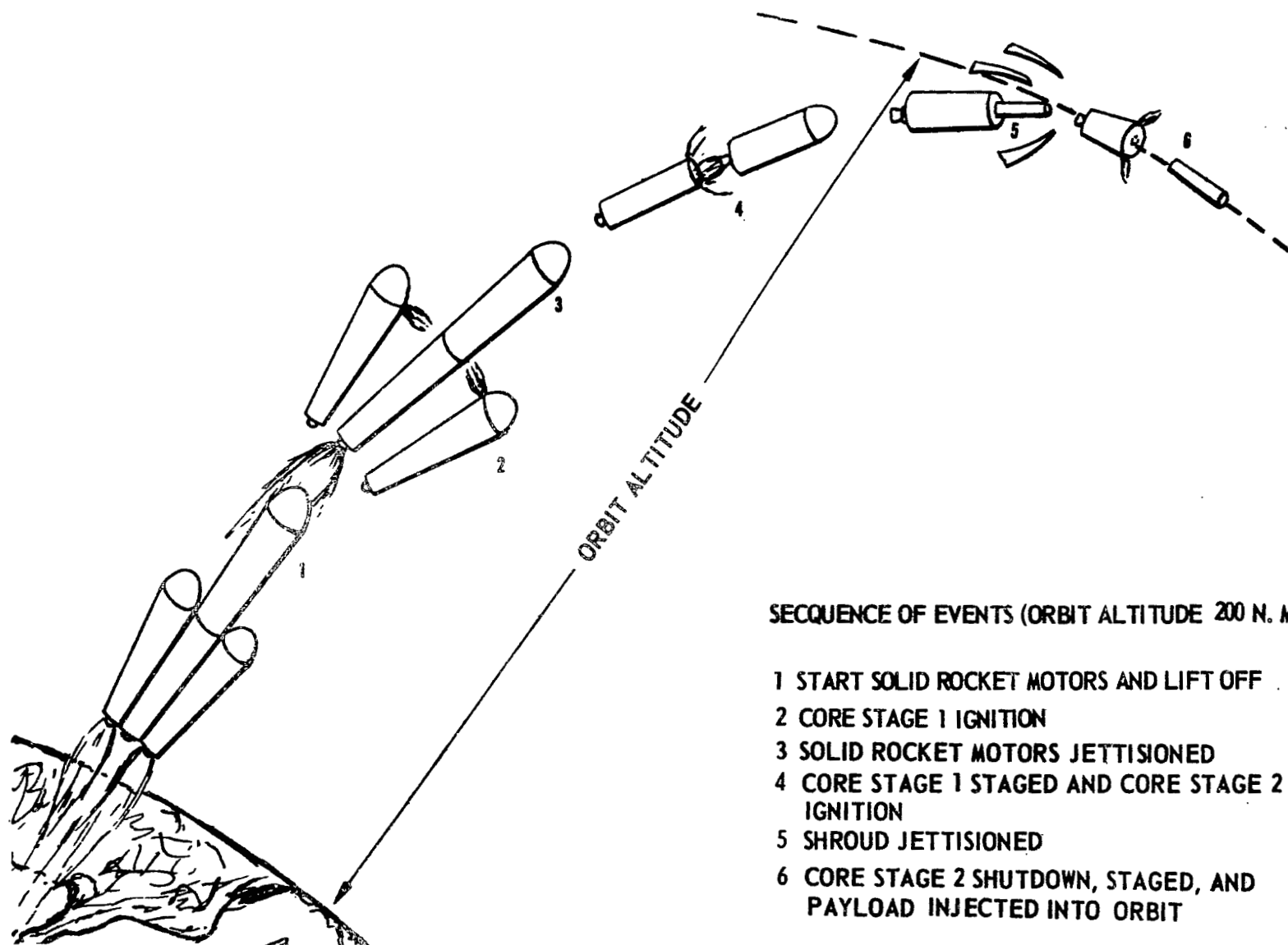
Figure II-2.   Typical Titan IIID launch-to-orbit profile.

RCS	MAGNETIC TORQUE	RCS	MAGNETIC TORQUE	RCS	RCS MAGNETIC TORQUE

HEAO INITIAL ORBIT S/C SEPARATION & STABILIZATION

ORBIT DETERMINATION

SOLAR VECTOR ACQUISITION & SOLAR PANEL THERMAL STABILITY

FLYWHEEL & S/C SPIN UP (CELESTIAL SCAN ATTITUDE)

ACQUIRE INITIAL GALACTIC SCAN ATTITUDE

GALACTIC SCAN MODE SOLAR OFFSET (12 MANEUVERS)

ACQUIRE CELESTIAL SCAN ATTITUDE

CELESTIAL SCAN MODE (SOLAR POINTING) (NO MANEUVERS)

DESPIN SPACECRAFT

ACQUIRE FIRST CELESTIAL POINTING ATTITUDE

CELESTIAL POINTING MODE (ANY ATTITUDE) (MANEUVERS TO BE DETERMINED)

1/6 ORBIT   1 2/3 ORBITS   2 ORBITS   5 1/2 ORBITS   1 ORBIT   1 ORBIT

31 DAYS   180 DAYS   154 DAYS
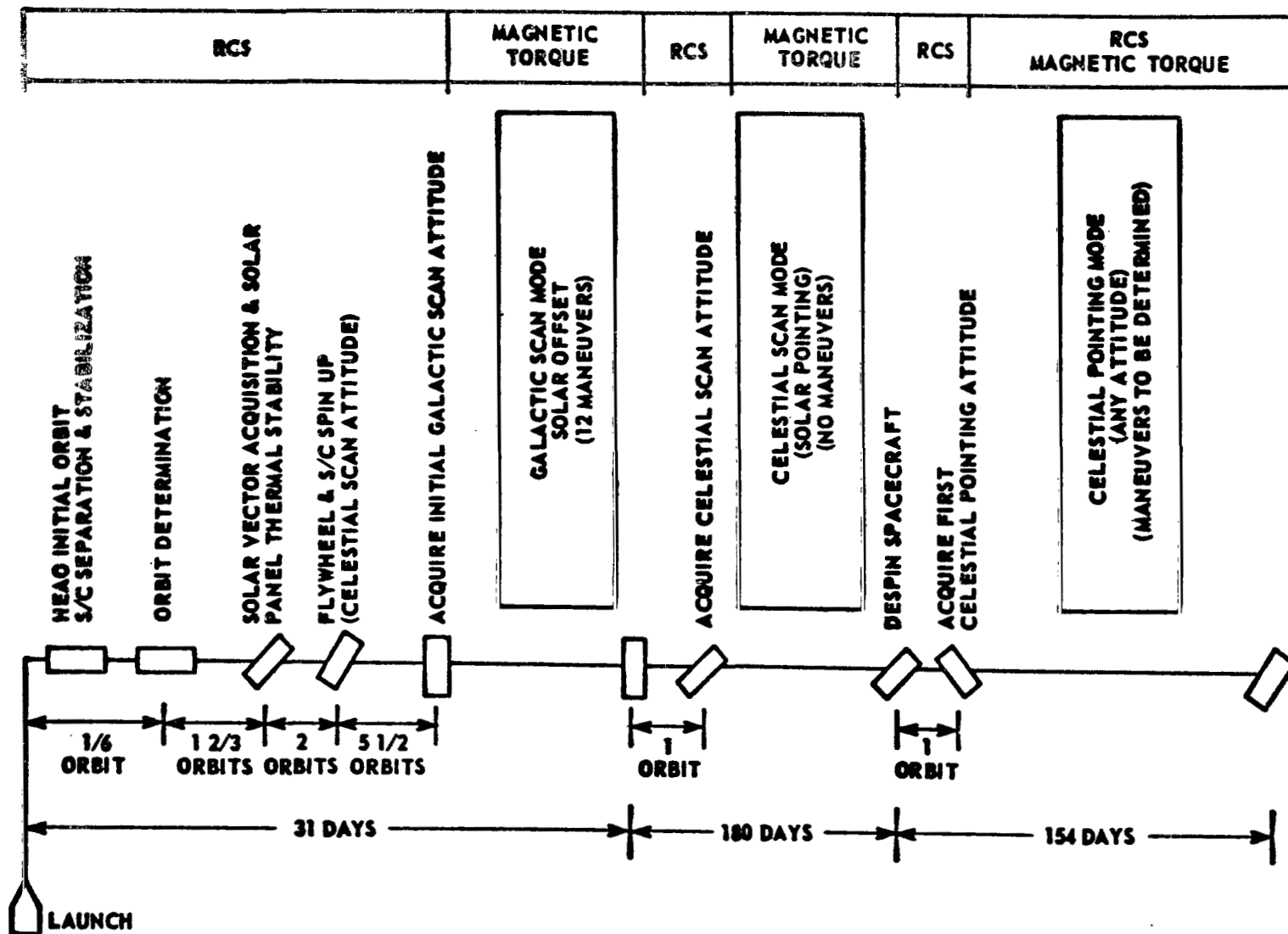
LAUNCH

Figure II-3. Baseline mission timeline.

events and the three mission modes are shown. The approximate time intervals involved and the primary control subsystem employed during each mission phase are also shown. The second year of the mission will be a repeat of the first year, with some variations to be determined from the first year results. This overall mission sequence and timeline was used as the design reference for determination of requirements and sizing of subsystems for the spacecraft.

Contact with the ground during the course of the mission will be accomplished through the geographically appropriate stations in the Space Tracking and Data Acquisition Network (STADAN).

Additional details of the baseline mission profile are given in the appropriate sections of this report.

SECTION III. LAUNCH VEHICLE

TABLE OF CONTENTS

TABLE OF CONTENTS (Continued)

LIST OF FIGURES

LIST OF FIGURES (Concluded)

LIST OF TABLES

In keeping with the overall philosophy of the HEAO project, the selection of the Titan IIID launch vehicle was based on the use of the lowest cost existing system with sufficient payload capability. Other considerations in the launch vehicle selection were the use of systems which will be used by other automated space projects during the operational time frame of the HEAO missions, and the availability of facilities and equipment on a schedule which involves no interference with other high-priority projects.

This philosophy eliminated all but existing launch vehicle systems, and the requirements of the HEAO project quickly polarized the selection to the Titan family of launch vehicles. While the Titan IIIC can accomplish the HEAO launches without modifications to the primary vehicle system, the Titan IIID with modifications to adapt to Eastern Test Range (ETR) may be more cost effective if the same modifications required by the Viking program can be utilized. The Titan IIID, as shown in Figure III-1 (without transtage upper stage and therefore less expensive than Titan IIIC), is capable of meeting the requirements of the HEAO launches, but some modification to the Titan IIID guidance system (either on the ground or on board) is required to use this system at ETR. The cost of the Titan IIID, including modifications, is expected to be lower than the cost of Titan IIIC. The Titan IIID is therefore the selected baseline launch vehicle for the HEAO launches. Since the Titan III with Centaur upper stage is being developed and will be launched from ETR in 1972 and 1973, the alternative of using the Centaur guidance system in the Titan IIID for the HEAO launches becomes attractive and was selected as the baseline system for the Phase A study effort.

The final selection of the astrionics system and other modifications to the Titan IIID launch vehicle for the HEAO missions must be made during Phase B launch vehicle studies in concert with the overall HEAO mission requirements.

Use of the Titan IIID at ETR involves two primary launch vehicle hardware configuration decisions: (1) guidance system and (2) payload fairing selection.

The following sections describe the basic Titan IIID launch vehicle and the modifications required to adapt it as the launch vehicle for the HEAO missions to be launched from the ETR. The launch vehicle capabilities and the environments which the payload will experience are presented and a section is devoted to the discussion of the payload shroud and its interface with the launch vehicle and the payload.
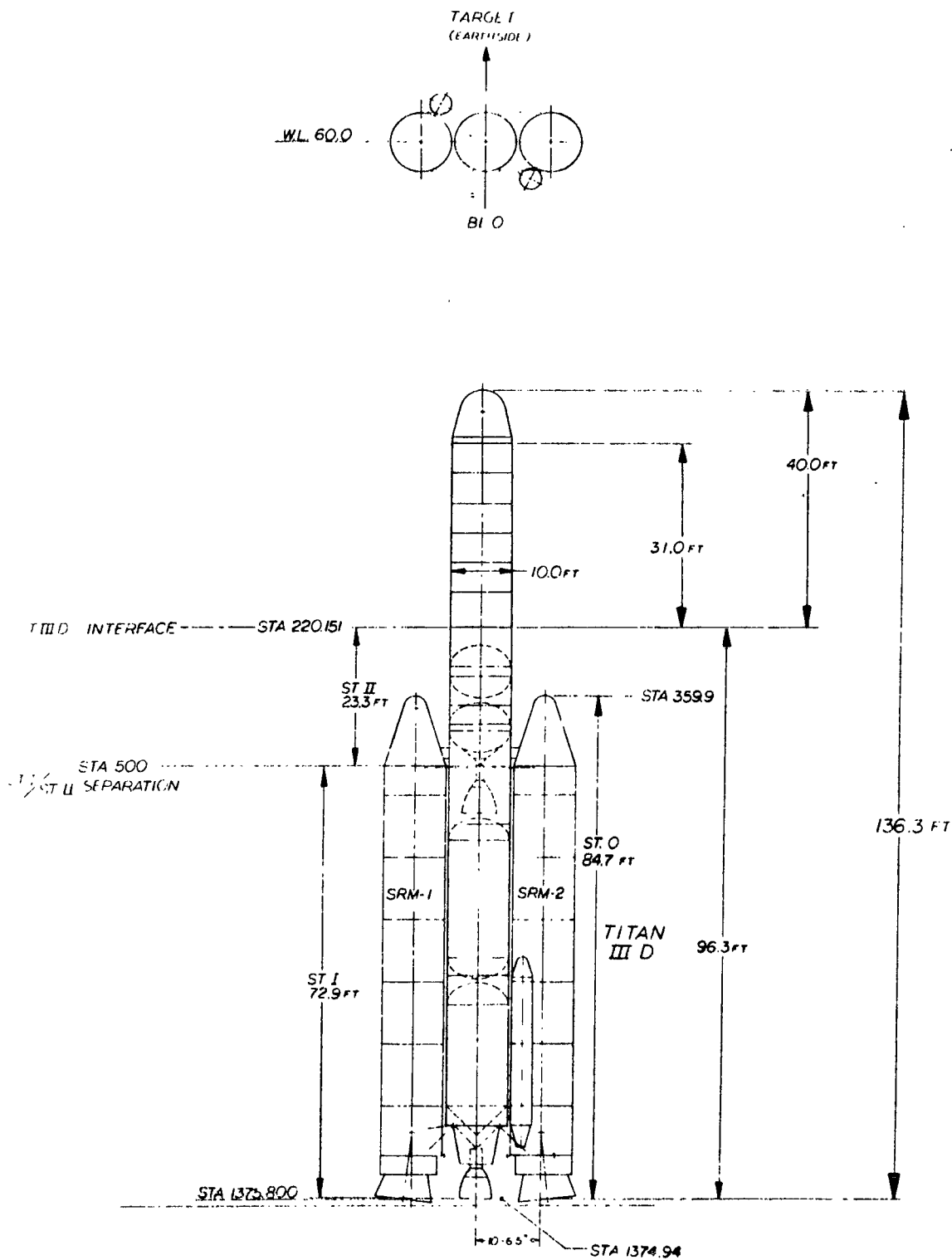
Figure III-1. Titan IIID launch vehicle (HEAO-A Mission).

A. Titan IIID Baseline Vehicle

This section presents a general description of the Titan IIID launch vehicle as it is now configured for launch from Western Test Range (WTR).

1. <u>Configuration.</u> The Titan IIID vehicle is a three-stage/solid and liquid propellant vehicle as shown in Figure III-2. It was developed from, and is nearly identical to, the Titan IIIC space launch vehicle and is described more fully in Reference 1, except that the Titan IIIC Transtage is deleted. The Titan IIID uses the solid rocket motors that were developed on the Titan IIIC program. Stage 0 consists of two solid rocket motors, each consisting of five solid segments, two closures, an ignition system, a nozzle assembly, and an ullage blowdown type thrust vector control system. The approximate burn duration of the solid rocket motors is 120 seconds.

The Titan IIID Stage I and Stage II is the "common core" used on other Titan III family vehicles, with Titan IIID-peculiar requirements added. These stages use earth-storable liquid propellants.

2. <u>Guidance System.</u> The Titan IIID guidance system consists of a BTL/WECO Series 600 Radio Guidance System which operates in conjunction with a ground guidance station located approximately 13 miles north of the launch pad at WTR. The system is capable of performing the guidance function during all of Stage I operation and during the first 70 percent of Stage II operation. It is limited by SRM plume attenuation during Stage 0 operation and by radar antenna look-angle constraint during the latter portion of Stage II flight.

3. <u>Flight Control System.</u> The Titan IIID flight control system consists of an analog computer, a programmer, a velocity meter, a staging timer, a three-axis reference (gyro) system, a rate gyro, and on each stage a thrust vector control system. The flight control system performs open-loop guidance (programmed trajectory) during Stage 0 operation and during the latter portion of Stage II flight. During Stage I and early Stage II operation, the flight control system reacts to a steering command issued by the radio guidance system. The velocity meter is initiated late in Stage II flight by radio guidance, and upon achieving the preset velocity-to-be-gained, issues the shutdown command and initiates payload staging. Except for initiation of the velocity meter, the flight control system is the primary source for discrete signals, and also performs open-loop guidance throughout flight in the event of guidance failure.
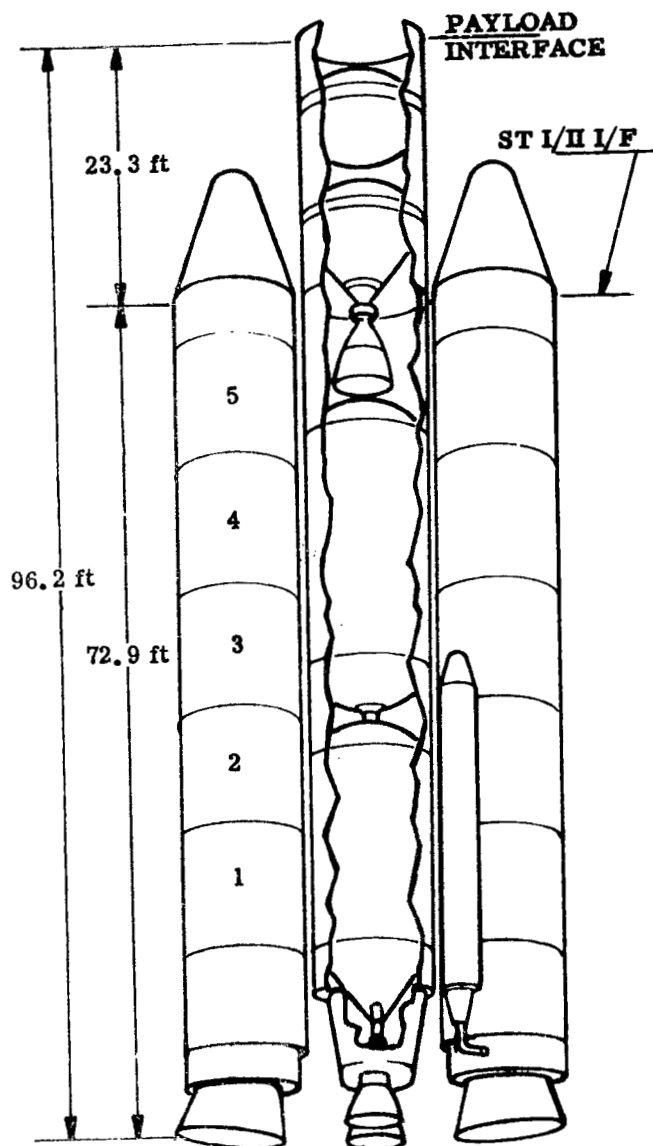
HARDPOINTS - 36
EQUALLY SPACED
GUIDANCE - RADIO INERTIAL

PAYLOAD INTERFACE

ST I/II I/F

23.3 ft

96.2 ft

72.9 ft

5

4

3

2

1

STAGE II
PROPELLANTS LOADED 67,338 lb
I_{sp} NOM 316.9(vac) sec
THRUST 101,890 (vac) lb
LOADED WEIGHT 73,254 lb

STAGE I
PROPELLANTS LOADED 258,860 lb
I_{sp} NOM 299 (vac) sec
THRUST 523,000 (vac) lb
LOADED WEIGHT 274,452 lb

STAGE 0
PROPELLANT WEIGHT 848,494 lb
TVC (N_2O_4) LOADED 16,848 lb
I_{sp} NOM 231.8 (S.L.) sec
THRUST 2,340,000 (S.L.) lb
LOADED WEIGHT 1,016,050 lb

LIFT OFF
- THREE STAGES WITHOUT PAYLOAD OR PAYLOAD FAIRING
WEIGHT 1,362,976 lb
THRUST 2,327,430 lb

Figure III-2. Standard Titan IIID launch vehicle.

4. Other Systems. The Titan IIID vehicle also includes an airborne electrical system, flight safety system, instrumentation system, and propulsion system.

B. Launch Vehicle Modifications

The launch vehicle hardware modifications result primarily from the guidance and payload fairing systems. The modifications required include the guidance system support truss, packaging of added guidance components, and installing a pull-away umbilical. Installation of the Titan IIIC payload fairing requires increasing the forward ring frame size on Stage II. The above items are discussed in more detail in the following paragraphs.

1. Guidance System. The guidance system requiring minimum changes for use in the Titan IIID vehicle at ETR is the currently used radio guidance system. However, according to current planning, the BTL ground station at ETR will not be used by NASA after late 1971. Unless other programs require its usage — and none are foreseen at this time — the total costs of operation, update, and maintenance would be imposed on the HEAO program. Since yearly operation is currently estimated to be about 2 million dollars, its cost has been judged to be prohibitive. Therefore, an inertial guidance system for the Titan IIID appears necessary; however, should other programs use the radio guidance system, it would become very cost effective. For these reasons, other systems have been considered.

Five optional guidance systems which are either developed or being developed for use in the 1973 period are as follows:

● BTL/WECO radio guidance/analog flight control (Fig. III-3) Titan IIID.

● ACED inertial guidance/digital flight control system (Fig. III-4) (Titan IIIC).

● Thor Delta strapdown inertial guidance/digital flight control with specially developed input/output electronics (Fig. III-5).

● The same as Thor Delta system above but with Ascent Agena strapdown inertial guidance hardware (Fig. III-5).

● Improved Centaur inertial guidance/analog flight controls (Fig. III-6).
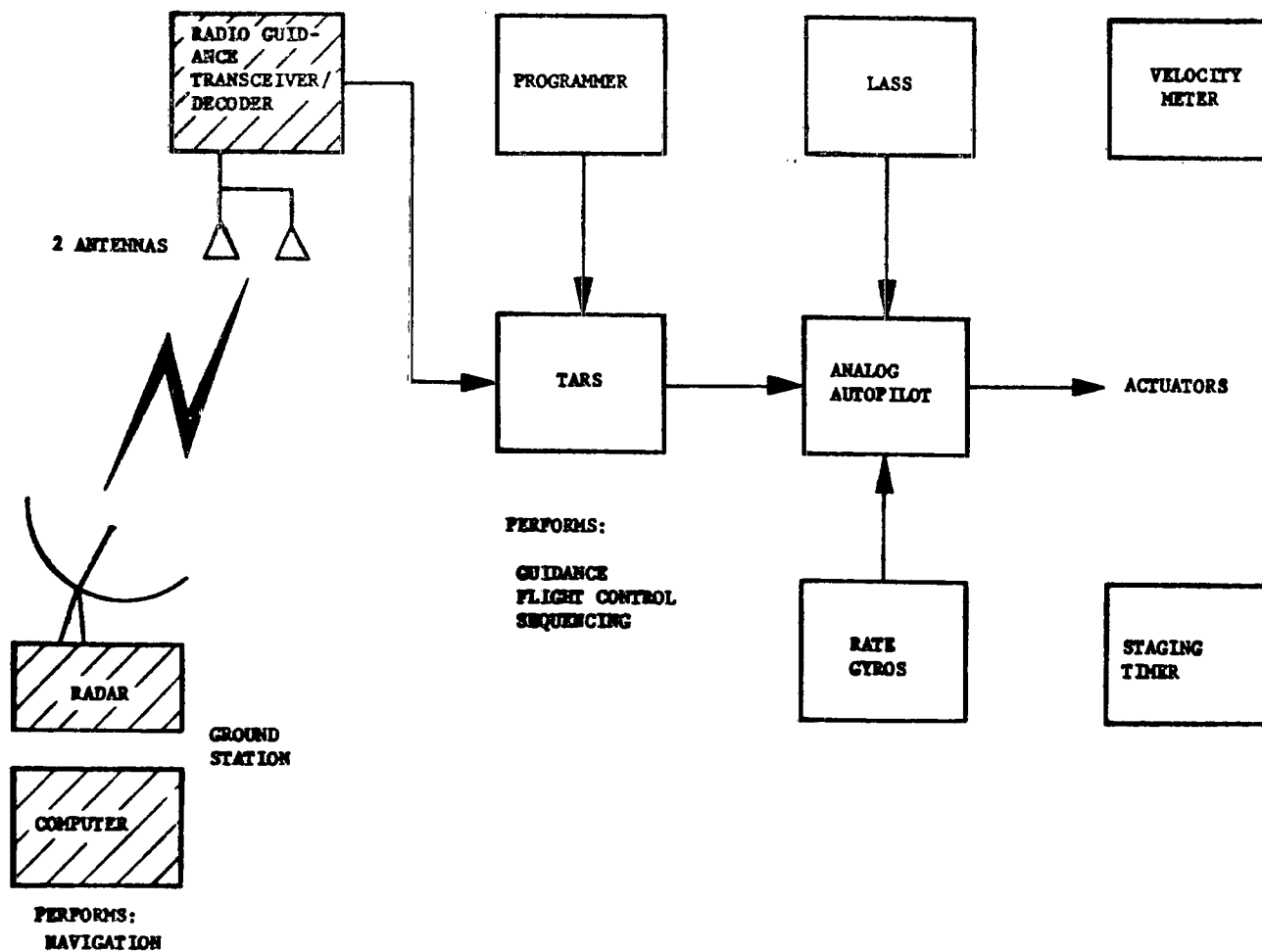
Figure III-3. BTL/WECO radio guidance/analog flight control — Titan IIID.
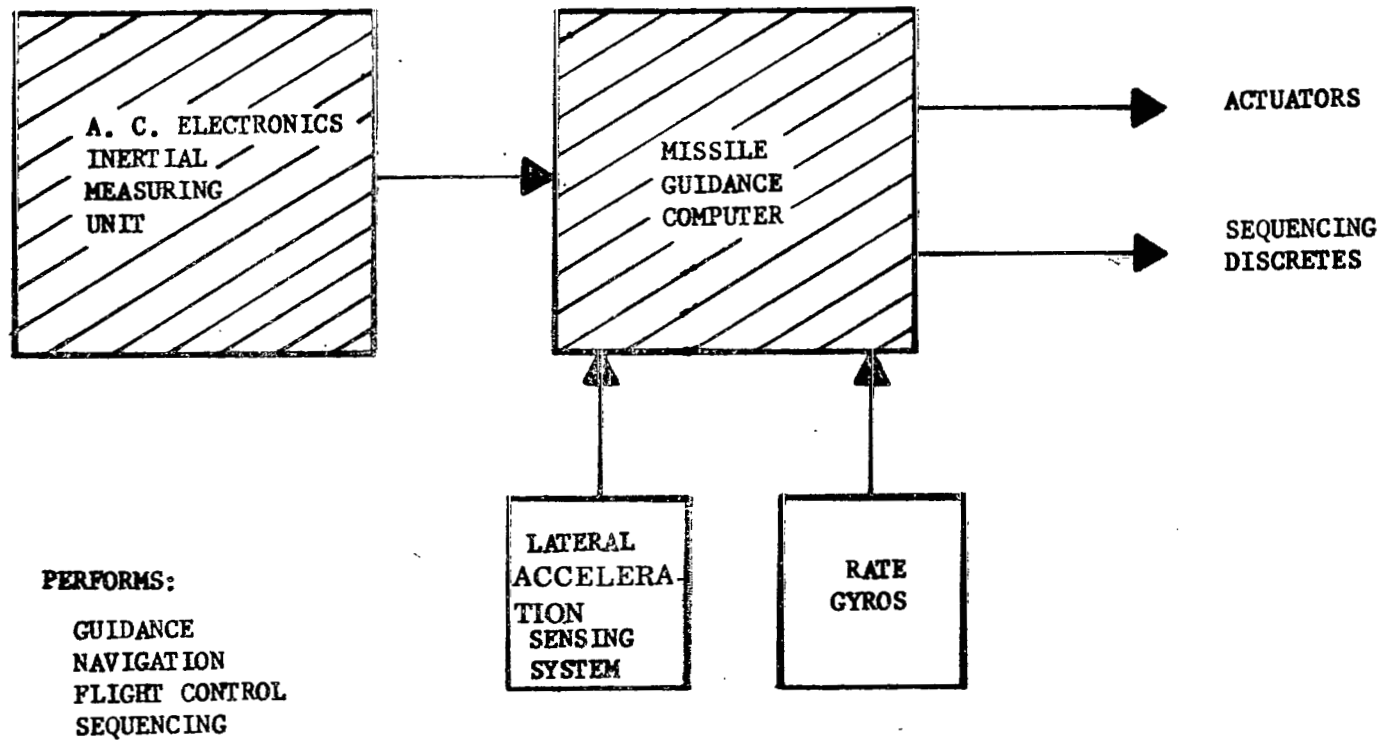
Figure III-4.   Titan IIIC ACED inertial guidance/digital flight control.

INPUT
BUS

SENSOR
REMOTE MULTIPLEX UNITS

PROGRAMMING
AND
CONTROL

OUTPUT
BUS

ACTUATOR
REMOTE OUTPUT UNITS

DIGITAL
DATA BUS

CENTRAL
PROCESSOR
UNIT
(8 K)

SEQUENCER

INERTIAL
SENSOR
ASSEMBLY
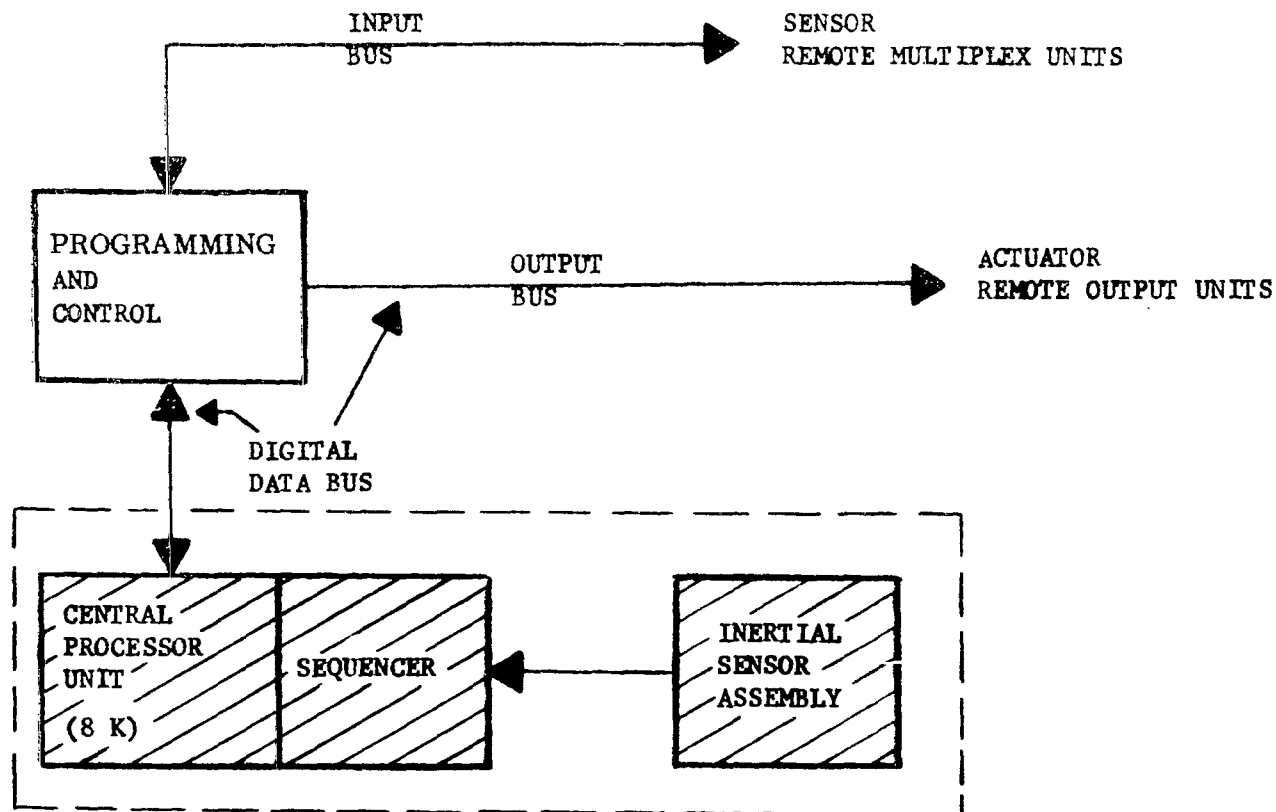
PERFORMS:

GUIDANCE
NAVIGATION
FLIGHT CONTROL
SEQUENCING

Figure III-5.   Ascent Agena or Thor-Delta inertial guidance/digital flight control.
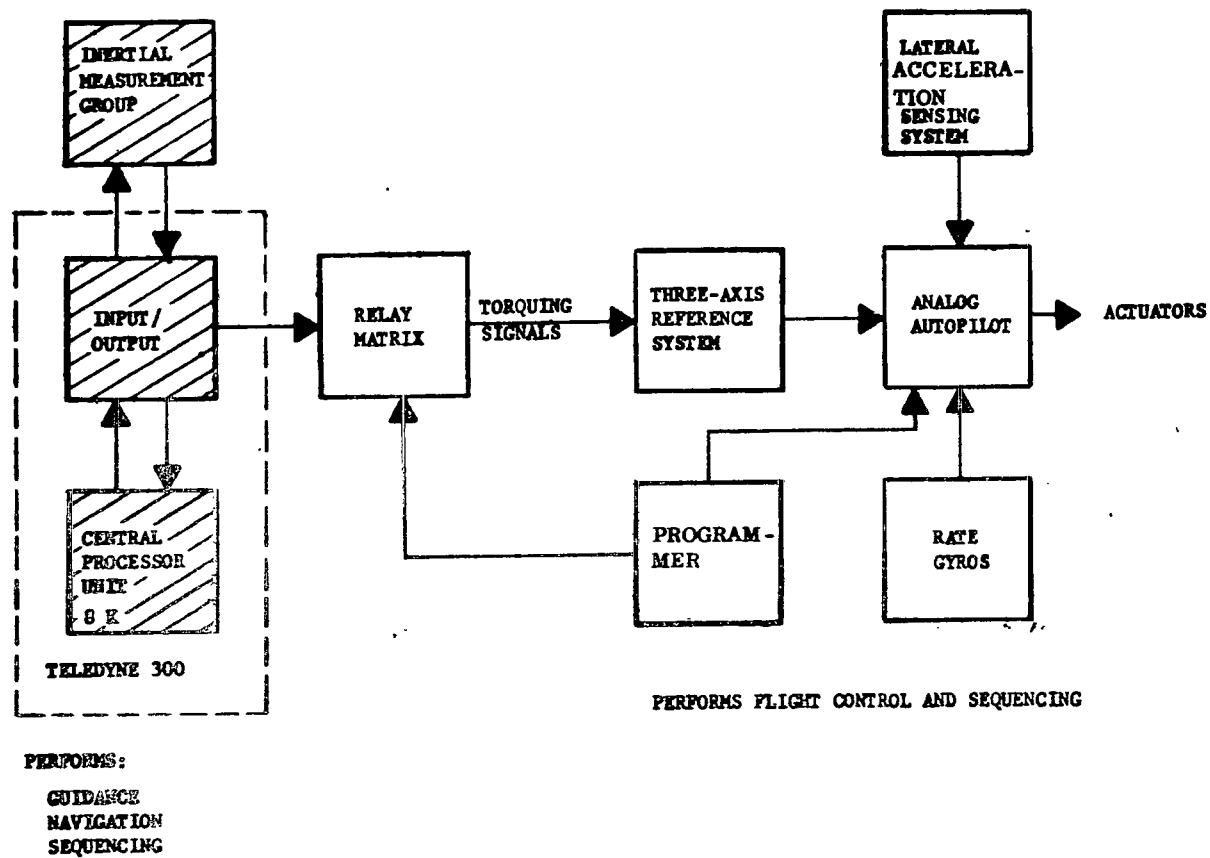
Figure III-6. Centaur inertial guidance/analog flight control.

These systems are more fully described in the following paragraphs.

    a. BTL/WECO radio guidance system. The changes required to the existing Titan IIID radio guidance and flight controls are as follows: .

    (1) Use Titan IIID/Centaur autopilot.

    (2) Relocate radio guidance dorsal and ventral antennas.

    (3) Install repeater antennas.

    (4) Update WECO/Univac ground guidance computer.

    (5) Relocate RIME to AGE van.

These changes are depicted in Figure III-7 and described below.

    The Titan IIID/Centaur flight controls computer includes a modification to change the direction of the pitch program. Because of on-pad alignment differences, the pitch down open-loop trajectory program at WTR becomes pitch up at ETR. This is accomplished by internally reversing pitch program polarity within the Titan IIID/Centaur flight controls autopilot. This same autopilot will be available for this mission.

    A second required change is to relocate the dorsal and ventral radio guidance antennas. This will require analysis to evaluate the look angles, followed by antenna relocation and waveguide modification.

    Repeater and pickup antennas must be installed on the mobile service tower, vertical integration building, and BTL ground station to permit prelaunch test and checkout.

    The major area of change is updating the BTL/WECO radio guidance ground station with an improved Univac computer. The existing 8000-word Athena drum machine will be replaced by a much faster general-purpose Univac 1230 with a random access core. This improvement will provide increased computation capability and improved reliability.

    The remaining change is installation of an existing RIME set into an existing AGE trailer to permit radio guidance subsystem checkout.

Figure III-7.   BTL/WECO system modifications for usage at ETR.

b. ACED inertial guidance system. The ACED system in its present configuration with the Titan IIIC IMU and MGC is not as cost competitive as the other systems. However, the MGC will be replaced with a new low-cost computer by 1972. This Titan IIIC configuration with the low-cost computer has been included in the cost comparison based on projected computer costs. The new computer that will be developed for Titan IIIC will include all of the I/O electronics to properly interface with the Titan IIID flight control sensors and actuation devices, as well as the electrical sequencing system so no new black box development is required for this system. The ACED configuration utilizing the new computer has the largest weight and power penalty of any of the inertial systems.

c. Strapdown inertial guidance system. The Thor-Delta or Ascent Agena configurations would use the inertial sensor assembly as presently configured, but the central processor unit (airborne computer) would require a memory expansion from 4000 to 8000 words (expansion capability provided in the Ascent Agena configuration). Special I/O electronics would be required to interface the Thor-Delta or Ascent Agena CPU's to the Titan IIID vehicle. Martin Marietta has a developed I/O electronics concept that can effectively provide this interface by using a PAC, two RMU's, and t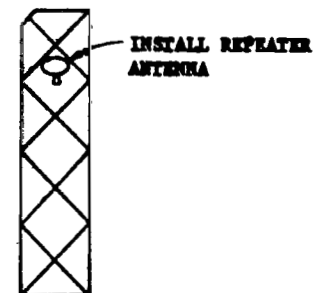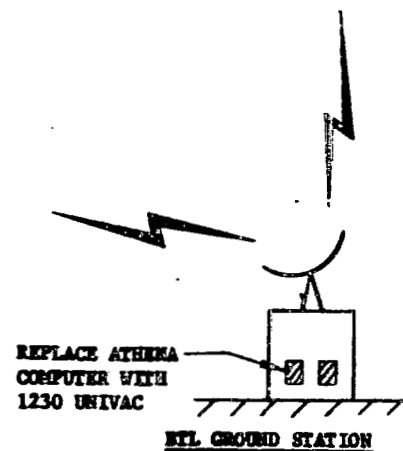hree ROU's. The CPU communicates with the vehicle sensors, actuation devices, and sequencing system through the PAC with addressed digital signals on one input and one output data bus. The RMU's convert analog sensor data at the rate gyros and lateral accelerometers (load relief sensors) to digital data for the data bus and the ROU's convert digital data to analog commands for the actuation devices. The inertial guidance/digital flight control configurations using Thor-Delta or Ascent Agena hardware present the lowest weight and power utilization of any of the inertial systems.

d. Centaur inertial guidance system. The Improved Centaur configuration would use the same guidance and flight control components presently designed for the Titan IIID/Centaur vehicle that is scheduled to launch the Viking payload in 1973. The Honeywell IMG and Teledyne computer would be moved into Stage II of the Titan IIID which results in a weight and power penalty, although not as severe as the ACED inertial system.

e. Weight and cost comparison. Table III-1 presents a preliminary weight and cost comparison of the various guidance and control systems examined. (These data must be reverified during the Phase B effort.) Delta costs compared to a baseline of Titan IIID at WTR using radio guidance with the present multiprogram utilization of the ground station are shown. The recurring costs per launch include selected airborne hardware costs and

TABLE III-1. TITAN IIID AT ETR

GUIDANCE AND CONTROL WEIGHT COST COMPARISON
ROM ($M)

	Δ Weight (lb)	Nonrecurring Cost ($)	Recurring Cost/Launch ($)	Delta Cost Per Launch ($)	4 Vehicles/1/yr Total Delta Cost ($)
BTL Radio @ WTR (baseline)	0	0	0.28	0	NA (Baseline)
BTL Radio @ ETR (Titan IIID launches only)	0	1.2	2.2	1.9	8.8
ACED Inertial	+385	2.9	0.72	0.44	4.7
Thor-Delta or Ascent Agena Inertial	0	3.5	0.40	0.12	4.0
Improved Centaur	+175	1.5	0.75	0.47	3.4

the proper portion of the radio guidance ground station maintenance costs. Common guidance and control airborne hardware such as rate gyros, actuators, and hydraulic power supplies were excluded because they did not impact the estimate of delta costs.

f.   Conclusions.   Based on this preliminary study, the following conclusions have been reached:

(1) If one or more other programs use radio guidance and have a combined launch rate of two or more vehicles per year, then radio guidance should be used on Titan IIID at ETR.

(2) All of the inertial systems can meet the anticipated accuracy requirements of Titan IIID at ETR although the ACED system is significantly more accurate than the other inertial concepts.

(3) The Improved Centaur inertial system has the lowest schedule and cost risk based on the advanced state of development of the components involved.

(4) The costs of the inertial systems examined are approximately equal.   Since weight is not a dominant factor, the inertial systems should be examined in more depth in the near future because of the near equivalent cost comparison.

(5) For the purpose of a baseline, for use in performance determination, the Improved Centaur system was selected.

2.   <u>Titan IIID Modifications To Adapt Payload Fairing</u>.   The Titan IIID Stage II forward skirt requires an increase in the Titan Station 220 ring frame size.   This modification is shown in Figure III-8 and is judged to be a minor modification.

C. Performance Capability

The performance capability of the Titan IIID launch vehicle to the proposed orbit of 200-n. mi. altitude and 28.5-degree inclination is 20 920 pounds.   The assumptions made for the performance calculations are given in Appendix B.   This payload was injected by direct ascent to a 200-n. mi. altitude.   The Titan IIID vehicle was designed for placing payload in low earth orbit (altitude < 150 n. mi.).
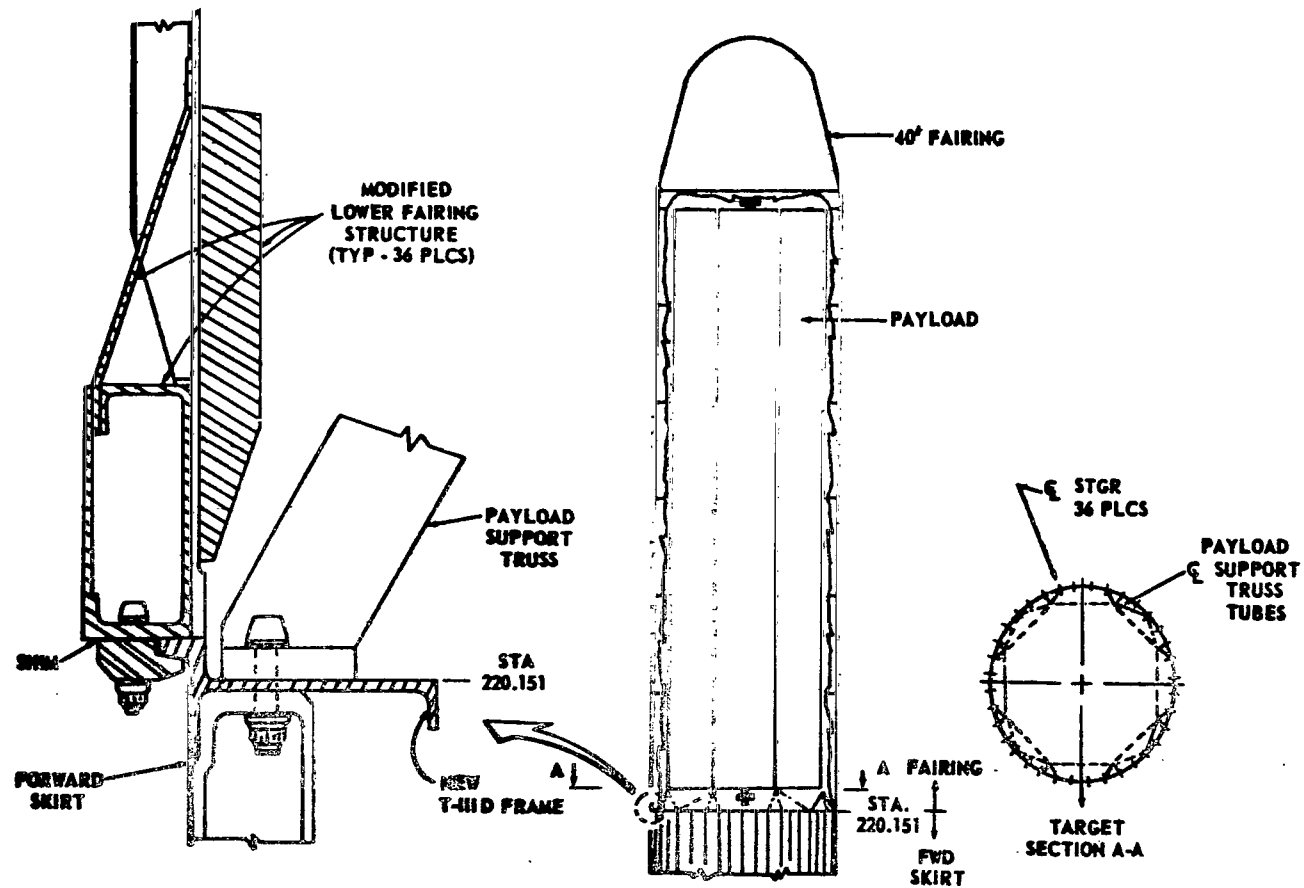
Figure III-8. Titan IIIC PLF adaption to Titan IIID forward skirt.

Improvement in performance capability of the Titan IIID can be attained by either (1) modifying the HEAO orbit to an elliptical orbit which would have a perigee and apogee sufficient to guarantee a minimum lifetime of 1 year for the $+2\sigma$ solar activity or (2) modifying the Titan IIID by adding a kick stage to the vehicle so that a trajectory could be achieved whereby the main stage would inject kick stage and payload into a 90- by 200-n.mi. elliptical orbit and the kick stage would inject the payload from the 90- by 200- to 200- by 200-n.mi. circular orbit. Adding the kick stage, a payload increase of up to 6000 pounds could be realized. Choosing an elliptical orbit of 1-year lifetime, a payload increase of up to 4800 pounds could be achieved.

Table III-2 contains the Titan IIID performance weight summary and trajectory data for direct injection into a 200-n.mi. circular orbit.

Recent performance data from Lewis Research Center on the Titan IIID vehicle indicated a payload of 20 641 pounds and is presented in Appendix B for comparison. This variation in payload is probably caused by the heavier payload shroud and the time that it was jettisoned; however, differences of this nature will become items for closer scrutiny during Phase B.

D. Payload Fairing

A payload fairing is required to enclose the payload. The payload fairing will interface with the Stage II forward skirt (Titan Sta. 220), and inflight separation of the fairing will occur at this interface. Two payload fairing configurations meeting the basic requirements are available for use in this program. They are as follows:

1. Titan IIIC universal operational fairing used at ETR.

2. Titan IIID fairing used at WTR.

The Titan IIIC fairing was selected for this application because the fairing has been used in previous missions launched from ETR. All major facility and launch pad (Pad 41) modifications required to accommodate the Titan IIIC fairing will have been made and the necessary GSE will be available. No GSE for the Titan IIID fairing will be available at ETR. Therefore, use of the Titan IIIC fairing will induce minimum program costs. Trisection separation of the Titan IIIC fairing also provides better payload/fairing clearance during separation than the two-section separation of the Titan IIID fairing.

TABLE III-2. TITAN IIID PERFORMANCE AND TRAJECTORY DATA FOR A 200-n.mi.
26. 5-DEGREE-INCLINATION CIRCULAR ORBIT

Stage	Parameters[a]	Engine Characteristics	Weight (lb)
0	Effective sea level thrust (lb)	2 340 000	
	Sea level specific impulse (sec)	232	
	Lift-off weight		1 387 272
	SRM Propellant consumed		842 960
	SRM TVC Injectant		14 561
	Service items expended		9 089
	Heat shield jettisoned		513
	Core stage propellant consumed		19 440
	Vehicle weight at SRM cutoff (lb)	500 709	500 709
	SRM weight at separation		153 953
	Thrust-to-weight ratio at lift-off	1. 687	
I	Vacuum thrust (lb)	532 000	
	Vacuum specific impulse (sec)	299	
	Weight at SRM separation		346 756
	Core stage propellant capacity		251 523
	Propellant consumed (after SRM cutoff)		232 082
	Vehicle weight at stage cutoff		114 674
	Stage weight at separation		17 197

a. 90-degree azimuth angle lift-off.

TABLE III-2. (Continued)

Stage	Parameters[a]	Engine Characteristic	Weight (lb)
II	Vacuum thrust (lb)	100 893	
	Vacuum specific impulse (sec)	310	
	Weight at ignition		97 477
	Standard payload fairing		2 310
	Propellant consumed		64 967
	Vehicle weight at stage cutoff		30 200
	Stage weight at separation		6 978
	Gross Payload		23 222
	Weight to be subtracted		
	Flight performance reserves		1 500
	Astrionic equipment		800
	Total weight to be subtracted		2 300
	Net payload		20 922

a. 90-degree azimuth angle lift-off.

1. <u>Titan IIIC Payload Fairing.</u>

a. Basic configuration. The Titan IIIC UPLF is 10 feet in diameter. The building block concept for this fairing is illustrated in Figure III-9. A 9-foot-long nose module and a 6-foot-long base are assembled to build a 15-foot UPLF. Longer lengths, up to 50 feet, may be assembled by utilizing the nose, base, and one or more 5-foot-long cylindrical, or intermediate, modules. A 40-foot-long baseline configuration for this mission is shown in Figure III-9. The UPLF is divided longitudinally into three sections as shown in Figure III-10. Each longitudinal joint contains a contamination-free separation system. The major characteristics of the fairing are described in the following paragraphs:

(1) Nose section. The nose section has a 45-inch-radius hemispherical nose, a cone with a 15-degree slope, and a cylindrical section 1 foot long. This section is of monocoque construction, with aluminum skin and ring frame stiffening.

(2) Midbody modules. The 5-foot cylindrical modules consist of aluminum skin, ring frames, and external hat-shaped stringers. They are configured in three basic type modules: a forward unit containing the air-conditioning inlet, a standard lightweight module, and a version of increased structural load capability. The increased strength is provided by thicker gage stringers and closer rivet spacings. The lighter modules are used in the upper portion of the midbody and the stronger modules are used in the lower region.

(3) Base section. The 6-foot base, like the 5-foot cylindrical module, is made of aluminum skin, ring frames, and external hat-shaped stringers. In addition, there are eight machined longerons and tension hooks to provide tension and compression load capability. An access door, 2 feet by 2 feet, is provided in each section of the base to allow access to the PLF systems and the payload compartment. The fairing air-conditioning inlet is also installed in a 2-foot by 2-foot door. There is also a large standard access door in the nose of Trisection III to provide payload access. All doors are structural doors to provide continuity to the structural shell.

(4) UPLF separation subsystems. The UPLF separation subsystems include the base separation shear pin system and the longitudinal thrusting joint that stages the PLF trisections. The longitudinal thrusting joint is activated by an electroexplosive detonator which initiates a linear explosive contained in a flexible bellows. The thrusting joints run the length of the fairing from the base to the nose. Initiation causes the gas to inflate

MID-BODY
SECTION (TYP)

10 FT DIA

5 FT

BASE SECTION

ACCESS DOOR
(24x24, 3PLACES)

NOSE SECTION

120 DEG
(TYP)

6 FT — 9 FT

15 FT

MINIMUM CONFIGURATION

ACCESS DOOR (31 IN. HIGH
x 58 IN. WIDE, 1 PLACE.
8x8 IN. INSPECTION HOLE
IN OTHER TWO TRISECTIONS.)

ACCESS DOOR

5 MID-BODY MODULES

BASE SECTION

NOSE SECTION

TARGET

6 FT

9 FT

40 FT

BASELINE CONFIGURATION
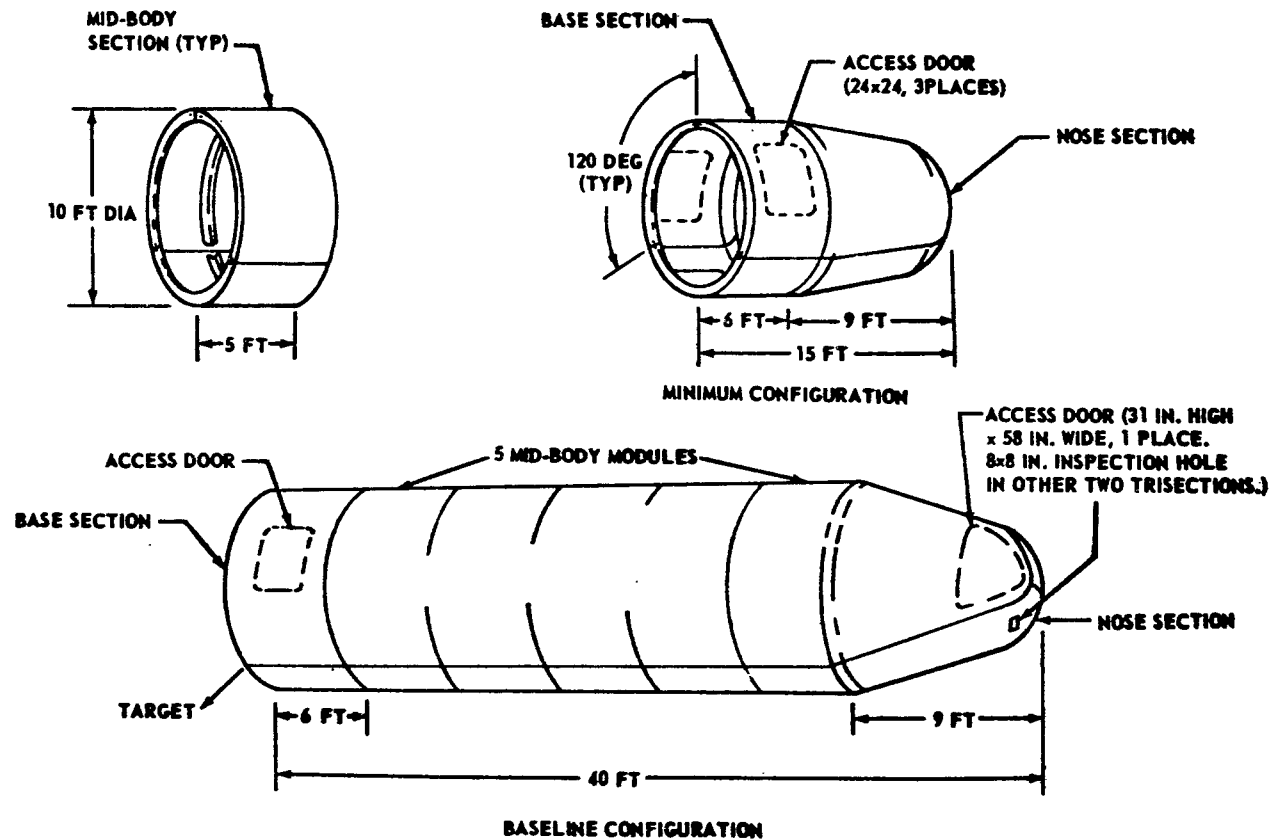
Figure III-9. PLF building block concept (HEAO-A PLF configuration).

OUTER SKIN

BELLOWS

ATTENUATOR TUBES

PRIMALINE (8 GR/FT)

ALUMINUM CYLINDER

ALUMINUM PISTON

OPEN

FIELD SPLICE BOLTS

CLOSED

NOTE: THE PAYLOAD FAIRING SEPARATION DETAILS SHOWN ARE A McDONNEL−DOUGLAS CORP. PROPRIETARY ITEM. THE NONCONTAMINATING THRUSTING JOINT IS PROTECTED BY US PATENT NO. 3,362,290.
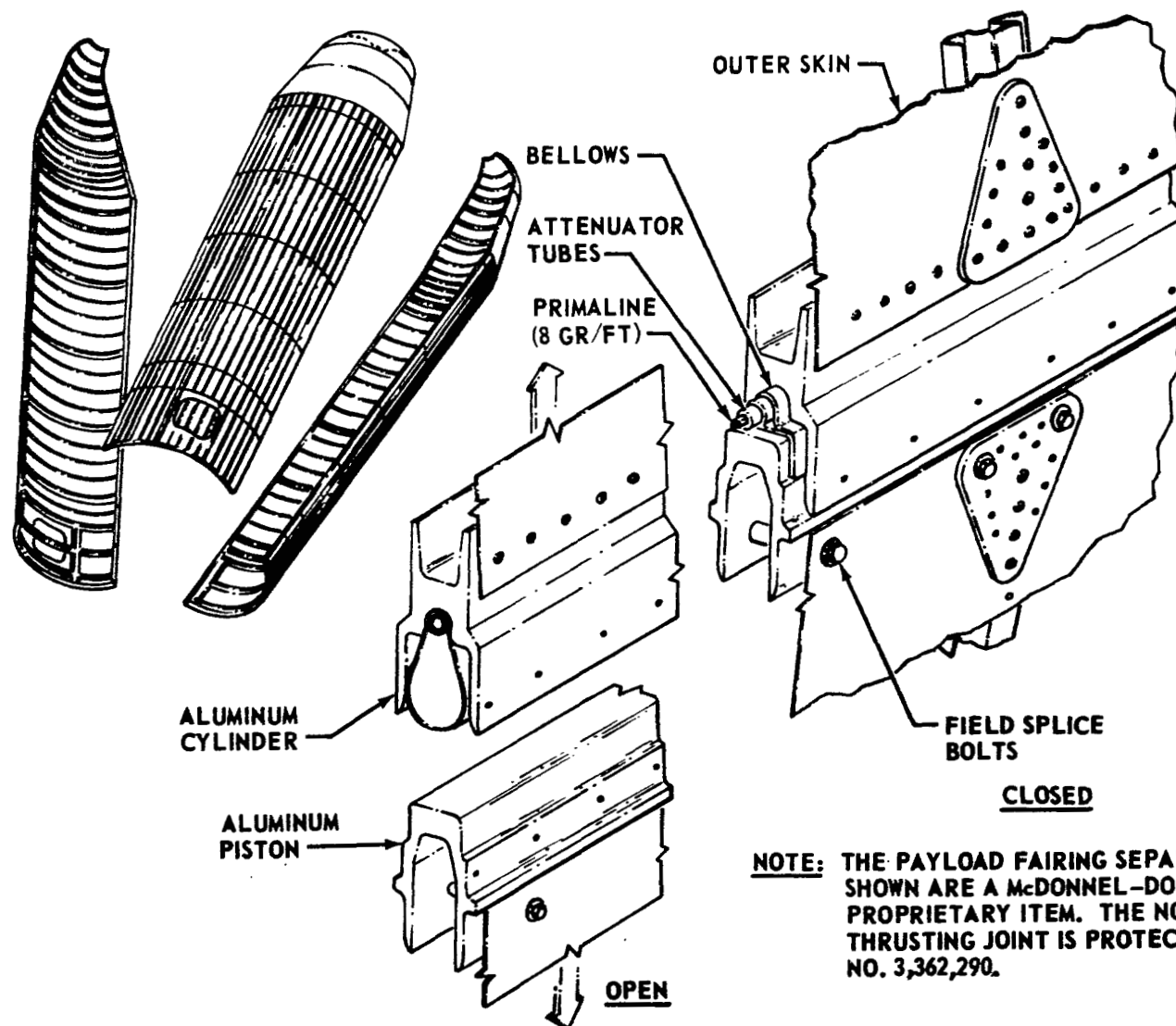
Figure III-10. PLF separation.

the bellows which, upon expanding, shears the structural rivets and parts the trisections.

(5) Thermal characteristics. The PLF is designed such that no point on its internal wall exceeds 300° F. Internal surfaces of the PLF have an emissivity less than 0. 30 to minimize aerodynamic heating heat flux to the payload. Thermal protection is provided by external insulation.

(6) UPLF/launch vehicle assembly. The UPLF is assembled to the launch vehicle in three longitudinal sections as shown in Figure III-10. The assembly is accomplished at the launch pad after the payload has been assembled on the launch vehicle.

b. Modifications for Titan IIID. The basic fairing will be modified at the 6-foot base section to provide a load introduction at 36 points to match the 36 stringers of the Titan IIID forward skirt at Station 220. Also, the Stage II forward skirt would require an increase in frame size. One concept for these modifications is illustrated in Figure III-8. The structural load capability of this combination is shown in Figure III-11. It is probable that the fairing strength will exceed that shown after the 36-stringer modification. Further analysis and definition of both the structural modification concept and the structural load capability of the final design selected must be accomplished in a Phase B definition effort.

c. Payload dynamic envelope. The basic payload dynamic envelope is shown in Figure III-12. Based on a conservative estimate of the structural and dynamic characteristics of the modified Titan IIIC UPLF, a maximum payload dynamic envelope of 107.27 inches was selected (Ref. 1).

E. Payload Environment

1. Flight Loads. On the recommendation of the Martin-Marietta Corporation, Denver Division, the conceptual designs developed in this study were based on maximum load conditions of 6. 0 g's longitudinally at burnout of Stage I and 1. 5 g's laterally at lift-off. Additional iterative loads analysis will be required during follow-on study phases when the payload is more clearly defined. Individual components, e. g. , antennas, will experience substantially higher acceleration loads.

2. Interior Acoustics. The predicted maximum interior acoustic levels for the payload are shown in Figure III-13. The acoustical environments
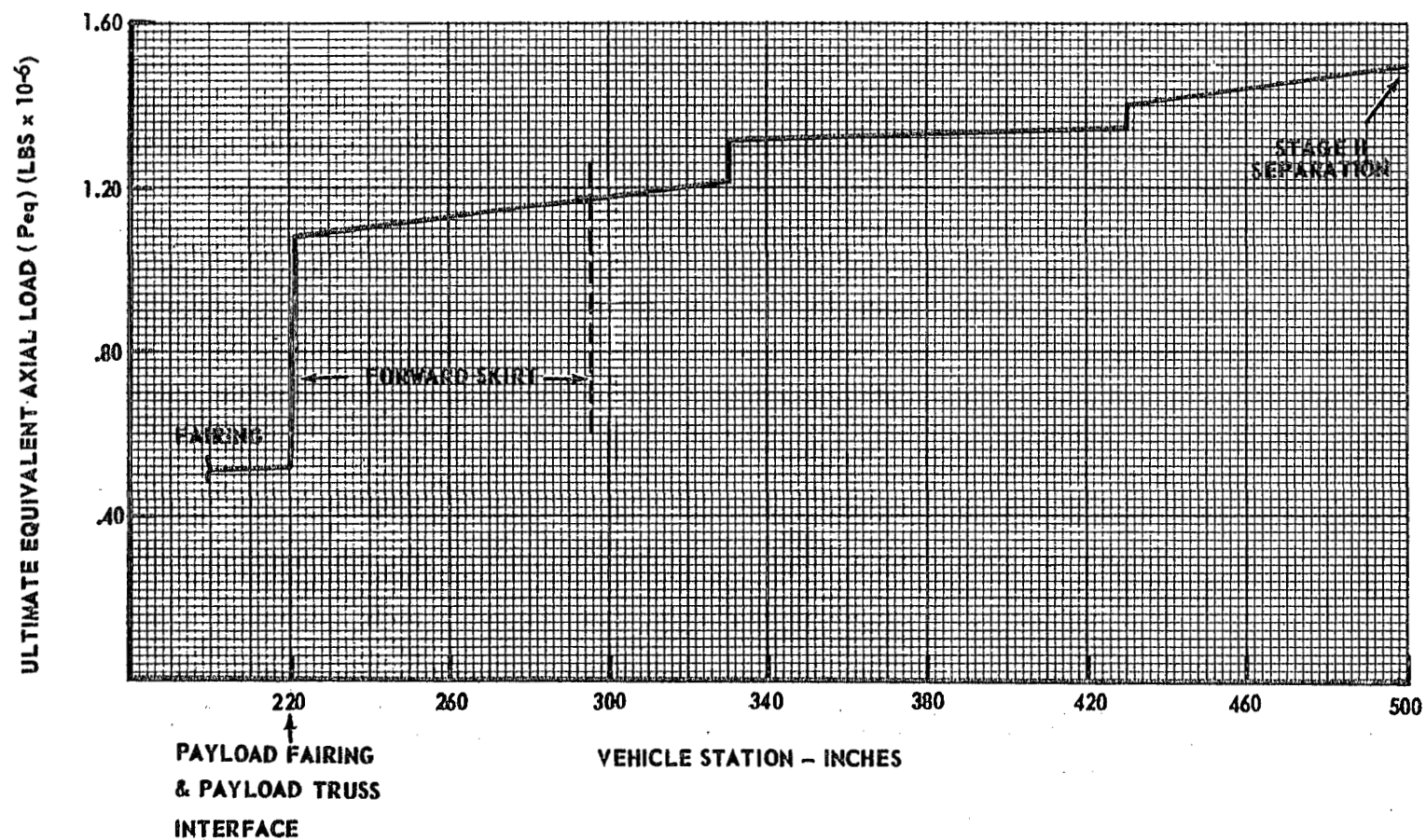
Figure III-11. Titan IIID forward skirt and Titan IIIC PLF ultimate design equivalent axial load.

ALLOWABLE PAYLOAD DYNAMIC ENVELOPE

96

12

480

1.00 (TYP) NOT TO BE VIOLATED BY PL OR PLF

TITAN III D PAYLOAD FAIRING

PAYLOAD

107.27

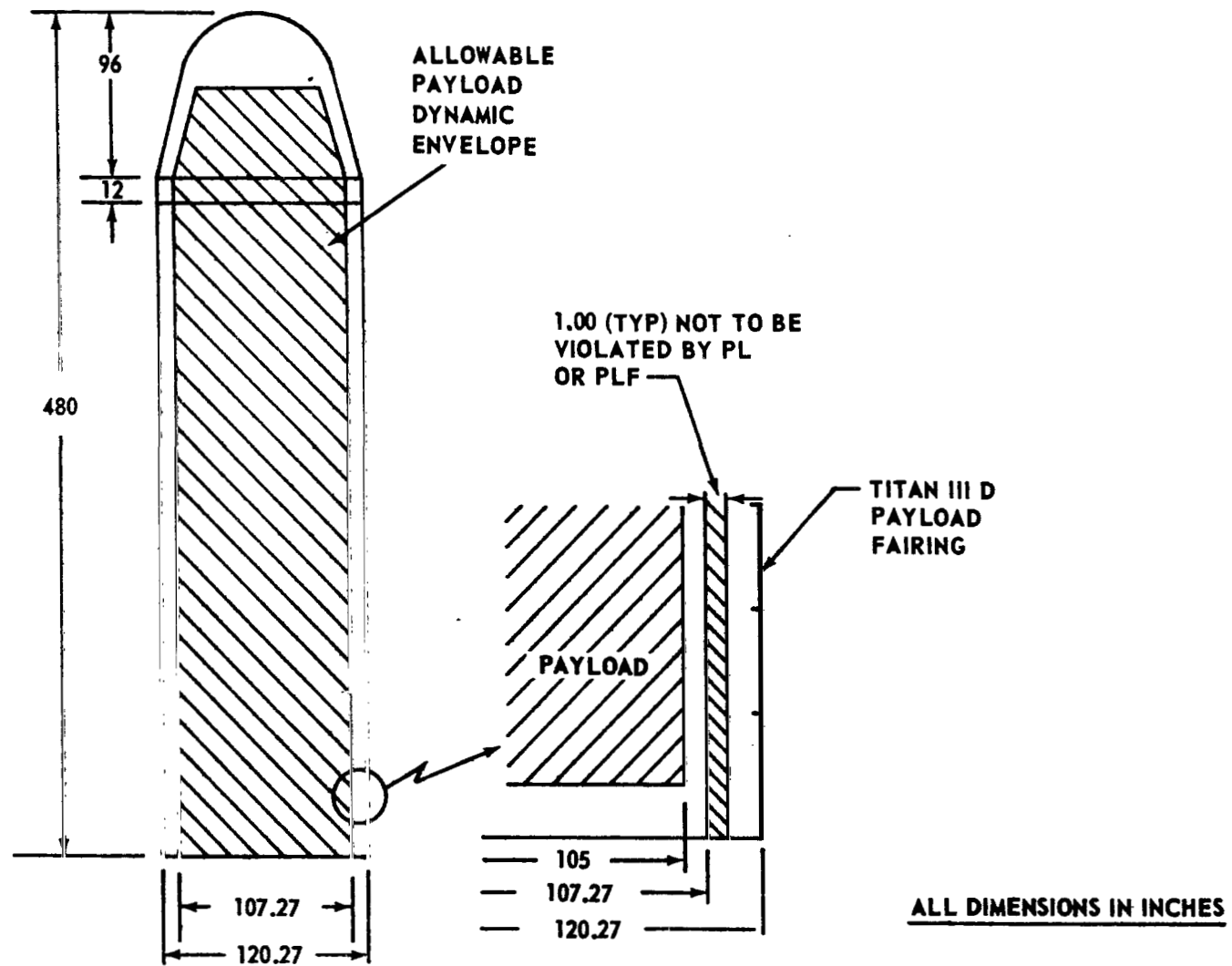120.27

105

107.27

120.27

ALL DIMENSIONS IN INCHES

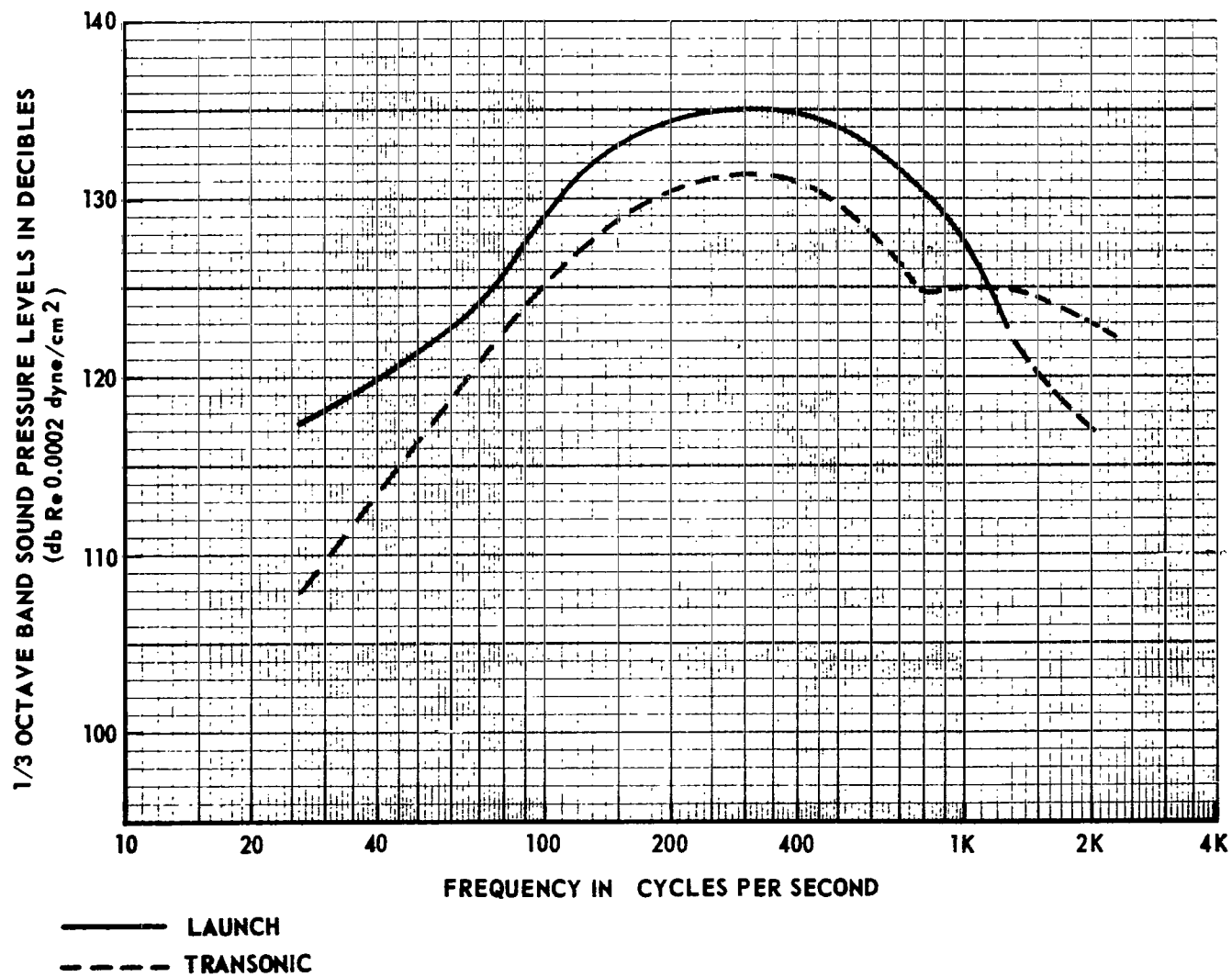Figure III-12. Payload dynamic envelope.

Figure III-13. Predicted maximum interior acoustic levels.

shown are based on extrapolation of measured data obtained from flights of the Titan IIIC vehicle and wind tunnel test programs. The data presented are based on the following assumptions:

    a.   The payload fairing does not include thermal and/or acoustic insulation.

    b.   The maximum dynamic pressure (q max) will not exceed 900 pounds per square foot.

    Extrapolation from measured internal acoustic data together with external measurements on Titan IIIC flights have permitted the establishment of external/internal noise reduction levels for both launch and transonic periods of flight. These noise reduction values were applied to the predicted external levels to obtain the predicted internal acoustic levels shown in Figure III-13. These levels are considered to be conservative since they are based on the maximum external levels measured during Titan IIIC flights.

    3.   <u>Vibration.</u> The vibration environments are based on data measured during flight tests of Titan IIIC. Figure III-14 presents predicted vibration levels transmitted to the payload from the Titan IIID.

    4.   <u>Shock.</u> The shock environments specified are from pyrotechnic devices used to separate the payload fairing and the payload. Data on which these shock environments are based were taken during various ground tests conducted by the Martin-Marietta Corporation and associates. The shock environment due to payload fairing separation is based on data from the Titan IIIC fairing, and is given in Figure III-15. The payload separation is assumed to consist of eight explosive nuts at the payload/payload truss interface, generating levels as specified in Figure III-16. Due to the high levels near the explosive nut and their location at the interface, a curve showing shock attenuation with distance is given in Figure III-17.

    Additional analysis and reevaluation of data shown in this paragraph will be necessary when the payload is more clearly defined and more details of the payload support truss structure design are available.

    5.   <u>Temperature.</u> There are three primary temperature conditions that may impose design constraints on the payload under consideration. These conditions are as follows:

3-26
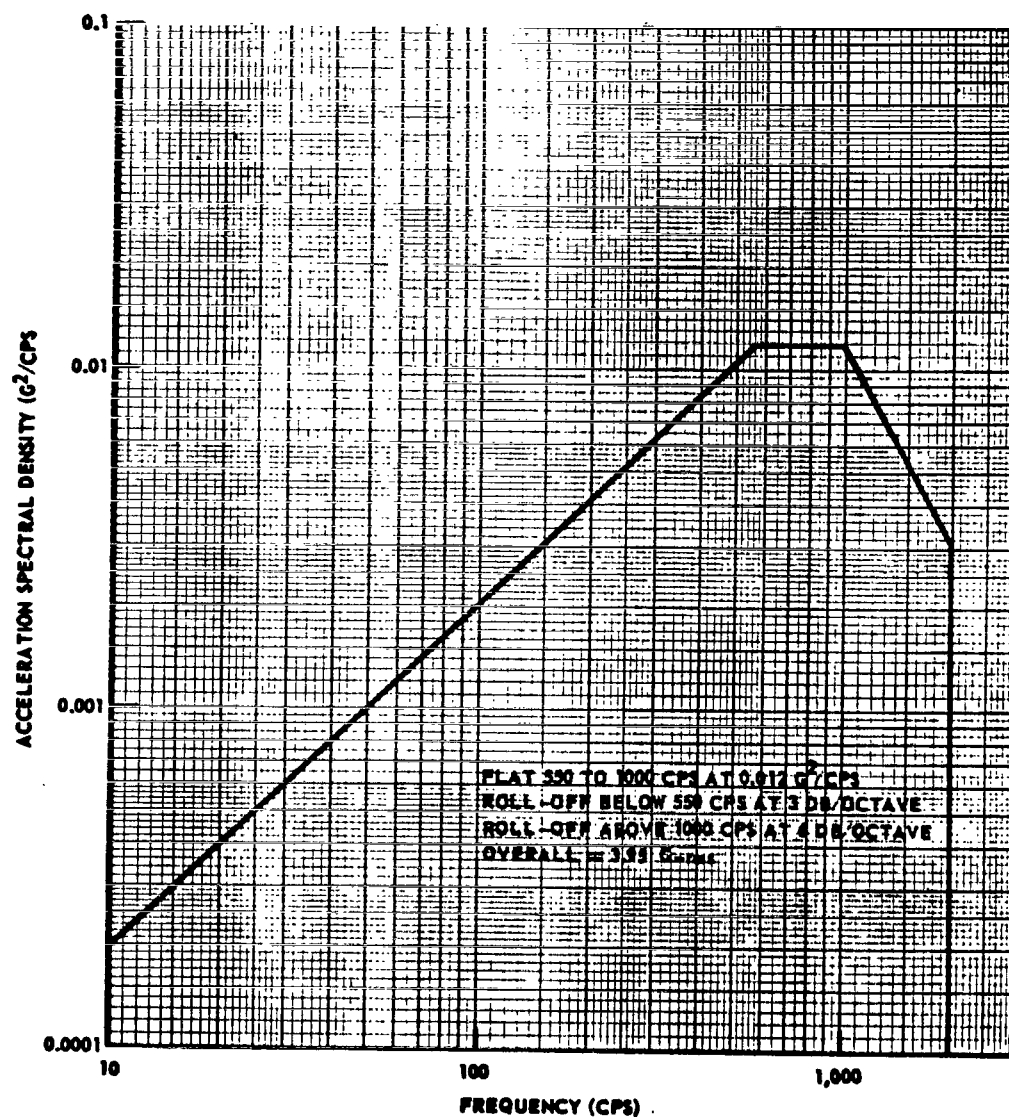
Figure III-14. Random vibration specification at payload interface, launch and flight environment.

MAXIMUM ABSOLUTE RESPONSE – g, PEAK
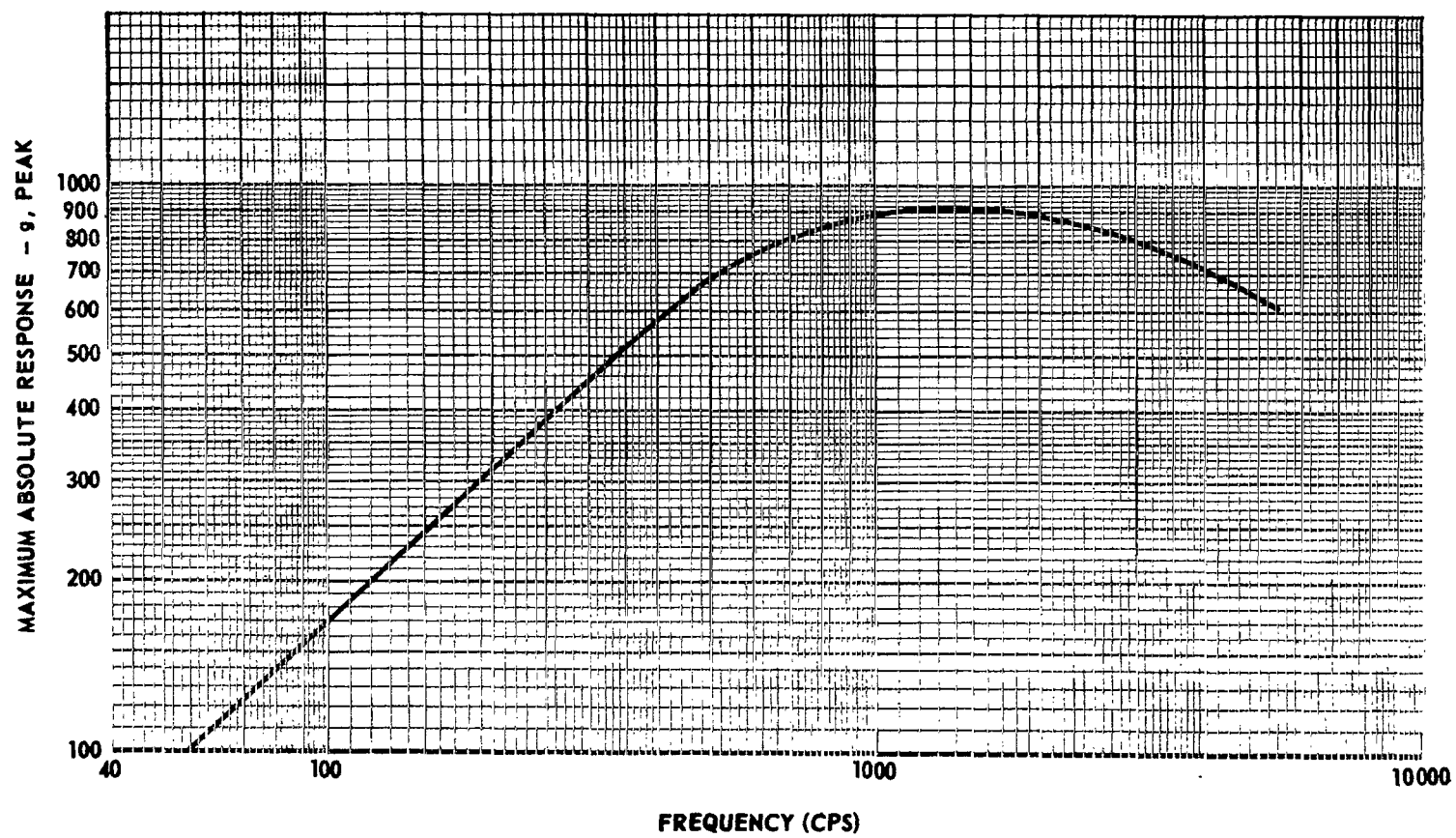
FREQUENCY (CPS)

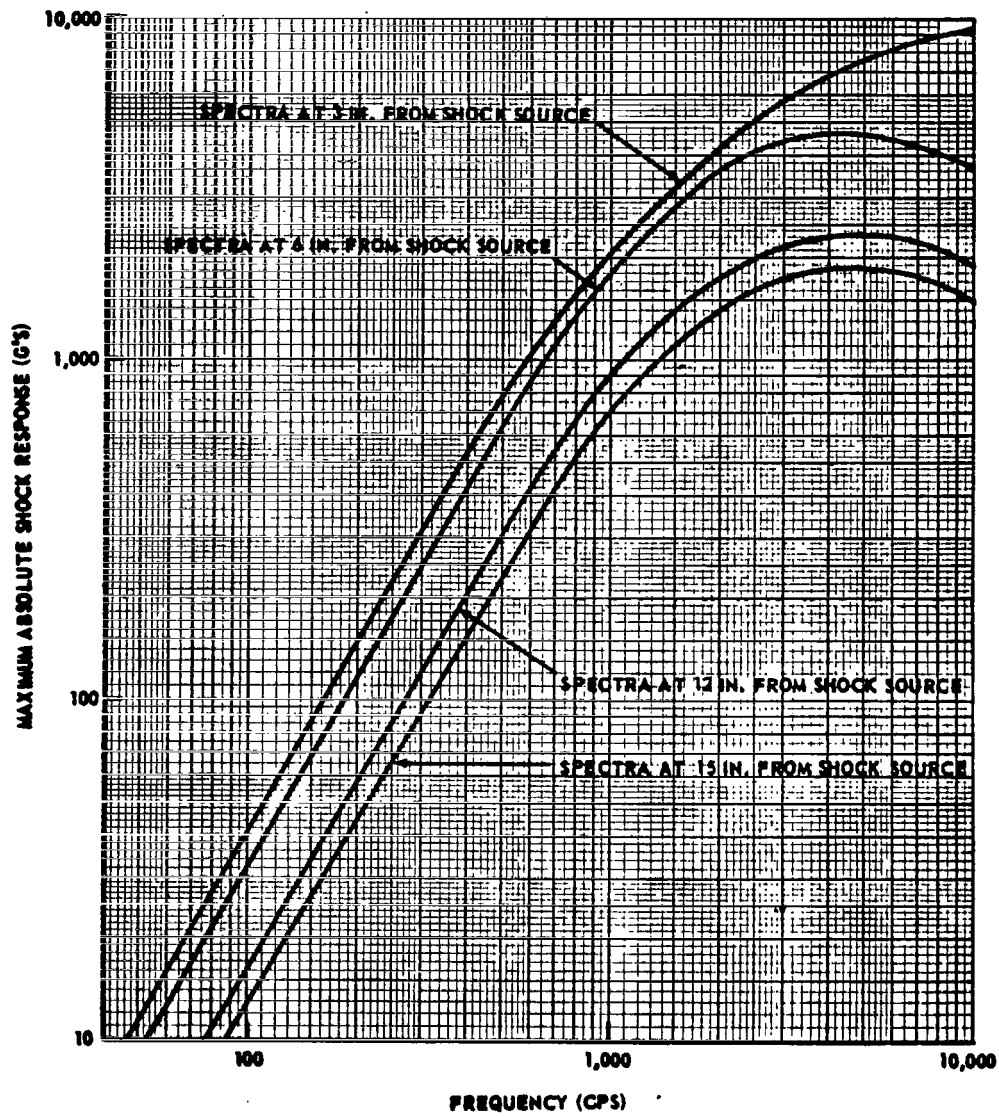Figure III-15.   PLF separation shock level at PLF to PLF adapter interface.

Figure III-16. Shock response spectra explosive nut shock
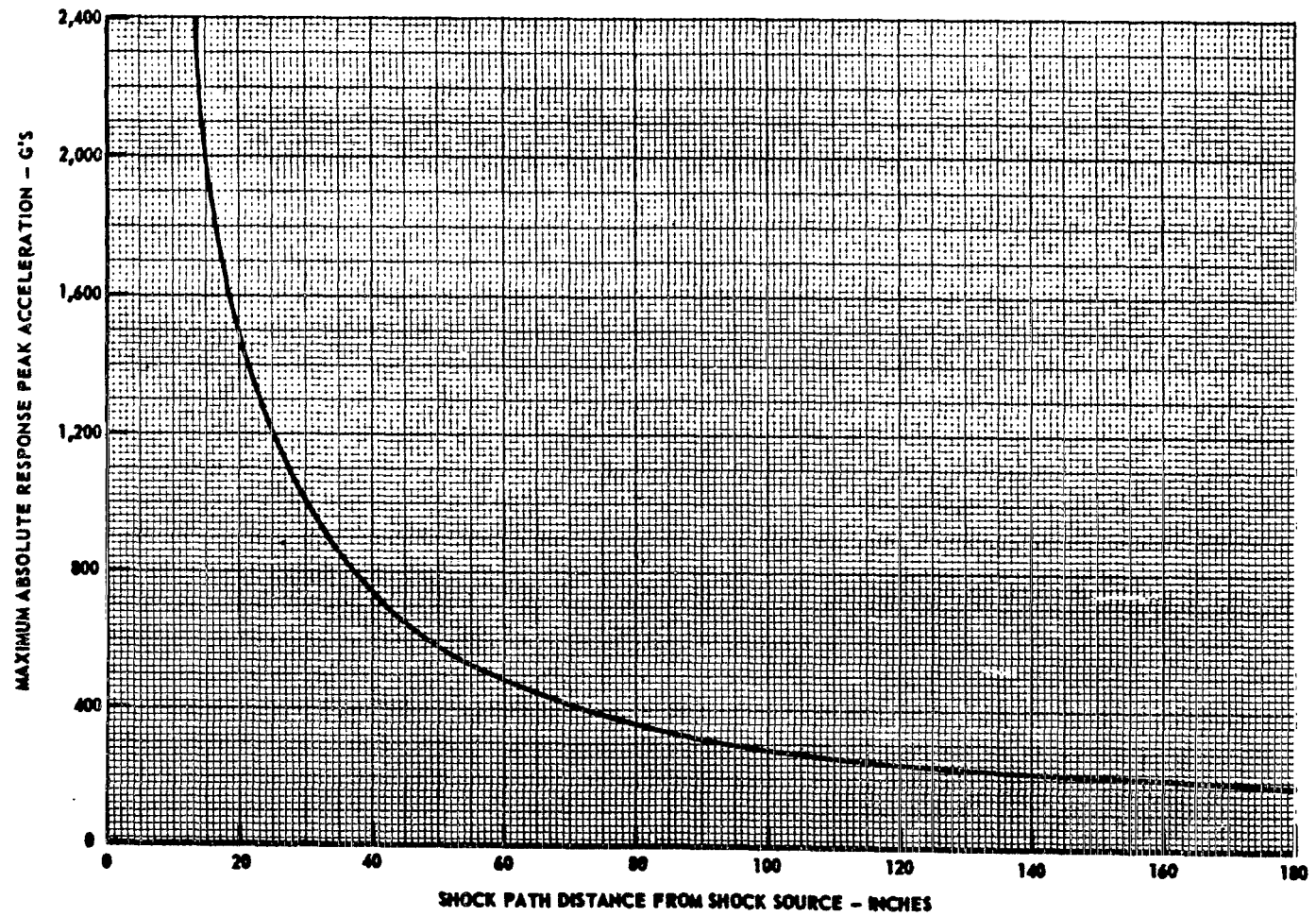(with 5-percent damping).

Figure III-17. Ordnance shock response decay curve.

a. Prelaunch. After the payload is erected, the environmental enclosure at the launch facility provides the following environment:

Temperature:	72° F ± 5° F
Relative Humidity:	50-percent maximum
Positive Pressure:	0. 25 inch of H_2O minimum
Filtration:	35-percent efficiency when tested with atmospheric dust per National Bureau of Standards test

After MST removal, the payload fairing with the payload inside would be exposed to ambient conditions for 2 to 3 hours prior to launch. Solar heating is a major temperature variable which is partly compensated for by an air-conditioning umbilical.

b. Ascent phase (with payload fairing). The fairing is designed to protect the payload from aerodynamic heating during ascent with an internal surface temperature < 300° F. Figure III-18 shows a typical payload fairing temperatures versus flight time curves.

F. Launch Operations

1. ETR Existing Facilities. The Titan facilities at the ETR are shown and described in Reference 2. In addition to the SRM segment receiving and processing facilities, ITL consists of the Vertical Integration Building where the core (Stage I and Stage II) is placed on the transporter and checked out; the SMAB, where solids are added to the core on transporter; and the two launch pads. This mobile mode of operation can provide quick turnaround capability. On-pad assembly of the launch vehicle can also be accomplished.

2. Titan IIID/Centaur. A NASA application of the Titan IIID vehicle with Centaur is now underway for the Pioneer-G and Viking missions. The Titan IIID/Centaur vehicle is derived by mating Centaur to Stage II of the Titan IIID vehicle. Launch Pad 41 will be modified to meet a launch date of the first Titan IIID/Centaur in the last quarter of 1972. Use of this pad for the HEAO mission would avoid mixing the Titan IIID mission with the Titan IIIC launches from Launch Pad 40, and would benefit from previous modifications at Pad 41 for the Titan IIID/Centaur.
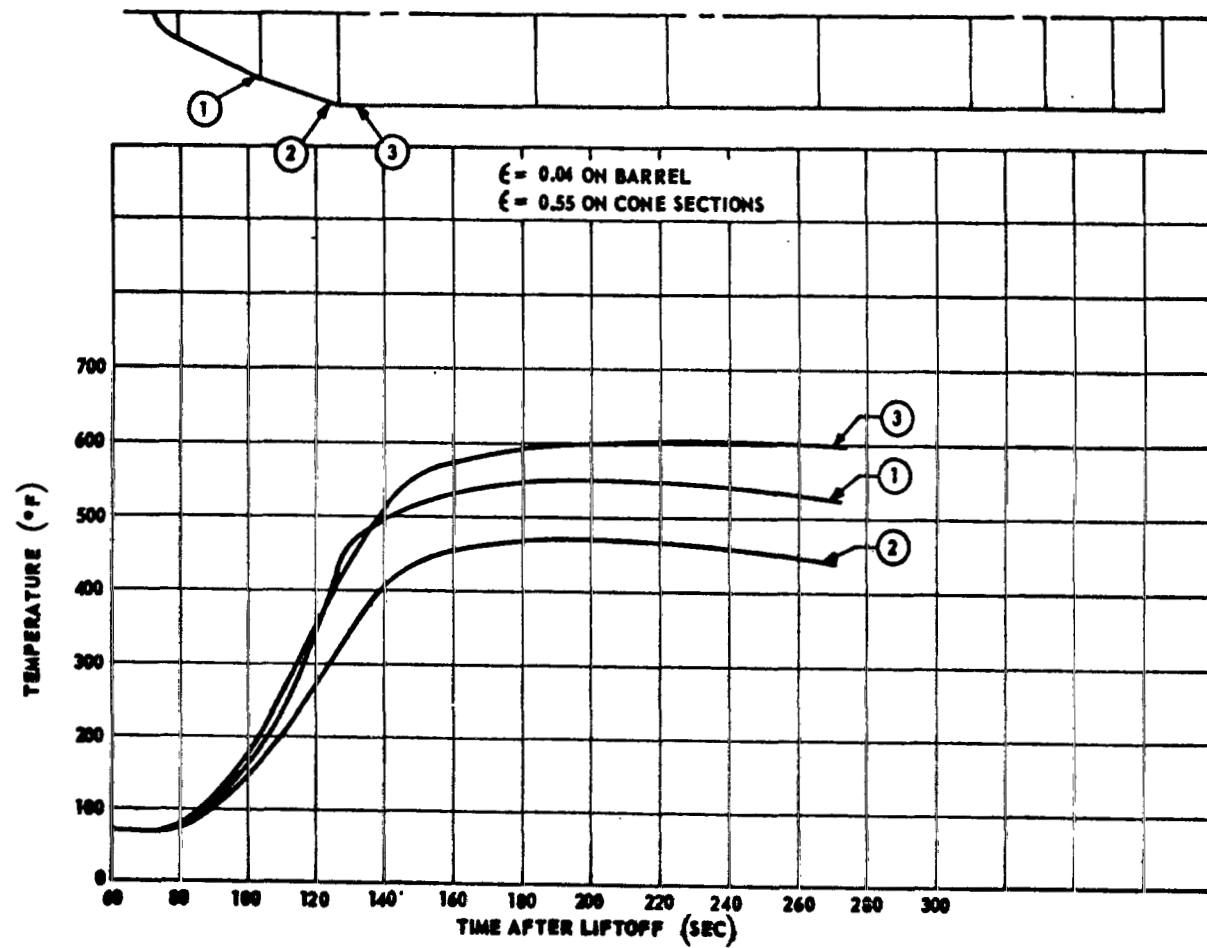
Figure III-18. Typical PLF temperature versus flight time.

3.   Launch Complex Modifications. The launch complex requires
minimum modifications resulting from astrionics changes and implementing
of Titan IIID because the facility will have previously been adapted to the
Titan IIIC and the Titan IIID/Centaur vehicles. Minor changes to the launch
tower may be required for umbilicals. Additional studies are required to
define these modifications, but no major impact is anticipated.

4.   Space Vehicle Assembly. The Titan IIID launch vehicle will be
checked out on Launch Pad 41 prior to the integration of the spacecraft and
payload adapter on top of Stage II. The payload fairing is then added to the
space vehicle and necessary checkout functions performed by the spacecraft
integration contractor under the direction of KSC. Additional studies are
required to define the on-pad assembly processes required for the HEAO
missions.

REFERENCES

1.   T-IIID Launch Vehicle at ETR for High Energy Astronomical Observatory, Revision 1, Martin/Denver, September 19, 1969.

2.   MCR-68-62 Titan IIIC Payload Users' Guide. Revision 1, Martin Marietta Corporation, Denver Division, Systems Engineering, April 17, 1969.

SECTION IV. ORBIT SELECTION AND OPERATIONS

TABLE OF CONTENTS

LIST OF ILLUSTRATIONS

LIST OF ILLUSTRATIONS (Continued)

LIST OF ILLUSTRATIONS (Concluded)

LIST OF TABLES

SECTION IV. ORBIT SELECTION AND OPERATIONS

A. Orbit Selection

Preliminary analyses accomplished early in the study led to the adoption of a 200-n. mi. , 28. 5-degree inclination, circular orbit for the baseline HEAO-A mission. Subsequent analyses have indicated that this initial orbit selection, although feasible, is not necessarily optimum. Detailed mission and systems trades will be required during the follow-on Phase B effort to select the optimum orbit.

There are many considerations affecting spacecraft orbit selection. One of the primary questions is how high the orbit must be to guarantee a 1-year lifetime. At the same time, if the chosen altitude is too high, the launch vehicle may not be able to carry enough payload. The accurate determination of orbit lifetime for various candidate spacecraft configurations and for various possible orbits thus becomes a major factor in choosing the optimum orbit for the HEAO-A mission. Other mission constraints which are important in selecting the proper orbit are discussed in the following paragraphs.

1. <u>Orbit Lifetime.</u> One of the primary considerations in choosing the orbit of the HEAO-A satellite is the requirement of a lifetime of 1 year. The lowest possible orbit altitude, subject to this constraint, is desired so that (1) maximum payload may be placed into orbit, and (2) possible interference by the South Atlantic Anomaly on the scientific instruments may be avoided or minimized.

For relatively close-earth satellite orbits, lifetime is primarily a function of the aerodynamic drag. Drag, in turn, depends upon the atmospheric density and the characteristics of the satellite (mass, drag coefficient, and area).

a. <u>Atmospheric density.</u> The accurate prediction and calculation of atmospheric density has been a subject of much investigation since the launching of the first satellite. It has been discovered that radiation from the sun in the extreme ultraviolet region (EUV) has a very pronounced effect on density at altitudes above 120 km (64. 7 n. mi.). The intensity of this radiation is dependent upon the general level of activity on the sun, one common

measure of which is sunspot number. Sunspot numbers exhibit large, some-what random variations from day to day, but also show a very clear cyclic pattern, over the years, with an average length of 11.08 years.

There presently exist two types of problems in computing future values of density caused by the sun's heating of the atmosphere. The first is acquiring a complete understanding of the mechanisms by which density is increased with an increase of solar radiation. Many scientists have addressed themselves to the problem, with the anticipated results of several theories now being available. It is therefore highly desirable to use the theory which best matches experimental evidence when computing density.

Table IV-1 demonstrates the amount of disagreement that can be obtained in computing orbit lifetime because of the choice of density theory (or density model). Here, nine satellites which decayed somewhere near 1 year after evaluation of orbit elements are shown. The computed lifetimes based upon six different density models are also presented. Notice that for satellite 1962 sigma, with an actual lifetime of 492 days, the computed life-times vary between 152.8 and 531.3 days.

The second problem in computing future values of density is, of course, the problem of predicting future levels of solar activity. This mystery has existed and has been investigated since the cyclic nature of solar activity was first discovered. Here again, there are several theories available which may be used to make a forecast. Unfortunately, none are practical for accurate forecasting of daily variations in activity level, and only a few are but barely adequate in predicting the yearly mean. The accuracy of prediction methods, moreover, is of such poor quality that it represents the only error source which needs to be considered when predicting orbit lifetime, provided state-of-the-art techniques are employed elsewhere where applicable.

An example of a "good" prediction on an actual past cycle is shown in Figure IV-1. The actual data of sunspot cycle number 11 are shown with the nominal, ± 2σ forcasts of the cycle, based on a 1-year knowledge of the cycle. (The prediction was made with data that would have been available 1 year after the start of the cycle.) Notice that the forecast is quite uncertain in the region of maximum activity, but improves in the region of minimum activity.

Launch of the first HEAO satellite is expected in March 1974. At this time, a period of near-minimum solar activity is predicted, as shown in Figure IV-2. This figure presents an atmospheric heating parameter

TABLE IV-1. VARIATION OF COMPUTED LIFETIMES (DAYS) WITH DENSITY MODELS

Satellite	Density Models					
	Actual Lifetime	Poe Density	1962 Standard Density	Special 1962 Density	1967 LMSC	1966 Jacchia
1958δ2	404.1	369.4	431.1	364.4	363.2	357.0
1958δ	197.7	174.6	202.4	180.8	176.3	172.4
1959ε2	362.0	349.8	330.0	359.6	327.0	324.0
1961ε	525.5	404.6	237.1	602.9	463.8	573.0
1961ξ	422.6	369.8	234.9	486.6	407.9	445.3
1961λ	372.9	263.0	157.0	391.6	307.3	367.6
1961λ2	391.2	399.1	247.9	468.3	373.7	389.5
1961αε	394.3	366.2	184.9	435.3	353.5	386.4
1962σ	492.0	392.4	152.8	490.8	420.9	531.3

which is a measure of the effect of solar activity. The heating level near 100 represents a sunspot number of zero. Since the sunspot number cannot drop below zero, the -2σ level of heating parameter cannot go below 100.

b. Satellite physical characteristics. Three parameters are important in describing the HEAO-A physical characteristics when computing lifetime: mass, drag coefficient, and reference area. The weight of the HEAO-A was assumed to be the total payload capability for the baseline orbit, 20 920 pounds.

Drag coefficients were calculated for three proposed configurations of the HEAO-A satellite, as shown in Figures IV-3, IV-4, and IV-5 (Configurations I, II, and III, respectively). The coefficients were computed assuming free molecular flow with diffuse reflection at an altitude of 200 n. mi. The angle-of-attack (shown in the figures) is defined to be in the plane formed by the X and Z axes. The plane of spin is parallel to the XY plane. For a given angle-of-attack, the vehicle spins parallel to the XY plane so that the drag force is continually changing. To account for this variation, drag coefficient was averaged over one revolution of the satellite for each angle-of-attack. The resulting drag coefficients are presented in Figures IV-6, IV-7, and IV-8. The reference area upon which these numbers are based is 55. 946 square feet.

c. Lifetime results. The predicted orbit lifetimes for three proposed configurations of the HEAO-A satellite in a circular 200-n. mi. , 28. 5-degree inclination orbit, assuming a 2σ high level of solar activity and using the 1962 Special U. S. Standard density model, are given in Table IV-2. As given in Table IV-2, Configuration I has the longest lifetime, and Configuration III would remain in orbit the shortest time.

TABLE IV-2. PREDICTED ORBITAL LIFETIME

Configuration	Ballistic Coefficient $(M/C_D A)$ Slugs/ft^2		Lifetime (days)
	Max	Min	
I	1. 585	1. 21	833
II	1. 44	0. 725	681
III	1. 14	0. 816	531

4-4

Using the data for Configuration I, a study was conducted to determine the minimum altitude orbit necessary to ensure a 1-year lifetime. Results are shown in Figure IV-9 for inclinations between 0 and 90 degrees. For a 28.5-degree inclination, the minimum altitude is slightly greater than 183 n. mi. The lowest altitude required is for an 80-degree inclined orbit, with a 179.3-n. mi. altitude. The highest altitude required is for a 0-degree inclination orbit with a 184.6-n. mi. altitude. The nominal lifetimes corresponding to points on this curve are approximately 550 days.

Figure IV-10 shows the nominal, $\pm 2\sigma$ decay histories for a 200-n. mi. 28.5-degree inclination orbit. The lifetimes are 833 days for the -2σ, 1075 days for the nominal, and 1315 days for the $+2\sigma$ prediction. The only error source considered in obtaining this spread of decay is that caused by the uncertainty in predicting future levels of solar activity. The 2σ high forecast of activity would produce the 2σ short lifetime.

For the 200-n. mi. orbit, Figure IV-11 shows how lifetime varies with inclination, and the nominal and -2σ lifetimes are given. The -2σ curve varies from a low of 762 days at 0 degree to a high of 980 days at 80 degrees.

Finally, Figure IV-12 presents the apogee/perigee combination required to provide a 1-year lifetime for various types of orbits. Orbit types vary from a 183-n. mi. circular to a 140 by 266-n. mi. elliptical orbit.

2. Launch Vehicle Trajectory and Payload Capabilities. Parametric data for the payload capability of both the Titan IIID and Titan IIIC launch vehicles are presented in Appendix B of Volume II. Those curves which best illustrate the interaction between orbit selection and vehicle performance are discussed here.

Figure IV-13 shows the net payload as a function of orbital altitude for the Titan IIIC and Titan IIID launch vehicles. For these missions, the trajectories were direct ascent to a circular orbit with an inclination of 28.5 degrees. Both vehicles have about the same capability for about 110-n. mi. circular orbit; but for a 200-n. mi. circular orbit, the Titan IIID can insert 20 920 pounds, while the Titan IIIC can insert 25 420 pounds.

Figure IV-14, in conjunction with Figure IV-12, shows the capability of the Titan IIID to inject into an elliptical, rather than a circular, orbit. Figure IV-14 is a graph of net payload versus perigee altitude for the Titan IIID launch vehicle. The trajectories were direct ascent to an elliptical orbit

with an apogee altitude sufficient for a 1-year lifetime at an inclination of 28.5 degrees. The apogee altitudes which meet this requirement are given in Figure IV-12. For example, the Titan IIID could inject 22 350 pounds into a 183-n. mi. circular orbit, or 25 790 pounds into a 140- by 266-n. mi. elliptic orbit.

Finally, Figure IV-15 shows the penalty involved for inserting into an orbit with an inclination different from 28.5 degrees. For these missions, the trajectories were direct ascent to 100-, 200-, and 300-n. mi. circular orbits, with and without yaw steering. For the northerly launch, the vehicle was launched with a 45-degree azimuth, and yaw steering was initiated at 90 seconds after liftoff. Net payload would be reduced by 2000 pounds for inserting into a 60-degree inclination rather than a 28.5-degree inclination, 200-n. mi. orbit.

The Titan IIIC provides superior payload capability because of the Transtage, which has a restart capability. Some of this deficit for the Titan IIID, which has no restart capability, could be made up by using a kick stage on the spacecraft. Use of a circularizing kick stage is discussed in Appendix G of Volume II.

There are launch vehicle tradeoffs other than payload which should be considered when choosing an orbit. For instance, the added complexities of a yaw maneuver on the guidance system may be important for high-inclination orbits. Also, range safety characteristics will vary with orbit parameters.

Table IV-3 summarizes payload capability alternatives for a 28.5-degree inclination orbit having a minimum lifetime based on a +2σ solar activity of 833 days.

Table IV-4 summarizes the payload capability alternatives for a 28.5-degree inclination orbit having a minimum lifetime based on a +2σ solar activity of 365 days.

3. Experiment Interference From the South Atlantic Anomaly. The most serious radiation problem which will be encountered by any low-altitude orbiting spacecraft is in the South Atlantic Anomaly. For an orbit with a 30-degree inclination, nearly all of the particle flux encountered will be localized in the anomaly region.

The term "anomaly" is rather a misnomer. A cross section of the earth's radiation belts, shown in Figure IV-16, illustrates the actual reason for the anomaly; i.e., an asymmetry of the geomagnetic field with respect to the geographic axis of the earth. Not only is the magnetic axis inclined to the polar axis, but it is also displaced at the center of the earth by approximately

TABLE IV-3.   PAYLOAD CAPABILITY ALTERNATIVES FOR A
28.5-DEGREE INCLINATION ORBIT WITH MINIMUM LIFETIME
OF 833 DAYS (+2σ SOLAR ACTIVITY) (CONFIGURATION I)

Alternatives	Payload (lb)
Titan IIID direct ascent to 200-n. mi. circular orbit	20 920
Titan IIID Hohmann transfer from 90- to 200-n. mi. circular orbit (solid rocket kick stage on spacecraft)	27 580
Titan IIIC direct ascent to 200-n. mi. circular orbit	25 420
Titan IIIC Hohmann transfer from 90- to 200-n. mi. circular orbit	26 900

TABLE IV-4.   PAYLOAD CAPABILITY ALTERNATIVES FOR A
28.5-DEGREE INCLINATION ORBIT WITH MINIMUM LIFETIME
OF 365 DAYS (+2σ SOLAR ACTIVITY) (CONFIGURATION I)

Alternatives	Payload (lb)
Titan IIID direct ascent to 183-n. mi. orbit	22 350
Titan IIID Hohmann transfer from 90- to 183-n. mi. circular orbit (solid rocket kick stage on spacecraft)	≈ 27 700
Titan IIIC direct ascent to 183-n. mi. circular orbit	25 950
Titan IIIC Hohmann transfer from 90- to 183-n. mi. circular orbit	27 430
Titan IIID direct ascent to 140 by 266-n. mi. elliptical orbit (365-day lifetime)	25 790

342 kilometers (184 n. mi.). This displacement causes the inner radiation belt to be displaced toward the earth's surface in the South Atlantic at 30-35 degrees West longitude and 35 degrees South latitude; this location is the South Atlantic or Brazilian Anomaly. In this area, the inner belt dips down to within 200 kilometers (108 n. mi.) of the earth's surface. A more detailed discussion of the South Atlantic Anomaly is given in Appendix C of Volume II.

From the data presented on integral particle flux in Appendix C, it is seen that the majority of flux above 500 keV is composed of electrons. The primary effect on the mission of this large electron flux ($>10^9$ particles/ cm^2/day) would be upon the gas proportional counting devices which record radiation in the 0- to 500-keV range. The assumed upper limit of the counting rate for these counters is 10^3 counts/cm^2-sec. Above this rate, saturation occurs and data are not relevant. Thus, data cannot be taken during the time when the spacecraft is in that region of the anomaly where the count rate is greater than 10^3 counts/cm^2-sec. One effect of the anomaly on the mission is therefore a loss of data during those periods.

Preliminary calculation of average experiment dead time caused by the spacecraft passing through the anomaly has been determined for various orbital altitudes and inclinations. For those calculations, it was assumed that particle fluxes greater than 10^3 particles/cm^2-sec at energies greater than 500 keV would completely saturate the instruments. Figure IV-17 depicts the experiment dead time for a count rate greater than 10^3 counts/ cm^2-sec as a function of orbit altitude. For the 200-n. mi. orbit, this gives a dead time of 4.2 percent which would amount to 3.9 minutes per orbit. Figure IV-18 shows experiment dead time for orbit altitudes as a function of orbit inclination. Percent dead time increases from 0 percent at a 17-degree inclination to a maximum of approximately 22 percent at a 72-degree inclination for the 200-n. mi. altitude. Because of the unsymmetrical shape of the anomaly with respect to the orbit path, the fluxes which the spacecraft will encounter will vary in magnitude and duration from orbit to orbit. Approximately half of the orbits will experience very small fluxes, and hence the experiments will experience no dead time then. Maximum dead time expected for any single revolution of the baseline orbit would be approximately 15 percent, or 14 minutes.

An elliptical orbit for the HEAO spacecraft may be considered as a means to increase the orbital payload for the Titan IIID launch vehicle. Figure IV-19 presents estimated experiment dead time (as compared to baseline mission) as a function of the perigee altitude of an elliptic orbit which will maintain a lifetime of at least 1 year. The apogee altitudes corresponding to these perigee altitudes are given in Figure IV-12; e. g., experiment dead time is approximately 4 percent for a 183-n. mi. circular orbit and 5 percent for a 140- by 266-n. mi. elliptical orbit. From this figure, it appears that the average dead time does not vary greatly over the range of orbits considered for the spacecraft.

4. Ground Station Coverage. A detailed discussion of the communications requirements between the spacecraft and ground stations is given in Section X. The STADAN network is presently being considered for data receipt. In this network, the Rosman, North Carolina station may be used as the control center. It will thus be desirable to obtain as much communication time as possible with this particular station as well as with the STADAN network in general.

The orbit parameters selected for the HEAO-A mission will influence the amount of tracking time by the STADAN network. In general, the higher the orbit altitude, the longer the contact times obtained for each station. A change in orbit inclination can greatly affect the amount of contact time with Rosman. For instance, a 200-n. mi. orbit with an inclination less than 20 degress cannot communicate with Rosman.

5. Sun and Star Occultation. The sun and specific stars will be blocked from view by the earth during various portions of the orbit. When the sun is shadowed, a loss of power from the solar panels is experienced. The occultation of various stars, or portions of the celestial sphere, will result in a loss of data for that time period. Appendix C of Volume II presents a more detailed discussion of the occultation variation with orbit parameters. Within the realm of orbit parameters presently being considered, occultation does not appear to be a major factor in regards to orbit selection.

6. Conclusions. This section outlined some of the more important factors to be considered when selecting the orbit for the HEAO-A mission. Of primary concern is to place the maximum amount of payload into an orbit which will guarantee at least a 1-year lifetime. It is highly desirable to minimize experiment interference by the South Atlantic anomaly. It is desirable to maintain maximum communication time with the STADAN network, and in particular with the Rosman, North Carolina, station. It is important to keep account of the occultation characteristics of the orbit. Detailed trade-off studies are required in the Phase B effort to select the optimum orbit based upon these considerations.

B. Orbital Operations

1. Initial Orbital Operations. The first mission operation is to place the satellite into the specified orbit at the correct time. As a result of injection, the longitudinal axis of the spacecraft is initially parallel to the direction of motion. Several operations must now be accomplished before the vehicle is ready to begin the job of data collection. The major sequence of events for the launch-to-orbit phase is summarized in Table IV-5 and Figure IV-20.

TABLE VI-5. HEAO MISSION SEQUENCE FOR LAUNCH PHASE

Time	Event Description	Mission Operational and Satellite System Requirements
T-12 hr	Update stored commands	Update satellite stored commands; charge onboard batteries.
T-10 min	Initialize satellite-to-launch mode	Switch from external to onboard power; turn on G&C power, turn on and check beacon and S-band communications system.
T-60 sec	Umbilical release	
T-3 sec	Launch vehicle ignition	
T-0	Liftoff from Cape Kennedy at 90-degree azimuth	
T+53 sec	Maximum dynamic pressure region	TVC system must be capable of nulling out any misalignments during this critical phase of the trajectory.
T+121 sec	Stage "O" separation	
T+253.7 sec	Stage I/II staging	
T+283.7 sec	Jettison payload shroud	
T+453.3 sec (EOI)	Earth orbit insertion; Stage II cutoff	Transmit satellite engineering data; arm pyrotechnics.

It is first necessary to correct errors where possible and adjust transients in the vehicle because of anticipated imperfections of the boost/ injection sequence. Some of these corrections will have to be completed prior to the initiation of the solar vector acquisition sequence; others may continue as more sequences are started. Vehicle launch time should be planned so that after all necessary corrections are made, the vehicle will be entering sunlight. This constraint is not mandatory, but is desirable to reduce the initial discharge demand on the batteries (during prelaunch and launch phase). The solar panels will begin to furnish power and recharge batteries as soon as possible. Also, spacecraft thermal equilibrium should be achieved more quickly, thereby reducing heater and startup power requirements and the initial load on the power system.

Figure IV-21 provides a schematic representation of the operations during the first orbit. After compensating for injection transients, the spacecraft should be ready to acquire the sun. Initial acquisition is made with the coarse sun sensor, and the vehicle rotated so that the spin axis (Z axis) is pointed toward the sun. The satellite is held in this attitude for two orbits, allowing enough time to assure that batteries are fully charged prior to initiating deployment or startup of equipment that may require   g large peak power.

Figure IV-22 provides a schematic representation of operations during the second through the seventh orbit. With the batteries fully charged and the solar array oriented, enough power is available to begin spinning the flywheel. It is expected that flywheel spinup will require 3 times the maximum electrical load as normal flywheel operation and will require from 4 to 6 orbits (up to 9 hours). As the electrical load stabilizes, the power available increases and the various experiment equipment and supporting systems may be started. Initial checks of their operational status should be conducted as the load permits.

The final step of the initial orbit operations is to spin the spacecraft up to its nominal rate of 0.1 rpm. Once the spin rate has been achieved, and all equipment and systems checked out, the vehicle is ready to begin the major function of data collection.

2. Major Orbital Operations. Table IV-6 and Figure IV-23 summarize the major orbital operations necessary for the satisfactory completion of the mission. The first 30 days are planned for an initial mapping of the galactic plane, discussed in more detail later. During this time, the satellite will be operating in a galactic scan mode (Fig. IV-24). A maximum offset angle of 37 degrees from the solar vector is anticipated. The optimum means for scanning the galactic plane dictates a launch date of either September 7 or

TABLE IV-6. HEAO MISSION SEQUENCE FOR ORBIT PHASE

Time, EOI	Event Description	Mission Operational and Satellite (S/C) System Requirements
0 to 5 min	Initiate S/C separation sequence	Initialize G&C system with transfer of data from launch vehicle computer receive separation command. Perform release and separation (ΔV - 2 ft/sec); launch vehicle maintain attitude hold for separation.
5 to 15 min	S/C stabilization	Necessary action is now initiated to correct or adjust all errors or transients which have occurred to the S/C caused by orbit insertion. The time necessary to correct these transients, which must be removed prior to solar vector acquisition, will determine the launch time of day.
15 to 165 min	Earth orbit coast orbit determination	Coast in orbit and make necessary adjustment to assure desired orbit is acquired.
2 3/4 to 5 3/4 hr	Celestial reference acquisition	Coarse sun sensor picks up the sun's rays; perform pitch and yaw turns to acquire sun orientation lock with spin axis (Z). Maintain inertial attitude hold during solar occultation.
5 3/4 to 14 hr	Flywheel spin-up experiment & system checkout	Receive ground command for flywheel spin-up's perform spin-up. A total of $\approx$8 1/4 hr at an average load of 170 watts is required for full spin-up of flywheel. The experiment equipment and the various supporting systems (data storage and transmission, aspect determination, power supplies attitude control, etc.) are turned on and run through initial checks. This phase may continue for the $\approx$8 1/4-hour flywheel spin-up period as long as total power available (with overload for flywheel) is not exceeded.

TABLE IV-6 (Concluded)

Time, EOI	Event Description	Mission Operational and Satellite (S/C) System Requirements
14 hr to 1 day	S/C spin-up & acquire galactic scan attitude	At completion of flywheel spin-up, RCS system perform spin-up of S/C to nominal 0.1 rpm rate about Z axis and orientates S/C for galactic scan.
1 to 31 days	Galactic Scan	Upon completion of the initial orbital operation, the S/C is oriented for the galactic scan mode. (The RCS must rotate the S/C 37 deg for the galactic scan orientation). To scan a galactic band of ±8.5 deg, 10 realignments of the S/C spin axis of ≈3 deg and one realignment of 17 deg are required. The maneuvers are made every 2 1/2 days.
31 to 211 days	Celestial scan	The S/C is oriented for normal scanning of the celestial sphere. The spin axis is aligned with the earth-sun line. This mode is continued for 180 days for complete coverage of the celestial sphere. G&C system must keep the spin axis aligned with the earth-sun line.
211 days	Despin S/C	RCS zeros out the 0.1 rpm S/C spin rate, 2 1/2 orbits for despin of S/C, & orientate S/C for celestial pointing.
211 to 365 days	Celestial pointing	Selected areas of major interest are monitored for time periods determined by S/C requirement and principal investigators. RCS & magnetic coils will perform S/C orientation maneuvers. There will be a minimum of 3 hours allocated for viewing each target.
2nd year	Repeat of first year operation	The first year sequence of operations is repeated with any modification necessitated by experiment findings or equipment failure.

March 8. This initial 30-day operation will require major scan axis reorientations at the beginning and end, with frequent small reorientations throughout the period.

The second through seventh months will be spent in the normal celestial scan mode (Fig. IV-25). All experiments and subsystems will be operating continuously and sweeping the celestial sphere at 0.1 rpm scan rate. Small reorientations of the spin axis are anticipated to counteract effects of drift and sun tracking. A survey of the entire celestial sphere will have been completed at the end of this phase.

For the eighth through twelfth months, the spacecraft will be despun so that individual points of major interest may be monitored (Fig. IV-26). Periodic major reorientations of the satellite will be required of the control system so that these areas of interest may be located. Again, frequent, small reorientations are expected to be required to counteract drift. While in this pointing mode of operation, only those experiments on the side facing the area of interest can monitor the area. Other experiments could either be turned off to conserve power or used to monitor random points on the opposite side of the celestial sphere. A more complete discussion of the rationale for celestial pointing is given later. The remainder of the time in orbit, as long as instruments are operating, will be a repetition of the first through twelfth month sequences.

3. Celestial Scan Mode. For determining the areas of the celestial sphere which will be scanned for a given orientation of the spacecraft spin axis, the spacecraft can be considered to be stationary and at the center of the celestial sphere. The spacecraft will remain at the center and during celestial scan mode will rotate at 0.1 rpm about the earth-sun line. This means that in Figure IV-27 the motion of the spacecraft about the earth, and even the position of the earth in its orbit about the sun, has no influence except for earth occultations determining the viewing disc of the spacecraft on the celestial sphere. The reason for neglecting these positions is because of the extremely large distance between the solar system and the nearest star. As shown in Figure IV-28, the extreme positions of the earth in its orbit about the sun subtends an angle of less than 2 arc seconds at the nearest star. Thus, the only direction that matters, for the celestial scan mode, is the direction from earth to sun.

The manner in which the celestial sphere is scanned for the celestial scan mode is illustrated in Figure IV-29. The viewing disc cuts the celestial sphere at right angles to the ecliptic plane at 90 and 270 degrees from the earth-sun line. The viewing disc moves along the ecliptic at the same rate as the earth in its orbit, while the spacecraft makes approximately 144 revolutions per day. Thus, the instruments will make more than one sweep through various points on the sphere.

4-14

Notice that in this mode it will take 6 months to completely cover the celestial sphere. If this mode were used to conduct an initial scan of the galactic plane during the first 30 days of operations, only a small part of the galaxy would be covered; as shown in Figure IV-30, the amount scanned would be a function of the launch time. Figures IV-31 through IV-36 depict the galactic plane as a band 360 degrees long and approximately 30 degrees wide (± 15 degrees from the center). The zero-degree points on the horizontal scale start at the intersection of the galactic plane with the ecliptic plane on the "ascending" side. Prominent stars are indicated on each strip by darkened circles with their names immediately above or below. Constellations are indicated by open circles and numbers to provide their names, both Latin and English. The names corresponding to each number are given in Tables IV-7 and IV-8. Each strip on these figures has shaded areas which represent the amount of coverage of the galactic plane during scanning. For instance, in Figure IV-31, looking at the strip for January, the plane would be swept between a line just to the right of constellation 14 and the line just to the right of the star Algol, if scanning started on January 1 and continued for 30 days. The plane would, of course, also be cut in a similar fashion 180 degrees away for the same time period (the area between the line to the right of Centaur and the line through constellations 3 through 7). Should this type of scanning be continued through 60 and then 90 days, the area between the broken lines would be covered. This set of figures shows the type of coverage of the galactic plane that could be obtained for 30-day periods beginning on the first of each month. For this type of scan, it is seen that starting in September or March would be the way to obtain the greatest coverage.

4. Galactic Scan Mode. Most of the X-ray and gamma-ray sources found to date lie very close to the galactic plane. The galaxy, or Milky Way, when observed through the spring, summer, fall, and winter, is seen to encircle the sky and divide it into two approximately equal parts. It is composed of many groups, or "clouds," of stars that seem to form a band across the celestial sphere. Since a high concentration of areas of interest lie near the galactic plane, it is desirable to conduct an initial scan of this region as quickly as possible in the early phases of the mission. This scanning will provide a great deal of data in a very short period and thus will provide insurance should components of one or more experiments or of the spacecraft fail at any early time in the mission.

The baseline concept for the galactic plane scan is described in detail in Section XI of this report. This description includes a discussion of the control system sensors and actuators to be used and their functions. The baseline concept provides for scanning a 17-degree belt in the galactic plane during a 30-day period, while limiting the maximum solar offset angle to 37 degrees.

TABLE IV-7. NAMES OF CONSTELLATIONS

1.	Monoceros	Unicorn
2.	Musca	Fly
3.	Norma	Carpenter's Level
4.	Puppis	Stern of Ship
5.	Scorpius	Scorpion
6.	Scutum	Shield
7.	Triangulum Aus	Southern Triangle
8.	Vela	Sail of Ship
9.	Vulpecula	Fox
10.	Ara	Altar
11.	Auriga	Charioteer
12.	Canis Major	Big Dog
13.	Carina	Keel of Ship
14.	Cassiopeia	Queen
15.	Circinus	Compass
16.	Crux	Southern Cross
17.	Cygnus	Swan, N. Cross
18.	Lacerta	Lizard
19.	Lupus	Wolf
20.	Pyxis	Compass of Ship
21.	Sagitia	Arrow
22.	Sagittarius	Archer
23.	Antlia	Air Pump
24.	Apus	Bird of Paradise
25.	Centaurus	Centaur
26.	Cepheus	King

O Constellations
● Stars   See Figures IV-3 through IV-36.

TABLE IV-8. STARS

	Visual Apparent Magnitude
Vega	0.1
Cappella	0.2
Castor	1.2
Centaur	0.3
Antares	1.2
Canopus	-0.9
Sirius	-1.6
Altair	0.9
Deneb	1.3
Algol	3.0

5. Pointing Mode. In addition to the solar-vector scanning mode, which will be used to map the entire celestial sphere, another mode of observation will be incorporated into the HEAO mission. This additional operational mode is utilized because in the original mapping of the celestial sphere, using the celestial scan mode, certain stars or positions on the sphere may prove to be interesting enough scientifically to warrant further study. This additional investigation should be carried out after the entire celestial sphere has been scanned by the celestial scan operational mode and the results carefully studied. The interesting stars or positions on the sphere which require further investigation should be isolated and their locations carefully defined. To view a particular location on the celestial sphere, for a considerable amount of time, the spacecraft will be despun and reoriented for the star to remain in the sensor's field of view. This fixed orientation will be maintained by an attitude sensing and control subsystem contained in the spacecraft for this purpose. This additional operational mode of the spacecraft is called the celestial pointing mode.

The attitude control system on board the spacecraft for major reorientations will be of the reaction jet type. To conserve the propellant contained within this system, it is desirable to minimize the attitude control firings. It will therefore be necessary to set up a schedule of the interesting stars which are to receive further study.

The area or star on the celestial sphere which may be viewed for an extended period of time in the off-solar vector mode is restricted by the position of the spacecraft with respect to the sun and the size and orientation of the solar panels. The axis of the spacecraft normal to the solar panels may be inclined by an angle of 37 degrees from the solar vector and still enable the panels to generate enough power to operate all spacecraft experiments and subsystems simultaneously. This 37-degree angle can be interpreted as forming a cone with a half-angle of 37 degrees in which full operation of the spacecraft can be assumed. The axis of the cone is the earth-sun line. If a star which requires further study is located outside of this cone, the power produced by the solar panels would be less than that required for full operation of the spacecraft. This problem could be overcome in two ways. First, the cone of visibility will rotate around the celestial sphere as the earth moves in its orbit around the sun. Thus, most of the points could be covered by following a proper time schedule for viewing. Second, for those points which do not fall within the 37-degree cone at any time during this operating mode, the power loss could be overcome by switching experiments on and off.

As the earth moves around the sun, the spacecraft will be in a different position with respect to the sun at various times of the year. Because of this different orientation, not all points on the celestial sphere are visible to the spacecraft's sensors at any particular time during the year without reorientation. All points become visible during the course of the year and the orientation of the spacecraft with respect to the sun plays an important role in the scheduling of the stars to be studied in the celestial pointing mode.
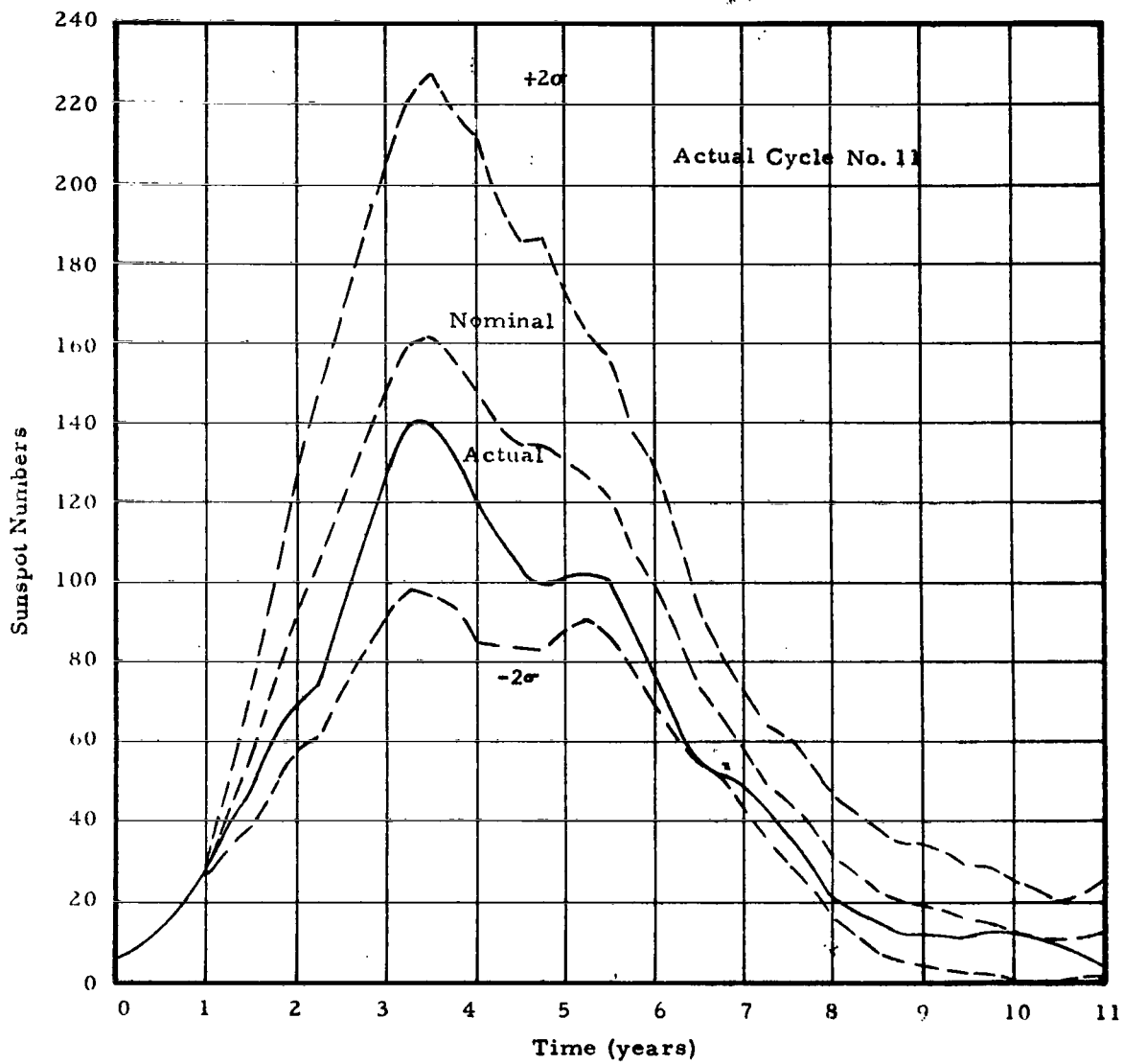
Figure IV-1. Example of a "good" prediction.
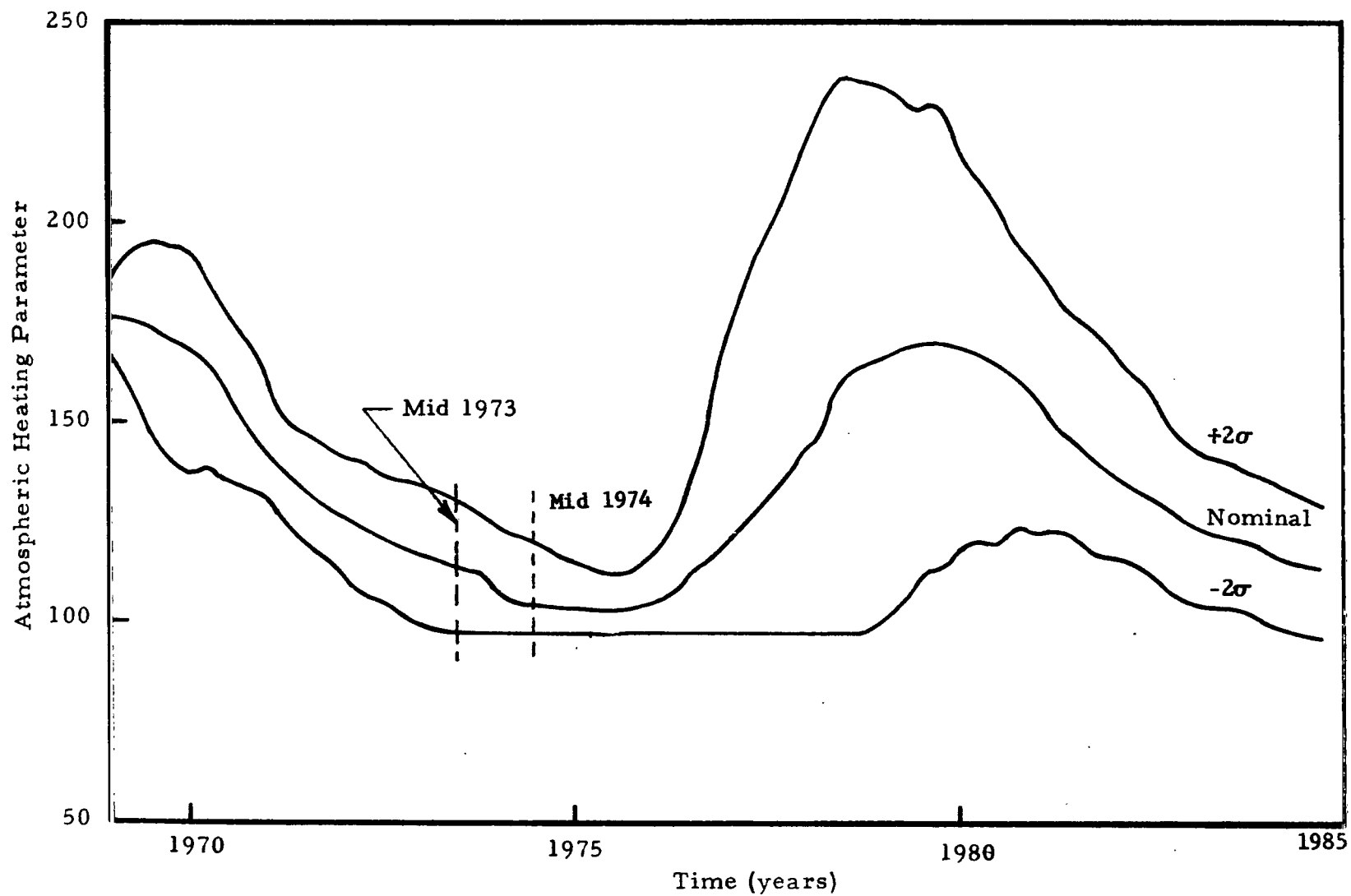
Figure IV-2. Current forecast of solar activity.
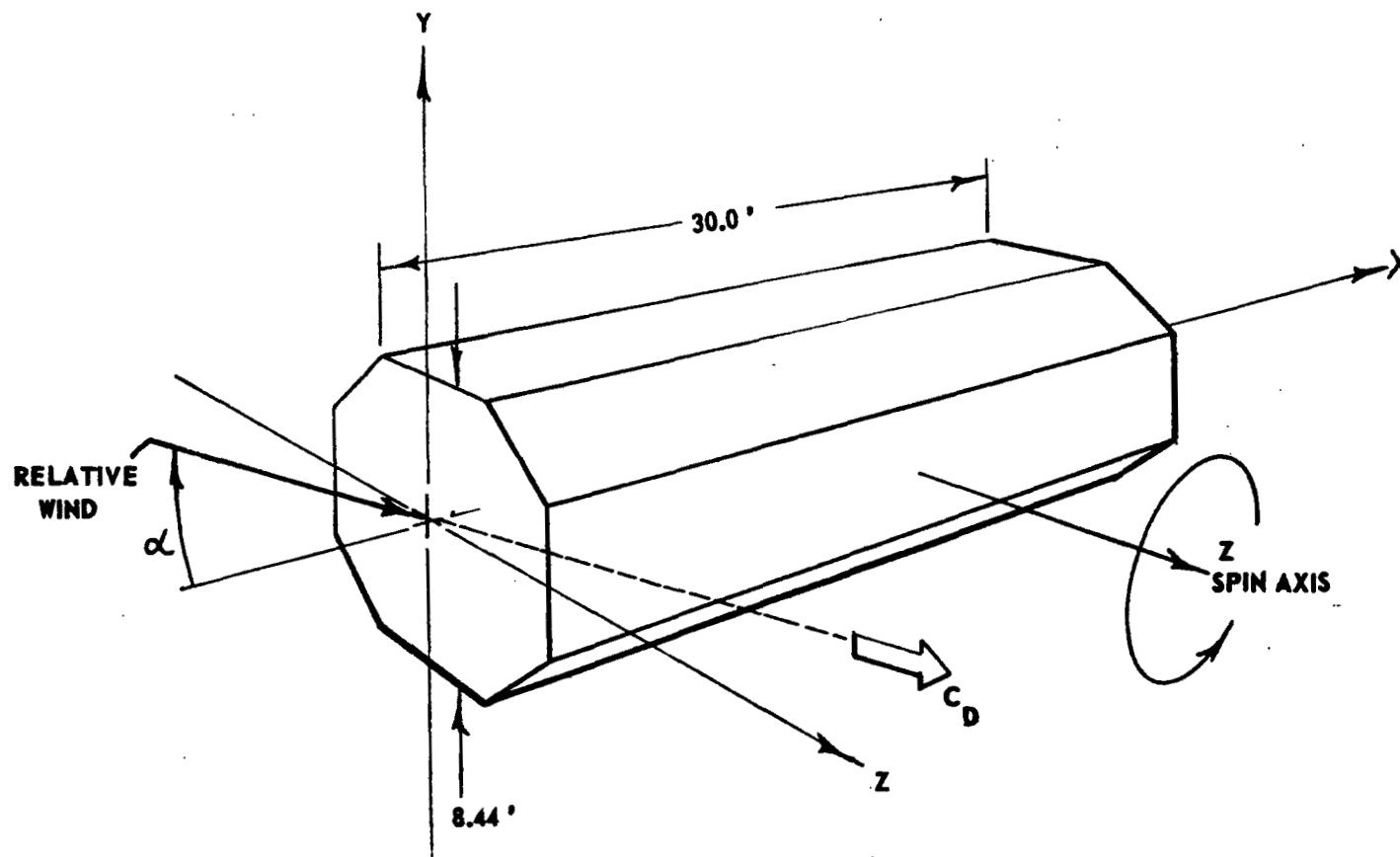
Figure IV-3. HEAO Satellite Configuration I.
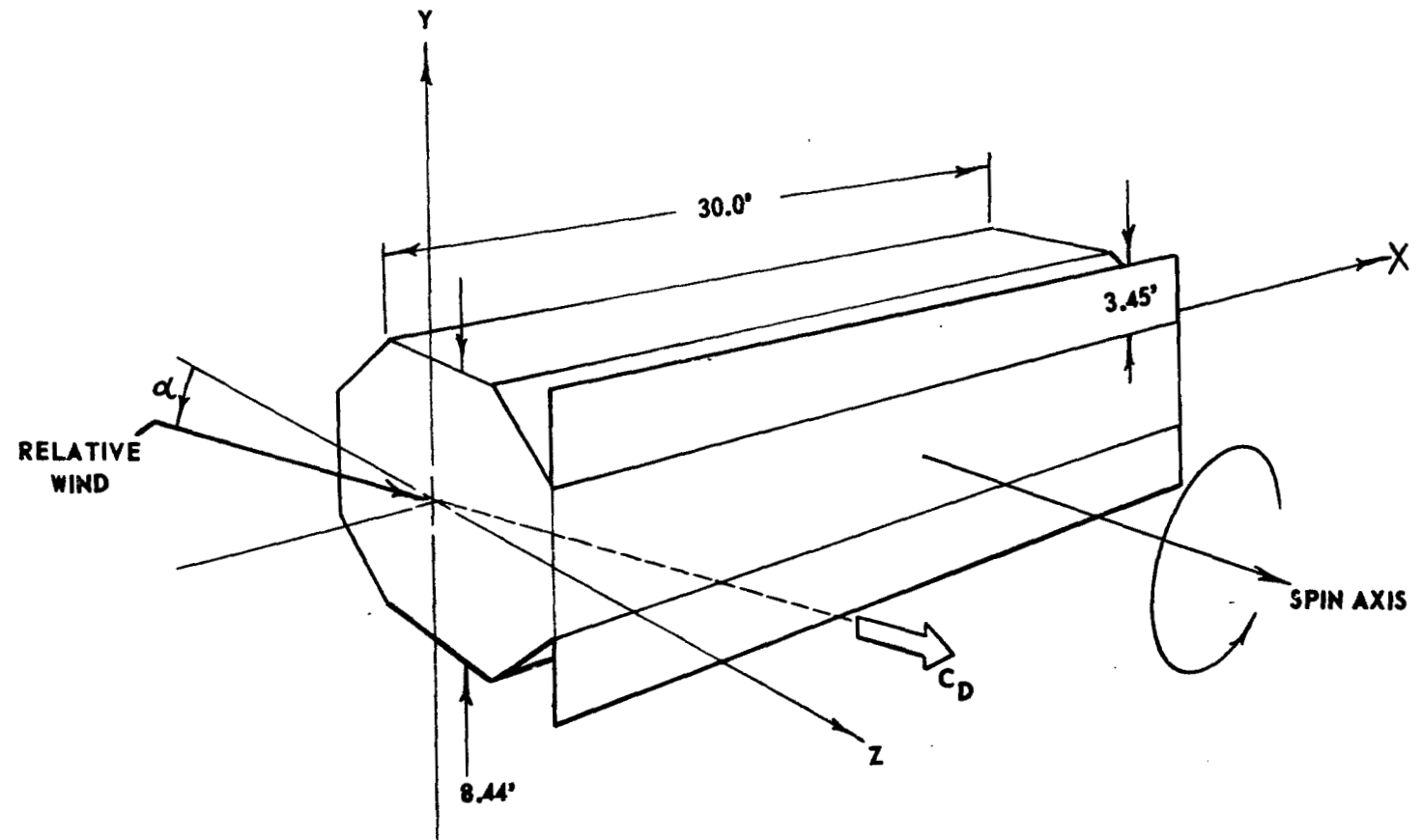
Figure IV-4. HEAO Satellite Configuration II.
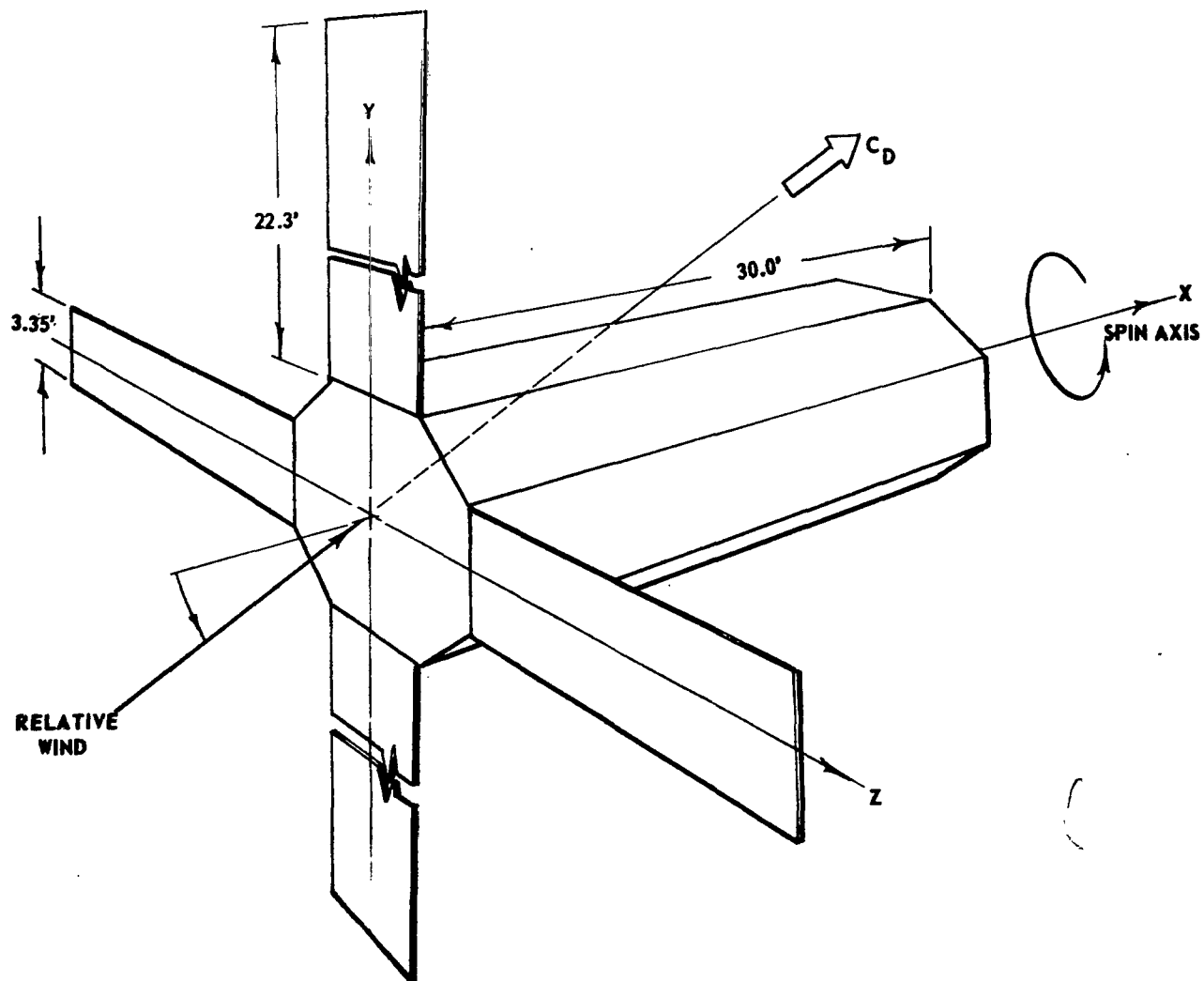
Figure IV-5. HEAO Satellite Configuration III.
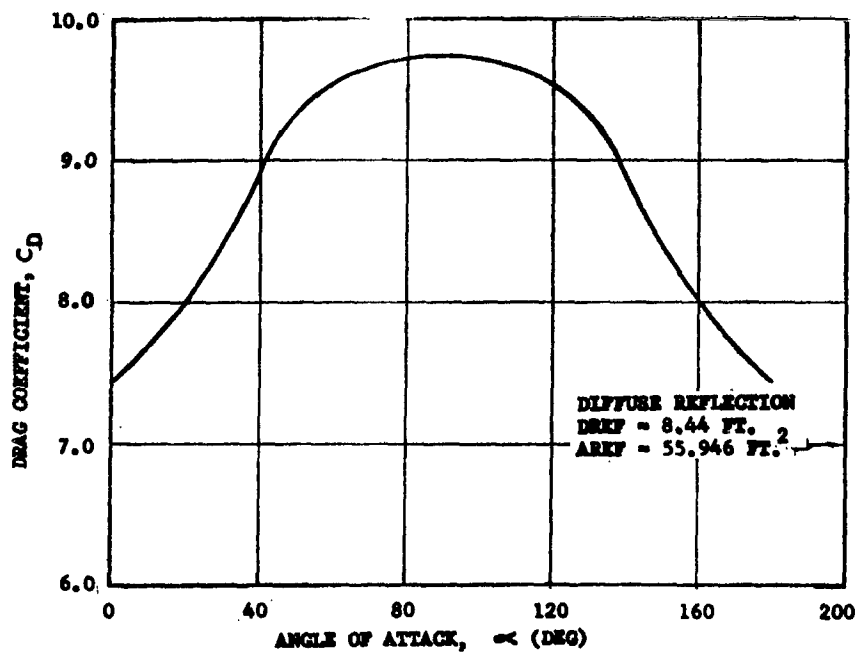
Figure IV-6. Drag coefficient for Configuration I.
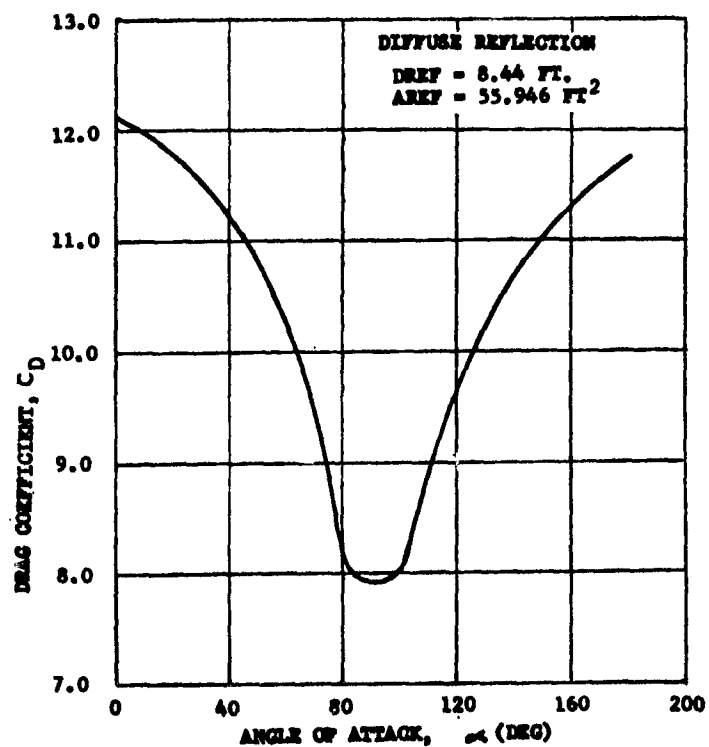
Figure IV-7. Drag coefficient for Configuration II.
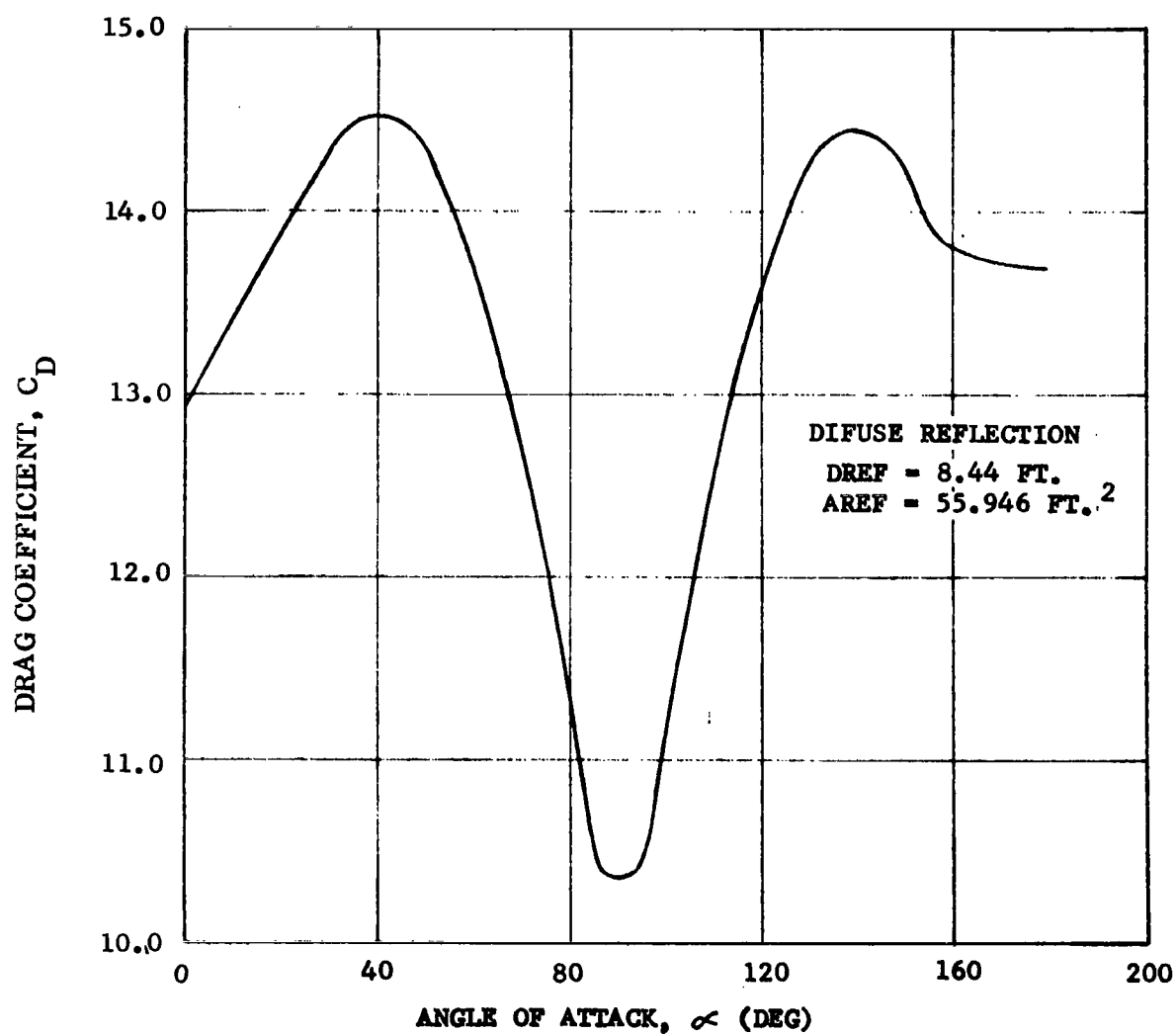
Figure IV-8. Drag coefficient for Configuration III.

The figure shows drag coefficient C_D plotted against angle of attack α (DEG). The y-axis, labeled DRAG COEFFICIENT, C_D, ranges from 10.0 to 15.0. The x-axis, labeled ANGLE OF ATTACK, α (DEG), ranges from 0 to 200.

DIFUSE REFLECTION
DREF = 8.44 FT.
AREF = 55.946 FT.^{2}
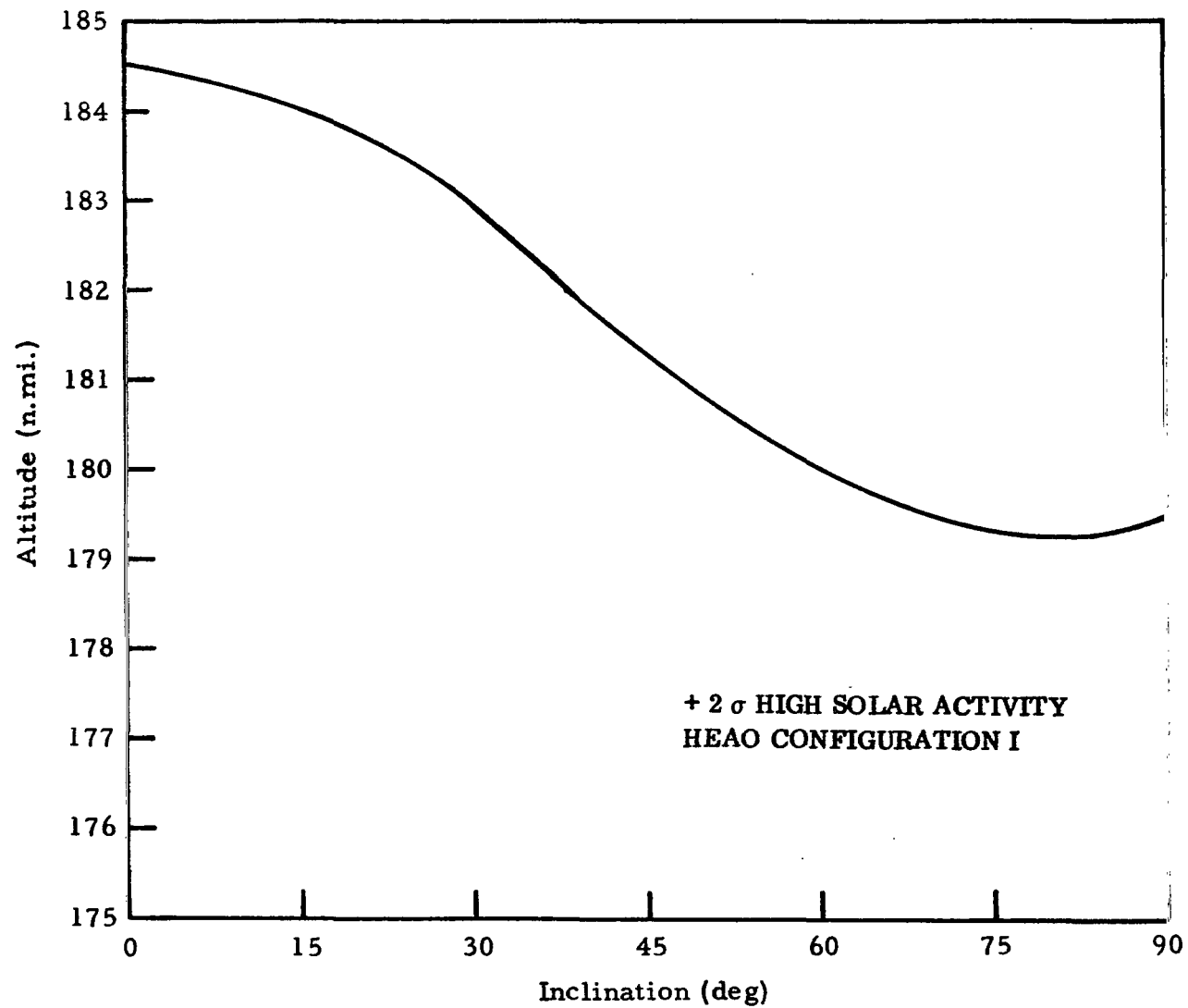
Figure IV-9. Solar activity variation of the orbit altitude required for a
1-year lifetime with orbit inclination.
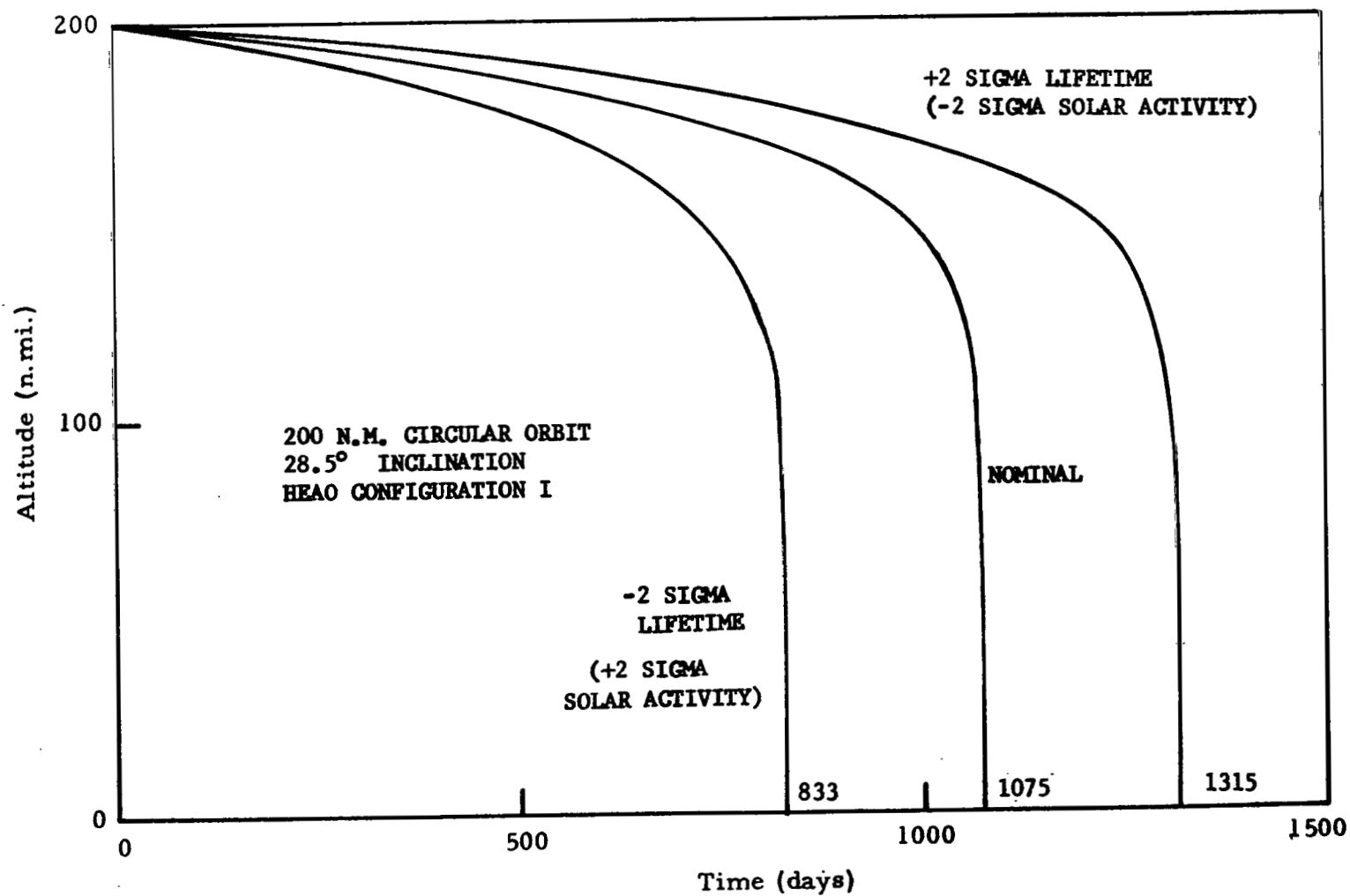
Figure IV-10. Nominal, ±2σ altitude decay histories.

The figure shows altitude decay curves with the following labeled elements:

- Y-axis: Altitude (n.mi.), marked 0, 100, 200
- X-axis: Time (days), marked 0, 500, 1000, 1500
- +2 SIGMA LIFETIME (-2 SIGMA SOLAR ACTIVITY)
- 200 N.M. CIRCULAR ORBIT
  28.5° INCLINATION
  HEAO CONFIGURATION I
- NOMINAL
- -2 SIGMA LIFETIME (+2 SIGMA SOLAR ACTIVITY)
- 833, 1075, 1315
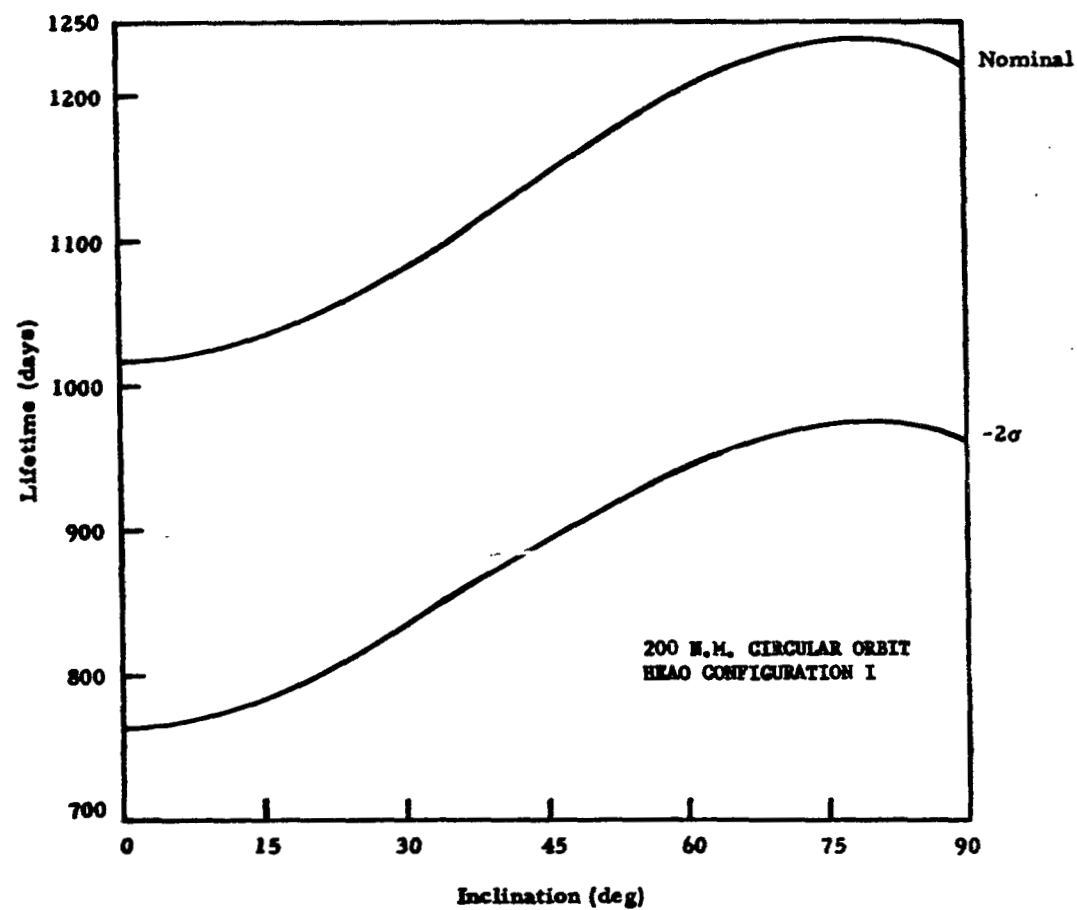
Figure IV-11.   Variation of orbit lifetime with inclination.
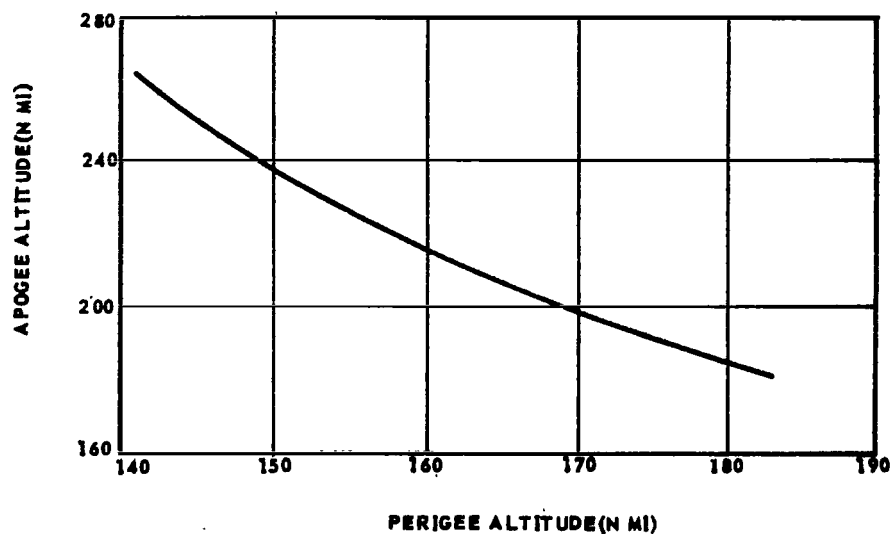
Figure IV-12. Apogee versus perigee altitude of HEAO Spacecraft with 1-year
orbital lifetime and +2σ solar activity.
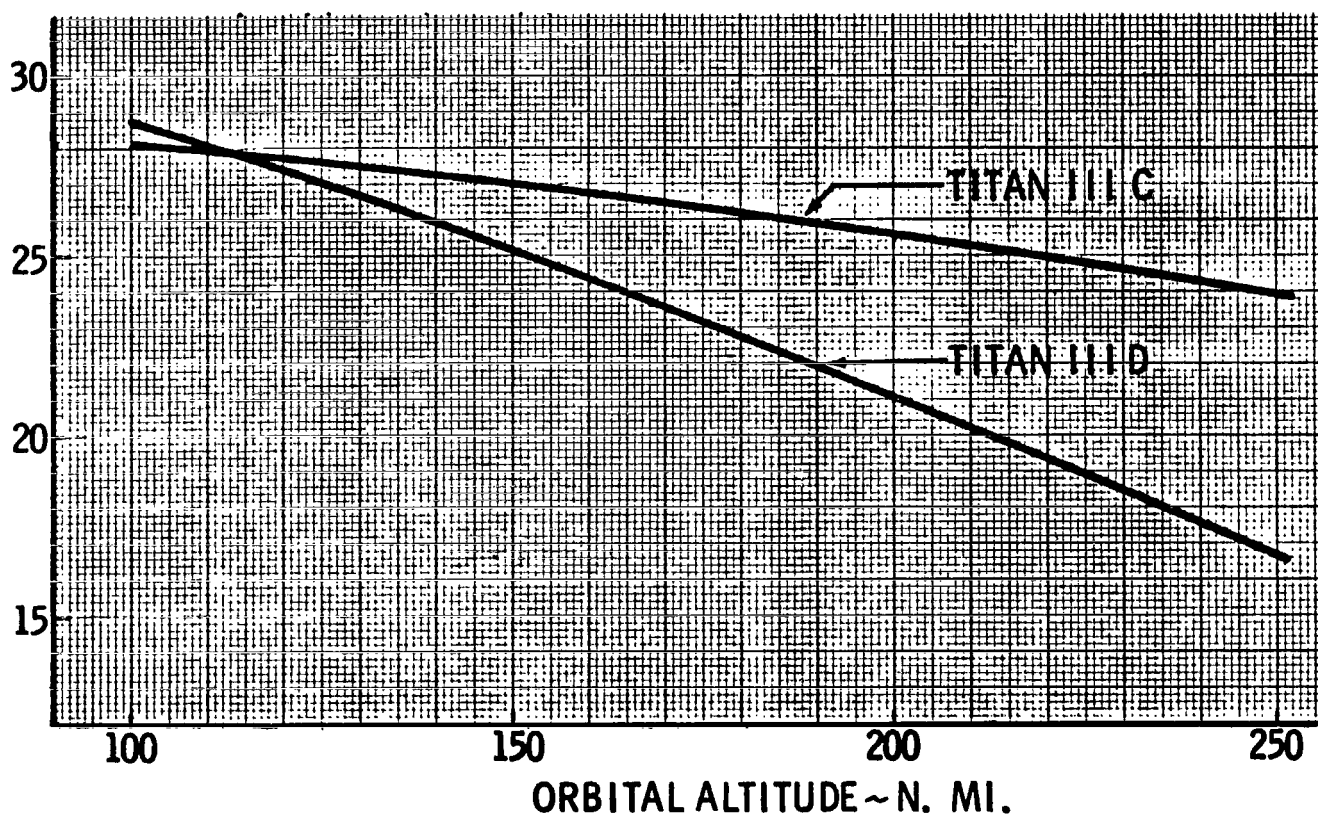
Figure IV-13. Titan IIID and IIIC performance-to-circular orbit
inclination 28.5 degrees.
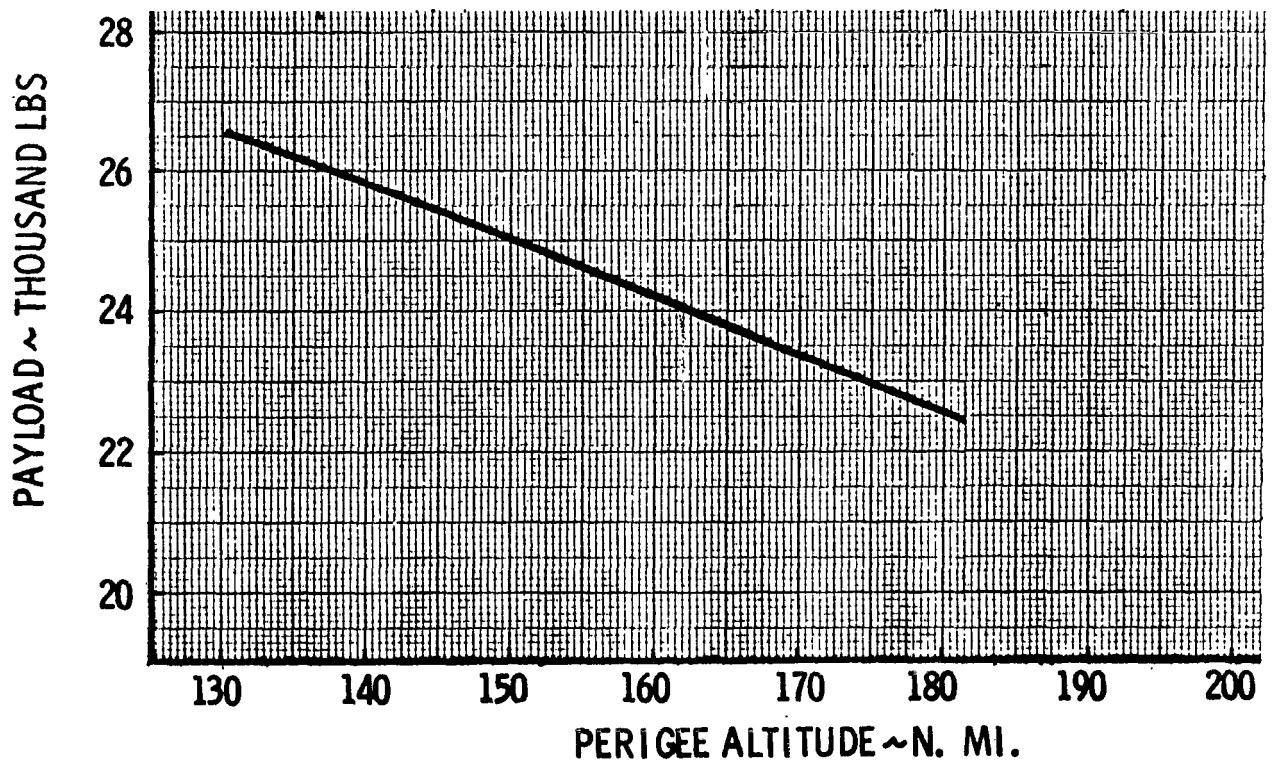
Figure IV-14. Titan IIID payload capability for elliptical orbit injection, orbit lifetime of 1 year with +2σ solar activity.

NORTHERLY LAUNCH   SOUTHERLY LAUNCH
—— NO YAW
---- YAW INITIATED AT 90 SECONDS AFTER LIFTOFF
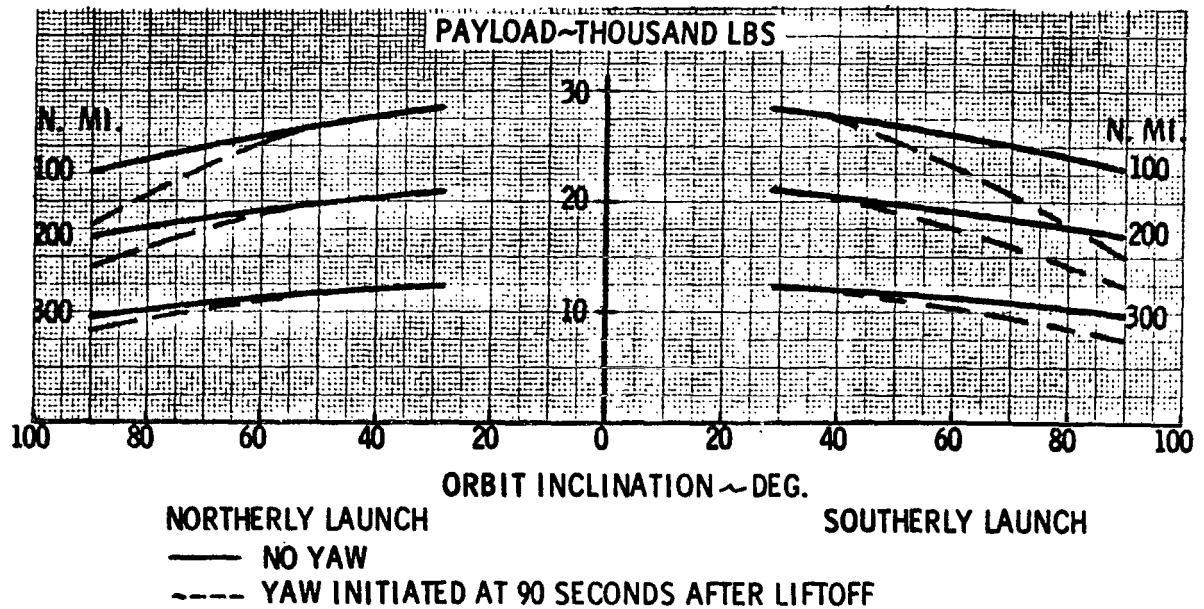
Figure IV-15. Titan IIID payload capability to circular orbit.
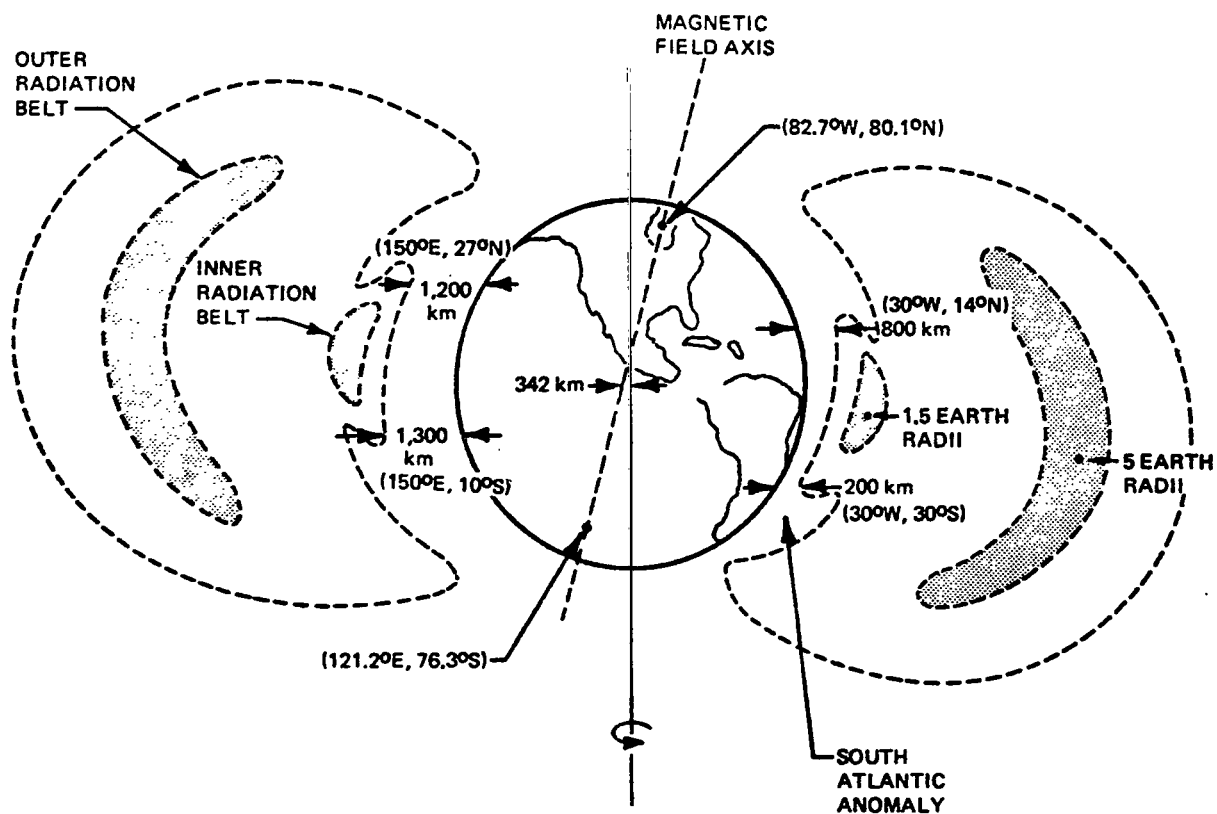
EXAGGERATED OUTLINES OF RADIATION BELTS. MAGNETIC FIELD AXIS APPROXIMATES LOCATION
OF AXIS OF AN OFFSET MAGNETIC DIPOLE. TRUE EARTH'S FIELD APPROXIMATES A DIPOLE, BUT IS
ASYMMETRICAL. CROSS-SECTION OF THE RADIATION BELTS IS IN THE PLANE OF THE 30°W GEOGRAPHI-
CAL MERIDIAN AND ILLUSTRATES RELATIVE ALTITUDES AT WHICH THE SOUTH ANOMALY PARTICLES
MIRROR IN THAT PLAN.

Figure IV-16. Van Allen Belts [1].
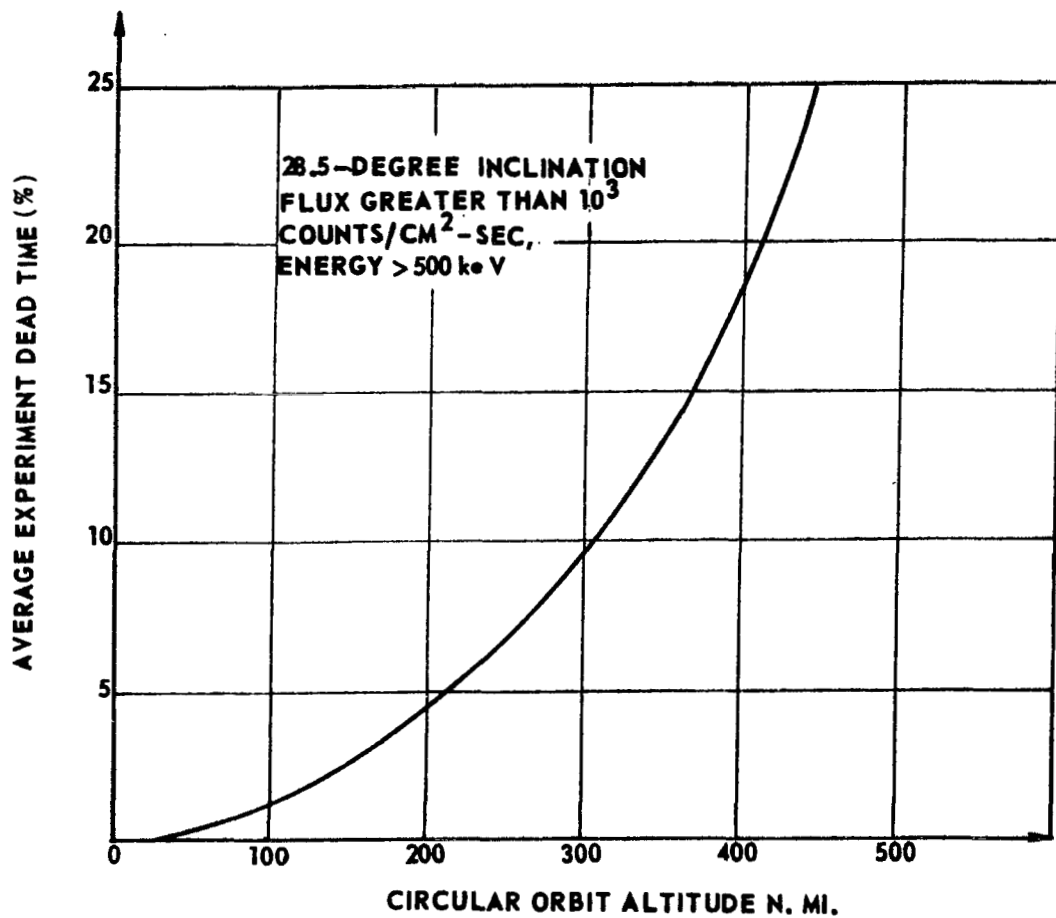
Figure IV-17.   Effect of orbit altitude on average
experiment dead time.
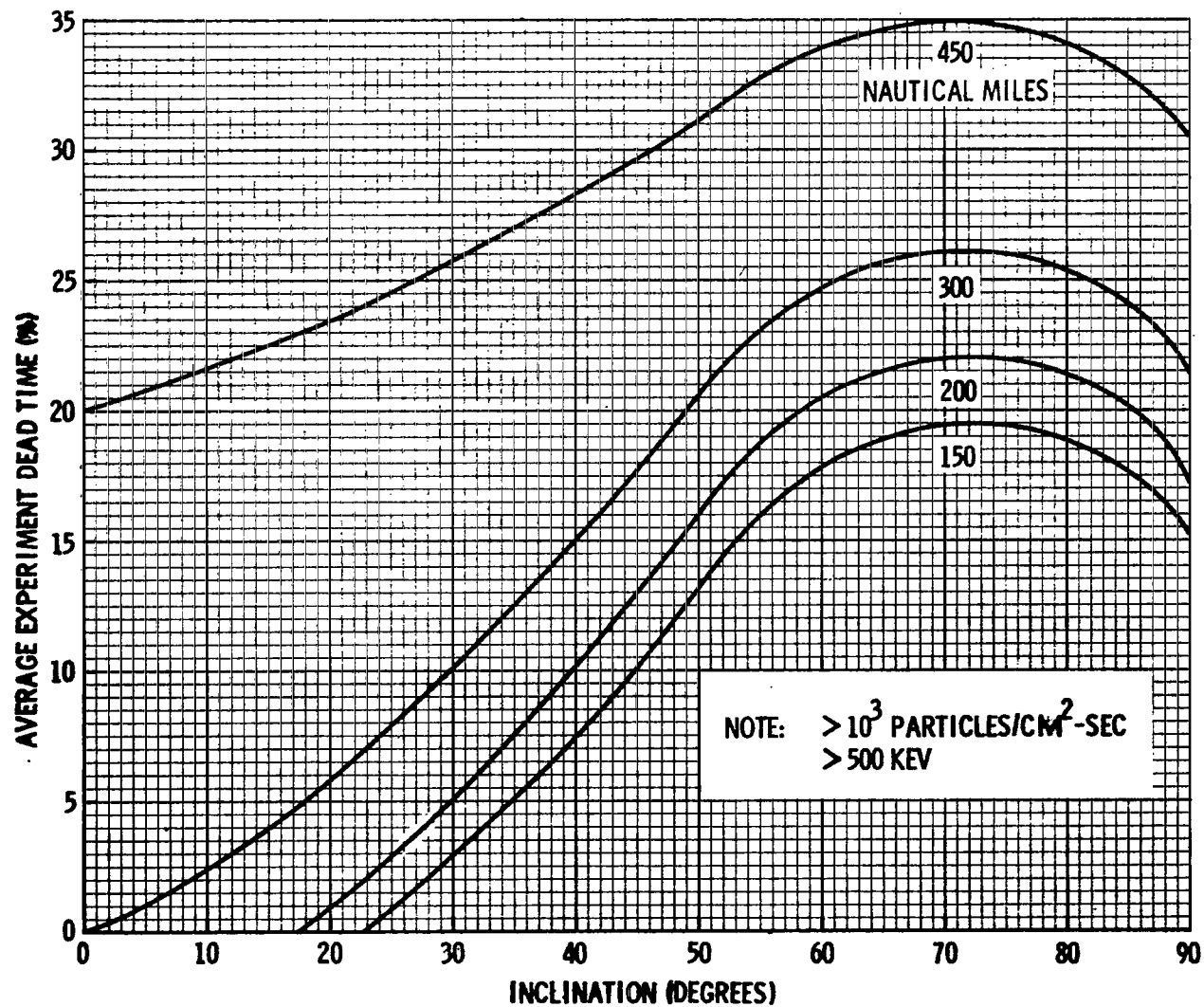
Figure IV-18. Effect of inclination on average experiment dead time.
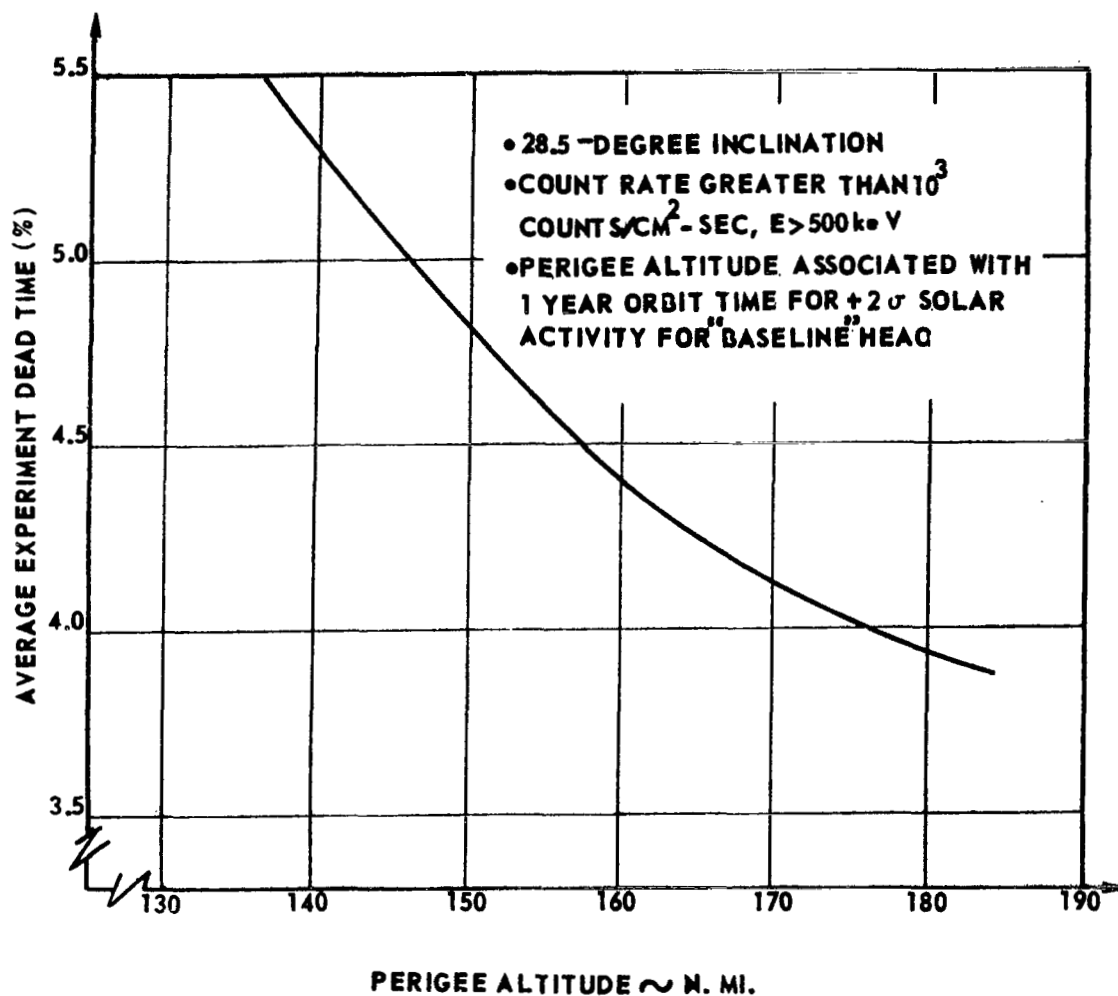
Figure IV-19. Effect of perigee altitude on average
experiment dead time.

SEQUENCE OF EVENTS (ORBIT ALTITUDE 200 N. MI.)

1 START SOLID ROCKET MOTORS AND LIFT OFF
2 CORE STAGE 1 IGNITION
3 SOLID ROCKET MOTORS JETTISIONED
4 CORE STAGE 1 STAGED AND CORE STAGE 2 IGNITION
5 SHROUD JETTISIONED
6 CORE STAGE 2 SHUTDOWN, STAGED, AND PAYLOAD INJECTED INTO ORBIT
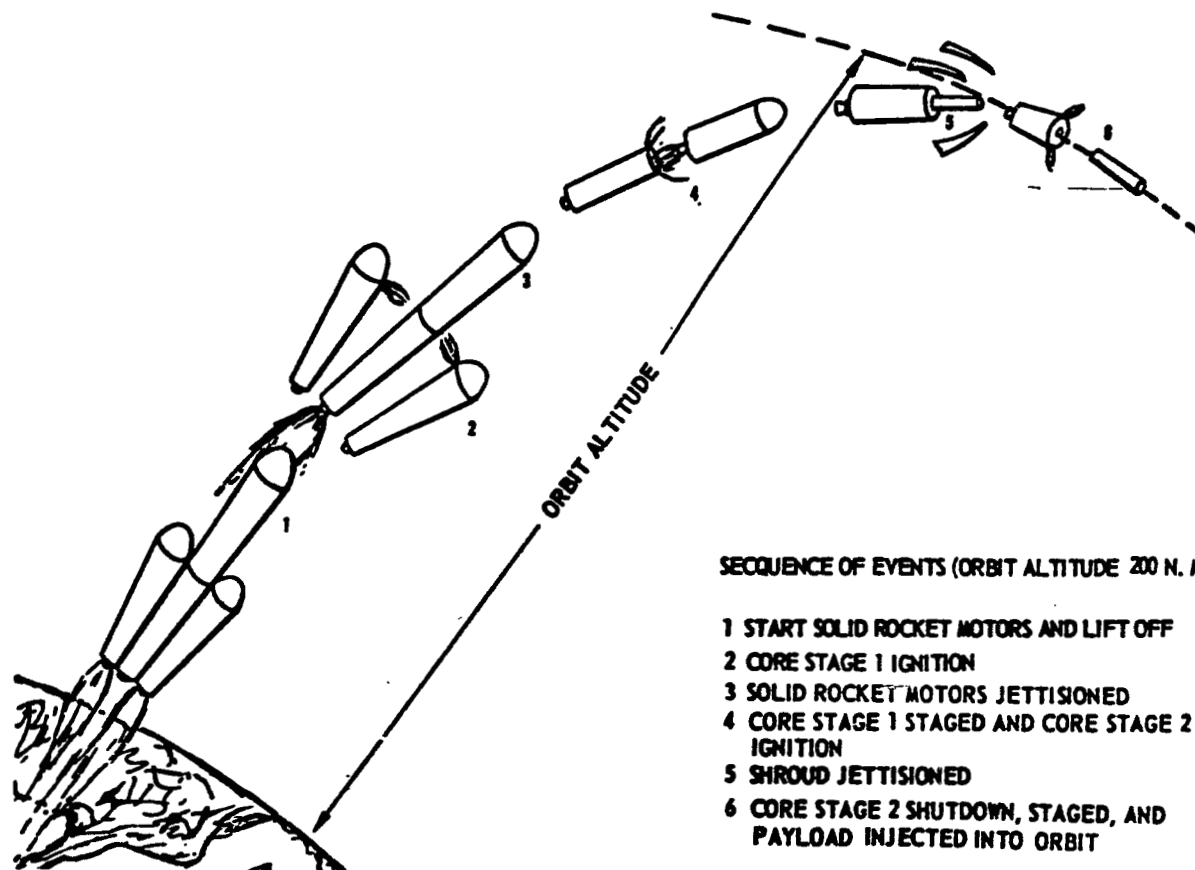
ORBIT ALTITUDE

Figure IV-20.   Typical Titan IIID launch-to-orbit profile.
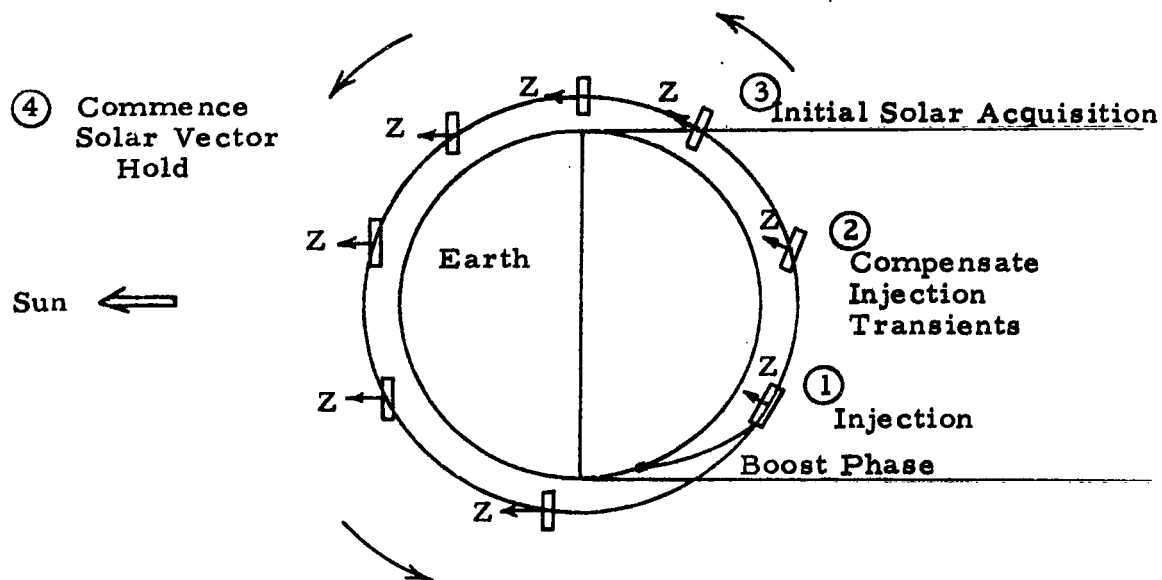
Figure IV-21. Initial orbital operations, the first orbit.
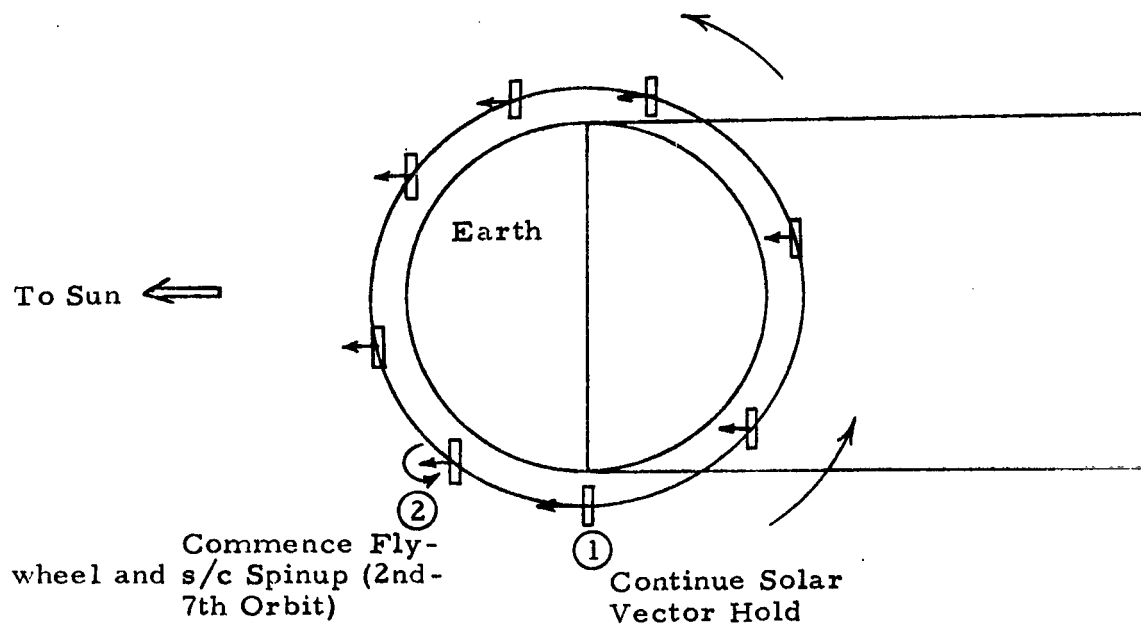
Figure IV-22. Initial orbital operations, the second through seventh orbits.
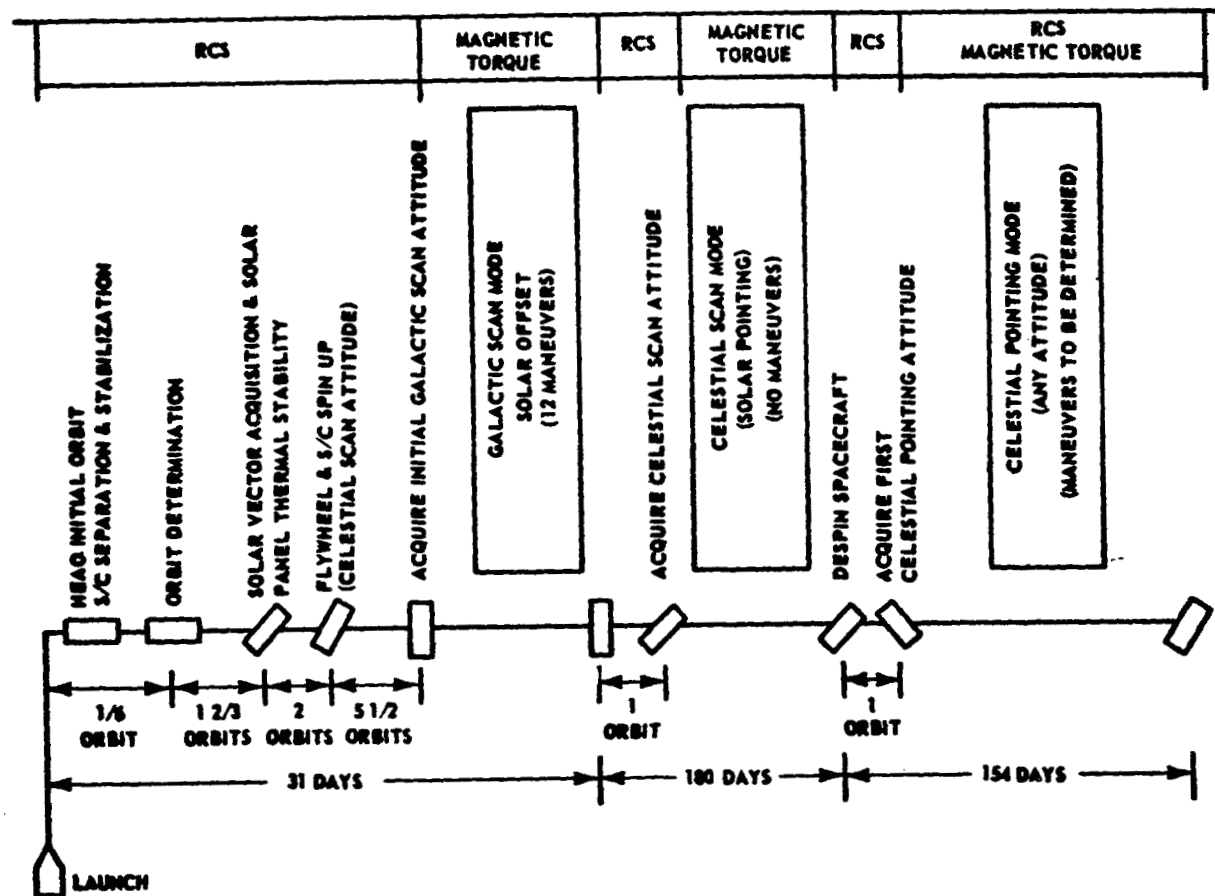
Figure IV-23. HEAO mission attitude control requirements.

Earth

To Sun ⇐

s/c Orbit

Off-Solar Vectors

Solar Vector

The s/c is rotated
to various angles
of off-solar-vector viewing to scan
the galactic plane. Each off-solar
vector is held for one or more orbits
(s/c spin rate is 0.1 rpm)
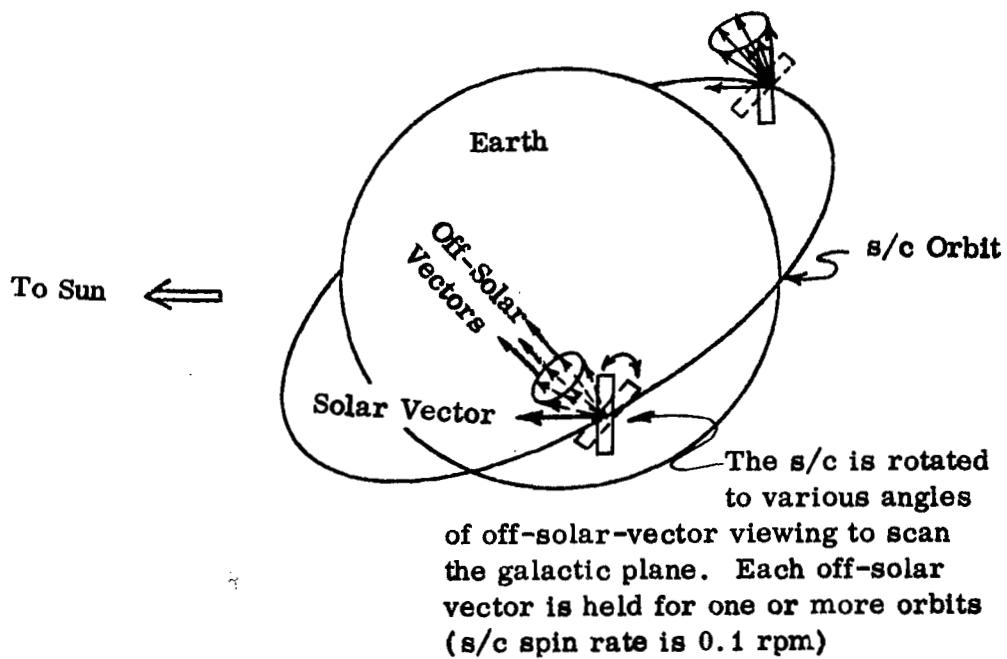
Figure IV-24. Major orbital operations: Galactic scan.

Earth

To Sun ⇐

The s/c
spin axis is
aligned with
the Earth-
Sun line.

s/c spin rate = 0. 1 rpm
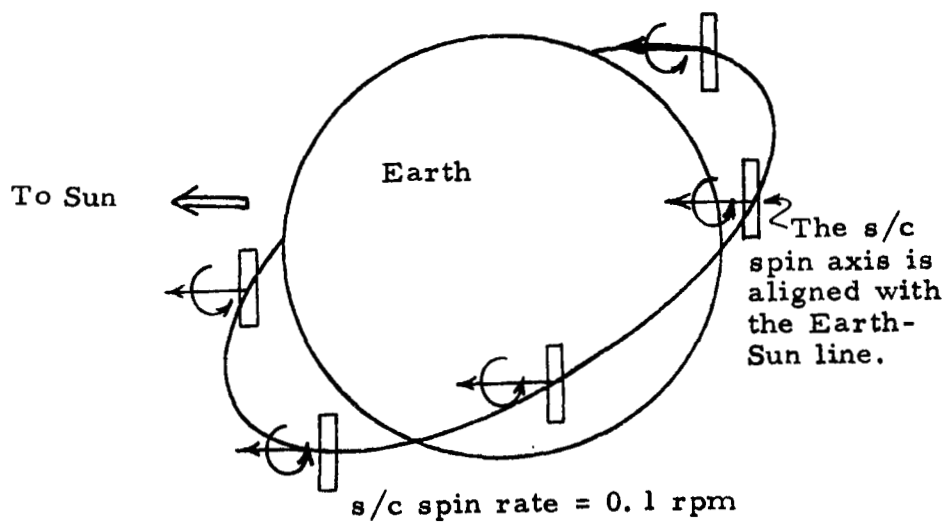
Figure IV-25. Major orbital operations: Normal celestial scan.

Earth

To Sun ⬅

The s/c is not
spinning. The
major axis is
aligned so that
the instruments
view the area
of interest.
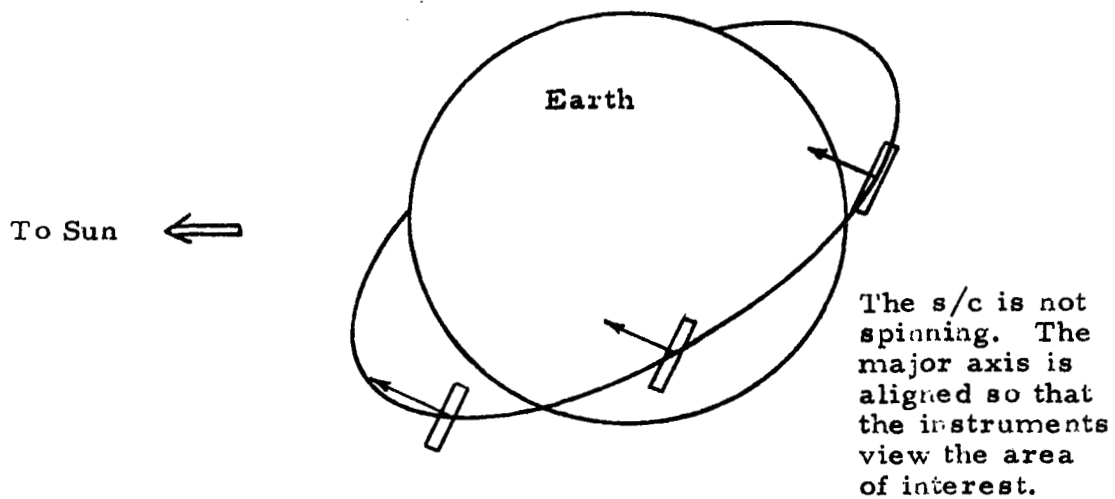
Figure IV-26. Major orbital operations: Celestial Pointing.

GALACTIC PLANE

TO SUN

EARTH

ECLIPTIC
PLANE

VIEWING DISK
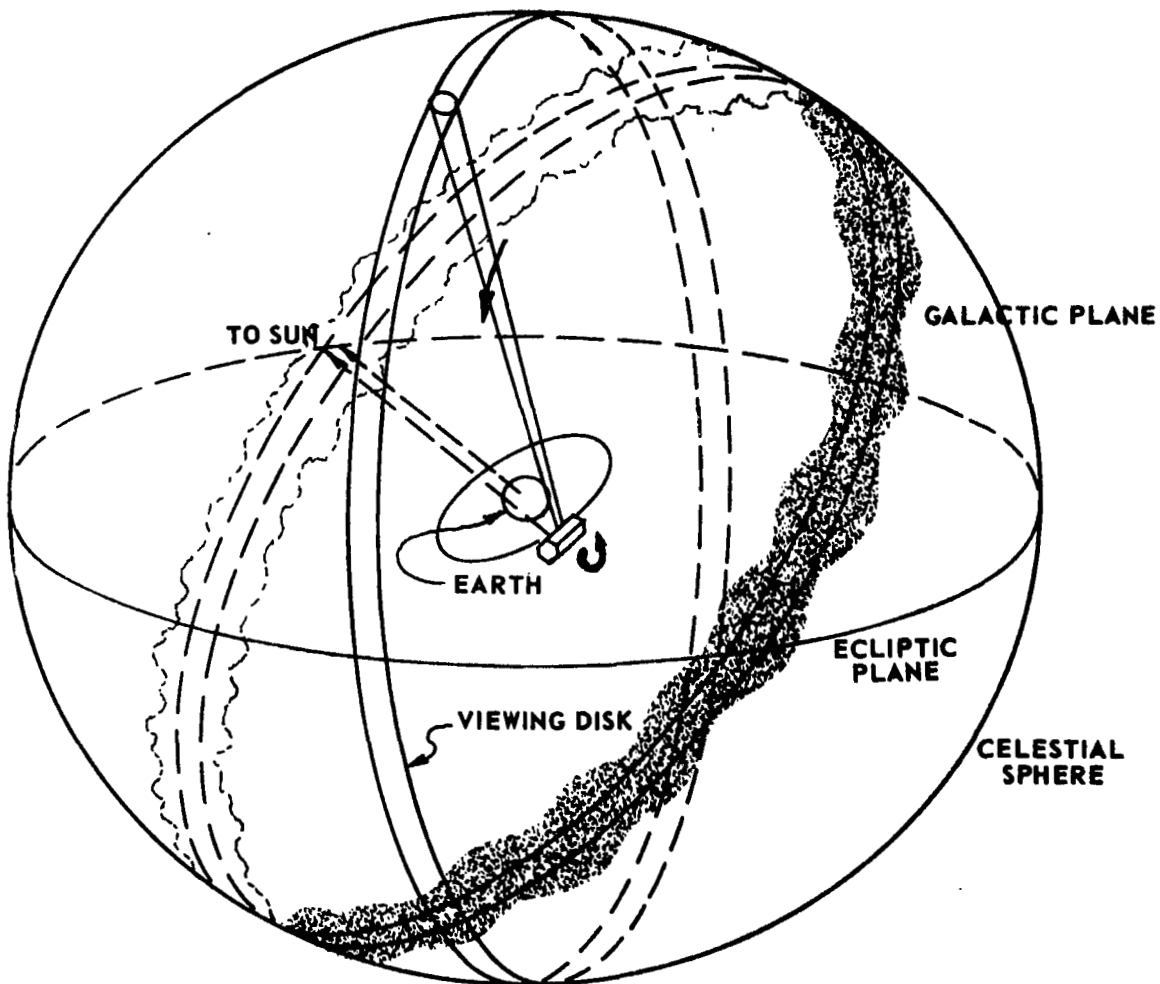
CELESTIAL
SPHERE

Figure IV-27. Scanning of the celestial sphere.
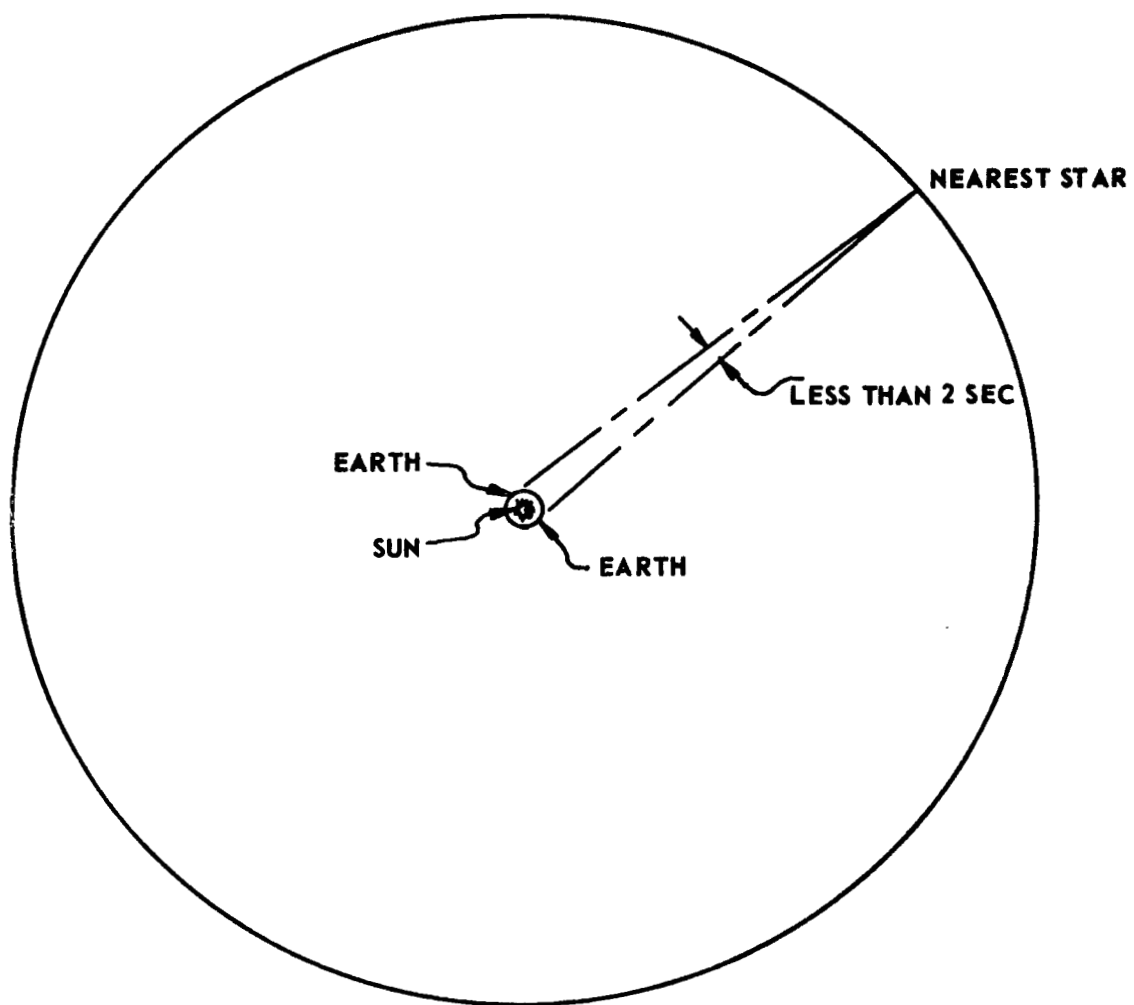
Figure IV-28. Stellar parallax.

GALACTIC PLANE

S/C SCAN RATE IS 0.1 RPM

₵ OF SCAN MOVES THROUGH 1 DEG/DAY

VIEWING DISKS

TO SUN

ECLIPTIC PLANE
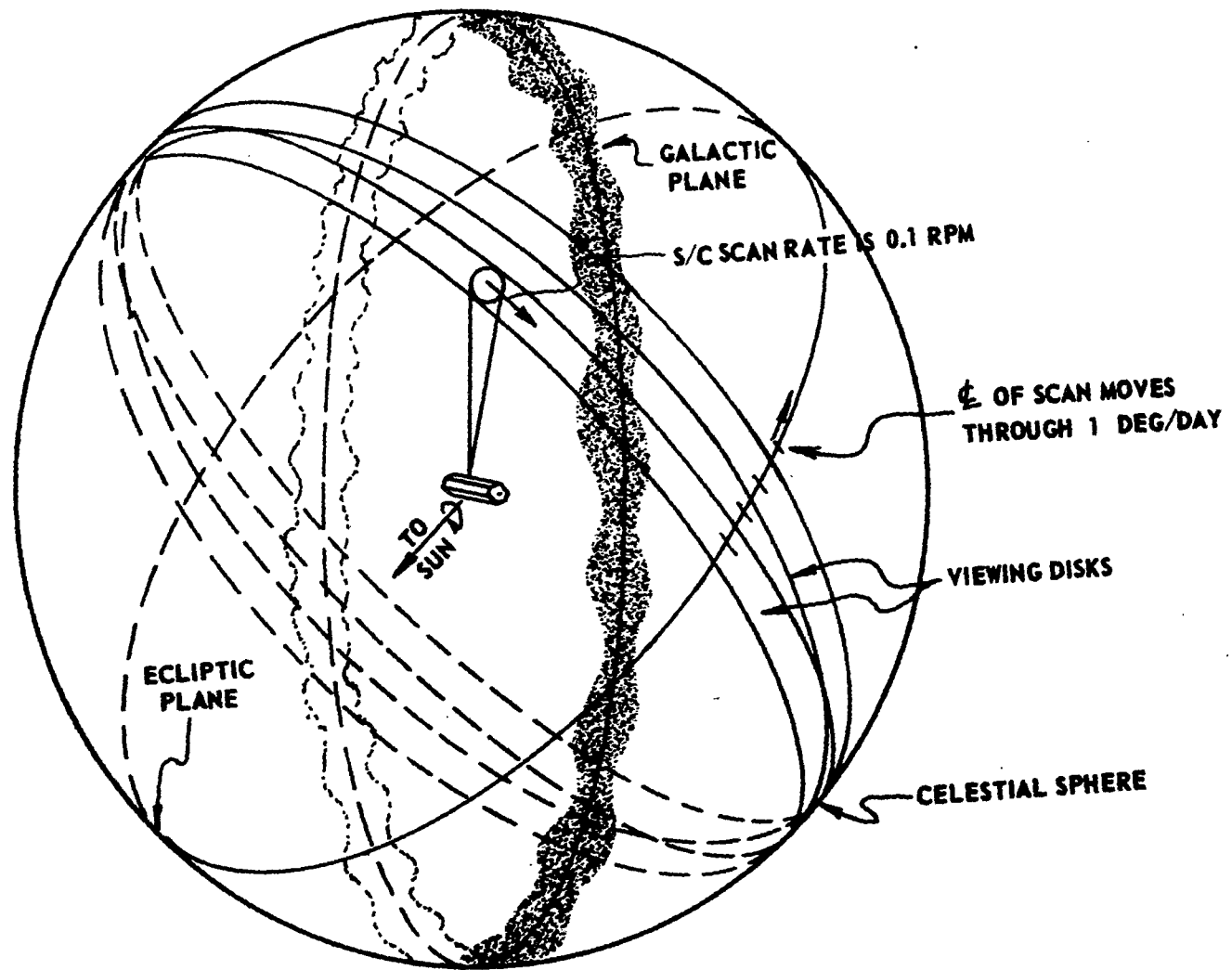
CELESTIAL SPHERE

Figure IV-29. Solar-vector-oriented scan mode.

SCAN PATH OF OCTOBER
6 (OR APRIL 3)

SCAN PATH OF
SEPTEMBER 6 (OR MARCH 4)

GALACTIC PLANE

JUNE 19

ECLIPTIC

MARCH 21
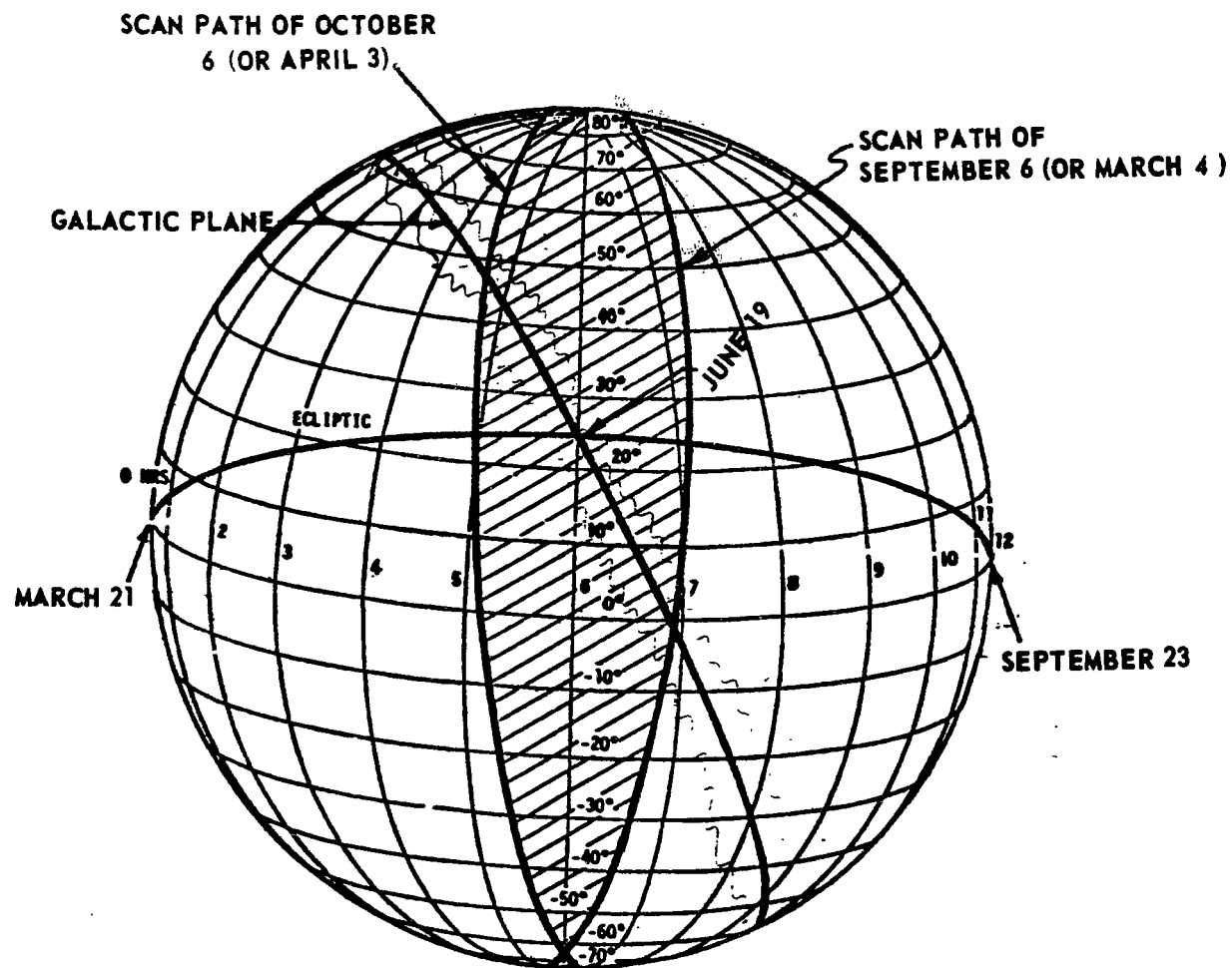
SEPTEMBER 23

Figure IV-30. Scanning pattern on the celestial sphere from September 6 through
October 6 (or March 4 through April 3).
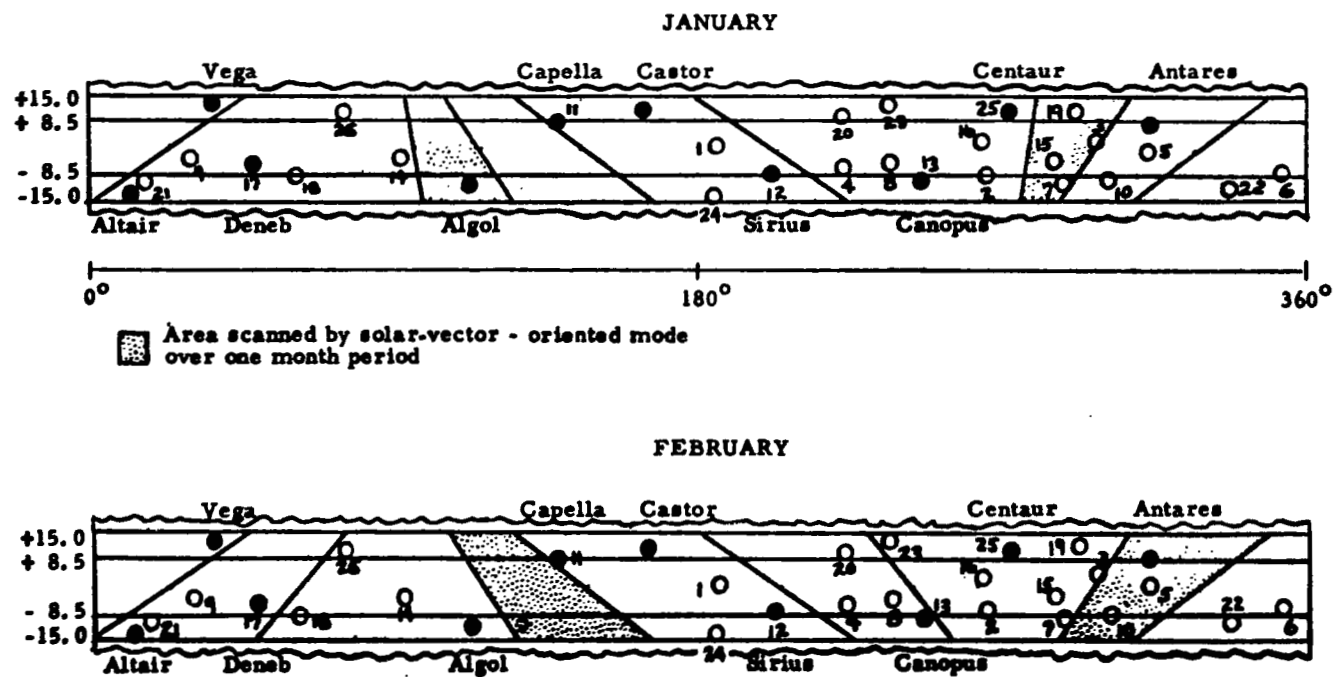
Figure IV-31.   Scanning of galactic plane for experiment iniation in January and February.
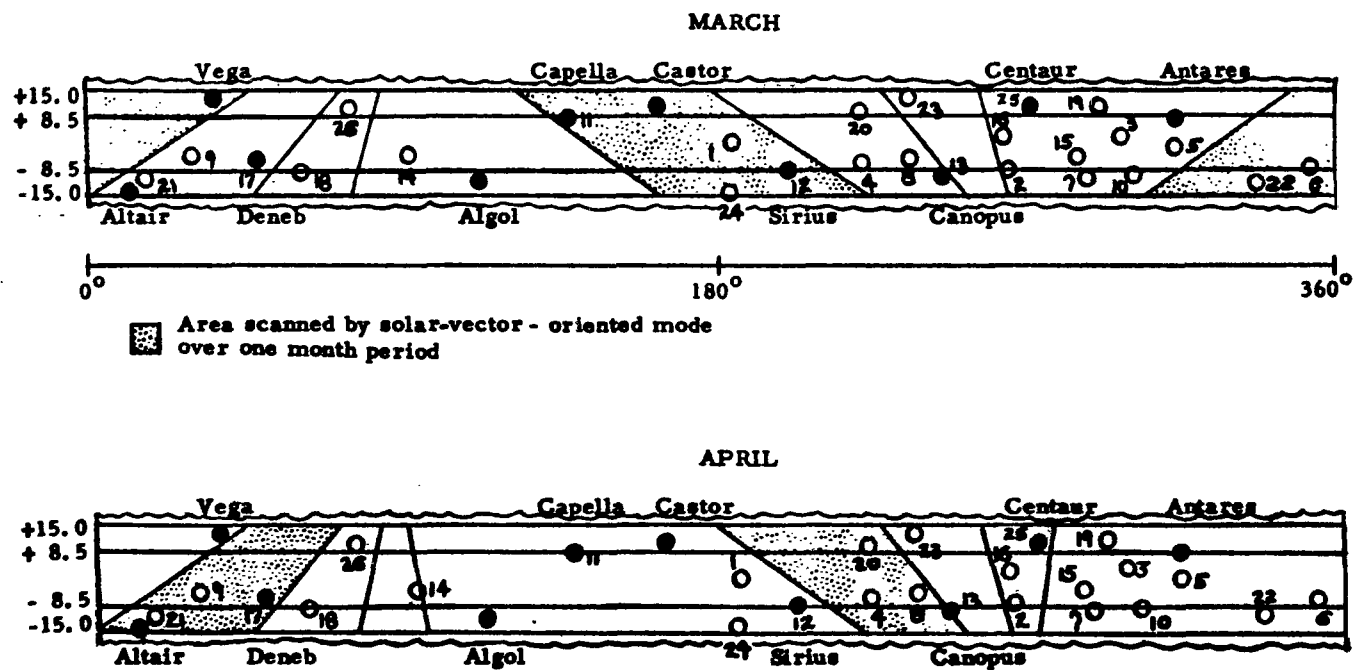
Figure IV-32. Scanning of galactic plane for experiment initiation in March and April.
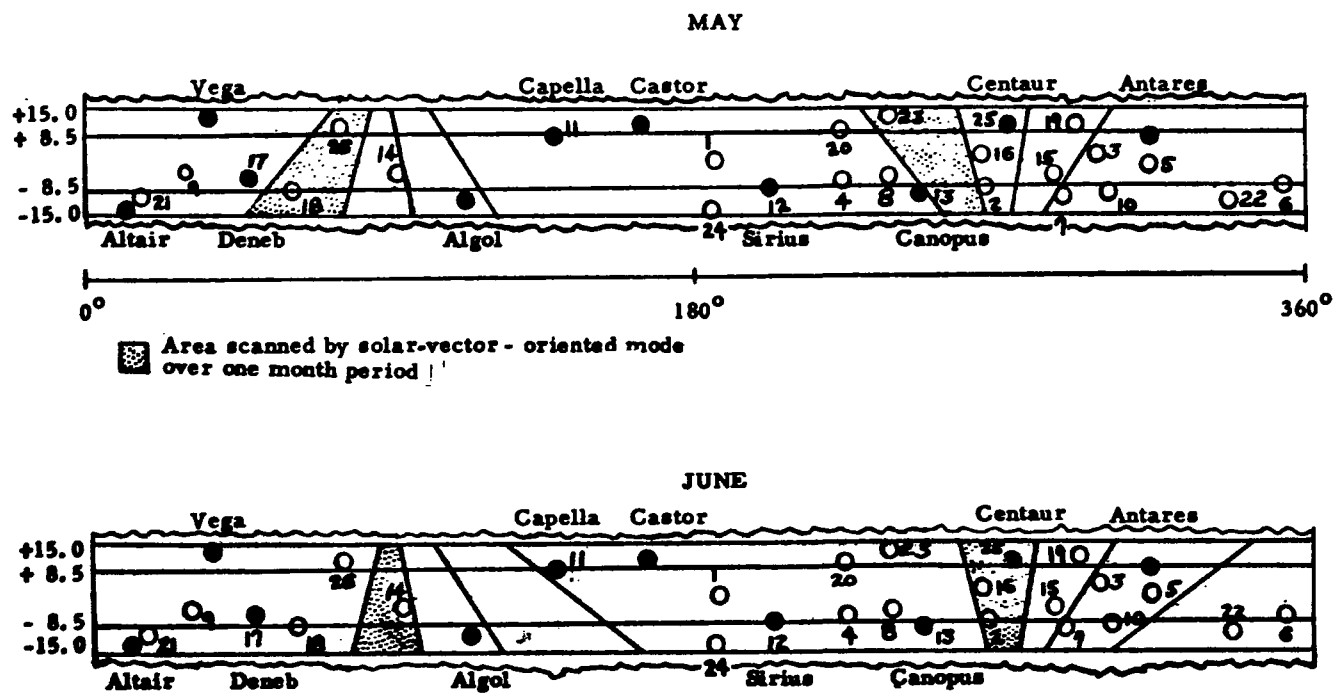
Figure IV-33. Scanning of galactic plane for experiment initiation in May and June.
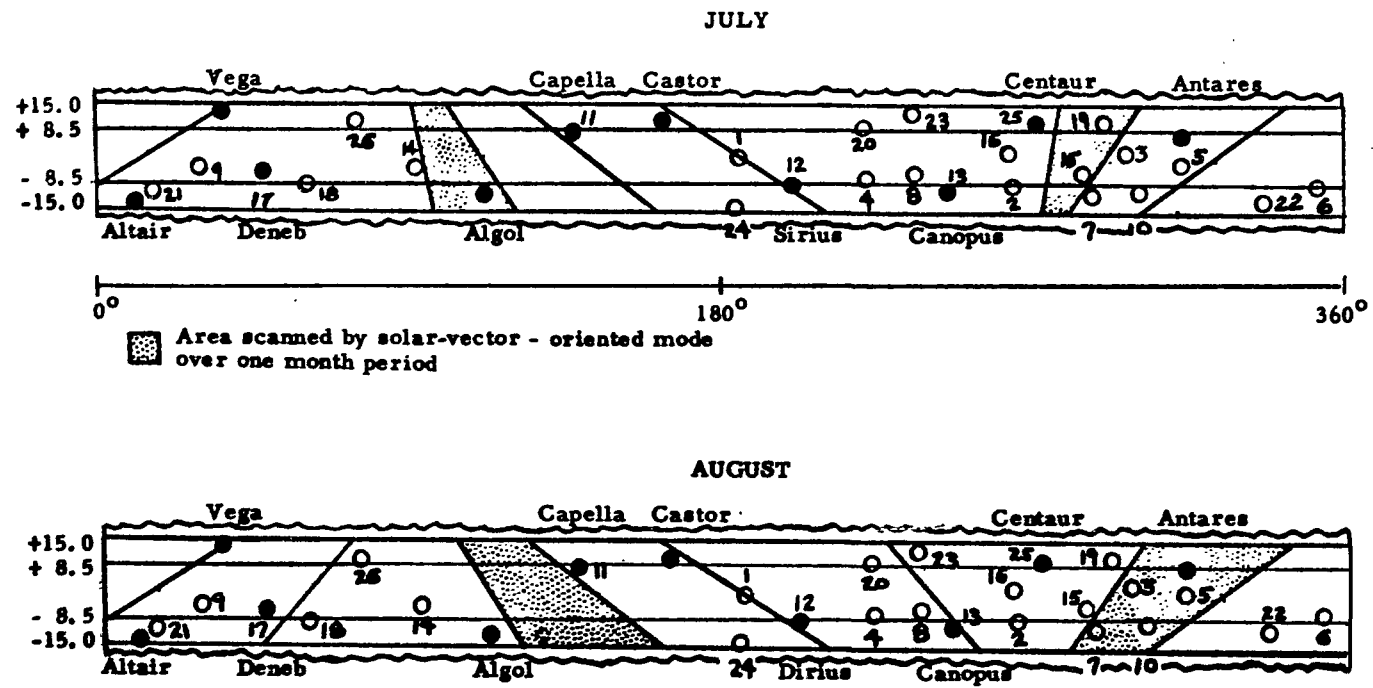
Figure IV-34. Scanning of galactic plane for experiment initiation in July and August.

SEPTEMBER

Area scanned by solar-vector - oriented mode
over one month period
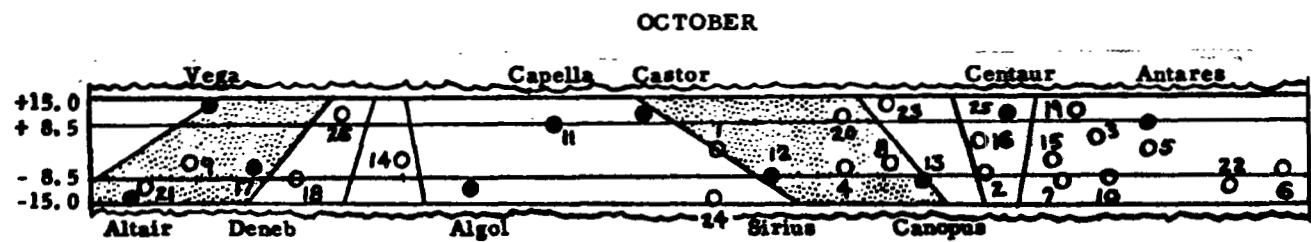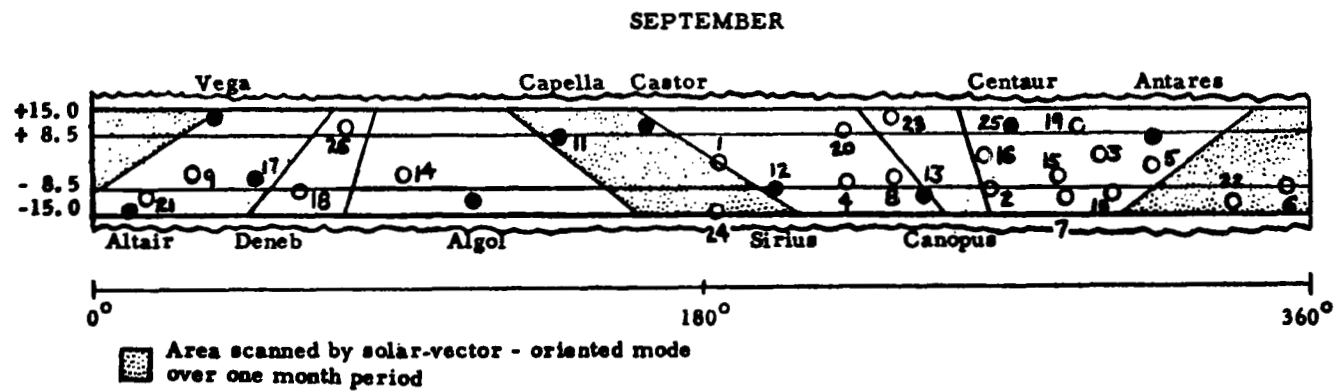
OCTOBER

Figure IV-35. Scanning of galactic plane for experiment initiation in September and October.

4-47
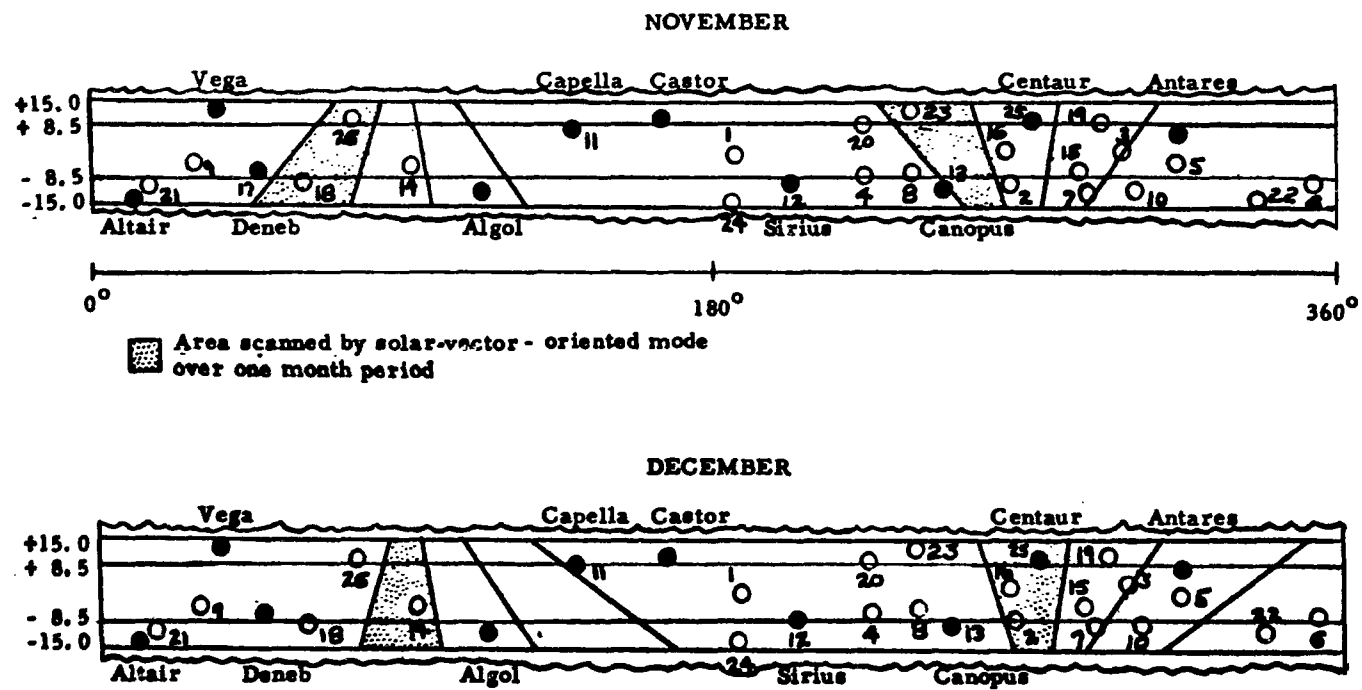
Figure IV-36. Scanning of galactic plane for experiment initiation in November and December.

REFERENCES

1. Smalley, V. G.; Smart, D. F.; and Filz, R. C.: Corpuscular Radiation
   Environment of a Low-Altitude, Polar-Orbiting Earth Satellite — A Brief
   Summary. Air Force Report Number CRL-66-540, 1966.

SECTION V. SPACECRAFT DESIGN

TABLE OF CONTENTS

LIST OF ILLUSTRATIONS

LIST OF TABLES

SECTION V. SPACECRAFT DESIGN

A. General Considerations N 70 - 22905

During this study, several competing approaches were examined for each aspect of the mission and hardware design. A concept was selected for further analysis and design; this concept was designated as the "baseline." The term "baseline" does not infer selection of the concept for final design; it merely designates the one to which the most detailed effort was devoted in the Phase A study. Unless otherwise noted, the discussion in this section applies to the baseline. The alternate concepts are discussed in the appendixes.

The primary objective of the mission is to operate a group of X-ray, gamma-ray, and cosmic-ray experiments in earth orbit aboard an automated spacecraft for 1 to 2 years and perform celestial scanning and pointing maneuvers. The specific experiments to be flown on this mission have not been chosen; therefore, a representative group of six scientific experiments was selected as the basis for spacecraft design. Total experiment weight is 12 500 pounds.

The spacecraft will rotate slowly about its scan axis to permit the experiments, which will be hard-mounted to the spacecraft, to scan the celestial sphere. The scan axis will be aligned within 1 degree of the solar vector during most of the mission. Operation of the spacecraft in this mode will permit the experiments to scan the entire celestial sphere in 6 months. The solar panel area provided on the spacecraft must permit the deviation of the scan axis off the solar vector for galactic belt scanning and pointing maneuvers while still sustaining the average electrical load. Off-solar vector viewing is necessary early in the mission to get early data from sources in the galactic belt and later in the mission to point the experiments at particular celestial sources for uninterrupted viewing.

To provide the required orbital lifetime, an initial orbital altitude of 200 n. mi. was selected. If a spacecraft having the weight and size of the present conceptual design is placed into this orbit, its nominal orbital lifetime is expected to be approximately 2.94 years, and the probability is only 0.02 percent that its orbital lifetime will be less than 1.0 year. An orbital inclination of 28.5 degrees was chosen for maximum payload.

B. Baseline Configuration

1. <u>Layout.</u> The major variables in spacecraft configuration are the experiment location, the solar panel arrangement and location, the structural support and arrangement, and the systems layouts.

The most significant factor in determining the overall dimensions of the baseline configuration is the Titan IIID launch vehicle payload envelope. The shroud dimensions dictated a spacecraft roughly cylindrical in shape in the launch configuration. To obtain a spacecraft of high reliability, simple design, and small aerodynamic drag, the use of a minimum number of moving and deployable parts was stressed. These considerations resulted in the selection of a baseline configuration having no large foldout members and having an approximate cylindrical shape in flight as well as in the launch configuration. The baseline configuration is illustrated in Figure V-1. The alternate configurations are discussed in Appendix D.

The baseline HEAO spacecraft has an octagonal shape. The maximum cross-section dimension is 105 inches; the dimension between opposite faces is 97 inches; and the width of each octagonal face is 40.2 inches. The spacecraft length is 30 feet; and the maximum payload design weight is 20 920 pounds. Three of the octagonal sides are covered by solar cells mounted on 0.375-inch honeycomb sandwich panels. The remaining outer surface of the spacecraft is covered by 0.025-inch-thick aluminum sheet, except for experiment cutouts.

The octagonal cross-sectional shape of the baseline configuration was chosen for several reasons. Flat surfaces on opposing sides of the spacecraft facilitate flush mounting the large area X-ray detector modules. The center solar panel is mounted on one of the sides normal to the scan axis; the other two solar panels are on sides adjacent to the center panel. To generate the maximum electrical power, a maximum projected array area must be provided perpendicular to the solar vector. At the same time, interior volume of the spacecraft must be adequate to contain all the experiments plus the required spacecraft systems. Appendix H gives a comparison of the projected areas available for solar panels for several different spacecraft cross-sectional shapes. The baseline power budget is summarized in Table IX-1. The octagonal shape provides a large projected side area, flat surfaces for experiment mounting, and a large interior volume.

The baseline spacecraft configuration has a relatively high ballistic coefficient and, therefore, a long orbital lifetime. One disadvantage
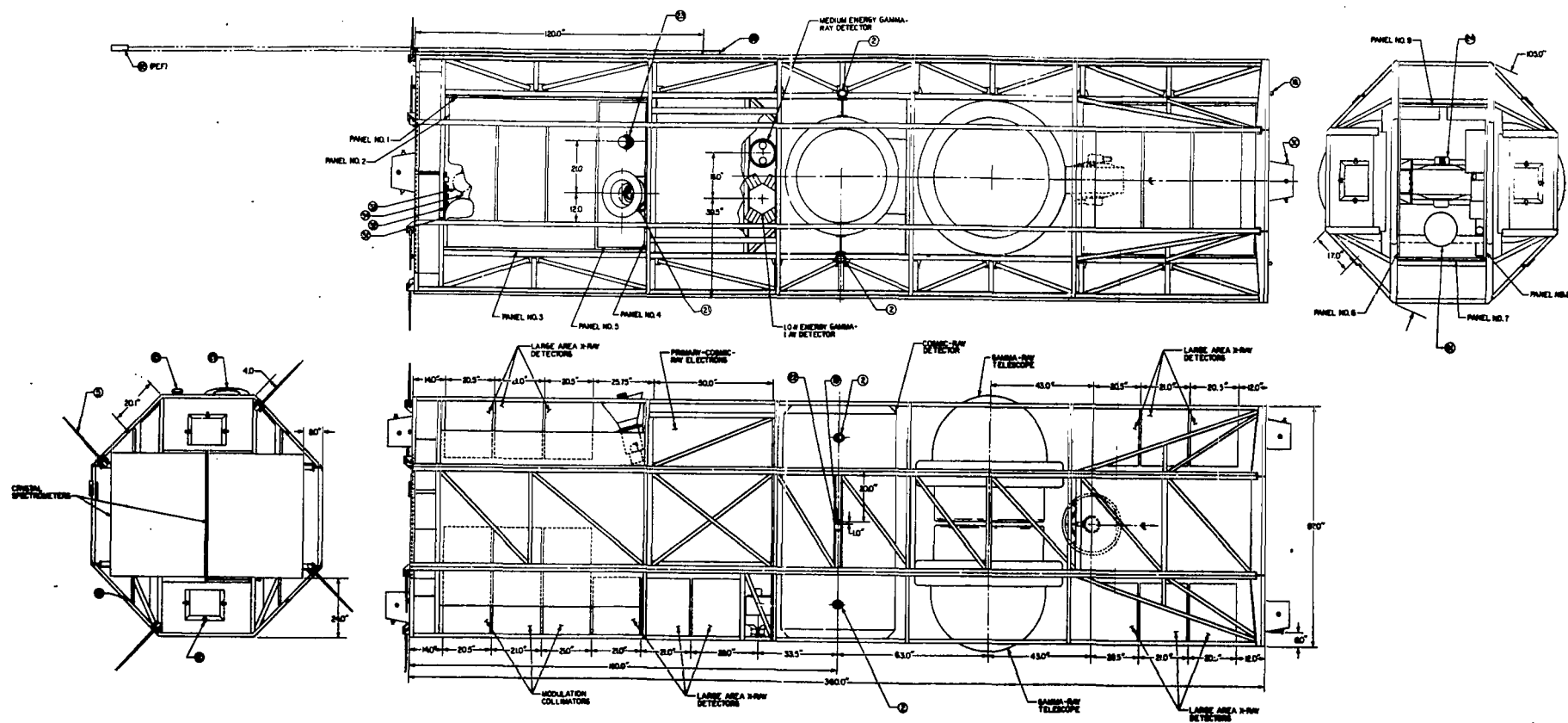
Figure V-1. Baseline spacecraft configuration.

PANEL NO 8

PANEL NO. 4

PANEL NO 9
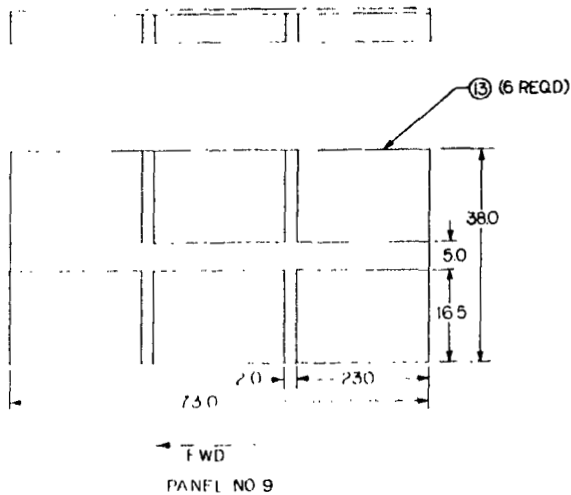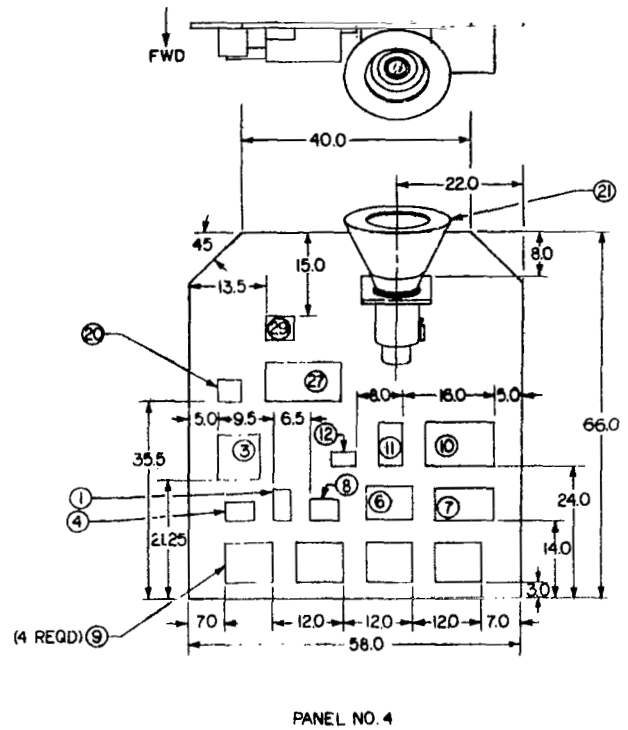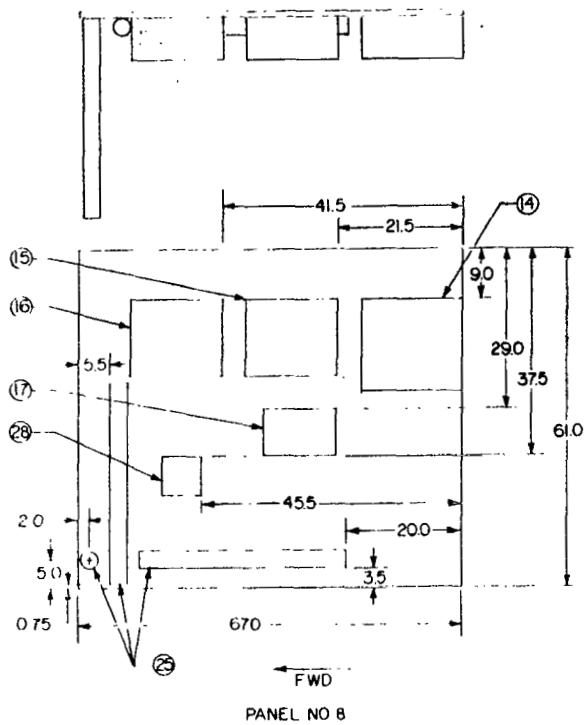
Figure V-1. (Concluded)

5-5

of the baseline configuration is that the mass moment of inertia about the longitudinal principal axis is much lower than the moments about the other two principal axes. This results in higher gravity gradient torques acting to disturb spacecraft attitude than if the moments about all three principal axes were more nearly equal.

One side of the spacecraft will face the sun and will contain the solar cells. The experiments will be hard-mounted to the spacecraft, allowing the experiments to scan in a plane perpendicular to the solar vector. Some consideration was given to mounting one or more of the experiments so that they would point along the scan axis away from the solar panels. Such a mounting would permit these experiments to point at a single position in the sky, or to sweep out a band centered in the ecliptic at the apparent rate at which the sun moves, while the other instruments were scanning at the rotation (scan) rate of the spacecraft; however, the disadvantages of this arrangement is that these scan-axis-pointed experiments would sweep only a small portion of the celestial sphere during the time that the other instruments are sweeping out the entire sphere. Also, it is desired that the experiments point in as few different directions as possible to facilitate pointing the experiments at specific targets with the least number of reorientation maneuvers. Hence, all of the experiments are located to view in the X-Y plane, which is perpendicular to the spin axis. The two Bragg crystal X-ray detectors are located in one end of the space-craft. Two of the heaviest experiments (gamma-ray telescope and cosmic-ray calorimeter) are mounted near the geometric center. The motivation for this arrangement is the reduction of the moments of inertia which result. This consideration is of particular importance in reduction of gravity gradient torques. The location of the next heaviest experiment (X-ray detectors) is largely constrained by the requirement for two viewing directions. These constraints are discussed in detail in Appendix A. The remaining spacecraft volume is available for location of the subsystems. The flywheel represents one of the more difficult problems because of its size.

To reduce spacecraft deflection during launch without increasing structural weight, a different packaging arrangement with the heavy experi-ments mounted near one end (bottom end during launch) was considered (Fig. V-2), although the center-experiment arrangement was kept as the base-line. The moments of inertia which result are discussed in a later paragraph. The structural considerations are discussed in Appendix E.

Figure V-2. Layout of baseline configuration with bottom-mounted experiments.

The RCS thrusters are located on both ends of the spacecraft. Exhaust impingement on the experiments and solar cells is avoided by the specific location and orientation selected.

An approach has been selected which permits the use of passive thermal control and provides flexibility for internal layout of the systems in the spacecraft. Passive thermal control is provided through use of thermal coatings, insulation, and location and packaging of equipment (a limited number of electrical heaters will also be required).

A summary of the subsystems components to be incorporated in the baseline has been tabulated and shown in Table V-1. (Columns in this table were left blank where data were not available.) The equipment will be mounted directly to internal equipment-mounting assemblies. Location of subsystem components is illustrated in Figure V-1. It will probably be necessary to thermally isolate equipment from the structure to reduce thermal distortion and help control temperature.

The payload support ring on the Titan IIID has 36 holes for attaching the payload to the launch vehicle. The HEAO configurations defined herein have 8 points available for attaching to the launch vehicles. Therefore, a payload truss is provided to support the payload and adapt it to the launch vehicle.

2. Mass Characteristics. The mass characteristics are based on a total spacecraft weight of 20 920 pounds. This weight was selected on the basis of the launch capability of the Titan IIID vehicle. Thus far, only 18 884 pounds of spacecraft weight has been identified; however, it is expected that the weight margin will decrease as the design progresses.

The HEAO weight summary is given in Table V-2. These data do not include selected redundancy which will probably be recommended as a result of reliability analyses to be performed later. A 2036-pound margin (10 percent) is available for growth, but this growth margin will be partially consumed as redundancy is added.

The system inertias given below are based on the total 20 920-pound payload capability, with the margin distributed to each end of the spacecraft.

Coordinate System. The mass characteristics are defined in terms of a set of body coordinates, X, Y, and Z, drawn through the CG of the spacecraft:

TABLE V-1. SYSTEM EQUIPMENT LIST

Identification Number		Number Required	Unit Weight (lb)	Unit Size (in.)	Unit Power Required (W)	Percent Operating Time	Unit Heat Dissipated (W)	Operational Temperature Allowed (°F)
	COMMUNICATIONS AND DATA HANDLING SYSTEM							
1	S-band transmitter	2	9.5	8 × 5 × 4	220 maximum (each)	5 min/orbit	200 each	0 to 100
2	S-band antenna	4	1	4.2 diam.	N/A	5 min/orbit	N/A	0 to 100
3	Power combiners and diplexer	1	26		N/A	Continuous	N/A	0 to 100
4	Command receiver	2	1.25	3.5 × 5 × 1.25	4	Continuous	2	0 to 100
5	VHF antenna	4	1	22 long	N/A	Continuous	N/A	0 to 100
6	Command decoder	1	6	8 × 6.25 × 2.5	4 maximum	Continuous	4	0 to 100
7	Digital multiplexer	1	8	6 × 6 × 10	5 maximum	Continuous	5	0 to 100
8	Analog signal conditioner	1	3	4 × 4 × 5	8 maximum	Continuous	8	0 to 100
9	Tape recorder	4	15	5.4 × 8.1 × 7.1	25 maximum (play) 5 minimum (record)	5 min/orbit Continuous	25 5	30 to 100
10	Switching network	1	10	8 × 8 × 12	8 maximum	Continuous	8	0 to 100
11	Diagnostic logic	1	4	4 × 4 × 8	3	Continuous	3	0 to 100
12	Minitrack beacon transmitter	2	0.4	0.82 × 2.1 × 4.8	4 maximum (each)	Continuous	4	0 to 100
	Cable and connectors		30	-	-	Continuous	-	0 to 100
	ELECTRICAL POWER SYSTEM							
	Solar modules	84	3.5	19.75 × 25.00 × 0.375		60 to 67		
13	Charger-battery regulator module	6	110	23 × 16.6 × 5		~100	74 day 64 night	32 to 86°F preferably 32 to 68°F
14	Power distributor	1	35	17.25 × 16.25 × 7.65	20		20	
15	Control distributor	1	25.5	16 × 14 × 7.5	20		20	
16	Solar Power distributor	1	35	16 × 14 × 7.5	20			
17	Switch selectors Cables & Connectors	1	20 150	12.5 × 8.5 × 5.5	20		20	
	ATTITUDE SENSING AND CONTROL SYSTEM							
18	Coarse Sun sensors	8	1	1 diam. × 5/8	-	5		-40 to 158
19	Fine Sun sensor	1	2	1 × 2 × 1/2	-	100		-67 to 122
20	Summing network	1	3	4 × 4 × 4	4	100	.4	

TABLE V-1. (Concluded)

Identification Number		Number Required	Unit Weight (lb)	Unit Size (in.)	Unit Power Required (W)	Percent Operating Time	Unit Heat Dissipated (W)	Operational Temperature Allowed (°F)
21	Star mapper	1	15			100	5	-45 to 165
	Star mapper electronics			7 diam. × 16	10	100		-45 to 165
22	Digital sun sensor and electronics	1	3 2	3 × 3 × 1 5 × 7 × 2	2	75	2	-57 to 185
23	Star tracker	1	15	5 diam. × 11		100	5	-45 to 165
	Star tracker electronics	1			10	100		-45 to 165
	*Earth horizon sensor	2	30	10 × 10 × 10	20	80		-30 to 165
24	Flywheel (CMG rotor)	1	240		458 start 40 running	100	55	
25	Magnetic coils and Mounting hardware	3	87	3 diam. × 36	34		100	
26	Magnetometer and Boom	1 unit	17	10 × 5 × 5	2	100	2	
27	Signal Processor (Including computer)	1	40	6 × 7 × 13	50		55	
28	Rate gyros with electronic modification	3	2.33	2 diam. × 3.5	57 start 12 running		12.4	
29	Star tracker high voltage supply	1	2	4.8 × 4.9 × 2	20			
30	PROPULSION (RCS) SYSTEMS Thruster modules	4	3.75					+35 to +350
31	Propellant tanks	2	7.5	10" diam. sphere		N/A		+35 to +350
32	Propellant valves and lines	2 units	3.5					+35 to +350
33	Propellant pressurization tank	1	46	21 diam. sphere				-65 to +350
34	Propellant pressurization valves, lines, and reg.	2	2.5					+35 to +350

*Alternate

TABLE V-2. HEAO WEIGHT SUMMARY

Experiments	Weight (lb)
Gamma-Ray Telescope	2 500
Cosmic-Ray Calorimeter	6 000
Cosmic-Ray Electrons	800
X-Ray Detectors	2 650
Medium-Energy Gamma-Ray	200
Low-Energy Gamma-Ray	350
	12 500
Electrical Power System	
Solar Panels	294
Solar Power Distribution	35
Control Distributor	25
Power Distribution	35
Voltage Supply (Measuring)	2
Charger Battery Regulator	660
Wiring	150
Power Supply	10
Measuring Distribution	25
Switch Selector	20
	1 256
Attitude Sensing and Control System	
Signal Processor	40
CMG (Flywheel)	240
Magnetic Coils, Insulation, & Mounting	262
Rate Gyros	7
Optical Sensors and Electronics	45
Magnetometers & Booms	17
Sensor Wiring	12
	623

TABLE V-2. (Continued)

Communications and Data Handling System	Weight (lb)
Antennas	10
Power Combiners and Diplexer	26
Transmitters	20
Command Receivers	3
Command Decoder	12
Recorders	60
Multiplexer	8
Switching Network	10
Analog Signal Conditioner	3
Diagnostic Logic	4
Cable and Connectors	30
	186

Propulsion System

Pressurization Tanks, Valves, & Reg	51
Propellant Tanks and Valves	15
Lines	6
Thrusters	15
Miscellaneous	1
Nitrogen	38
Hydrazine	35
	161

Structures

Basic Structure	2 770
Skin	300
Equipment Mounting Panels	600
Payload Truss	120
	3 790

Separation System

Separation Joints	100
Electronics and Pyrotechnics	20
	120

TABLE V-2. (Concluded)

Thermal Control System	Weight (lb)
Insulation	248
Subtotal	18 884
Contingency (10 + Percent)	2 036
Total (Titan IIID Capability at 200-n. mi. Altitude and 28.5-degree Inclination)	20 920

a. Positive X - launch direction.

b. Positive Z - toward sun.

c. Positive Y - right-hand rule to complete the triad.

The inertias are:

Baseline Configuration
(Center-Mounted Experiments)

$$\begin{cases} I_x = 18.51 \times 10^6 \text{ lb-in.}^2 \\ I_y = 163.16 \times 10^6 \text{ lb-in.}^2 \\ I_z = 171.20 \times 10^6 \text{ lb-in.}^2 \end{cases}$$

These inertias result from the heavy experiments being mounted toward the center of the spacecraft. Inertias associated with the bottom-mounted experiments approach are given below:

Bottom-Mounted Experiments

$$\begin{cases} I_x = 17.12 \times 10^6 \text{ lb-in.}^2 \\ I_y = 237.39 \times 10^6 \text{ lb-in.}^2 \\ I_z = 242.96 \times 10^6 \text{ lb-in.}^2 \end{cases}$$

Weight advantages resulting from this arrangement are given in Appendix E.

The distribution of the mass for the EC case resulted in a 1.5-degree misalignment between the geometric and principal axes; the misalignment occurs in the X-Y plane. For the EB case, the misalignment is 0.4 degree. The principal Z axis is aligned with the body Z axis for both cases. Arrangement of subsystems or components can be varied to improve this misalignment.

All of the above inertias are based on bulk location of the subsystems, rather than discrete locations for subsystem components. CG locations for both variations are given below. The location of the reference axes is shown in Figure V-3.

| Axis | CG Location (in.) | |
	Experiments Center-Mounted (EC)	Experiments Bottom-Mounted (EB)
X'	188.90	168.40
Y'	- 0.68	-0.17
Z'	1.20	1.40

The change in the CG is only slight, although the inertia around the Y and Z axes vary by a factor of 1.4.
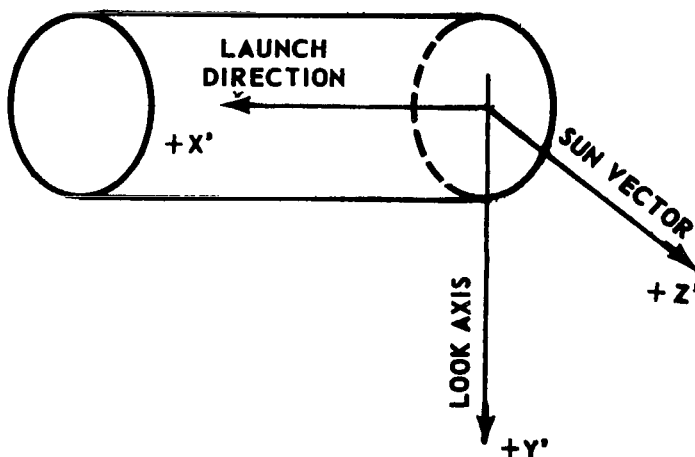
Figure V-3. Position of reference axes for purposes of locating the CG.

C. Systems Description/Integration

1. <u>General Approach</u>. The basic overall functional requirements for the spacecraft to perform its mission (such as performing a scan of the galactic belt) were analyzed; then the basic requirements were broken down into more detailed functional requirements (such as tilting the spin axis out of the ecliptic and pointing it at specific points in a prescribed pattern to perform the scan). End-to-end systems functions were then defined, and preliminary systems assessments were made, with particular emphasis on how the systems could be designed using a maximum amount of flight-proven hardware.

The major constraints and advantages of different approaches were weighed against each other to help determine the design approach and establish the feasibility of a concept. For example, to increase solar array power, the approach of lowering the temperature of the arrays with heat pipes was examined and compared with approaches which increased the array area (fold-out panels and lengthened body).

The end-to-end systems analyses extended beyond the flight hardware area to consider such areas as ground equipment and operations and their effects on the flight hardware design. For example, the data management system investigation included considerations beginning at the source of the data in the experiments or spacecraft systems, extending through the spacecraft data/communication system, the down-link, the ground receiving station, and the data processing system, to final dissemination of the data to the experimenter. Orbital altitude and inclination effects on ground contact time were considered also. In some systems analyses, the ground equipment and/or ground operations considerations proved to be the strongest configuration drivers for certain characteristics of the system; for example, the onboard data storage subsystem had to be sized primarily on the basis of the data receiving capability in the ground tracking stations and on station contact times.

Lists of equipment in each system were compiled showing estimated power requirements and weight as a part of the integration effort. Mass characteristics were generated and major systems interfaces were analyzed and defined. Growth and modularity aspects of systems were investigated, and considerations of reliable operation and long life were given special attention during the study.

EMC was not investigated because more design details are required before any meaningful assessment can be made; however, several general

problem areas are anticipated. Some of the experiments have high voltages
which are switched, causing transients in the systems. Also, it will probably
not be possible to operate the magnetic control coils simultaneously with the
magnetometers because of their distortion of the magnetic field near the
magnetometers. Magnetic materials in the spacecraft must be closely con-
trolled. There may be a danger of magnetizing the large iron cores of some
of the heavier experiments and all other ferrous material while operating the
control coils. Most of the experiments in the typical package studied have
metal enclosures around them which should help prevent large amounts of
radiated electromagnetic energy from entering or leaving them. The conducted
electromagnetic energy may be more of a problem and may require extensive
corrective measures. Packing density of experiments and systems in the HEAO
and cable routings will have to be examined extensively from an EMC stand-
point.

    2. <u>Systems Identification and Description.</u> The major spacecraft end
items which are recommended for the HEAO program are shown in Figure V-4.
The systems and components for the mockup, thermal-vacuum test article,
structural (static) test article, and vibration/acoustic test article are defined
in Section XIII. The systems and components for the prototype (identical to
flight) HEAO are shown in Figure V-4. The spacecraft consists of the following
systems and subsystems:

        a.   Attitude sensing and control system.

             1.   Attitude sensors subsystem.

             2.   Signal processing subsystem.

             3.   Actuator subsystem.

             4.   Flywheel subsystem.

        b.   Electrical power system.

             1.   Solar array subsystem.

             2.   CBR subsystem

             3.   Networks subsystem.

MAJOR SPACECRAFT END ITEMS

| BREADBOARD | MOCKUP | THERMAL VACUUM TEST ARTICLE | PROTOTYPE (IDENTICAL TO FLIGHT ARTICLE) | STRUCTURE TEST ARTICLE | VIBRATION/ ACOUSTIC TEST ARTICLE | FLIGHT ARTICLE (IDENTICAL TO PROTOTYPE) |

SYSTEMS

ATTITUDE SENSING AND CONTROL	COMMUNICATIONS AND DATA HANDLING	ELECTRIC POWER	STRUCTURE	*SEPARATION	THERMAL CONTROL	PROPULSION	EXPERIMENTS
FLYWHEEL	S-BAND TRANSMITTERS	SOLAR PANELS WITH SUBSTRATE BACKING	BASIC LOAD CARRYING TRUSS	PYROTECHNICS	COATINGS	GN₂ TANKS AND PLUMBING	COSMIC X-RAY
SIGNAL PROCESSOR	S-BAND ANTENNAS	CBR UNITS	OUTER SKIN COVERING (MICROMETEOROID PROTECTION)	CHARGE CIRCUIT	INSULATION	HYDRAZINE TANKS AND PLUMBING	LOW ENERGY GAMMA RAY
MAGNETOMETER (3-AXIS)	POWER COMBINER	POWER DISTRIBUTOR	EQUIPMENT MOUNTING PANELS AND SUBSTRUCTURE	ELECTRICAL CONTROL CIRCUIT	ELECTRIC HEATERS	THRUSTORS	MEDIUM ENERGY GAMMA RAY
MAGNETIC COILS (3)	COMMAND RECEIVERS	CONTROL DISTRIBUTOR	*PAYLOAD SUPPORT TRUSS				GAMMA RAY TELESCOPE
THRUSTOR CONTROLS	COMMAND ANTENNAS	MEASUREMENT DISTRIBUTOR					COSMIC RAY ELECTRONS
COARSE SUN SENSORS (4)	COMMAND DECODERS	SWITCH SELECTOR					COSMIC RAY CALORIMETER
SUMMING NETWORK	DIGITAL MULTIPLEXER	MASTER MEASURING VOLTAGE SUPPLY					
FINE SUN SENSOR (1)	ANALOG MULTIPLEXER	CABLES AND CONNECTORS					
STAR MAPPER (1)	ANALOG SIGNAL CONDITIONER	NETWORKS					
STAR MAPPER ELECTRONICS	TAPE RECORDERS						
STAR TRACKER	SWITCHING NETWORKS						
STAR TRACKER ELECTRONICS	DIAGNOSTIC LOGIC						
RATE INTEGRATING GYROS (3)	MINITRACK BEACON TRANSMITTERS						
DIGITAL SUN SENSOR (1)	CABLING AND CONNECTORS						
	BUFFER						

*Part of the payload, but not part of the HEAO in orbit.

Figure V-4. Prototype hardware breakdown.

    c.   Communications and data handling system.

        1.   Communications subsystem.

        2.   Data handling subsystem

    d.   Propulsion (Reaction Control)[1] system.

        1.   Thruster subsystem.

        2.   Propellant subsystem.

        3.   Pressurization subsystem.

    e.   Separation system.[2]

    f.   Structure.

        1.   Main box truss supports.

        2.   Skin.

        3.   Internal equipment panels.

        4.   Payload Truss[2]

    g.   Thermal control system.

    h.   Experiments.

A block diagram showing interfaces, inputs, and outputs of the major active systems is shown in Figure V-5.

---

1. Although this equipment can be considered as part of the attitude control equipment, it is listed as a separate system for the purpose of writing this report. The term "propulsion system" is used interchangeably with "RCS" in this report, although the system is not utilized for "propulsion" in the usual sense of the term (at one time in the study, the use of the system for periodic altitude boost was considered).

2. Although these items are part of the payload, they remain with the launch vehicle after HEAO separation.
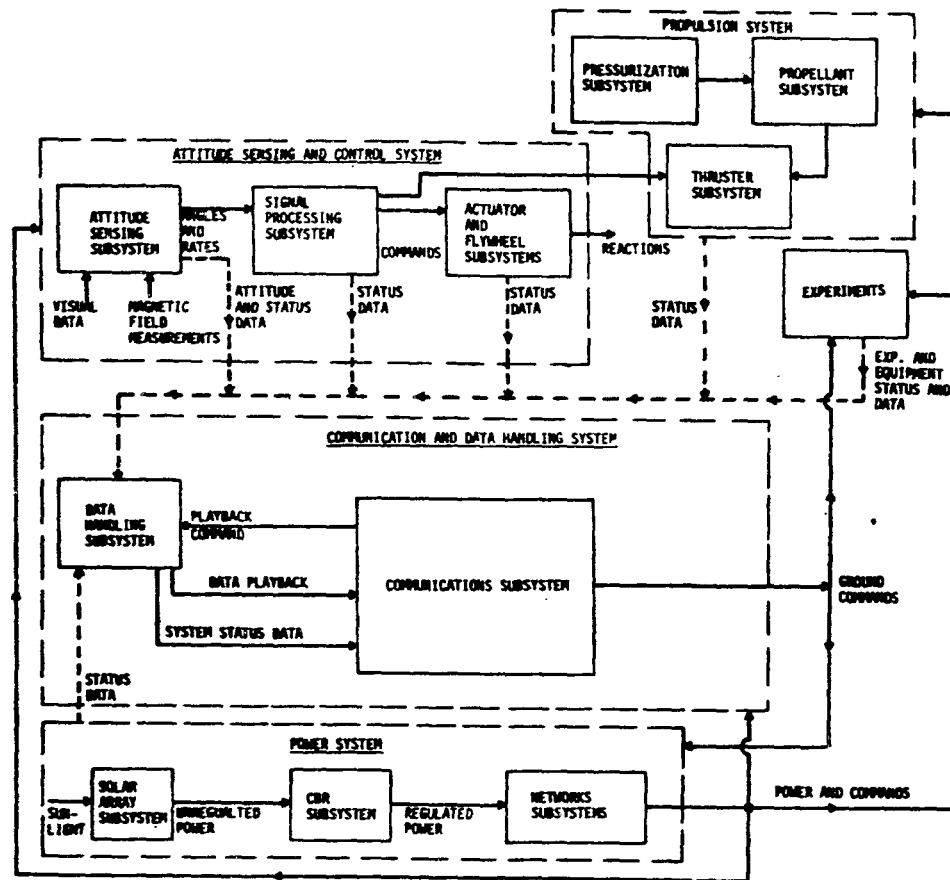
Figure V-5. Spacecraft block diagram.

a. Attitude sensing and control system. The location on the spacecraft of the major components of this system are shown in Figure V-6. The primary function of the attitude sensing and control system is to measure and maintain spacecraft attitude within the limits stated below. The requirement for maintaining spacecraft attitude is ±1.0 degree from a desired orientation. Attitude determination must be ±0.1 degree for purposes of data correlation; it is accomplished by a star mapper which generates signals in response to stars passing through its field of view as the spacecraft rotates. These data are stored temporarily on the spacecraft and are later transmitted to a ground receiving station and processed to determine precise spacecraft orientation at any given time. The map generated by the star mapper is not used on board the spacecraft.

The spacecraft attitude control system consists of four subsystems: (1) attitude sensing subsystem; (2) signal processing subsystem; (3) actuator subsystem; and (4) flywheel subsystem. The reaction control system can be considered a fifth functional subsystem, but it is treated as an independent system in this and other sections of the report.

For onboard control purposes, the spacecraft attitude is sensed or measured by one or more optical or inertial instruments in the attitude sensor subsystem. The optical instruments include coarse and fine sun sensors, a digital sun sensor, star tracker, and a star mapper. The inertial instruments are rate gyros. The output of the rate gyros is integrated to provide a reference during earth occultation of the visual reference. The signals generated by the sensors are processed by the signal processing subsystem to determine whether an attitude correction is required and, if it is, the magnitude and direction of the required correction. The signal processor then sends a command to the proper element in the actuator subsystem, with no ground contact required.

The actuator subsystem includes three magnetic coils and the control signal to the propulsion system thrusters. The thrusters are used for initial stabilization and orientation of the spacecraft after booster separation, and to make major reorientations. The magnetic coils generate a magnetic field which reacts with the earth's magnetic field to produce a torque. The magnetic coils are used to maintain a given spacecraft attitude and to make small reorientations, such as those required for maintaining solar pointing of the scan axis. Use of the magnetic coils is dependent upon the presence of a favorably oriented earth magnetic field. The magnitude and orientation of this field are measured by a three-axis magnetometer on board the spacecraft. If the orientation is favorable, an attitude correction is made; if the field orientation is unfavorable, the correction is deferred until orientation becomes favorable. Major spacecraft reorientations are commanded from the ground. These commands are either acted on immediately or stored. If a command is
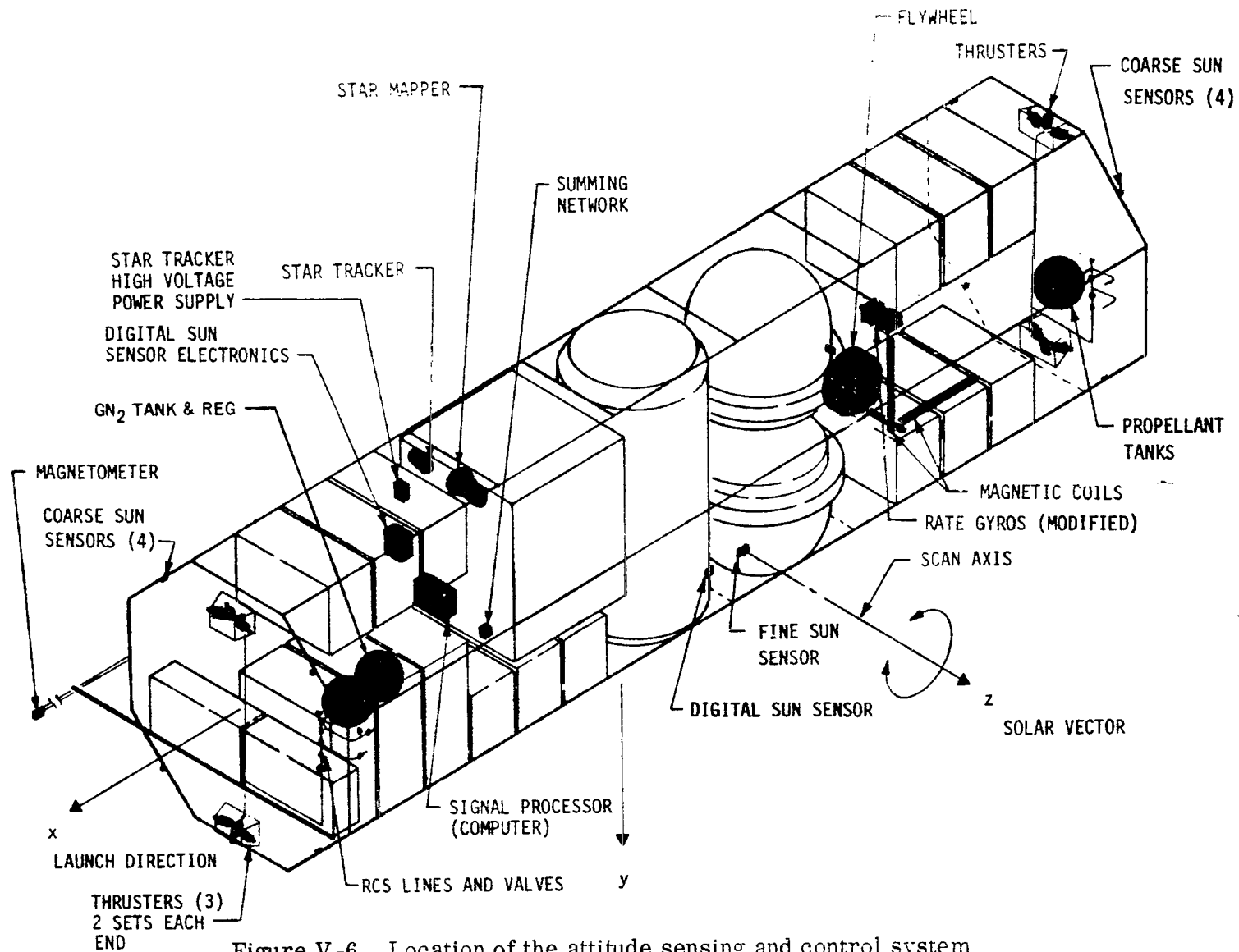
Figure V-6. Location of the attitude sensing and control system and propulsion system.

for reorientation at a particular time, and the magnetic field is unfavorably oriented or of insufficient strength, thrusters are used.

The flywheel subsystem consists of an IGRA from an ATM-type control moment gyro. The flywheel is mounted with its spin axis parallel to the spacecraft scan axis. The function of the flywheel is to stabilize the spacecraft by providing a momentum vector (2000 foot-pound-second) along the scan axis.

More details on this system are provided in Section XI.

b. Electrical power system. The locations of the major components in this system are shown in Figure V-7. The function of the electrical power system is to supply all systems with regulated electrical power at 28 volts dc and to provide interlocks, logic, and switching for control of spacecraft functions. During the daylight portion of each orbit, the solar panels generate enough power to supply the spacecraft and recharge the batteries. During the dark portion of each orbit, the batteries supply the power for the spacecraft.

The electrical power system consists of three subsystems: (1) the solar array subsystem; (2) the CBR subsystem; and (3) the networks subsystem. The solar array subsystem is rigidly fixed to the structure on three sides, and covers approximately 100 square feet of surface area per side; however, since two of the sides are at an angle of 45 degrees to the center one, the maximum effective solar array area, with the spin axis pointed at the sun, is approximately 240 square feet. The CBR subsystem takes the unregulated solar array output and regulates it for subsequent distribution to the loads. It also contains the batteries and provides controls for charging and discharging the batteries. The networks subsystem consists of the power distribution and circuit protection equipment, interlocks and logic, switch selector, and the electrical controls to each spacecraft component. More details on the electrical power system are provided in Section IX.

c. Communication and data handling system. The location of this system on the spacecraft is shown in Figure V-8. The communication and data handling system is composed of two subsystems:

1. The communications subsystem which consists of the RF equipment associated with the VHF beacon, the two command receiver/decoders, and the two S-band data links.

2. The data handling subsystem which consists of all the elements between the data sources and the inputs to the transmitters.

CHARGER-BATTERY
REGULATOR UNITS

DISTRIBUTION
BOXES

SOLAR
PANELS ON
THREE SIDES

SCAN AXIS

z

SOLAR VECTOR

x

LAUNCH DIRECTION

y
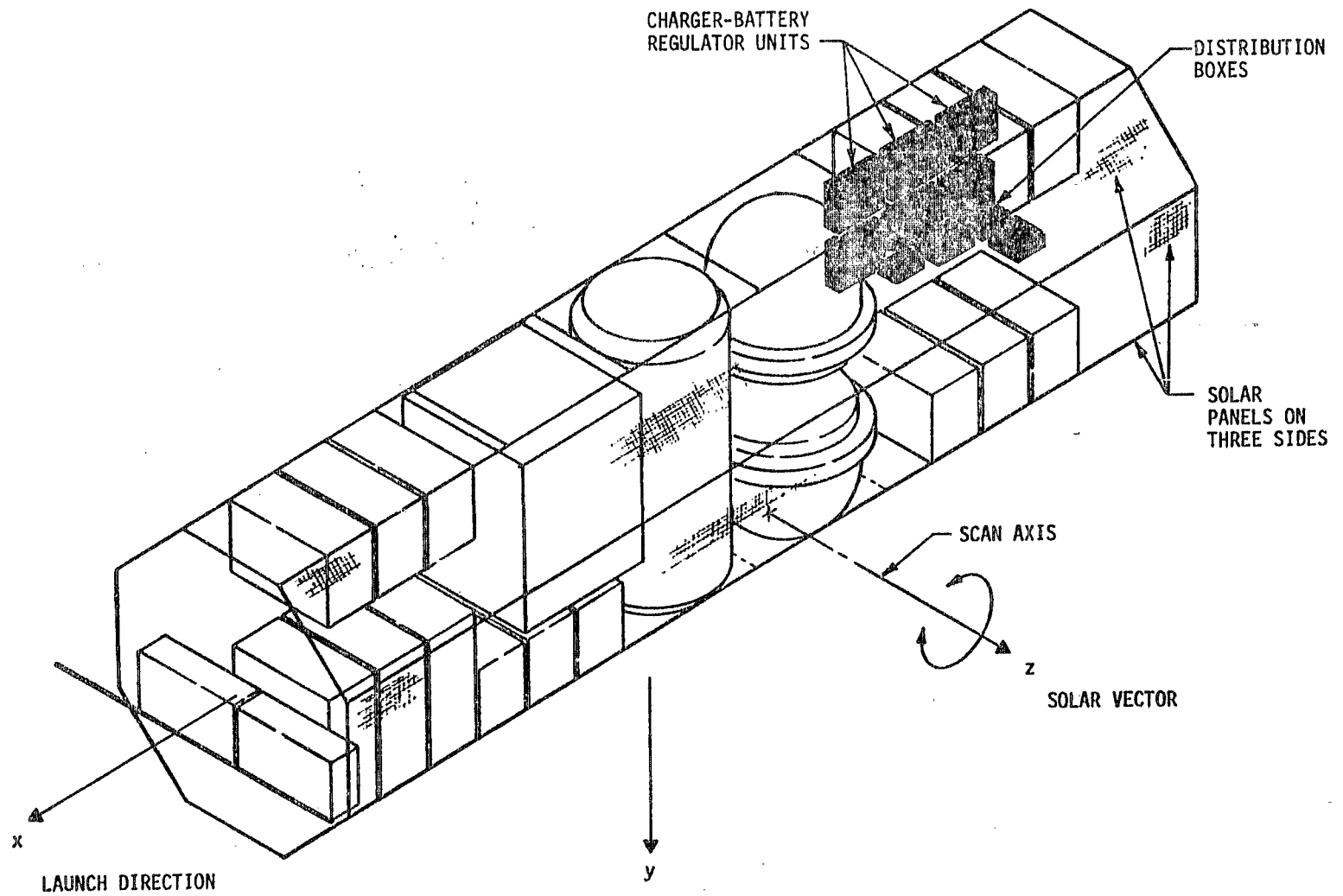
Figure V-7. Location of the electrical power system.

S-BAND ANTENNAS

TRANSMITTERS, TAPE
RECORDERS, AND OTHER
COMPONENTS

(BACK SIDE)

VHF
ANTENNAS (4)

SCAN AXIS

S-BAND
ANTENNA

z

SOLAR VECTOR

x

LAUNCH DIRECTION
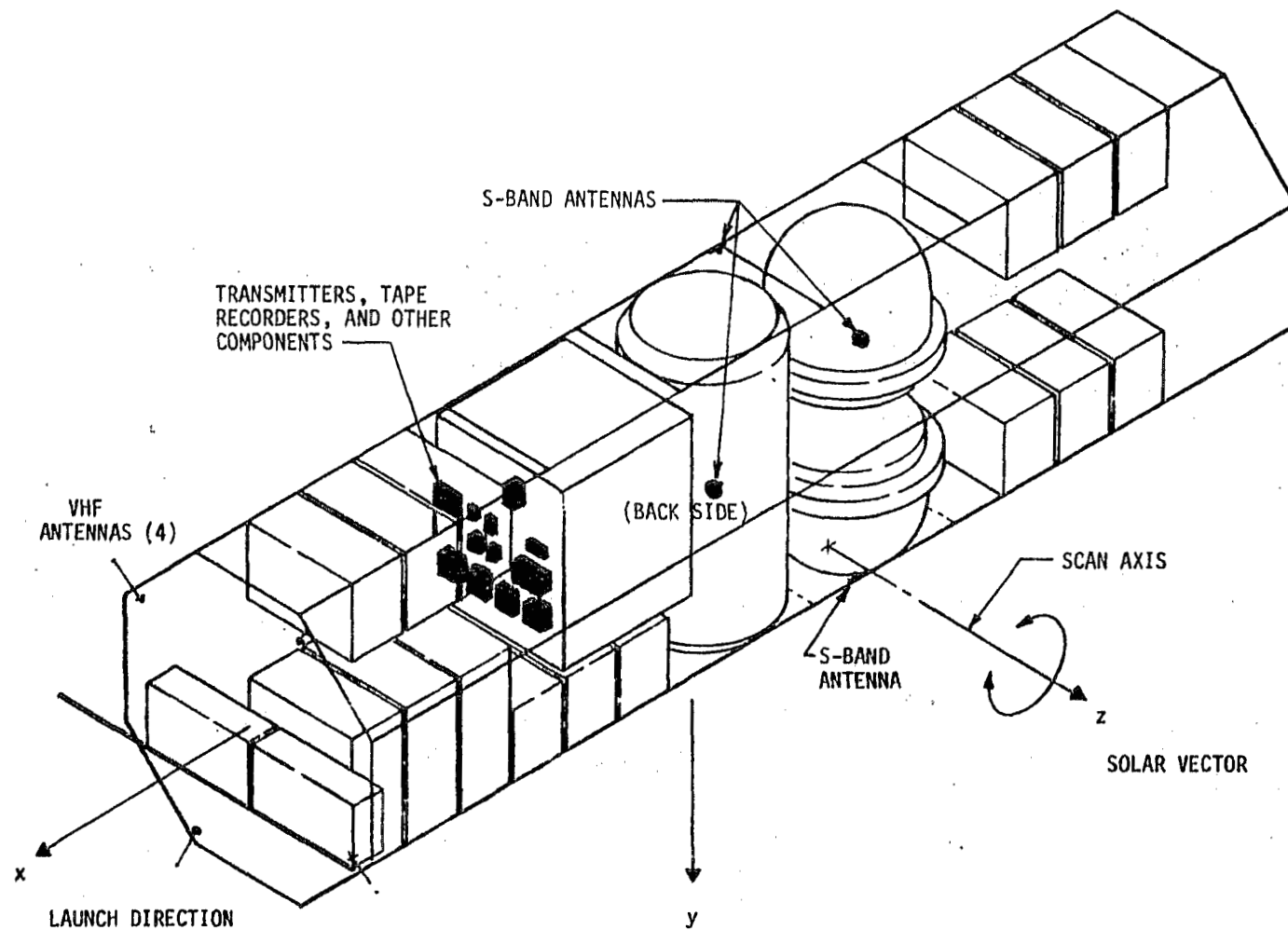
y

Figure V-8. Location of the communication and data handling system.

In the communication subsystem, the VHF minitrack beacon link consists of two low-power transmitters operating at 136 MHz, coupled to four VHF antennas. The beacon serves to facilitate ground acquisition and tracking of the spacecraft, to acknowledge ground commands, and to transmit very limited spacecraft system status in real time at a low data rate. The VHF ground command up-link is received by the onboard command receivers through use of the same four VHF antennas. The commands are routed to all other onboard systems. A total capacity of 1024 commands is provided. The two S-band links operate simultaneously and independently to transmit stored spacecraft and experiment data to ground stations. The two RF links operate in the 2200- to 2300-MHz band through four S-band antennas.

The function of the data handling subsystem is to accept, condition, sample, and store data on magnetic tape recorders. Upon ground command, the tape recorders are played back into the S-band transmitters. The subsystem consists of signal conditioners, analog-to-digital converters, digital and analog multiplexers, switching networks, and tape recorders. The system provides for a data recording rate of 27.5 kilobits per second (25 kilobits of experiment data and 2.5 kilobits of spacecraft systems status data). Four dual-track tape recorders are provided, with only one being used for recording at any one time (both tracks). A total storage capacity of 1728 megabits is provided using all four recorders. When over a ground station, one recorder will be playing back data to the ground while another is recording. The present standard for STADAN limits the data rate per link to 200 Kb/s. More details on this system are provided in Section X.

d. Propulsion (RCS) system. This system consists of three subsystems: (1) the thruster subsystem; (2) the propellant subsystem; and (3) the pressurization subsystem. The thruster subsystem consists of four thruster assemblies each containing three 0.5-pound thrusters. The thrusters are used for initial stabilization, for reorientations of a considerable size or which have to be made within critical time constraints, and for spin-up and despin when changing from pointing to scanning modes and vice-versa. The spacecraft has been sized for 60 maneuvers during the 2-year mission period. Total propellant requirement is 35 pounds, including a 100 percent contingency factor. The total impulse required is sufficiently small that either cold gas, monopropellant, or bipropellant systems could be used; however, hydrazine monopropellant has been selected for the baseline. The propellant subsystem consists of two 10-inch-diameter tanks and the associated plumbing and valves. The pressurization subsystem consists of one GN_2 tank and the associated plumbing, valves, and regulators. The GN_2 is separated from the hydrazine by a bladder in each propellant tank.

The components of this system are shown in Figure V-6. More details on the propulsion aspects of the spacecraft are provided in Section VIII.

Heaters will be required for the thrusters, since hydrazine freezes at approximately 35° F; but these have not been included in the baseline design.

e. Separation system. This system was not defined in any depth during the study. . Any of several existing, flight-proven techniques could be used. The essential elements would have to be pyrotechnic devices (explosive nuts, primacord, etc), latching, unlatching, and deployment mechanisms, electrical charging and firing circuits, and electrical control and instrumentation circuits. Although it is part of the payload, this system is not part of the in-orbit HEAO. It will remain with the payload truss and launch vehicle after HEAO separation.

f. Structure. The structure of the HEAO consists of three main assemblies: (1) main box truss supports; (2) internal equipment panels; and (3) skin. In addition, there is a payload adapter which is part of the payload, but not part of the in-orbit spacecraft.

The basic structure supports the primary cosmic-ray electrons experiment, the cosmic-ray calorimeter, the gamma-ray telescope, the medium-energy gamma-ray detector, and the low-energy gamma-ray detector.

The basic structure configuration is impacted by and tailored for the two larger experiments: (1) gamma-ray telescope (48-inch diameter), and (2) cosmic-ray calorimeter (50-inch diameter). The longitudinal box truss member sizes vary, depending on the particular location of these large experiments. The spacecraft's primary structural members are constructed of standard extruded sections of aluminum alloy.

The experiments mentioned above are attached directly to the box truss supports.

Internal equipment panels are used to support other experiments and the subsystems equipment. All loads from the subassemblies will be carried by the box truss assemblies and their interconnecting members.

The skin covers and completes the structure, except for the three sides covered by the solar array and the cutouts for experiment viewing angles. The skin serves for thermal and micrometeoroid protection. Accessibility to internal equipment is obtained through removable skin and solar array panels.

All structural loads are transmitted to outrigger members and crossbeams at one end of the spacecraft, and thence to the payload truss assembly at 8 places. The payload truss assembly transmits the load from these 8 places to 16 places on the Titan IIID forward skirt. This truss assembly remains with the launch vehicle after payload separation in orbit.

The structure is discussed in more detail in Section VI.

g. Thermal control system. The function of the thermal control system is to maintain all experiments and spacecraft components within prescribed temperature limits. This is accomplished by the proper selection of coatings on the outer and inner surfaces of the spacecraft, the proper location and mounting of equipment, and the use of electric heaters and insulation where required. Coatings which have low thermal absorptivity and high thermal emissivity will be used to prevent overheating of the spacecraft. System components are arranged within the spacecraft, and insulated as required, so that heat radiated and conducted from some components is absorbed by others to prevent them from becoming too cold, and vice versa. Thermal control of all items will probably not be possible by location alone. It is anticipated that electrical heaters will be required on some items, such as thrusters, although power requirements are expected to be low. The thermal aspects of the spacecraft are discussed in more detail in Section VII.

h. Experiments. The locations of the baseline experiments are shown in Figure V-9. The function of these experiments is to measure the flux and spectra in the X-ray, gamma-ray, and cosmic-ray regions from 10^2 to 10^{15} ev. Data generated by the experiments will be recorded on magnetic tape and transmitted to ground tracking stations as contact opportunities permit.

3. Interfaces. Four major areas of interface were considered during the study: (1) spacecraft/experiments; (2) spacecraft/GSE; (3) spacecraft/launch vehicle; and (4) spacecraft internal systems interfaces. The three main areas of concern in defining and controlling the interfaces are the physical, functional, and procedural considerations. No procedural considerations were analyzed during this study.

a. Spacecraft/experiment interface. The spacecraft/experiments interface is the largest configuration-driver of the three, and will probably be the most difficult interface to control because of its complexity and because of the diversity of hardware and contractors involved. Although usually spoken of as one interface, in actuality each spacecraft system has as many different interfaces as there are experiments. The complexity of the interface

GAMMA-RAY
TELESCOPE

COSMIC-RAY
CALORIMETER

PRIMARY COSMIC-
RAY ELECTRONS

LARGE AREA
X-RAY DETECTORS

SCAN AXIS

z
SOLAR VECTOR

MEDIUM ENERGY
GAMMA-RAY DETECTOR
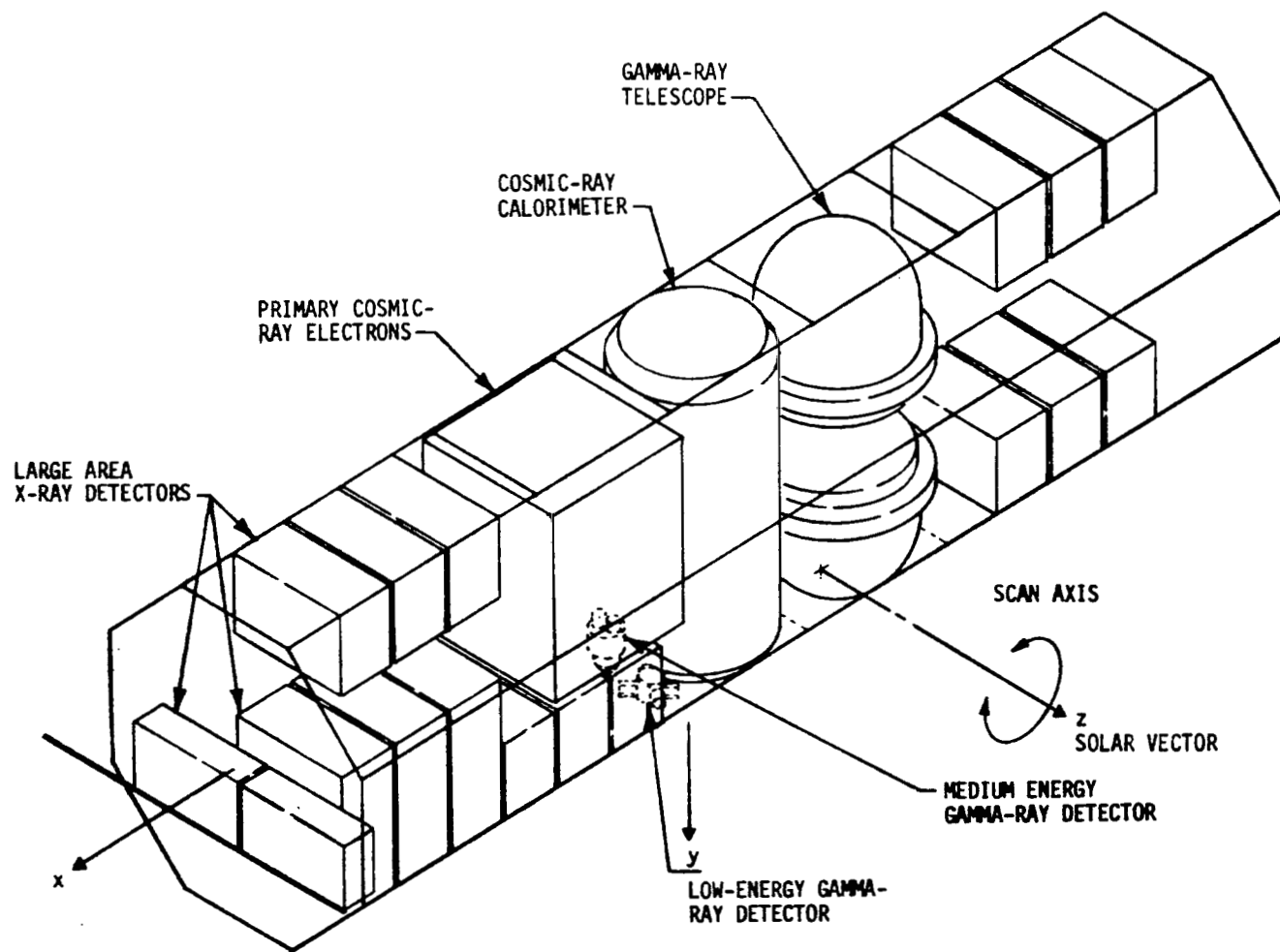
x

y

LOW-ENERGY GAMMA-
RAY DETECTOR

Figure V-9. HEAO baseline configuration showing location of the baseline experiments.

is shown in Figure V-10. The data formats, word lengths, and data rates vary considerably from experiment to experiment. Also, the voltage and power requirements, viewing angles, masses, and structural mounting requirements vary greatly from experiment to experiment. On the other hand, there are cases where the experiments have common requirements, or at least can all be compatible with the most stringent requirement, such as correlation of data with time and pointing angle.

Obviously, one approach to defining the interface would be to allow each experimenter to place his own requirements on the spacecraft and let the spacecraft be designed to handle a diversity of quantities flowing across the interface; another approach would be to specify to each experimenter what will be available at the interface and let each one provide the parameter conditioning required. The approach recommended as a result of the study thus far is somewhat of a compromise between the two. The data transfer could be a 10-bit per byte parallel transfer of digital data from experiment data registers and buffers within each experiment to the data handling equipment on the spacecraft side of the interface. A time clock (possibly 0.5 MHz) and a star mapper capable of providing 0.1-degree resolution of pointing angle will be provided on the spacecraft and will serve to correlate all experiment data, rather than having separate clocks and mappers in each experiment. A dc voltage level of 28 volts will be provided to each experiment at the interface, at a power level commensurate with experiment requirements. The experimenter will step the voltage up or down, or provide better regulation, as required. The spacecraft structure is designed to allow for the viewing angles required by each experiment, and to provide adequate mounting provisions.

b.   Spacecraft/GSE interface. The spacecraft/GSE interface must be analyzed for the applicable ground operations phases. It is anticipated that most of the HEAO systems will not be active during launch. The most likely candidates for being active are portions of the control system, some of the heaters, the portions of the data system which are all transmitted on the minitrack beacon link, the command system, and the portion of the power system required to sustain the other activated systems. Electrical controls and plumbing to RCS propellant and pressurization subsystems must be provided. Capability to control all these foregoing functions would have to be provided through umbilical connections. To conserve weight, all other functions required for operating the spacecraft systems during ground operations will probably be provided through test connections internal to the spacecraft. Drag-in test cables will be used to mate the GSE with these test connections for operations testing. RF links will exist between spacecraft and ground equipment. These consist of two S-band telemetry data links, one tracking beacon link, and one
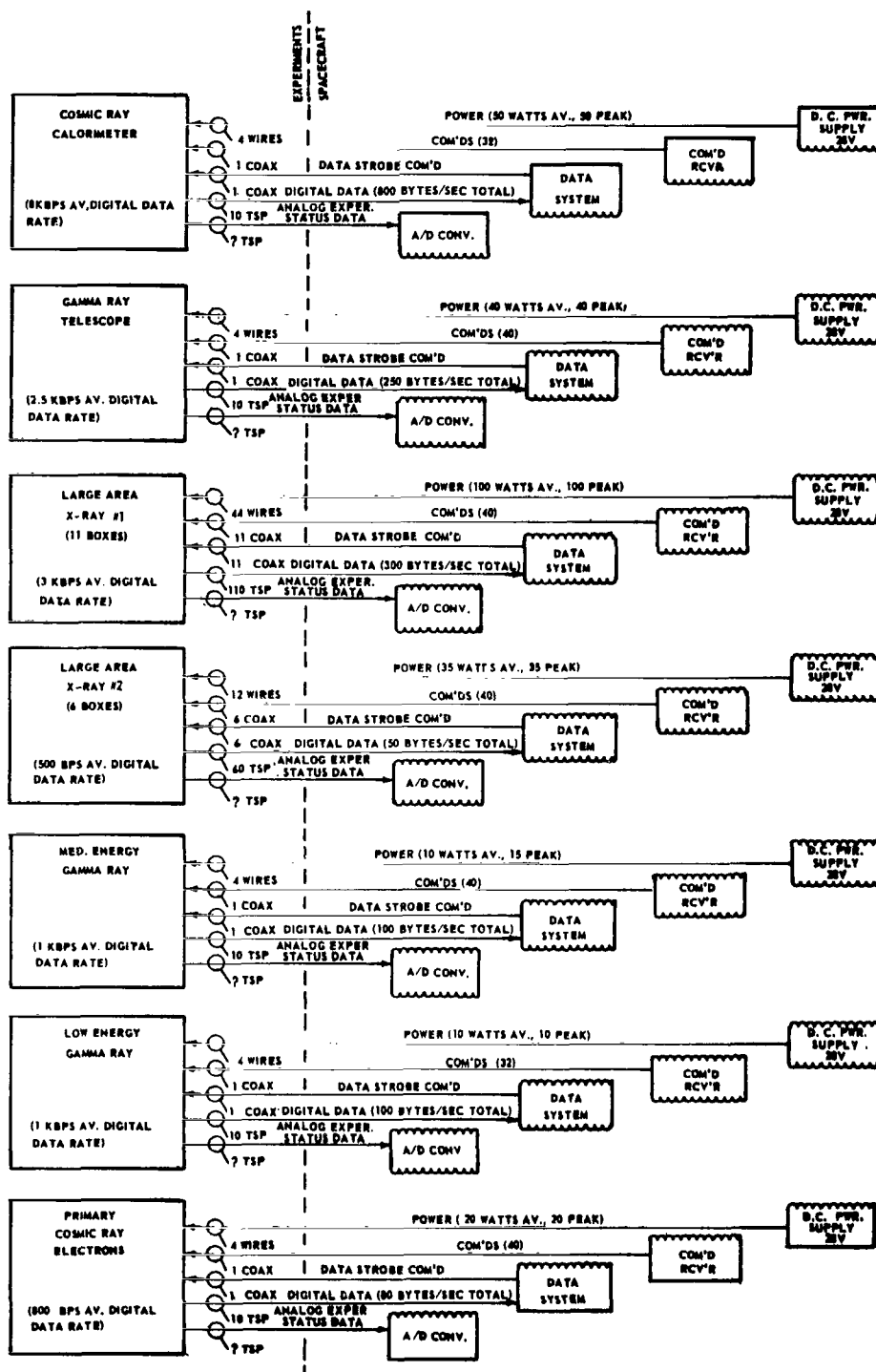
Figure V-10. Typical spacecraft/experiments interface.

command link. For ground test operations, coaxial cables will be provided for each link (two for the command link). Provisions for transmitting space-craft data to the ground may require radiating elements external to the launch vehicle shroud.

c. Spacecraft/launch vehicle interface. The structural interface with the launch vehicle is the only aspect of this interface which has been considered in the study. A minimum of 16 attach points is required for this interface. The functional interface is expected to be extremely small. Commands and power will probably be required from the launch vehicle to the spacecraft separation system. Dynamic sensor data from the spacecraft or shroud area to the launch vehicle guidance system is a possibility.

d. Spacecraft internal systems interfaces. The interfaces between systems and interfaces internal to each system are included in this category. The major interfaces between systems are in the areas of structure, electrical power and networks, and the data/communication system. The sizes of these interfaces can be estimated from the systems power statement (Table IX-1), the systems data summary (Table X-3), the system command summary (Section X), and in the systems block diagrams. The complexity of the interfaces internal to each system depends on the nature of the off-the-shelf hardware selected from other programs, the systems layout, modularity, redundancy, and growth potential provided in the system. The nature of these internal systems interfaces is depicted in the subsystems block diagrams.

4. Growth

a. System weight/power growth trends. Growth aspects of the entire spacecraft and of each system were considered in the study. The base-line configuration was sized for the maximum payload capability (20 920 pounds) of the Titan IIID in a 200-n.mi. circular orbit at 28.5 degrees inclination. A cursory analysis of spacecraft weight growth trends indicates that such an unmanned system could be expected to have weight growth of 10 to 30 percent from the beginning of the program to flight. The present weight estimate on the HEAO is 18 884 pounds. This results in a weight margin of 2036 pounds (10+ percent). The percentage of growth available with the present HEAO weight estimates is below the average amount to be expected. Although historical data have not been compiled on power growth rate throughout a pro-gram, the margin which presently exists (approximately 260 watts) in the celestial scan mode may well be insufficient for a normal program at the end

of Phase A. Methods of increasing power capability and payload weight have been studied, and the data are presented in the appropriate sections and appendices within the study. Additional aspects of growth are covered in Appendix D.

b. System capability improvement. In the study, modularity was considered as one of the prime methods of achieving growth, both by the addition of add-on units and by possible replacement of an entire unit with one of greater capability. The degree of modularity depends on the nature of the function, the nature of the off-the-shelf hardware selected, and the systems layout, packaging, redundancy, and maintainability considerations.

In multiple-input systems like the communications and data-handling system, in which there are many identical input components, or in multiple-input and multiple-output systems like the power distribution sub-system, in which there are many identical input and many identical output components, a high degree of modularity can be achieved. In such cases, hardware is usually highly standardized and much of it is available as off-the-shelf equipment. The nature of the growth to be expected in such systems is usually an increase in the quantity of inputs or outputs, which can be achieved by adding more input or output modules. Systems such as the attitude sensing and control system are usually more "customized" and have less inherent modularity. The nature of the growth to be expected in such systems is not usually an increase in the number of inputs and outputs, but an increase in the amplitude of the output (force) already being provided. Some modularity is possible by designing for add-on output elements (magnetic coils, RCS thrusters, etc.).

The anticipated systems growth, mentioned in the examples above, are growth in numbers or amplitudes of inputs or outputs. Growth in accuracy of the systems is another desirable aspect, particularly when Mission B and later missions are considered. Modularity will enhance the capability for the growth in accuracy of the systems, since modules can be replaced by up-dated ones of greater accuracy. The same modular configuration of the systems which give optimum advantages for growth in numbers or amplitudes of functions should give adequate or even optimum advantages for growth in accuracy. Maintainability is also enhanced by modularity, and the number of spares can be minimized because of it.

To help assess the associated advantages and penalties for each system, growth was considered from both a functional and physical growth standpoint. With each growth in systems capability, there is a corresponding penalty in weight, power required, etc. Some indication of the degree of modularity, the growth capability, and the associated penalty can be seen from

the Systems Equipment List (Table V-1), together with the systems block diagrams and the power, data, commands, and weight lists in the various systems sections. From these sources, it can be seen how many modules can be added to the input or output of a particular component before the component's capability is exceeded. The weight, space, and power required for each module can also be seen from the table. Since the baseline structure was sized for 20 920 pounds, the payload can grow to that extent with no anticipated structural problems.

Growth in flight performance of the spacecraft was also investigated; these data are presented in Section IV. Performance capability beyond that required for the final payload weight can be used for going to a higher altitude to increase orbital lifetime, or for going to a higher inclination to increase ground station contact time.

5. Reliability

General. Since it is desired that the HEAO spacecraft be a long-life spacecraft, considerable emphasis must be placed on reliability and long-life aspects of the systems in the early phases of the design. Although manned space flight hardware end items have reliability goals on the order of 0.95 and higher, the reliability goals of scientific satellites in the past usually have been considerably lower, on the order of 0.70 or so at best [V-1]. Although the HEAO is not man-rated, it is a very large and complex scientific satellite, and because of its importance, it would desirably have a reliability goal somewhere between that of a "typical" satellite and a manned spacecraft. It is anticipated that selected redundancy will have to be added to increase the spacecraft reliability. The increase in power required for this increased reliability would be extremely low, since most of the redundancy could be "standby." It is estimated that six items of hardware account for over 70 percent of the reliability problems of the baseline spacecraft. These are the solar panel and CBR assemblies, tape recorders, signal processor, flywheel, power converter, and gyros. Therefore, future efforts should be concentrated in these areas. When the flight experiments are defined, their reliability should be established at a level commensurate with the desired mission reliability, and an overall reliability analysis should be performed.

REFERENCE

V-1. Corliss, William R.: Scientific Satellites. NASA SP-133, 1967.

SECTION VI. STRUCTURAL DESIGN

TABLE OF CONTENTS

LIST OF ILLUSTRATIONS

LIST OF TABLES

SECTION VI. STRUCTURAL DESIGN
A. General Requirements and Design Approach

The structural design approach of the HEAO spacecraft is essentially determined by configuration constraints which result from considerations of the launch vehicle envelope, the location, size, and viewing requirements of the major experiments, and flat area requirements for fixed solar cell arrays. The configuration layout of the baseline spacecraft, as discussed in Section V, results in a structural shape which has an octagonal cross section, and dimensions of 97.0 inches face to face, and 30.0 feet in length. An additional constraint which affects the structural design approach is the requirement to locate the spacecraft center of gravity near the geometric center to minimize gravity gradient torques. This constraint requires that the heavier experiments be placed toward the center of the spacecraft and results in a significant structural penalty, due to longer load paths and greater bending moments acting on the aft portion of the structure. As a result of this penalty, an alternate structural design which considers location of the heavier experiments in the aft portion of the structure was developed and is discussed in the appendices of this report.

The design approach taken for the structural system of the spacecraft is an open truss assembly, as illustrated in Figure VI-1. The primary structural load paths are through two opposing box truss sections, each parallel to the longitudinal axis of the spacecraft. These parallel sections provide unobstructed volume for location of the major experiments in a common viewing direction, with minimum load path lengths to the primary structure. In the aft portion of the structure, the primary loads in the box truss sections are distributed by outrigger members and cross beams to the eight outer corners of the octagonal cross section. These support points interface with a payload adapter described in Section VI-E which further distributes and carries the loads to the vehicle interface. Secondary members of the structural truss assembly are attached to the box truss sections to maintain the external octagonal cross section and provide support for the solar arrays and external thermal shroud/micrometeoroid bumper skin. Other members are required for transfer of loads laterally between the primary box truss sections and provide overall structural stiffness.

Although designed specifically for the assumed experiment characteristics and requirements described in Section II, the design approach provides
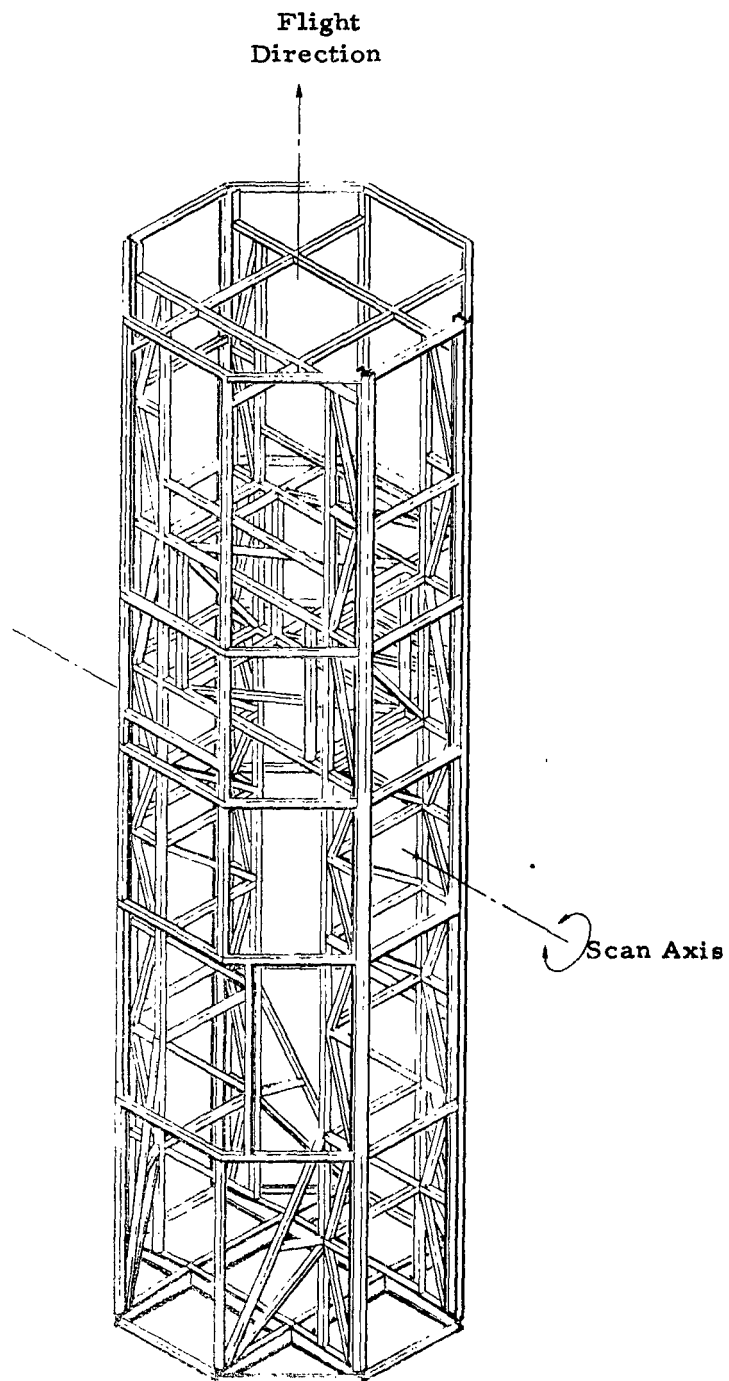
Flight
Direction

Scan Axis

Figure VI-1. Baseline spacecraft structural concept.

inherent flexibility, within reasonable constraints, for accommodating experiments varying from the baseline experiments in size, shape, and weight. Structural support of the experiments will be through structural brackets attached to the primary structure such that the primary constraint to experiment shape and size would be essentially the volume available between the box truss sections. Also, by utilizing an open truss assembly for the structural system, maximum accessibility to the experiments and spacecraft systems is provided by removing the external solar arrays and external skin.

B. Structural Design Requirements

The HEAO spacecraft will be contained within the Titan IIID payload fairing during launch within the sensible atmosphere and therefore will not be subjected to aerodynamic loading. The flight loads for which the spacecraft structure is sized are therefore those resulting from launch vehicle accelerations. The lateral and longitudinal accelerations imposed upon the spacecraft for three critical phases of Titan IIID launch, i.e., lift-off, maximum dynamic pressure, and cutoff, were specified by the Martin-Marietta Company, Denver Division, for purposes of this conceptual design phase and are presented in Table VI-1.

The dynamic envelope of the launch vehicle as shown in Figure VI-2 is specified as a cylinder of 107.27 inches in diameter. The envelope of the spacecraft is a cylinder 105.0 inches in diameter and 30 feet long. Thus, the total allowable deflection is 1.13 inches. For purposes of structural analysis, 1.0 inch of this total allowable deflection was allocated to the spacecraft structure and 0.13 inch to the payload adapter.

TABLE VI-1. EQUIVALENT STATIC LOADS CONDITIONS

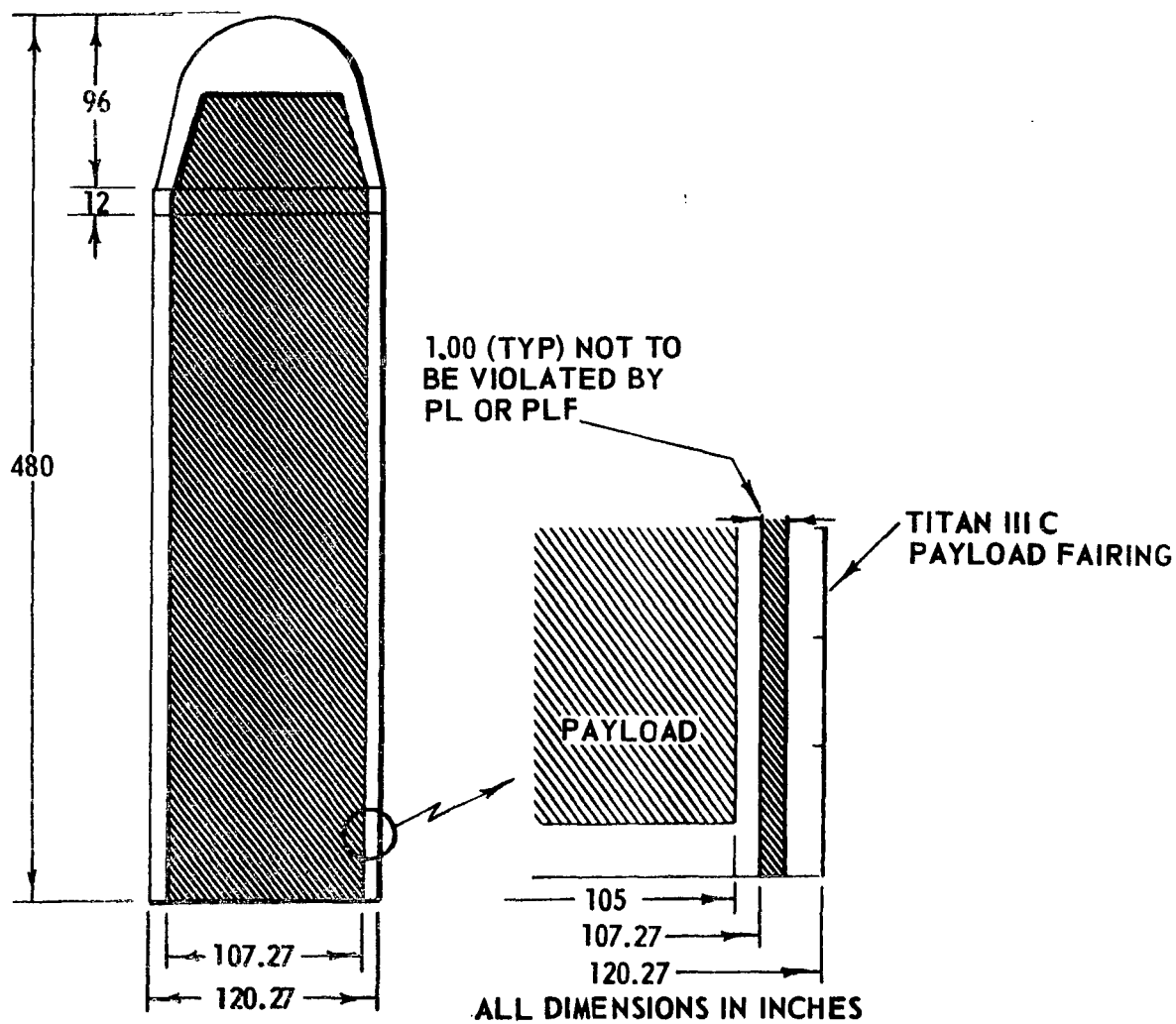| Boost Flight Conditions Titan IIID	Longitudinal Acceleration (g)	Lateral Acceleration (g)
Lift-off	1.7	1.5
Max qα	2.2	0.4
Cutoff	6.0	0.75

Figure VI-2. Dynamic payload envelope.

C. Structural System Description

The structural system developed for the baseline HEAO spacecraft configuration is shown in Figure VI-3.

The major load paths are through eight longerons which serve as chord members for the two parallel longitudinal box truss sections. Two angles are used to form T-sections for these longerons. Struts and diagonals are angle sections and cross beams used between the two truss assemblies at various levels are I-sections. Specific sizes for these members are shown in Figure VI-3 and all members are 2024-T4 aluminum.

The members of the box truss sections will serve as attach members for the experiments and subsystems when applicable. Other subsystems and secondary experiments are to be mounted on transverse internal panels. All panels are assumed to be of 1-inch-thick aluminum honeycomb sandwich construction. These panels will carry the equipment load to the box truss sections as shown in Figure VI-3.

The outer skin of the spacecraft, which is on all sides except where the solar panels are installed, serves as thermal shielding as well as a micrometeoroid bumper. The skin is 0.025-inch aluminum sheet. Cutouts are provided to accommodate the view angle of the experiments as required.

It is assumed that experiments are contained in their own enclosures and chassis, and this material will provide the remaining requirement for micrometeoroid protection.

The solar panel substrate is aluminum honeycomb sandwich construction 0.375 inch thick. The face sheets are 0.008-inch-thick aluminum sheet and the core is 3.1 pounds-per-cubic-foot aluminum honeycomb, having an 0.125-inch cell size and an 0.007-inch wall thickness.

The total thickness of the solar panel substrate will be more than adequate to serve as the micrometeoroid bumper in the area that they are installed.

Figure VI-3. Baseline structural design.
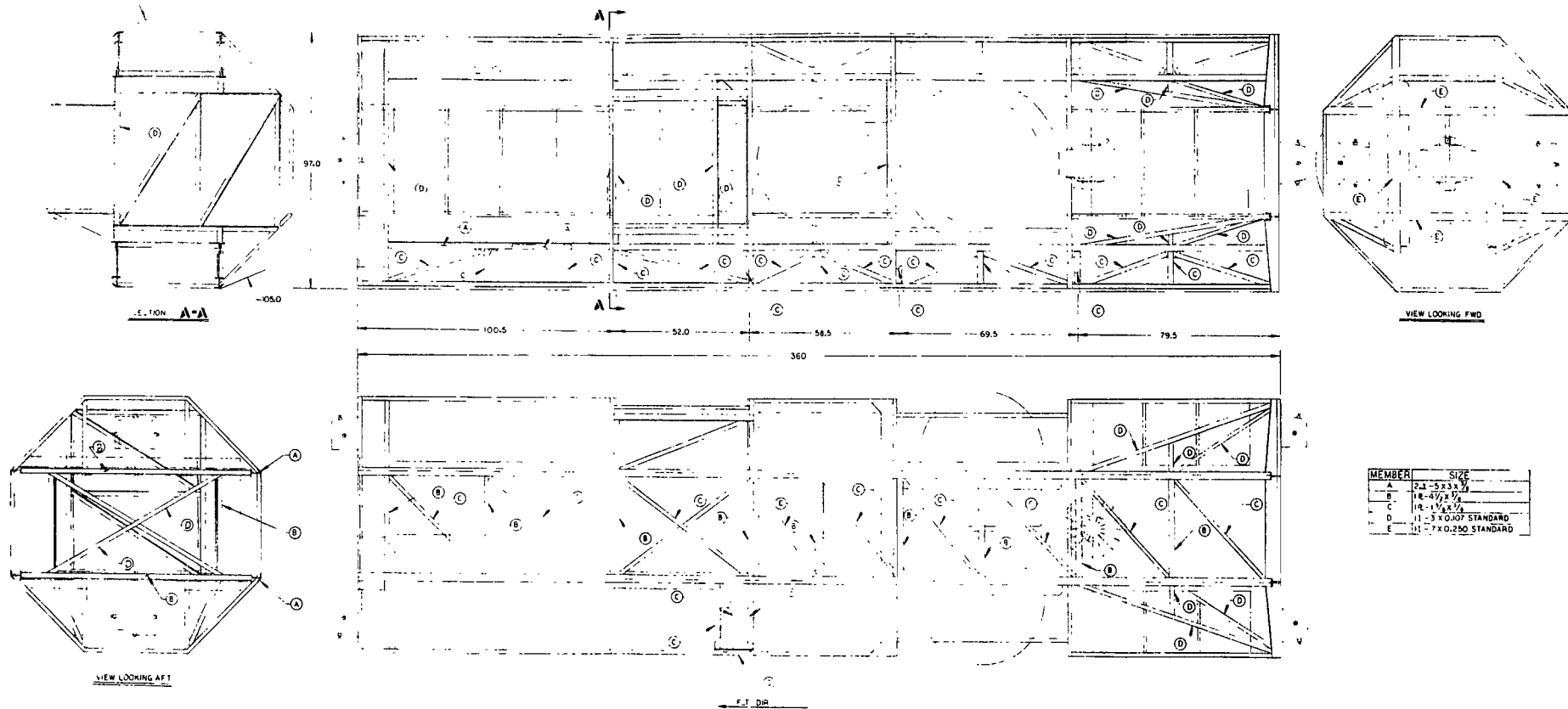
MEMBER	SIZE
A	2.1 - 5 X 3 X 3/8
B	1R - 4 1/2 X 1/2
C	1R - 1 1/2 X 1/2
D	11 - 3 X 0.107 STANDARD
E	11 - 7 X 0.250 STANDARD

SECTION A-A

VIEW LOOKING FWD

VIEW LOOKING AFT

D. Weight Analysis

The total payload weight assumed for the structural analysis is 20 920 pounds. The total weight of the six major experiments is 12 500 pounds and is distributed according to the location of the experiments as shown in Figure VI-3. The remaining 7580 pounds is taken as the weight of the secondary experiments, subsystems, and structures, and is assumed to be uniformaly distributed along the longitudinal axis.

Other assumptions made for the purpose of conducting the weight analysis are summarized as follow:

- All joints are considered pinned for analysis simplification.

- A factor of safety of 1.25 on the ultimate strength is used.

- The maximum deflection shall be 1.0 inch.

The weight breakdown and deflection for the structure designed for loads only and for loads and deflections are given in Table VI-2.

TABLE VI-2. COMPARATIVE WEIGHTS AND DEFLECTIONS

Component	Designed for Loads and Deflection	Designed for Loads Only
Basic structure (truss, bulkhead, etc.), lb.	2770	1950
Skin (0.025-inch aluminum), lb.	300	300
Internal equipment mounting panel (estimated), lb.	600	600
Total weight, lb.	3670	2850
Maximum Deflection, in.	0.998	2.6

As can be seen from the table, the deflection requirement imposes a large weight penalty on the spacecraft designed for load only.

No optimization, other than a general rearrangement which is discussed in the appendix, was performed to reduce the weight of the structure designed by limited deflection; however, several trades exist and should be considered in subsequent design iterations. These trades in general are the following:

- Tapering the envelope of the spacecraft to allow more clearance at the forward end.

- Type of construction.

- Material changes.

- Snubbers between the spacecraft and payload shroud.

E. Payload Adapter

The payload adapter is required for structural support of the HEAO spacecraft and provides distribution of the flight loads to the launch vehicle interface. The adapter also provides the means for separation of the spacecraft from the launch vehicle which could consist of a spring and explosive bolt at each of the eight spacecraft support points.

The Titan IIID launch vehicle has 36 longerons on the forward skirt at station 220.154. Each longeron provides an available point at which spacecraft loads can be introduced. The ultimate compressive capability of each of these load points is summarized for three critical flight conditions in Table VI-3, and were derived from the vehicle's ultimate compressive capability which is shown in Figure VI-4.

TABLE VI-3. TITAN IIID INTERFACE ULTIMATE CAPABILITY

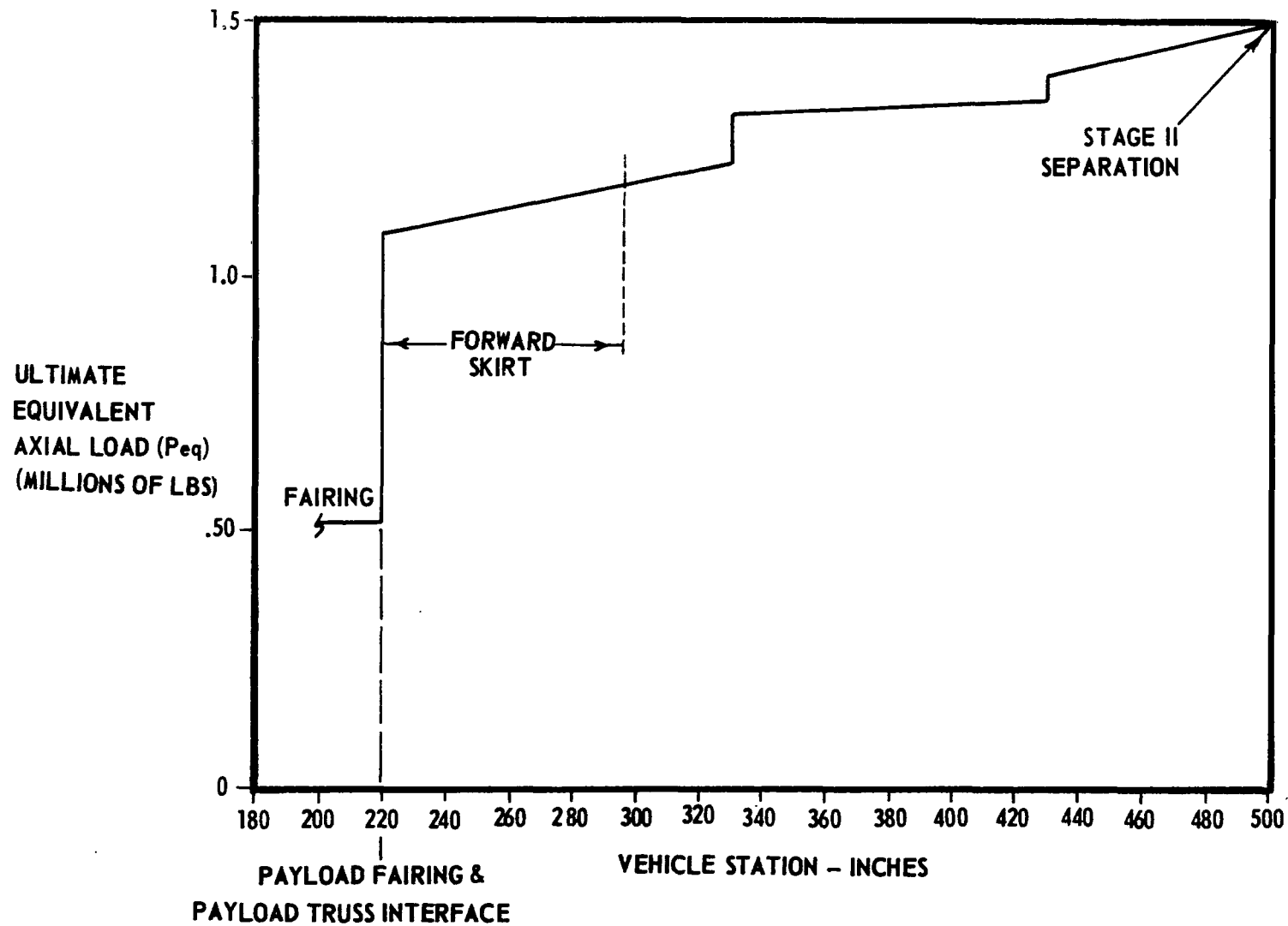| Boost Flight Conditions	Titan IIID Capability (lb/support point)
Lift-off	30 000
Max $q\alpha$	15 560
Cutoff	30 000

Figure VI-4. Titan IIID ultimate axial load.

The loads at the spacecraft/launch vehicle interface were derived from the equivalent static load conditions of the launch vehicle which are listed in Table VI-1. The loads were calculated for a 16-point distribution at the launch vehicle interface. The limit compressive loads and the shear limit loads are given in Table VI-4.

TABLE VI-4. MAXIMUM COMPRESSIVE AND SHEAR LOADS AT TITAN IIID/SPACECRAFT INTERFACE

Boost Flight Conditions	Maximum Compressive (lb)	Maximum Shear (lb)
Lift-off	11 150	8450
Max qα	7 625	4100
Cutoff	10 790	8250

The payload support adapter shown in Figure VI-5 was designed to transfer the eight spacecraft support point loads to 16 points at the launch vehicle. This is a minimum requirement to maintain a good safety factor over the vehicle capability. The adapter consists of a forward ring which picks up the load at 8 points and transfers this load through 16 struts to an aft ring which is mated to the launch vehicle interface ring. The aft ring, when attached to the launch vehicle ring, was designed to withstand the shear load acting at the interface.

The adapter is designed to be fabricated from 7079-T6 aluminum alloy. The primary consideration for the selection of this material is high compressive strength and modulus of elasticity.

The 16 struts are considered to be short columns which take all the compressive load without buckling, and their deflection is in the elastic range. The preliminary structural analysis, based on maximum limit load, indicated an adapter deflection which exceeds the 0.13-inch deflection defined in Section VI-B. The 16 struts were therefore sized according to the deflection criteria. A weight summary for the payload adapter is given in Table VI-5.
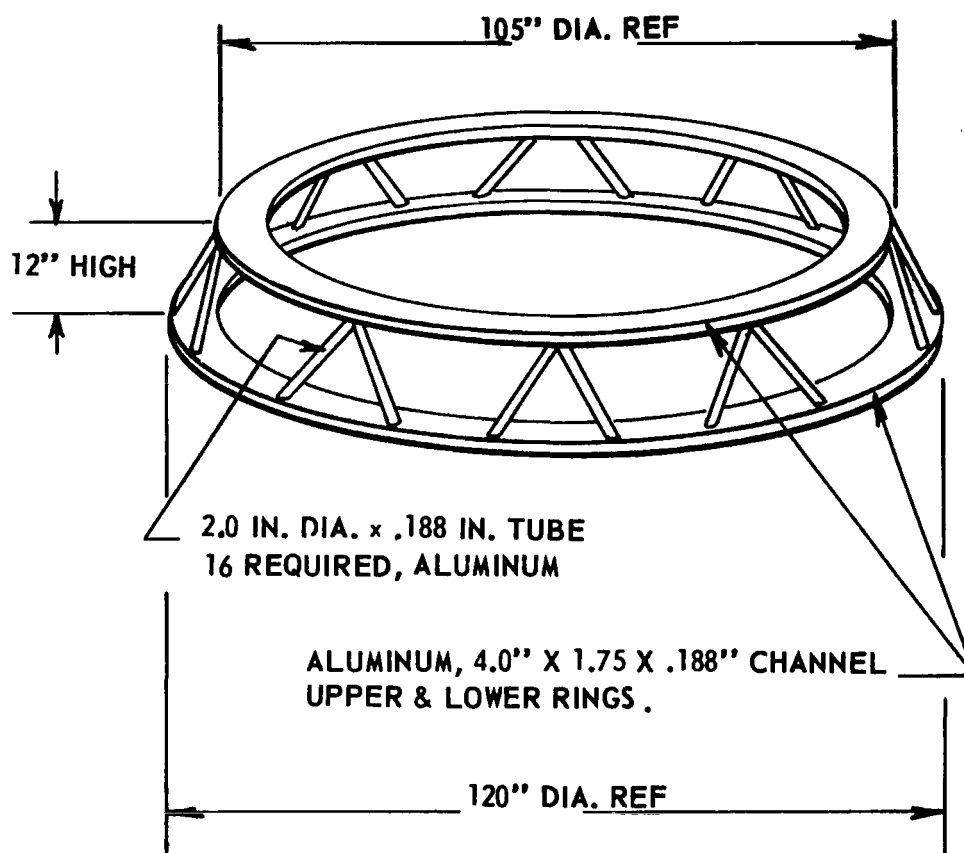
105" DIA. REF

12" HIGH

2.0 IN. DIA. x .188 IN. TUBE
16 REQUIRED, ALUMINUM

ALUMINUM, 4.0" X 1.75 X .188" CHANNEL
UPPER & LOWER RINGS.

120" DIA. REF

Figure VI-5. Payload adapter.

TABLE VI-5. ADAPTER WEIGHT SUMMARY

Description	Weight (lb)
Forward Ring	47
Aft Interface Ring	49
Struts and Fasteners	24
Total	120

SECTION VII. THERMAL SYSTEM DESIGN

TABLE OF CONTENTS

LIST OF ILLUSTRATIONS

LIST OF TABLES

SECTION VII. THERMAL SYSTEM DESIGN

A. Requirements

The first consideration was to define the thermal problem areas and to ascertain component temperatures which must be maintained for the vehicle to perform its intended function. The solar panel temperature must be maintained below 140° F average if the desired power is to be obtained from the solar panels. This temperature limit could not be exceeded because of the inherent characteristic of the solar module power to decrease as the temperature increases as shown in Figure IX-5, Section IX. Environmental temperature limits for the experiments are 14° F to 86° F. The CBR's are to operate below 85° F. Hydrazine tanks and distribution lines must be held above the fuel freezing point of 35° F.

B. Baseline System Description

A thermal analysis of a vehicle design is dependent upon the structure, skin, material, surface coating, and component characteristics such as physical size, weight, location, power dissipation, and orbit orientation. A thermal model of the HEAO baseline spacecraft configuration was constructed which included all individual panels, experiments, subsystem components, and structural members. The outside skin and solar panels were broken down into nodes of reasonable size; i. e., a total of 416 nodes were used in the thermal model. The Lockheed Orbital Heat Flux computer program [VII-1] was used to calculate the external environment, and the "CINDA" thermal analyzer program [VII-2] was used to calculate the temperature distribution within the model.

For this analysis, the spacecraft was considered in a pointing (non-scanning) mode whereas the HEAO rotates about the scan axis at 0.1 rpm.

The orbit used for the analysis was as specified in the guidelines. The orbit orientation, with respect to the earth's ecliptic plane, was chosen to expose the spacecraft to maximum sunlight. This was done to simulate the worst-case condition, since the primary thermal control problem is the disposal of excess heat. As shown in Figure VII-1, the orbit plane is oriented so that the imaginary line made by the orbit plane cutting the ecliptic plane is 90 degrees to the sunline. This condition sets the angle between the sunline
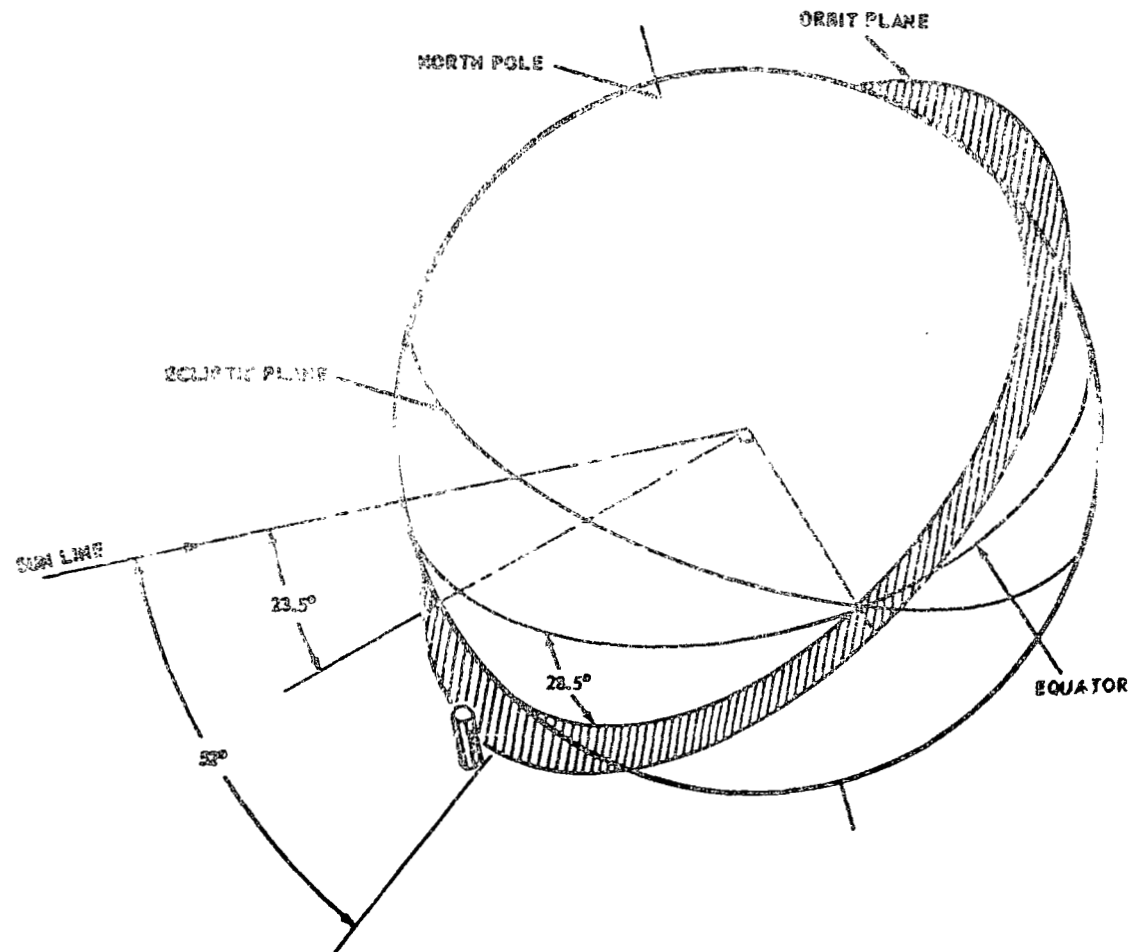
Figure VII-1. Assumed orbit orientation with respect to the sun.

and the orbit plane at 52 degrees. This occurs at either the summer or winter solstice. Summer solstice is shown in Figure VII-1. The maximum sunlight time for a satellite in a 28.5-degree, 200-n. mi. orbit is 62.3 minutes. The minimum sunlight (55.7 minutes) occurs when this imaginary line lies on the sunline.

Figure VII-2 shows the structural layout and configuration of the HEAO spacecraft. Figures VII-3 and VII-4 present the box truss structure, and the panel and experimental layout for the baseline vehicle used in the thermal model. The vehicle is the baseline and represents the latest configuration. Other configurations studied are shown in the Appendix F. Table VII-1 presents the subsystems component listing and location.

Guidelines and assumptions used in performing this analysis were as follows:

- Baseline design box truss structure, panels, and experiment layout as shown in Figures VII-2, VII-3, and VII-4, respectively, were used in the analysis.

- Substrate for solar cells was 3/8-inch aluminum honeycomb paneling (face sheet thickness = 0.008 inch).

- Meteoroid shielding and/or thermal shielding was 0.025-inch aluminum sheet.

- Equipment panels and radiation shielding was 1-inch honeycomb.

- Solar absorptivity and emissivity values used were:

	α_s	ϵ_t
X-ray detectors	0.34	0.04
Solar panels	0.70	0.80
All other surfaces	0.30	0.80

- The spacecraft was in a 200-n. mi. circular orbit and at a 28.5-degree inclination with respect to the equatorial plane.
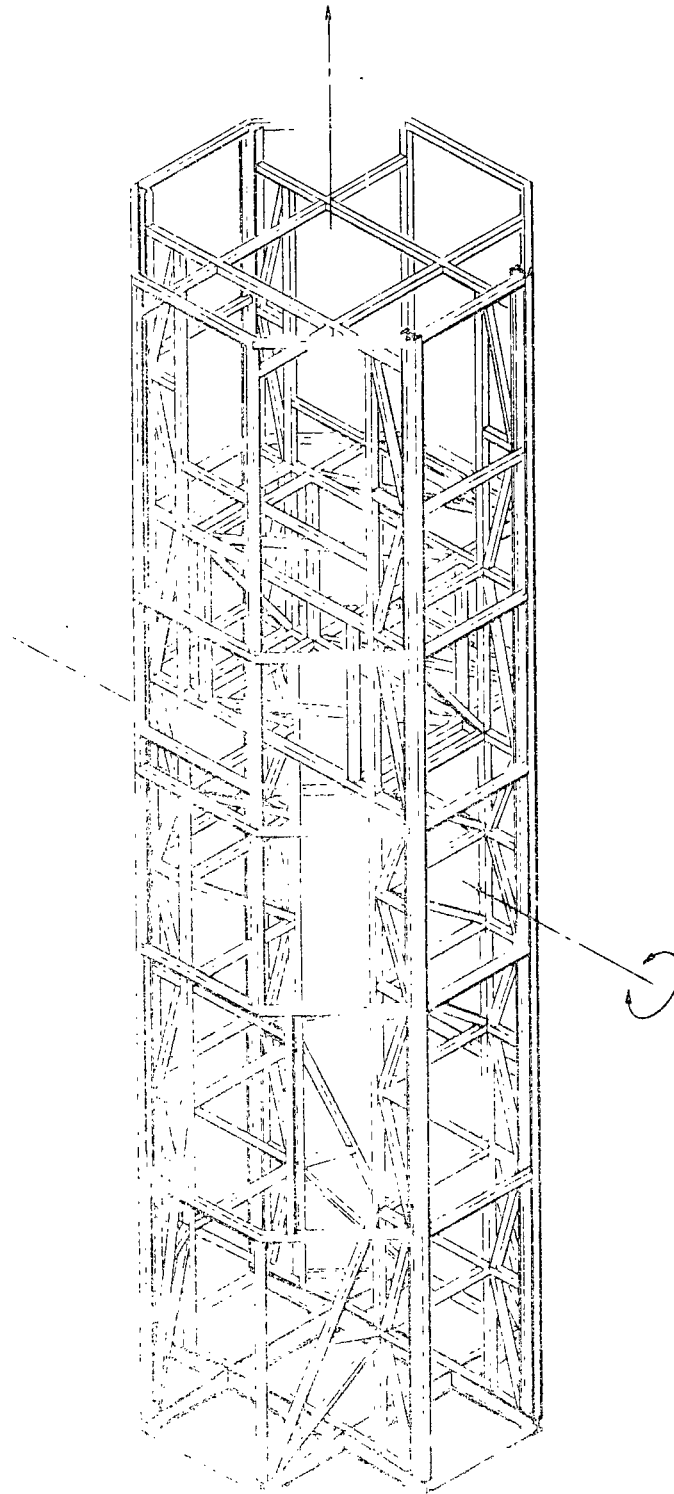
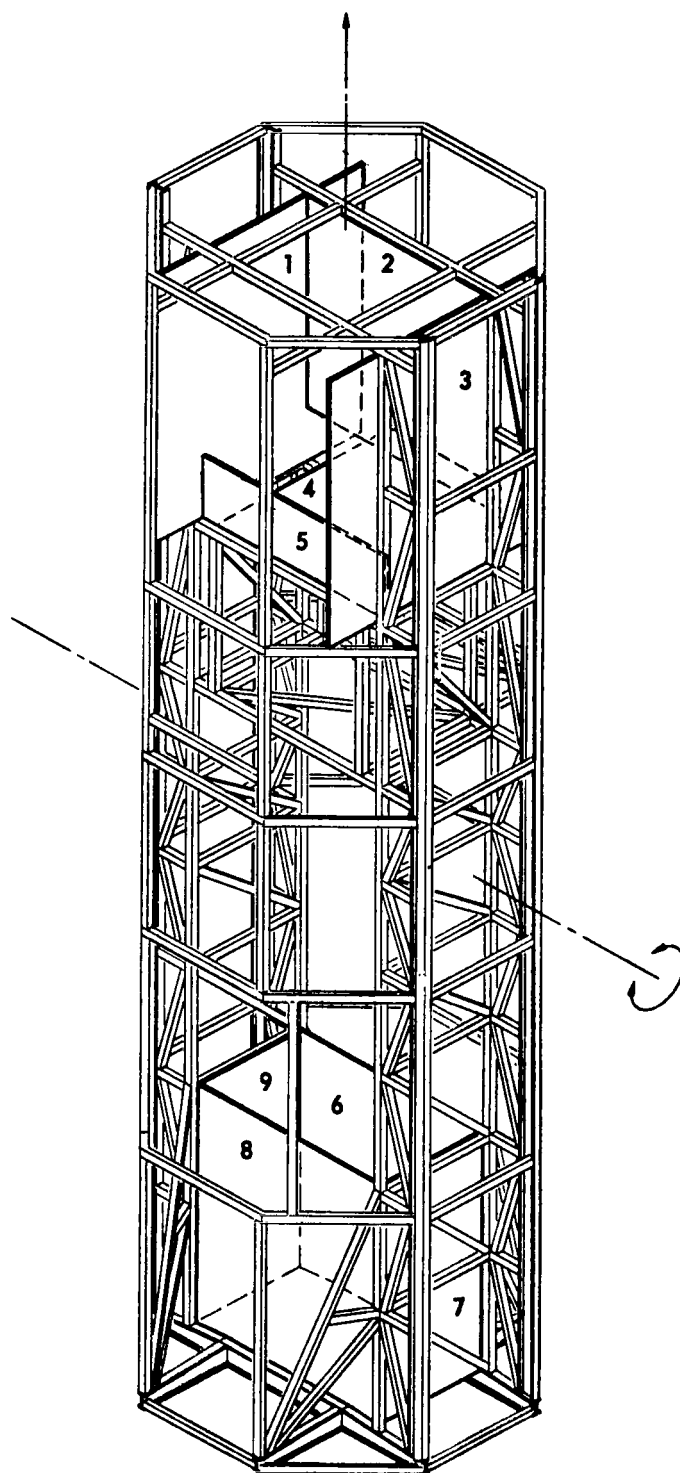Figure VII-2. HEAO structural configuration utilized in this analysis.

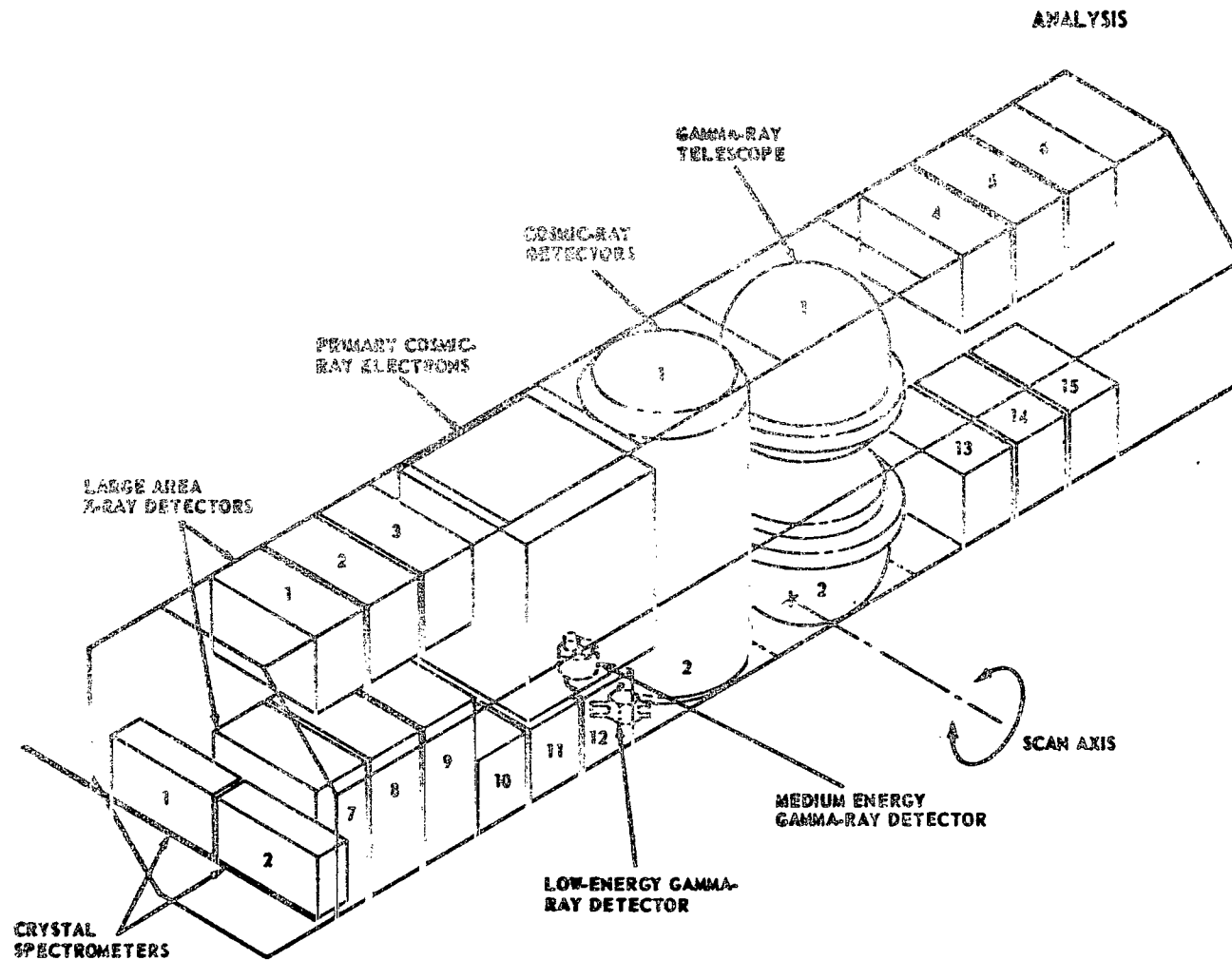Figure VII-3. HEAO subsystems panel layout utilized in this analysis.

Figure VII-4. HEAO baseline configuration showing experiment locations utilized in this analysis.

TABLE VII-1. SUBSYSTEM COMPONENT LOCATION

Component	Number of Units	Location
Tape Recorder	4	Panel 4
Switching network	1	Panel 4
Command receiver	2	Panel 4
Analog signal conditioner	1	Panel 4
Digital multiplexer	1	Panel 4
Diagnostic logic	1.	Panel 4
Power combiner	1	Panel 4
Minitrack beacon transmitter	2	Panel 4
Command decoder	1	Panel 4
Summing network	1	Panel 4
S-band transmitter	2	Panel 4
Signal processor	1	Panel 4
Digital sun sensor electronics	1	Panel 4
Star mapper number 1	1	Panel 4
Star tracker	1	Panel 4
Rate gyro	3	Panel 8
Magnetometer electronics	1	Panel 8
Magnetic coils	3	Panel 8
Switch selector	1	Panel 8
Measurement distributor	1	Panel 8
Control distributor	1	Panel 8
Master measuring voltage supply	1	Panel 8
Charger battery regulator	5	Panel 9
Power distributor	1	Panel 9
Magnetometer	1	On boom extending 10 feet from end of spacecraft
Star mapper number 2	1	Attached to structure by gamma-ray telescope number 1
RCS modules	4	Attached to ends of spacecraft

TABLE VII-1. (Concluded)

Component	Number of Units	Location
Flywheel	1	Attached to structure near gamma-ray telescopes
Digital sun sensor	1	Attached to structure which supports middle solar panel (insulated from solar panel)
S-band antenna 1 and 2	2	Attached to end of spacecraft adjacent solar panels
S-band antenna 3 and 4	2	Attached to end of spacecraft adjacent shaded side panels
Gas bottles	4	Attached to structural member near end of spacecraft
Propellant tanks	2	Attached to structure near end of spacecraft

● Heat dissipated by each component is shown in Table VII-2.

● All subsystems components had good metal-to-metal contact with the mounting panels.

● Heat source constants used were:

Solar constant	447 Btu/hr-ft^2
Earth albedo	43 percent
Earth IR	68.2 Btu/hr-ft^2

TABLE VII-2. HEAT DISSIPATION RATE UTILIZED IN THIS ANALYSIS FOR EACH COMPONENT AND EXPERIMENT

Component	Number of Units	Heat Dissipation per Unit (w)
Large area X-ray detector (Basic Module)	6	9
Large area X-ray detector (Modulation Collimators)	3	10
Large area X-ray detector (Bragg Spectrometers)	2	8
Large area X-ray detector (Experiment 2)	6	6
Low energy gamma-ray detector	1	10
Medium energy gamma-ray detector	1	10
Gamma-ray telescope	2	20
Primary cosmic-ray electrons	1	20
Cosmic-ray calorimeter	1	50
Flywheel	1	55
Star mapper	2	5
Digital sun sensor	1	2
Signal processor	1	55
S-band transmitter	2	18
Summing network	1	4
Command decoder	1	4
Minitrack beacon transmitter	2	1
Diagnostic logic	1	3
Digital multiplexer	1	5
Analog signal conditioner	1	8
Command receiver	2	0.4
Switching network	1	4
Tape recorder	4	0.05
Magnetometer	1	2
Star tracker	1	5
Digital sun sensor	1	2
Charger battery regulator	5	70
Power distributor	1	20
Rate gyros	3	12.4
Magnetometer electronics	1	2
Magnetic coil	3	100
Switch selector	1	20
Measurement distributor	1	20
Control distributor	1	20
Master measuring voltage supply	1	20

The absorptivity (α) and the emissivity (ϵ) values assumed for the panel coatings were chosen to hold the overall vehicle temperature down. These values ($\alpha = 0.3$ and $\epsilon = 0.8$) are considered to be within the realm of the state-of-the-art for spacecraft coatings. Two typical examples are S-13G (ZnO/Silicone) and Z 93 (ZnO/K_2SiO_3). Figures VII-5 and VII-6 show the degradation of the two paints with regard to solar exposure only [VII-3]. Reference VII-4 gives a more realistic indication of the paint deterioration including meteoroid bombardment and solar exposure as reported from Pegasus flights (Fig. VII-7). Note the value of α_s/ϵ_t after 1800 hours of solar time is 0.40, and in this analysis 0.375 was used. This will cause a small temperature rise; i.e., approximately 2 percent.

Future studies should look into this aspect of thermal coatings in greater depth and detail. The solar panel values, $\alpha = 0.7$ and $\epsilon = 0.8$, were chosen based on former satellite solar panel (ATM) characteristics. The values used for the viewing surface of the X-ray detectors are those of polished aluminum or aluminized Mylar which is the specified surface for these instruments. A thermal coating cannot be applied because of the sensing characteristics.

C. Results

Preliminary results from an effectiveness analysis of the HEAO thermal control system have been obtained [VII-5]. The analysis consists of establishing characteristic parameters associated with the HEAO thermal control system, determining the values of the parameters, and generating a numerical measure of effectiveness for two thermal control, active and passive, concepts considered for HEAO. The values of the characteristic parameters were related to the solar arrays only; i.e., the parameter values associated with the spacecraft were not considered in this preliminary analysis. The thermal control concepts analyzed consisted of a baseline system which utilized paint only; alternate systems which utilized both paint and heat pipes are discussed in Appendix F. The vehicle configuration considered was the baseline consisting of the solar arrays mounted to the sides of the spacecraft with the center panel perpendicular to the sunline.
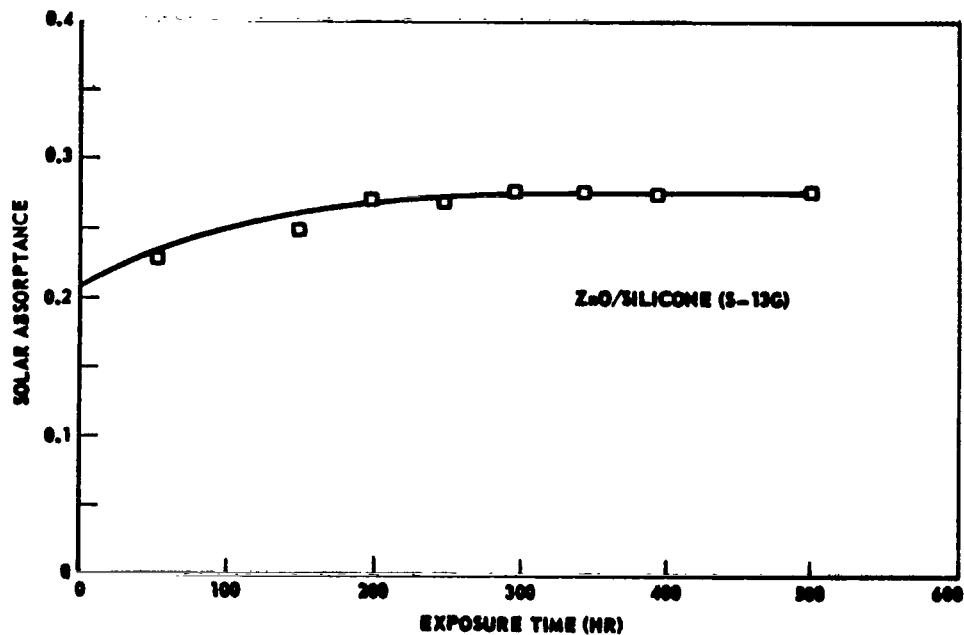
Figure VII-5. Solar absorptance of S-13G thermal control coating as a
function of exposure time at a one-sun level (0. 2 to 0. 4μ xenon) and 710° R.
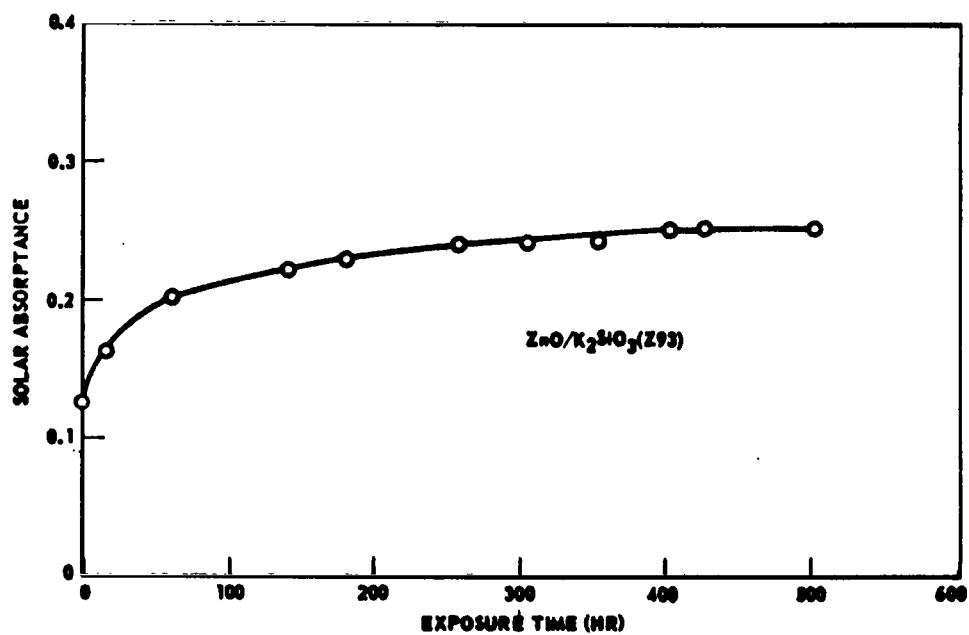

Figure VII-6. Solar absorptance of Z-93 thermal control coating as a function
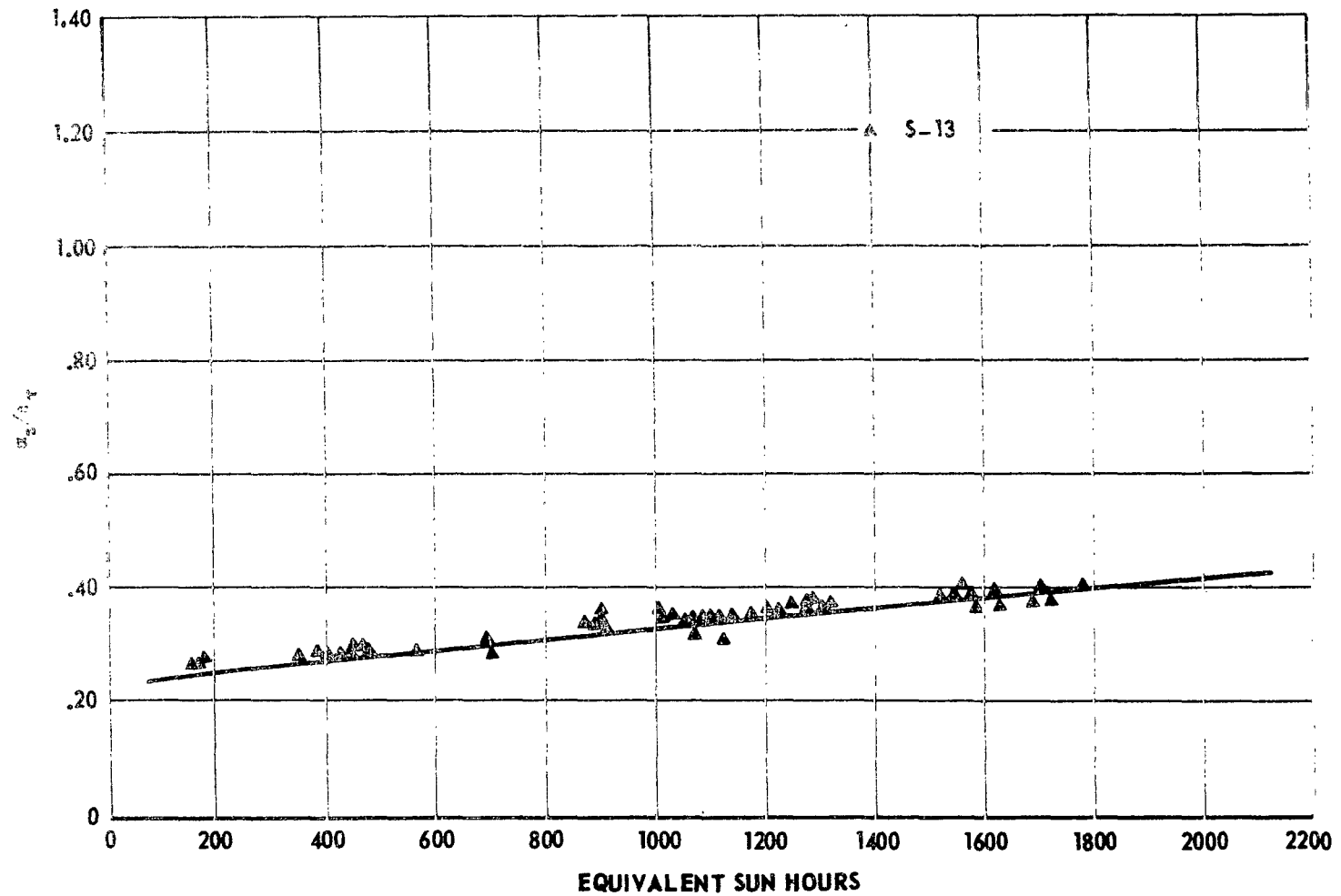of exposure time at a one-sun level (0. 2 to 0. 4μ xenon) and 960° R.

Figure VII-7. α_s/ϵ_t degradation history.

The characteristic parameters considered are as follows:

(1) The range of temperatures (maximum to minimum) experienced by the array during an orbit.

(2) The difference between the average orbital array temperature and an optimum array temperature (140° F) is chosen as the optimum temperature to reflect power requirements.

(3) The temperature gradient across the surface of the array.

(4) The effect of the mass of the thermal control system on mission lifetime (the ballistic number, B_n, is expressed in terms of any increase in total mass).

(5) The lifetime of the elements (paint and heat pipes) of the thermal control system.

The lifetime of the elements is considered to be the time that the system will control the temperature of the HEAO arrays within specified limits. This value is certainly a strong function of element degradation. Only a rough estimate has been made as to the quantitative value of this degradation. This estimate is based on micrometeoroid and thermal degradation tests and satellite data. It should be noted that all parameters were considered to be equally important in this preliminary analysis.

The numerical values of the temperature-related parameters were obtained from the thermal analysis. The values for the other parameters were obtained from estimates of control element weights and degradation as mentioned above. The two thermal control concepts were compared relative to a base consisting of no active thermal control elements. Using the analytical data, the concept utilizing heat pipes and paint is approximately 19 percent more effective than the concept utilizing paint alone. To achieve an indication of the effect of trade-offs of parameters between concepts, a computation was made assuming that the paint would last twice as long as was considered in the above case. This consideration reveals that the heat pipe concept is now approximately 12 percent more effective, thus indicating the importance of obtaining accurate degradation data. The above results indicate that the heat pipe concept is more effective than the paint-only concept. It should be noted that these results are based on the available values of the parameters considered and do not include difficulty in manufacturing, cost, or schedule time consideration. The relative importance of the above parameters also needs to be defined in Phase B and the results of this considered.

It is to be emphasized that these results and conclusions are preliminary and related to the solar array only. A more thorough effectiveness analysis should be conducted and include the cost and schedule time consideration, a more accurate determination of thermal control element lifetime, further definition of the relative importance of the parameters, and the incorporation of the spacecraft parameters.

Table VII-3 lists the resulting equilibrium temperature ranges of the experiments, equipment mounting panels, and various components located in or on the spacecraft at points other than the mounting panels. Temperature ranges for the components that are shown to be located on the mounting panels in Table VII-1 are not listed in Table VII-3. This is because these components were assumed to have good metal-to-metal contact and remain essentially at the same temperature as the panel to which they are mounted.

Note the temperature range of Panel No. 8 is 126° F to 130° F. This high temperature range is caused by the three magnetic coils which are attached to this panel. They are assumed to dissipate a total of 300 watts of heat, most of which is transferred into the panel. The temperature of this panel and the other attached components can be lowered to an operating range of 80° F to 85° F by removing these magnetic coils. There are several locations within the spacecraft where the coils could be mounted so that the heat could be dissipated at a rate that would lower this operating temperature to a desirable level. Simulation of the spacecraft dynamic behavior using a computer program indicates that the power required by the magnetic coils will be much less than 300 watts, so this local heating problem is not as severe as presently indicated.

The fuel tank location is acceptable because of the temperature range of 55° F to 70° F which is well above the hydrazine freezing point. The RCS thruster modules and some fuel lines will definitely require heaters because the temperatures will fall below the freezing point of the fuel.

The CBR's were mounted on Panel No. 9, which has a temperature range of 84° to 86° F. It is believed that by relocating the magnetic coils from this area the CBR temperature will drop to the required temperature level.

The crystal spectrometers will require heater blankets to raise their temperatures.

Figure VII-8 presents the solar panel temperature variations throughout one orbit. These curves represent the temperature of a 4.8-foot section

TABLE VII-3. ORBITAL COMPONENT TEMPERATURE RANGE

Component	Temperature (°F)
Experiments	
Large area X-ray detector 1	78 to 80
Large area X-ray detector 2	78 to 80
Large area X-ray detector 3	78 to 80
Large area X-ray detector 4	67 to 70
Large area X-ray detector 5	67 to 70
Large area X-ray detector 6	67 to 70
Large area X-ray detector 7	61 to 64
Large area X-ray detector 8	63 to 66
Large area X-ray detector 9	63 to 66
Large area X-ray detector 10	63 to 67
Large area X-ray detector 11	70 to 72
Large area X-ray detector 12	68 to 70
Large area X-ray detector 13	71 to 73
Large area X-ray detector 14	72 to 73
Large area X-ray detector 15	70 to 71
Cosmic ray calorimeter cover 1	61 to 66
Cosmic ray calorimeter core 1	64 to 66
Cosmic ray calorimeter cover 2	43 to 50
Cosmic ray calorimeter core 2	63 to 64
Low energy gamma-ray detector	63 to 64
Medium energy gamma-ray detector	60 to 61
Primary cosmic-ray electrons cover	50 to 56
Primary cosmic-ray electrons core	51 to 57
Gamma-ray telescope cover 1	30 to 34
Gamma-ray telescope core 1	35 to 39
Gamma-ray telescope cover 2	27 to 39
Gamma-ray telescope core 2	33 to 38
Crystal spectrometer 1	-31 to -20
Crystal spectrometer 2	- 7 to 4

TABLE VII-3.   (Concluded)

| Component	Temperature (°F)
Subsystems Not Mounted on Panels	
Flywheel	93 to 97
RCS modules	-51 to -21
Gas bottles	48 to 73
Propellant tanks	55 to 70
RCS valves and plumbing	26 to 52
Magnetometer	-53 to -46
S-band antenna 1 and 2	79 to 122
S-band antenna 3 and 4	-19 to - 7
Digital sun sensor	95 to 157
Star mapper 2	69 to 71
Panels	
Panel 1	0 to 12
Panel 2	80 to 86
Panel 3	82 to 127
Panel 4	63 to 65
Panel 5	70 to 85
Panel 6	69 to 78
Panel 7	93 to 121
Panel 8	126 to 130
Panel 9	84 to 86
Shady side skin panel adjacent to cosmic-ray detector 1	-53 to 11
Shady side skin panel adjacent to cosmic-ray	-65 to - 5
Shady side skin panel adjacent to cosmic-ray detector 2	-62 to 4
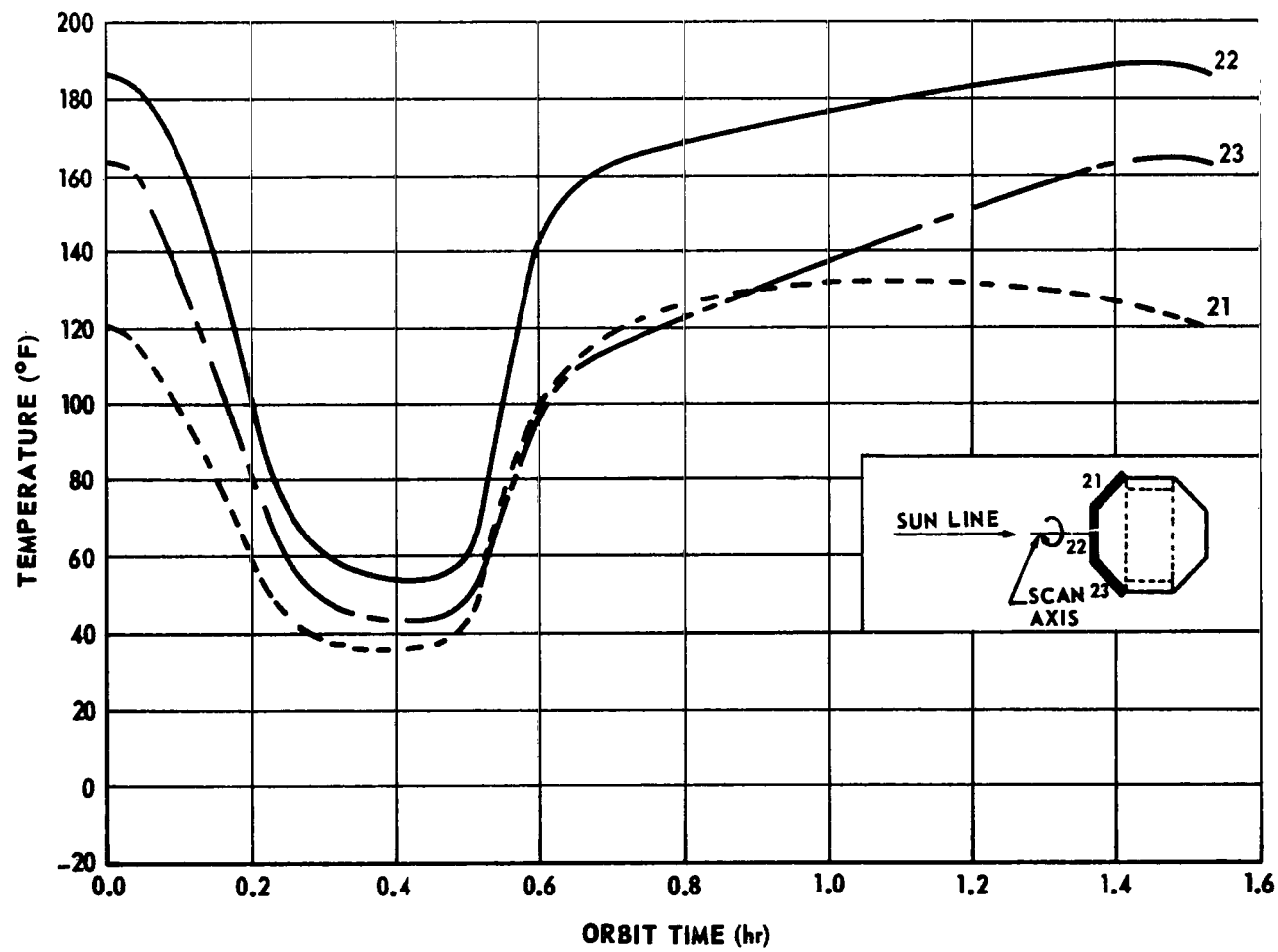
Figure VII-8. Orbit temperature variation at the center of each solar panel.

from the center of the three panels. The solid curve represents the middle panel that is perpendicular to the sunline. The two dashed curves represent the two side solar panels angled at 45 degrees to the sunline. There are some variations in the temperature along the length of the panels. These variations are caused by the different radiating paths from the solar panel substrate. For instance, the ends of the solar panels are a few degrees higher because of the radiation shields which are placed behind them to protect the subsystem components. Also, there is a faster solar panel temperature rise on the baseline configuration than on the other configurations, as given in Appendix F, as the spacecraft comes from the earth's shadow into the sunlight. There is a larger temperature variation for one orbit on this configuration as compared to studies in the appendix. This is caused by the 3/8-inch substrate having less heat capacity than the 1-inch material used on the configuration in Appendix F.

Overall, the results from this configuration are not significantly different from those in Appendix F.

D. Conclusions

The thermal system analyzed indicates a satisfactory passive system. By proper coatings, location of equipment, experiments, and panels, a satisfactory temperature range can be obtained. A thermal shield must be used, as this increases the heat capacity of the vehicle and reduces the temperature variations for the experiment and equipment.

If there is an increase in power on the vehicle, a high conductive device such as the heat pipe could be employed to maintain the desired temperature levels. Also, one must not overlook the advantages of using a capacitance device to overcome excessive temperature variation in an orbit. These two devices give the designer a backup tool in choosing systems having greater power requirements or higher temperature.

REFERENCES

1.   Newby, T. S.; and Eurich, R. G.: Heat Flux Study. LMSC Report
      M-16-64-1, July 15, 1964.

2.   Gaski, J. D.: Chrysler Improved Numerical Differencing Analyzer.
      TN-AP-66-15, April 30, 1966.

3.   Breuch, R.: Handbook of Optical Properties for Thermal Control
      Surfaces. Final Report, Vol. III, Contract No. NAS8-20353,
      Lockheed Missile and Space Company, Sunnyvale, California.

4.   Schafer, C. F.; and Bannister, C. B.: Pegasus Thermal Control
      Coatings Experiment. AIAA Paper No. 66-419.

5.   Ryberg, A., et al.: A Summary Report on System Effectiveness and
      Optimization. Contract No. NAS8-20412, ITT Federal Electric
      Corporation, September 17, 1969.

SECTION VIII.   REACTION CONTROL SYSTEM DESIGN

TABLE OF CONTENTS

LIST OF ILLUSTRATIONS

LIST OF TABLES

iv

SECTION VIII. REACTION CONTROL SYSTEM DESIGN

A. Requirements

In designing an RCS for the HEAO, the following objectives or guidelines were considered as requirements:

(1) The RCS will be designed for a 2-year on-off operating capability, thus requiring almost an unlimited number of restarts.

(2) Only existing and proven components will be used; i. e. , those components used on previous flights or proven by ground tests.

(3) The RCS design will be based upon a low total system weight, low cost, simplicity, and reliability.

(4) The HEAO will have two independent RCS units, one at each end of the spacecraft, each having six thrusters. Each unit will be capable of performing all maneuvers required of the total RCS in the event one unit becomes inoperable.

(5) The RCS of the attitude control system will provide for spin-up, despin, attitude control, and orientation maneuvers required of the HEAO. The RCS will be used primarily in conjunction with a flywheel and magnetic torquers for attitude control and orientation; however, only the RCS will be used for some maneuvers.

B. Baseline System Description

The baseline HEAO is equipped with two identical N_2H_4 monopropellant RCS units, one located at each end of the spacecraft; however, the two units are connected by a common pressurization system. Each unit has two thruster modules. Each thruster module consists of three thrusters, making a total of 12 thrusters for the HEAO. The thruster modules are attached to the spacecraft in the XY plane which provides two pitch thrusters, four roll thrusters, and four yaw thrusters for each unit (Fig. VIII-1).

Two separate RCS units are required to prevent having to use long propellant lines from a single propellant tank which could present severe thermal problems; i.e., vaporized or frozen propellant in the lines; however,
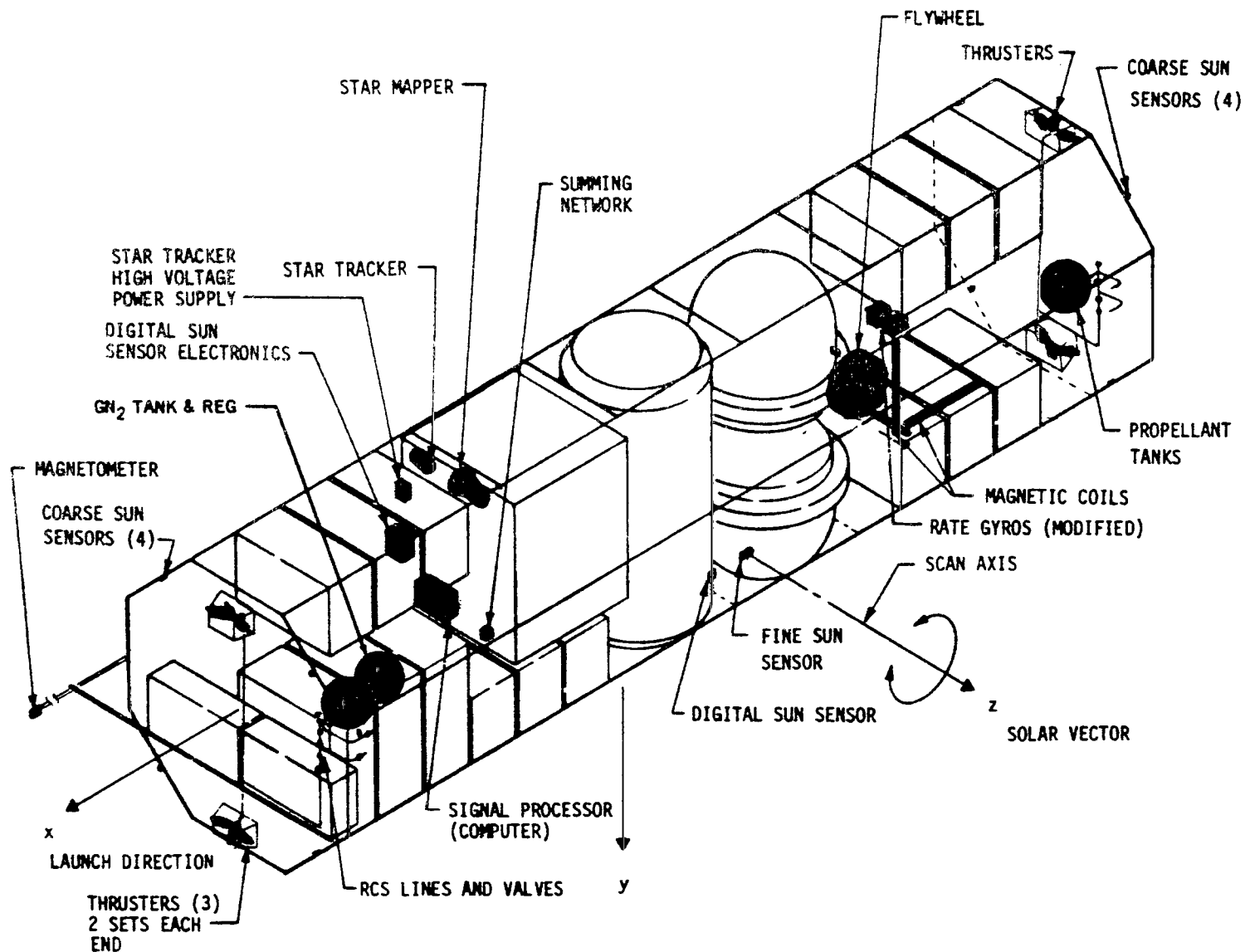
Figure VIII-1. Location of the propulsion system components and attitude sensing and control system components.

the two separate propellant tank systems are connected. In the event that some thrusters on one end become inoperable, the propellant in the tank on that end can be transferred to the thrusters on the other end. The connecting propellant line can run along the inside wall of the solar panel side of the spacecraft to help prevent the propellant from freezing. This backup system will be activated by opening and closing appropriate valves should control of the spacecraft become critical because of thruster failure. Activation of this system includes the shutdown of the inoperable RCS unit. In the event one RCS unit has to be shut down, the other unit will be capable of performing all RCS required maneuvers of the HEAO.

Severe thermal problems with the propellant can result by attaching the thruster modules to the spacecraft in such a manner that one thruster module will be in the shade of the spacecraft most of the time and its opposite in the solar environment. Since the spacecraft is required to have a solar pointing spin vector (Z axis), attaching the thruster modules to the spacecraft in the XY plane will provide an equal solar thermal environment at each module. However, during some particular orientation modes required of the spacecraft, one thruster module can be in the solar environment while its Y opposite can be in the shade of the spacecraft. But, for the entire mission, attaching the thruster modules in the XY plane will provide the best equal thermal environment for each module.

Table VII-3 summarizes the environmental temperature distribution experienced by various components within the HEAO. The RCS thruster modules can be expected to experience a temperature variation of –51° F to –21° F during the 2-year HEAO mission; the propellant tanks will experience a temperature variation of 55° F to 70° F; valves and plumbing can be expected to experience a temperature variation of 26° F to 52° F. Thus, it is apparent that electrical heaters will be required in the RCS thruster modules to prevent the N_2H_4 propellant from freezing (35° F), and some type of thermal protection will be required for the valves and plumbing. N_2H_4 should not be allowed to exceed 350° F, since it could start spontaneously decomposing at this temperature.

During this study, four types of RCS units were considered as possible candidates for use on the HEAO:

(1) N_2H_4 monopropellant system.

(2) Cold N_2 gas system.

(3) Bipropellant system.

(4) Resistojet system.

The choice as to which system to use for the baseline HEAO was narrowed down to the N_2H_4 monopropellant system and the cold N_2 gas system. Of these two systems, the N_2H_4 monopropellant was chosen as the baseline HEAO RCS. This choice was made only on the basis that the N_2H_4 monopropellant system weighed less than the cold N_2 gas system. The N_2H_4 monopropellant system is discussed in detail in the following paragraph; the other three candidates are discussed in detail in Appendix G.

C. Analysis and Trends

1. Analysis. Table VIII-1 presents a HEAO mission simulation which summarizes the maneuvers requiring the use of the RCS, the total impulse required of the RCS for each maneuver, and the propellant weight required for each maneuver. Each maneuver or reorientation involves thruster impulses which start precessional motion toward the new direction and a second impulse some time later which stops motion once the desired direction is reached. The propellant weight is based on an expected average pulsing specific impulse of 200 sec provided by the baseline RCS. A schematic drawing of the proposed baseline RCS for the HEAO is shown in Figure VIII-2. This schematic is a modified version of an N_2H_4 RCS concept as presented in Reference VIII-1. A summary weight statement of the baseline RCS is presented in Table VIII-2. The main subsystems of this RCS are pressurization, propellant, and thruster. Each of these will be discussed in detail.

a. Pressurization subsystem. Both units of the baseline RCS are connected to a common N_2 gas pressurization system. Since the thermal effects upon N_2 gas in space are not severe, pressurant feedlines can be allowed to run the entire length of the spacecraft if necessary. Thus, by using a common pressurization system rather than a separate system for each RCS unit, the pressurization system is simplified with a savings in weight.

During the 2-year mission of the HEAO, the RCS will require approximately 2.12 pounds of N_2 gas as a pressurant. The leak rate of the pressurant gas is expected to be about two standard cubic centimeters per minute per valve. Thus, the leakage over a 2-year period was calculated to be about 36 pounds. The total pressurant gas required for the entire mission will weigh 38.12 pounds. This gas is stored under a pressure of about 3000 psia in a titanium storage bottle.

TABLE VIII-1. SUMMARY OF TOTAL IMPULSE AND N_2H_4 PROPELLANT REQUIREMENTS FOR JET THRUSTER MANEUVERS

Event	Total Impulse (lb_f-sec)	Propellant Weight (lb) (I_{sp}-200 sec)
First Year		
Nulling of assumed spacecraft rates of 3 deg/sec about each axis after separation from launch vehicle	340	1.70
Solar acquisition (rotation of 90 deg about X and Y axes)	212	1.06
Maintain spacecraft attitude for 8 hours during spin-up of flywheel	173	0.87
Flywheel spin-up counteract torque imposed on spacecraft	133	0.67
Spin-up of spacecraft to 0.1 rpm about scan Z axis	29	0.15
Reorientation of first galactic scan position	105	0.53
Galactic scan reorientations during 30-day period	140	0.70
Reorientation to sun (25 deg) after completion of galactic scan	71	0.36
Solar vector guiding mode[a]	none	none
Despin spacecraft after first 7 months	29	0.15

a. Requires a period of 6 months.

TABLE VIII-1. (Concluded)

Event	Total Impulse (lb_f-sec)	Propellant Weight (lb) (I_{sp}-200 sec)
First Year		
Reorient spacecraft to 30 positions 12 deg apart for pointing mode operation	849	4.25
Totals for first year	2081	10.44
Second Year		
Spin-up of spacecraft to 0.1 rpm	29	0.15
Reorientation to first galactic scan position	105	0.53
Galactic scan reorientations during 30-day period	140	0.70
Reorientation to sun after completion of scan	71	0.36
Solar vector guiding mode[a]	none	none
Despin spacecraft after 7 months of second year	29	0.15
Reorient spacecraft to 30 positions 12 deg apart for pointing mode operation	849	4.25
Totals for second year	1223	6.14
Totals for 2 years	3304	16.58

Note: For contingencies and safety, the required propellant is multiplied by a factor of 2 and rounded off: N_2H_4 ≈ 35 lb required; total impulse ≈ 7000 lb_f-sec.
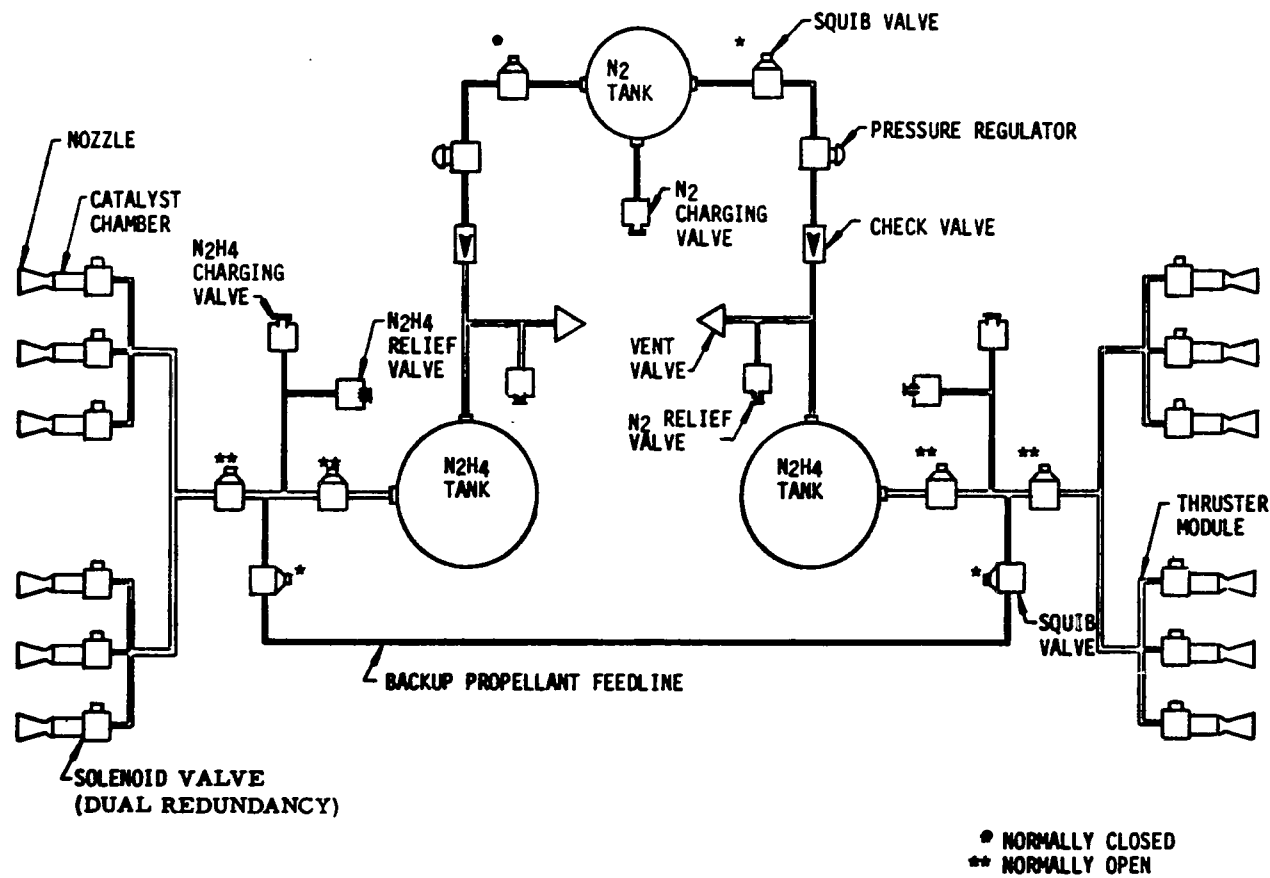
a. Requires a period of 6 months.

Figure VIII-2. System schematic of an N_2H_4 monopropellant RCS.

TABLE VIII-2. WEIGHT SUMMARY OF THE N_2H_4 MONOPROPELLANT RCS

Item	Component Weight (lb) (Total Impulse $\approx$ 7000 lb_f-sec)
N_2 Tank	46.00
Squib valve (8)	2.80
Check valve (2)	0.22
N_2 charging valve	0.12
Pressure regulator (2)	0.60
N_2 vent valve (2)	0.24
N_2 relief valve (2)	0.52
N_2H_4 tank (2)	14.60
N_2H_4 relief valve (2)	0.52
N_2H_4 charging valve (2)	0.24
Thruster modules (4)	15.00
Lines	6.00
Miscellaneous	1.00
System dry weight	87.86
N_2 charged (36-lb leakage)	38.12
N_2H_4 charged	35.00
Total system weight	160.98

The RCS propellant tanks are not pressurized until the HEAO is placed into orbit. This is done because of the danger of rupturing a bladder in the propellant tanks during launch. Once in orbit, two squib valves (one for each RCS unit) open and the pressurant gas flows through a pressure regulator which adjusts the pressure for use in the propellant tank. The propellant tank feed pressure is about 290 psia.

b. Propellant subsystem. The properties of monopropellant N_2H_4 are presented in Table VIII-3. As shown previously, 35 pounds of N_2H_4 propellant are required of the RCS for the entire mission of the HEAO. Since two units are used, 17.5 pounds are put into each tank. Each tank utilizes a positive expulsion system to force the propellant to the thrusters. The expulsion system consists of a collapsible bladder around an expulsion tube. N_2H_4 fills the bladder and the pressurant gas enters the propellant tank on the other side of the bladder, collapsing it to force the propellant out of the tank at 290 psia.

In the event of a thruster failure on one end of the spacecraft, and the control of the spacecraft becomes critical, a squib valve can be activated to shut down that entire RCS unit. Control can be maintained by the RCS at the other end. When the propellant at the operating end is depleted, however, the activation of squib valves allows the propellant at the nonoperating end to flow through a backup propellant feedline to the thrusters at the operating end. Aluminum propellant tanks are used.

c. Thruster subsystem. The engine type proposed is the Rocket Research Corporation MR-6A. This engine is capable of generating 0.5 pound of thrust with a chamber pressure of 200 psia. A steady-state vacuum specific impulse of 221 sec is maintained at this chamber pressure. This specific impulse was degraded to 200 sec to account for pulsing. Shell 405 catalyst is employed to obtain spontaneous decomposition of the hydrazine monopropellant. The minimum impulse bit is 0.005 lb_f-sec with repeatability within ± 10 percent. Another version of this 0.5-pound-thrust engine has operated at 110 psia chamber pressure and duty cycles of 100 percent to 0.017 percent for 24 consecutive hours (1 011 383 pulse cycles) without failure [VIII-3]. Electrical signals from the spacecraft guidance and control system operate the engines' dual, redundant solenoid valves to allow the propellant to flow through to initiate thrust. This engine is also capable of operating with a blowdown pressurization system so that thrust decreases to 0.25 pound at 100 psia chamber pressure. This engine has operated in space and is a reliable and proven component. Table VIII-4 gives data on this engine. A total of 12 engines are used on the spacecraft.

TABLE VIII-3. PHYSICAL, CHEMICAL, AND THERMODYNAMIC PROPERTIES OF N_2H_4

Item	Data
Mean molecular weight	32.0453
Density	62.8 lb_m/ft^3 at 68° F
Freezing point	34.8° F
Boiling point	235.9° F
Critical pressure	2132 psia
Critical temperature	716° F
Vapor pressure	0.28 psia at 68° F
Heat of formation	+677 Btu/lb_m at 77° F
Heat of vaporization	602 Btu/lb_m at 77° F
Specific heat	0.736 Btu/lb_m-° F at 68° F
Thermal conductivity	0.205 Btu/hr-ft-° R at 68° F
Gas constant	48.2 $ft-lb_f/lb_m$-° R
Gamma	1.197 at 76° F
Viscosity	0.972 centipoise - 68° F
Cost	$1.50/lb
	Reference VIII-2

TABLE VIII-4. RCS ENGINE FOR USE ON HIGH-ENERGY ASTRONOMY OBSERVATORY

Item	Data
Manufacturer	Rocket Research Corp. Seattle, Washington
Designation	MR-6A
Type	Liquid monopropellant
Propellant	N_2H_4
Thrust (maximum), lb_f	0.5
Chamber pressure (maximum), $lb_f/in.^2$	200
Feed pressure (maximum), $lb_f/in.^2$	290
Specific impulse (maximum thrust) sec	221
Thrust (minimum), lb_f	0.25
Chamber pressure (minimum), $lb_f/in.^2$	103
Feed pressure (minimum), $lb_f/in.^2$	150
Specific impulse (minimum thrust), sec	218
Rated duration	1 000 000 + pulses
Weight, lb	0.9
Expansion ratio (ϵ)	100
	Reference VIII-3

2.   Trends. As a monopropellant, N_2H_4 is used in rocket engines to produce a thrust which ranges from 0.5 pound to 600 pounds. All of the JPL Ranger and Mariner spacecraft have used such thrusters for making precise trajectory corrections, and several communication satellites maintain their position in a synchronous earth orbit with the aid of N_2H_4 engines. N_2H_4 midcourse correction engines were used on the Rangers and the 1967 Mariner; both probes used a nonspontaneous H-7 catalyst. For this catalyst to begin decomposing N_2H_4, the catalyst had to be preheated to a temperature of about 600° F to 800° F. Thus, an auxiliary ignition system was required which consists of operating the thruster for a short time with an oxidizer, such as nitrogen tetroxide, which is hypergolic with N_2H_4. The 1969 Mariner used the spontaneous Shell 405 catalyst which eliminated the auxiliary ignition system. Thus, the 1969 Mariner had a simpler and more reliable propulsion system than that used on the 1967 Mariner. It had 30 percent fewer components, 45 percent fewer leak paths, and weighed 4.6 pounds less. The next major new use of an N_2H_4 system will probably be in the Viking spacecraft. The principal objective of the Viking 1973 Project is to "soft" land a scientific payload on the surface of Mars with the aid of throttleable N_2H_4 thrusters.

Liquid N_2H_4 is not shock sensitive and can be heated to a practical limit of 350° F before thermal decomposition becomes significant. Since many materials begin to act as catalysts with N_2H_4 well below 500° F, any part of a propulsion system which will be exposed to N_2H_4 must be clean and free of rust and scale. Since N_2H_4 is almost like water in its capacity for absorbing heat, local heat transfer rates must be limited; and, in designing a monopropellant N_2H_4 propulsion system, any heat to be transferred from the thruster area to parts of the system containing the liquid must be taken into account.

A limitation of N_2H_4 is a freezing temperature of about 35° F. Adding certain substances lowers this freezing point, but at a price. Water and NH_3 are effective, for example, but they also lower performance. Hydrazinium nitrate is effective, too, and even improves performance; but it raises the decomposition temperature and makes handling the propellant slightly harder. Electric heaters will be required in the thruster modules of the HEAO to prevent the freezing of N_2H_4 in the feedlines. Table VII-3 shows that the RCS thruster module temperature will vary from -51° F to -21° F, as mentioned previously.

N_2H_4 is readily compatible with many common materials used for construction of a propulsion system, such as the 18-8 series of stainless steels, aluminum, titanium, Teflon, and butyl rubber.

From a handling and safety point of view, mixtures of air and N_2H_4 vapor are extremely flammable, and care must be taken to exclude air from any N_2H_4 system. The breathing of N_2H_4 vapors should be avoided because its tolerance limit value is one part per million for an 8-hour daily exposure.

Hydrazine's popularity really stems from the discovery of the catalyst, Shell 405, which spontaneously and repeatedly initiates decomposition of the fuel. The disadvantages of having to use an auxiliary ignition source when N_2H_4 was used with the old H-7 and HA-3 catalysts, however, prompted a search for a spontaneous catalyst that culminated in the development of Shell 405 by the Shell Development Company under contract to NASA-JPL. A "spontaneous catalyst," in this context, is one that will start to decompose N_2H_4 after being in contact with it only a short time (10 to 1000 msec), and when both substances are at a temperature no higher than 70° F. Shell 405 is made up of an aluminum oxide carrier of high surface area — about 7.80 x $10^5 ft^2/lb_f$ — and impregnated with the active material, iridium. It is reusable, available in several particle sizes, and costs about $2100 per pound. Naturally, its high cost and the use of a strategically scarce metal tend to restrict its use. But it is very attractive for applications which require many hundreds of operations of the propulsion system.

Shell 405 has not proven physically as durable as either of its predecessors, H-7 or HA-3. As a result of its apparent reduction in strength at high temperatures, there may be a physical loss of catalyst from a thruster, which in turn results in very rough thruster operation — or even in no operation at all. The rate at which catalyst is lost is affected by the propellant flow rate per unit of bed cross-sectional area, the uniformity of the injector, and the technique used for retaining the catalyst. Though the problem has not prevented the widespread use of Shell 405, it has required an extensive development effort in some cases. NASA is currently sponsoring further investigations aimed at improving the durability of the new catalyst.

When N_2H_4 decomposes with the proper catalyst, 12 kcal of energy per mole of liquid N_2H_4 are released. Once the decomposition begins, the reaction is self-sustaining. The products of decomposition are clean and the flame temperature is low. The products of the decomposition are gaseous NH_3, N_2, and H_2. Though the details of the reaction are not completely understood, it can be represented in overall terms as:

$$2N_2H_4 \rightarrow 2NH_3 + N_2 + H_2 \qquad .$$
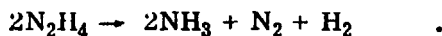
This is followed by a much slower endothermic reaction (i.e., one that absorbs energy) in which NH_3 is catalytically decomposed:

$$2NH_3 \rightarrow N_2 + 3H_2 \qquad .$$
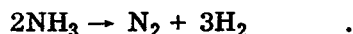
While the first reaction is controlled by transport processes, the second reaction is kinetically rate-limited. The practical usefulness of the second reaction lies in the fact that the composition, and temperature, of the exhaust products can be controlled over fairly wide limits by varying the length and thus the residence time of the catalyst bed [VIII-4].

D. Conclusions

A summary comparison is made between the baseline RCS N_2H_4 monopropellant system and the three alternate RCS concepts: bipropellant, cold N_2 gas, and resistojet.

Based on the impulse requirements of the RCS, an N_2H_4 monopropellant propulsion system was chosen. Even though a bipropellant system would weigh less, a monopropellant system was chosen because it is simpler and hence affords greater system reliability. Monopropellant fuels can also achieve a higher fraction of their theoretical performance and form a large proportion of the system mass. Their main drawback, however, is a comparatively low absolute level of performance. Currently operational bipropellant systems deliver at least 18 to 25 percent more specific impulse than an N_2H_4 monopropellant system.

Based on the total impulse requirements (7000 lb_f-sec) of the RCS, a cold N_2 gas RCS will weigh approximately 100 pounds more than the monopropellant N_2H_4 RCS. An N_2H_4 monopropellant system will produce at least three times the specific impulse of a cold N_2 gas system. Based on the weight difference of the two systems, the monopropellant system was chosen; however, the cold N_2 gas system has higher reliability, greatest simplicity, shorter lead time, more advanced state-of-the-art, and lower cost than the monopropellant or bipropellant systems. During the Phase B study a determination should be made as to whether the weight difference between the monopropellant system and the cold gas system is critical enough to rule out the cold gas system.

The N_2H_4 monopropellant system was chosen over the resistojet system because the weight and electrical power requirements of the resistojet system were considered excessive.

For a detailed discussion and comparison of the three alternate RCS's see Appendix G.

A study should be performed during Phase B to determine if the Shell 405 catalyst is capable of operating for a 2-year period through many cycles without significant deterioration.

REFERENCES

VIII-1.   Anonymous: Weight Comparison of Low Thrust-Low Impulse
           Attitude Control Systems. Walter Kidde & Company, Inc.,
           Belleville, New Jersey, Report No. 0310-275.

VIII-2.   Iwen, A. C.: Propellant Properties Data. Brown Engineering
           Company, Huntsville, Alabama, Summary Report SMS-PVEL-078,
           Contract No. NAS8-20073, T.D. A2-AVB-3-057, Revised
           April 1969.

VIII-3.   Anonymous: Satellite Attitude Control Engine, from Data Sheet
           on Rocket Research Corporation MR-6A (TA 1.5-0.5), Liquid
           Propellant Engine Manual (U). Chemical Propulsion Information
           Agency, Unit 1, December 1967, (C).

VIII-4.   Price, T. W.: Hydrazine Monopropellant Provides 0.5-600 Lb
           Thrust. Space/Aeronautics, Vol. 52, No. 5, October 1969,
           pp. 70-72.

SECTION IX. POWER SYSTEM DESIGN

TABLE OF CONTENTS

LIST OF ILLUSTRATIONS

LIST OF ILLUSTRATIONS (Concluded)

LIST OF TABLES

SECTION IX. POWER SYSTEM DESIGN

A. Requirements

1. <u>Guidelines.</u> The power for the HEAO payload is to be provided by a solar cell array and rechargeable battery system. The proposed design has been developed around the following guidelines and constraints which are applicable to this system:

    a. Orbit characteristics - 200-n.mi. altitude
                                  28.5-degree inclination circular orbit.

    b. Solar vector pointing and off-axis pointing.

    c. Use of available hardware.

    d. Simplicity and economy.

    e. All systems can accept 28-vdc power.

    f. Modular design.

    g. Reliability - 1-year design goal
                          2-year desirable lifetime.

    h. Titan launch vehicle envelope.

The orbital characteristics determine the time in sunlight, temperatures, and radiation levels to be encountered by the array. The solar cell array has dictated that the primary mode of operation for the HEAO shall be based on a solar-oriented position. The effects of off-sun pointing on the design have also been considered for the various operating modes proposed for this mission.

      Based on a preliminary analysis of the power system, it was determined that the ATM solar cell modules were not suitable for this application. Therefore, a new solar cell module was designed for the HEAO application. This module is similar to the ATM module, except that efficiencies are slightly higher and the physical dimensions are different to meet the HEAO requirements. Other portions of the power system make extensive use of modified ATM equipment.

A modular design approach has been followed by which additional solar panel modules and energy storage and conversion units can be added or deleted according to changes in total power requirements. The addition of panel modules would require a change in the baseline spacecraft configuration; deletions would cause no configuration changes. A great deal of flexibility has been provided to allow for tailoring the system to the final spacecraft requirements.

It is difficult to confidently predict reliability for lifetimes in excess of 1 year because of inadequate statistics and test history on the rechargeable batteries. Careful test and selection of flight hardware, conservative design ratings, and good control of battery temperatures are means by which adequate reliability can be achieved. Simplicity and design to avoid single-point failure modes is proposed rather than extensive redundancy to obtain the desired reliability.

The Titan launch vehicle payload envelope has constrained the overall configuration and the area available for body-mounted solar panels. Several alternative configurations have been evaluated in this study; the baseline configuration which has been selected is an octagon shape 30 feet long, having a maximum diagonal dimension of 105 inches, with body-mounted solar panels on three sides. Simple foldout solar panels are proposed as an alternate if more power is required.

    2.   <u>System Power Requirements.</u> Preliminary investigations have shown that a power system which operates at 28 vdc ± 5 percent will accommodate the HEAO subsystems and experiments. Should special requirements arise later, better regulation and/or special voltages can be furnished with little impact on the system.

The power requirements for the spacecraft have been estimated at 560 W for the Phase A study. This power requirement does not include contingency to allow for growth or unexpected degradation of power system capability. At the completion of the study, it became evident that the spacecraft will probably require additional power for the ASCS, the RCS, and for the communications and data handling systems. The power requirement is shown as 560 W, although the maximum power system capability using the available surface is 820 W. The power system was designed for the maximum capability to allow for the expected additional requirements. The difference between capability and 560 W is carried as a contingency, as shown in the power summary of Table IX-1. The peak power indicated for the various subsystems is a temporary demand, and these peaks do not normally coincide.

The system transient capability is 2490 watts, not to exceed 90 watt-hours
per orbit. A typical power profile is shown in Figure IX-1. Tables IX-2
through IX-4 break down the individual system requirements. Three operating
modes have been defined, and are described in the following paragraphs.

TABLE IX-1. POWER SYSTEM CAPABILITY AND REQUIREMENTS

Power available initially	820 W maximum
Power available after 1 year	780 W maximum
Power available after 2 years	740 W maximum

System	Power (W)	
	Peak	Average
Experiments	275	265
Communication and data handling system	503	65
ASCS	616	200
Redundant systems	30	30
		560

TABLE IX-2. POWER SUMMARY FOR HEAO BASELINE
CONFIGURATION EXPERIMENTS

Item	Power (W)	
	Peak	Average
Large area x-ray	135	135
Low-energy gamma ray	15	10
Medium-energy gamma ray	15	10
Gamma-ray telescope	40	40
Cosmic-ray electrons	20	20
Cosmic-ray calorimeter	50	50
Total		265

TABLE IX-3. POWER SUMMARY FOR HEAO BASELINE CONFIGURATION
COMMUNICATION AND DATA HANDLING SYSTEM

Item	Power (W)	
	Peak	Average
S-band transmitter (2)	440	30.0
Command receiver (2)	0.4	0.2
Command decoder	4	0.1
Digital multiplier	5	5.0
Analog signal conditioner	8	8.0
Tape recorders (4)	30	6.7
Switching network	8	8.0
Diagnostic logic	4.0	3.0
Minitrack beacon transmitter (2)	4.0	4.0
Total		65.0

TABLE IX-4. POWER SUMMARY FOR HEAO BASELINE CONFIGURATION, ASCS

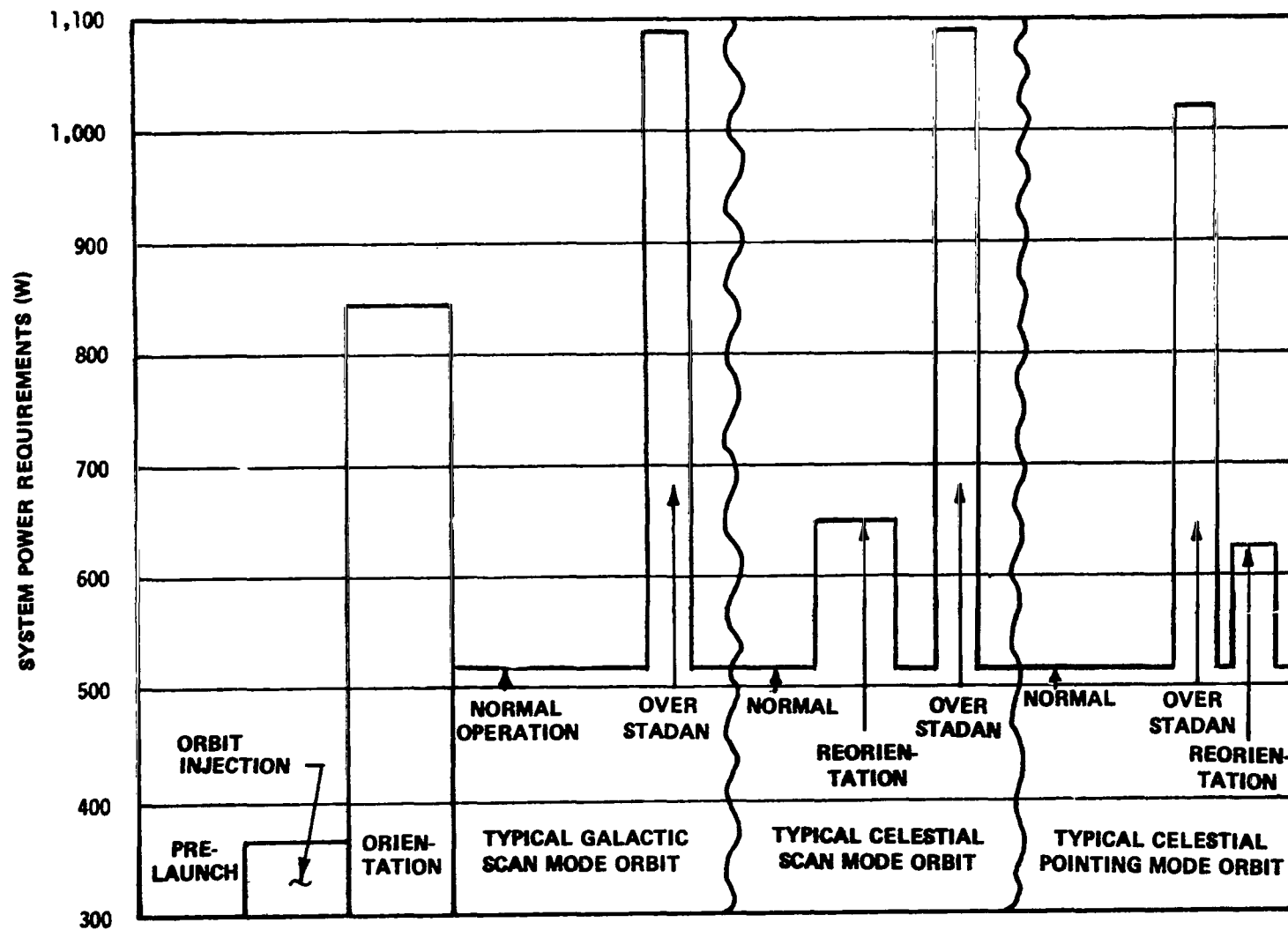| Item	Power (W)	
	Peak	Average
Star mapper/electronics	10	10
Star tracker	10	10
Digital sun sensors	2	2
Gyros, rate (3), and electronic modifications	173	36
Magnetometers	2	2
Flywheel	268	40
Magnetic coils	100	50
Signal processor	50	50
		200

Figure IX-1. Typical power profile for various operational modes.

a. Celestial scan mode. In the celestial scan mode, the space-craft will remain sun oriented and will perform the desired observations by rotating at a one-tenth rpm rate while tracking the sun through its ~1 degree/day movement along the ecliptic. This orientation provides the maximum power output.

b. Galactic scan mode. The galactic scan mode provides a survey of the galactic plane during the first 30 days of the mission. This would require the spacecraft scan axis (Z) to move off the solar vector at various angles up to approximately 37 degrees, the worst condition anticipated for the power system. Adjustments in the power requirements may be required for this mode. The cosmic-ray electron and cosmic-ray calorimeter experiments could be completely turned off for this period if necessary.

c. Celestial pointing mode. The celestial pointing mode provides detailed study of points of interest. The spacecraft scan axis can be pointed to any point within 37 degrees of the solar vector. To compensate for the loss of power from the off-axis maneuver, it may be necessary to reduce the power requirements for this mode. The experiments on one side of the spacecraft could be completely shut down.

B. Baseline System Description

1. Functional Description. The spacecraft baseline configuration is shown in Figure IX-2 with the location of the power system components indicated. A block diagram of the proposed power system is given in Figure IX-3.

The solar array normally supplies power to the spacecraft systems and charges the batteries during the daylight portion of the orbit. The batteries furnish power during the dark portion of the orbit or any other time the solar panel voltage drops below the open circuit voltage of the battery. This occurs during peak load requirements. Because of the problems anticipated in connecting the power conversion system to the output of panels with different incidence angles, a solar power distributor has been shown.

The CBRM's can accept power from the solar panels at voltages from approximately 80 to 26 V and provide output power at approximately 28 vdc.

Power distribution is through a power distributor and one or more control distributors, depending on the number of circuits required. Redundant
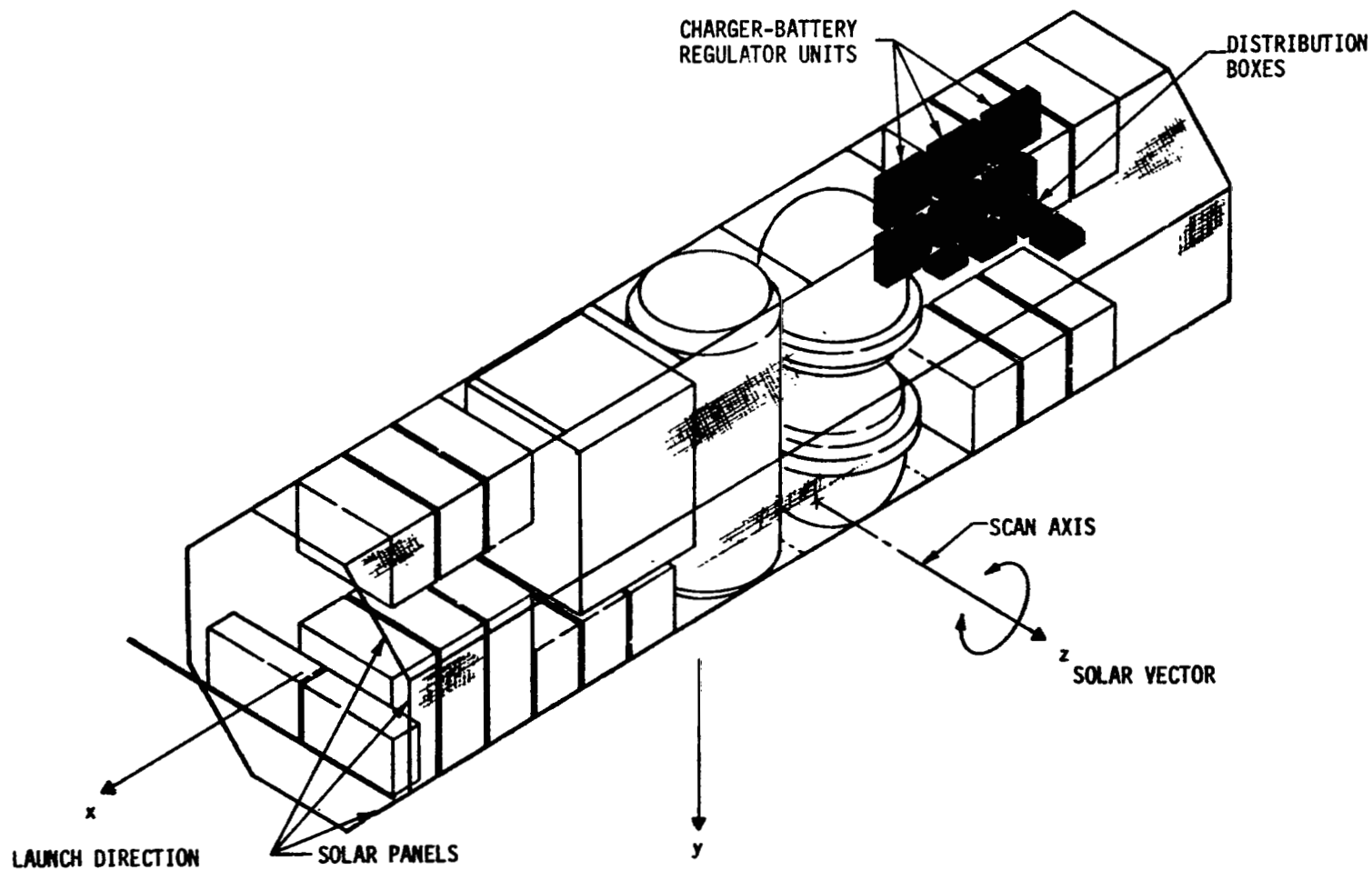
Figure IX-2. Spacecraft baseline configuration indicating location of power system components.
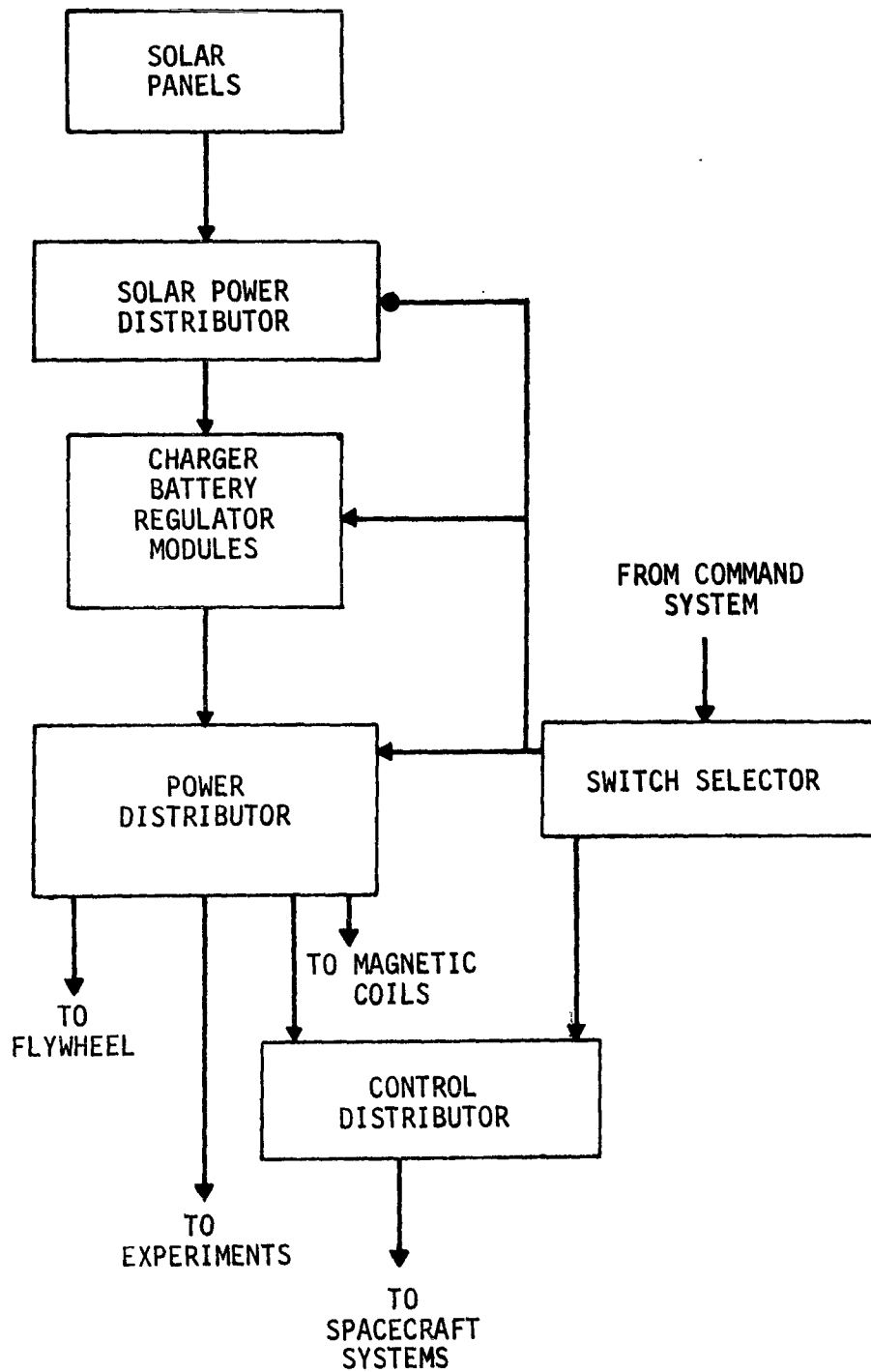
Figure IX-3. Power system block diagram.

buses and cables will be provided in the distributors and in the main power distribution lines. Each line will be provided with short circuit protection. Diode isolation would be within the equipment being furnished with power or in one of the distributors, as required.

Ground commands control selective power system functions. These commands are routed through the command receiver and command decoder of the telemetry system to the switch selector. This unit provides control of switches or relays in the distribution system.

2. Hardware Description

a. Solar panels. The HEAO baseline solar array covers three adjacent sides of the octagonal spacecraft configuration. The limitation of 105 inches for the maximum diameter of the structure dictates a width of 40.2 inches for each side panel. The overall spacecraft length is 30 feet.

Although the baseline array is considered as being body mounted, the array consists of individual modules small enough in size to minimize handling and fabrication problems. These modules would be mounted in a structural framework for support of the modules and associated wiring harness. The solar array layout is shown in Figure IX-4.

A custom solar cell module is proposed. This module would be similar to the ATM module, but more efficient, and sized to meet the HEAO requirements. Improvements for this HEAO module include:

     a. A better packing factor (active cell area/module area).

     b. Fabrication and soldering improvements.

     c. Improved or more economical cover slides.

     d. Improved adhesives.

     e. Increase in output from solar cells having different dimensions.

     f. Weight or thermal advantages with a change in substrate.

The module configuration is shown in Figure IX-5. The power output of this module is plotted as a function of temperature in Figure IX-6.
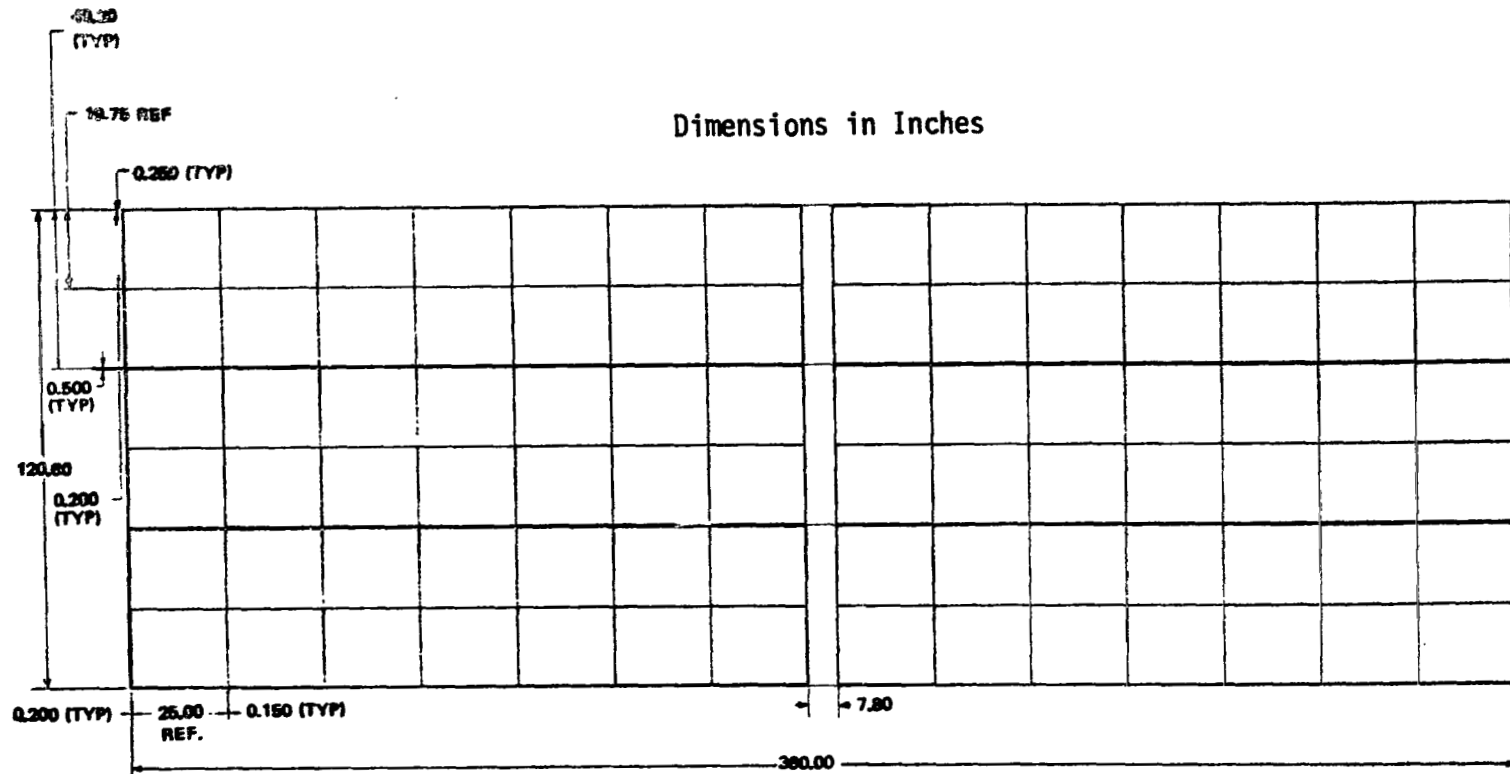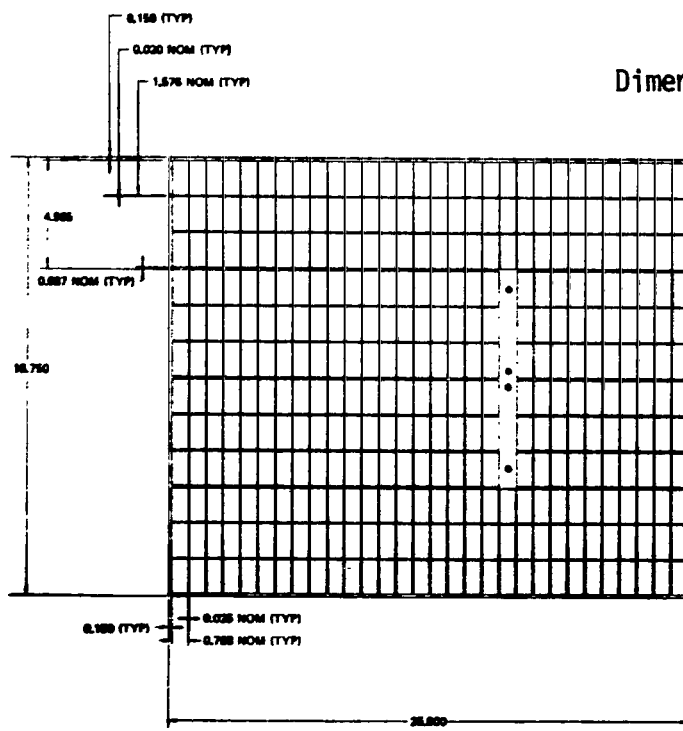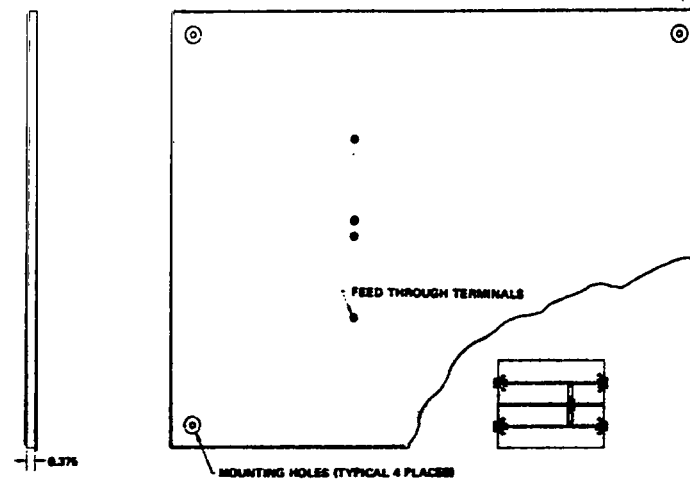
Dimensions in Inches

Figure IX-4. Solar panel layout for baseline configuration.

Dimensions in Inches

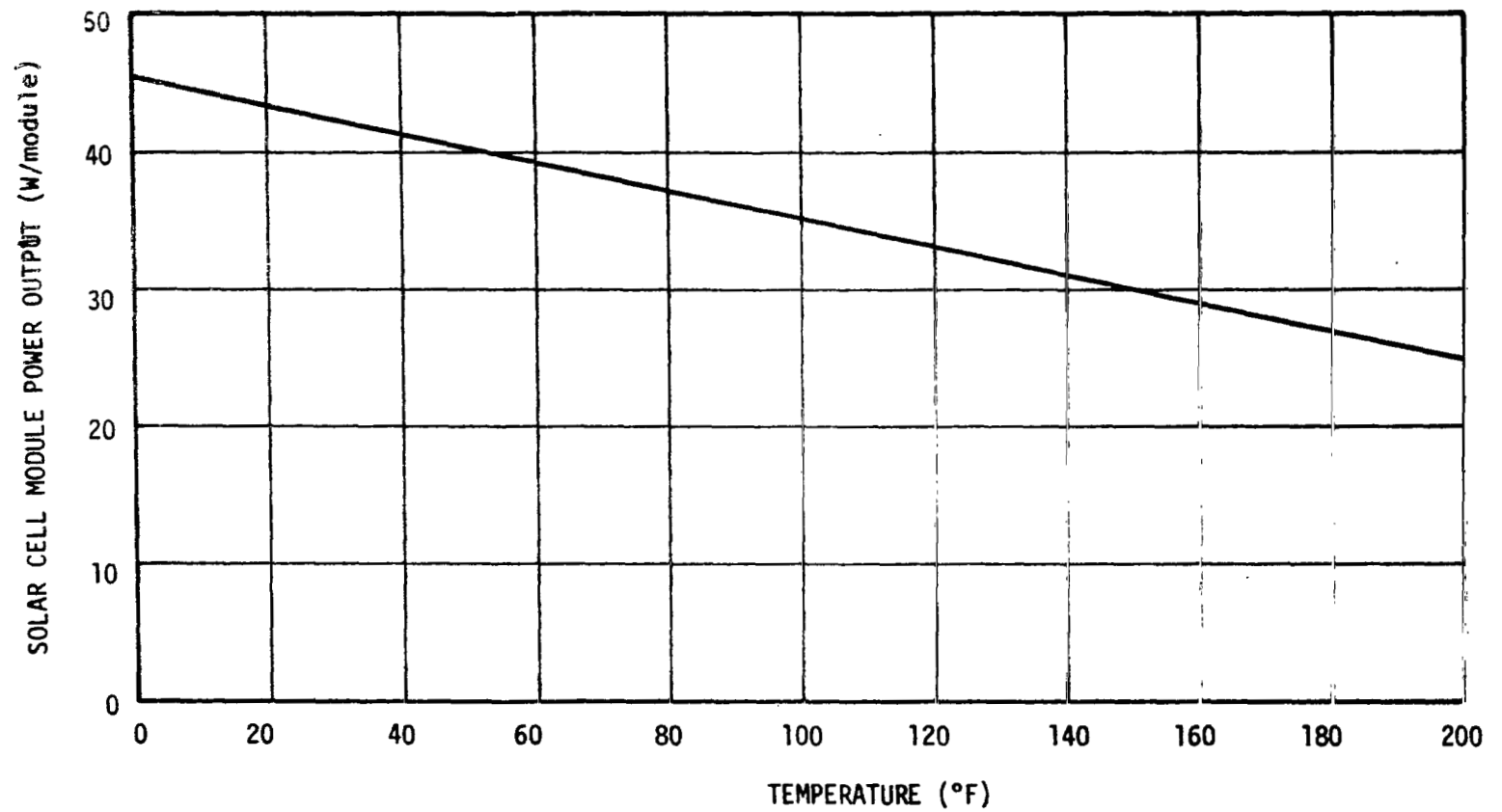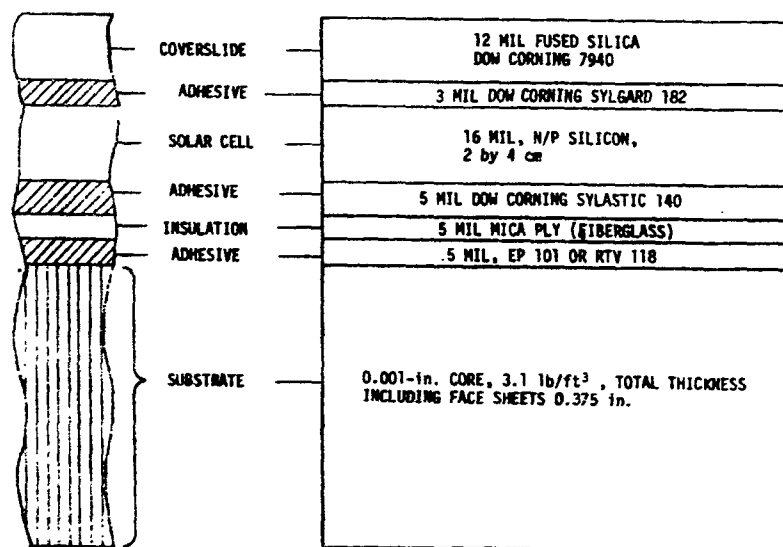Figure IX-5. Possible HEAO solar cell module configuration.

Figure IX-6. Solar cell module power output as a function of temperature.

Figure IX-7 shows the cross section of the module, gives a list of components and materials used and lists the characteristics of the solar cells. The packing factor for this module configuration is approximately 89 percent.

The module shown in Figure IX-5 has 354 two- by four-centimeter (0.788 by 1.576 inches) solar cells connected in 3 strings of 118 cells connected in series. For one possible hookup, using six CBRM's, 4 2/3 modules on each of the three solar panels would be connected to each CBRM. The problem of matching inputs to the CBRM's would be eliminated if foldout side panels were used to form a flat array surface.

The coverslides for the solar cells are 0.012-inch-thick fused silica, although consideration may be given to microsheet since it is less expensive. The coverslides provide protection to the solar cell from radiation and micrometeoroid damage. The coverslides have an antireflective coating on the side exposed to the sun to allow maximum transmission of energy in the region of solar cell peak spectral response. The side of the coverslide attached to the solar cell has a reflective coating to reject ultraviolet energy, providing protection from ultraviolet damage to the adhesive used in bonding the coverslide to the cell. The cut-on wavelength (wavelength where 50 percent of the light is transmitted) of the ultraviolet reflective coating is specified as 0.400 ± 0.015 micron. Since the solar cell and coverslide are very brittle, the module substrate must provide maximum freedom from bending. To provide the required stiffness and a lightweight structure, a 3/8-inch aluminum honeycomb substrate is proposed. This substrate would consist of 0.008-inch face sheets sandwiching 3.1 lb/ft^3-0.001-inch ribbon core material. A more thorough analysis will be required to verify this selection. The total weight of a solar cell module, including solar cells, coverslides, intercell connections, adhesives, and substrate, is estimated at 3.5 pounds.

b. CBRM's. The CBRM is a single unit containing a battery, a battery charger, a load regulator, and the associated controls, protection, monitoring, and auxiliary circuitry. The total unit weight is approximately 110 pounds. The CBRM accepts power from the solar array during the illuminated portion of the orbit and supplies power to a load bus during the entire orbit. During the illuminated portion of the orbit, the power from the solar array supplies the load bus and recharges the battery. During the dark portion of the orbit, the battery supplies power for the load bus. An ATM CBRM of modified design is used in the HEAO power system. A combination schematic and block diagram of the ATM CBRM is shown in Figure IX-8. An outline drawing (Fig. IX-9) shows the dimensions of the present 20-ampere-hour capacity unit. The present design has the following characteristics:

COVERSLIDE		12 MIL FUSED SILICA DOW CORNING 7940
ADHESIVE		3 MIL DOW CORNING SYLGARD 182
SOLAR CELL		16 MIL, N/P SILICON, 2 by 4 cm
ADHESIVE		5 MIL DOW CORNING SYLASTIC 140
INSULATION		5 MIL MICA PLY (FIBERGLASS)
ADHESIVE		.5 MIL, EP 101 OR RTV 118
SUBSTRATE		0.001-in. CORE, 3.1 lb/ft³ , TOTAL THICKNESS INCLUDING FACE SHEETS 0.375 in.

TYPE:	N/P SILICON
THICKNESS:	NOMINAL 0.016 in.
CONVERSION EFFICIENCY:	NOMINAL 10 PERCENT AT AIR MASS ZERO
BASE RESISTIVITY:	7 TO 14 ohm-cm
CONTACTS:	SINTERED SILVER-TITANIUM, SOLDER- DIPPED, 62 PERCENT TIN, 36 PERCENT LEAD, 2 PERCENT SILVER.

SOLAR CELL CHARACTERISTICS

Figure IX-7. Solar cell module cross-sectional view.

Note: Connections to the CBRM are made through connectors J1, J2, J3, and J4.

Figure IX-8. Block diagram and schematic of CBRM.

- Independent operation.

- No single-point failure will result in the loss of the total power system.

- No single-point failures will result in a high voltage on the CBRM output buses.

- Overload protection.

- Equal load sharing by all modules.

- Automatic fault detection and recovery.

CONTROL
FUNCTIONS

TELEMETRY

INPUT-OUTPUT POWER

BATTERY MONITORING AND CONDITIONING

BATTERY AREA

ELECTRONICS AREA

MOUNTING PANEL

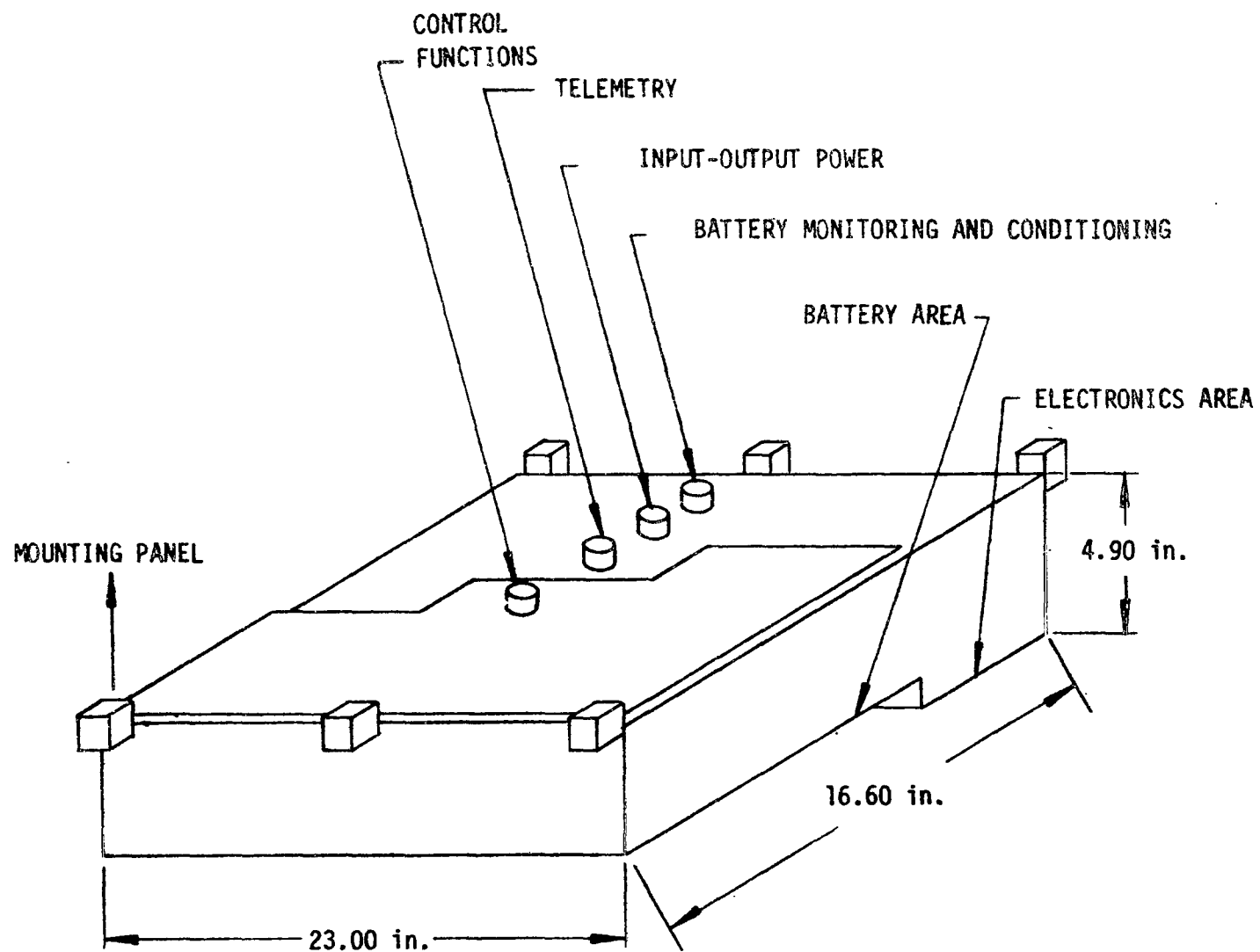4.90 in.

16.60 in.

23.00 in.

Figure IX-9. CBR module configuration.

Several problems will be encountered by the HEAO power system which were not a factor in the ATM design. A 2-year spacecraft lifetime with a 92-minute duration orbit dictates an operating life of about 11 400 cycles for each CBRM. The specified operating lifetime of the ATM CBRM is 4000 cycles. The operating lifetime may be extended by decreasing the depth of discharge. Since a total of only six CBRMs are to be used on the HEAO, instead of 16 to 18 as on the ATM, the design for independent operation will mean a greater percentage loss for each malfunction. The loss of any one unit will reduce the total system capacity of the HEAO by 16.7 percent, if the original depth of discharge is maintained. The use of common bussing or other means of providing redundancy will cause a reduction in overall system efficiency. This is a problem which should be considered more thoroughly in the next phase of study.

Another problem which will have to be investigated is the effect of varying voltages and currents to the CBRM's caused by the 45-degree side solar panels and the off-axis viewing. Several methods for connecting the panels are available. The use of fold-out side panels would alleviate this problem, and allow CBRM operation under design conditions.

The presently defined mission requirements of 560 W would require an average electrical output of 93 W from each of the six CBRMs. The full 820-W capability of the power system would increase this to 137 W from each. The mission requirements are not well enough defined to estimate the maximum transient demand, although the 415-W peak capacity of the present CBRM designs is adequate for those shown in Table IX-1.

The requirement for six CBRM's is shown in Figure IX-10. As indicated on the chart, an increase in power requirements to more than 670 W would dictate the need for an additional CBRM if the 15 percent depth of discharge level is not to be exceeded. If the 820 W capability is used, the depth of discharge would increase to 20 percent with six CBRM's. A 15-percent depth of discharge was chosen to provide a long battery cycle life and to reduce the effect on the system of a single CBRM failure. The calculations are based on a dark period of 36 minutes, which is the worst case situation.

(1) Battery charger. The battery charger is a switching regulator type that is capable of converting the solar array voltage to the level required for charging the battery. The charger will sense the condition of the battery, the load requirements, and the solar array parameters; it will then condition the power not needed by the load bus to charge the battery.

NOTES:
[1] 15 PERCENT DEPTH OF DISCHARGE
[2] 20 PERCENT DEPTH OF DISCHARGE
[3] 25 PERCENT DEPTH OF DISCHARGE
[4] 30 PERCENT DEPTH OF DISCHARGE

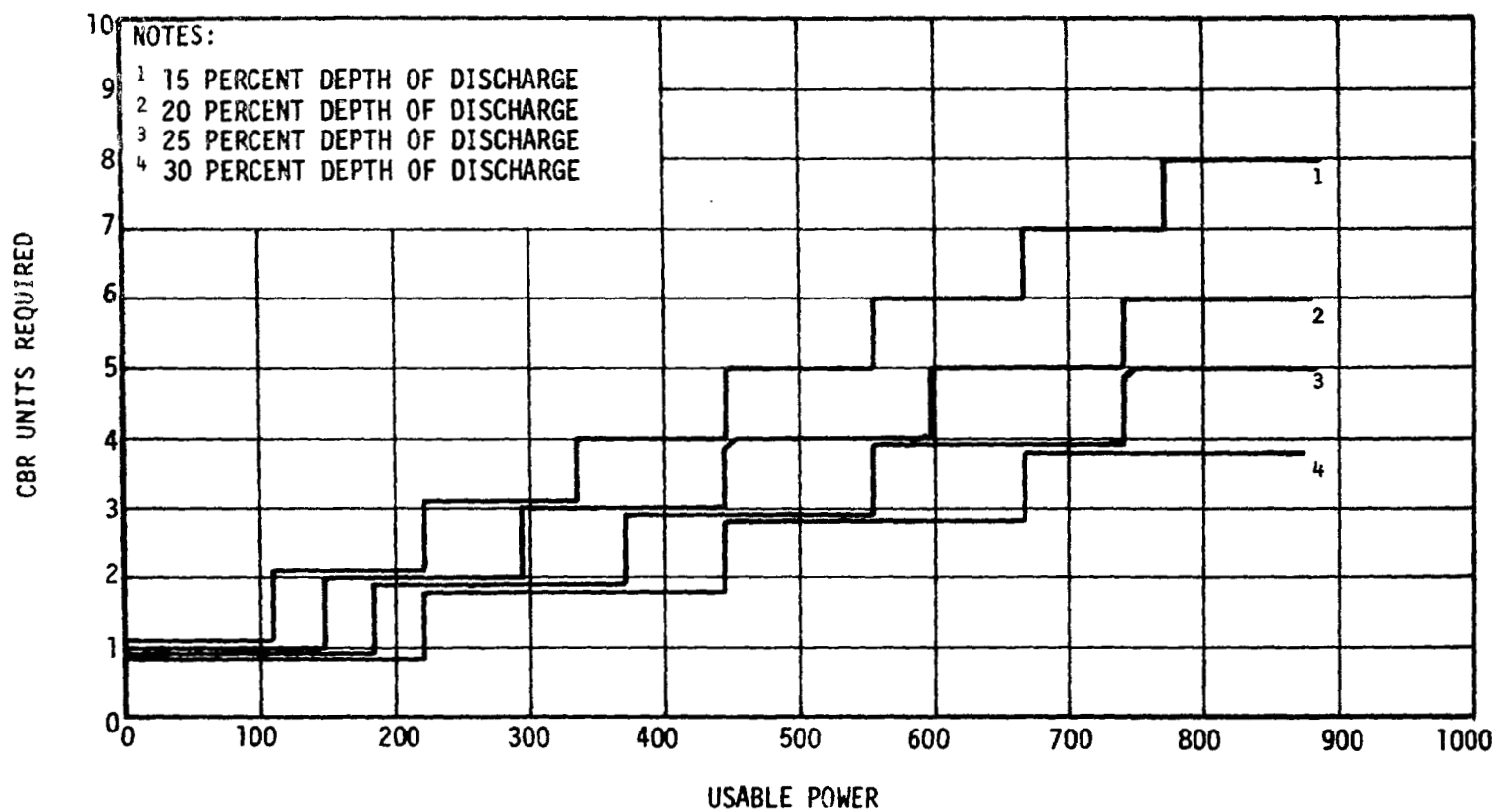CBR UNITS REQUIRED

USABLE POWER

Figure IX-10. CBR modules required for different depth of discharge values and power values.

The battery charge control sequence is illustrated in Figure IX-11. The initial charging is done at a constant current. When the battery terminal voltage reaches a predetermined value, which is a function of battery temperature, the charger reduces the battery charging voltage and continues with constant voltage charging. Battery charging will be terminated when the fully charged condition is signaled by the battery third electrode or when the input voltage to the CBRM drops below a specified value. The charger efficiency is specified at a minimum of 92 percent.
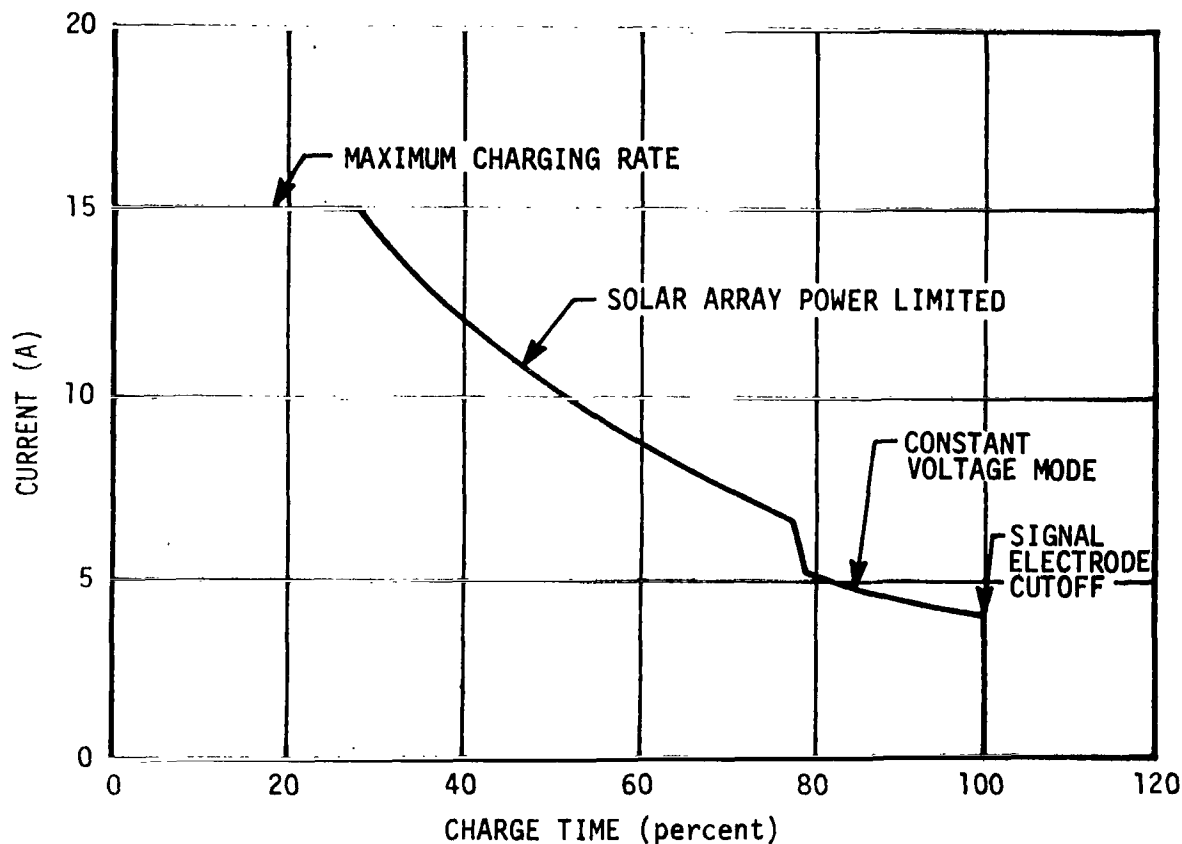

Figure IX-11. Battery-charging regime.

(2) Battery. The battery contains 24 series-connected, hermetically-sealed, nickel-cadmium cells of the three- or four- electrode type. Total battery capacity is 20 A-hr, and total weight is not more than 50
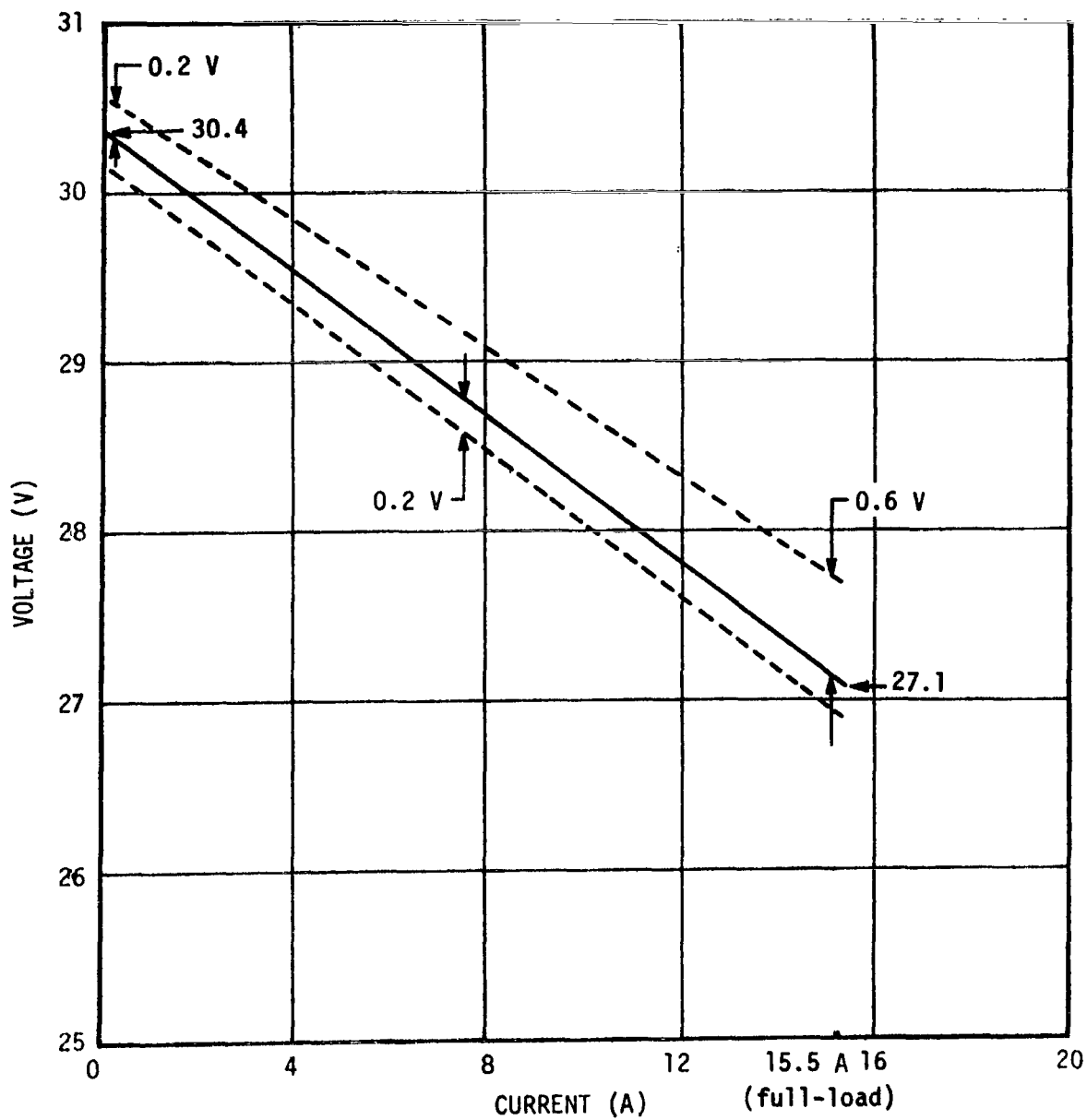
Figure IX-12. Regulator output voltage slope.

pounds. One parameter which is very important in achieving extended battery life is cell matching. Close coordination with the work being done in this area should provide a better design for the HEAO battery units. Other parameters which are even more critical in terms of battery lifetime (number of cycles) are temperature control and depth of discharge limitation. The specifications for ATM batteries give a battery lifetime of 4000 cycles to a depth of discharge of 30 percent when operated at temperatures from -20°C to 10°C(-4°F to 50°F). The cycle life is expected to be increased if depth of discharge is limited to 10 to 20 percent and the thermal limits are not exceeded. Preliminary thermal analysis for this spacecraft does not indicate any immediate problems from an environmental temperature standpoint. The anticipated 15-percent depth of discharge should lengthen the life of the batteries. Short-circuit protection is provided by a contactor in series with the battery which opens if the battery discharge current exceeds 25 A. Overcharge of the batteries is prevented by a charge control system which monitors the third electrode signal voltage of three cells in each battery unit and terminates the charge when a fixed signal level is reached.

(3) Load regulator. The load regulator is a switching regulator designed to be capable of converting widely varying input voltages into a closely regulated output voltage. It regulates power from either batteries or solar panels. The regulator can deliver a peak transient load of 415 W under transient limitations of 15 W-hr/orbit above an average load of 200 W. The regulator output voltage is maintained within the values shown in Figure IX-12. The regulator efficiency is a minimum of 89 percent for loads between 100 and 200 W and not less than 85 percent for peak load. Short-circuit protection is provided by limiting regulator output current to 20.0 A maximum. The output voltage starts to drop off above 15.5 A and decays to zero at 20 A.

(4) Auxiliary circuits and controls. The CBRM operates from externally supplied commands and performs the functions described in Table IX-5. In addition, automatic malfunction responses are included as well as monitoring signals which can be telemetered for ground evaluation of the power system operation.

c. Networks. The power is distributed from the CBRM's to the individual power-consuming components through normally redundant circuits. The power distributor separates the main power drains upon the system. This unit contains the primary circuit protection for the major loads. The flywheel, magnetic coils, and experiments will probably be fed directly from the power distributor.

TABLE IX-5. CBRM COMMAND SYSTEM

Command	Signal Required	CBRM Response
Charger on	24 - 31 vdc, 18 - 60 msec duration	Turns on charger; closes battery contactor and input contactor if they are not already closed
Regulator on	24 - 31 vdc, 18 - 60 msec duration	Turns on regulator; closes input contactor if it is not already closed
Charger off	24 - 31 vdc, 18 - 60 msec duration	Turns off charger; opens battery contactor and input contactor if regulator is off
Regulator off	24 - 31 vdc, 18 - 60 msec duration	Turns off regulator; opens battery contactor and input contactor if charger is off
System on	System common	Turns on charger and regulator; closes battery contactor and input contactor.

Power will also be supplied through the power distributor to the control distributor. This unit furnishes power to the communications and data handling and to the ASCS.

It is proposed that developed Saturn-type distributors be used for this program, assuming they can be adapted to meet the requirements. This should be no problem since approximately 10 standard plug-in printed circuit modules have been developed under the ATM program for use in the existing control distributor. The appropriate standard modules already available should provide sufficient flexibility. In any case, individual modules with special relays, diodes, or logic circuitry could be designed for use in the existing distributors.

Coded command signals are sent from the ground stations, through the command link and decoder, to the switch selector. This unit routes a 28-V discrete signal to the appropriate relays in the distributor panels to switch equipment or operating modes.

Additional capability will be necessary within the electrical network so that ground operations can be performed. Typical functions of this system would be to:

● Provide power input during calibration, test, and checkout of systems during all test phases.

● Interface the electrical support equipment with the spacecraft systems.

● Provide test points for power system tests, such as dark cell tests.

● Provide vehicle power prior to launch.

The electrical network should be designed to minimize the amount of cabling and the number of connectors to reduce weight and increase reliability.

The cabling system layout has not been designed. Factors which will strongly affect the system design are power losses from a low voltage dc distribution system and problems of grounding or shielding associated with the other systems.

The total weight of the power system is summarized in Table IX-6. The solar panel module weight includes the honeycomb substrate, but does not include the structure necessary to support the individual modules. The solar panel area is assumed to cover three sides of the 30-foot-long structure.

The individual components of the power system may be moved to improve the mass characteristics of the spacecraft; however, the proximity of certain units to each other is important and must be maintained. Line losses and interference should also be considered in locating the power system components.

The thermal considerations of some of the components, especially the CBRM's, are critical for their successful performance.

In addition to the power interface to the spacecraft systems, other interfaces are necessary. The command subsystem interfaces at the switch selector where the ground command signals are implemented. Data indicating the condition of the power system will be transmitted via the telemetry link.

3. Performance

a. Design factors. In converting solar panel generated power into usable power, system losses must be considered. The locations of these losses are depicted in Figure IX-13. The efficiency figures for the CBRM sections are representative numbers based on ATM hardware. The transmission and distribution losses are also typical figures estimated for this configuration.
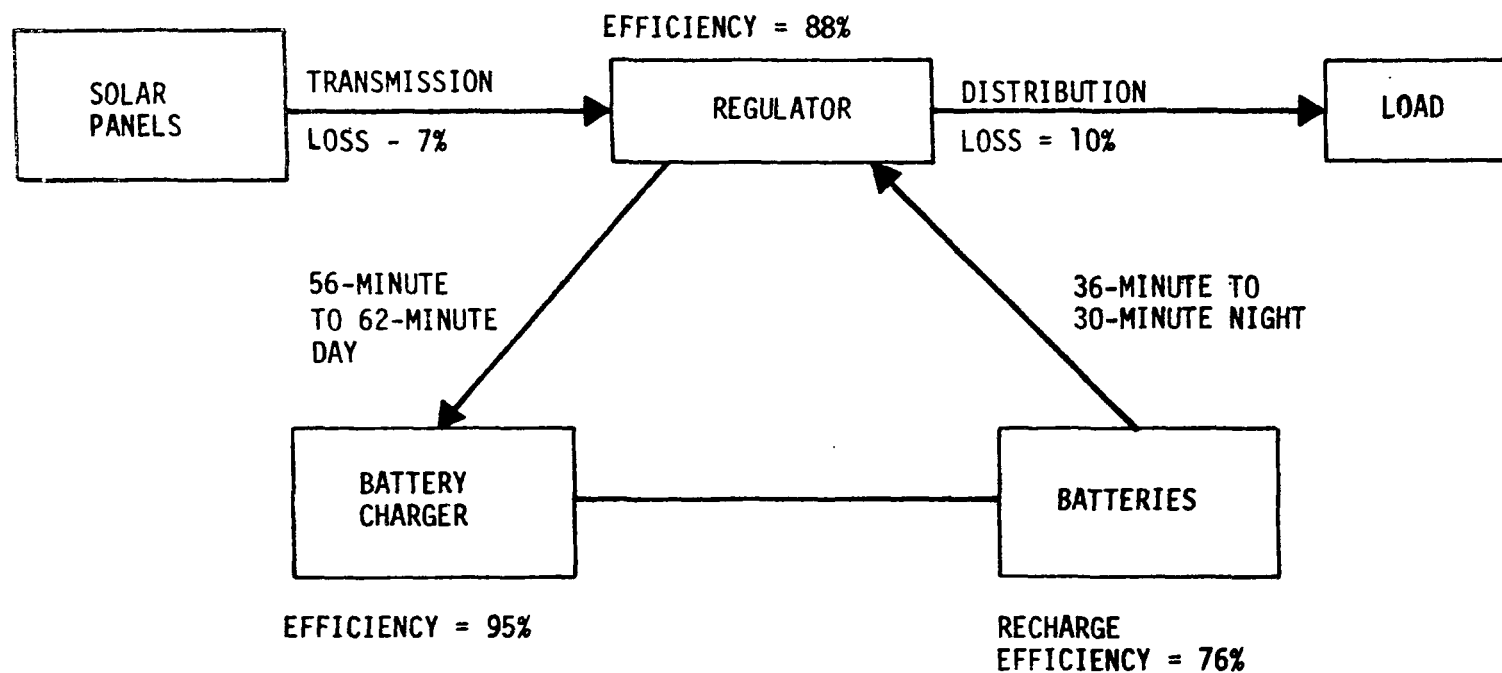
EFFICIENCY = 88%

| SOLAR PANELS | | TRANSMISSION | REGULATOR | DISTRIBUTION | | LOAD |

```
┌──────────┐    TRANSMISSION        ┌───────────┐    DISTRIBUTION      ┌──────┐
│  SOLAR   │ ──────────────────────▶│ REGULATOR │ ────────────────────▶│ LOAD │
│  PANELS  │    LOSS - 7%           └───────────┘    LOSS = 10%        └──────┘
└──────────┘
```

TRANSMISSION

LOSS - 7%

DISTRIBUTION

LOSS = 10%

56-MINUTE
TO 62-MINUTE
DAY

36-MINUTE TO
30-MINUTE NIGHT

BATTERY
CHARGER

BATTERIES

EFFICIENCY = 95%

RECHARGE
EFFICIENCY = 76%

Figure IX-13. Power system losses.

TABLE IX-6. POWER SYSTEM WEIGHT STATEMENT

Item	Weight (lb)
Solar panel modules	294
CBR units	660
Solar power distributor	35
Power distributor	35
Control distributor	25
Switch selector	20
Cables and connectors	150
Measuring supply	2
Measuring supply distributor	25
Power supply	10
Total	1256

The range of times indicated for the day-night period are based on the 200-n. mi., 28.5-degree-inclination circular orbit. In calculating the power output, the shortest daylight period has been assumed. At the same time, the temperature calculations are based on the longest daylight period and will indicate the hottest case with the least power output. As a result of this procedure, the calculated power figures should be a conservative value.

The power system performance factor calculations are shown in Table IX-7. Several things may degrade the electrical output of the solar array. Radiation and micrometeoroid damage are the major anticipated sources of degradation. The function of the coverslide is to protect the solar cells from this damage. However, the solar cells will not be completely covered by the coverslide and certain portions of the active surface will be directly exposed to the radiation flux. Also, the micrometeoroid degradation is mainly caused by surface erosion of the coverslide. Although the reaction control thrusters have been located so that their exhausts will not directly impinge on the solar array,

TABLE IX-7. POWER SYSTEM PERFORMANCE FACTOR

Solar array output required with 7% transmission loss	2110 W
Average regulator input plus average charger input	1960 W
Average battery charger input at 95% efficiency	920 W
Average battery recharge power required: $818 \text{ W-hr} \times \dfrac{60}{56}$	875 W
Average battery recharge power at 76% recharge efficiency	818 W-hr
Average night power requirements for 56-minute day,	
36-minute night: $1040 \text{ W} \times \dfrac{36}{60} \text{ hr}$	620 W-hr
Average regulator input at 88% efficiency	1040 W
Average CBRM output at 10% distribution loss	910 W
Maximum average power capability, based on array output	820 W
Power system performance factor: $\dfrac{2110 \text{ W array output}}{820 \text{ W system output}}$	2.57

exhaust gases are a possible source of degradation. The thermal cycling under vacuum conditions may also have a damaging effect on the solar panels. A 5-percent-per-year solar cell degradation factor has been assumed for the conditions of this mission.

Other factors which will affect the total solar panel output will be module mismatch, assembly wiring losses, and degradation from testing. No additional degradation or power loss has been attributed to these factors at this time. Total available power calculations have been made on summation of module outputs. The anticipated module output is based on average ATM module test results adjusted for the additional number of solar cells on the HEAO module.

b. Solar angles. The solar panels located at 45-degree angles to the center solar panel in the baseline configuration and the motion of the space-craft about its scan axes will complicate the calculations for effective power. The viewing program for the proposed mission profile has indicated a maximum angle off the solar vector of 36.5 degrees for the center panel axis. This will cause the solar incidence angle on the panel away from the sun to be 81.5 degrees. For the purposes of this study, the panel output has been calculated using a cosine function, although it is realized that this generates an optimistic figure for the large angles, because of surface reflection. Another problem brought about by the panel angles is the variation of input into the CBRM's. The variation of solar cell current with a change in incidence angle coupled with the solar cell voltage shift caused by the temperature change will impact the CBRM design. The use of fold-out panels would simplify many of the power system design problems.

Figure IX-14 shows the relationship of temperature, sun angle, and output power from one solar cell module. This chart is based on the predicted outputs at beginning of life.

c. Thermal impacts. The configuration and assumptions used to calculate the solar panel temperatures are described in the thermal analysis section of this report. The temperatures for the various cases investigated have been used to plot power output curves as a function of temperature.

Figure IX-15 is a plot of the power output from each panel as a function of orbit time for the baseline thermal case (Section VII), with the scan axis pointing along the solar vector. No heat conductors are used in this configuration. The output of the two side panels has been corrected for incidence angle using the cosine of the 45-degree angle. As noted in the thermal analysis section, the spacecraft rotation has not been considered. This should have very little effect in this instance.
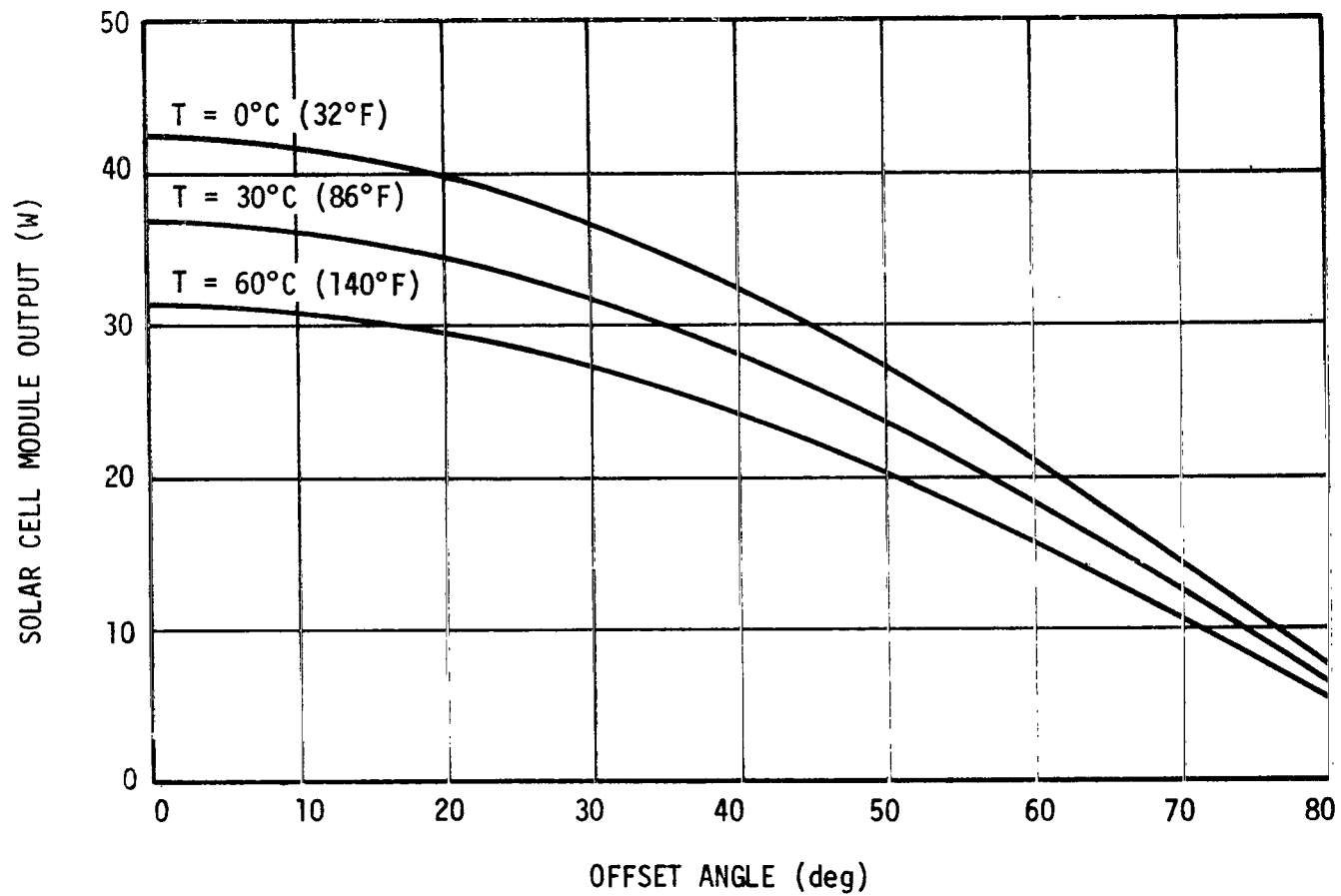
Figure IX-14. Solar cell module power as a function of temperature and offset angle.
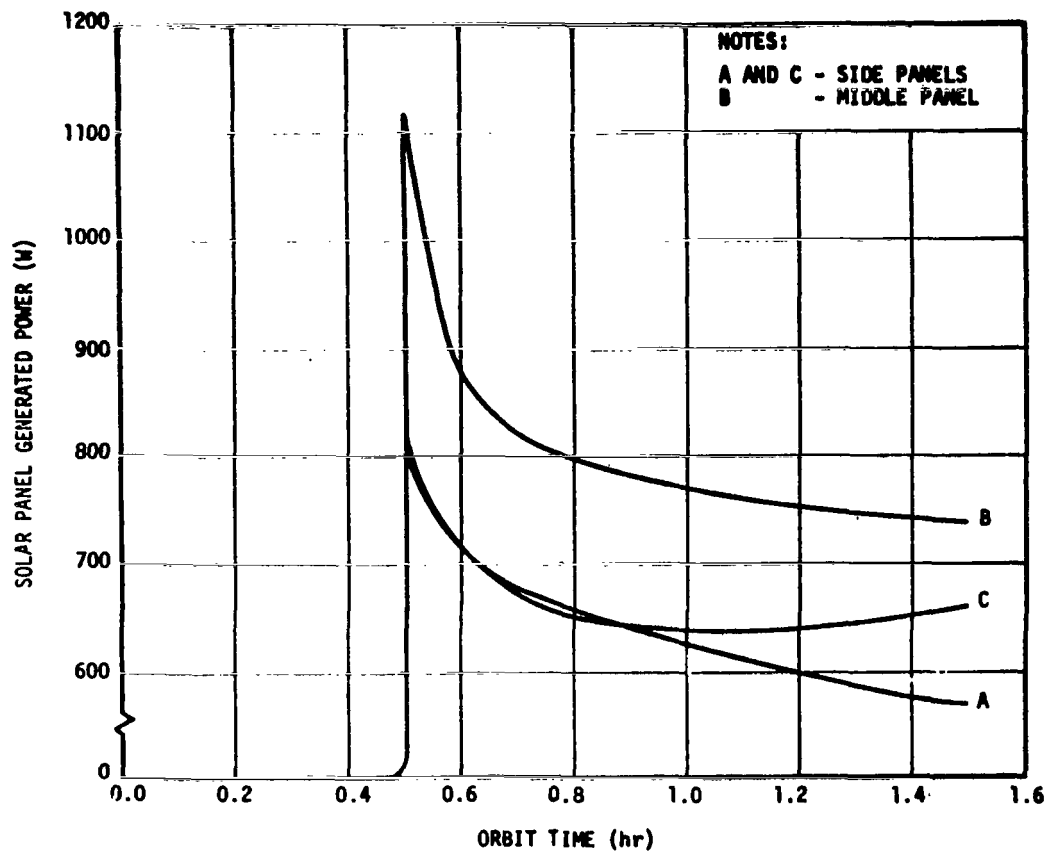
Figure IX-15. Power as a function of orbit time for the baseline configuration with the scan axis aligned with the solar vector.

Thermal Case F (Appendix F) is used to plot the panel outputs in Figure IX-16. This is the same as the baseline thermal condition, except that heat conductors were used.

The cyclic nature of the side panel outputs is depicted in Figure IX-17 for a spinning spacecraft, with the scan axis pointed off the solar vector. The dashed line indicates the average output of the two panels. The situation where the spacecraft points with no scanning motion off the solar vector is shown in Figure IX-18. Although the maximum angle considered for the spinning case was 36.5 degrees and for the pointing case was only 30 degrees, the temperatures are from Thermal Case C (Appendix F) which used 35 degrees as the solar offset angle.
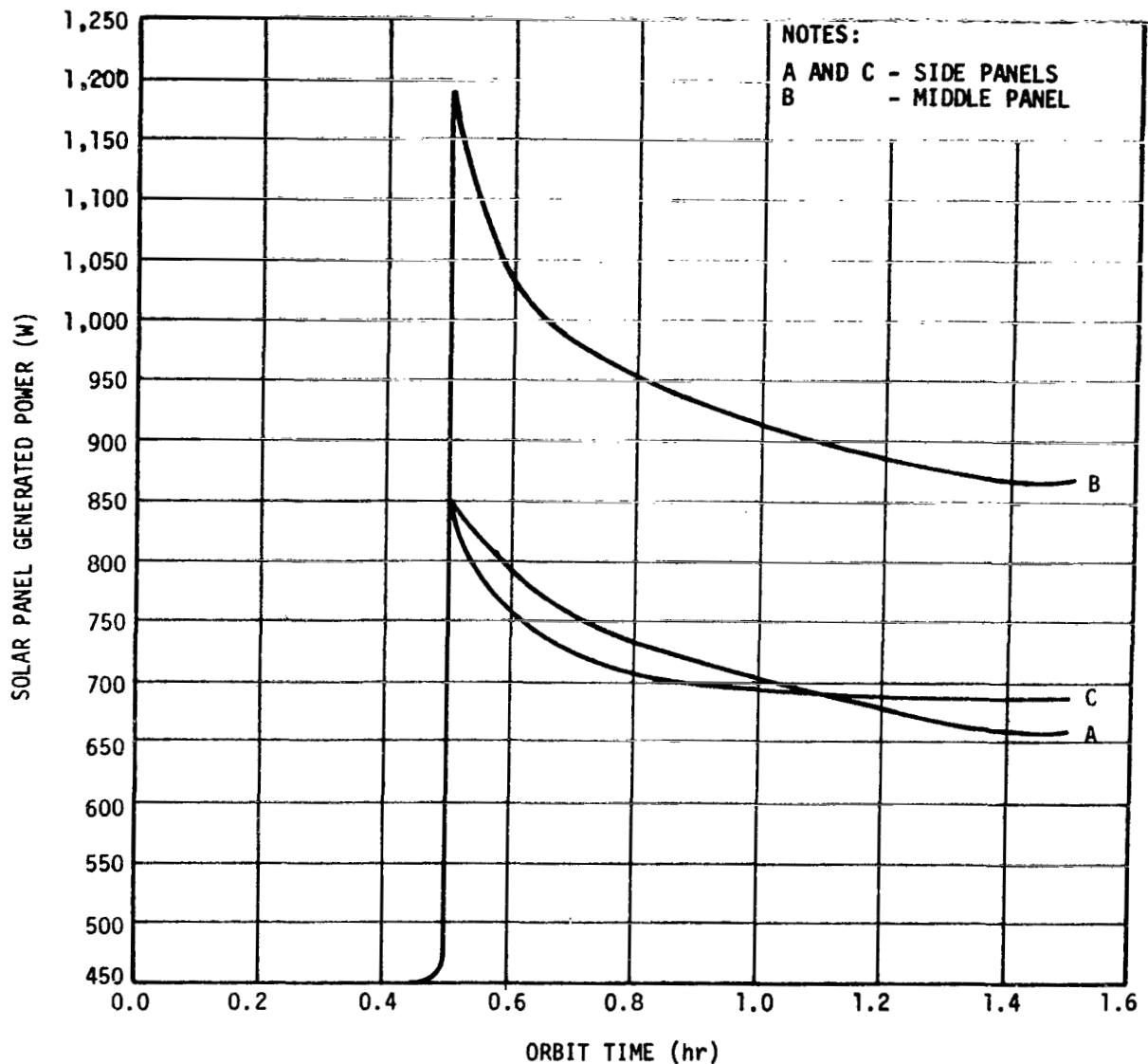
Figure IX-16. Power as a function of orbit time for baseline configuration with heat conductors.

The individual panel outputs for Thermal Case E (Appendix F) have been plotted in Figure IX-19. This configuration has fold-out side panels with no thermal control.

A plot of average power output for the five different situations has been shown as a function of orbit time in Figure IX-20. These are total power curves which represent the sums of the individual panel outputs shown
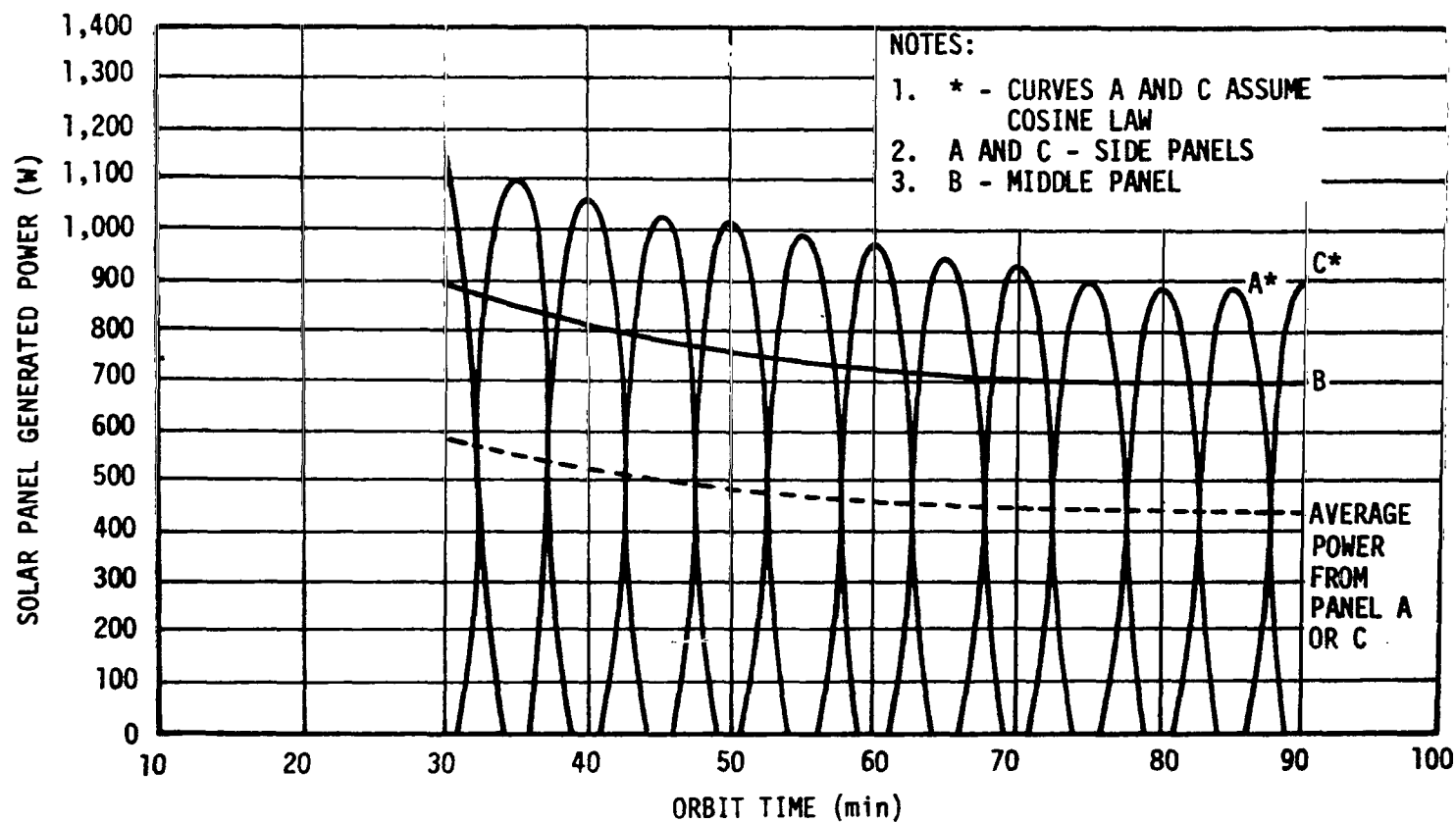
Figure IX-17. Power as a function of orbit time for baseline configuration 36.5-degree pointing angle (based on temperatures from 35 degrees off-axis thermal analysis).
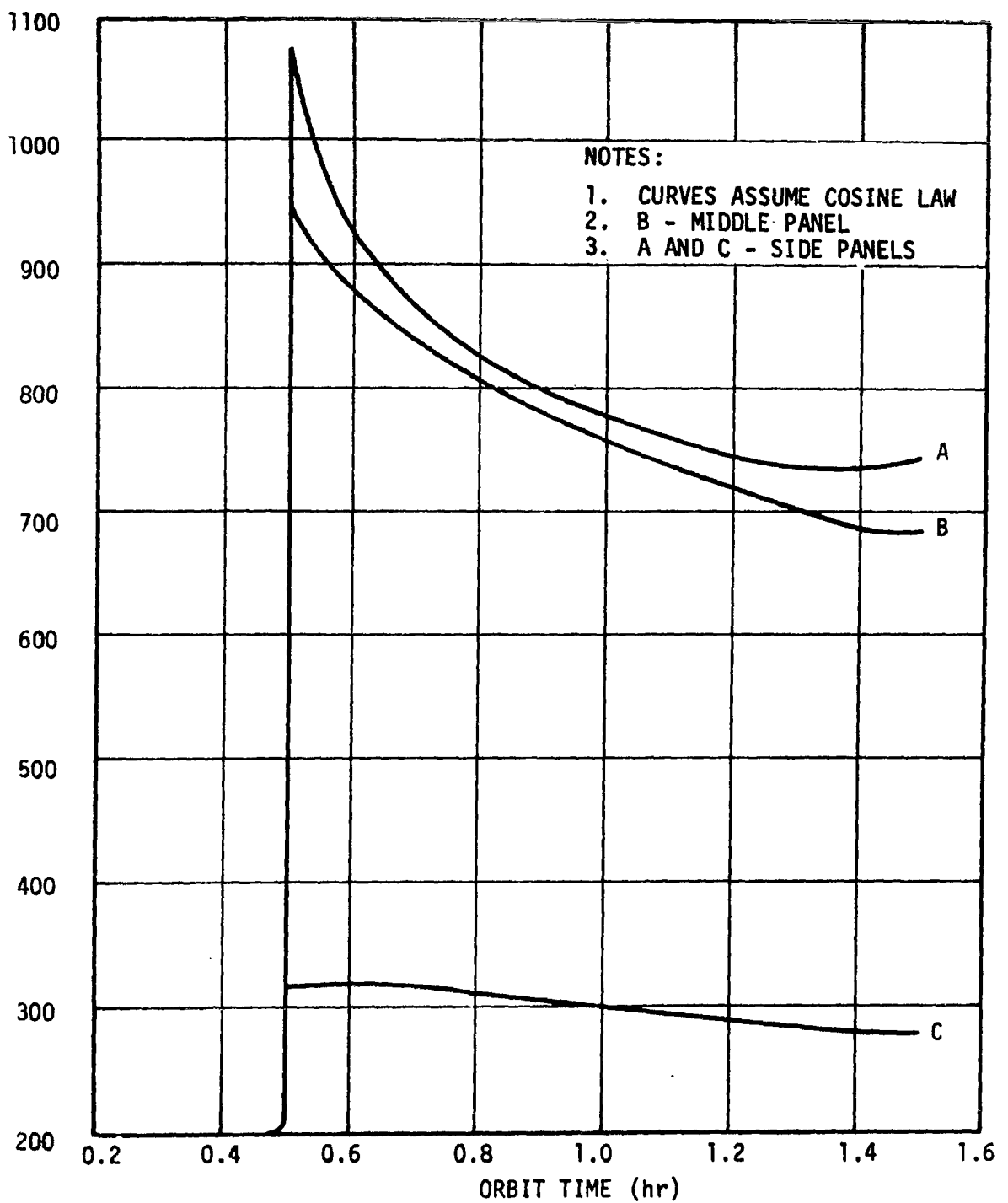
Figure IX-18. Power as a function of orbit time for baseline configuration 30-degree scan angle (based on temperatures from 35 degrees off-axis thermal analysis).

NOTES:
A AND C - SIDE PANELS
B - MIDDLE PANEL
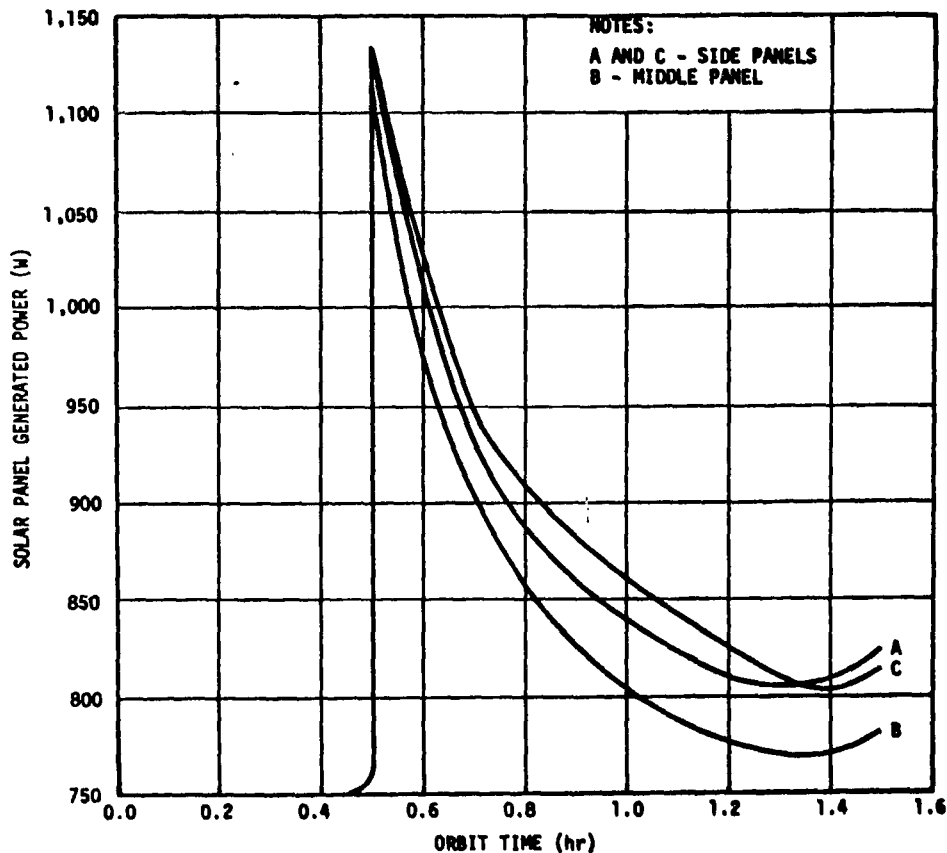
Figure IX-19. Power as a function of orbit time for foldout solar panels
perpendicular to solar vector.

in the preceding figures. The usable average power figures shown in the notes
have been calculated with the use of a single performance factor and degradation
factor. The relative system merits or additional design losses for special
cases have not been factored into these calculations.

The chart presented in Table IX-8 is a summary of the power
situation for the various orientations. The column showing available power
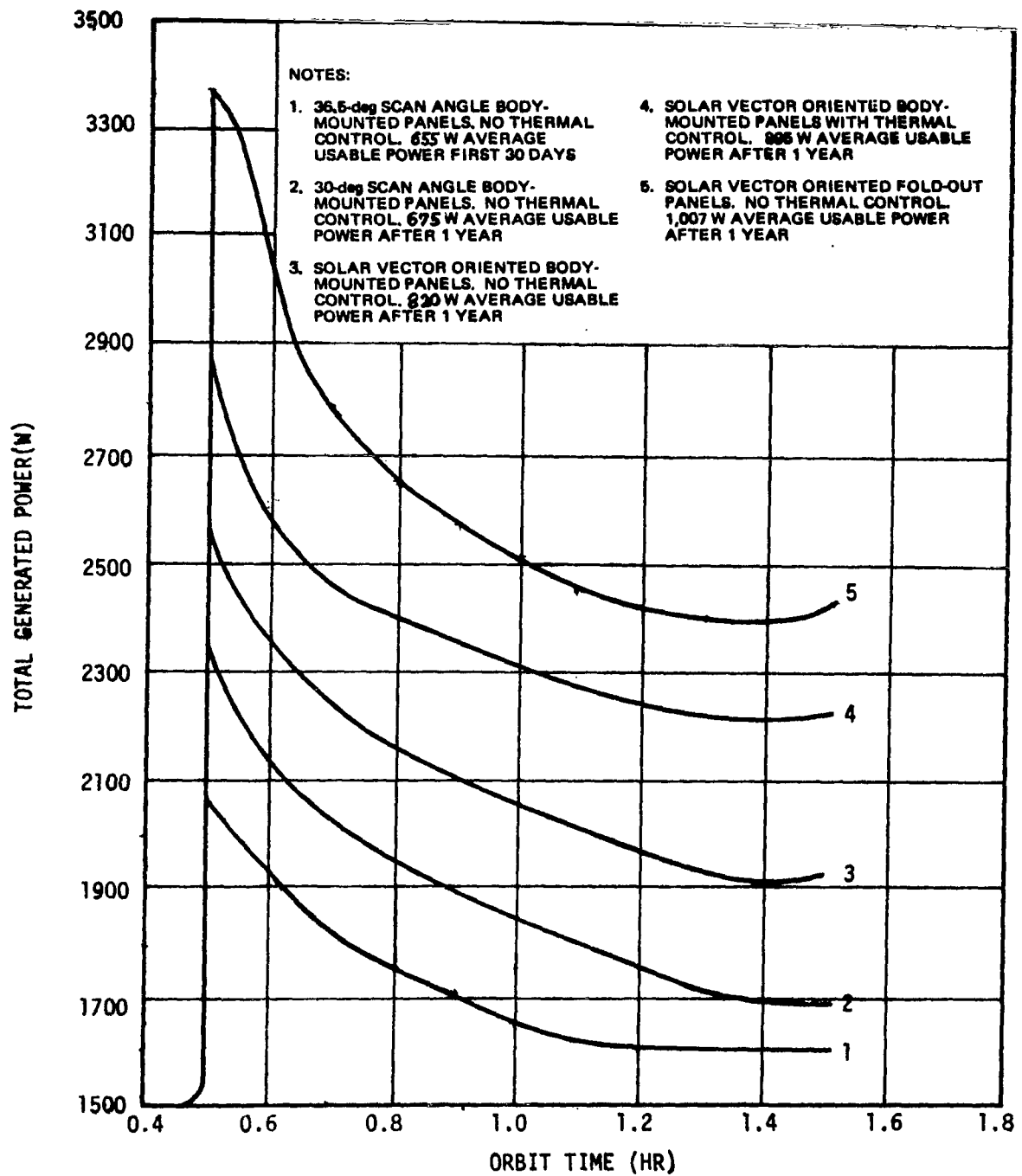
Figure IX-20. Power output as a function of orbit time for various orientations.

9-34

TABLE IX-8. POWER SUMMARY

Configuration	Available Power (W)	Power Available for Contingency (W)
Celestial Scan		
Start of mission	820 W	260 W
After 1 year	780 W	220 W
Galactic Scan		
Start of mission, 36.5-deg offset angle	655 W	95 W
After 1 year, 36.5-deg offset angle	625 W	65 W

Note: This table is based on a 5-percent/year solar cell degradation and the baseline thermal case (Section VII).

is based on an optimistic analysis of the solar array output at the various offset angles. The contingency power is power in excess of the 560 W defined as a basic requirement.

C. Conclusions

The study of electrical power system configurations and capabilities has identified those portions of the conceptual design requiring further definition or refinement during Phase B. The establishment of definite, detailed power profiles and mission timelines will be a prerequisite for this task. Tasks requiring more work are summarized in the following paragraphs.

1. Solar Array Summary. This study considered alternate solar array configurations as shown in this section and in Appendix H. It appears that the solar cell modules are adequate for the baseline HEAO. If power requirements should increase or mission requirements change, it could be necessary to increase the power systems capability. The easiest way to obtain a substantial increase is to fold out the solar panels.

The requirement for two of the solar panels to be at an angle of 45 degrees to the center panel complicates the power system and introduces losses in matching the solar cell outputs; but the losses are within the performance

factor margin. A consequence of the varying outputs is that the CBRM will require some redesign to adapt it to operation at a constant input voltage, rather than a constant current, as in the ATM.

a. Definition of solar array/structure interface. Mounting of the solar cell module to the structure was not studied for the baseline. The proposed structure is such that there should be no problems in affixing the modules. If fold-out solar panels are incorporated, some structure change would be necessary to meet the launch envelope restrictions and maintain the rigidity required. A mounting concept was developed for the fold-out alternate.

b. Foldout array. Fold-out solar arrays were studied because the available contingency does not appear sufficient if requirements increase. The study considered only the power outputs, and no consideration was given to the weight of the fold-out arrays. This limited study of fold-out arrays is presented in Appendix H. Reliability of the fold-out array is not expected to be a problem since there is substantial history of successful fold-out arrays with very few failures.

2. CBR Summary. The ATM CBRM used for this study was designed for use in a power system with a flat, solar oriented array and relatively short mission. The HEAO solar array, as baselined, is not flat, is not solar oriented for all of the mission, and the required power system lifetime is considerably longer than ATM.

Solar cell modules on the different sides of the HEAO have different temperatures and illumination; therefore, their characteristic power curves and output voltages vary. Matching the outputs from the different sides to the input of the CBRM will degrade overall efficiency and peak power which could be used to charge the batteries. This loss does not appear to be critical.

Operation of the CBRM at a constant voltage (rather than constant current as in ATM) is expected to yield maximum utilization of the solar array output under the worst conditions expected. Further study of this problem is necessary to determine the feasibility of the constant input voltage approach. If the results of the study show this to be an undesirable approach, it will be necessary to develop a peak power tracking circuit.

3. Reliability. Reliability of the power system was not studied in depth. A detailed reliability engineering effort is required to determine requirements and the configuration of the power system to meet the mission guidelines. Several possible reliability problems have been identified.

a. Batteries. The rechargeable nickel-cadmium batteries in the CBRM are sensitive to temperature, depth of discharge, and number of charge-discharge cycles. Batteries are usually the weakest link in long-duration power systems. One suggested improvement in this area would be the procurement of battery cells under GSFC proposed specification S-716-P-23, dated April 30, 1969. This specification offers the best quality and design control of space batteries if a qualified source can be established.

b. Solar cells. Solar cell modules seem to be adequately reliable, although some provision may be necessary to isolate failed modules.

c. Networks. The only significant reliability consideration in the network's portion of the electrical power system is the reliability of the power distributors, switch selectors, and command functions. History of these items seems to indicate that there should be no problems for the baseline mission.

SECTION X. COMMUNICATIONS AND DATA SYSTEMS

PRECEDING PAGE BLANK NOT FILMED.
TABLE OF CONTENTS

LIST OF ILLUSTRATIONS

LIST OF TABLES

SECTION X. COMMUNICATIONS AND DATA SYSTEMS
Requirements

The telemetry and command system must provide for adequate communication between the spacecraft and ground tracking stations. In addition, the system must acquire, process, and store a variety of scientific data, as described in Section II of this report. A few ground rules, assumptions, and constraints are peculiar to the communications system and have been treated as requirements so that a baseline could be accomplished in a reasonable time frame. In Appendix I, several of the parameters were analyzed to determine how they influenced the design and selection of the hardware for the baseline. The following assumptions were made at the beginning of the study in relation to the tracking system:

(1) The carrier frequency of the wide band telemetry system would be 2200 MHz to 2300 MHz.

(2) STADAN would be used for communication with the vehicle.

(3) The errors in the command system should not exceed one in 10^9 bits. The telemetry data received at the tracking station could tolerate one error in 10^5 bits.

(4) The system should be sized to provide at least a data-rate capability of 27 500 bits per second. At least 2500 bits would be allocated to spacecraft engineering data.

These are not particularly difficult requirements and certainly do not require technological advances. The basic operation requires that the system provide a means of sampling and gathering data from the various experiments and spacecraft system into the telemetry system where a bulk storage capability is provided for time between tracking stations. When the satellite has been acquired by the tracking station, the data in the storage system are dumped through the telemetry links to the ground station. The data are forwarded by the station to the mission control center for further processing.

1. <u>On-Board Data Handling Requirements</u>. This portion of the system is not well defined primarily because the actual experiments have not been selected. The experiments described in Appendix A were used as typical examples of what the flight experiments would be. Table II-2 indicates an

arithmetical total of 16.8 kb/s for the scientific data. To provide a telemetry system that would be adequate and provide growth and flexibility, this estimate has been increased by a factor of 50 percent. Thus, throughout this section, a scientific data rate of 25 kb/s plus 10 percent for spacecraft engineering data was used.

2. <u>Data Storage Requirements</u>. The STADAN is comprised of some 15 stations. This number is reduced to only 6 for this study because of geographic location and because S-band equipment will not be available at all sites. The stations considered as being available are listed below:

Rosman, North Carolina (Link with GSFC)

Quito, Equador

Santiago, Chile

Johannesburg, South Africa

Orroral, Australia

Tananarive, Republic of Malagasy (Madagascar)

When the tracking station geographical locations and the earth trace of the spacecraft are considered, it becomes apparent that the stations fall into three groups spaced approximately 120 degrees apart. That is, Rosman, Quito, and Santiago contacts would be nearly simultaneous and thus cannot be considered as separate contacts for the purpose of storage dumping. The same is true for Tananarive and Johannesburg. To scope the bulk storage requirements, the orbital mechanics indicate that the period of the orbit at 200 n. mi. is 92 minutes. At a constant bit rate, which was assumed for this study, the total storage requirement is 1.5×10^8 bits. It would be desirable to have a data dump for each orbit. A backup station would also be very desirable to allow for station down time or higher priority spacecraft preempting and preventing the unloading of the data. This is not always obtainable; in fact, after a first look, it appears that the down-link capabilities may have a very significant impact on the design. A run was made of the GSFC computer program which gives STADAN station contacts. This program includes actual composite command and telemetry masks. The station contact time does not allow for signal acquisition and playback command. As the station operating procedure is formulated, these two conditions will have to be factored into the actual times, and used for the definitized design. The results of the run are summarized in Table X-1 over a 30-revolution span. This appears to be the time interval after which the trajectory repeats itself rather closely.

10-2

TABLE X-1. SUMMARY OF GROUND CONTACTS

200 n. mi. i = 28.50 deg	
Number revolutions	30
Total number contacts	42
Number contacts >6 minutes	19
Number contacts >5 minutes	32
Number contacts <5 minutes	5
Revolutions with more than one 5-minute contact	8
Revolutions with at least one 5-minute contact	16
Revolution without any contacts	2

Note that if only 5-minute contacts are considered, the maximum out-of-contact time is about 3 revolutions on the 8, 9, and 10 orbits and periodically throughout the hundred or so orbits examined. The station location and the 8, 9, and 10 orbits are shown on Figure X-1. There are several requirements to be deduced from this summary as follows:

(a) A prime tape-dump station and a backup will not always be available.

(b) The time for a tape replay for a single orbit should not exceed 5 minutes.

(c) The maximum bulk storage capability should be at least three orbits of data or more.

3. Antenna Requirements. The spacecraft antenna coverage should be continuous throughout the mission. Considering the sun orientation, orbital inclination, and spinning of the spacecraft, a total spherical coverage would be required. The antennas must be compatible with ground stations and the physical shape of the spacecraft, and provide a minimum electrical loss. The
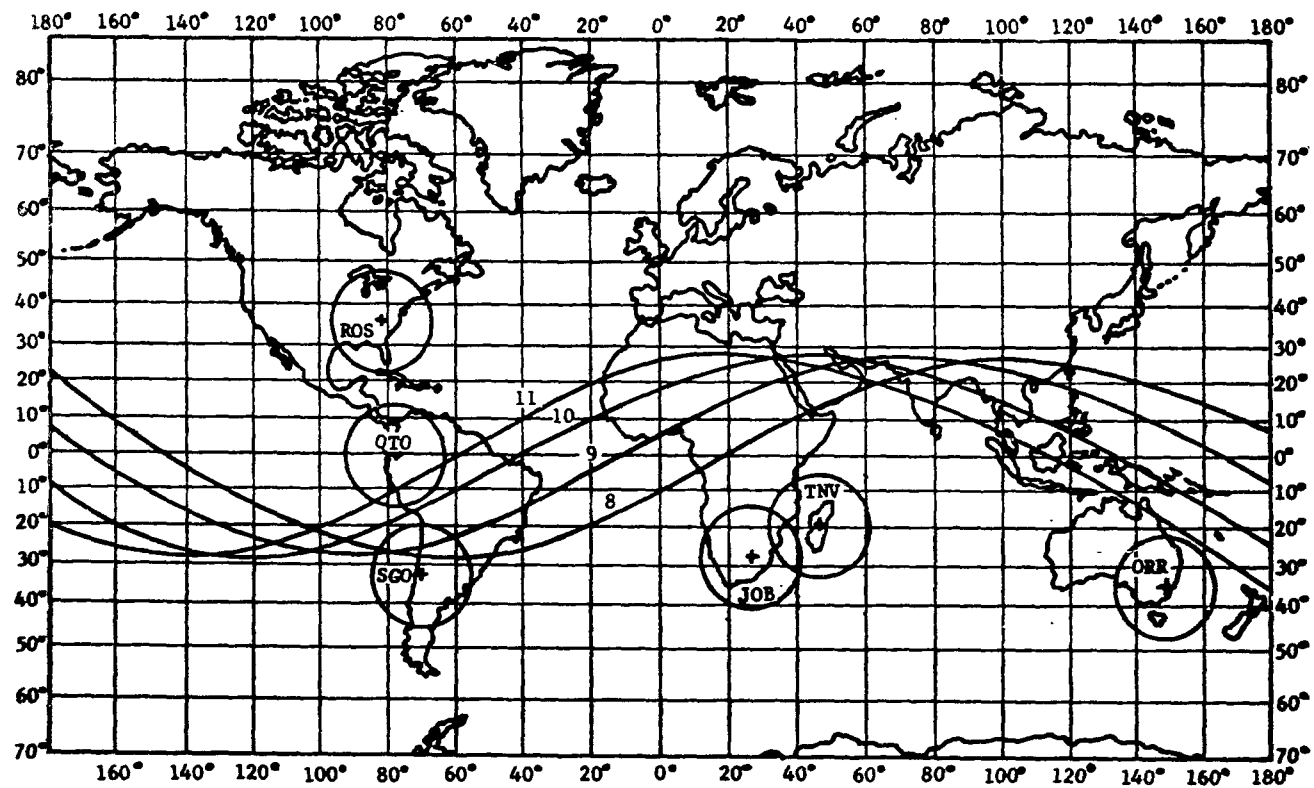
Figure X-1. STADAN Stations for HEAO.

ground station will determine such parameters as frequency and polarization. The spacecraft will influence the selection of the radiating elements. It is well known that it is impossible to obtain an isotropic single polarization pattern. The size and shape of this spacecraft certainly impact this problem. In Appendix I, the various approaches are covered in more depth; but they are outlined briefly below:

(a) Use several antennas properly phased for the narrowest beam possible and fewest nulls.

(b) Use dual polarization diversity receiver on the ground.

(c) Use frequency diversity.

(d) Switch antennas either from ground commands or on board generated commands.

The spacecraft physical configuration would require six S-band radiating elements, four elements around the longitudinal axis, and one on each end. Each S-band element should ideally have a 90-degree cone of coverage. The four S-band elements around the spacecraft should alternate polarization to allow diversity polarization techniques to be used on the ground or the elements must be switched. The ground station is probably only capable of receiving circular polarization, thus establishing a scheme of alternating right-hand circular polarization (RHCP) and left-hand circular polarization (LHCP). The circular polarization limitation would mean that only four elements around the spacecraft could be used. This results in a gap in the pattern but simplifies operations. Because exact pattern characteristics cannot be predicted accurately by analytical methods, experimental methods ultimately will have to be used. The BW requirements of the antenna are a function of the information rate and the modulation scheme. The data cannot exceed 200 kb/s because of ground station limitations, and the modulation scheme will be some type of wideband angular modulation. If a modulation index of five is used, then for a complex signal

$$BW = 2(\Delta f + 2 f_m)$$

where

Δf – carrier deviation

f_m – baseband

$$M = \frac{\Delta f}{f_m} = 5$$

$$BW = 2(200)(5+2) \quad .$$

$$= 2.8 \text{ MHz/transmitter}$$

Two down links will have to be diplexed onto the antenna. In the S-band range of 2200 - 2300 MHz this would be

$$BW \text{ percentage} = \frac{5.6}{2300} \times 100$$

$$= 0.2 \text{ percent}$$

This is certainly easy enough to achieve. The power-handling capability is a function of several parameters. If it is assumed that as many as two transmitters may be multiplexed onto a single radiating element, then the antenna must handle twice the output of the unit transmitter, divided by the number of antenna elements. This is the case where multielements are active at all times to provide omnidirectional coverage. The dual link is required because the dumped data rate exceeds the data handling standards of a single link.

    4. _Transmitter Requirements_. To obtain tracking data and aid in lock up of the very narrow beam S-band antenna on the ground, a minitrack beacon is required. Since the beacon is radiating continuously for the life of the mission, the power drain must be extremely low. Considering the percentage of the time the satellite is in contact with a ground station, it doesn't seem advisable to require that the beacon be turned off after S-band lock-up. The beacon must be capable of being modulated to provide certain critical engineering data associated with the reception of ground commands and the decision to command palyback and erasure of the tape recorder. Two IRIG-FM channels would be required to provide the capability, one for command acknowledge and one for status data. The status data are also contained in the 2.5 kb/s of engineering data on the wide band link; however, the remote tracking stations do not have a capability to decommutate the digital data and, hence, that status data will not be available in real-time at the remote stations; thus the status data provided on the beacon link is used in decision making during the pass. These data can also be transmitted directly to mission control for near real-time analysis of the situation, in the event a ground station is linked to Mission Control. It does not contain scientific data. Two standard FM channels were chosen to establish requirement; these were Channels 7 and 9. A margin

above the threshold was established at 3 db and the calculations shown in Table X-2 establish that a beacon of at least 10.9 milliwatts will be required.

TABLE X-2. MINITRACK LINK REQUIREMENTS

C/N in IF	13	(Assumed threshold of 10 db and 3 db margin above threshold)
Noise spectral density	-168 dbm	Receiver NF = 3.5 db Receiver T = 360° Sky T = 800°K System T = 1160°K
Bandwidth	26.8	485 Hz from $B_{If} = 2(f_c + f_m)$
KTBW	-141.2	
Power required in the Side bands	-128.2	
The modulation loss	-7.7 db	$M_1 = 0.7$ $M_2 = 0.7$
Received power required	-120.5	
Received antenna gain	+22.2	401 Antenna
Space loss	-142.6	
Polarization loss	-3.0	
Spacecraft antenna losses	-6.0	
Circuit loss	-1.5	
Required transmitter power	+8.6 dbm	
Transmitter power	8.6 dbm	
Losses	-151.3	

TABLE X-2. (Concluded)

Receiving antenna	+22.2	
Total received power	-120.5	
Modulation loss	-2.2	
Power in carrier	-122.7	
Bandwidth	+24.7	
Received noise power	-143.3	
C/N in loop	+20.6 db	
Subcarrier channel 2	-128.2	
Noise spectral density	-168.	
Bandwidth	+26.1	(408 Hz)
Noise in the IF	-141.9	
C/N	13.7	

10.4 dbm = 10.9 Milliwatts

Each S-band link is required to provide a 10^{-5} bit error rate.
The PCM standard specifies that the data rate will not exceed 200 kilobit
NRZ data. At an orbital altitude of 200 n. mi., the slant range would be
approximately 1200 n. mi. A receiver IF signal to noise ratio of approximately
13 db results in errors of about 1 bit in 10^5. The transmitter power output
is determined as follows:

$$P_t = L_{space} + L_{ckt} + M - G_r - G_t + K + T + B + C/N - L_{mod} .$$

Where:

    a. L_{space} = space loss= $37.67 + 20 \log F_{MHz} + 20 \log d_{nm}$

              = $37.67 + 20 \log 2300 + 20 \log 1280$

              = 167.1 db

    b. L_{ckt} = 6 db (includes polarization, cable, etc.)

    c. Margin = 6 db

    d. $-G_r$ = -46 db ($\approx$ 40 foot dish)

    e. $-G_t$ = 8 db (4-way power split)

    f. K = Boltzman's constant = 1.38×10^{-23} = -228.6 dbw/Hz

    g. T = effective system noise figure = 200° K = 23 db

    h. B = system noise BW

    i. C/N = 13 db(NBFM) and 10 db (WBFN)

    j. L_{mod} = modulation loss .

Thus,

    P_t = $-66.5 + C/N + B + L_{mod}$

    B = 500 KHz = 57 db

    P_t = $-66.4 + 13 + 57.0 + 9.6$

       = 13.2 dbw

       $\approx$ 20 watts

An important parameter of the transmitters is the DC to RF conversion efficiency. The 136 MHz carrier frequency and the low output power of the beacon makes a solid-state design achievable; however, in the S-band case this was not quite as straight forward as for the minitrack beacon. The solid-state devices usually have a cutoff frequency in the VHF range and the power output is very low at S-band. The TWT devices have much better efficiency but are not as reliable. The TWT also has an inherent characteristic that, for a small change in bias of the helix, a phase noise is generated. This has been tolerated in many satellites designed for communications; but the trend is toward modulations at a VHF and, then, by the use of varactors or transistors, to multiply the signal up to S-band. To establish a reasonable and meaningful efficiency estimate, a solid-state design concept was generated as shown in Figure X-2. The scheme was to amplify the VHF output of the exciter/modulator to power level where the losses through multipliers and hybrids would result in an output in the range of 20 watts.

EXC/MOD	–	10
PA 1		20
PA 2 A&B		50
PA 3 A-D		120
Total input		200 watts

The overall efficiency, $\eta = \dfrac{+20}{200} \times 100 = 10\%$

The DC to RF efficiency of solid-state devices at S-band have been improving at a rate of 2 percent per year for the last several years; the conservative 10 percent should allow for at least a 2:1 derating in power dissipation.

The two areas that are still difficult to predict as far as solid-state designs are concerned, are the following:
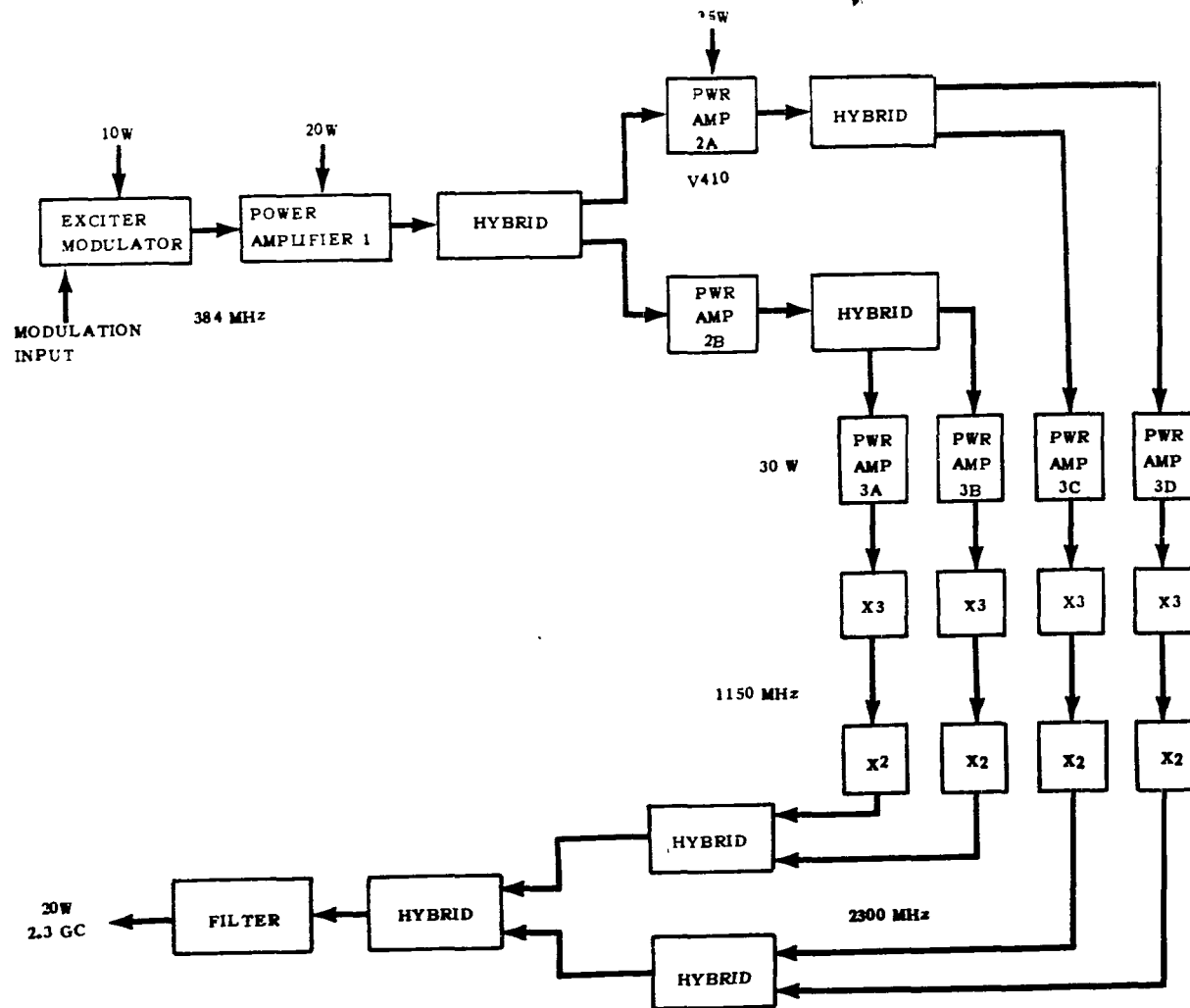
Figure X-2. Solid-state S-band transmitter.

(a) Long-term frequency stability with aging.

(b) Output power stability.

These will not be addressed at this time since they would not impact the design in selection of other elements of the system.

5. Command System. Command system requirements for the experiments are not well defined at this time; however, current estimates of the number of commands required to control experiments and spacecraft are as follows:

Experiment	No. of Commands
X-Ray Experiment 1	40
X-Ray Experiment 2	40
Low-energy gamma-ray detector	32
Medium-energy gamma-ray detector	40
Gamma-ray telescope	40
Cosmic-ray electrons	40
Cosmic-ray calorimeter	32
Sub Total	264

Spacecraft	No. of Commands
Attitude control system	70
Communication & data system	60
Power system	25
Sub Total	155
Total	419

Some experimenters prefer to decode a digital pulse train, while others lean toward relay closures or discrete levels supplied to the experiment control logic. To satisfy all requirements, including spacecraft system requirements, a central command decoder must be included in the spacecraft. The total number of commands available depends on the number of bits in the

serial binary command word. Since experiment control will require 264 commands, the next available number of total spacecraft commands is 512. However, since more than 155 other spacecraft commands have already been identified, for a total of 419, it is recommended that the command system be configured for 1024 commands, which requires a 10-bit command word.

It is necessary for the HEAO spacecraft to utilize the 148 MHz STADAN up-link. Since a 10-bit command word is necessary to meet system requirements, the STADAN 400 bits per second command rate should be adequate for this system. This would allow approximately 16 commands per second to be transmitted to the spacecraft, assuming that each command is repeated three times. In 1 minute, 960 commands (almost the complete repertoire) could be transmitted.

In summary, one STADAN 148-MHz command link operating at 400 bits per second should be adequate for up-link requirements.

B. Baseline System Description

1. Functional Description. The functions of the HEAO communications/ data system are defined in the requirements portion of this report. A block diagram is shown in Figure X-3 and described below.

a. Communications and data. There are two independent communications systems. The 136-MHz minitrack beacon is used to acknowledge commands from the ground and to transmit spacecraft systems status and attitude in real time at a low data rate.

The S-band system consists of two RF links operating in the 2200- to 2300-MHz band. The stored spacecraft data are dumped to the ground stations over these links.

The spacecraft antenna systems include S-band and VHF elements. A basic four-element S-band array and four-element VHF array should be adequate for the mission. Optimum methods of feed, polarization, and phasing will have to be determined empirically. The conceptual design of the antenna system provides, to a degree, omnidirectional operation of both S-band and VHF systems. The nulls at each end of the spacecraft are not expected to be a serious problem.
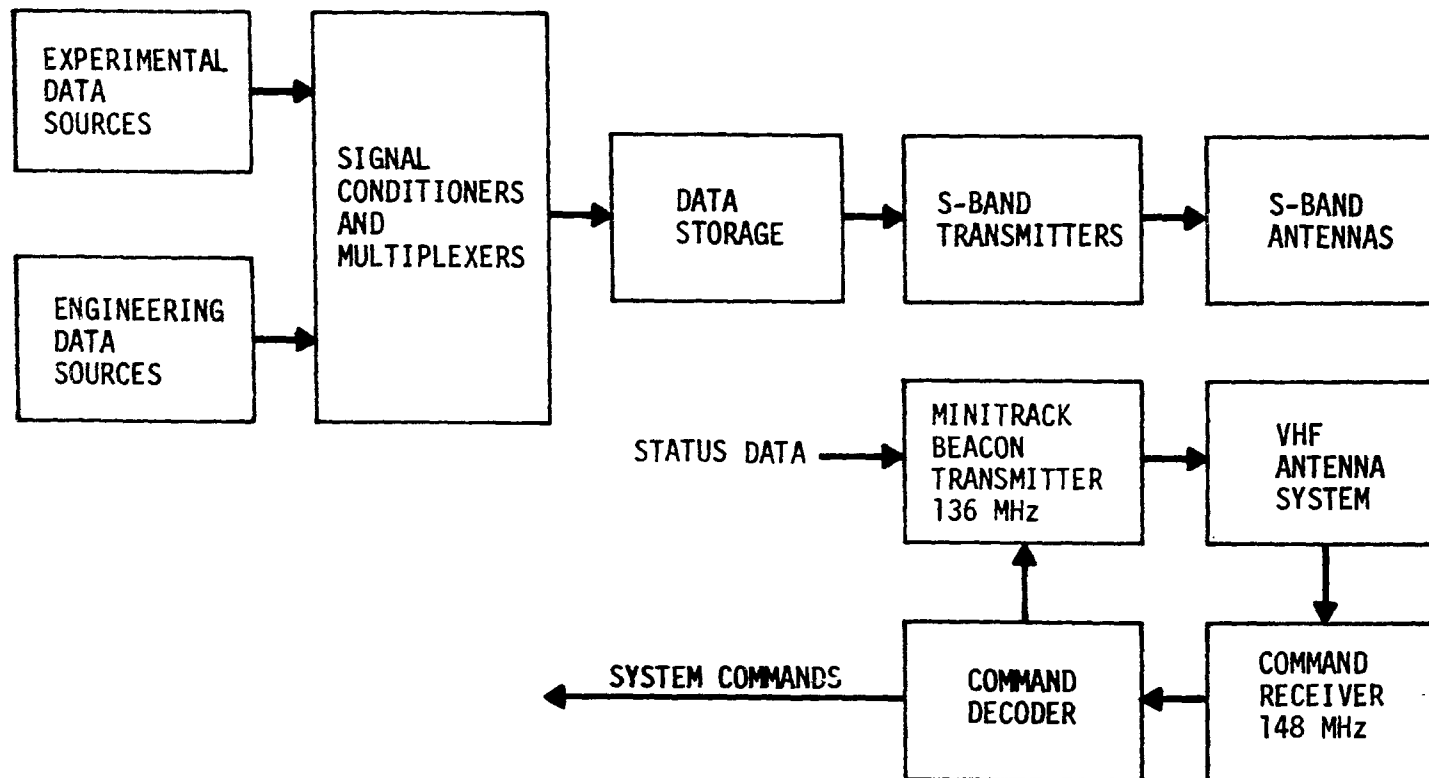
Figure X-3. Functional block diagram-spacecraft communications and data handling system.

b.   Data acquisition and storage subsystem. This portion of the system includes all the elements between the data output sources and the inputs to the transmitters. The function of this subsystem is to accept, condition as necessary, sample, and store data on magnetic tape recorders. On ground commands, the tape recorders are played back into the S-band transmitters.

c.   Command subsystem. The command subsystem consists of command receivers and a command decoder. The purpose of this subsystem is to receive commands from ground stations, decode the commands, and either route the binary command word to the appropriate spacecraft system or provide a command signal to activate relays, solid-state switches, or other control devices.

d.   Tracking beacon. The primary purpose of the 136 MHz beacon is to provide an acquisition aid for the 85-foot antennas when operation at S-band. The beacon signal will be used to establish orbital parameters in the early phase of the mission and to transmit spacecraft systems status and attitude data in real time. It will also be used to acknowledge STADAN command signals.

2.   Acceptable Implementation

a.   Antennas. The spacecraft antennas consist of two separate subsystems. The first is the S-band transmitting antenna system. The second is a VHF antenna system shared by the minitrack beacon transmitter and the command receivers.

Final testing of antenna configurations will have to be carried out on model spacecraft installations at an antenna test range. Antenna performance characteristics must be determined by actual measurement; this is a Phase C function.

(1) S-band telemetry antennas. The telemetry antenna system consists of six radiating elements. These four antennas will be mounted symmetrically around the vehicle at 90-degree intervals. Detailed design of the antenna system will be possible only after the vehicle configuration is finally defined.

Although final selection of a radiating element is not possible at this time, it is believed that the antenna would be physically similar to the Electronic Specialty Company Model 03-44-00010. Estimated size is 4.2-inch diameter by 1.5-inch thickness; the weight is less than 1 pound. The telemetry antenna is illustrated in Figure X-4.
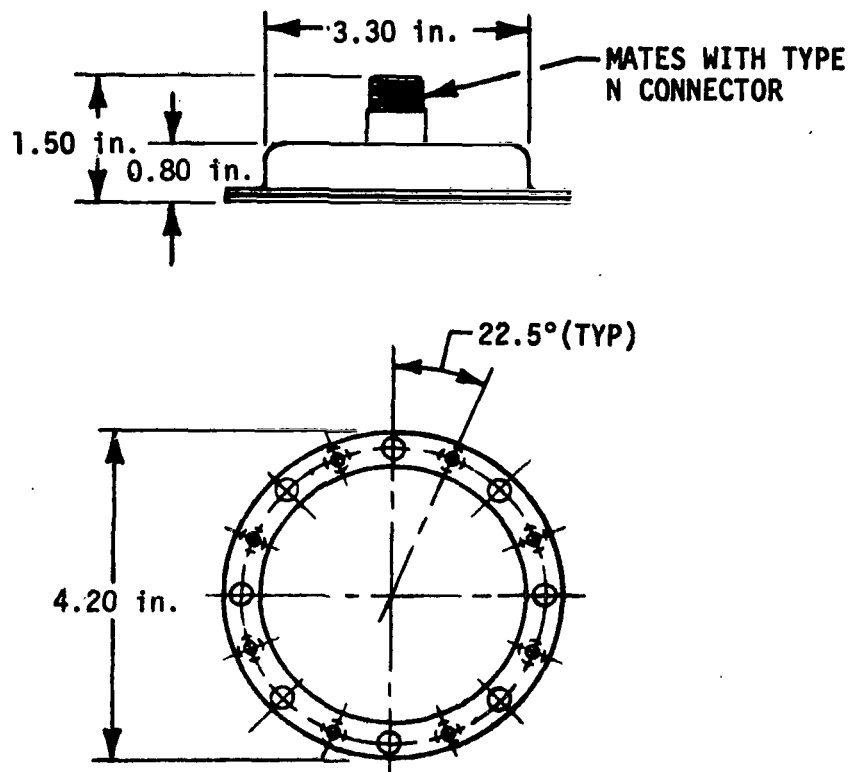
NOTES:

1. WEIGHT: 1.0 lb
2. MANUFACTURER: ELECTRONIC RESOURCES
3. MODEL NO.: SPECIAL

Figure X-4. S-band telemetry antenna.

(2) VHF antennas. The VHF antenna system will consist of
four VHF quarter-wave stub elements spaced at 90-degree intervals about the
spacecraft cross section. This antenna system will be shared with the minitrack
beacon. A notch filter rejecting 136 MHz would be used to provide isolation of
the command receiver system from the minitrack transmitter.

The VHF antenna elements will project approximately
22 inches from the spacecraft skin. The antenna would have a spring in its
base which would erect the antenna after shroud separation. The VHF antenna
is illustrated in Figure X-5.

VHF RECEPTACLE

2.63 in.

1.46 in.

45°

21.88 in.

23.88 in.

3.00 in.
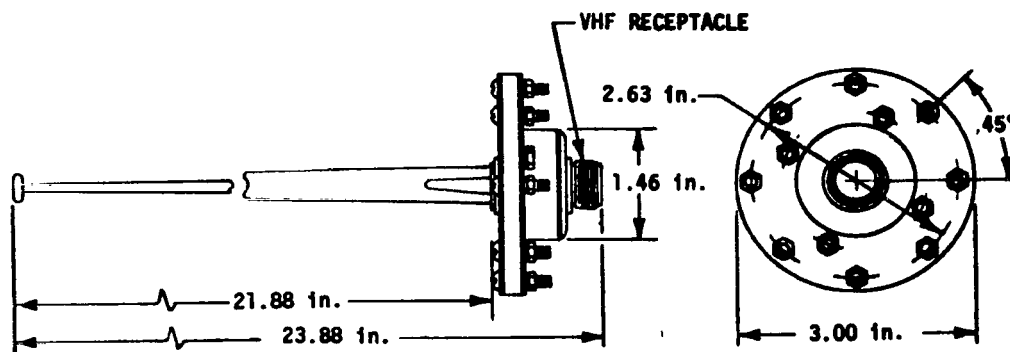
NOTE:

1. WEIGHT: 1.0 lb

Figure X-5. VHF antenna.

b. Transmitters. Two S-band transmission links and one Minitrack transmission link are required in the spacecraft.

The recommended S-band units are EMR model 3620-05. These transmitters are rated at 20 watts, the outline dimensions are 8.00 by 4.00 by 4.00 inches, and the weight is 9.5 pounds. The case isolation and circulator/load options would be selected for this application; this unit is illustrated in Figure X-6.

The Minitrack beacon recommended for HEAO is the Spacecraft Model T400 transmitter. This unit has been flown on Pegasus 1, 2, and 3, Saturn I, OSO 1 and 2, and several other scientific satellites. It is designed to operate on the 136-MHz band at an output of up to 2 watts. It has phase modulation capability, with a modulation sensitivity of 2 radians/volt, the physical envelope is 0.82 by 2.1 by 4.8 inches, and the weight is 0.4 pound. Figure X-7 illustrates the beacon transmitter configuration.

c. Data handling subsystem. The data handling subsystem is currently the least defined area of the spacecraft electronics systems. The reason for this lack of definition is that this subsystem must serve as an interface between the experiments and the telemetry system, and the experiment telemetry requirements have not been fully defined. However, some assumptions can be made that will allow "envelopes" to be defined.
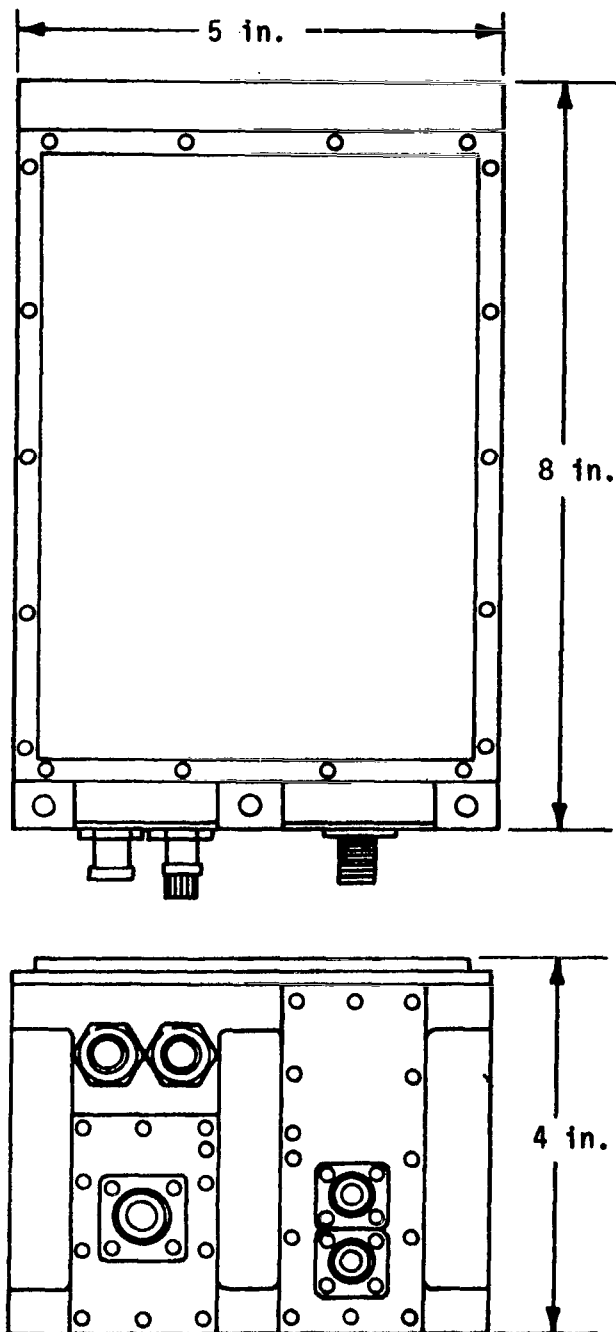
NOTES:

1. WEIGHT = 9.5 lb
2. POWER = 220 W (MAXIMUM); 0 W (MINIMUM)
3. MANUFACTURER: ELECTRO MECHANICAL RESEARCH
4. MODEL NO: 3620-05

Figure X-6. S-band telemetry transmitter.
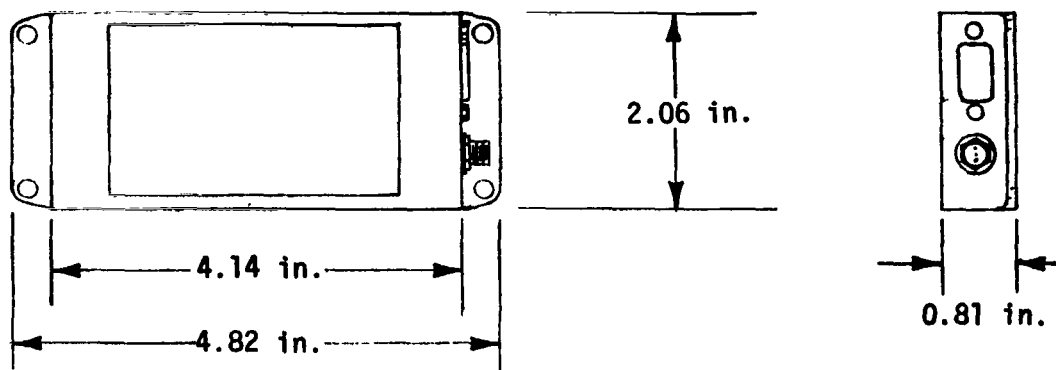
NOTES:

1. WEIGHT: 0.4 lb
2. POWER: 4.0 W (MAX) 4.0 (MIN)
3. MANUFACTURER: SPACECRAFT
4. MODEL NO.:   T-400

Figure X-7. Minitrack beacon.

(1) Magnetic tape recorders. Since the tape recorder has moving parts, it is intuitively the least reliable element in the entire data system. Several methods by which the recording system reliability may be improved are:

• Redundancy

• Machine selection

• Operational techniques.

The baseline on-board data storage system consists of four dual-track Leach 2000 tape recorders. Each recorder is configured to record and reproduce two channels of digital data. The Leach 2000 recorder offers several desirable features for the HEAO system. It was designed specifically for satellite use. The high-packing density allows high bit rate replay at a relative low tape speed. This should enhance reliability and use a minimum of electrical power.

Recorder data storage capacity is computed from the relationship of the reel capacity in inches times the packing density or (1800) (12) × 10 000 = 216 megabits per track. Total storage capacity for the two-track configuration is 432 megabits. Total system capacity is 4 × 432 = 1 728 megabits.

The two digital data channels in the HEAO Communications/ Data System operate at 13.75 kilobits per second. At a recording bit density of 10,000 bits per inch, a recording tape speed of 1.375 inches per second is required. Playback speed is determined by the 200 kb/s limit of the STADAN downlink. This leads to a playback speed of 200 000/10 000 = 20 inches per second. Playback-to-record ratio is computed as 20.00/1.375 = 14.545.

The recorder will accept the two-channel digital input continuously until the end of the reel is reached. At this point, the recorder control logic will automatically shut off the machine and switch on another machine in the record mode.

When ground station contact is made, the full recorder(s) will be switched to the playback mode. The playback will be continued until the tape dump is complete, even if more than one ground contact is required to accomplish the complete playback. The data dump will be done with the tape moving in the opposite direction to the record mode. No rewinding operations are required, thus minimizing tape system wear and power requirements.

Use of two data tracks per recorder offers several advantages. These include lower system power demand, increased data storage capability, less tape wear, and increased redundancy. These advantages are gained at negligible increases in weight and unit power demand.

The four-recorder system requires only one two-channel tape machine to be on line recording at any given time. The other three would be in a stand-by mode except during ground station contact when one machine would be in a playback mode.

If one of the four tape machines fails, no mission degradation occurs. The main result would be that system storage capacity would drop from 1728 million bits to 1296 million bits.

Should two of the four tape units fail, again no direct mission impact will result. In this case, data storage capacity drops to 864 million bits. This is still 123 percent of the maximum storage requirement.

If three out of four tape units fail, the ability to record while dumping data will be lost. This will cause an average loss of 380 seconds of data per orbit. This amounts to about 7 percent of the total data. In addition, data storage capacity will drop to 432 million bits, which will cause loss of about 30 percent of data during unfavorable contact times.

Should all tape recorders fail, the system could still transmit real time data, rather inefficiently, during approximately 7.5 percent of the total orbital time.

Leach series 2000 tape recorders have an envelope of 5.3 by 7.6 by 7.1 inches. Weight is 15 pounds. Power required is 5 watts for record and 25 watts for playback. The Leach 2000 recorder is illustrated in Figure X-8.

PURGE TUBE OR VALVE (2 PLACES)

DTK1H-14-15PW-085 OR 057 CONNECTOR HERMETIC (DEUTSCH)

DTK1H-14-15P-085 OR 057 CONNECTOR HERMETIC (DEUTSCH)

152 20-F1-20 INSERT (4 PLACES)

7.10 in.

7.60 in.

5.31 in.

0.50 in.

NOTES:

1. WEIGHT: 15 lb
2. POWER: 25 W (MAX) 5 W (MIN)
3. MANUFACTURER: LEACH
4. MODEL NO.:   SERIES 2000
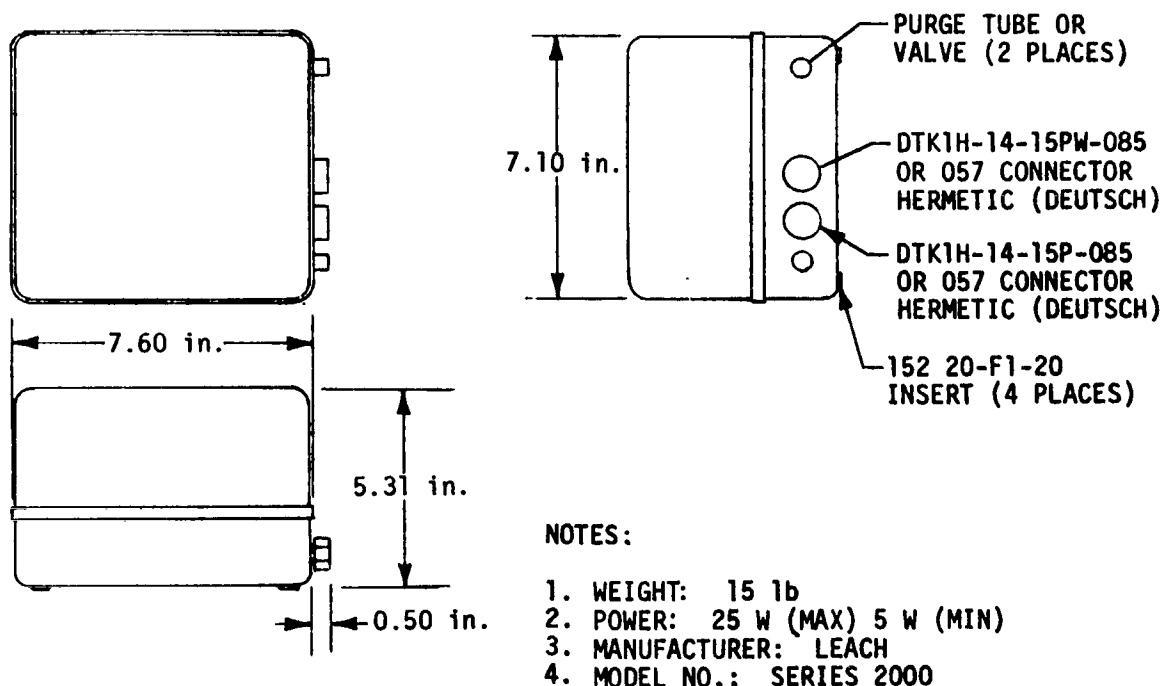
Figure X-8. Tape recorder.

(2) Multiplexer. The flexibility and reliability required by the HEAO data multiplexer is believed to be attainable only with a special design. A literature search has discovered no "off-the-shelf" unit with the

capabilities required by the HEAO system. It is possible that, when experiment data outputs are well defined, an existing multiplexer may be found which is suitable. The baseline assumes that a unit with a 6- by 6- by 10-inch envelope and 8-pound weight is adequate. The multiplexer dimensions are shown in Figure X-9.
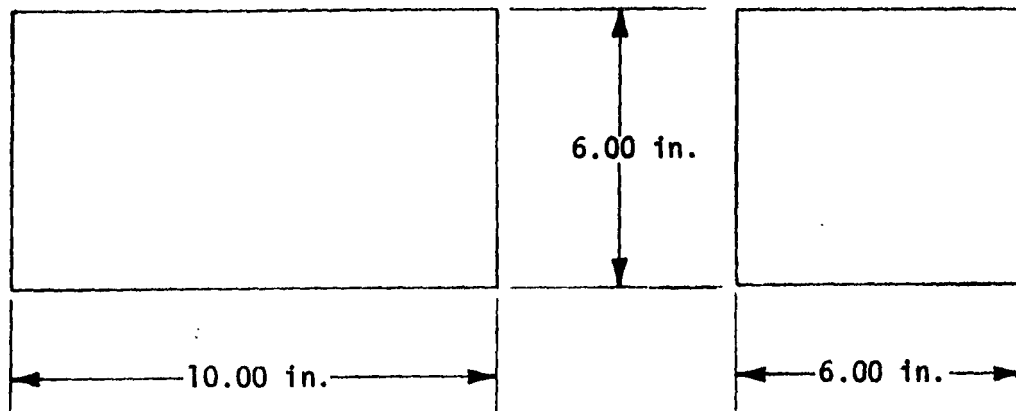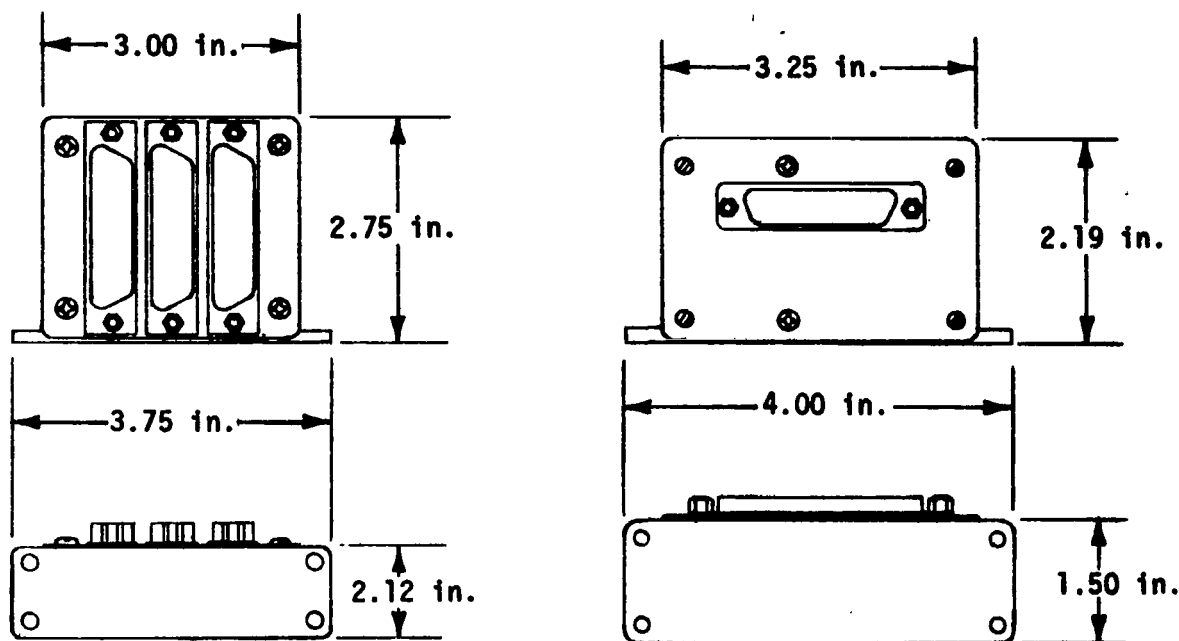

NOTES:

1. WEIGHT: 8 lb
2. POWER: 5 W (MAX) 5 W (MIN)
3. MANUFACTURER: SPECIAL

Figure X-9. Multiplexer.

(3) Signal conditioner. The baseline design signal conditioners will attenuate the analog diagnostic signals to basic system voltage levels, multiplex them, and convert them into digital form. Two units will be required: a commutator and an analog-to-digital converter. The system cannot be completely defined before "housekeeping" signals to be monitored and experiment outputs are determined; however, the Teledyne Telemetry Model 378 commutator and the AD-610 analog-to-digital converter are typical of the hardware available for this application (Fig. X-10).

(4) Switching network. The switching network serves to route the data flow to and from the recorder subsystem. The two digital multiplexer outputs are switched to the proper pair of digital recorders for data storage. When the HEAO passes over a STADAN network data acquisition station, the outputs of the pair of tape recorders to be dumped are routed to the S-band transmitter modulation inputs.

NOTES:

1. WEIGHT: 3 lb
2. POWER: 8 W (MAX) 8 W (MIN)
3. MANUFACTURER: SPECIAL

Figure X-10. Analog signal conditioner and multiplexer.

       The switching network final design will result in a specialized module that will not be an off-the-shelf component. For conceptual design purposes, it can be considered to be contained by an 8- by 8- 12-inch envelope weighing 10 pounds.

       (5) Sync generator. The sync generator is considered to be a part of the digital multiplexer subsystem, whose volume and weight are included in the envelope described for that subsystem.

       (6) Diagnostic logic. The diagnostic logic for HEAO will perform "housekeeping" functions. Inputs will be available from a variety of subsystems, including data systems, command decoder and switching networks, and attitude control and experiments.

d. Command Receiver. The command receiver recommended for the HEAO is the AVCO model AED-301A. This receiver has outline dimensions of 3.5 by 5 by 1.125 inches, power requirements of 0.18-watt standby and 0.40-watt operating, and weight of 1.25 pounds. This receiver has flown on the OSO-H, ISIS, and SERT-II spacecraft.

e. Command Decoder. The command decoder will not be defined until experiment definition is complete; however, a typical AVCO command decoder designed to interface with the AED-301A command receiver can be used for preliminary design purposes. A typical decoder has outline dimensions of 8 by 6.25 by 2.5 inches, a standby power consumption of 0.1 watt, and weight of 6 pounds. The operating power consumption will vary with the operating mode.

C. Performance

In the following paragraphs the baseline system is assessed as to how well the requirements outlined in the first part of this section have been met.

1. Data Rate. To establish a format, frame rate and consequently a data rate, a typical measurement program was devised. The multiplexing scheme is based on the sample rates and bytes per sample shown in Table X-3. The mean sample rate of the experiments is about 200 samples per second. If this is selected as the minor frame rate, those sample rates that exceed this rate will be supermultiplexed and those that are less submultiplexed. The calorimeter experiment would occupy the first four words of each minor frame. The low-energy gamma-ray experiment would occupy a single word in only half the subframes. The very low sampling rates such as in some of the engineering channels may appear as a single word in only one subframe of the entire major frame. A matrix of 12 x 200 is slightly more than the required capability but indicates that the data requirements can be met within the limitation of the Goddard Pulse Code Modulation Standard now in effect. A 16 x 148 matrix would probably be more efficient; the data rate would be slightly less. The 12 x 200 matrix is shown in Table X-4. The standard allows 256 minor frames per major frame and 8192 bits per major frame. The word length in the standard is restrained to 32 bits. This results in a maximum matrix of 256 x 256. The 12 x 200 or the 16 x 148 matrix is well within these boundary conditions.

The 12 x 200 matrix contains 24 000 bits. At a frame rate of one per second, the bit rate is 24 000 bit/sec. This bit rate is within the design requirements and capability of the baseline spacecraft.

TABLE X-3. SPACECRAFT DATA SAMPLING RATES

Code	Data Source	Type of Data	Samples/sec
	Experiment Data Summary		
A	Cosmic-ray calorimeter	Digital	800
B	X-ray Experiment 1	Digital	300
C	Gamma-ray telescope	Digital	250
D	Low-energy gamma-ray detector	Digital	100
E	Medium-energy gamma-ray detector	Digital	100
F	Cosmic-ray electrons	Digital	80
G	X-ray Experiment 2	Digital	50
H	Experiment status	Digital	50
	Engineering Data Summary		
I	16 ch. aspect; 1 ch. comm. sig. strength; 5 ch. ASC current; 4 ch. tape current (total, 26 ch.)	Analog	5
J	48 ch. elect.; 10 ch. pressure; 1 ch. flywheel speed (total, 59)		8
K	30-switch position		1
L	Clock (1 or more words/frame)		
SYN	Synchronization (3 words/frame)		

TABLE X-4. MAJOR FRAME MATRIX

WORDS

	1	2	3	4	5	6	7	8	9	10	11	12
1	A	A	A	A	B	B	C	C	F	I	J	J
2	A	A	A	A	B	B	C	C	F	I	J	J
3	A	A	A	A	B	B	C	C	F	I	J	J
4	A	A	A	A	B	B	C	C	F	I	J	J
5	A	A	A	A	B	B	C	C	F	I	J	J
6	A	A	A	A	B	B	C	C	F	I	J	J
7	A	A	A	A	B	B	C	C	F	I	J	J
8	A	A	A	A	B	B	C	C	F	I	J	J
	A	A	A	A	B	D	C	Q	I	J	J	V
194	A	A	A	A	B	D	C	Q	I	J	J	V
195	A	A	A	A	B	D	C	Q	I	J	J	V
196	A	A	A	A	B	D	C	Q	I	J	J	V
197	A	A	A	A	B	D	C	Q	I	J	J	V
198	A	A	A	A	B	D	C	Q	I	J	J	V
199	A	A	A	A	B	D	C	Q	I	J	J	V
200	A	A	A	A	B	D	C	Q	L	SYN	SYN	SYN

(Left axis label: MINOR FRAMES)

Note: Subframes 166 through 199 contain only 11 words; therefore, the last words are coded V for vacant.

2. <u>Power Consumption.</u> The average and peak power consumptions are the factors of primary concern to the sizing of the power system. The peak power occurs only during contacts with a ground station when the transmitters are "powered up" and the recorders are in playback. The summary of the tracking station contacts indicates that on about half of the orbits a 5-minute contact would occur; therefore, the average power is based on one 6-minute 45-second maximum time contact per revolution. The average power is found by inspection of Figure X-11 to be

$$P_{avg} = \frac{(T_o - T_c) P_s + T_c (P_{peak})}{T_o} \; ,$$

where

T_o – orbital period (92 minutes)

T_c – ground station contact time (6 minutes 45 seconds)

P_s – Steady-state power demand

P_{peak} – Peak power (S-band transmitter on)

$$P_{avg} = \frac{(92 - 6.75)(30.2) - (6.45)(503)}{92}$$

$$P_{avg} \cong 65 \text{ watts}$$
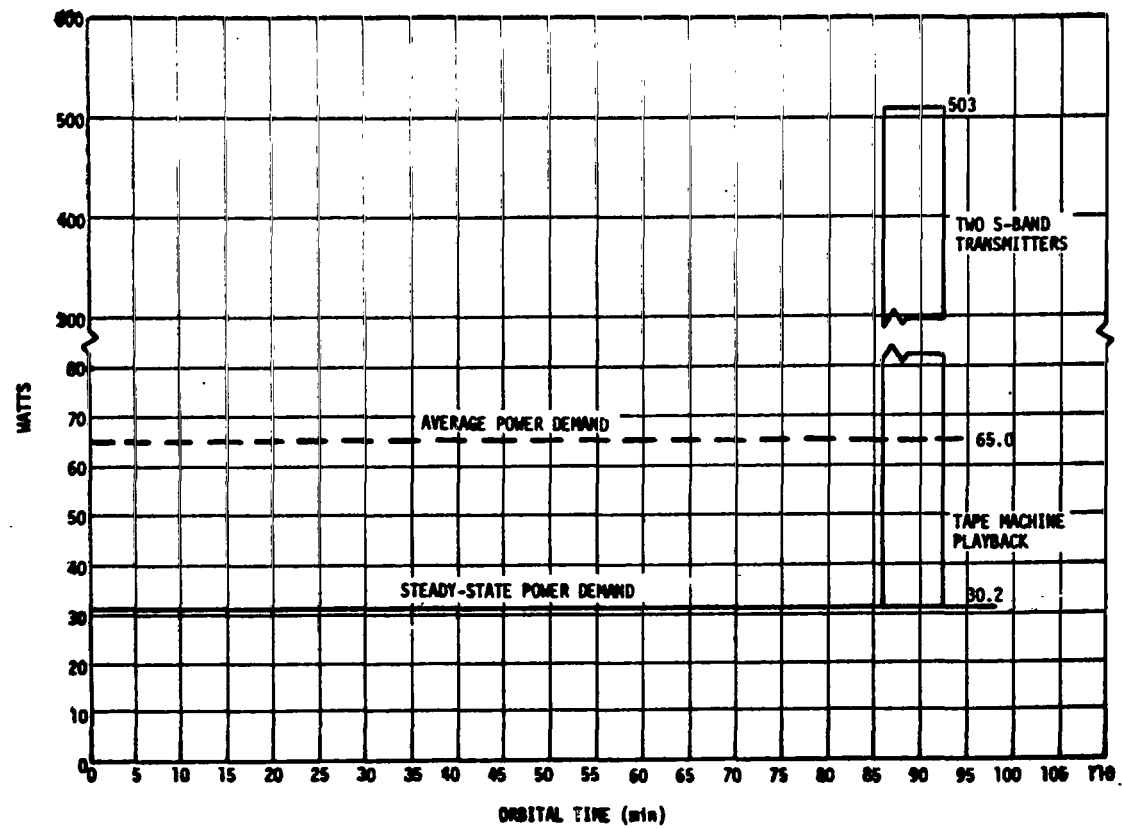
Figure X-11. HEAO communication and data handling system power profile.

The peak power is approximately 503 watts. This is a conservative estimate and in the later refinement it is not expected to increase.

3. <u>Bulk Data Storage Requirements</u>. The item having the greatest impact on the baseline system is the 200-kb/s limit on the data transmitted to the STADAN stations. Goddard Space Flight Center published a memorandum showing STADAN contact times for HEAO's first 107 orbits. A total of 152 000 000 bits of data are generated by the HEAO systems, each orbit at the baseline data rate of 27.5 kb/s. Since two RF down links are used, data are effectively dumped at a 400-kb/s rate. At this rate, the required contact time per orbit can be computed to be 380 seconds.

A plot (Fig. X-12) was made of the data stored on board at the end of each orbit for the first 107 orbits. As can be seen, the system is able to dump data down to zero storage on orbits 1, 2, 3, 4, 5, 19, 20, 34, 35, 66, 81, 96, and 97. At certain times during the out-of-contact period, the total bits in the recorders approach 700 megabits. The total capability of the baseline system is computed from the reel capacity and packing density.

$$1800 \text{ ft} \times 12 \times 10\ 000 \text{ bits/inch} = 216 \text{ megabits/track}$$

$$2 \text{ tracks/ recorder} \times 4 \text{ recorders} \rightarrow 1728 \text{ megabits}$$

This would be considered a very comfortable margin if it were the only satellite active at that particular time.

D. Conclusions

The salient conclusion that should be drawn from this portion of the study is that while the baseline is not optimum from the standpoint of power consumption or data handling efficiency, it is the current state of the art. The one exception requiring development is the tape recorder. Many of the components are available as catalog items from the vendor and those requiring design are straightforward engineering problems.

The baseline system performance in most all areas exceeded the requirements. The only possible marginal condition was the total data storage at a time when many spacecraft could be competing for time on the STADAN
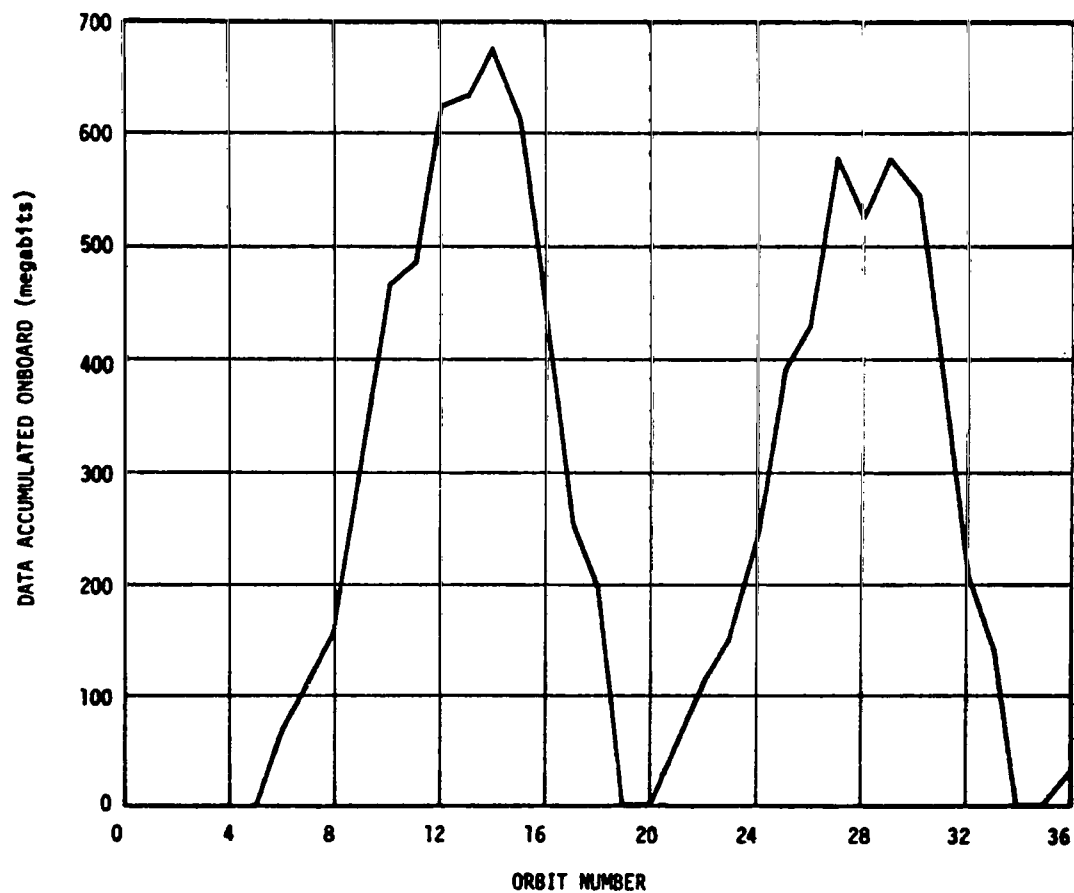
Figure X-12. Data accumulation as a function of orbit numbers.
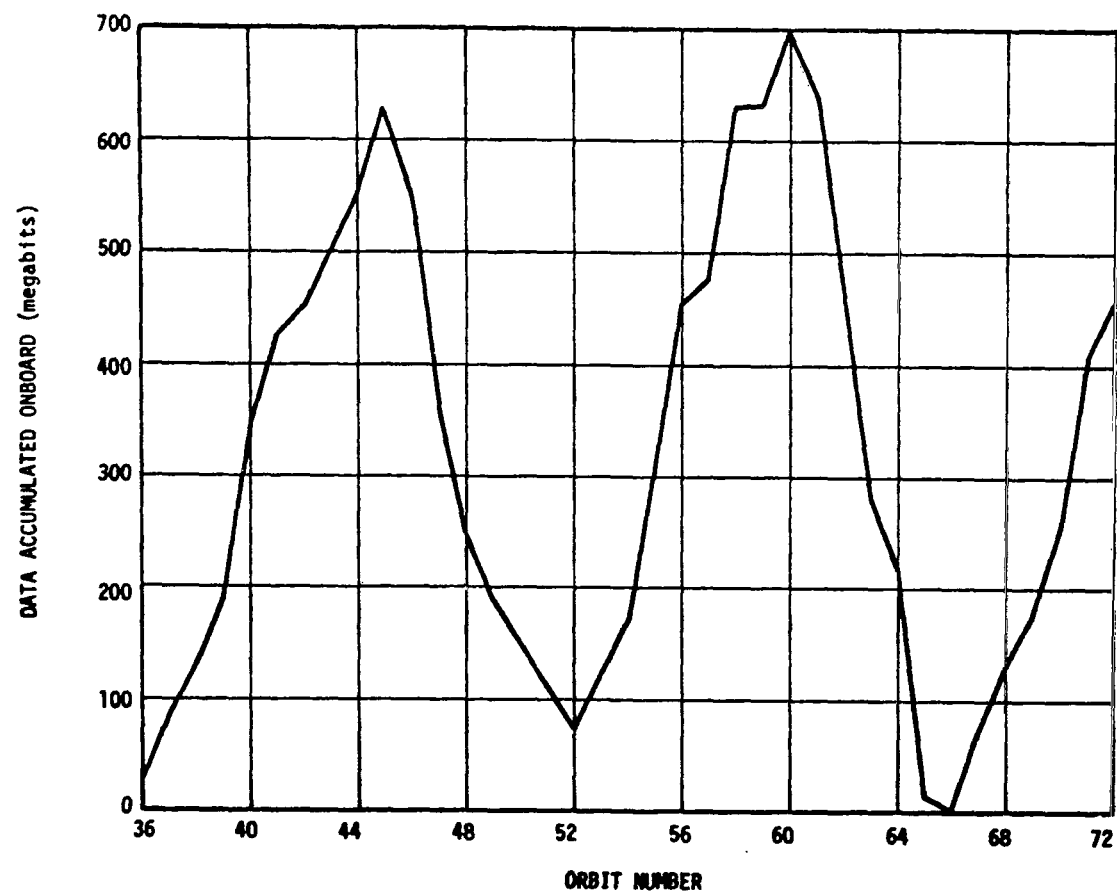
Figure X-12. (Continued)
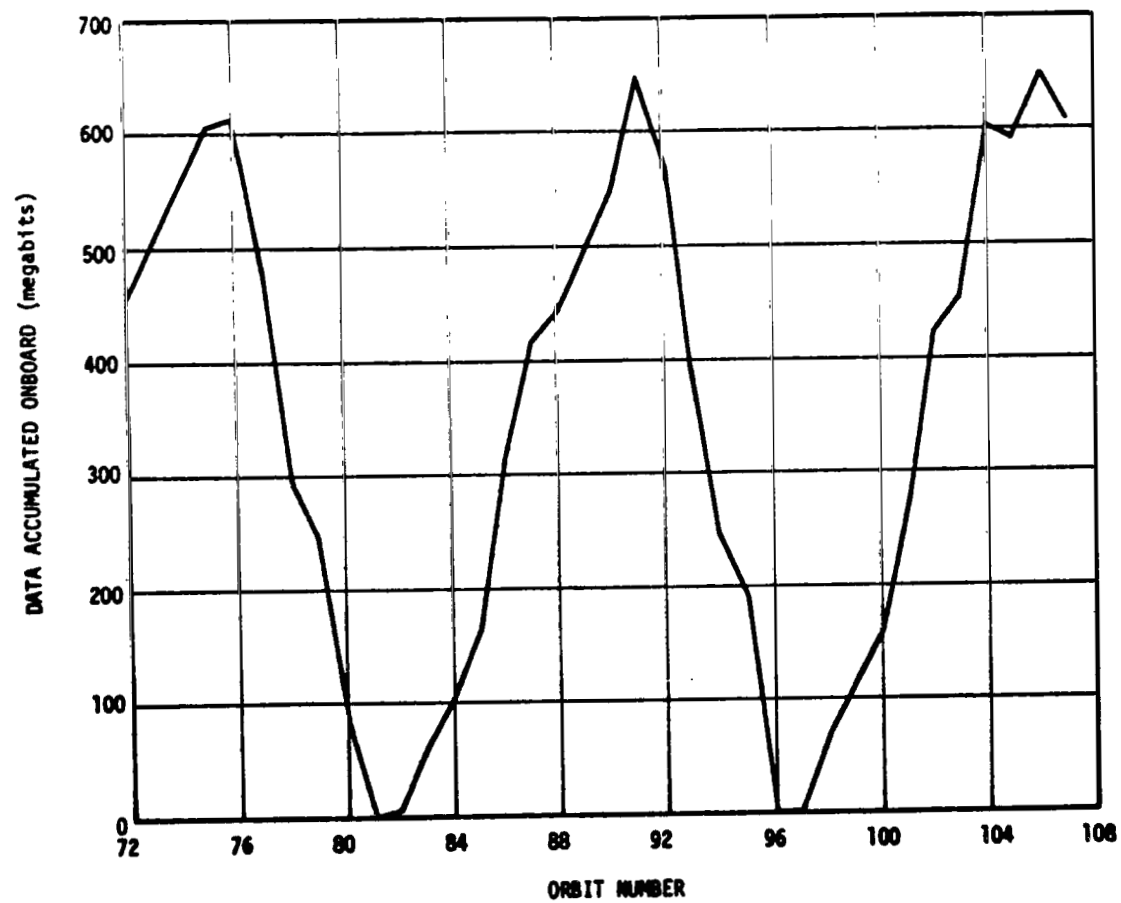
Figure X-12. (Concluded)

net. This condition cannot be altered by increasing data storage. Over the long term, the satellite cannot produce data faster than STADAN can accept it. There are several alternatives. The first is to increase down-link data rate standard above the 200 kb/s. Another would be to decrease experimental data rate. A third would be to explore higher orbits and different inclination angles. This should be traded against the reduced experiment data mentioned above. The 200 kb/s standard is based on existing data-handling equipment. The majority of the stations of interest now have the more up-to-date equipment that has a capability greater than the current standard.

SECTION XI. ATTITUDE SENSING AND CONTROL SYSTEM

TABLE OF CONTENTS

TABLE OF CONTENTS (Concluded)

LIST OF ILLUSTRATIONS

LIST OF ILLUSTRATIONS (Continued)

LIST OF ILLUSTRATIONS (Concluded)

LIST OF TABLES

DEFINITION OF SYMBOLS

X, Y, Z Body principal axes

X_s, Y_s, Z_s Solar fixed coordinates with X_s to the sun, Z_s PEP pointed northerly and Y_s completing a triad in the ecliptic plane.

ψ, θ, ϕ Euler angles defining vehicle attitude relative to sunline. ψ in the ecliptic, θ in a plane perpendicular to the ecliptic plane, and ϕ about scan axis.

δ Scan axis solar offset angle

T_{xG}, T_{yG}, T_{zG} Gravity gradient torques in spacecraft body axes

GM_e Gravitational parameter, 1.4077×10^{16} ft^3/sec^2

I_x, I_y, I_z Moments of inertia

T_x, T_y, T_z Vector troque components, spacecraft axes

SECTION XI. ATTITUDE SENSING AND CONTROL SYSTEM

A. Requirements

1. Guidelines and Constraints. Basic mission guidelines and space-craft constraints affecting the design of the ASCS consist of experimental pointing and control accuracies, power and thermal constraints, spacecraft configuration, and spacecraft operational mode requirements.

Attitude determination accuracy for experimental data correlation has been established at ±0.1 degree for each of the three spacecraft axes (Fig. XI-1). This is to be provided in two of the three spacecraft operational modes on a non-real-time basis for ground data reduction and in the third mode real time. Since the spacecraft solar panels must be kept sun oriented to provide power to the onboard subsystems, there is a limit to the degree of solar panel (Z-axis) offset from the sunline. This maximum Z-axis offset requirement has been set at approximately 37.0 degrees. Within this constraint, attitude pointing accuracy limits for the spacecraft have been established such that the axis required to be pointed is maintained within 1.0 degree of the desired orientation. Two of the three spacecraft operational modes require that the spacecraft be rotated at a rate of 0.1 revolution per minute (rpm) about its Z-axis to produce an experiment scanning motion. Scan-rate control has been tentatively set at a tolerance of ±10 percent of the 0.1 rpm scan rate.

Occultation of solar and celestial references dictate a requirement for an inertial reference system. Thermal considerations impacting the ASCS result in hardware location constraints, particularly in locating the electronics equipment.

The spacecraft onboard ASCS will be designed on the basic assumption that spacecraft control is initiated after separation from the booster and is sized primarily to meet the requirements of the three basic operational modes, as defined by the mission sequence.

2. Reference Attitudes. Based on the guidelines and constraints, several reference attitudes must be defined along which the body principal axes are to be oriented during various operational modes. In Figure XI-1 the body principal axes and the body geometric axes are assumed to be
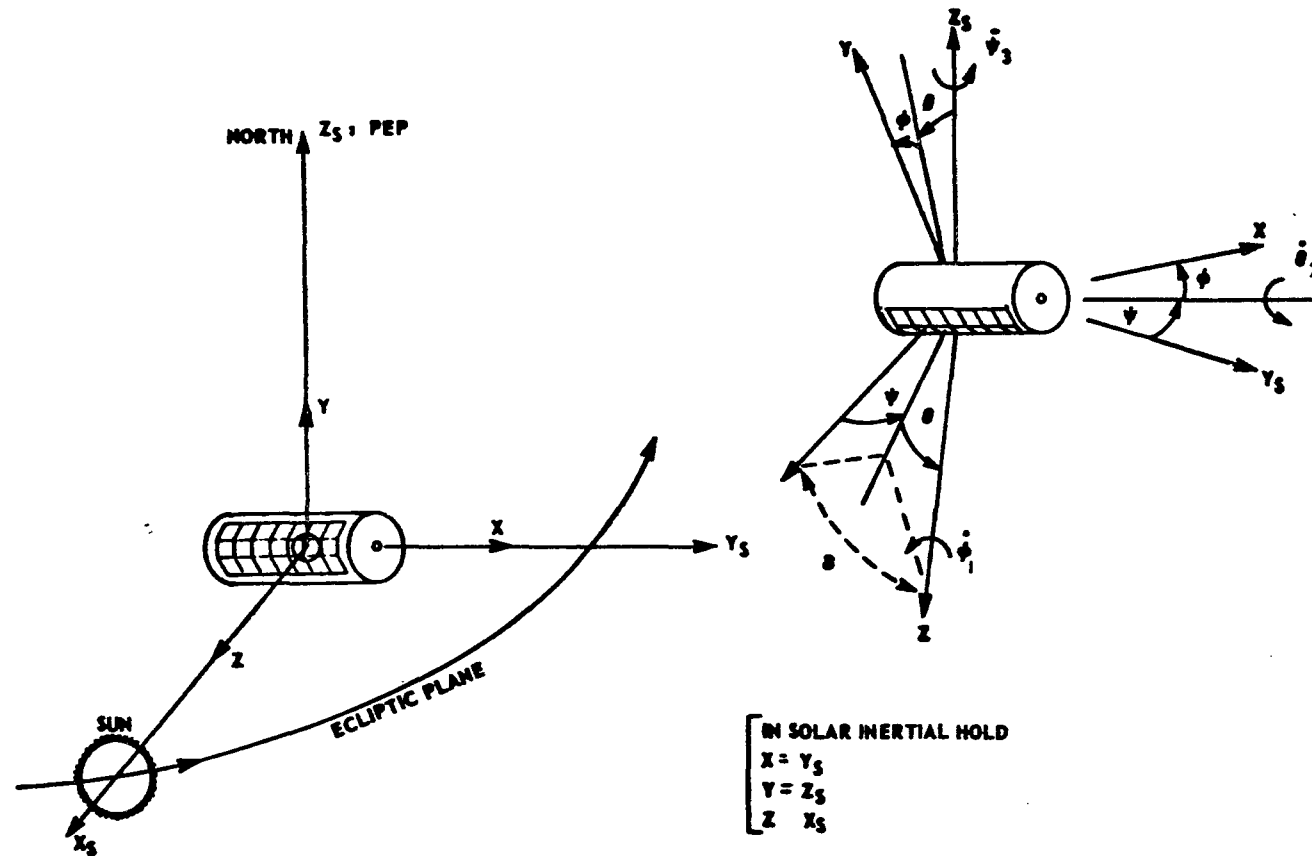
Figure XI-1.   HEAO solar reference and Euler angles (sequence 3, 2, 1).

identical and are denoted by the right-hand triad (X, Y, Z). To facilitate vehicle-spacecraft integration and structural studies, the spacecraft axes have been selected to correspond to the launch vehicle coordinates: the X-axis is aligned with the launch vehicle longitudinal (minimum inertia) axis at lift off; the majority of the experiments are aligned with the Y-axis (intermediate inertia) which is aligned with a launch vehicle bench mark at lift-off; and the center solar panel is aligned normal to the Z-axis (maximum inertia) to complete the right-hand triad. The origin is located at the geometric center of the spacecraft which for preliminary design purposes is assumed to be the center of mass in the baseline configuration. During much of the operational lifetime, the vehicle slowly rotates or scans about the Z-axis so that the experiments cover either the galactic belt or celestial sphere. Hence, the Z-axis is referred to as the "scan" axis in this report.

Since the HEAO depends upon solar energy to supply its power needs, the Z-axis must not exceed an angle of approximately 37 degrees off the sunline during any operational mode. Solar coordinates are selected as a basis for describing the HEAO reference attitudes. Either an earth-or vehicle-centered solar coordinate system is defined relative to the ecliptic plane by the right-hand triad (X_s, Y_s, Z_s), as illustrated by Figure XI-1. The X_s-axis (in the ecliptic plane) is directed from the earth to the sun, the Z_s axis is perpendicular to the ecliptic plane directed in a northerly direction, and the Y_s axis completes the triad in the ecliptic plane. Table XI-1 lists four reference attitudes for the HEAO relative to solar coordinates.

The vehicle's attitude relative to the sunline in either of the four reference attitudes can be specified by three Euler angles: ψ in the ecliptic plane, θ in a plane perpendicular to the ecliptic plane, and ϕ about the scan axis. Moreover, each reference attitude has been defined to satisfy an operational mode.

To facilitate performance, simulation, and analysis studies, the body axes are redefined in terms of solar axes such that the body and solar coordinates are identical in a solar inertial hold mode. Appendix J, Paragraph 4 contains a more detailed description of the coordinate systems and axis definitions that are necessary to evaluate the HEAO performance with respect to the reference attitudes.

3. Mission Sequence

a. Description. Figure XI-2 illustrates a typical HEAO mission sequence used to determine the ASCS configurations and operating sequences.

TABLE XI-1. REFERENCE ATTITUDES

Reference Attitude	Orientation	Use
Initial solar acquisition	Z-axis (scan axis) points to the sun $(Z \equiv X_s)$, the longitudinal X-axis is perpendicular to the sunline in the ecliptic plane $(X \equiv Y_s)$, and the Y-axis is perpendicular to the ecliptic plane $(Y \equiv Z_s)$.	Initial solar acquisition and hold
Celestial scan	Z-axis (scan-axis) points to the sun $(Z \equiv X_s)$. Scan rotation about Z-axis (0.1 rpm).	Survey of entire celestial sphere by onboard experiments.
Galactic scan	Z-axis points near the galactic pole. Scan rotation about Z (0.1 rpm)	Survey of entire galactic belt by all experiments aligned with the spacecraft X and Y axes.
Celestial pointing	Z-axis constrained to point within 37 deg of the sunline. Either the X, Y, or negative Z axis points to target.	Point experiment fields-of-view to various selected targets on the celestial sphere.

There is considerable flexibility in the time line shown, but the major events, reference attitudes, and operational modes have the same definition and impose basically the same requirements on the ASCS regardless of the sequence of performance. All of the major operational modes are initiated by ground commands.
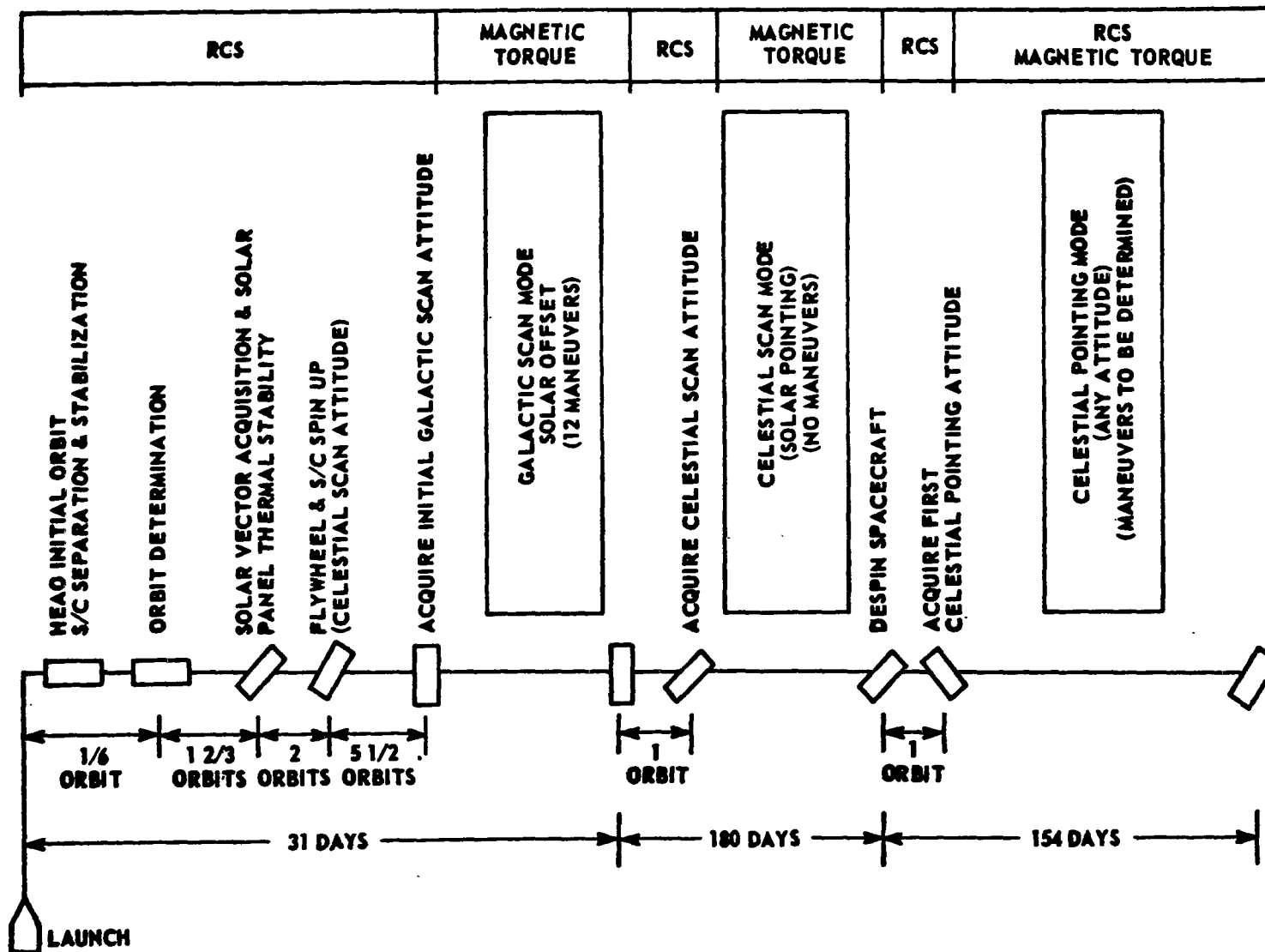
Figure XI-2. Mission profile.

The ASCS assumes control of the HEAO after spacecraft separation from the launch vehicle. Shortly after separation, the spacecraft launch transients must be reduced to acceptable levels, and after approximately one orbit, the Z-axis must be aligned to the solar vector. Baseline performance analysis indicates that attitude hold using the rate gyros must be provided during the sun occultation periods.

After Z-axis alignment to the sun, the flywheel must be brought up to full speed, and for the selected baseline mission sequence, the spacecraft is maintained in its initial solar acquisition attitude until completion of flywheel run-up. Following flywheel run-up, the spacecraft must be spun up to the required 0.1 rpm. This flywheel and spacecraft spin-up sequence requires about seven orbits, of which one orbit is required for solar vector alignment and the remaining six orbits are required primarily for flywheel spin-up. Upon completion of the spin-up sequence, the spacecraft will be in the celestial scan reference attitude (Table XI-1).

The Galactic scan reference attitude (Table XI-1) and the Galactic scan operational mode are to be used during the first 30 days of the mission (based on a launch date of either September 7 or March 7) to scan a 17-degree galactic belt. If the use of a favorable launch date is not possible, the galactic scan mode will be delayed until a favorable time occurs; the spacecraft will be kept in the celestial scan attitude, and a survey of the celestial sphere will be performed.

Assuming the galactic scan has been completed, the spacecraft must be positioned to the celestial scan reference attitude. A complete survey of the celestial sphere will be accomplished in a 6-month period by tracking the solar vector (moves approximately 1 degree per day) with the Z-axis of the spacecraft while rotating the spacecraft at 0.1 rpm about its Z-axis.

Upon completion of the celestial sphere survey, the spacecraft will be positioned to the celestial pointing reference attitude (Table XI-1). The ground reduction of data obtained during the galactic scan and celestial survey parts of the mission must determine the points of interest on the celestial sphere about which more information is desired. To obtain this information, the spacecraft rotation must be stopped and the experiment LOS pointed at the specific point of interest. The experiment LOS is shifted to other points of interest as commanded.

Figure XI-2 also contains a profile for the use of the RCS jets and magnetic torquer actuators. This profile is predicated on the guideline that RCS jets will be used for all major spacecraft maneuvers and the magnetic torquers will be the primary actuators for maintaining spacecraft attitude while it is in a reference attitude and for making small angle maneuvers.

b. Operational Modes

(1) Celestial scan mode. The primary mission objective is a survey of the entire celestial sphere by all the experiments on board the spacecraft. This objective will be accomplished in a 6-month period by the spacecraft operating in the celestial scan mode. In this mode the alignment of the Z-axis (scan axis) of the spacecraft is maintained within 1 degree of the solar vector, and the spacecraft is revolved about the scan axis at the rate of 0. 1 rpm. The rotation of the spacecraft about its scan axis causes the FOV of the experiments aligned along the X- and Y-axes to sweep out a band of the celestial sphere on each revolution. Maintaining the scan axis alignment on the solar vector results in the survey of the entire celestial sphere in 6 months as the earth orbits the sun. Figure XI-3 illustrates the spacecraft orientation in this mode.

The alignment of the spacecraft Z-axis to within 1. 0 degree of the solar vector and the 0. 1 rpm scan rate are maintained by the ASCS. Attitude determination to ±0. 1 degree is provided by ground processing of data generated by the onboard star field mapper.

(2) Galactic scan mode. To obtain the maximum amount of useful data early in the mission, it is planned to scan the region of the galactic plane during the first 30 days of the mission. It will be possible to scan the galactic plane with the experiments by orienting the spacecraft Z-axis near the galactic axis (the axis normal to the galactic plane), as illustrated by Figure XI-4. The time at which this can be done is limited by the spacecraft power requirements and the location of the solar vector relative to the galactic axis. At the optimum time for a 30-day galactic scan, the maximum angle that the Z-axis must be positioned off the solar vector is approximately 37 degrees. If a launch date is suitable, this time will be during the first 30 days of the mission; if not, the galactic scan will be performed at some other time during the mission.

In this mode, the spacecraft Z-axis will be aligned at various angles to the galactic axis, varying from 0 to 8. 5 degrees. The angle from the Z-axis to the solar vector during this time will vary from
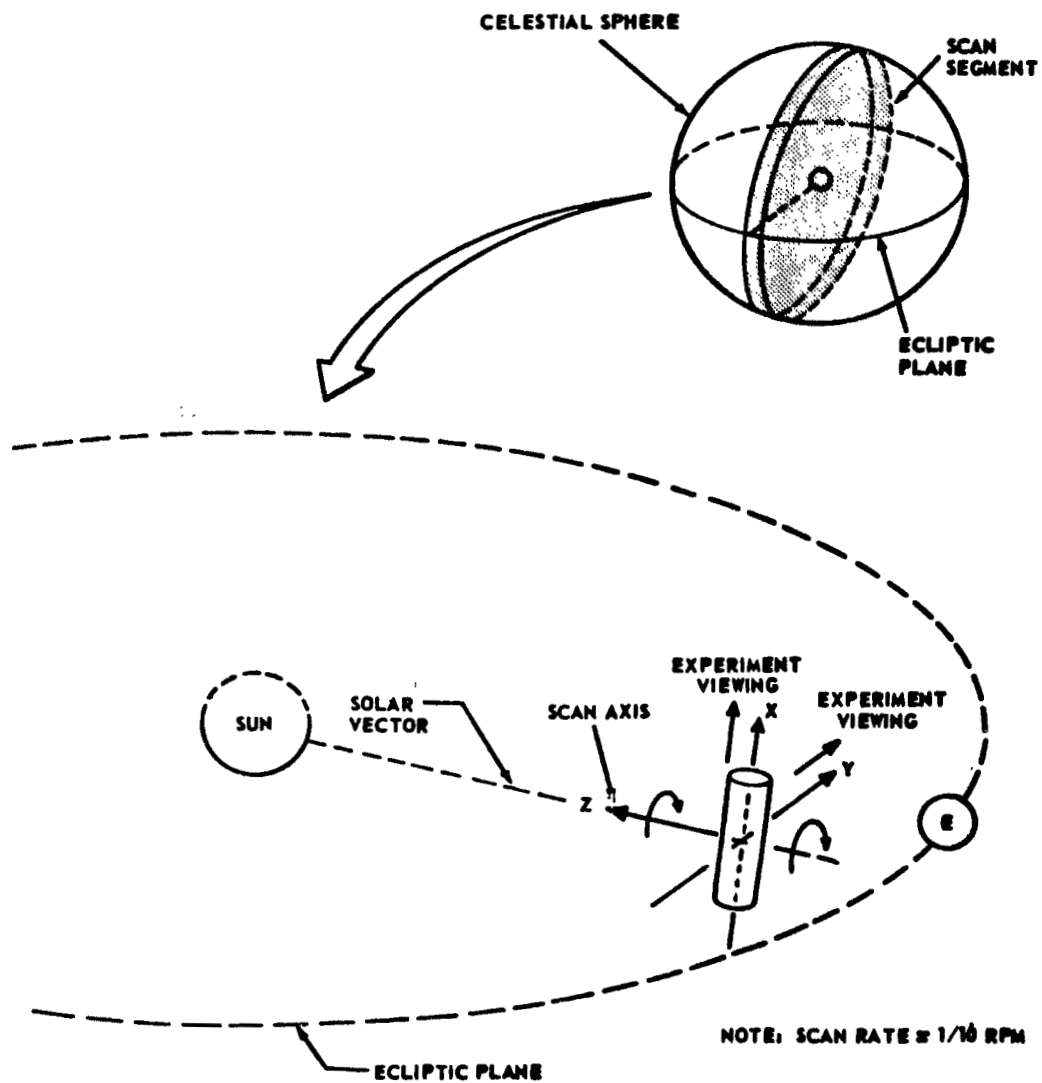
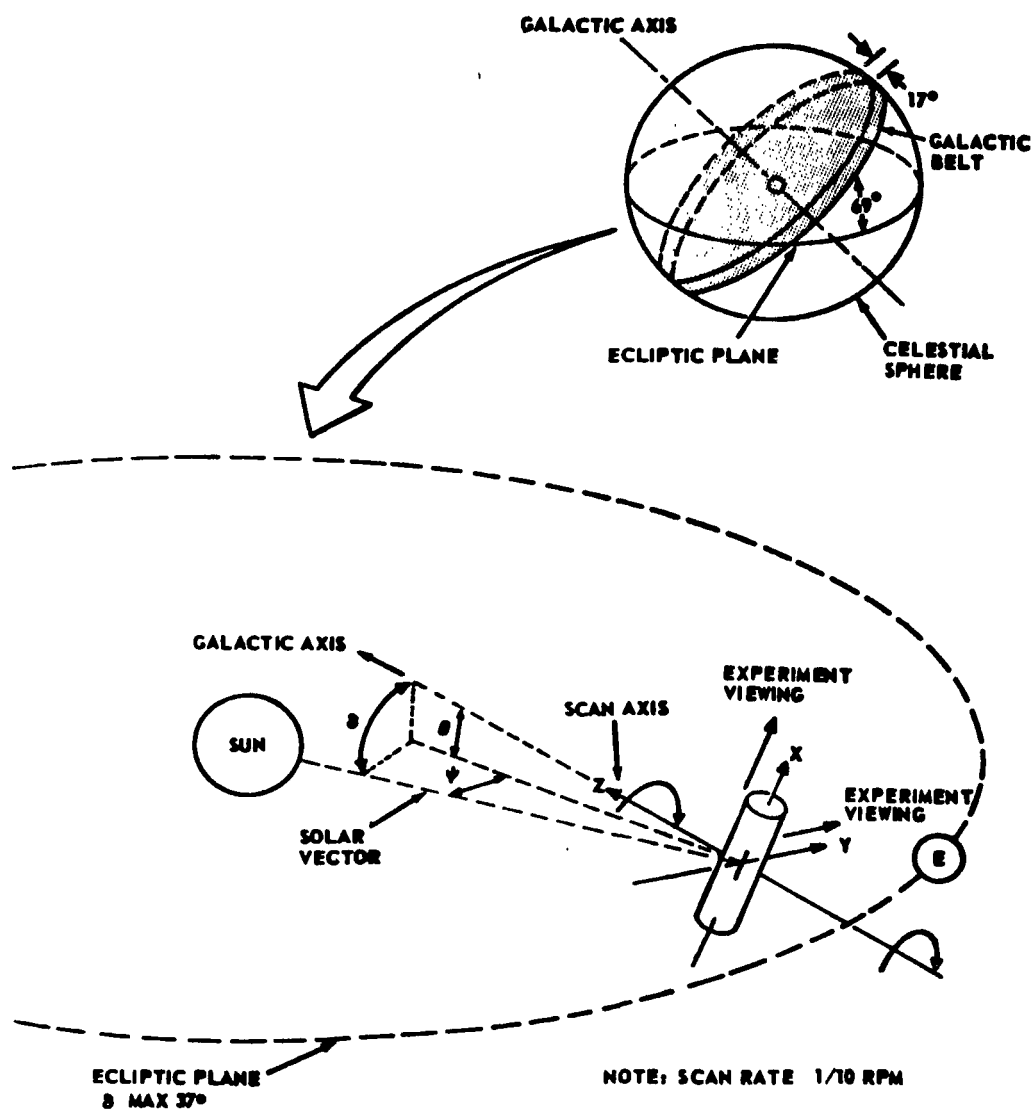Figure XI-3. HEAO celestial scan mode.

Figure XI-4. HEAO galactic scan mode.

about 24 to 37 degrees. Further definition and discussion of the maneuvers
to satisfy this mode is given in Section XI, Paragraph C. 3. The specified
spacecraft scan rate and the orientation of the spacecraft Z-axis within 1. 0
degree of the desired position is maintained by the onboard ASCS. Attitude
determination to ±0. 1 degree for all three spacecraft axes is provided by
ground processing of data generated by an onboard star field mapper.

(3) Celestial pointing mode. In the celestial pointing mode,
the rotation of the spacecraft about its Z-axis (scan axis) is reduced to near
zero. The experiments' FOV will be pointed to various selected targets on the
celestial sphere, as illustrated by Figure XI-5. In this mode, the orientation
of the experiment LOS axis is maintained to within 1. 0 degree of the desired
direction. Attitude determination via ground data processing is not required
in this mode, since the spacecraft is stabilized about 3 axes and optical sensors
are tracking targets with an accuracy of ± 0. 1 degree. During periods when
the targets are occulted and spacecraft control is referenced to inertial
sensor (gyro) inputs, the attitude accuracy of ±0. 1 degree must still be
maintained. It is anticipated that the duration of the occultation periods will
not be long enough for inherent gyro drift errors to reduce the overall system
accuracy to less than ±0. 1 degree. Additional study of gyro designs and
items affecting overall system accuracy will be required to verify the capabil-
ity of meeting this requirement during occultation periods.

B. Baseline System Description

1. <u>System Configuration.</u> The approximate physical locations and
orientations of the baseline ASCS components are presented in Figure XI-6.

Four coarse sun sensors are located around the X-axis and four
coarse sun sensors are located around the Y-axis so that their FOV can sense
the solar vector offset of the Z-axis from any spacecraft attitude. The fine
sun sensor has its FOV aligned with the Z-axis and measures solar offset
angles about the X and Y body axes.

The star tracker LOS is aligned with the Y-axis and obtains star
sightings in the X-Y plane. Also aligned with its LOS perpendicular to the
Z-axis is the star field mapper so that it can scan a segment of the celestial
sphere as the spacecraft rotates.

The rate gyro package has its triad of gyro input axes aligned with
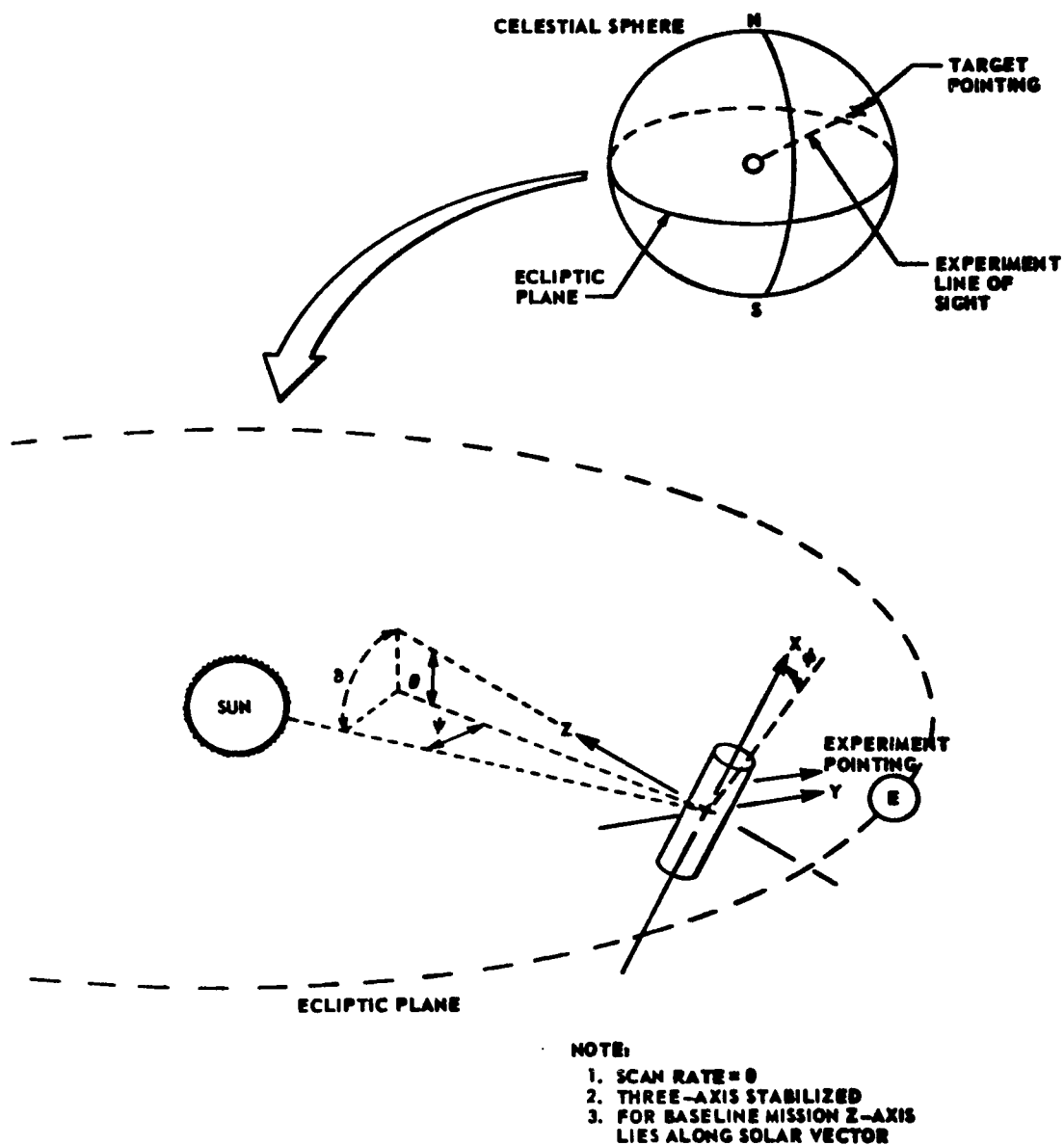the spacecraft body axes and senses rates about all three body axes. The

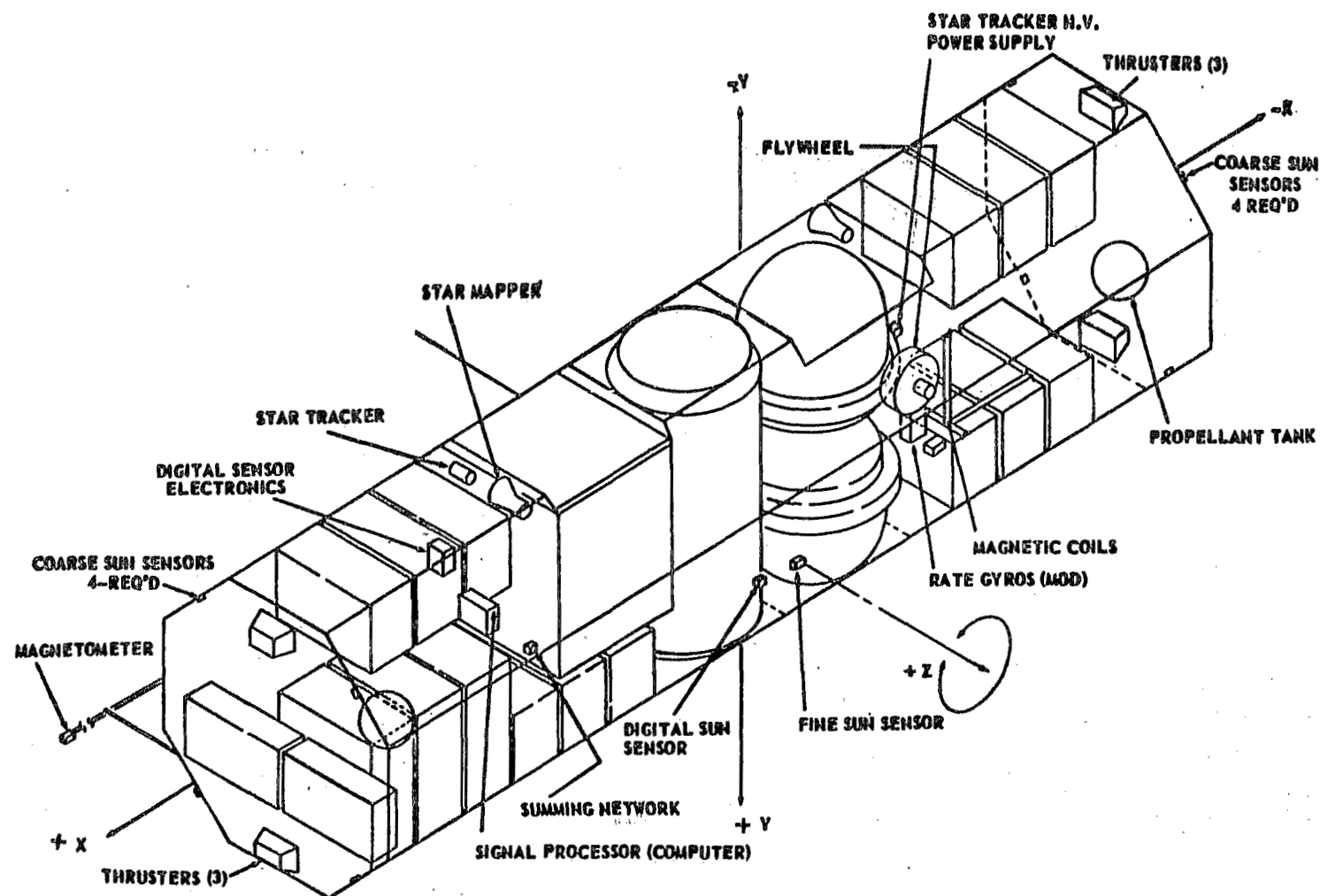Figure XI-5.   HEAO celestial pointing mode.

Figure XI-6. Approximate physical locations and orientations of baseline ASCS components.

flywheel is aligned with its momentum vector parallel to the Z-axis. Spacecraft rotation is about the Z-axis and in a direction to add its momentum to that of the flywheel.

A three-axis magnetometer is provided to sense the earth's magnetic field and the magnetic torquing coils with which the magnetometer operates are oriented to provide torques about the body axes. Likewise, the RCS thrusters are oriented to provide torques about the body axes.

The locations of the remaining components are arbitrary and in the final design will be located to satisfy thermal, structural, and volume constraints.

Figure XI-7 provides a functional block diagram of the baseline ASCS. The complete grouping of all sensors and actuators required to perform all the mission phases is provided. The use of each of these components in the various operational phases is described in Section XI. C. While the electronics portions of the system are represented as separate blocks from a functional standpoint, it should be noted that these functions can be combined into a central signal processor and computer. Optional sensor choices are discussed in Appendix J, Paragraph 1.

2. Sensors.

a. Magnetometers. The primary attitude control scheme of using magnetic coils requires that the earth's magnetic field strength and direction be determined with respect to the spacecraft body axes. This requirement applies to all the spacecraft operating modes where magnetic coils are used as the means for attitude control. A three-axis magnetometer will produce a voltage proportional to the field strength along each axis, the polarity of the signal indicating the field direction along each axis. The present location of the baseline configuration shows the magnetometer assembly mounted on an extendable boom. This boom location was chosen because of the residual field of the magnetic coils, after the current has been removed, which was thought to be sufficient to disturb the accuracy of the magnetometer readings. Additional study has indicated that the coil location with respect to the magnetometers may not require an extended boom mounting; however, this cannot be validated until the spacecraft as well as the coils are further defined.

b. Star field mapper — slitted reticle design. Spacecraft attitude determination to an accuracy of ±0.1 degree is required for each of three axes to identify the position of the experimental data source on the celestial

Figure XI-7. HEAO ASCS — system functional block diagram.

sphere. Spacecraft position as a continuous function of time is necessary, but on a non-real-time basis. By ground plotting spacecraft position, experimental data source locations can be identified. The basic scheme involves a passive stellar mapping device which senses a star position in its optical FOV. Star positions are recorded and then telemetered to a ground station as contact opportunities permit. The attitude of the spacecraft is then determined as a function of time in a computer program operation (Fig. XI-8).

Stellar mapping can be accomplished using a slitted reticle mapping instrument with its LOS located in the X-Y plane of the rotating space-craft. Figure XI-9 illustrates the application of this sensor. The problem of attitude determination using mapping devices involves reconstructing the space-craft pointing direction by first identifying the star field seen by the mapper, and then resolving the positions of spacecraft axes in this field as a continuous function of time. The star locations on the celestial sphere as tabulated in a Reference Catalogue (Star Catalogue) have specific angular separation values. The star identification process involves matching measured angular separations obtained by the mapper with a Star Catalogue listing the known angular separations between stars. For the slit reticle mapper, at the time the star LOS crosses the slit pattern located behind the imaging optics, the coordinates of the star are measured with respect to the sensor optical axis and thus with respect to the spacecraft axes. Transit of a star across the slits produces electrical impulses. The transit time recorded between two slits, Δt, is proportional to the distance of the star off the optical axis; and the time between two star intercepts ΔT_2 is related to the right ascension value between the two stars. These transit time values provide the data for the star identification program and subsequent calculation of three-axis attitude for the space-craft.

Defining the spacecraft position involves relating the star intercept time in body coordinates to an inertial coordinate system. This is accomplished by determining the three Euler angles and their rates $(\psi, \theta, \phi, \dot{\psi}, \dot{\theta}, \dot{\phi})$ in the solution of simultaneous equations for the unknowns. Star intercept times yield the values required for solution of the equations. Figure XI-10 shows the coordinate systems and the angles involved in the solution of the spacecraft attitude equations. The unit vectors $\bar{i}, \bar{j}, \bar{k}$ define the inertial coordinate system. The unit vector $\bar{i}$ lies in the plane of the celestial equator and is aligned with the first point of Aries on the celestial sphere. The unit vector $\bar{j}$ also lies in the plane of the celestial equator at an angle of 90 degrees to $\bar{i}$. The unit vector $\bar{k}$ makes a right-hand orthogonal system.
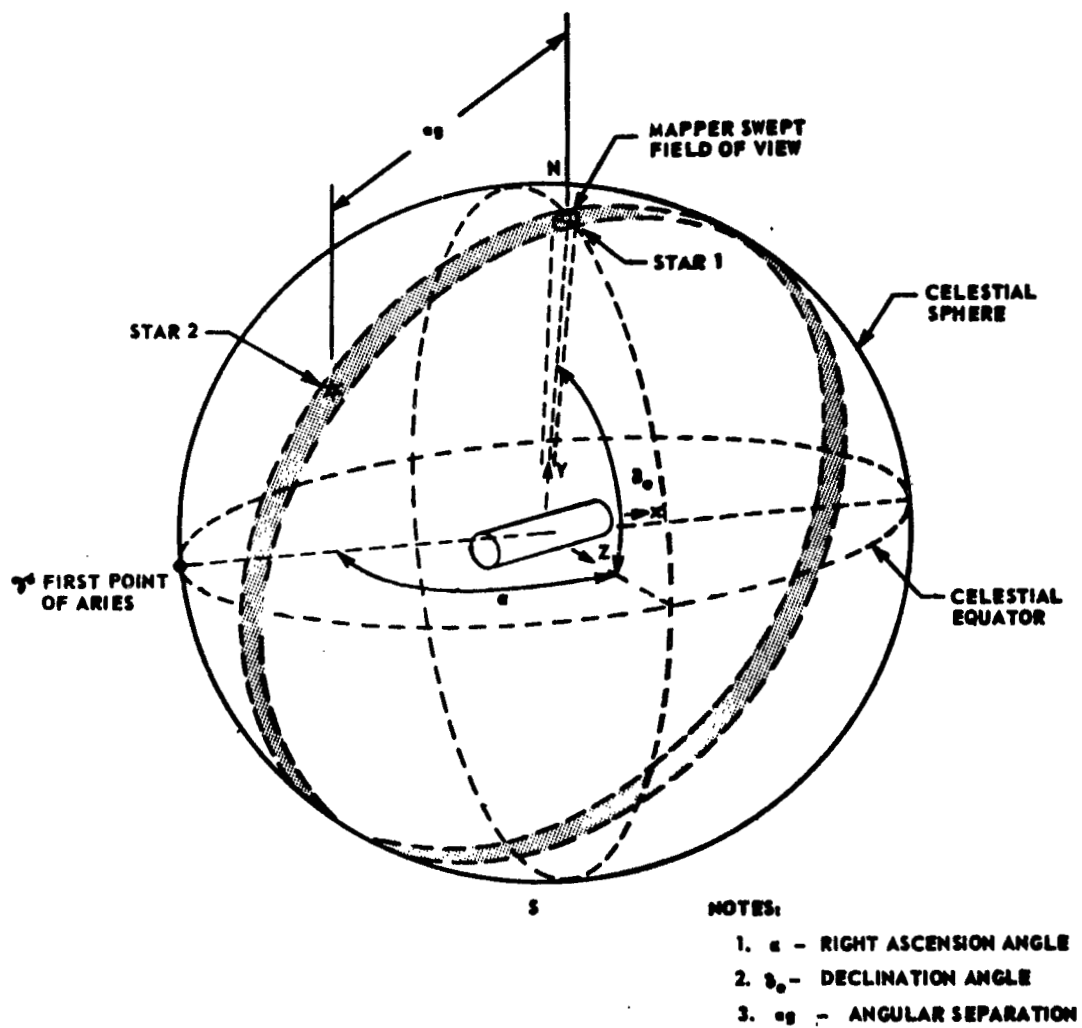
Figure XI-8. Star field identification.
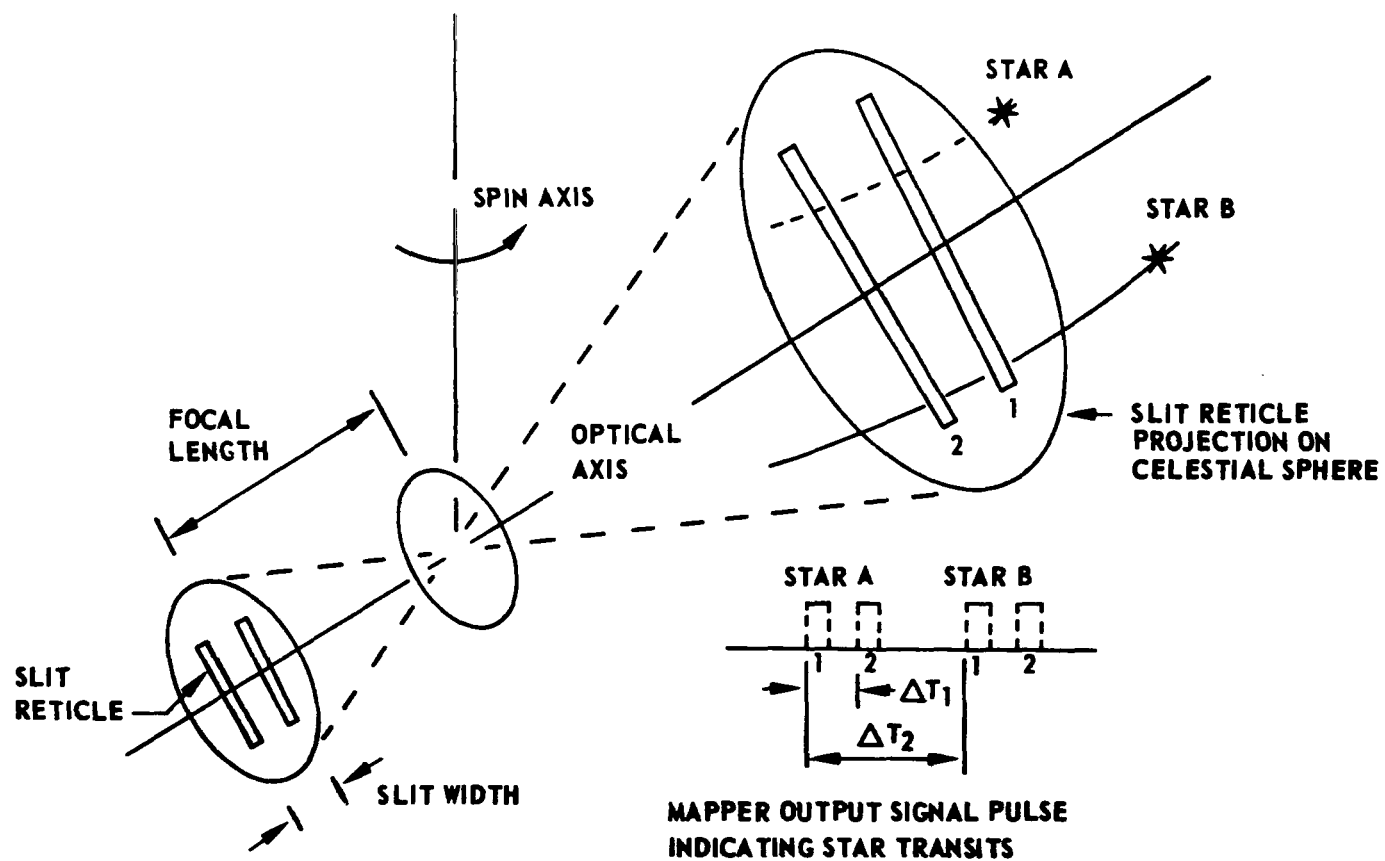
Figure XI-9. Operation of the slit reticle star mapper.

$\overline{K}_B$

$\overline{K}$

CELESTIAL SPHERE

ψ_o

β

TARGET STAR

FIRST POINT OF ARIES

δ_o

$\overline{J}_B$

θ_o

$\overline{J}$

$\overline{i}$

ψ_o

α

λ

$\overline{i}_B$

CELESTIAL EQUATOR

NOTES:

1. α – RIGHT ASCENSION TO TARGET

2. δ_o – DECLINATION TO TARGET

3. $\left. \begin{array}{cc} \theta_o & \dot{\theta}_o \\ \phi_o & \dot{\phi}_o \\ \psi_o & \dot{\psi}_o \end{array} \right\}$ EULER ANGLES AND RATES

4. λ – SENSOR AXIS ASCENSION TO TARGET

5. β – SENSOR AXIS DECLINATION TO TARGET

6. $\overline{i}, \overline{j}, \overline{k}$ – INERTIAL COORDINATE UNIT VECTORS

7. $\overline{i}_B, \overline{j}_B, \overline{k}_B$ – BODY AXIS UNIT VECTORS

Figure XI-10. Attitude determination.

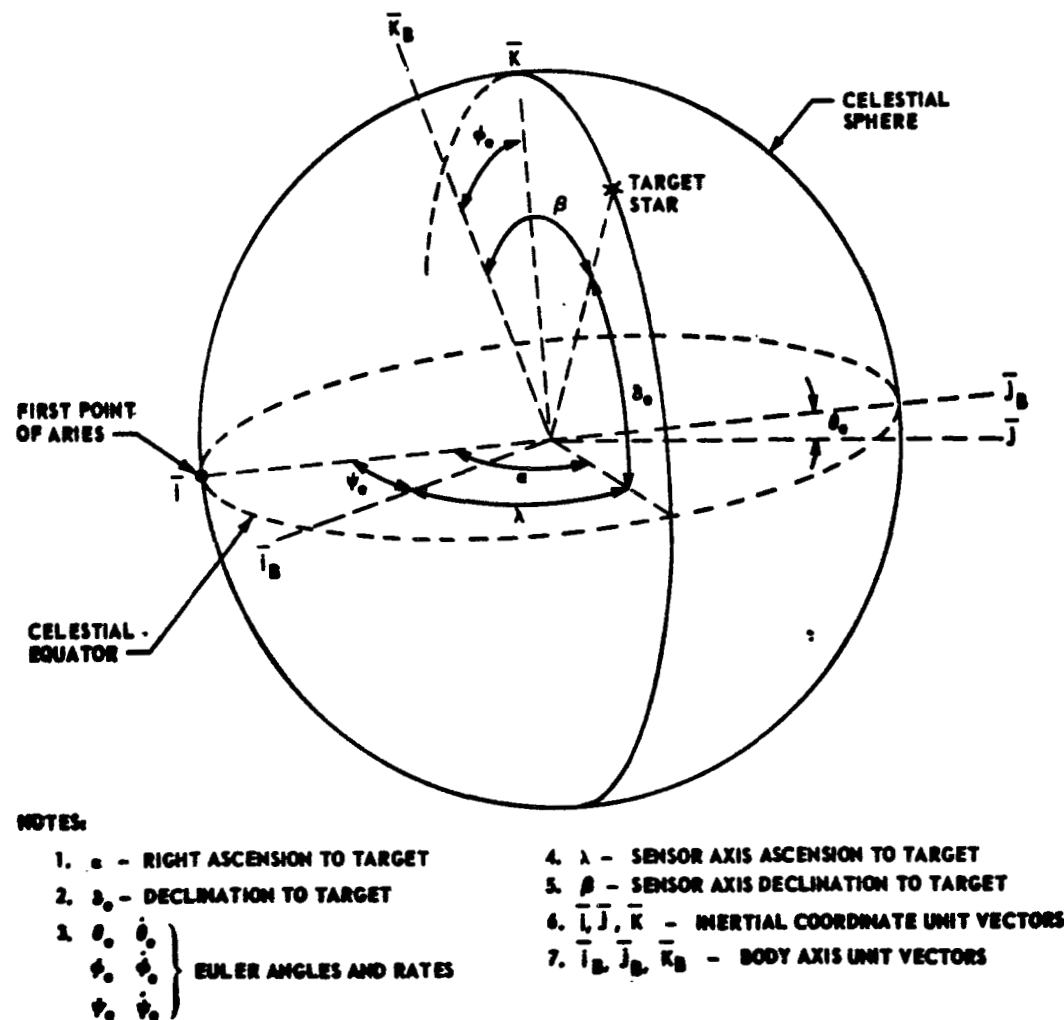Vectors $\bar{i}_B$, $\bar{j}_B$, $\bar{k}_B$ represent unit vectors along the space-craft body axes. Euler angles ψ, θ, ϕ define the position of the spacecraft in the inertial coordinate system. At star intercept, the angles λ and β locate the star with respect to the body coordinates $\bar{i}_B$, $\bar{j}_B$, $\bar{k}_B$. The relationship between the spacecraft body coordinates and the inertial coordinates is a function of the angles α, δ, λ and β and the Euler angles as well as their rates.

$$\begin{Bmatrix} \bar{i}_B \\ \bar{j}_B \\ \bar{k}_B \end{Bmatrix} = f \begin{bmatrix} \text{(known)} & & \text{(unknown)} \\ (\alpha, \delta, \lambda, \beta) & , & (\theta, \phi, \psi, \dot{\theta}, \dot{\phi}, \dot{\psi}) \end{bmatrix} \begin{Bmatrix} \bar{i} \\ \bar{j} \\ \bar{k} \end{Bmatrix} .$$

The angles λ and β are measured by the star mapper. The right ascension and declination angles, α and δ, are known for each identified star from the results of the star identification program. The Euler angles and their rates must be determined before the coordinate transformation from body-to-inertial axes can be made. Thus the star transits provide the values required in the equations necessary to determine the attitude of the spacecraft.

c. Coarse sun sensors. After the spacecraft is separated from the booster and body rates have been nulled, it must have the capability of acquiring the sun from any orientation; therefore, sensors giving total spherical viewing are required. A coarse sun sensor system consisting of eight sensors, each having an FOV of ±80 degrees, will assure sun acquisition. Figure XI-11 illustrates the positioning of the sensors on the spacecraft base-line configuration and the sensor output signal format. A null accuracy of ±5 degrees has been determined to be sufficient for switching from coarse to fine sun acquisition. By defining the sensor axis system with respect to the three spacecraft axes, summing networks can be designed to give sun position with respect to the spacecraft. This will provide data to the attitude control system where the required rotational direction in two planes will be implemented to move the Z-axis (solar panels) toward the sun.

d. Fine sun sensor — analog. Locating a fine sun sensor on the spacecraft Z-axis, as shown in Figure XI-12, will provide the capability of the terminal phase of acquisition; i. e., aligning the Z-axis on the solar vector. This sensor will also provide the capability of tracking the sun for both the
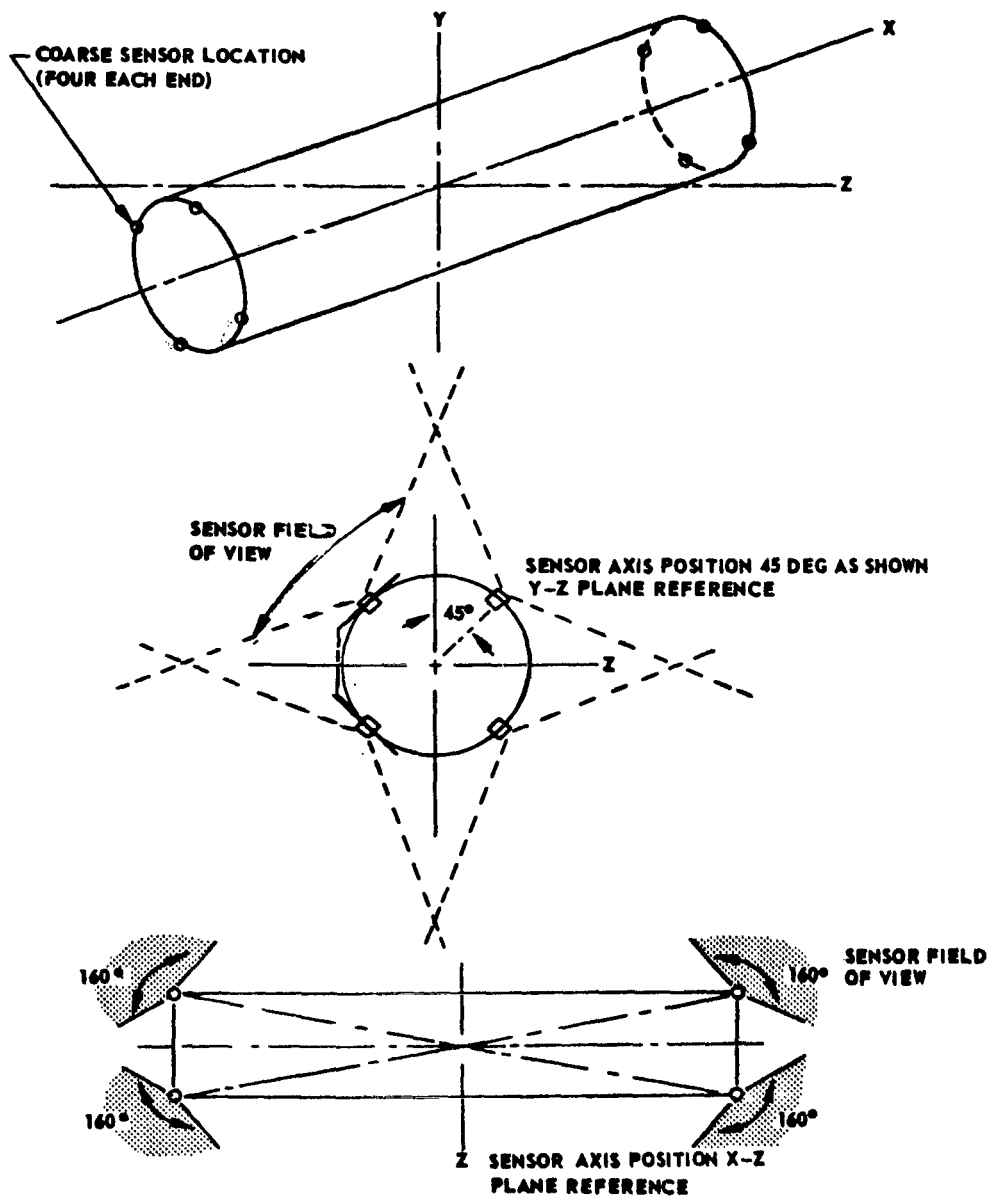
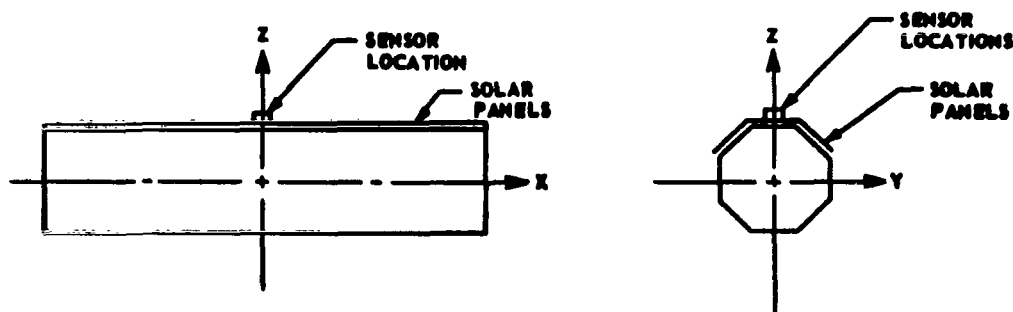Figure XI-11. Coarse sun sensor layout.

Figure XI-12. Location of the fine sun sensor on the spacecraft.

celestial scan and the celestial pointing modes. Establishing a fine sensor FOV approximately 15 degrees and a coarse sensor null accuracy of 5 degrees assures sufficient overlap as the sun enters the fine sensor FOV to switch out of the coarse acquisition phase into the terminal fine acquisition phase. A fine sensor null accuracy of 2.0 arc-minutes is sufficient for scan axis alignment on the solar vector and for tracking requirements during the celestial scan mode.

The output of the analog sensor is voltage directly proportional to the angular error of the sun position about the null position. The null position is obtained when the solar vector is approximately normal to the sensor optics. The proportional relationship for the sun sensor is constant only over the linear response region of the output signal as shown in Figure XI-13 where V is the sensor output voltage and ϵ is the angle of the sun from the null position. The sensor response should have a linear range of at least ±1.0 degree. Sensor saturation at 15 degrees is based on initial sun acquisition requirements.
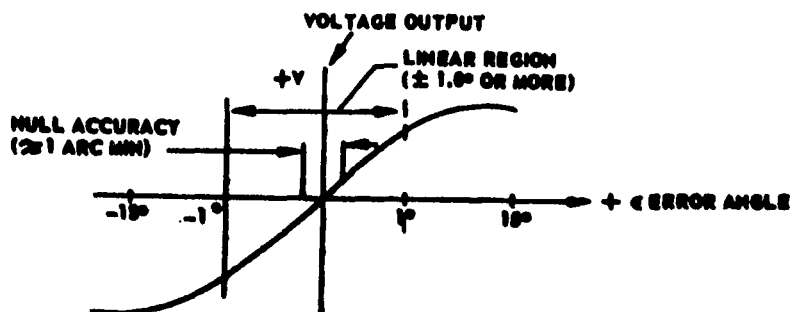

Figure XI-13. Response curve of an analog sun sensor.

A typical sensor design which would meet the HEAO mission requirements consists of four silicon sensors mounted on a common base with a fifth sensor designated as a disable eye. The function of the disable eye will be covered in the discussion of initial sun acquisition. The two control axis error signals are generated by the four cells.

The sun rays striking the optical surface of the sun sensor (Fig. XI-14) are focused by each of the four lenses onto the slit plane. If the sensor is in the null position, i.e. , the sun's rays are perpendicular to the optics plane, the image from each lens falls upon a photocell located on the photocell plane and each photocell is illuminated equally. This condition is indicated by the generation of equal voltages by each photocell. If the sensor is not in the null position, the photocells are not illuminated equally, because of the geometry of the slits and unequal voltages are produced. The sun orientation relative to the null position is measured about the spacecraft X and Y axes (Fig. XI-15) by comparing the output voltages from each photocell.
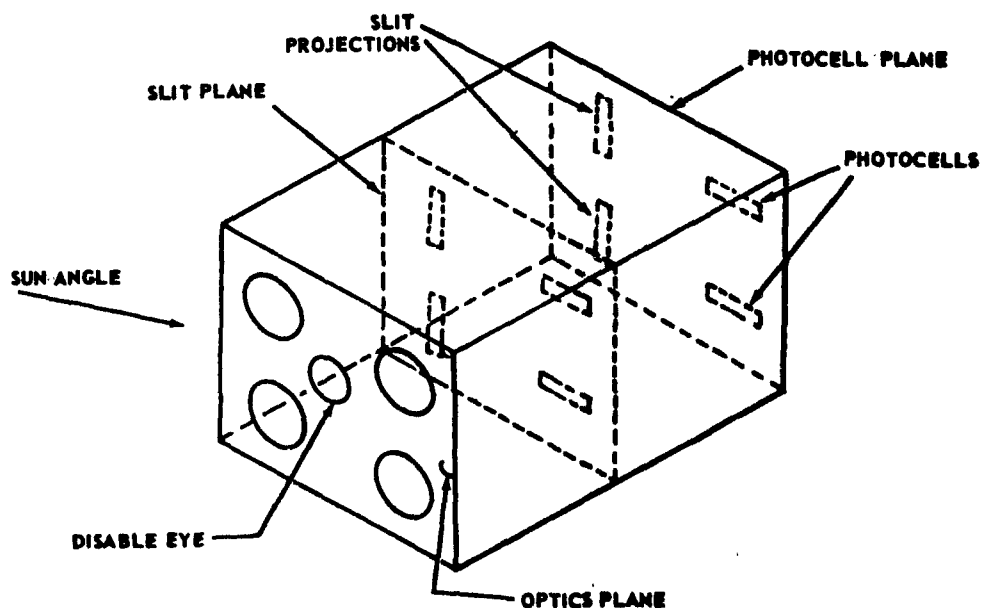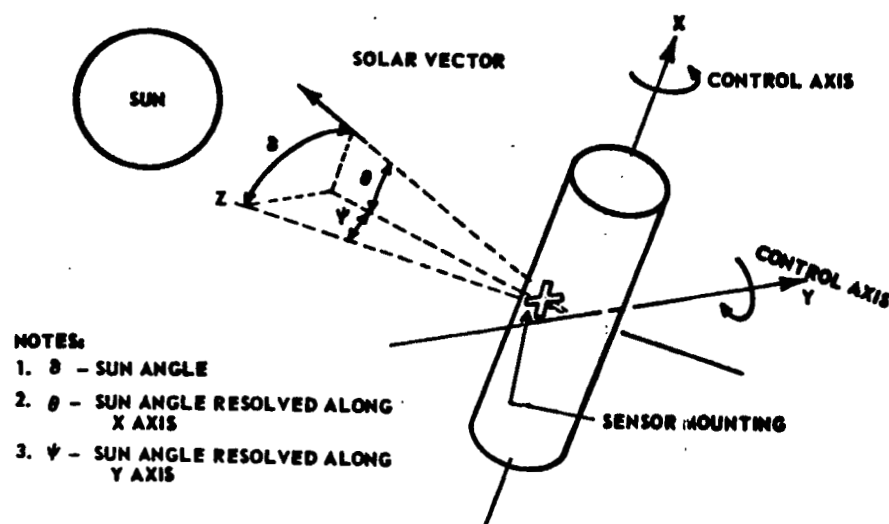

Figure XI-14. Analog sun sensor.

Figure XI-15. Sun orientation relative to the null position.

NOTES:
1. $\mathfrak{s}$ – SUN ANGLE
2. θ – SUN ANGLE RESOLVED ALONG X AXIS
3. ψ – SUN ANGLE RESOLVED ALONG Y AXIS

Because of the spacecraft rotation at 0.1 rpm, the two channel outputs of the sensor, which represent the location of the solar vector along the X and Y body axes of the spacecraft, will be time-varying sinusodial-type functions 90 degrees out of phase, as shown in Figure XI-16. Since for the
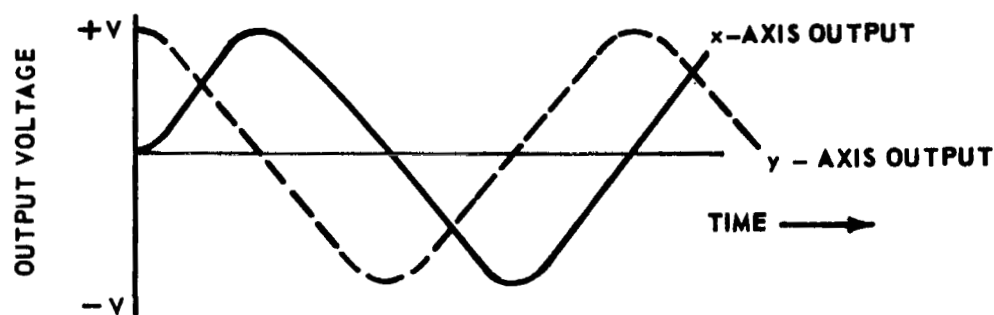

Figure XI-16. Sun sensor X- and Y-axis output variation versus time with rotating spacecraft.

baseline approach this sensor is only used to return to its null reference, the X and Y error signals are automatically resolved into body axes components,

thus permitting production of body restoring torque control with no transformation necessary. Spacecraft precession and wobble will cause the output waveforms given in Figure XI-16 to be somewhat modified with respect to those shown.

e. Digital sun sensor. The digital sun sensor is used for the galactic scan mode where the Z-axis is offset some angle from the solar vector. It also provides sun angle reference in the celestial pointing mode. Designing a digital sensor with an adequate FOV and the required degree of resolution does not appear to be a problem. Digital sun sensors which have the capability of measuring sun angles up to 128 degrees have been designed and flown in spacecraft. Figure XI-17 illustrates the principle of operation of this type of sensor. Sunlight passes through an entrance slit on the front surface of the reticle and forms an illuminated image of the slit on the gray coded pattern in the rear surface. The image position is dependent on the angle of incidence. Behind each column of the code pattern is a silicon photocell. If the light falls in a clear portion of the pattern, the photocell behind it is illuminated, producing an output "one." If the light falls in an opaque segment, the photocell is not illuminated and the output is "zero." The outputs of the cells are amplified and stored in a buffer storage. The sequence of numbers in storage represents the sun angle read. Measurement of sun angles to an accuracy greater than 0.5 degree requires changing from the gray code to binary, and electronically interpolating since the least bit change in the gray code pattern represents 0.5 degree. For two-axis error signals, a two-headed sensor will be required with the entrance slits parallel to the two spacecraft control axis, as shown in Figure XI-18.

Because of the rotation of the spacecraft, the command register read in/read out cycle will be timed at some frequency dependent on attitude control usage and reference data demand. The two-headed sensor, mounted as shown in Figure XI-18, will resolve the sun angle along the spacecraft X and Y axes.

Use of the digital sun sensor requires a second celestial reference to compensate for scan axis drift.

f. Star tracker. The star tracker has its FOV aligned with the spacecraft Y-axis. Its primary function is to provide attitude position reference for maneuvers and attitude control reference in the galactic scan and celestial pointing modes. The star tracker design selected provides acquisition and tracking capability. This type of tracker is normally termed a dual-mode tracker. Figure XI-19 illustrates the two modes of operation. In the acquisition
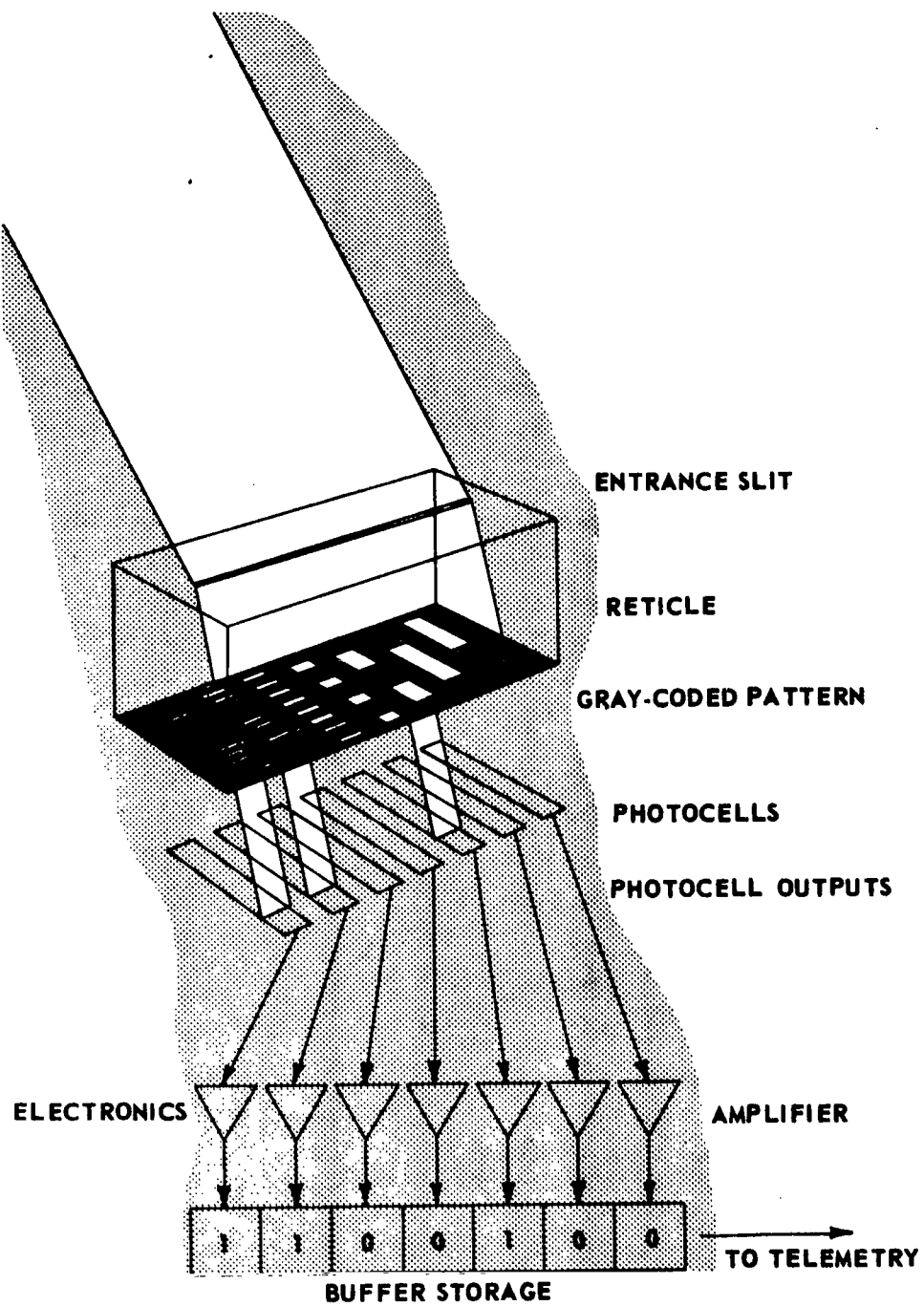
11-24

ENTRANCE SLIT

RETICLE

GRAY-CODED PATTERN

PHOTOCELLS

PHOTOCELL OUTPUTS

ELECTRONICS

AMPLIFIER

TO TELEMETRY

BUFFER STORAGE

Figure XI-17. Schematic: Digital sun sensor.

SENSOR
AXIS ALIGNMENT   Y

SUN

ENTRANCE
SLIT
ALIGNMENT

Z

X

SPACECRAFT
AXIS
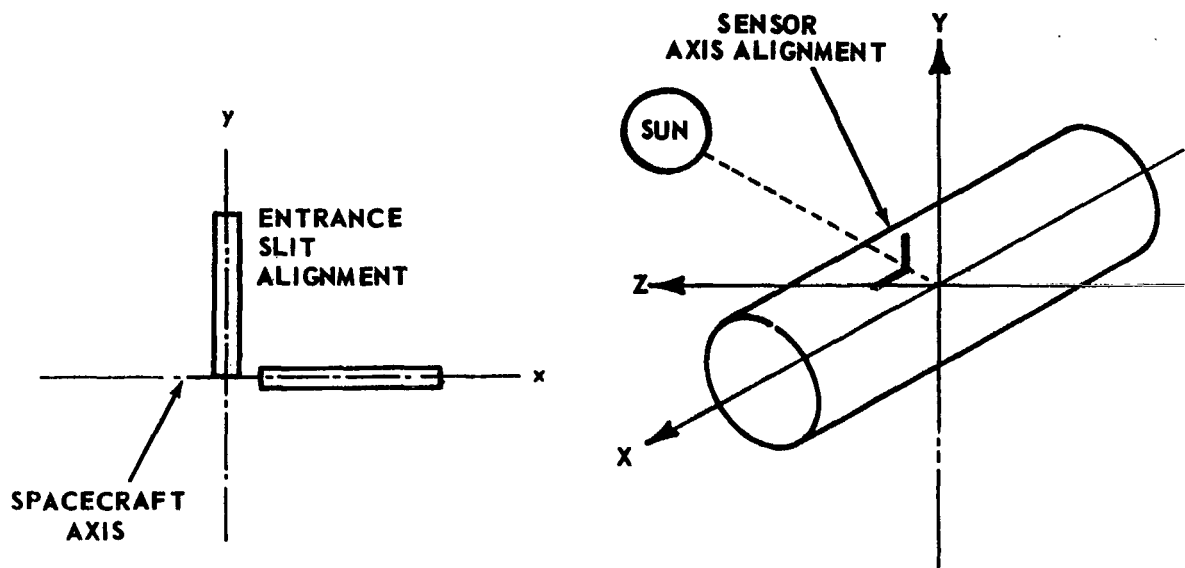
Figure XI-18.   Two-headed digital sun sensor, hard mounting.

PATH OF FIELD OF VIEW SWEEP

SCAN PATTERN
CENTERED ON
STAR IMAGE

INSTANTANEOUS
FIELD OF VIEW

Y

X   OPTICAL AXIS

SCANNED
PHOTOCATHODE
AREA

ACQUISITION MODE   TRACK MODE
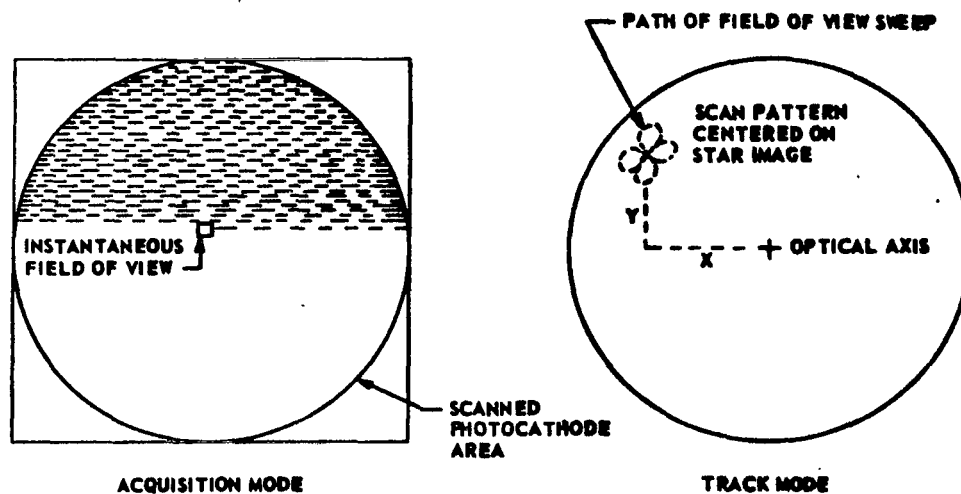
NOTES:
1. X ERROR MEASURED FROM OPTICS AXIS
2. Y ERROR MEASURED FROM OPTICS AXIS

Figure XI-19.   Star tracker.

11-26

mode, a small FOV is electronically swept through the larger instrument FOV. The smaller FOV scans in steps until the entire field is covered. At the instant the known target is intercepted by this sweep, the tracker automatically switches to the track mode and the scanning FOV begins to sweep a much smaller pattern (i.e., a rosette pattern) through the star. The coordinates of the star are measured at each intercept with a much higher accuracy than provided in the acquisition mode. A star tracker having an FOV of 20.0 degrees with a tracking accuracy of ±1.0 arc-minute, and capable of identifying fourth magnitude (visual) stars and brighter stars, should satisfy HEAO mission requirements.

g. Rate gyros. Rate gyros are required for initial spacecraft rate nulling and for attitude reference during celestial occultation periods. Three rate gyros aligned with the spacecraft body axes are sufficient to give rate data for the initial rate nulling of the spacecraft. To provide attitude position reference, the rate output is electronically integrated to give position. Use of integrating circuits with the rate gyro output permits the use of ATM type rate gyros for the HEAO spacecraft. This also provides the capability of obtaining rate and position data from the same gyro package.

h. Sensor characteristics. Table XI-2 provides a listing of the types of sensors discussed in each spacecraft operating mode. Data presented were obtained from existing hardware designs available within the industry which represent characteristics applicable to the HEAO mission. These data are presented to provide initial estimates for weight, power, and size, and to illustrate that attitude sensing requirements can be readily achieved. The coarse sun sensors are used primarily for initial sun acquisition rather than in any of the spacecraft operating modes. The total weight for the baseline system is estimated at 81.0 pounds with the power requirement estimated to be 66.0 watts. Alternate system considerations for a star mapper, digital sun sensor, and an earth horizon scanner are given in Appendix J, Paragraph 1.

3. Actuators. Reaction jets and magnetic torquers are used for the production of control torques. The magnetic torquers were sized to produce control torques equal to the maximum disturbance torque expected to be encountered during the mission. Reaction jets having a thrust of 0.5 lb_f were selected for the baseline design. An engine having this thrust will provide sufficient torque to reduce spacecraft body rotation rates and reorient the spacecraft in a reasonably short period of time, and will also have a small minimum impulse. The major disturbance torques acting on the spacecraft are gravity gradient and aerodynamic torques. Other disturbance torques,

TABLE XI-2. SENSOR CHARACTERISTICS

Sensor	Number	FOV (deg)	Accuracy	Size (in)	Weight* (lb)	Power (watts)
Coarse sun sensor	8	± 80	± 5 deg	1 diam × 5/8	8.0	4.0
Fine sun sensor	1	± 15	± 2 arc min	1 × 2 × 1/2	2.0	2.0
Star mapper with electronics	1	20	± 1 arc min	7 diam × 16	15.0	10.0
Digital sun sensor	1	± 45	± 15 arc min	3 × 3 × 1	3.0	
Digital electronics	1			5 × 7 × 2	2.0	2.0
Star tracker with electronics	1	16 × 8	± 1 arc min	5 diam × 11	15.0	10.0
Magnetometer (3-axis) (includes boom)	1		100 gamma	10 × 5 × 5	17.0	2.0
Rate gyro	3	Full-scale output 6 v/± 15 deg	Threshold rate 0.01 deg sec	8 × 6 × 4	7.0	36.0
Wiring					12.0	
				TOTAL	81.0	66.0

* Weights in this column are the totals for the number of units given in the second column and include mounting hardware

such as magnetic, solar radiation, etc., have been neglected, since their magnitudes are very small in comparison to gravity gradient torques.

a. Disturbing torques. Maximum values of gravity gradient torques in the spacecraft body axes are calculated from the following equations:

$$T_{xG} = \pm\frac{3}{2}\frac{GM_e}{R^3}\left(I_y - I_z\right)$$

$$T_{yG} = \pm\frac{3}{2}\frac{GM_e}{R^3}\left(I_z - I_x\right)$$

$$T_{zG} = \pm\frac{3}{2}\frac{GM_e}{R^3}\left(I_x - I_y\right)$$

where

T_{xG}, T_{yG}, T_{zG} = gravity gradient torques about X, Y, Z axes

GM_e = gravitational parameter, 1.4077×10^{16} ft^3/sec^2

R = spacecraft distance from the center of the earth, ft

I_x, I_y, I_z = spacecraft moments of inertia about the principal body axes; I_x=3970 ft-lb-sec^2; I_y=35 210 ft-lb-sec^2; I_z=36 900 ft-lb-sec^2.

Substituting the values of the different parameters into the above equations gives

$$T_{xG} = 0.00328 \text{ ft-lb}_f$$

$$T_{yG} = 0.0639 \text{ ft-lb}_f$$

$$T_{zG} = 0.0606 \text{ ft-lb}_f$$

Aerodynamic torques are estimated from parameters given in Appendix J, Paragraph 8 at about 10 percent of the gravity gradient torques. The total disturbance torques acting on the spacecraft axes due to gravity gradient and aerodynamics are thus estimated to be

$$T_x \text{ (maximum)} = 0.0036 \text{ ft-lb}_f$$

$$T_y \text{ (maximum)} = 0.0703 \text{ ft-lb}_f$$

$$T_z \text{ (maximum)} = 0.0667 \text{ ft-lb}_f$$

b.   Reaction jets.   The reaction jets are provided only for initial stabilization and rate damping, initial solar acquisition as well as reacquisitions and for large Z-axis attitude reorientations.   Three-axes spacecraft control is required and 12 engines are provided on the baseline spacecraft for this control.

A preliminary summary of propellant requirements for different maneuvers is given in Table XI-3.   The propellant weight was calculated on the basis of a specific impulse of 200 seconds.   As mentioned previously, jet thrusters will not be utilized for spacecraft attitude hold (after flywheel spinup is complete), but will be used only for major spacecraft scan-axis reorientations.   Magnetic torquers will be used for attitude hold and solar tracking of the scan axis.

c.   Magnetic torquers.   Magnetic control, utilizing a magnetic moment produced on the spacecraft to react with the earth's magnetic field is an attractive means of generating control moments.   The system weight is not dependent upon the length of the mission and should have greater reliability than a system with on-off actuated valves, pressure regulators, etc.

TABLE XI-3. SUMMARY OF PROPELLANT REQUIREMENTS AND TIMES FOR JET THRUSTER MANEUVERS

Event	Total Impulse (lb-sec)	Propellant Weight (lb)
1. Nulling of assumed spacecraft body rates of 3 deg/sec about each axis after separation from launch vehicle	340	1.70
2. Solar acquisition (rotation of 90 degrees about X and Y axes	212	1.06
3. Maintain spacecraft attitude during spin-up of flywheel (8 hours)	173	0.87
4. Flywheel spin-up counteract torque imposed on spacecraft (8 hours)	133	0.67
5. Spin-up of spacecraft to 0.1 rpm about scan (Z) axis	29	0.15
6. Reorientation to first galactic scan position (30 min)	105	0.53
7. Galactic scan reorientations during 30-day period	140	0.70
8. Reorientation to sun (25 deg) after completion of galactic scan (15 min)	71	0.36
9. Solar vector guiding mode	None	None
10. Despin spacecraft after first 7 months	29	0.15

TABLE XI-3. (Concluded)

Event	Total Impulse (lb-sec)	Propellant Weight (lb)
11. Reorient spacecraft to 30 positions 12 deg apart for pointing mode operation	<u>1126</u>	<u>5.62</u>
Totals for first year	2358	11.81
1. Spin-up of spacecraft to 0.1 rpm	29	0.15
2. Reorientation to first galactic scan position (30 min)	105	0.53
3. Galactic scan reorientations during 30-day period	140	0.70
4. Reorientation to sun after completion of scan	71	0.36
5. Solar vector guiding mode (6 months)	None	None
6. Despin spacecraft after 7 months of second year	29	0.15
7. Reorient spacecraft to 30 positions 12 deg apart for pointing mode operation (5 months)	<u>1126</u>	<u>5.62</u>
Totals for second year	<u>1500</u>	<u>7.51</u>
Totals for 2 years	3858	19.32

NOTE: For contingencies and safety, the required propellant is multiplied by a factor of 2 and rounded off: 19.32 × 2 = 38.64 ~ 40 pounds of propellant required.

The initial baseline magnetic control system selected consists of two large coils and one small coild each of which is aligned along one of the three spacecraft axes. The two large coils (one along and the other normal to the scan axis) were sized equally assuming each capable of compensating the maximum disturbance torque expected. The small coil (aligned normal to the scan axis) was primarily sized to provide scan rate control. All three coils are capable of simultaneous use to provide three-axis attitude control.

The large coil located along the Z-axis of the spacecraft was sized to be capable of producing a control torque that is some factor greater than the maximum value of the disturbance torque which acts in a plane normal to the Z-axis. The resultant torque of Tx maximum and Ty maximum is ± 0.0704 ft. lb. A value of ± 0.0727 ft-lb has been taken for initial sizing of each of the large control coils.

The components of the earth's magnetic field in solar coordinates are plotted in Figures XI-20, XI-21, and XI-22 as functions of the orbital time. The definition of the solar coordinates X_s, Y_s, Z_s have previously been defined in Figure XI-1. The strength of the earth's magnetic field (Appendix J, Paragraph 7) at an altitude of 200 n. mi. varies from 0.263 to 0.372 gauss (Fig. XI-23) along the orbital path, depending upon geographical location. Solar activity will cause these limits to vary, but this effect has not been considered. The component of the earth's field that is effective for scan axis pointing control lies in the plane normal to the scan axis (Figs. XI-21, XI-22). The value of this component in the Y_s-Z_s plane varies from 0 to 0.22 gauss. A value of 0.10 gauss was used to size the z-axis coil required for effective scan axis pointing control. The magnetic moment (M) required to produce a control torque (T) of 0.0727 ft-lb in a field of 0.1 gauss is 9858 amp-meters^2 (Appendix J, Paragraph 2).

The size of the coil having a core of Permendur material capable of producing a magnetic moment of 9858 amp-meters^2 is as follows:

Length of the coil = 4.6 feet
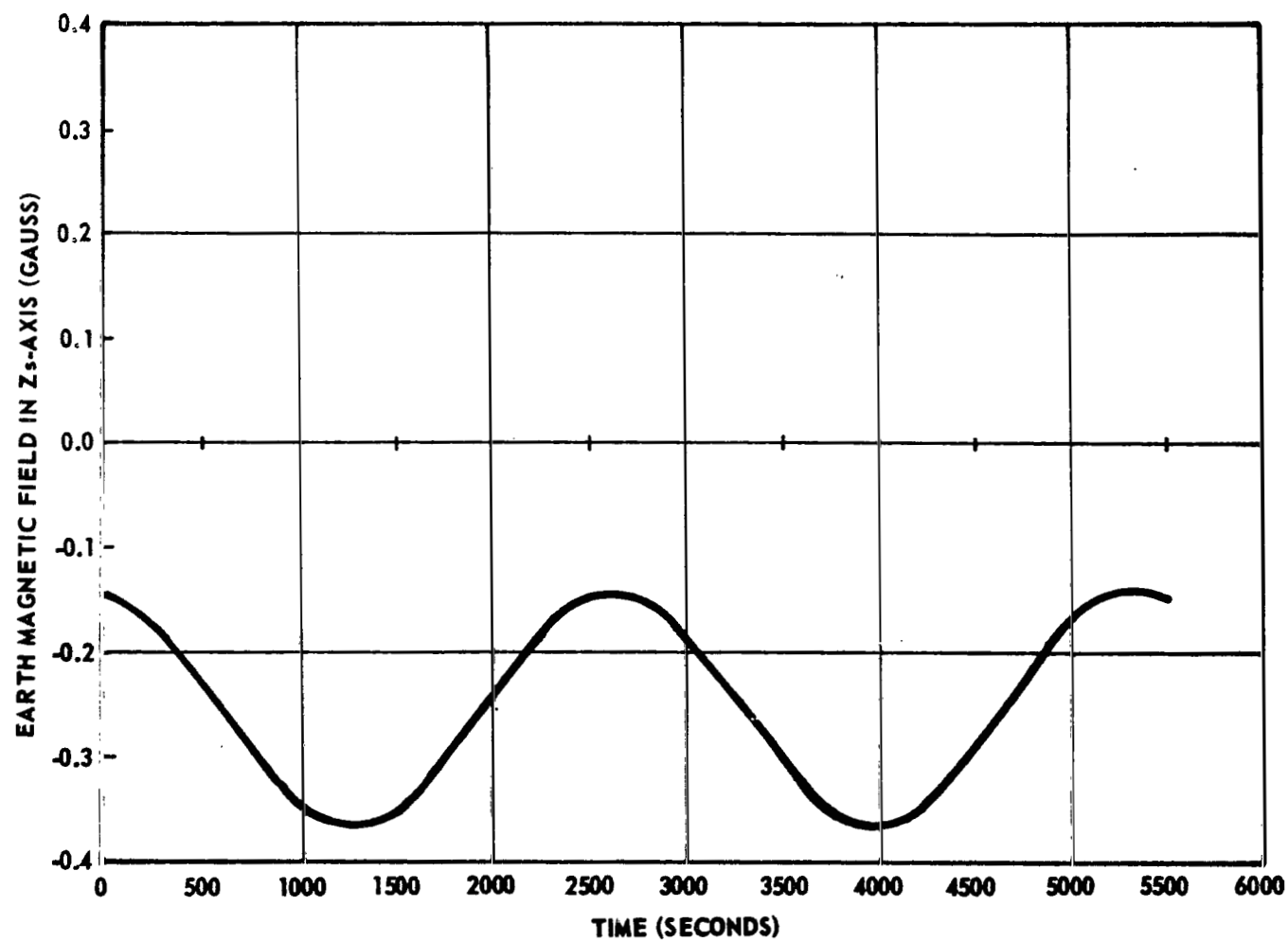
Diameter of the core = 2.8 inches

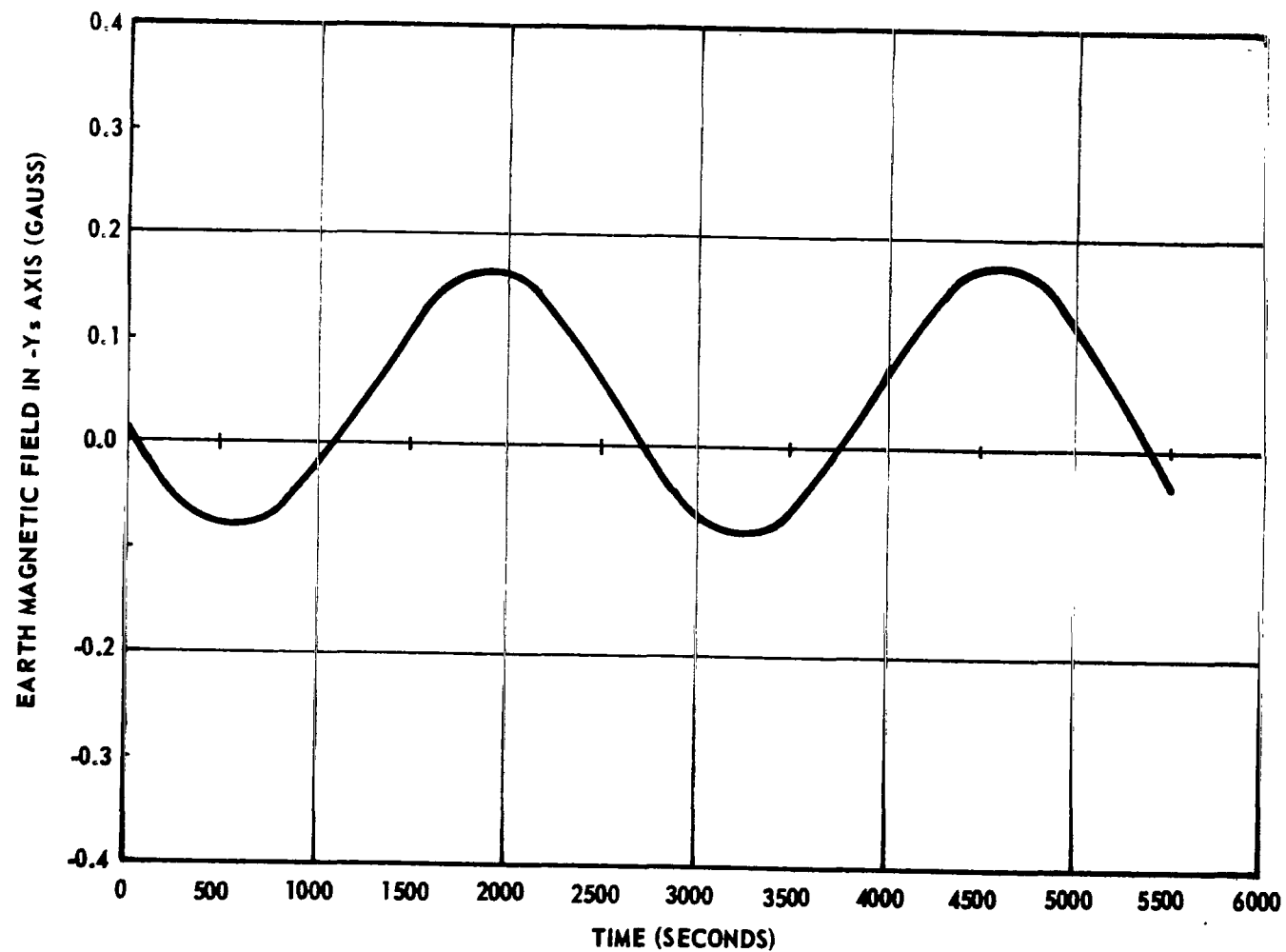Figure XI-20.   Variation of the earth's magnetic field component along X_s-axis during each orbit.

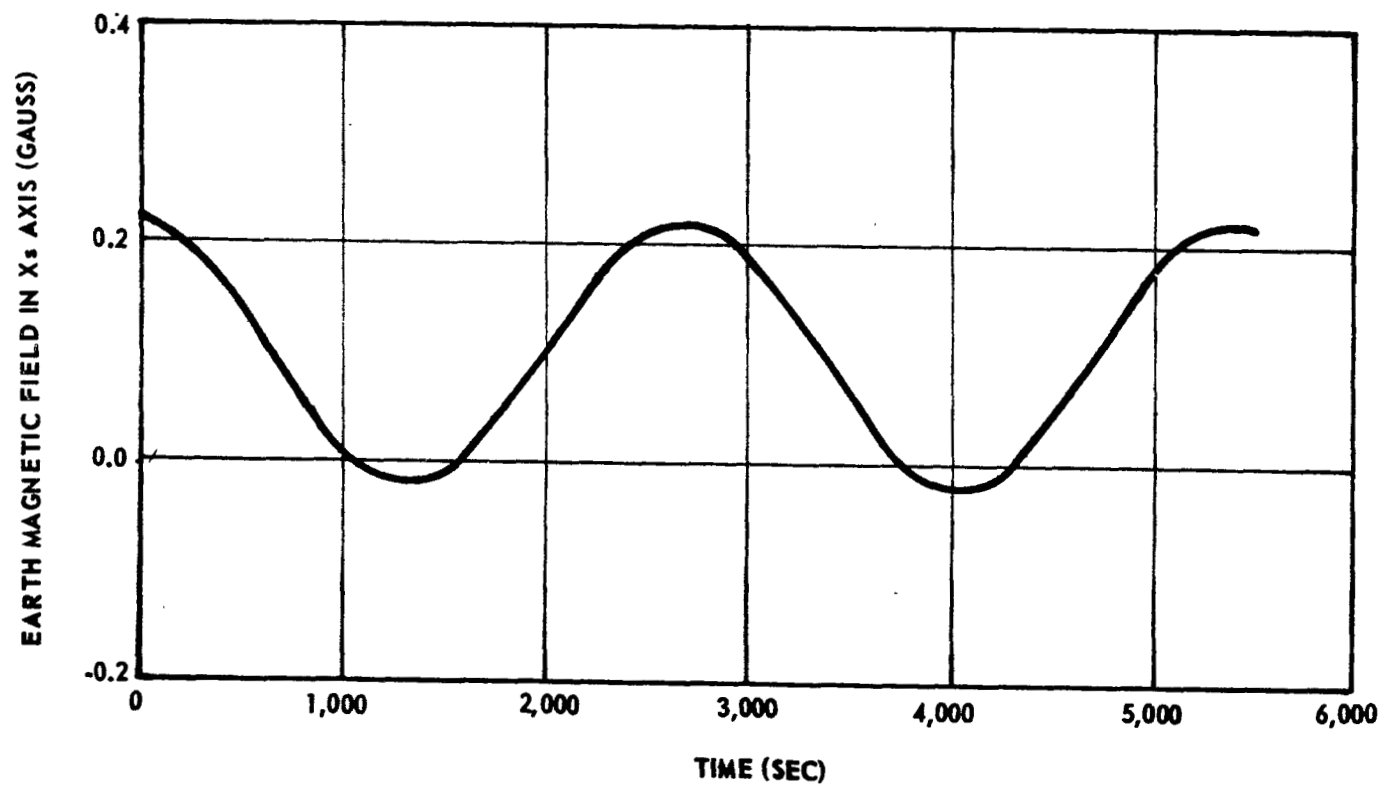Figure XI-21. Variation of the earth's magnetic field component along the Y_s-axis.

Figure XI-22. Variation of the earth's magnetic field component along Z_s-axis during each orbit.
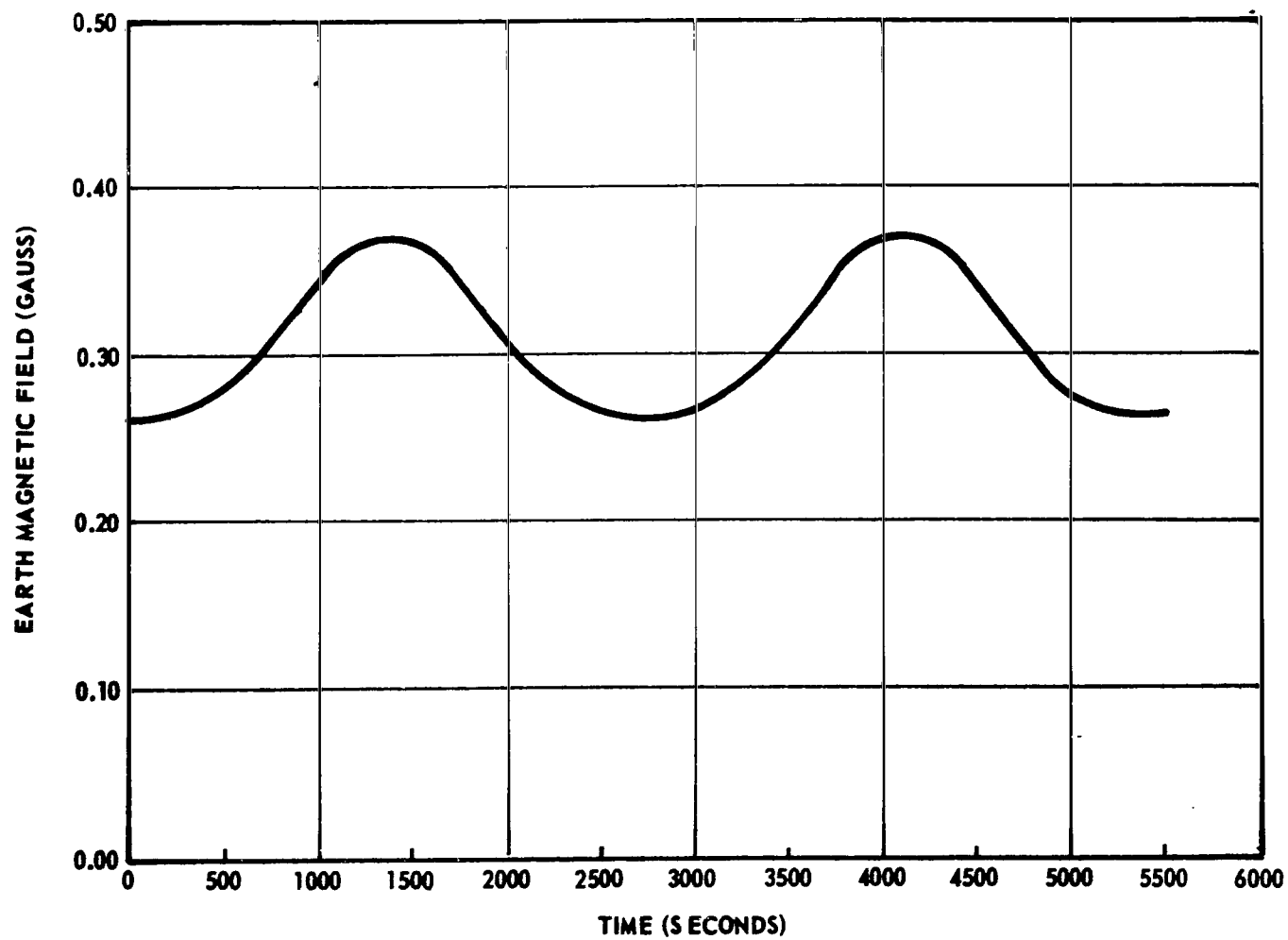
Figure XI-23.   Variation of total earth magnetic field in each orbit.

Weight of the core = 97. 6 pounds

Mass power product for
the coil of aluminum wire
(excluding core)   = 245 W-lb

The calculations used to determine these parameters are
given in Appendix J, Paragraph 2 and the total weight of the coil core using a
maximum of 100 watts is (97. 6 + 2. 5) = 100 pounds. This coil will be located
with its axis parallel to the spacecraft scan axis.

Preliminary results of spacecraft motion simulation indicate
a variation of about 1 percent in the scan rate during one orbit of the space-
craft. Therefore a control torque which is capable of changing the scan rate
by 1. 1 percent in a 60-second period would appear to be adequate. On this
basis, one of the coils located on an axis normal to the scan axis was sized to
produce a change in the scan rate of 0. 0067 deg/sec in a 60-second period.
The torque required for this change is 0. 072 ft-lb$_f$.

Scan rate control is ideally carried out whenever the earth's
magnetic field component along the scan axis is as small as possible to
minimize the cross-coupling effect of rate control torques on the scan axis.
For this condition the major component of the earth's field which varies from
0.26 to 0.37 gauss should lie in the plane normal to the scan axis. Therefore,
a lower value of 0.26 gauss was used as the strength of the earth's field for
sizing the scan rate control coils. The magnetic moment required for each
coil is 3756 amp-meters^2.

The size of the coil having Permendur as the core material
is:

Length of the coil = 9 inches

Diameter of the core = 0. 45 inch

Weight of core = 37. 12 pounds

Mass power product
for the coil of aluminum
wire (excluding core) = 15 W-lb .

Total weight of one coil
and core using a maximum
of 20 watts = 37.87 pounds.

In the celestial pointing mode of spacecraft operation, any one of the three axes of the spacecraft may be required to point in some inertial direction and its attitude held within ±1 degree. This will require a three-axis attitude control system. Since the angle about the pointing axis is not required to be precisely controlled, and can vary as much as ±37 degrees, a two-coil or a three-coil system can be used for pointing mode operation [XI-1, XI-2].

The coil aligned with either the X or Y spacecraft axis should be the same size as the coil located on the scan (Z) axis. The third coil may be smaller than the other two because its primary use will be scan rate control.

The total weight of the three coils is, therefore, (100 + 100 + 37.87) = 237.87 pounds and requires a maximum of 100 watts. Providing 24 pounds for insulation cover, mounting, connection, etc., the total weight of the three coils becomes (237.87 + 24) = 262 pounds.

Figure XI-24 shows a schematic for the mechanization of the coils (electromagnets). This scheme has been used in the DME-A satellite [XI-3]. A capacitor is used for storing energy which is discharged through the windings when torque is needed. The sense of the magnetic dipole can be made either positive or negative by command of the reversing relay. The magnetic dipole produced is a function of the voltage, which is variable. The null sensing magnetometer placed between the two electromagnets senses the state of magnetization of the magnets. This measure is used to determine the current required to demagnetize the magnets. The electromagnets are magnetized for a certain period of time (about 10 seconds) and then demagnetized (state of zero dipole moment) for about 1 second so that the three-axis magnetometers located on the spacecraft boom can sense the earth's field. The electromagnets are again magnetized and then demagnetized in sequence until the desired attitude of the spacecraft is attained.

One of the serious operational difficulties with this scheme is the nulling (state of zero dipole moment of the electromagnets) operation. The empty coil system has an advantage over this system in this regard.
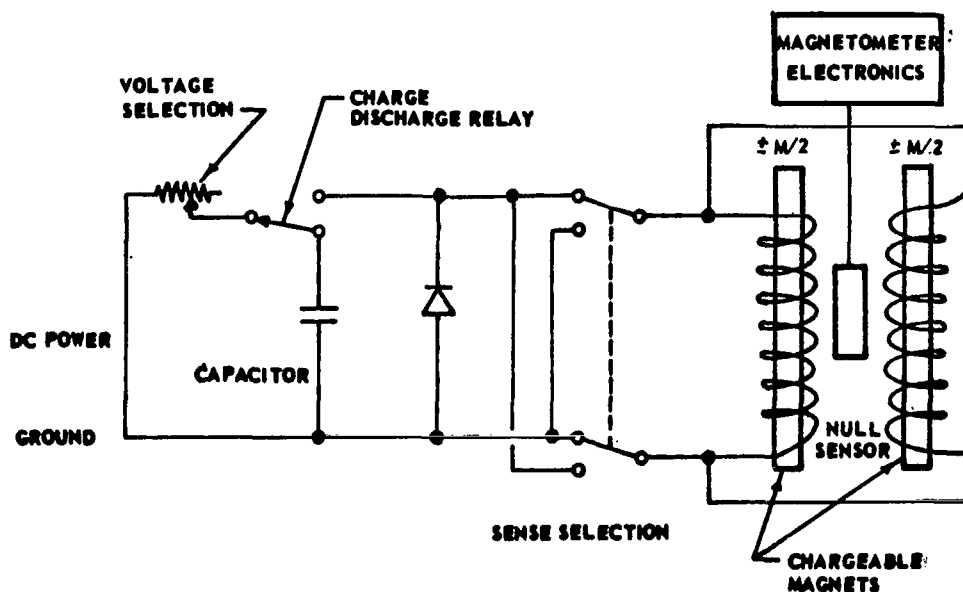
Figure XI-24. Magnetic coil system for attitude control.

4. Flywheel

a. Hardware description. The flywheel selected for use on the HEAO spacecraft consists of the Inner Gimbal Rotor Assembly (IGRA) in the Control Moment Gyro (CMG) developed for application on the Apollo Telescope Mount (ATM) space vehicle. By stripping the outer gimbal assembly and associated electronics directly applicable to its operation as a CMG, the modified assembly can serve as a flywheel. Consequently, no major design or development effort is required to obtain a flywheel for HEAO.

The modified inner gimbal assembly will consist of the rotor, induction motors for rotor spinup and operation, and heaters mounted to the rotor bearing housing. The assembly is operated at an internal pressure of approximately 10^{-3} mm Hg. The rotor is driven by two squirrel cage induction motors mounted symmetrically on the rotor shaft for thermal balance. The rotor is supported by a simple pair of bearings lubricated by a self-lubricating system. A tachometer is mounted to the rotor shaft through a gear reduction assembly.

The power supply for the ac motors is contained in an inverter assembly which converts the spacecraft 28-volt input to a 115-volt, 400-cycle, 3-phase current for motor operation. There is no voltage regulation on the inverter output to the motors, and no provision for speed control in the rotor in the present design. The inverter assembly also contains diagnostic instrumentation for the system operation such as heater power control, vibration pickups, pressure transducers, and temperature pickups.

A typical power profile (referred to the dc bus) for the inverter assembly is shown in Figure XI-25. Normal spinup time for the rotor is approximately 8 hours. Four heaters, each drawing 60 watts, are turned on for approximately 1 hour in the initial warmup period. After the initial warmup period of full heater power, the heaters are operated intermittently to maintain temperature in the lubricant; the average wattage is estimated at 12 watts for each of four heaters.

Estimated weight of the stripped CMG is 180 pounds, mounting hardware 20 pounds, and inverter assembly 40 pounds, giving a total weight estimate of 240 pounds.

b. Flywheel application. The purpose of adding a flywheel to the spacecraft is to provide some additional degree of stability, primarily during the scanning modes where the spacecraft rotation rate of 0.1 rpm is not sufficient to provide the required stability. The flywheel spinning at a rate of approximately 8000 rpm produces a momentum which tends to counteract the effects of disturbing torques on the spacecraft. This results in a decrease of the precession rate of the scan axis (Z-axis), thus reducing the number of times corrections would be required to maintain spacecraft attitude with respect to a reference source. This has particular advantages if occultation periods do not require inertial reference hardware (gyros) because pointing error requirements are met.

Preliminary analysis of spacecraft response under the influence of disturbing torques indicates that the present flywheel does not provide enough stability to warrant exclusion of inertial reference hardware. Adding magnetic coils to the attitude control system for correction capability reduces somewhat the significance of the flywheel contribution to spacecraft stability. The initial spacecraft performance analysis is discussed in Section XI, Paragraph D. Considerable additional analysis is required to validate the effectiveness of the flywheel.
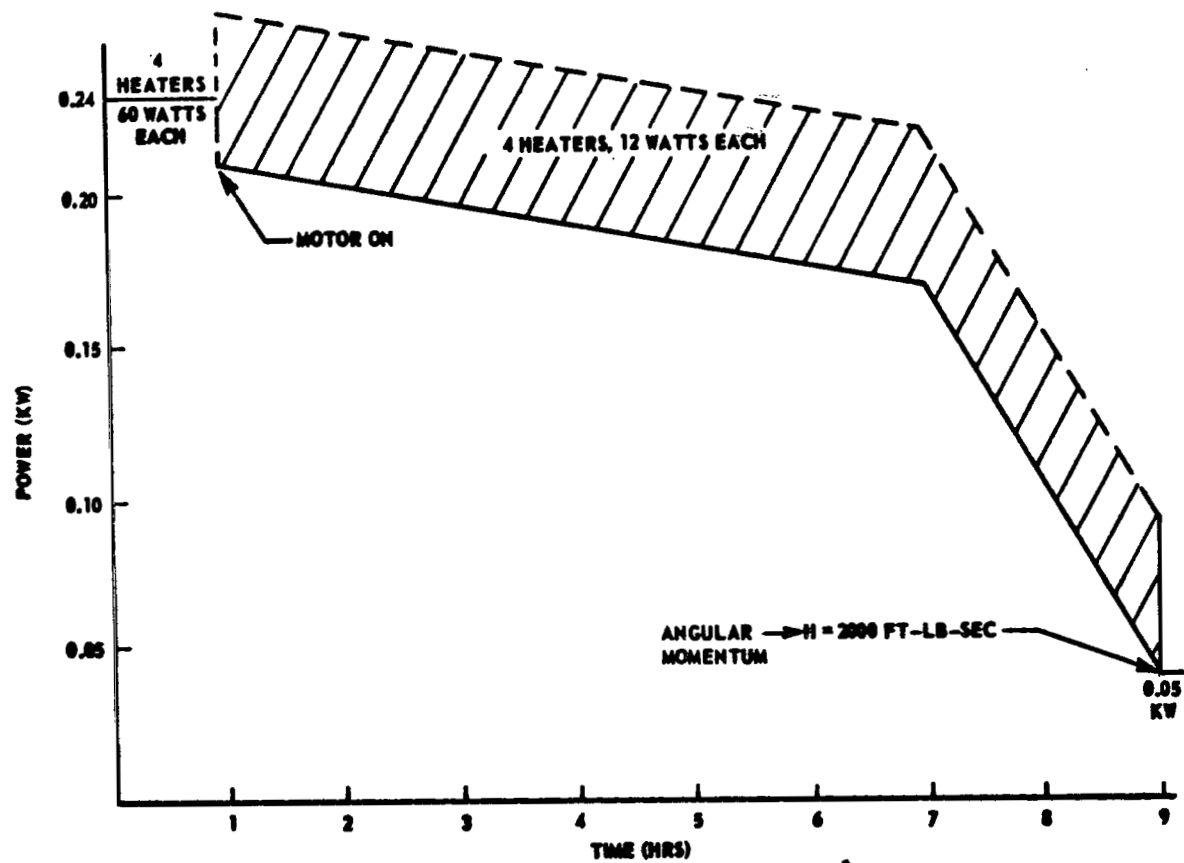
Figure XI-25. Typical flywheel spinup power profile.

5. <u>Signal Processing.</u> A functional block diagram of the attitude sensing and control system is illustrated in Figure XI-7. The gyro signals are electronically processed to provide both rate and position information to the system. The fine and coarse sun sensor signals are transmitted to summing networks. Processed signals from these sources, along with all other sensor signals, next go to the input signal selector and multiplexer.

The input signal selector and multiplexer selects the proper sensor signals for the spacecraft operating mode. The analog signals are multiplexed into the analog-to-digital converter. The digital sensor signals are transmitted directly to the control logic.

The control logic digital input interface is connected in parallel with the telemetry system digital interface. Digital aspect data are then sampled by the telemetry system for transmission-to-ground stations.

The control logic uses digitized sensor signals to compute the spacecraft attitude. This spacecraft attitude is then compared to aspect reference angles previously transmitted via the command link and stored in system memory. When the spacecraft attitude in a given axis differs from the reference attitude by a predetermined amount, a control signal is generated by the control logic and sent to the output selector. Here, a decision based on the error amplitude and operating mode is made to use the appropriate jet or coil system to correct the error. The control logic provides compilation of the required restoring torques based on the appropriate control law for each mode.

The on-board attitude sensing and control system will maintain the spacecraft in a predetermined attitude on the basis of coded signals stored in the computer memory. To make a major spacecraft reorientation and/or change the operating mode of the spacecraft, a command is transmitted from the ground. A new reference attitude is then stored in the computer memory.

C. System Operation

1. <u>Initial Acquisition (Fig. XI-26).</u> The primary functions of this mission phase are to align the spacecraft Z-axis within 1 degree of the solar vector and to obtain flywheel and spacecraft spinup. Upon completion of initial acquisition, the spacecraft is in the celestial scan reference attitude from which either the galactic scan mode or the celestial scan mode can be readily entered.
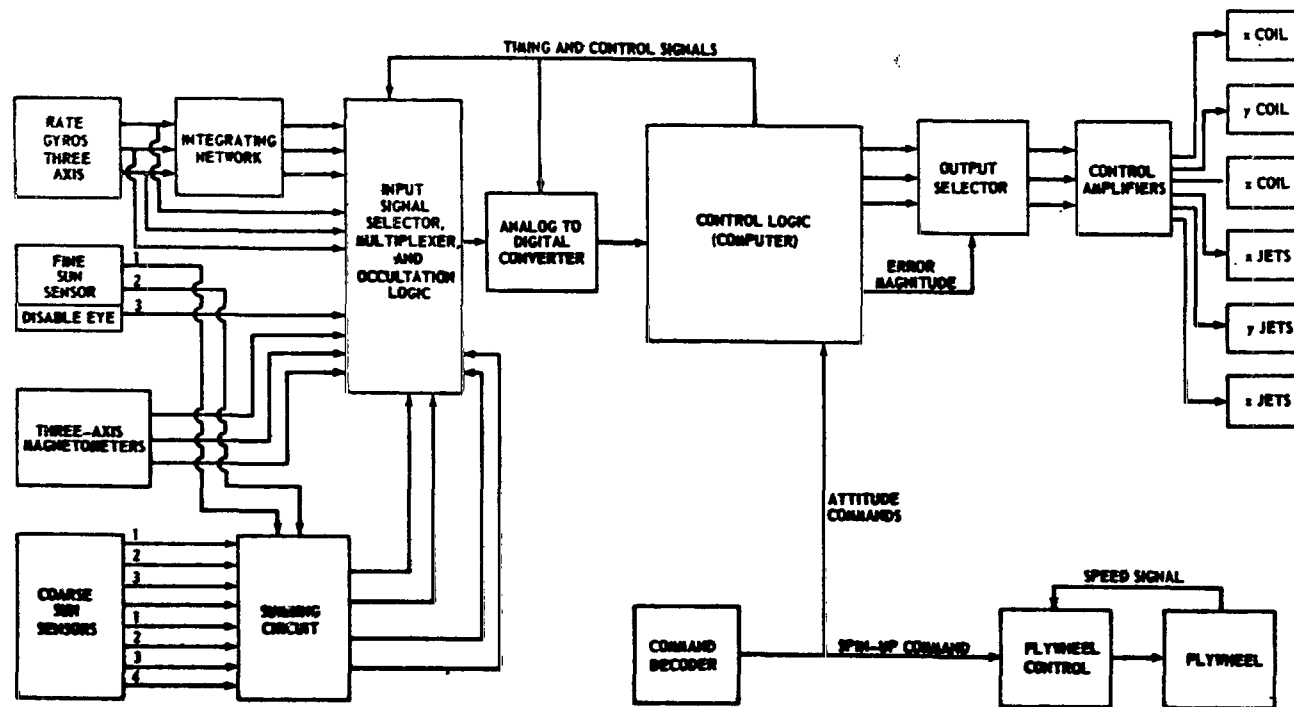
Figure XI-26.   HEAO — initial solar vector acquisition — signal flow block diagram.

At spacecraft separation from the launch vehicle, the spacecraft rates about all axes are sensed by the rate gyros. The gyro outputs are processed and routed to the control computer where control commands are generated to activate the RCS jets and reduce the body rates to acceptable levels.

The spacecraft Z-axis solar offsets about the X and Y axes are sensed by the eight coarse sun sensors (four per axis). The sun sensor error signals are processed in the summing networks and the analog-to-digital converter and routed to the control computer where actuator commands are issued to torque the spacecraft in a direction to align its Z-axis with the solar vector. When the Z-axis has been oriented to a position where the sun is in the FOV of the fine sun sensor disable eye, the disable eye issues a discrete signal that transfers spacecraft control from the coarse sun sensors to the two-axis fine sun sensor. The processed outputs of the fine sun sensor are now used to generate the control commands necessary to obtain precision alignment of the Z-axis with the solar vector.

Preliminary analysis indicates that an attitude hold for the spacecraft is required during sun occultations. This is accomplished by integrating the outputs of the rate gyro to obtain position information. This position information when supplied to the control computer is used to generate the necessary actuator commands to provide the attitude hold required. Further analysis may indicate that a simple integration of the gyro outputs is not sufficient and that a form of "strapdown" computation is required to obtain the correct position information. A typical sequence of events is listed as follows:

- Command of initial acquisition phase.

- Rate stabilization to acceptable thresholds.

- Attitude hold during sun occultations.

- Acquisition of sun by coarse sun sensors.

- Torque spacecraft into the fine sun sensor FOV.

- Disable eye switches control to the fine sun sensor.

- Final alignment to solar vector.

- Spinup flywheel while holding spacecraft attitude.

- Spinup the spacecraft.

2. Celestial Scan Mode (Fig. XI-27). In this mode, the spacecraft is near the celestial scan reference attitude with the Z-axis approximately aligned with the solar vector and the spacecraft rotating about the Z-axis at 0.1 rpm. The experiments are scanning segments of the celestial sphere as the spacecraft rotates.

The two-axis fine sun sensor measures the Z-axis solar vector offset error angles and generates outputs that are processed and used to generate commands to the magnetic coil actuators to maintain precision alignment of the Z-axis with the solar vector. By maintaining this solar vector alignment, the Z-axis is forced to track the sun at its approximate 1-degree-per-day angular rate, and, in the process, the experiments scan different segments of the celestial sphere. This permits scanning the entire celestial sphere in approximately 6 months.

The rate gyro package supplies rate and position information that is used for rate stabilization and for attitude holds during sun occultations. Attitude hold about the Z-axis is not required because of the spacecraft rotation about this axis.

Three-axis precision attitude determination is required for this mode to provide correlation between the experiment data and the spacecraft attitude. The star field mapper supplies star information on a non-real-time basis that is stored onboard and during contact periods transmitted to ground stations. Ground reduction of these data permits reconstructing a star map that provides the required correlation between experiment data and spacecraft attitude.

3. Galactic Scan Mode (Fig. XI-28). To scan a belt in the galactic plane with the LOS of the experiment during 30 days of the mission requires an initial solar offset of the spacecraft Z-axis to a position near the galactic pole followed by a series of programmed maneuvers near the galactic pole designed to scan approximately 100 percent of the region of interest during the specified time period. A September 8 launch was chosen in the example shown in Figure XI-29 which depicts a scan pattern suitable for scanning 100 percent of a 17-degree galactic belt in 30 days while minimizing the solar offset angle to meet solar power requirements.

The first maneuver performed on ground-command initiation of the galactic scan mode is to position the Z-axis to position 1. The star tracker is enabled prior to the start of the maneuver and its output resulting from a known star reference is used to update a calculated scan angle ϕ .
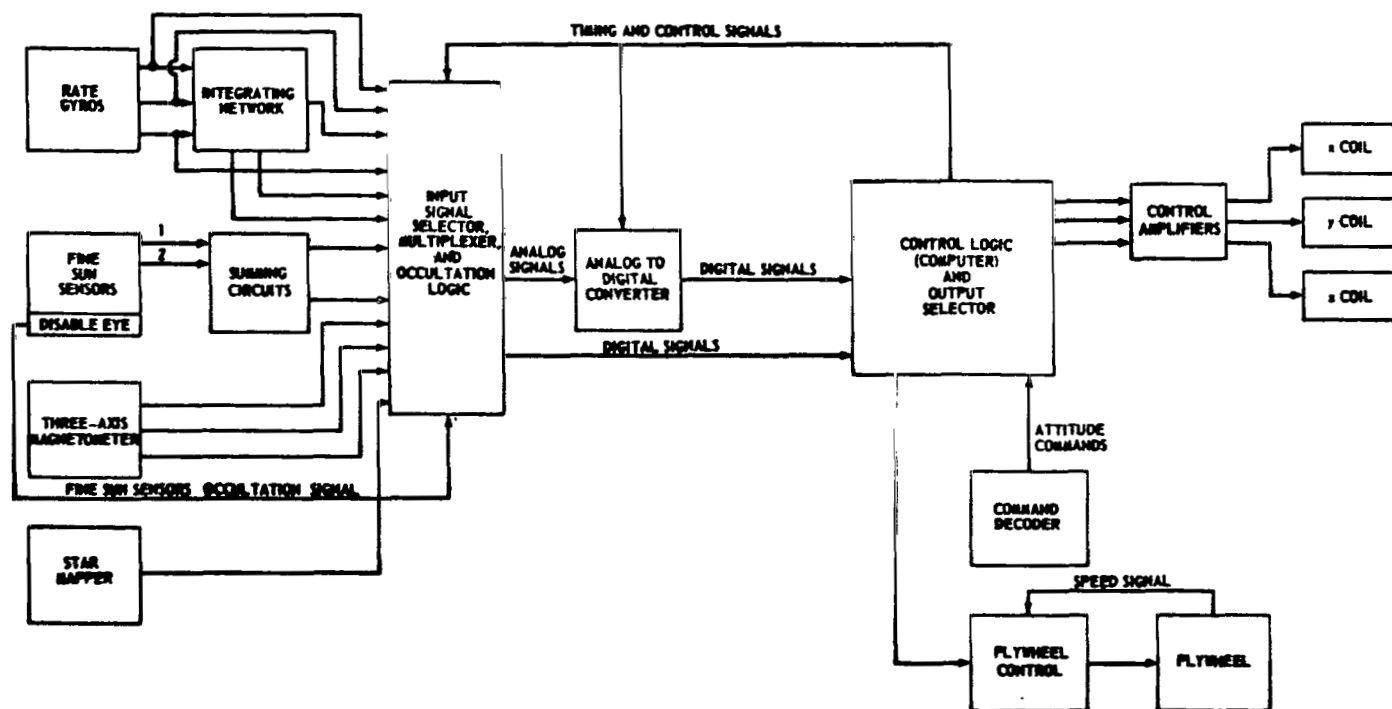
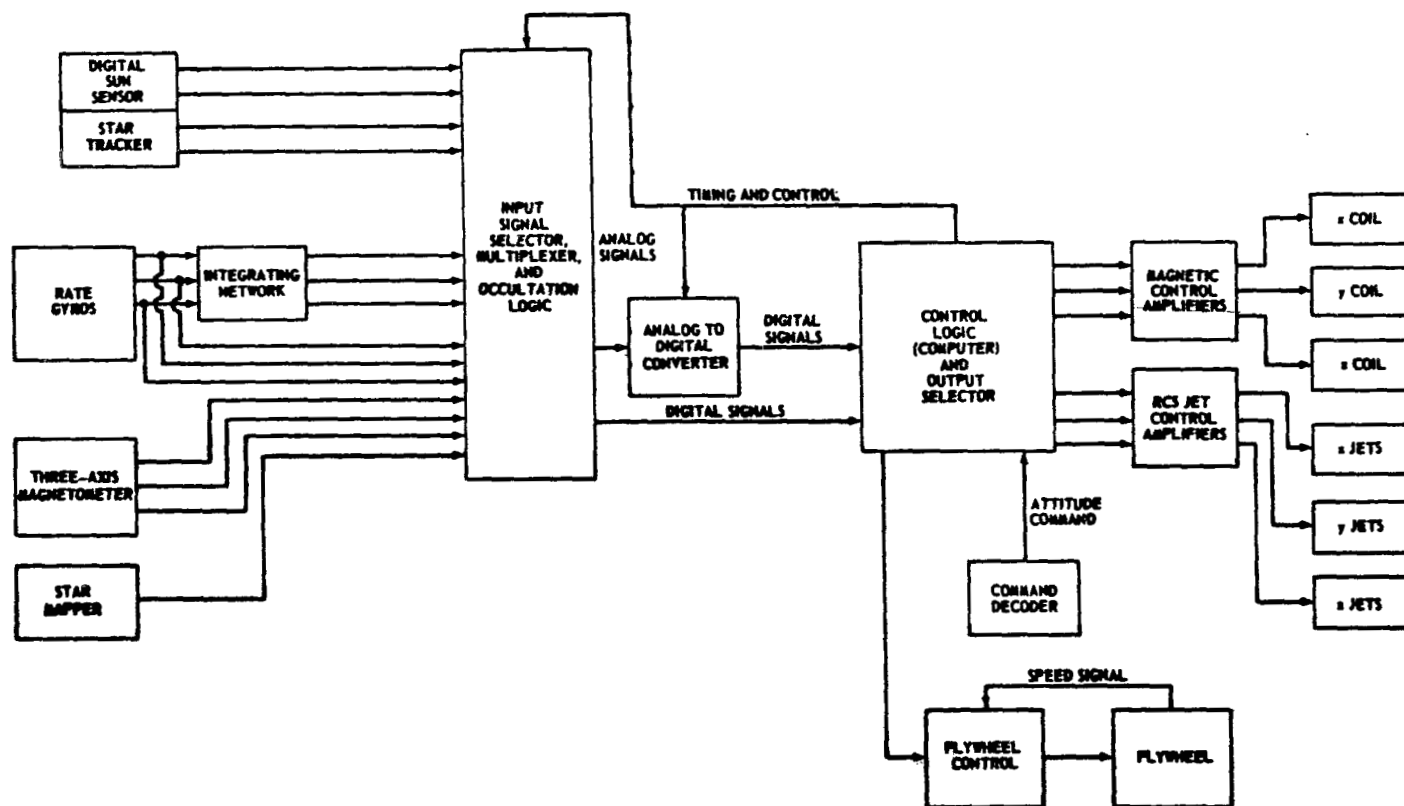Figure XI-27. HEAO — celestial scan mode signal flow block diagram.

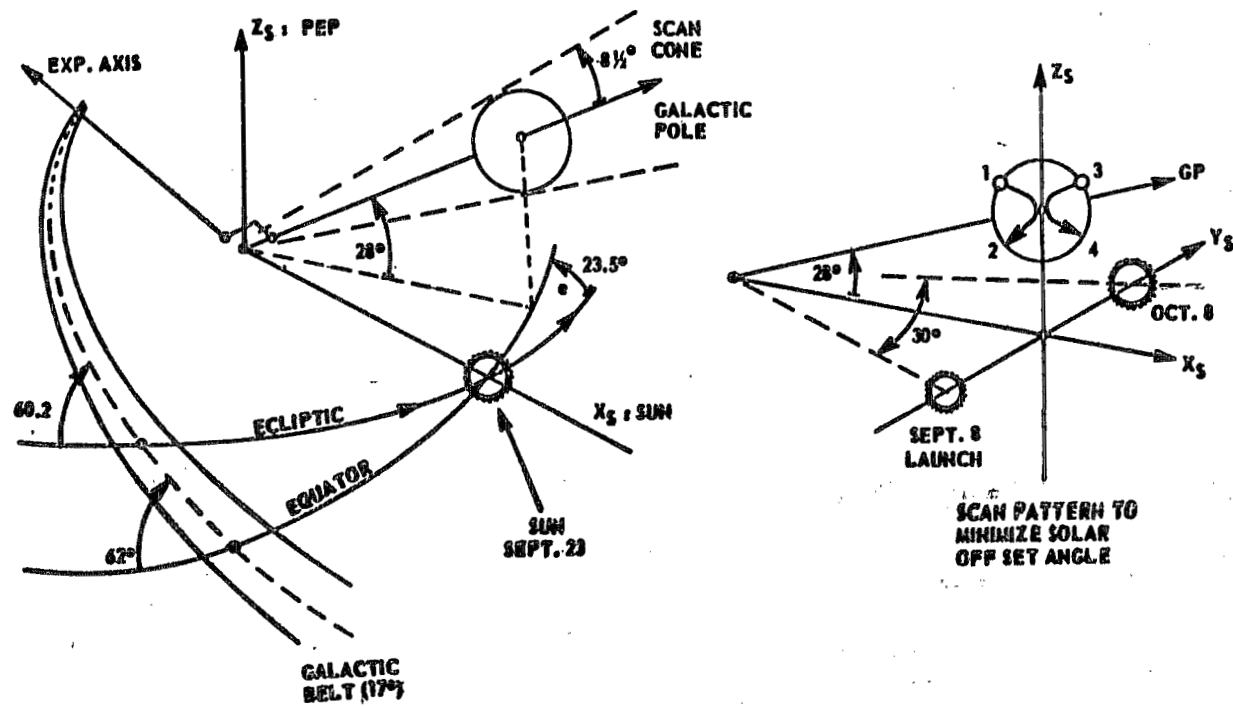Figure XI-28. HEAO — galactic scan mode — signal flow block diagram.

Figure XI-29. HEAO — galactic scan.

This updated angle ϕ is used to resolve the two-axis digital sun sensor out-puts into the proper values of position angles θ and ψ. The RCS jets are activated to move the Z-axis to position 1. This maneuver can be accomplished by two single axis maneuvers or one direct maneuver with suitable thrusters. The direct maneuver may require some form of strapdown computation to obtain the necessary parameters.

After remaining at position 1 for approximately 56 hours, the Z-axis is programmed along the locus from point 1 to point 2 in five discrete steps and is held at each new position for 56 hours while the experiments scan a portion of the galactic belt. The steps are 3, 3, 4, 3, and 3 degrees in that order.

From position 2, the Z-axis is moved approximately 17 degrees to position 3 where it remains for 56 hours. The Z-axis is now programmed along the locus in six discrete steps of 3 degrees each to position 4. The Z-axis dwells at each intermediate position for 56 hours. After the completion of the time at position 4, the desired galactic belt will have been scanned. A movement of approximately 24 degrees will reacquire the sun and place the spacecraft in the celestial scan reference attitude.

The two-axis digital sun sensor serves as the primary solar vector offset angle measuring device. By using known star sightings, the star tracker provides update information on the scan angle ϕ for resolution of the sun sensor outputs into the proper values of θ and ψ.

Rate and position information is obtained from the rate gyro pack-age for rate stabilization and for attitude holds during sun occultation periods.

The magnetometer and magnetic coils are used in combination to provide attitude control and to perform the small angle maneuvers. Large angle maneuvers are performed with the RCS jets.

Aspect determination to ±0.1 degree is accomplished by ground data reduction of the star transit information supplied by the star field mapper.

The galactic scan mode involves the operation of sensors offset from their null reference; therefore, careful consideration must be given to the effects of vehicle motion on the sensor outputs. Sensed signals for the X and Y axes must be processed and resolved by use of the rotation angle about the Z-axis to generate the correct commanded control torque signals. This consideration holds for any other operational manner that requires similar offset operation.

4. Celestial Pointing (Fig. XI-30). The primary function of the celestial pointing mode is to provide for investigations of selected locations on the celestial sphere. In this mode, the spacecraft is not rotating and the experiments are aimed at the selected locations under ground command control and using ground supplied pointing information.

For the baseline system, the Z-axis of the spacecraft is aligned with the solar vector at all times. This constrains the viewing of a specific target to a particular time of year, at which time the tracking of the solar vector has positioned the experiments LOS in a great circle of the celestial sphere that contains the target. When this favorable condition occurs, the spacecraft is rotated about its Z-axis until the experiments are looking directly at the target. Proper programming of the target viewings with respect to the time of year will minimize the waiting time for target viewing. Solar offset pointing is discussed in Appendix J, Paragraph 3.

Solar vector alignment is maintained by the processing and use of the fine sun sensor error signals. The disable eye provides a signal at sun occultations that configures the spacecraft control system into an attitude hold mode.

Rate and position signals are obtained from the rate gyro package for use in rate stabilization and for attitude holds.

Since this mode requires pointing the experiments' LOS at a particular point on the celestial sphere and maintaining this orientation for a given length of time, some means must be provided to control spacecraft drift about all three axes. The sun sensor provides this drift control about the X and Y axes. The star tracker produces an output as a result of known star sightings. This output is processed and used to provide updated information on the angle ϕ which, together with the sun sensor outputs, is used to generate the necessary control commands and magnetic coil actuation to compensate for spacecraft drift.

Spacecraft attitude determination to ±0.1 degree is obtained from the two-axis digital sun sensor and the star tracker.

5. Random Reacquisition. To be able to acquire the solar vector and thus position the spacecraft in basically the celestial scan reference attitude at any point in the mission, a random reacquisition capability must be provided. This capability does not require any new sensors or actuators, but does require that a switching sequence be available to configure the control system.
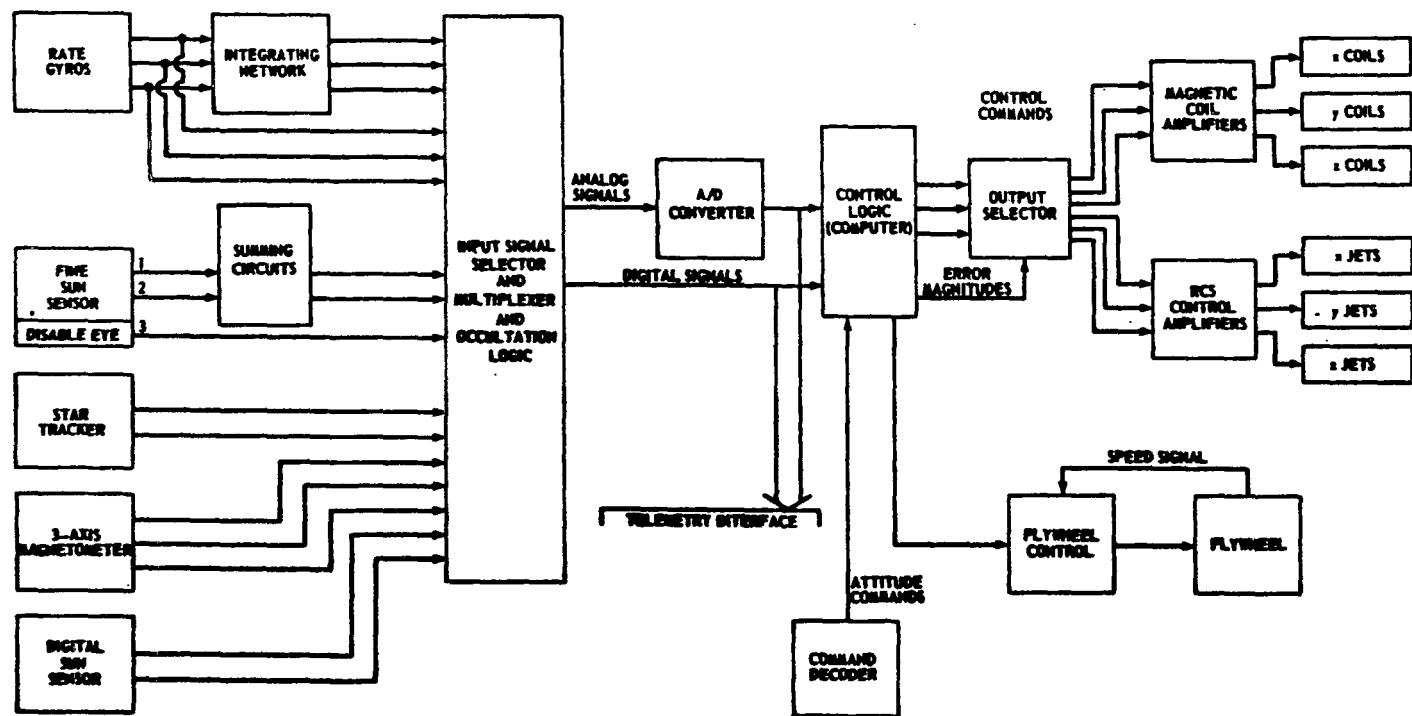
Figure XI-30. HEAO — celestial pointing mode functional diagram.

The course and fine sun sensors are used to acquire the sun in the same manner described in the initial acquisition operation sequence. Rate and position information is supplied by the rate gyros for stabilization and for attitude holds.

Actuation through large angles is supplied by the RCS jets, and attitude control actuations are supplied by the magnetometer and magnetic torquer combination.

Aspect determination is not considered a requirement for this operation.

D. Baseline Performance Simulation

1. **Description.** A computer program was written to simulate the dynamic behavior of the HEAO spacecraft in a 200-n. mi. circular earth orbit. Three effects are simulated in the program:

- The gyroscopic action of the rotating spacecraft having a flywheel aligned along its Z-scan axis. This effect is expressed using Euler's dynamic equations.

- The effect of gravity gradient disturbance torque on the spacecraft.

- The effect of magnetic control torque produced by current-carrying coils which react with the earth's magnetic field.

The equations which were programmed were Euler's equations for rotational motion about the principal body axes, Euler's kinematical relations which relate the body principal axes to the solar inertial reference, transformational matrices which relate the environmental torques to the body axes, and the magnetic control torque logic which relates the spacecraft's attitude errors and rates through appropriate feedback gains to applied torques about the body axes.

The Euler angles (ψ, θ, ϕ), shown in Figure XI-1, specify the spacecraft orientation relative to the solar reference coordinates. For small values of ψ and θ, the directional cosine angle between the vehicle scan axis and the solar vector is denoted by δ and is obtained by

$$\delta = (\psi^2 + \theta^2)^{\frac{1}{2}}$$

In a phase plane plot ψ and θ are related to the solar Z_s and Y_s axes in which a unit vector along the scan axis is projected onto the Y_s - Z_s plane.

The dominant environmental torque is that caused by gravity gradient effects. The gravity gradient disturbance torque components about the body principal axes are given in Appendix J, Paragraph 5. In computing the components of the local radius vector in body coordinates, the effects of orbital position, orbital inclination, orbital regression, time of year (solar position), and ascending line of nodes were considered in deriving the required transformational matrices. However, orbital conditions were selected such that the gravity gradient torques attained their maximum possible values, and those angles which vary slowly with time were held constant at their maximizing values over an orbital time period. As previously stated, the magnetic control torquers were sized to counteract the maximum gravitational torques about each axis.

Magnetic control torques are produced by the reaction of magnetic moments with the earth's magnetic field. These moments are produced by electromagnets located on the principal axes of the spacecraft. The basic equation for the torque produced is given in Appendix J, Paragraph 6, as

$$\overline{T} = \overline{M} \times \overline{B}$$

where

$\overline{T}$ — torque vector.

$\overline{M}$ — magnetic moment vector produced by the electromagnets.

$\overline{B}$ — earth's magnetic field vector.

For pointing control of the spacecraft scan axis (Z-axis), primarily only the electromagnet aligned on this axis is used; therefore, for this operation, $M_X = 0$ and $M_Y = 0$ and torques about the three spacecraft body axes X, Y, and Z are given by

$$T_{xm} = M_z B_y$$

11-54

$$T_{ym} = M_z B_x$$

$$T_{zm} = 0$$

where

T_{xm}, T_{ym}, T_{zm} — the magnetic control torque produced about spacecraft axes X, Y, Z (ft - lb$_f$)

M_x, M_y, M_z — the magnetic dipole produced about the spacecraft axes (ft - lb$_f$/gauss) by the magnetic coils.

B_x, B_y, B_z — the components of the earth's magnetic field along the spacecraft axes (gauss).

For control of the spacecraft scan (spin) rate, the electromagnet located on the scan axis (Z) is not energized, but the other two are. Therefore for this operation, $M_z = 0$, and torques about the three spacecraft body axes are given by

$$T_{xm} = M_y B_z$$

$$T_{ym} = -M_x B_z$$

$$T_{zm} = M_x B_y - M_y B_x$$

Only torque T_z is desired; torques T_x and T_y introduce disturbances to the attitude of the scan axis (Z). Therefore scan rate control torque

is applied only when the component of the Earth's magnetic field parallel to the spacecraft Z-axis (B_z) is very small, i.e., $B_z \leq 0.001$ gauss. This minimizes the disturbance acting on the scan axis.

All equations were solved simultaneously using the computer to find the values of ψ, θ, δ, and other parameters.

2. Parameters and Cases Simulated. The computer simulation results are based upon the following parameters:

- Orbit = 200 n. mi. circular

- Orbit inclination = 28.5 degrees with the earth's equator

- Spacecraft scan rate = 1/10 rpm

- Flywheel spin rate = 8000 rpm

- A simple dipole model of the earth's magnetic field inclined 11 degrees to the geographic north.

- Moment of inertia of the flywheel rotor is 2.43 ft-lb-sec^2

- The principal moments of inertia of the spacecraft are assumed to coincide with the geometric axes.

To simulate maximum gravity gradient disturbing torques (Appendix J, Paragraph 5) acting on the spacecraft, the sun was placed in its winter solstice position relative to the earth, and the orbit plane was placed in an orientation to give a solar vector-orbit plane angle of 45 degrees.

Computer simulations were performed for the baseline configuration, with the following principal moments of inertia:

$$I_x = 3970 \text{ ft-lb-sec}^2$$

$$I_y = 35\ 210 \text{ ft-lb-sec}^2$$

$$I_z = 36\ 900 \text{ ft-lb-sec}^2$$

3. **Simulation Results.** Figures XI-31 through XI-33 show the variation of the gravity gradient torque in the solar X_s, Y_s and Z_s axes (Figure XI-1) as the spacecraft moves in the orbit. The torque in X_s axis is cyclic, having a frequency twice that of the spin frequency. The torques in both the Y_s and Z_s axes are biased; however, the Z_s component is only slightly biased.

Without active control, the biased torques produce secular momentum terms which vectorially add to the spacecraft momentum vector to precess the scan axis in the direction of the sun's apparent movement and southward from the ecliptic plane. Figures XI-34 and XI-35 are plots of the angular momentum about the inertial axes, Y_s and Z_s, due to gravity gradient torque over an orbit time period. The angular momentum in Y_s axis is secular and its value at the end of one orbit is about 90 ft-lb-sec. The angular momentum in the Z_s axis has a secular component of about 13 ft-lb-sec at the end of one orbit period. The net total angular momentum gain at the end of the orbit time is about 103 ft-lb-sec. Control torques must counteract this gain in angular momentum.

In Section XI, Paragraph B. 3 and in Appendix J, Paragraph 6 it was shown that the effective earth's magnetic field for scan axis attitude control is the component of the field which lies in the Y_s - Z_s plane which is normal to scan axis. Figures XI-20, XI-21, and XI-22 show that the component of the earth's magnetic field in the Y_s-Z_s plane is small, in the 800- to 1300-second and 3500- to 4000-second intervals of the orbit time, and most of the field lies along the X_s scan axis. During these intervals, the production of control torques by coils for scan axis attitude control can not be optimally produced by the scan axis coil, M_z.

It was also pointed out that scan rate adjustments are carried out whenever the earth's magnetic field component along the scan axis is very small ($B_z \leq 0.001$ gauss); but, Figure XI-20 shows that $B_z = B_{xs}$ attains peak value of 0.35 gauss during the orbit. Thus, in such an orbit where B_z is not very small, scan rate adjustments, if required, can be carried out; but this will cause perturbation in the pointing attitude of the scan axis because of undesirable components of the torque produced in the plane normal to the scan axis.
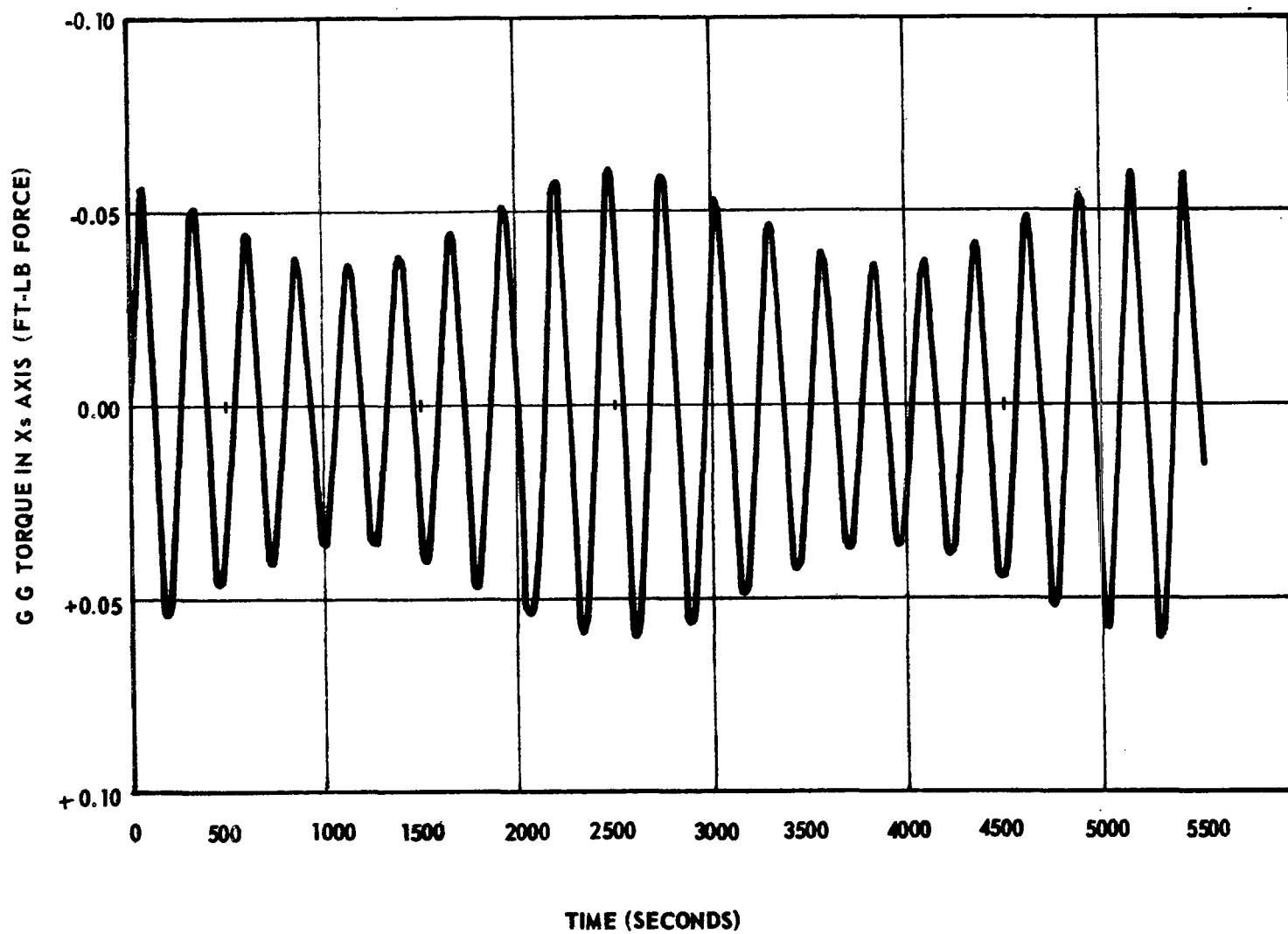
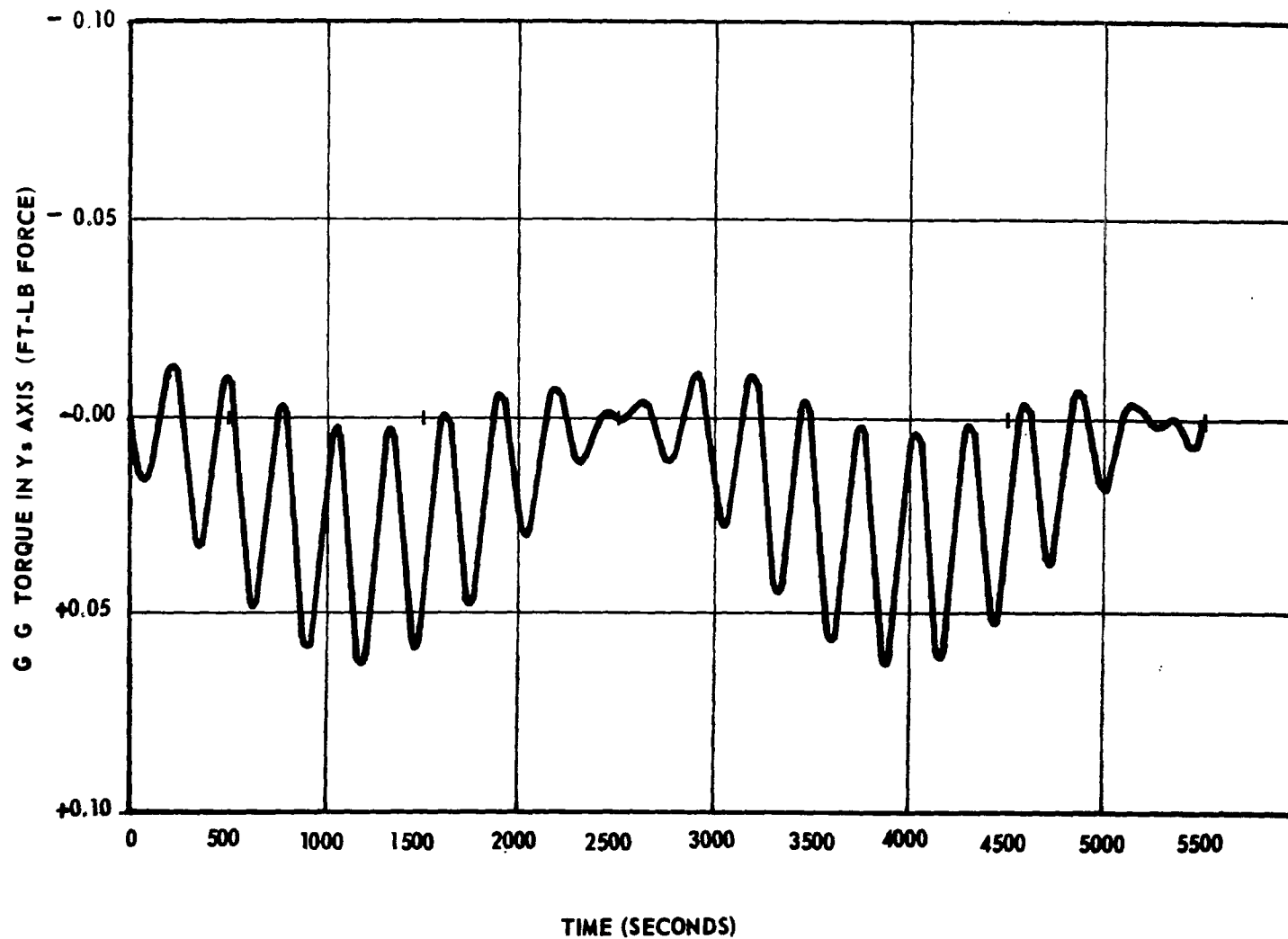Figure XI-31. Variation of gravity gradient torque in the X_s axis with orbit time.

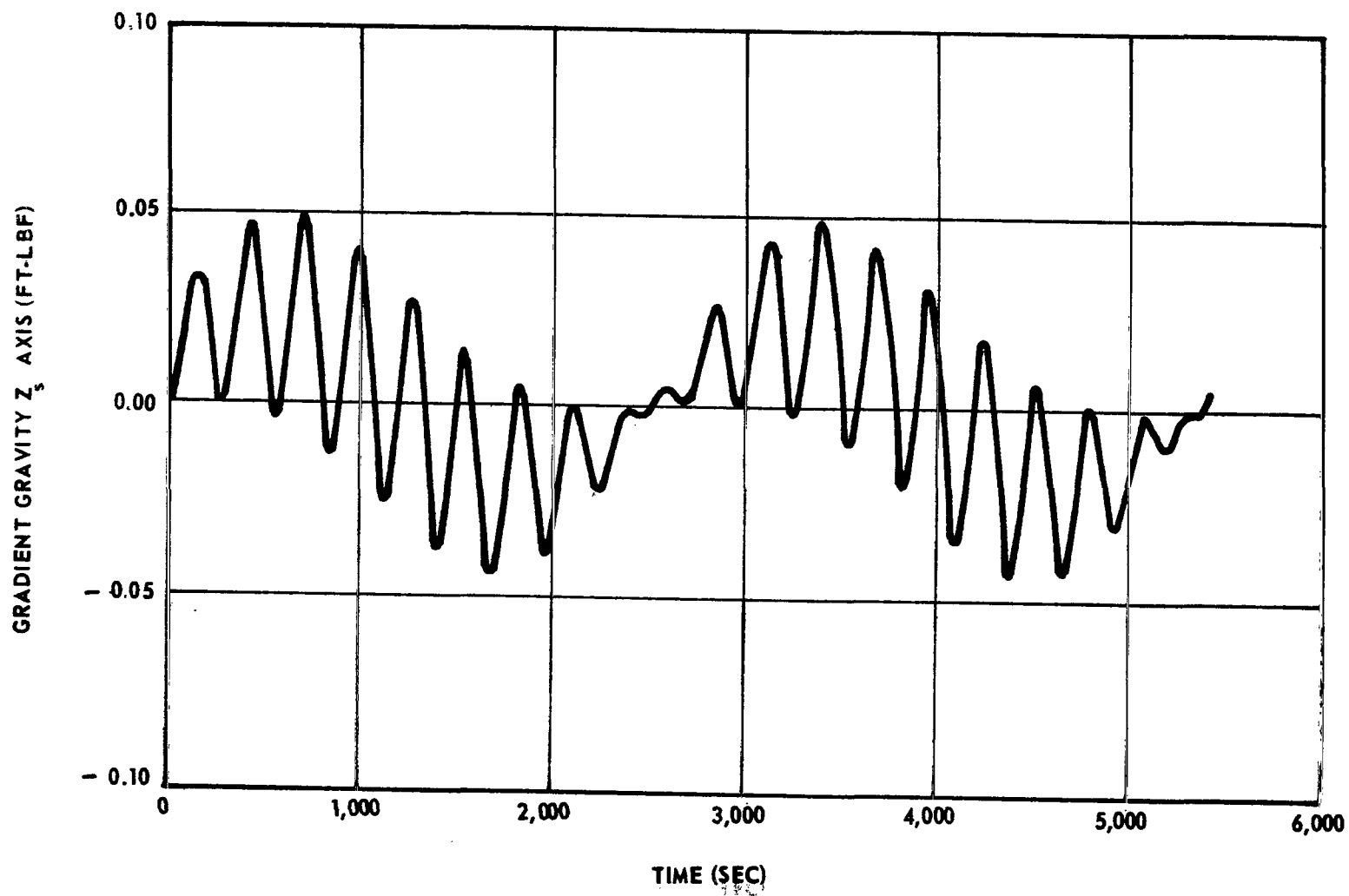Figure XI-32.   Variation of gravity gradient torque in the Y_s axis with orbit time.

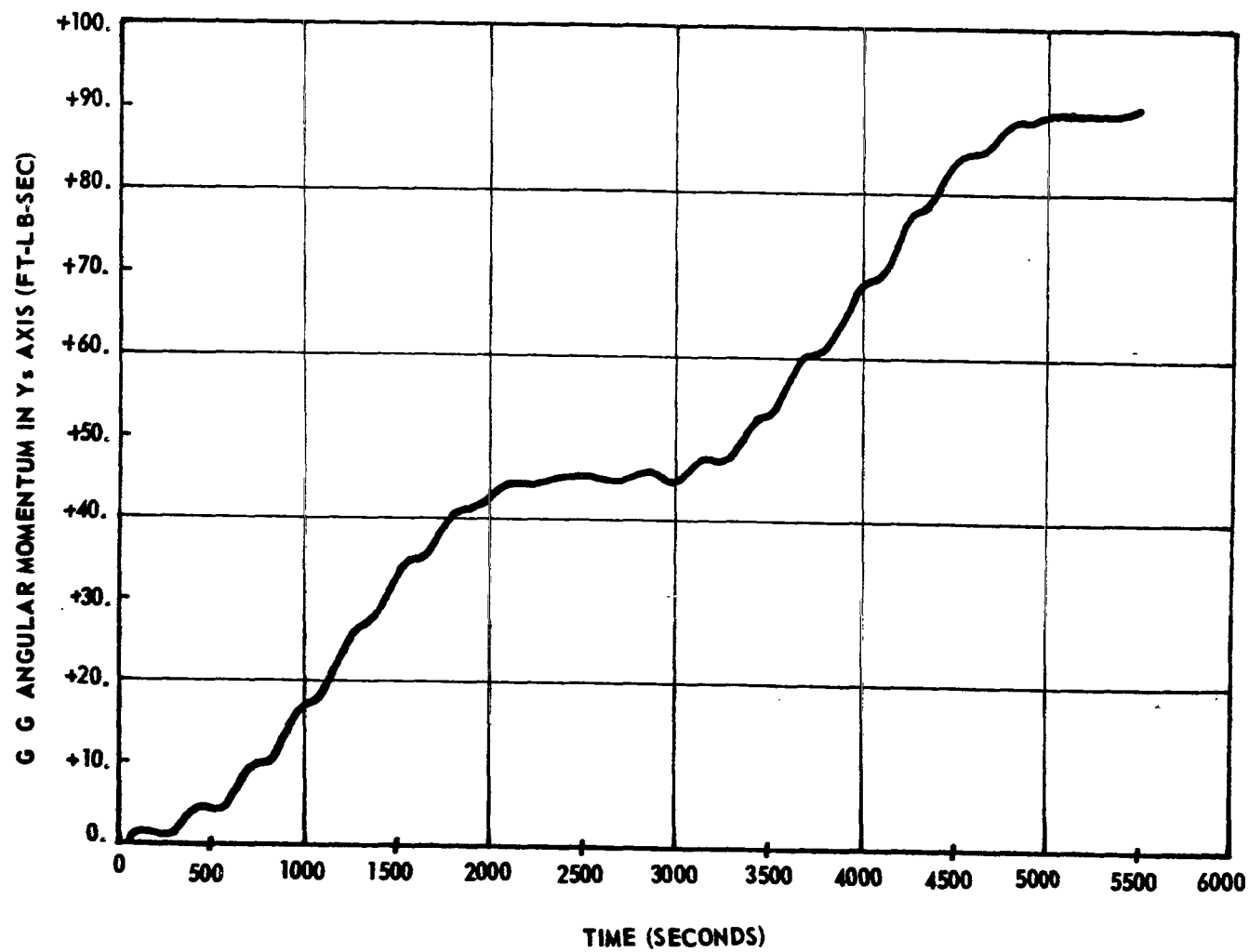Figure XI-33. Variation of gravity gradient torque in the Z_s axis with orbit time.

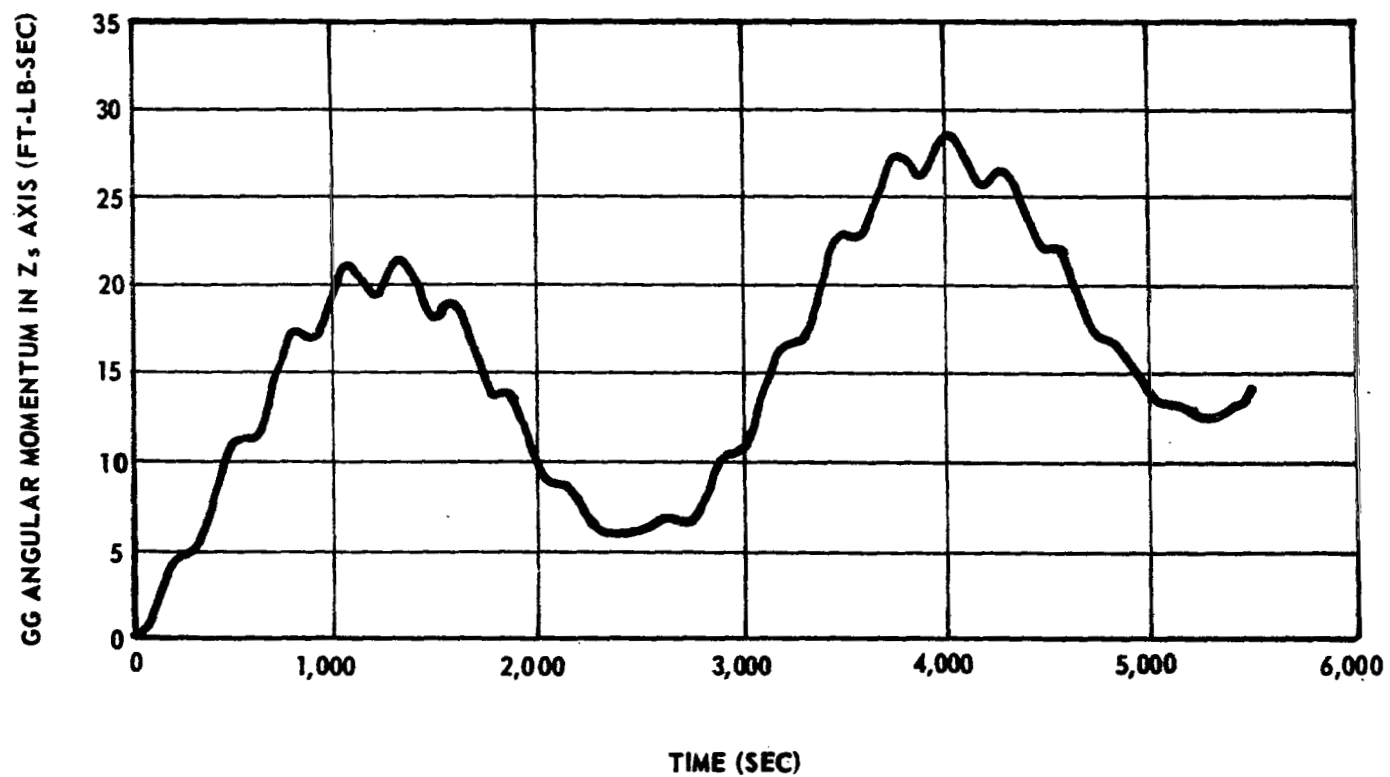Figure XI-34. Gain in angular momentum caused by gravity torque in the Y_s axis during one orbit.

Figure XI-35. Gain in angular momentum caused by gravity torque in the Z_s axis during one orbit.

The control logic for the magnetic torquers has been programmed to take advantage of favorable field components whenever possible and to minimize the undesirable torque components.

Figures XI-36 and XI-37 are the plots of the drift of the scan axis caused by the gravity gradient torques, as calculated by the Computer Simulation program. The case simulated is the baseline spacecraft configuration having a spinning flywheel with no control torques applied. Figure XI-36 shows the scan axis drift angle (δ) as a function of orbit time. The drift angle δ was set at zero at time zero. The scan axis drifts continuously and reaches a value of 2.25 degrees in one orbit time of 5520 seconds. Figure XI-37 is a plot of the trace of the scan axis in the ψ-θ plane, which is normal to scan axis for small values of ψ and θ angles. The angle ψ increases almost continuously caused by secular gravity torque in Y_s axis. The angle θ is near cyclic with a small secular component at the end of the orbit time. The variations in the angle θ are caused by gravity torque in Z_s axis.

Figures XI-38 and XI-39 are the plots of data generated by the Computer Simulation program for the case of the baseline spacecraft configuration having a spin flywheel with magnetic control torques applied. The disturbing torques are gravity gradient torques.

The magnetic control torques are applied to the spacecraft whenever the scan axis drift angle δ becomes equal to or greater than 0.100 degree. They are applied continuously as long as the orientation of the earth's magnetic field remains favorable, until δ decreases to 0.067 degree. These deadband limits on δ were selected for simulation purposes only.

Magnetic torquers are operated in an on-off fashion. A torque pulse with a 10-second duration is applied, shut off for 1 second, and then applied again. This sequence is repeated for as long as the torque is utilized. This on-off operation is required for the magnetometers to sense the earth's magnetic field during the off period.

Three coils were used for spacecraft control in the Computer Simulation program, with one coil mounted along each spacecraft principal axis. The resistance of each coil is 10 ohms and the physical constant K of each coil is 0.35 turn-meter^2. K is defined as the ratio of the coil magnetic moment amp-turn-meters^3 to the current in amperes. The power for the magnetic torquers has been limited to 100 watts maximum.
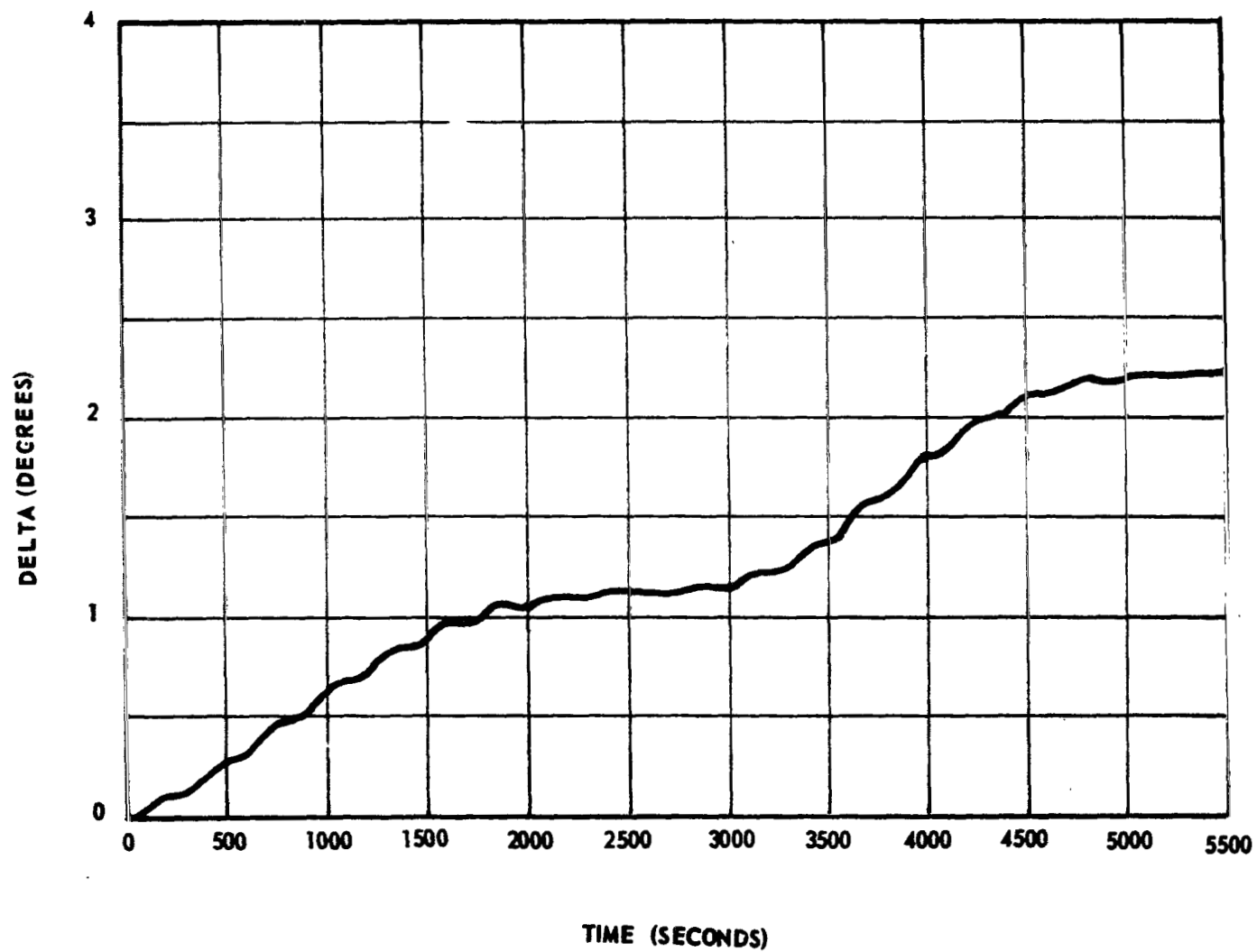
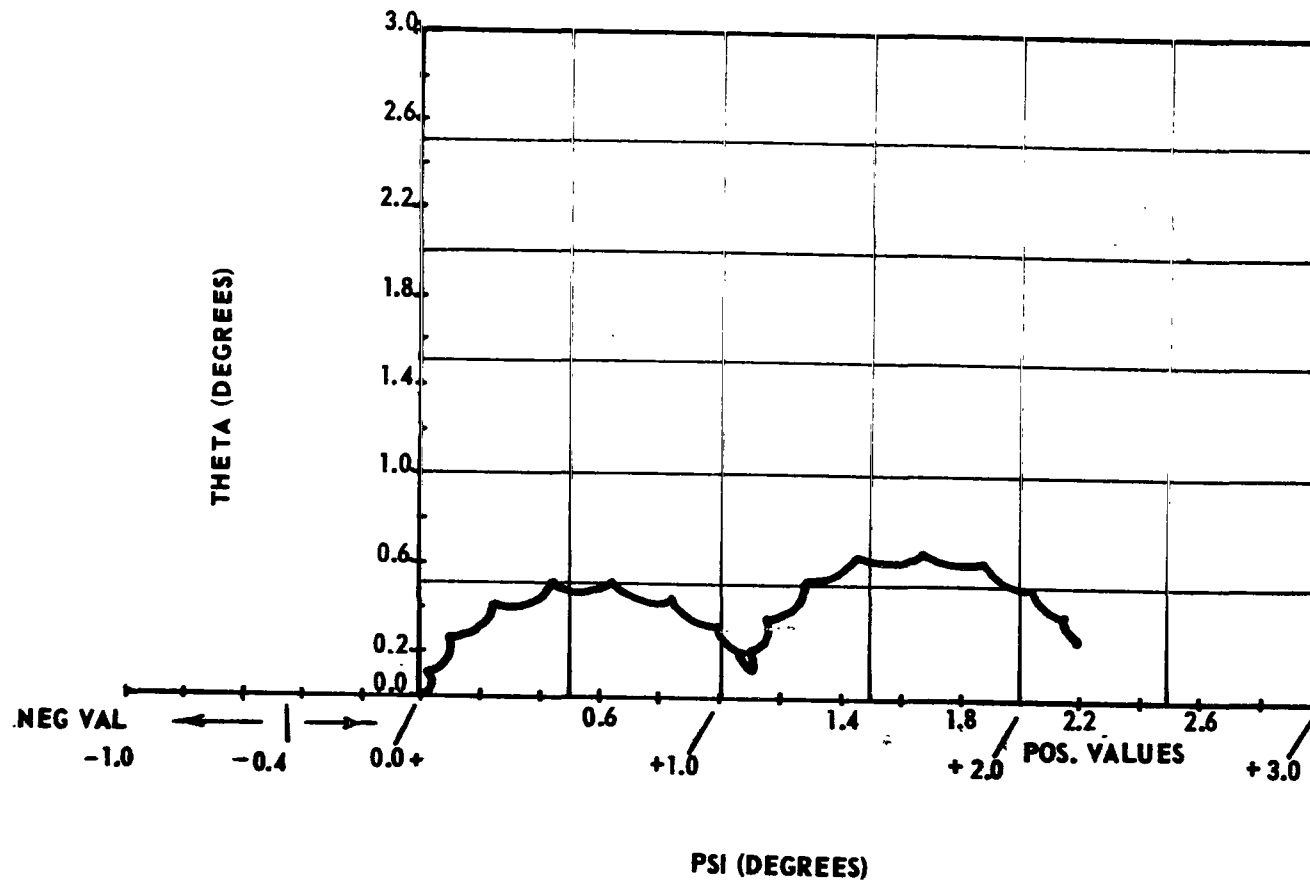Figure XI-36.   Scan axis drift angle δ of the uncontrolled spacecraft during one orbit.

Figure XI-37. Trace of the scan axis in ψ - θ plane caused by gravity gradient
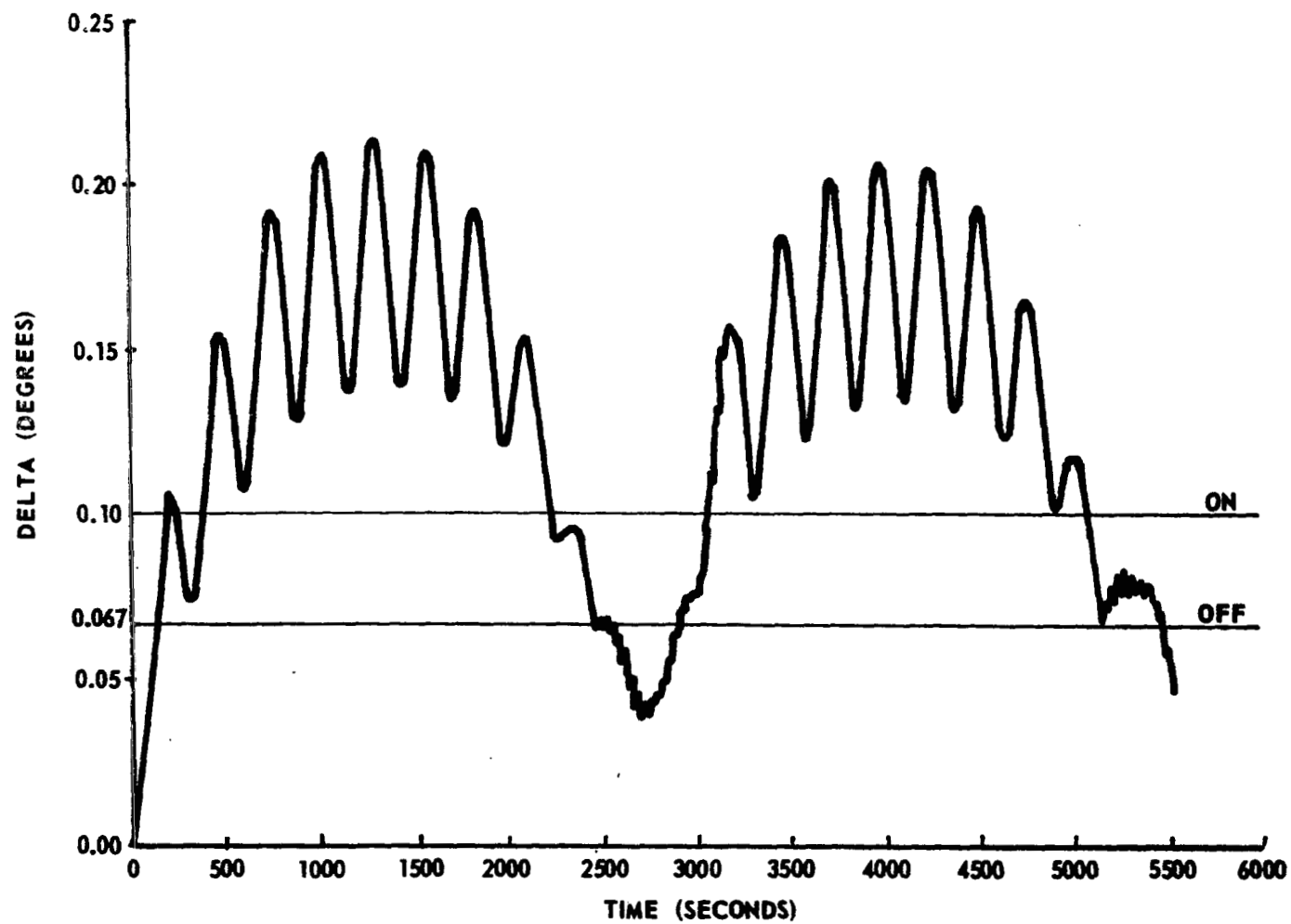disturbance torques, uncontrolled spacecraft.

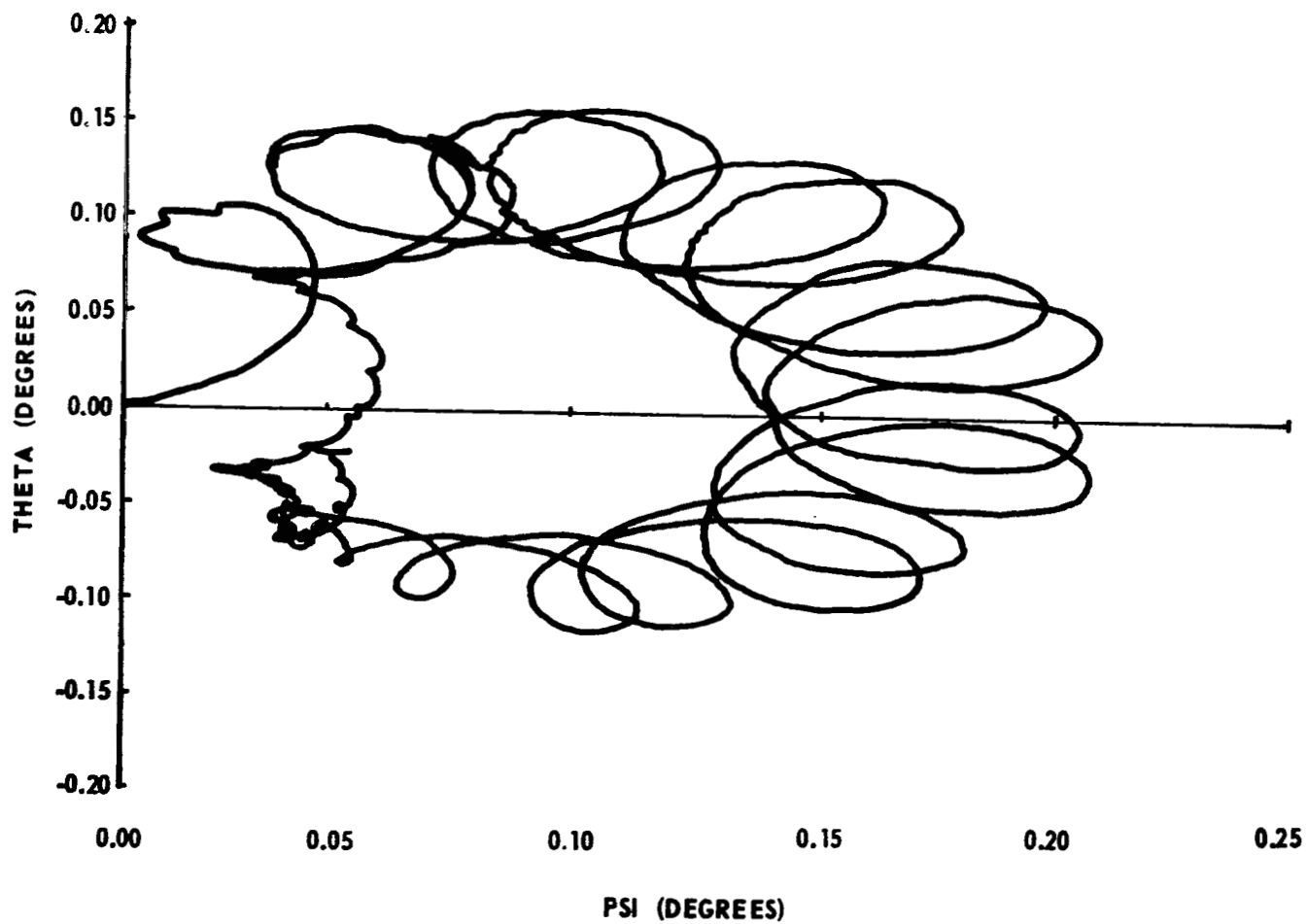Figure XI-38. Scan axis drift angle, δ, for the controlled spacecraft.

Figure XI-39. Motion of the scan axis in the $\psi - \theta$ plane for the controlled spacecraft.

Figure XI-38 is the plot of the scan axis drift angle δ with orbit time. The value of δ never exceeds more than 0.22 degree. The value of δ starts increasing at a faster rate at about 800 seconds and goes to its peak value of 0.22 degree at 1300 seconds, and then drops at a faster rate to less than 0.067 degree in the next 1200 seconds, at which time the magnetic torquers are cut off. This same cycle is repeated during the 3000- to 5000- second interval. The reason for the buildup of δ during 800 to 2000 seconds and 3600 to 4800 seconds is that the gravity gradient torque in X and Y axes nearly reaches maximum in these ranges. Figure XI-39 is the plot of the trace of the scan axis in $\psi - \theta$ plane. Figure XI-40 shows the variation of the scan rate in one orbit time. The variation in the scan rate is about ±1 percent.

The maximum available coil power of 100 watts is not required, as illustrated in Figure XI-41 for a nominal condition. Using a three-coil control logic scheme for scan axis pointing control less than 1.5 watts, continuous power usage is required. Much higher power levels are encountered in single coil situations, such as might be encountered at certain orbital positions or with a coil failure. For example see Figure J-26 in Appendix J.

Alternate spacecraft performance simulation results are given in Appendix J for the baseline vehicle, with a control logic which utilizes one coil for scan axis pointing control and for an alternate configuration with the longitudinal axis of minimum inertia directed toward the sun. The three-coil control logic appears to have several advantages over the one-coil logic, especially power usage and continuous rate feedback for spacecraft damping, and has been selected as the baseline control scheme for the HEAO.

E. Conclusions and Recommendations

Sensor hardware design types were selected for the baseline system configuration primarily on the basis of spacecraft operational mode attitude sensing requirements. The types of sensors selected appear to be feasible and readily adaptable designs for mechanization of attitude control. Alternate sensor designs, which warrant additional consideration for application in the HEAO spacecraft, are presented in Appendix J.

The slitted reticle star mapper selected for the baseline does not include a motor driven reticle; therefore, it is unsuitable for application in the celestial pointing mode; however, by adding a motor and angle encoder to
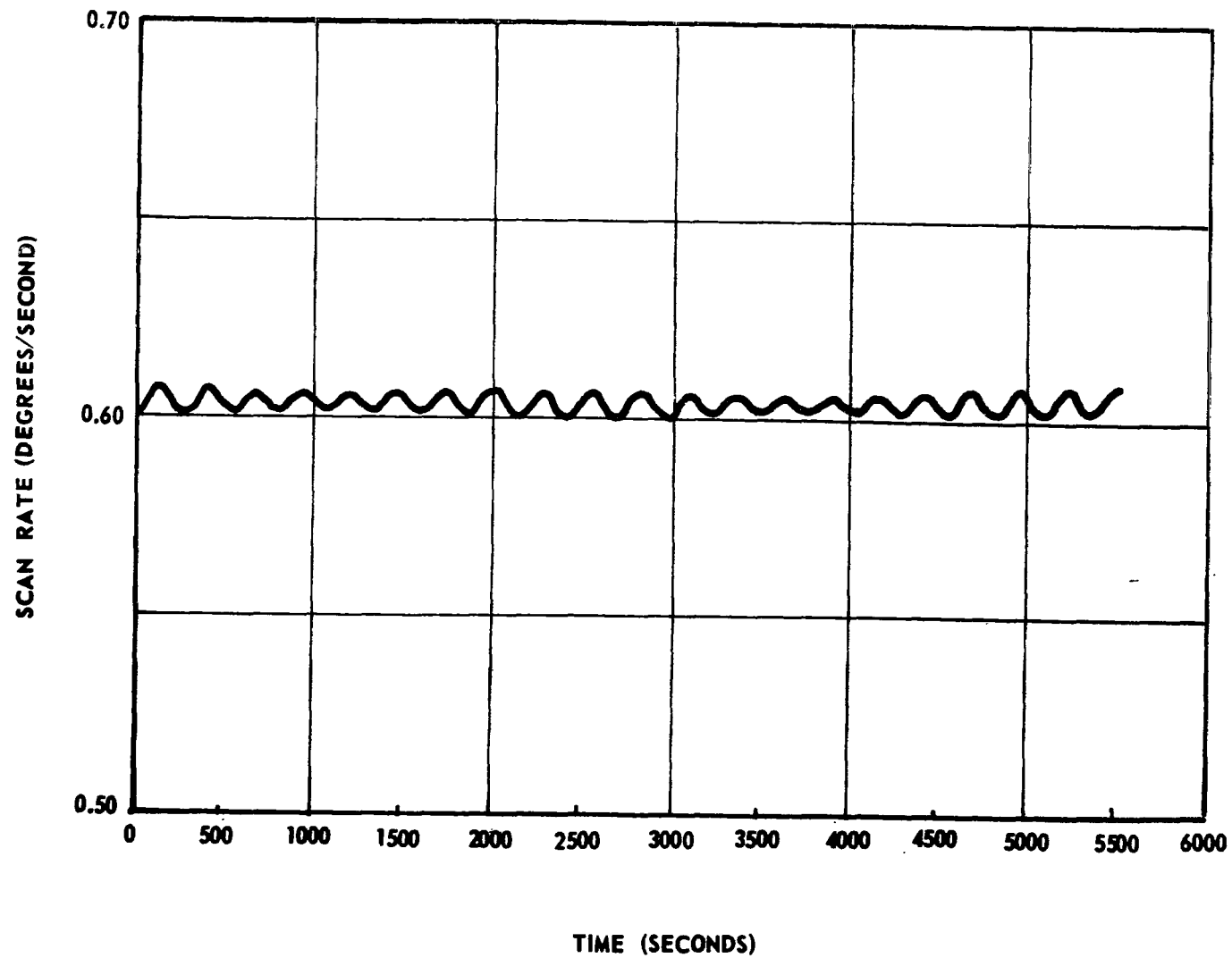
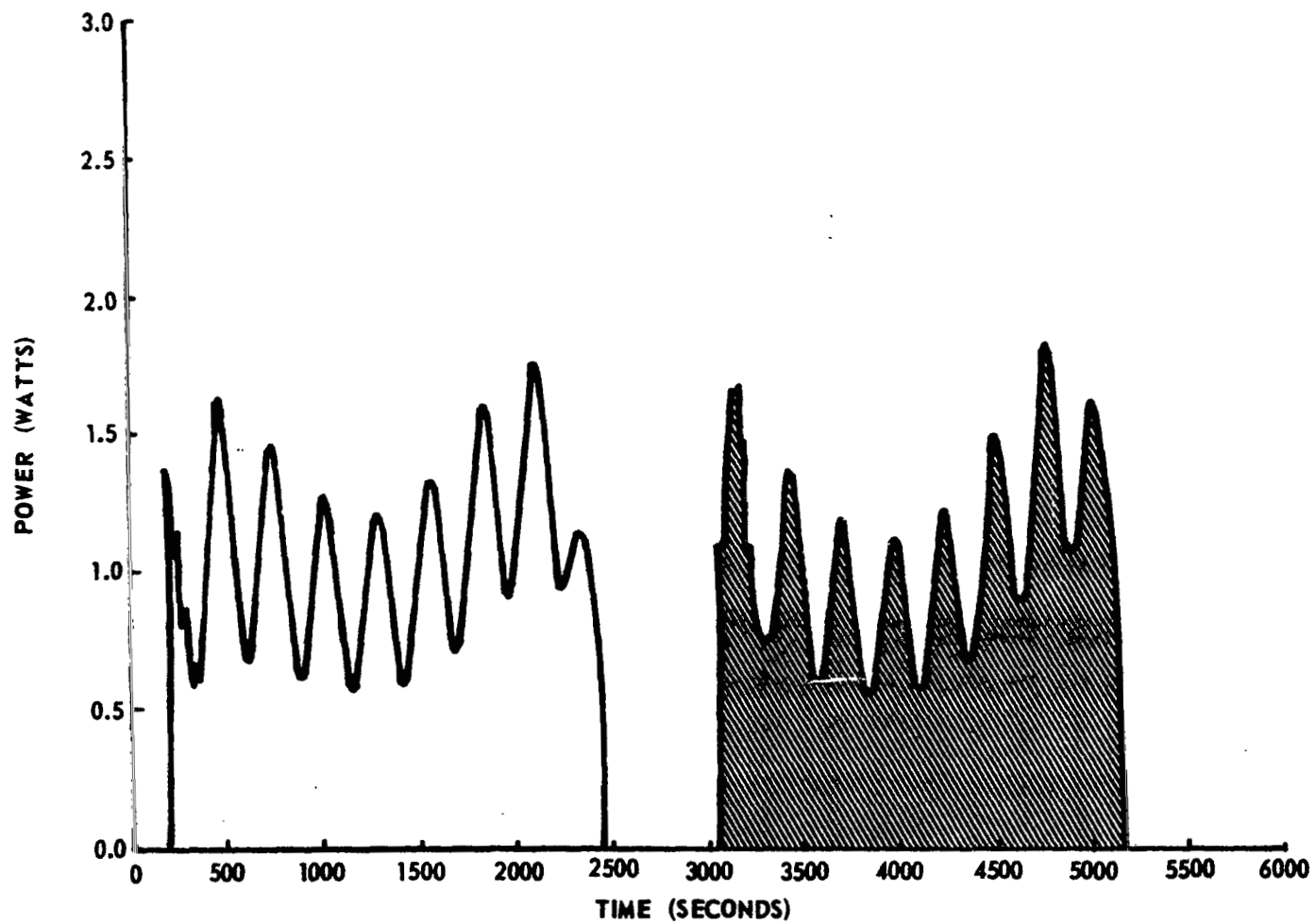Figure XI-40. Scan rate variation in one orbit of controlled spacecraft.

Figure XI-41. Power profile for the magnetic torquers.

the basic design, it can also function as a tracking sensor. The reliability of the motor driven reticle may be high enough to warrant consideration of using the slitted reticle mapper in the pointing as well as the scanning modes.

The dual mode (beam scanning) type star tracker would provide both stellar mapping and target pointing capability. The beam scanning mode would be used in the celestial and galactic scan modes. The track mode would be implemented for celestial pointing. For spacecraft maneuvers, the track mode could be switched in to identify a known star for a position fix to begin the maneuver. The tracker would be switched back to stellar mapping once the manuever was completed and the new spacecraft position verified. The tradeoff between the beam scanning star tracker and the slitted reticle star mapper is the degree of complexity in the mechanization scheme and the reliability assessment of the resultant hardware.

Use of the earth horizon scanner (conical design) as an alternate to the star tracker for a position reference in maneuvers has the advantage of viewing the earth continuously except for small time periods during the orbit as opposed to the star tracker which views the target only once per revolution of the spacecraft. In addition, the star tracker has to be able to recognize a known star to define attitude position. Horizon scanners are expensive and heavy, but the cost can be reduced by simplifying the design for a particular application. In the HEAO mission, more onboard calculations to determine attitude position might be performed by the signal processing subsystem. This would simplify the sensor design and cost. Spacecraft attitude position fixed by computation can be keyed to bypass the points in orbit where the horizon scanner would be "earth" saturated.

The magnetometer used for earth magnetic field sensing is mounted on an extendable boom in the baseline configuration. Use of an extendable member is somewhat undesirable from an operational reliability standpoint. It would be more desirable to have all sensors body-mounted to the spacecraft with no deployment mechanisms. When the magnetic coils are energized, a magnetic field is created that would interfere with magnetometer operation if the magnetometer is located in the proximity of the coils. A detailed design analysis must be made to determine the effect of the coils on the magnetometer and other items on the spacecraft. Shielding requirements and component location restrictions can then be determined.

Preliminary analysis has indicated that the magnetometer may not have to be boom-mounted. Computing earth field parameters is an alternative to direct measurement, but it appears to be too complex and subject to more error.

Gimbaled sensors' potential applications were discussed briefly; however, because of recognized low reliability, no in-depth study was pursued. It is recommended that any improvement in space-qualified bearing lubricants be reviewed for application in gimbaled sensors which have the potential of upgrading HEAO sensor performance.

Computer simulations of spacecraft responses to gravity gradient disturbance torques and magnetic control torques have been performed. Two different control schemes for scan axis attitude control have been simulated:

- A three-coil scheme in which one coil is mounted on each of the body axes.

- A single-coil control logic scheme in which only one coil is used for scan axis pointing control.

The results to date indicate that the three-coil control scheme gives better performance than the single-coil control scheme. With the three-coil control scheme it was possible to generate continuous control torque; whereas, with the single-coil scheme, it was not possible to generate continuous control torques because of the orientation of the earth's magnetic field.

Since continuous control is feasible using the three-coil scheme, the flywheel system for providing additional stability against disturbance torques may not be required. The power requirements for the three-coil control scheme is less than for the single-coil control scheme, because the magnetic moment generated by the three-coil system is always made normal to the earth's magnetic field. The only disadvantage of the three-coil scheme is that it produces undesirable torques about the scan axis. Since scan rate variations up to ±10 percent are allowed, this seems to be not much of a problem. It is therefore preferable to use the three-coil control scheme during the scan modes.

More computer simulation data are required to determine the feasibility of using the magnetic torques for the pointing mode, initial sun acquisition, flywheel spin-up, spacecraft spin-up, and for going from one mode to another mode. If magnetic torquers appear feasible for the above operations, then a jet control system may not be required for any phase of the mission. The feasibility of using 6 jets instead of the 12 jets now defined on the baseline configuration should be investigated.

The magnetic coils should be optimized with respect to the sum of coil weight and the additional weight penalty associated with their electrical

power requirements. Coil weight can be traded against coil electrical power requirements.

Although a limited number of simulation runs have indicated stable closed loop performance using the magnetic torquing system even though nutation or wobble damper devices were not utilized, consideration for including these devices for performance improvement of the ASCS should be given attention in the future iterations of the HEAO baseline. The requirements for a nutation damper should especially be evaluated and established for those portions of the mission using reaction jet thruster control since no performance simulation runs to date have been made for these mission phases.

Redundancy concepts for the ASCS must be given considerable attention in future studies. A logical approach is to determine how the baseline configuration of ASCS components can be modified on command by an onboard switching function to utilize certain components in a dual capacity. Possibilities that should be considered are the differentiation of certain angle measurements to obtain rates and the processing of certain sensor outputs in different ways to obtain attitude information. System performance should be assessed for any such multiple usage schemes. The extension of this approach would be to determine the minimum redundancies required to assure mission success.

REFERENCES

XI-1. White, J. S.; Shigemet, F. H.; and Bourquin, K.: Satellite Attitude Control Utilizing the Earth's Magnetic Field. NASA TND-1068, August 1961.

XI-2. McElvain, R. J.: Satellite Angular Momentum Removal Utilizing the Earth's Magnetic Field. American Astronautical Society, Goddard Memorial Symposium, Washington, D. C., March 16-17, 1962.

XI-3. Mobley, F. F., et al.: Performance of the Spin Control System of the DME-A Satellite. Presented at the AIAA Guidance and Control Conference, Seattle, Washington, August 15-17, 1967.

SECTION XII. MISSION OPERATIONS

TABLE OF CONTENTS

SECTION XII. MISSION OPERATIONS

A. Introduction N70-22912

1. <u>Scope.</u> The HEAO Mission Operations is an element of the overall HEAO program management and will be under the leadership of the mission director. The major operational elements will be combined to form the HEAO mission operations system. The HEAO Mission Operations system includes the following: plans, systems, interfaces, time-phased sequence of events, procedures and facilities necessary to perform launch and flight operations planning, produce mission software (computer programming), operate launch and mission control facilities, monitor and control the launch vehicle, spacecraft and experiments during launch operations and in flight, obtain data for operational control and manage the acquisition, and processing and distribution of launch and mission control and experiment data.

2. <u>Guidelines and Assumptions.</u> In arriving at a mission operations approach within the scope outlined above, the following guidelines and assumptions were considered:

    a. In the operations area, major interfaces will exist between elements of MSFC, OSSA, GSFC, KSC, AFETR and the launch vehicle management center concerning the prime operational considerations and as these considerations affect the spacecraft, experiments, launch vehicle, launch facilities, the tracking and data network and the control centers.

    b. The Unmanned Launch Operations (ULO) at KSC will be responsible for launch operations.

    c. The Titan III class vehicle will be the primary launch vehicle considered.

    d. The launch operations will use existing Titan III facilities at KSC which will be modified, as required, to accommodate the unique requirements of the HEAO mission.

    e. The mission operations system will be supported by the HEAO prime contractor.

f.   The launch of the first spacecraft will occur in March 1974; the second spacecraft is to be launched 1 year later. Due to the orbital lifetime goal of 2 years, the mission operations system must consider support of two spacecraft in orbit simultaneously.

g.   The Satellite Tracking and Data Acquisition Network (STADAN) will be utilized for acquisition of mission control operations data and the experiments data. A data relay satellite system may be available to HEAO in the desired time period; however, because of uncertainties of implementation, the data relay satellite system has not been considered as a primary system.

h.   GSFC will be responsible for implementation of the STADAN and other required network stations; Greenbelt, Maryland, will be the primary candidate for the mission control center. The final selection of a mission control center is still under consideration.

i.   The Huntsville Operations Support Center (HOSC) may be available to support mission operations with design information and recommendations in the event of contingencies.

B. Launch Operations

1.   Scope.   The HEAO launch operations system includes spacecraft and launch vehicle receiving, testing, prelaunch servicing; space vehicle assembly and integration with the launch facilities; verification of launch readiness; launch countdown and launch operations through spacecraft separation from the launch vehicle in flight. The launch operations system will also consist of personnel, facilities, ground support equipment, a ground instrumentation system, and associated software at KSC and the Air Force Eastern Test Range (AFETR). Program considerations having a significant impact on launch operations include the objective, due to scientific considerations of launching in either March or September of the selected launch year.

The HEAO Program Office will define and document launch operations requirements. These requirements will be forwarded to and coordinated with KSC/ULO for implementation.

2.   Approach to Vehicle Integration.   The major functions associated with the preparation of the launch vehicle include build up of the Titan core in the Vertical Integration Building (VIB), assembly and integration of the solid

stages at the Solid Motor Assembly Building (SMAB), transfer to the launch complex, and prelaunch checkouts and testing at the launch complex. The launch complex planned for the HEAO launch will be at pad 41. The Titan III Integrated Transfer and Launch (ITL) complex at Cape Kennedy Air Force Station (CKAFS) will be used for this operation. Launch pad 41 and transfer hardware will require modifications to process the Titan IIID/HEAO spacecraft integrated vehicle.

The spacecraft and the experiments will be initially delivered to one of the hangars in the KSC/CKAFS industrial area (hangar AE, AO, etc.) for receiving inspection. Clean rooms are available to accomplish this effort. The specific clean room (and hangar) used will depend on whether the spacecraft needs to be vertical during the checkout or whether the checkout can all be accomplished with the spacecraft in the horizontal position. All of the hangars do not have the height capability to handle the spacecraft in the vertical position.

When the spacecraft has been checked out, it will be transported to the Explosives Safe Area where installation of ordnance and pressurants and filling of the hydrazine tanks may be accomplished. From there it will go to the launch pad, where the launch vehicle has preceded it, to be mated to the Titan IIID vehicle.

3. <u>Approach to Prelaunch Verification.</u> As a goal, the spacecraft prelaunch operations at the launch complex will be limited to those functions which are necessary for assurance that all systems are functionally flight ready so that the launch schedule can be met. Prelaunch testing will also include limited performance verification tests and compatibility tests with the tracking and data system, Launch Control Center, and the Mission Control Center. An adequate number of spares will be prepared for each launch opportunity to provide an acceptable contingency for the limited launch periods. A refurbished prototype spacecraft may be available as a back-up or spare in the event of major failure.

Functional and compatibility tests of the spacecraft will be performed, after which composite space vehicle tests will be conducted. These tests will verify interfaces involving the systems, spacecraft, vehicle stages, space vehicle, and ground support equipment.

Readiness tests will be conducted to verify flight readiness of the launch, flight, and ground systems. A simulated launch countdown will be performed to verify readiness of the space vehicle and associated ground support equipment. In conjunction with these tests, operational readiness tests

(ORT) will be conducted to assure readiness of the complete ground-based tracking and data system, including the Mission Control Center. Simulated data will be entered at each ground tracking station utilized for launch operations and will be processed through the data system and displayed in the proper display devices at the Launch Control Center (LCC). The flight operations system will also participate in these tests and satisfactory completion of the tests will include the acquisition, processing, and display of the data and the exercising of command functions at the HEAO Mission Control Center.

Launch readiness will be certified in a Flight Readiness Review held at KSC prior to launch. The program manager will ascertain the readiness of the space vehicle and the operational elements of the HEAO Program and make decisions concerning the continuation of launch preparations.

4. Approach to Launch Operations Control. The launch countdown will be conducted from the Titan III ITL LCC. The KSC/ULO Launch Director will be responsible for the space vehicle countdown and ETR support. The launch director will be assisted by a space vehicle launch conductor and by test conductors for the spacecraft and each appropriate launch vehicle stage. The HEAO Mission Director will be responsible for the overall mission countdown and will coordinate the space vehicle countdown with the prelaunch preparations of the tracking and data systems and the flight operations system. The launch operations system will be responsible for mission control until separation of the spacecraft from the launch vehicle in flight, nominally expected to occur following the insertion burn of the launch vehicle.

The launch operations system will provide tracking, instrumentation, and data handling support from the beginning of launch countdown through spacecraft separation.

C. Flight Operations

1. Scope. The HEAO Flight Operations System consists of those elements required to perform flight planning, prepare mission software (computer programming), conduct flight team training, operate mission control facilities, monitor and control the spacecraft and experiments during flight, and obtain data for operational control and experiment evaluation. Flight operations encompasses the responsibility for mission control beginning with launch vehicle/spacecraft separation and continuing until the completion of the HEAO mission. The flight operations will normally be under the direct control of a flight director.

2. Approach. The primary objective of HEAO Flight Operations is to return the maximum amount of useful scientific data from the spacecraft. HEAO program considerations that will have a significant impact on flight operations are the length of each mission (1 to 2 years) for the anticipated four launches and the need to control two spacecraft in orbit simultaneously after the first year of operation.

Many of the flight operations techniques developed for previous orbiting satellite missions can be applied directly to the HEAO Flight Operations approach. The overall flight operations system design will be based on centralized control exercised from a central control center. The approach is also based on the use of the STADAN network for tracking and data acquisition.

A number of central control centers will be considered to provide flexibility when arriving at a final selection. The operational ground rules and preliminary requirements, mentioned in the following paragraphs, have been developed to conduct a survey of existing facilities that may serve as a central control center; these operational ground rules and preliminary requirements will be utilized in house by NASA and by the Phase B contractors in determining a primary control center and a number of alternatives. Final selection of the actual control center will include considerations such as availability, existing capability, network interfaces, compatibility with the scientific community needs, and cost of operation for the planned time period.

In conjunction with the centralized control approach, the Mission Control Center will require the capability for receiving, processing and display of tracking, telemetry, and command data for both the spacecraft and experiments, and, as mentioned earlier, must provide for control of two orbiting vehicles simultaneously.

The HEAO Flight Operations approach dictates that all command decisions be made at the mission control center and that the data required for command decisions be made available at the control center; also, where practical, the command action will be initiated at the control center. In conjunction with this command philosophy, the supporting network should allow for one command contact per orbit from the control center, with exceptions where ground site coverage is not available.

For Flight Operations System design considerations, the number of commands required has been estimated. (One estimate places the number at 419, but the actual number can vary significantly, depending upon system

sophistication and autonomy.) This is based on the need to accomplish orbital checkout after launch and includes commands necessary to get spacecraft systems and experiments into operational modes.

The orbital checkout period is estimated to require about eight orbits, or 12 hours. Wherever possible, preprogrammed sequences will be stored on board and will be backed up by ground command capability. The option to turn off some experiments or to intermittently operate some experiments will be exercised in real time by the mission or flight director after consultation with the affected principal investigators. In the event of intermittent operation it will still be possible to get representative data due to its repetitive nature covered by spacecraft rotation about the z-axis.

Tracking for orbit determination will be required on the first through the eighth orbits, as early orbit determination is needed; some assistance will probably be required from the MSFN sites during this early period. Intermittent tracking will be required for orbital decay determinations and the determination of communications, acquisition, and LOS times for the network sites.

The spacecraft systems operations data requirements for flight operation are estimated to be in the range of 100 to 150 status measurements for systems analysis. The experiments status measurement requirements cannot be accurately determined at this time. A continuous data recording will occur at a 27.5-Kb/s rate and tape data dumps will be scheduled approximately every 1 1/2 hours, depending on station coverage. Real-time data are required for both spacecraft and experiments status. Near real-time data are required to assess spacecraft and experiments operation between orbits to make corrective adjustments, as required. This approach is particularly true during the first month of operation, and during the seventh through the thirteenth months when numerous commands for repositioning are expected to occur.

A flight operations support facility may be established at MSFC, HOSC, to support the Mission Control Center's operation. The HOSC facility may be used to display flight data for spacecraft systems and experiment evaluation.

Operational personnel and computer programming will be required as early as 1 1/2 years prior to launch. One year prior to launch, operations personnel will be needed to begin initial activities, such as the initial flight operations planning, establishing procedural timelines, and conducting systems training and simulation. The operations team will include either principal investigators or their representatives.

D. Information Management

1. <u>Scope.</u> Information management includes plans, ground systems, and facilities necessary to provide for flight data acquisition transmittal, processing, distribution, and storage for all mission phases, including experiment data.

2. <u>Approach to Network Utilization.</u> It is anticipated that STADAN will be the primary network employed for spacecraft and experiment operation and control. If the needed coverage so dictates, other ground communication sites from other networks, such as the Manned Space Flight Network and sites operated by the AFETR, may be called into use. This would be especially true in the period immediately after launch when range safety and the determination of orbit are of prime importance.

Experiment and spacecraft system data needed for operational control will be transmitted to the control center in real time or in as near real time as possible for spacecraft/ experiment operation evaluation. All operations decisions will be made at or through the control center and all commands will be implemented from there.

3. <u>Approach to Information Processing and Distribution.</u> Mission data processing and distribution can be separated into two categories: the data processing which is required for operational evaluation for mission control purposes and the final processing, distribution, and analysis of the scientific and engineering data.

A mission software system will provide a data processing system compatible with STADAN (and any other sites employed) hardware and software, which will collectively perform the control, recording, transmission, display, and analysis functions required to process telemetry, tracking, and command data for up to two spacecraft in orbit simultaneously. Support software will also be prepared to complement the above operational software to support personnel training and data reduction. Development and integration of the software system will be controlled by the HEAO Program Office. Software requirement will be documented and preparation responsibilities assigned to specific organizations. Design of the software will be integrated with the spacecraft design and with the mission design activities. Integration of this software with the network software system will be accomplished in time to support the mission training and simulation activities.

The mission operations system will coordinate and document mission data requirements and will implement a plan for their collection, processing, and distribution. Final science data analysis and evaluation will be performed by the principal investigators and as required by sites designated by the HEAO Program Office.

The operating team will analyze sufficient mission data in real time to ensure that mission objectives are being satisfied.

SECTION XIII.   PROGRAM SUPPORT

TABLE OF CONTENTS

TABLE OF CONTENTS (Concluded)

LIST OF ILLUSTRATIONS

SECTION XIII. PROGRAM SUPPORT

A preliminary analysis of the HEAO-A program was accomplished to identify the major elements of program support, and to establish an approach and rationale for further study. All areas of program support identified are recommended for study in Phase B. The broad areas of program support requirements identified are discussed in the following paragraphs.

A. Ground Support Equipment N70-22913

1. General. The term "GSE" as used in this document refers to all mechanical and electrical ground equipment required for all ground operations except manufacturing. For purposes of discussion, the GSE is grouped into the following broad categories based on the principal functional area of utilization:

      a.   Acceptance Testing.

      b.   Transportation, handling, and access.

      c.   Launch site.

      d.   Mission operations.

      e.   Experiments.

The number of sets of GSE required is a function of the number of end items of hardware required, their frequency of manufacture, the launch schedule, the types and quantities of tests required, the quantities and locations of the various test facilities, and the number of flight articles in orbit at one time. Based on the current schedule estimates (Fig. XIII-1) there appears to be no major GSE requirements overlap between the various test articles and the first flight article, nor between the first and second flight article. For purposes of this study, the second flight article is considered to be the refurbished prototype article.

The greatest problem related to quantity of GSE required arises from the possibility that test facilities in different locations will be used for systems testing in ambient, magnetic, vibration, and thermal-vacuum environments. All systems should be functioning to varying degrees in each of these environments, which would require GSE during each test. It is not
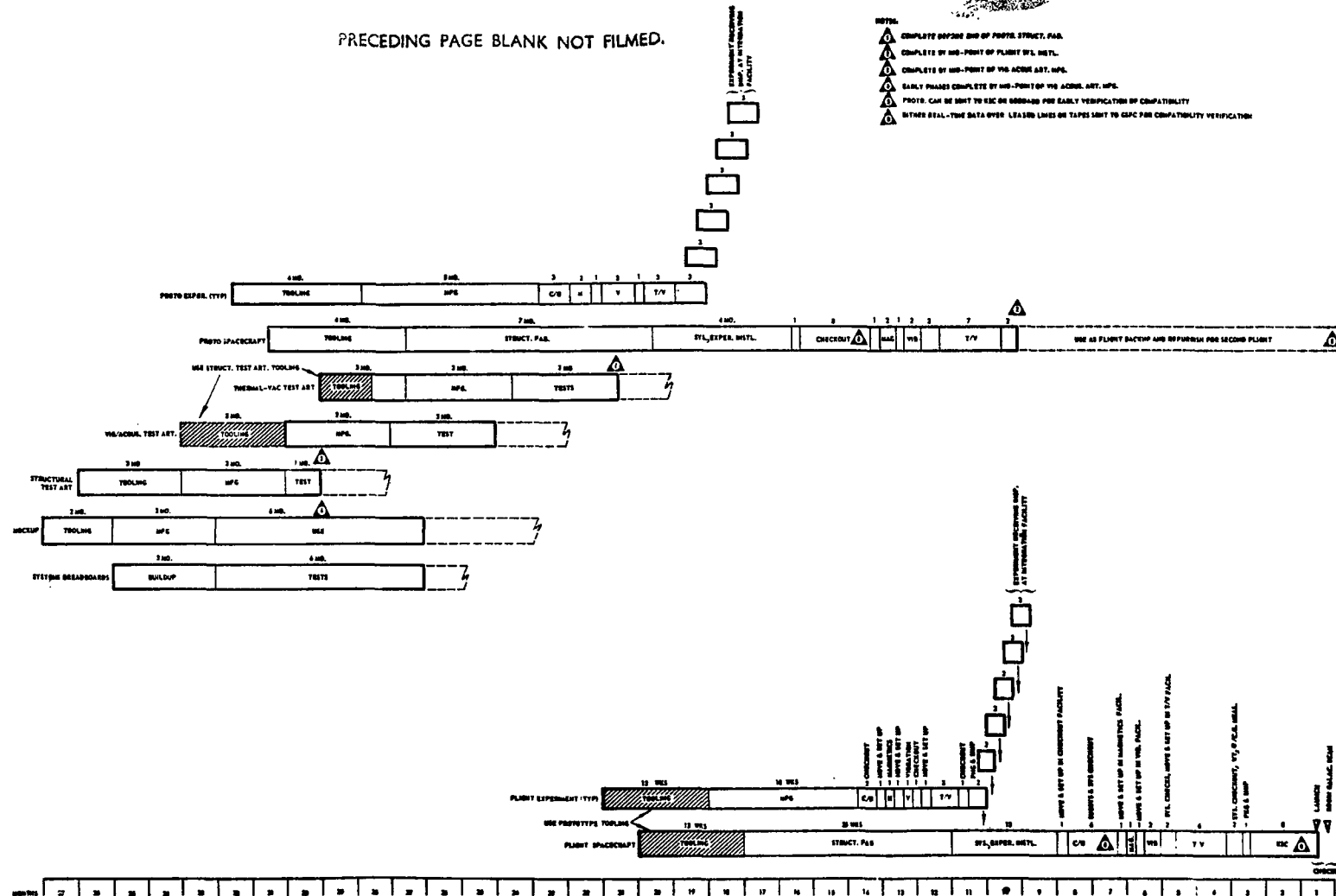
Figure XIII-1. HEAO Hardware Schedule

desirable to have a separate set of GSE at each facility. The two most apparent solutions to this problem are (1) to select a location which has all of these facilities in close proximity to each other and use remote control from one central location to each facility with limited supplementary GSE in each, and (2) to have a set of portable GSE which travels with the end item to each facility.

The applicable GSE must be available for use on test articles as well as flight articles. All GSE must provide fail-safe features and protection from damage to the end item being tested. Existing GSE from other programs should be used wherever possible.

2. Acceptance Testing. Acceptance test equipment is required for testing each end item after (and sometimes during) its manufacturing or assembly process is completed. This includes GSE for bench-level tests on components (black boxes) and assemblies and GSE for tests on subsystems, systems, and integrated systems after manufacturing of a major end item. The major elements of a typical checkout complex for a flight HEAO-A spacecraft are shown in block diagram in Figure XIII-2. It is expected that the number of umbilical functions and launch vehicle interface functions required will not be extensive (see Section V), and, to save weight, test connections will be provided internal to the HEAO-A spacecraft; therefore, drag-in test cables will be required for most functions. If the launch vehicle interface is small, the launch vehicle simulator will be small or unnecessary. However, it is shown here to indicate that it is a possible requirement. Coaxial cables are shown for the RF equipment. The primary use of the computer will be for data acquisition, formating, and display.

3. Transportation and Handling. Horizontal transporters for the HEAO-A end items, similar to those for stage handling, will be required. The possibility of modifying existing transporters for use on the HEAO-A should be investigated. All candidate transportation systems should be investigated. Environmental control and some instrumentation will be required during transportation. A cover for weather protection must be provided.

There must be handling rings on each end of the spacecraft for rotation while in the horizontal transporter, and to provide hard points for attaching slings, etc. Slings must be provided at both ends for lifting and attitude translation of the spacecraft.

4. Launch Site. Equipment must be provided for the prelaunch verification of the operational readiness of the spacecraft at KSC. This
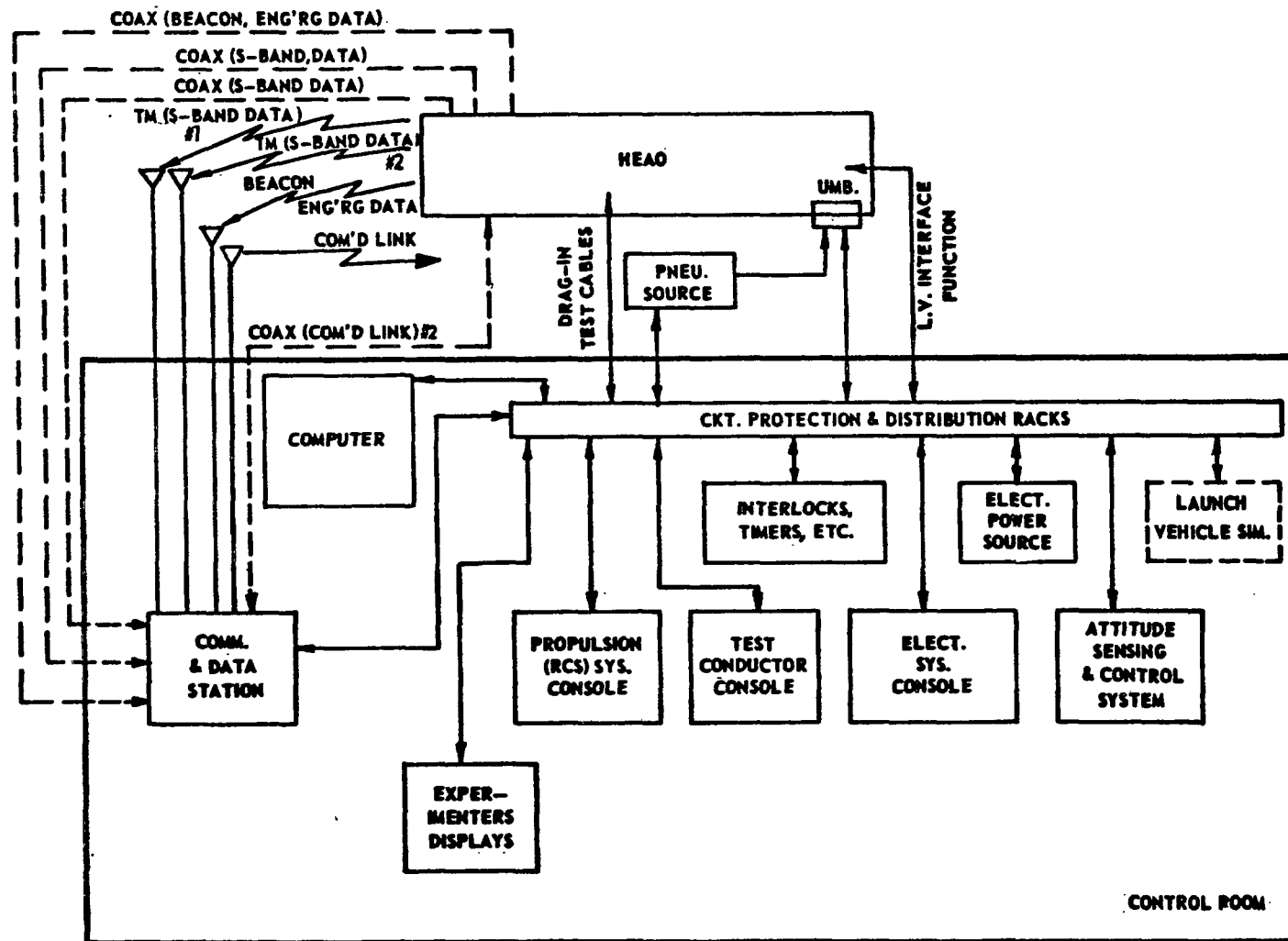
Figure XIII-2. Typical flight HEAO checkout complex.

equipment must be capable of operating all systems on board the spacecraft, but not necessarily to the same depth as with the upstream GSE. Communication and data handling must be provided to verify the transmitted data and the communications equipment.

Although it has not been established which HEAO-A systems must be active during launch, it is anticipated that most systems will not be active. Therefore, the quantity of umbilical functions required for launch is expected to be small, and, consequently, the quantity of active GSE for the spacecraft during launch should be small.

Capability for external and internal access to the spacecraft while in the stacked configuration on the launch pad must be provided at KSC.

5. <u>Mission Operations.</u> Equipment must be provided for ground tracking, data acquisition, command transmission, and data processing and display during the mission. The STADAN network has been recommended for use on HEAO-A, but its capability may require upgrading to handle the volume of data from HEAO-A plus other concurrent programs. The equipment available in STADAN stations and its capability has been investigated and is discussed in Section X.

6. <u>Experiments.</u> The experiment contractors should provide all GSE and perform all testing required for their experiments prior to their installation in the spacecraft. The capability of verifying each experiment while removed from the spacecraft is usually required at KSC as a contingency measure. In addition, there may be servicing, calibration, handling, inspection, access, repair, maintenance, replacement, and environmental control GSE required to travel with the experiment after its installation into the spacecraft. It may be feasible to integrate some of the experiment contractors' acceptance test GSE into the spacecraft checkout complex rather than designing duplicate equipment within the complex to operate each experiment. This must be investigated in more detail during follow-on studies.

B. Test Facilities

Preliminary analysis of the test facility requirements to support the HEAO-A program has not indicated any necessity for development of major new facilities. The need for extensive ground testing to assure high reliability in past programs through simulation of launch and orbital environments has resulted in construction of numerous test facilities by both government and

industry. It is anticipated that specific test requirements for the HEAO-A
program can be satisfied by minor modifications of selected elements of the
existing test facility complexes.

The principal spacecraft environments which require testing that can be
simulated on the ground are vibration, vacuum conditions, temperature, and
radiation. Table XIII-1 presents a summary of the capabilities of existing large
vacuum facilities which are potentially suitable for use in this program. This
is an indication of the extent of the existing test facility base. Further investi-
gation is required to identify potentially suitable static and dynamic testing
facilities; however, current indications are that adequate facilities exist for
component, subsystem and full-scale static and dynamic testing of the HEAO-A
spacecraft.

When the spacecraft and its supporting subsystems are more fully
defined, it will be necessary to determine specific test requirements and
select appropriate test facilities to accomplish the tests. Selection of the
facilities to be used will require a detailed analysis to ensure maximum cost
effectiveness through minimum modification, minimum movement of test
articles, and minimum interference with test schedules of concurrent programs.

C. Reliability and Quality Assurance

Reliability and quality assurance (R&QA) analyses must begin early in
any program and continue throughout the design and development phases.
Refinement and updating of this R&QA approach and data must be continued in
subsequent program phases.

Areas of Consideration. Specific areas that should receive special atten-
tion during these follow-on program phases are as follows:

1. Development and definition of reliability goals.

2. Failure mode effects analysis of each component, subsystem,
system, and spacecraft concept considered.

3. Reliability tradeoff analysis based on the long-life hardware
design approaches to emphasize the interrelationship of reliability, safety,
maintainability, and long-life assurance, and the design impact resulting
from the tradeoffs.

13-8

TABLE XIII-1. LARGE VACUUM CHAMBERS

Facility (Nominal Dim.)	Working Space or Specimen Size	Pressure Level	Solar Simulation	Other
Boeing 39 ft dia × 50 ft high	28 ft dia × 40 ft high (working space)	1×10^{-6} (ultimate) 1×10^{-5} Torr w/20 TL/sec O_2 or N_2 gas load	20 ft dia beam	Lunar plane cycle temp. from 325° F to -390° F
Douglas 39 ft dia sphere	30 ft dia sphere (working space)	1×10^{-6} (ultimate) 1×10^{-5} (working pressure)	Quartz lamps - Provisions for 20 ft dia beam	
GE 32 ft dia × 54 ft high	21 ft dia sphere (working space)	1×10^{-6} (ultimate)	22 ft dia Beam - Off axis xenon arc; collimated +3 to 5 deg at outer edge. Uniformity ±10% intensity 120 to 140 w/ft²	
GE 3(39 ft dia spheres)	21 ft dia × 30 ft high (working space)	1×10^{-6} (ultimate)	Iodine Quartzline lamps 300 w/ft² over 23 ft dia area	
Martin 29 ft dia × 45 ft high	24 ft dia × 36 ft high (test volume)	1×10^{-6} (clean, dry, and empty)	Infrared heating 1000 quartz lamps 500 kw each 260 w/ft² over 1100 ft² and 130 w/ft² over an additional 1100 ft²	
MacDonald 30 ft dia × 36 ft lg	27 ft dia × 33 ft lg (working space)	5×10^{-6}	Shroud temp. can be varied from -300° F to +275° F	Man-rated
AEDC 42 ft dia × 82 ft high	20 ft dia × 65.5 ft high (specimen size)	1×10^{-7} (ultimate)	Quartz - Iodine lamps; Uniformity ±3% over test field of 30 ft depth decollimation ±5 deg. Spectral adjustment by replacing source lamps with xenon short arc lamps	Rapid pump-down vibration capability
Goddard 28 ft dia × 40 ft high	27.5 ft dia × 40 ft lg (working space)	1×10^{-10} (ultimate)	Hg - Xenon; 70-140 w/ft² 20 ft dia beam; 130 w/ft² over 17.5 ft dia; uniformity ±10% over 17.5 ft area and 25 ft depth collimation 2.2 deg on ½ angle	
Goddard 33.5 ft dia × 59 ft high	33 ft dia × 59 ft high (working space)	1×10^{-8} (ultimate)		
MSC Chamber "A" 65 ft dia × 120 ft high	55 ft dia × 90 ft high (clear) 25 ft dia × 65 ft high (test specimen)	1×10^{-6} (ultimate) 6×10^{-5} w/27.6 TL/ sec gas load	Side sun - 13 × 33 ft - 65 to 145 w/ft² Top sun - 13 ft dia - 60 to 140 w/ft²	180 deg rotating lunar plane
MSC Chamber "B" 35 ft dia × 43 ft high	25 ft dia × 30 ft high (clear) 13 ft dia × 27 ft high (test specimen)	1×10^{-6} (ultimate) 6×10^{-5} w/27.6 TL/ sec gas load	Top - 5 ft beam - 60 to 140 w/ft²	Fixed lunar plane 80° - 400° K
Lewis Plumbrook	100 ft dia × 121 ft 5 in high	1×10^{-6} (ultimate) 1×10^{-9} pending future addition of shroud		Nuclear capability
Lewis Plumbrook ("B-2")	33 ft dia × 55 ft high (clear space) 22 ft dia × 50 ft high (test specimen)	5×10^{-6} (ultimate) 1×10^{-4} w/15 TL/ sec gas load	Radiant heat 130 w/ft² over 22 ft dia × 30 ft high area	
Lewis Cleveland	25 ft dia × 70 ft lg (clear space)	9×10^{-7} (ultimate)		
Lewis Cleveland	15 ft dia × 63 ft lg (clear space)	1×10^{-3} (ultimate)		

Lockheed, TRW, and Hughes have large chambers, but not large enough for a 9 × 30 ft test specimen.

4.	Overall program reliability and quality assurance assessment must be performed to identify any supporting research and new technology requirements, checkout system implications, new fabrication and testing techniques, and facility and equipment requirements which are necessary to obtain the long-life assurance desired. This assessment should provide a basis for overall comparison of different spacecraft configuration designs with regard to implementation schedules and costs.

D. Safety

A safety analysis was not performed during this study. However, safety criteria must be developed and a safety analysis accomplished during the Phase B study. Systems must be safe from the standpoint of personnel or hardware damage during ground operations, and safe from standpoint of hardware damage during the mission.

E. Logistics

Preliminary analysis of the logistics support requirements for the HEAO-A program failed to reveal any especially unique requirements for this program as compared to other long-life automated spacecraft programs. Obvious program characteristics which will influence the logistics support techniques to be employed are the long-life expectancy of the automated space-craft as contrasted to the manned GSE and mission operations elements, some of which must also operate throughout the mission lifetime. Some of the major elements of logistics support which will require additional analysis and definition in subsequent phases of the HEAO-A program are identified below.

1.	Maintainability. Maintenance of the GSE and the spacecraft systems prior to launch can be accomplished in the traditional manner, provided adequate emphasis is placed on accessibility and maintenance equipment and spares availability at all critical sites. On the other hand, maintainability of the automated spacecraft during mission operations requires special analysis of each functional hardware element to determine solutions to such problems as malfunction detection, fault isolation, environmental limitations, and redundancy techniques. Such analyses should be performed at the earliest possible time in the design phase to be most effective.

2.	Spares. Spacecraft and experiment system spares, per se, for the mission flight phase will not be a requirement since the necessary replacement capability will have been built into the equipment as redundant components. Off-the-shelf hardware history will greatly influence the automatic or on-call phase-in program for redundant components. A somewhat different spares support approach for the mission operation GSE is required. Many existing facilities will be utilized which may also be supporting other opera-

tional programs, and existing spares provisioning for these may prove adequate. A classical approach to spares selection and provisioning should suffice for the balance of the Support Equipment.

F. Manufacturing

Preliminary analysis of the conceptual design of the HEAO-A spacecraft indicates that conventional state-of-the-art methods and processes will be adequate for fabrication and assembly. Conventional facilities for manufacturing are available and no special problems are anticipated; however, special requirements for installation of the experiments and subsystems into the spacecraft structure may develop. Further analysis should be made to determine the level of cleanliness required and the size clean room needed during assembly and installation operations. Temperature and humidity control may be required.

Conventional air-frame-type assembly fixtures will be required to position the spacecraft during the assembly operations. Because of the mass of some experiments, consideration should be given to final assembly in the vertical position. Vertical assembly might minimize deflection and allow for better alignment of experiments and subsystems.

G. Testing

An adequate test program is essential in any space hardware development program and is an element of major cost in the program. Through maximum use of existing flight-proven hardware in the HEAO-A program, it is expected that some reduction in test requirements and costs can be realized. However, since there will be many new elements in the HEAO-A program, such as experiments, structures, components, and interconnections, the need for a comprehensive test program is still of paramount importance. Adequate development and qualification testing will verify the design adequacy early in the program and help reduce the changes normally experienced between design and flight. These changes greatly increase the cost and time of the test program and accumulate more operating time on the flight systems. The need for a comprehensive test program is further emphasized by the small number of "all-up" flights planned for the HEAO program.

In the following paragraphs the test phases, test approach, test articles, and schedules are discussed briefly to establish the overall test program rationale for the HEAO program.

1. Test Phases. The broad phases of testing which must be included in the HEAO program are as follows:

Development testing.

Qualification testing.

Acceptance testing.

Pre-launch testing.

In-orbit testing.

Development testing will include ambient and environmental testing to be performed on development test articles (breadboards, structural test article, vibration/acoustic test article, thermal vacuum test article, and prototype).

Qualification testing (ambient and environmental) will be performed on articles identical to flight hardware.

Acceptance testing (ambient and some environmental) will be performed on each end item after (and sometimes during) the manufacturing or assembly process.

Prelaunch testing will be performed on the launch vehicles and spacecraft separately and then on the total space vehicle to verify compatibility of the flight hardware with the launch GSE and readiness of both for the launch.

In-orbit testing will be performed before the spacecraft begins operation and periodically throughout the mission.

Development testing, qualification testing, and acceptance testing will be performed at the different levels of hardware complexity (components, assembly, subsystem, system, integrated systems, and spacecraft). Prelaunch and in-orbit testing will normally be high-level tests only, although provisions must be made to isolate malfunctioning components. Provisions should be made in the hardware to verify that the redundancy is still functional; this verification should be made in all phases of testing.

2. Test Approach. The test program approach should be well attuned to the size, complexity, cost, lifetime, and importance of the HEAO program. It has been found on other programs that subjecting the flight hardware to the expected mission levels of environmental stress raises the confidence level in the testing and enhances the probability of mission success, since failures and anomalies have been detected during these types of tests which were not detected during ambient tests. Hardware which is operating in a marginal fashion may appear to function properly in an ambient test, but environmental

stresses may shift the operational characteristics to the failure region. From GSFC experience [XIII-1] during systems tests of 22 spacecraft, over 50 percent of the experiment malfunctions and approximately 42 percent of the total malfunctions were detected during the thermal-vacuum tests. Approximately 50 percent of the 759 total malfunctions were caused by experiments. Since these data were from systems-level tests, these 759 malfunctions occurred after numerous tests at lower levels of hardware complexity. This indicates the importance of systems-level tests in the program. The importance of environmental testing for both the experiments and the other spacecraft systems is also indicated. Data from the Surveyor program [XIII-2] indicate that the greatest causes of in-flight failures (17 percent) were environmental causes, although solar-thermal-vacuum testing and vibration testing were performed on the Surveyor program. This also indicates a strong need for environmental testing.

The HEAO-A test program should be a logical, building-block sequence of tests progressing from lower to higher levels of hardware complexity. Each test should make maximum use of information and confidence gained from preceding tests to minimize duplication of tests. In-process testing should be performed during manufacturing or assembly phases whenever necessary to verify characteristics which cannot be verified after completion of the manufacturing or assembly, or to verify hardware in which a failure, if detected after manufacturing or assembly, would require considerable effort to disassemble and correct.

Ambient tests will be performed in all phases of the HEAO-A test program. In addition, environmental tests will be performed in the development, qualification, and acceptance phases. The levels of environmental stresses applied during the development and qualification phases shall be at least the qualification level and sometimes the failure level. Hardware to be flown shall not be tested to qualification levels, but shall be tested to the expected mission environment levels.

From GSFC experience, a good guideline for determining levels of environmental stress for flight acceptance testing for satellites has been shown to be those which will give 1 chance in 20 of their being exceeded in flight, and, for qualification testing, those which will give 1 chance in 100 of their being exceeded in flight. These guidelines are recommended as a starting point for the HEAO test program to be developed in subsequent program phases.

At the systems level of hardware complexity, or higher, the environments which should be considered are the launch environments and the temperature and vacuum aspects of the space environment. All the practical functional tests should be run under environmental stress at the systems level.

3. Test Articles Descriptions and Schedule. The schedule shown in Figure XIII-1 depicts a typical test program for the HEAO. In this schedule and the following discussion, several separate test articles are identified and briefly described. Further analysis is required to assess the possibility of utilizing a common test article for more than one test environment.
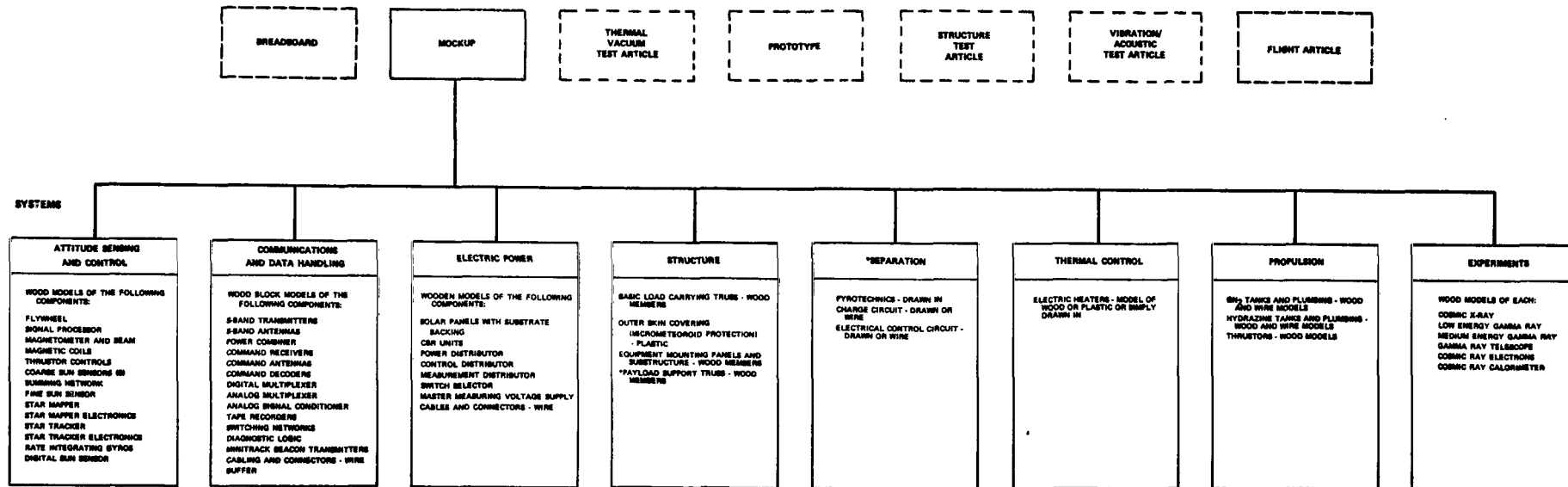
a. Mockup. The mockup is shown as the first major item of test hardware to be built. It will be a semihard mockup (wood, plastic, etc.) which will be used to assist in developing the systems layout, packaging, routing and lengths for cables and plumbing, access equipment, mounting provisions, etc. The mockup will be updated to more closely resemble the flight article in critical areas as the design becomes more completely defined. Figure XIII-3 indicates the type of hardware which will be installed on this article. As a result of the early phases of mockup use, the locations of the hardware, which will be specified in design drawings, will have been verified and changes will have been made to resolve problems. This information will then be used in determining locations of the mass simulators in the vibration/acoustic test article.

b. Structural (static) test article. The structural (static) test article will consist of the basic structural members, with no skin included. Figure XIII-4 indicates the type of hardware which will be installed on this article. Testing on this article is shown to be completed by mid-point of the vibration/acoustic test article manufacturing. The testing will be to qualification levels, and possibly to failure levels, although failure levels may not be required since the load-carrying capability is not expected to be as critical as the stiffness.

c. Vibration/acoustic test article. The vibration/acoustic test article will utilize the same tooling as used on the structural test article. It will be essentially the same as the structural test article, except that it will contain mass simulators and flight-type mounting hardware. Figure XIII-5 indicates the type of hardware which will be installed on this article. The testing on this article will be completed in time for the results to support the final manufacturing and testing of the thermal-vacuum test article. The testing will be to qualification levels and possibly higher levels.

d. Thermal-vacuum test article. The thermal-vacuum test article will be a flight-type structure, with skin and with thermal properties simulated for the components. There is a possibility that portions of the more thermally-critical systems may be installed on the article. Figure XIII-6 indicates the type of hardware which will be installed on this article. It will utilize the tooling used on the structural test article, with additions as required. The testing on the thermal-vacuum article will be completed in time for the results to support the fabrication of the prototype. The testing will be to qualification levels and possibly higher levels.

MAJOR SPACECRAFT END ITEMS

BREADBOARD | MOCKUP | THERMAL VACUUM TEST ARTICLE | PROTOTYPE | STRUCTURE TEST ARTICLE | VIBRATION/ ACOUSTIC TEST ARTICLE | FLIGHT ARTICLE

SYSTEMS

ATTITUDE SENSING AND CONTROL

WOOD MODELS OF THE FOLLOWING COMPONENTS:

FLYWHEEL
SIGNAL PROCESSOR
MAGNETOMETER AND BEAM
MAGNETIC COILS
THRUSTOR CONTROLS
COARSE SUN SENSORS (6)
SUMMING NETWORK
FINE SUN SENSOR
STAR MAPPER
STAR MAPPER ELECTRONICS
STAR TRACKER
STAR TRACKER ELECTRONICS
RATE INTEGRATING GYROS
DIGITAL SUN SENSOR

COMMUNICATIONS AND DATA HANDLING

WOOD BLOCK MODELS OF THE FOLLOWING COMPONENTS:

S-BAND TRANSMITTERS
S-BAND ANTENNAS
POWER COMBINER
COMMAND RECEIVERS
COMMAND ANTENNAS
COMMAND DECODERS
DIGITAL MULTIPLEXER
ANALOG MULTIPLEXER
ANALOG SIGNAL CONDITIONER
TAPE RECORDERS
SWITCHING NETWORKS
DIAGNOSTIC LOGIC
MINITRACK BEACON TRANSMITTERS
CABLING AND CONNECTORS - WIRE
BUFFER

ELECTRIC POWER

WOODEN MODELS OF THE FOLLOWING COMPONENTS:

SOLAR PANELS WITH SUBSTRATE BACKING
CBR UNITS
POWER DISTRIBUTOR
CONTROL DISTRIBUTOR
MEASUREMENT DISTRIBUTOR
SWITCH SELECTOR
MASTER MEASURING VOLTAGE SUPPLY
CABLES AND CONNECTORS - WIRE

STRUCTURE

BASIC LOAD CARRYING TRUSS - WOOD MEMBERS

OUTER SKIN COVERING (MICROMETEOROID PROTECTION) - PLASTIC

EQUIPMENT MOUNTING PANELS AND SUBSTRUCTURE - WOOD MEMBERS

*PAYLOAD SUPPORT TRUSS - WOOD MEMBERS

*SEPARATION

PYROTECHNICS - DRAWN IN
CHARGE CIRCUIT - DRAWN OR WIRE
ELECTRICAL CONTROL CIRCUIT - DRAWN OR WIRE

THERMAL CONTROL

ELECTRIC HEATERS - MODEL OF WOOD OR PLASTIC OR SIMPLY DRAWN IN

PROPULSION

GN_2 TANKS AND PLUMBING - WOOD AND WIRE MODELS
HYDRAZINE TANKS AND PLUMBING - WOOD AND WIRE MODELS
THRUSTORS - WOOD MODELS

EXPERIMENTS

WOOD MODELS OF EACH:

COSMIC X-RAY
LOW ENERGY GAMMA RAY
MEDIUM ENERGY GAMMA RAY
GAMMA RAY TELESCOPE
COSMIC RAY ELECTRONS
COSMIC RAY CALORIMETER

*Part of the payload, but not part of the HEAO in orbit.

Figure XIII-3. Mockup hardware breakdown.

MAJOR SPACECRAFT END ITEMS

| BREADBOARD | MOCKUP | THERMAL VACUUM TEST ARTICLE | PROTOTYPE | STRUCTURE TEST ARTICLE | VIBRATION/ ACOUSTIC TEST ARTICLE | FLIGHT ARTICLE |

SYSTEMS

ATTITUDE SENSING AND CONTROL	COMMUNICATIONS AND DATA HANDLING	ELECTRIC POWER	STRUCTURE	SEPARATION	THERMAL CONTROL	PROPULSION	EXPERIMENTS
NONE	NONE	MASS SIMULATORS	BASIC LOAD CARRYING TRUSS EQUIPMENT MOUNTING PANELS AND SUBSTRUCTURE *PAYLOAD SUPPORT TRUSS	NONE	NONE	NONE	NONE

*PART OF THE PAYLOAD, BUT NOT PART OF THE HEAD IN ORBIT.

Figure XIII-4. Structure test article hardware breakdown.

FOLDOUT FRAME

FOLDOUT FRAME 2

MAJOR SPACECRAFT END ITEMS

| BREADBOARD | MOCKUP | THERMAL VACUUM TEST ARTICLE | PROTOTYPE | STRUCTURE TEST ARTICLE | VIBRATION/ACOUSTIC TEST ARTICLE | FLIGHT ARTICLE |

SYSTEMS

ATTITUDE SENSING AND CONTROL	COMMUNICATIONS AND DATA HANDLING	ELECTRIC POWER	STRUCTURE	*SEPARATION	THERMAL CONTROL	PROPULSION	EXPERIMENTS
MASS SIMULATORS AND FLIGHT-TYPE MOUNTING HARDWARE	MASS SIMULATORS AND FLIGHT-TYPE MOUNTING HARDWARE	MASS SIMULATORS AND FLIGHT-TYPE MOUNTING HARDWARE	BASIC LOAD CARRYING TRUSS; EQUIPMENT MOUNTING PANELS AND SUBSTRUCTURE *PAYLOAD SUPPORT TRUSS	NONE	HEATER MASS SIMULATORS AND FLIGHT-TYPE MOUNTING HARDWARE	MASS SIMULATORS AND FLIGHT-TYPE MOUNTING HARDWARE	MASS SIMULATORS AND FLIGHT-TYPE MOUNTING HARDWARE

*PART OF THE PAYLOAD, BUT NOT PART OF THE HEAO IN ORBIT.

FOLDOUT FRAME 1

Figure XIII-5. Vibration/acoustic test article hardware breakdown.

FOLDOUT FRAME 2

MAJOR SPACECRAFT END ITEMS

| BREADBOARD | MOCKUP | THERMAL VACUUM TEST ARTICLE | PROTOTYPE | STRUCTURE TEST ARTICLE | VIBRATION/ ACOUSTIC TEST ARTICLE | FLIGHT ARTICLE |

SYSTEMS

ATTITUDE SENSING AND CONTROL	COMMUNICATIONS AND DATA HANDLING	ELECTRIC POWER	STRUCTURE	*SEPARATION	THERMAL CONTROL	PROPULSION	EXPERIMENTS
THERMAL SIMULATORS OF THE FOLLOWING COMPONENTS: FLYWHEEL SIGNAL PROCESSOR MAGNETOMETER (3-AXIS) MAGNETIC COILS (3) THRUSTOR CONTROLS SUMMING NETWORK STAR MAPPER ELECTRONICS STAR TRACKER ELECTRONICS RATE INTEGRATING GYROS (3) DIGITAL SUN SENSOR (5)	THERMAL SIMULATORS OF THE FOLLOWING COMPONENTS: S-BAND TRANSMITTERS (2) POWER COMBINER COMMAND RECEIVERS (2) COMMAND DECODERS (2) DIGITAL MULTIPLEXER ANALOG MULTIPLEXER ANALOG SIGNAL CONDITIONER TAPE RECORDERS (4) SWITCHING NETWORKS (2) DIAGNOSTIC LOGIC MINITRACK BEACON TRANSMITTERS (2) BUFFER	THERMAL SIMULATORS OF THE FOLLOWING COMPONENTS SOLAR PANELS WITH SUBSTRATE BACKING CBR UNITS POWER DISTRIBUTOR CONTROL DISTRIBUTOR MEASUREMENT DISTRIBUTOR SWITCH SELECTOR MASTER MEASURING VOLTAGE SUPPLY NETWORKS	BASIC LOAD CARRYING TRUSS OUTER SKIN COVERING (MICROMETEOROID PROTECTION) EQUIPMENT MOUNTING PANELS AND SUBSTRUCTURE *PAYLOAD SUPPORT TRUSS	NONE	COATINGS INSULATION ELECTRIC HEATER SIMULATORS	THERMAL SIMULATORS OF THE FOLLOWING COMPONENTS GN₂ TANKS AND PLUMBING HYDRAZINE TANKS AND PLUMBING THRUSTORS	THERMAL SIMULATORS OF THE FOLLOWING COMPONENTS COSMIC X-RAY LOW ENERGY GAMMA RAY MEDIUM ENERGY GAMMA RAY GAMMA RAY TELESCOPE COSMIC RAY ELECTRON COSMIC RAY CALORIMETER

*Part of the payload, but not part of the HEAO in orbit.

FOLDOUT FRAME /

Figure XIII-6. Thermal vacuum test article hardware breakdown.

FOLDOUT FRAME 2

13- 1

e. System breadboards. System breadboards will be utilized as required to develop each system. Testing will be done as early as possible to provide long leadtime for procurement of flight hardware. The breadboard testing will complement the operations on the mockup, and will be completed in time to support procurement of the hardware for the prototype.

f. Prototype. The prototype will be identical to the flight article, will serve as backup for the first flight article, and will be refurbished for use as the second flight article. Prototype experiments will be tested separately, and then installed in the prototype structure; all systems will be verified in ambient environment. Either real-time data over leased lines or data tapes from this checkout should be sent to the appropriate locations for early verification of compatibility with the spacecraft data. Schedule for testing in a magnetic test facility is shown in Figure XIII-1. Assuming there will be magnetometers and magnetic control coils on the spacecraft, it will be necessary to have such a facility to isolate the spacecraft from the earth's magnetic field and stray magnetic fields to measure the spacecraft magnetic characteristics and calibrate the magnetometers and coils as installed and deployed. A vibration test is shown next, and then a thermal-vacuum test. Between each of these tests, there is time shown for disconnection, movement, setup, and system checks. It is desirable that the prototype schedule lead the first flight article schedule by as much time as possible. However, because of overall time limitations, the end of prototype testing is shown to be constrained to approximately the mid-point of systems installation on the first flight article. The prototype can then be sent to appropriate centers, such as KSC and GSFC, for early verification of compatibility with hardware at those facilities.

g. Flight article. The flight article testing is essentially the same as the prototype. The time estimates shown for these tests in the schedule (Fig. XIII-1) are slightly decreased to reflect some learning curve. Prelaunch testing is shown at KSC. The acceptance test data and prelaunch data should be sent to GSFC and KSC.

h. Other considerations. A brief period of time for in-orbit checkout is shown immediately after launch. This will be required for turn-on and verification of on-board systems and verification of ground equipment prior to actually beginning the acquisition of data. In-orbit checkout will occur periodically throughout the mission to verify operation and calibration of equipment.

13-23

H. Miscellaneous

Many existing facilities and GSE elements will be used in the HEAO-A program which also may be supporting other programs. Existing spares-support procedures for these elements must be analyzed to determine if they are adequate for the additional HEAO-A program requirements.

No unusual packaging and handling requirements have been identified for the HEAO-A hardware. However, each phase of manufacturing, shipping, and storage must be analyzed in subsequent program phases to identify any special requirements that may\arise as the spacecraft systems and experiment payload become better defined. Some unique packaging, handling, or storage requirements for experiment components or experiment packages are anticipated.

No unusual transportation problems are anticipated because of the spacecraft size and configuration. The present configuration should be transportable by most conventional modes as determined necessary to accommodate the schedule. Methods of transportation will be influenced primarily by the manufacturing, test, checkout, and experiment integration schedules. Experiment and system sensitivity may influence the mode of transportation.

An approach to the acquisition and control of all essential technical support documentation must be formulated to support the program and to afford management with a continuous reference to assist in monitoring the operational equipment and hardware.

REFERENCES

XIII-1.   Proceedings of the Symposium on Long Life Hardware for Space.
           MSFC, Huntsville, Alabama, March 17-19, 1969.

XIII-2.   Netter, D. E.; and Trainer, T. M.: In-flight Failure Modes of
           Surveyor Spacecraft. Redstone Scientific Information Center
           Report Number RSIC-782, April 1968.

SECTION XIV. CONCLUSIONS AND RECOMMENDATIONS

TABLE OF CONTENTS

SECTION XIV. CONCLUSIONS AND RECOMMENDATIONS

A. Conclusions

1. <u>General.</u> The Phase A study has resulted in a definition of a baseline spacecraft and several alternate system and subsystem configurations. The primary effort has been directed toward analyzing and establishing the feasibility of the baseline and its associated subsystems; however, many of the alternatives remain as attractive potentials to consider.

The spacecraft concept used as a baseline appears to be well suited to the requirements for the HEAO mission as currently defined. Emphasis has been placed on spacecraft design and mission operation techniques which require little or no additional development, and which therefore offer the advantages of demonstrated reliability, low spacecraft and overall program costs, and short program maturation.

2. <u>Orbit Selection.</u> A circular orbit with an altitude of 200 n. mi. and an inclination of 28.5 degrees was selected for the baseline orbit on the basis of lifetime, maximum payload-to-orbit energy requirements, and radiation expected in the region of the South Atlantic Anomaly. This orbit appeared from our initial studies to yield approximately the required 1-year lifetime at $+2\sigma$ solar activity. Later in the study, calculations showed that this altitude is conservative. Orbital lifetime estimates are now approximately 833 days at $+2\sigma$ solar activity for this orbit.

Because of the South Atlantic Anomaly, there are advantages to an inclination lower than 28.5 degrees, and, conversely, there are advantages to a higher inclination, such as 35 degrees, because of improved telemetry contact with the STADAN station at Rosman, N. C. More effective use of this station may help alleviate the problem of getting data from the tracking stations to the PI in a minimum time. The choice among the orbit options will be made a part of the Phase B study. Payload considerations affecting orbit selection are discussed below.

3. <u>Payload Capability.</u> A spacecraft weight of approximately 19 000 pounds was identified. A weight growth to 20 920 pounds is possible, since that is the launch capability of the Titan IIID vehicle which was chosen as the baseline launch vehicle. This contingency of approximately 2000 pounds (10 percent) is considered very low for a large, complex spacecraft at this point in its design. Several approaches to increasing the payload are available. If the circular orbit is lowered to approximately 183 n. mi., the payload

capability is approximately 22 350 pounds, and the lifetime criteria can still be met. If an elliptical orbit of approximately 140 by 266 n. mi. were selected, the payload capability available would be approximately 25 790 pounds with the lifetime criteria still attainable. A kick stage could be used to circularize the orbit at 200 n. mi. from an initial 90- by 200-n. mi. orbit, with a resulting total payload capability of approximately 27 500 pounds.

Another possibility for potential growth in payload is through use of the Titan IIIC, which would yield a payload of 25 420 pounds to a 200-n. mi. circular orbit. In all the foregoing approaches, investigations would have to be made in the areas of attitude control, South Atlantic Anomaly effects, ground tracking station coverage, thermal effects, solar panel illumination, and celestial target occultation before choices of another approach could be made. The spacecraft structure would have to be sized for the increased static and dynamic loads in all cases where the above approaches were used for increasing payload.

The methods listed above as possibilities for increasing payload also can be used for increasing performance by changing either altitude, inclination, or orbit eccentricity. The use of the Titan IIIC may become even more attractive as more details on the costs of modifying and using the Titan IIID are defined (particularly costs associated with the guidance system).

4. Experiment Accommodation. The experiment support capability of the systems considered provides a reasonable degree of flexibility for accommodating a variety of experiment packages. Major impact would result from an experiment package which greatly increased in physical size, weight, or electrical power requirements; however, means are available, as represented by the alternates, to accommodate substantial changes relative to these aspects.

The baseline spacecraft can be operated in either a scanning or a nonscanning mode and with its scan axis either on the solar vector or off the solar vector by as much as 45 degrees during the initial portion of the mission (less than this later in the mission, because of solar cell degradation). This will permit mapping a portion of the galactic belt at an early time in the mission. The celestial sphere can be mapped by all experiments in a 6-month period using the celestial scan mode. The experiments can also be pointed at a particular location of interest to obtain a long period of uninterrupted viewing.

If payload contingency is not consumed by spacecraft growth, the excess could be used for additional experiments such as engineering experiments — a separate category of experiments which has been identified by OSSA as of interest.

5.   Power Capability.   The baseline concept can provide a maximum of 820 watts to the load in the celestial scan mode at the anticipated orbital temperatures.   This power would drop to 780 watts at the end of 1 year and to 741 watts at the end of 2 years.   A 15-degree-wide strip in the center of the galactic belt can be scanned by pointing the spin axis off-sun a maximum of approximately 37 degrees.   The power available to the load in this mode of operation is 655 watts at the anticipated orbital temperatures.   This power would drop to 625 watts at the end of 1 year.   A 30-degree-wide strip centered in the galactic belt can be scanned by pointing the spin axis off-sun a maximum of approximately 45 degrees.   The power available to the load in this case is 580 watts initially at the anticipated orbital temperatures.   This would drop to 550 watts at the end of 1 year, which is inadequate for the presently defined loads.   In the pointing mode of operation, the power available would vary with the off-sun angle involved, but would be approximately the same as for the galactic scan mode for the same angles.   There would be some differences because of the nonrotating nature of the pointing mode.

The power requirements identified to date total 560 watts, not including contingency.   Several additional probable requirements have been identified and are discussed in Appendix H.

Should power requirements grow beyond the baseline concept capability, several alternatives for increasing the power capability could be selected.   Simple techniques are available to fold out the solar array side panels on the baseline configuration, as one readily available means whereby the power capability can be increased by approximately 20 percent.   Power can also be increased through use of other types of deployable arrays, by lengthening the spacecraft to add more body-fixed arrays, and through use of heat pipes to help cool the arrays.   Another approach to resolving power problems would be to modify the mission requirements to selectively reduce power needs.   For example, the off-sun galactic belt scan could be eliminated, or experiments could possibly be turned off during the times when their viewing angles were occulted by the earth, when they were in the South Atlantic Anomaly, when opposing experiments were pointed at selected targets, or whenever operation of an experiment with higher priority took precedence.

6.   Attitude Sensing and Control.   The spacecraft can be stabilized and controlled by a combination of reaction jets, flywheel, and magnetic coils. After initial spin-up in orbit, the flywheel runs continuously.   It consists essentially of the inner gimbal rotor assembly of the ATM Control Moment Gyro.   The 12 reaction jets are used only for large or time-critical reorientation maneuvers, and for spin-up and spin-down.   The three coils are used for small attitude corrections and for spin rate control.   The coils and reaction jets may serve as limited backup systems for each other.

The most significant unknown in this area is the capability of the magnetic torquers. While they have been used very successfully on smaller satellites, there have been no applications involving large spacecraft of orbital parameters of interest to HEAO. The geomagnetic field and the magnetic field of the control system determine the magnitude and direction of the corrective torques which can be created. The latter can be controlled as desired, but the magnetic control system is nevertheless dependent on favorable orientations of the earth's field for effective control. There will likely be periods of time during each orbit which are unavailable for correction of drift; the duration of these periods will determine the ultimate performance of the attitude control system, at least in the range of HEAO-A performance requirements. A special study is now underway to assess this factor.

Small corrections in attitude made necessary by drift, etc., will be made in response to onboard attitude sensors; therefore, the requirements for ground contacts for attitude control will be limited to those necessary for updating stored commands in the onboard memory, which provide mission sequencing control. Spacecraft attitude determination to within ± 0.1 degree can be determined from an analysis on the ground of data generated by the star mapper. Pointing control of the spacecraft can be maintained within ± 1 degree during sun occultation and celestial reference occultation (approximately 45 minutes maximum) by using rate gyros; hence, pointing at a celestial target with a pointing accuracy within ± 1 degree can be accomplished for an unlimited length of time within the specified power and thermal constraints.

Late in the study it was determined that the 3-coil system would probably not require nearly as much power as the 100 watts which was originally estimated. However, it is expected that approximately 75 watts more power will be required for sensors and heaters than has been baselined; so these two power requirement changes would be somewhat off-setting. Also, late in the study, it was determined that the flywheel may not be required, which would be a savings of approximately 40 watts average power and 240 pounds, if this should prove to be true.

7. Reaction Control System. During this study, four types of reaction control systems were considered: hydrazine monopropellant, cold nitrogen gas, bipropellant, and resistojet. Based on weight, complexity, and power assessments, the hydrazine monopropellant system was chosen as the baseline, using 12 thrusters of 0.5-pound thrust each, and using GN_2 as the pressurant. This system is state-of-the-art.

14-4

8.   Thermal Control. An analysis of temperature distributions among the spacecraft subsystems and reference experiments shows that thermal control problems should not be severe, at least in the normal operating modes. With one exception (the Bragg Crystal Spectrometer), the temperature variations of all experiments fell within the required range of -10° C to +30° C. In the case of the experiment which did not remain in this temperature range, a relocation should alleviate the problem.

Since the baseline RCS utilizes hydrazine monopropellant, with a freezing point of 35° F, a limited quantity of electrical heaters on the thruster modules will be required to prevent freezing of the hydrazine.   Thermal shielding such as that provided by the spacecraft skin must be used, as this increases the heat capacity of the vehicle and reduces the temperature variations for the experiment and equipment.

If there is an increase in temperature on the vehicle, such as that caused by a large increase in dissipated power, a highly conductive device such as a heat pipe could be employed to maintain the desired temperature levels. Also, a heat capacitance device could be used to overcome excessive temperature variation in an orbit. These two devices give the designer a backup tool in choosing systems having greater power requirements or higher temperatures.

The impact of abnormal spacecraft attitudes on thermal control must be investigated in depth in future studies. No attempt has been made to explore this problem during the Phase A effort. Because such attitudes will usually involve greater exposure of the experiments to solar heat, the analysis is particularly sensitive to the nature of the selected experiment payload.

9.   Structure. The baseline structure concept was developed around the experiments being mounted near the geometric center of the spacecraft. There is a definite weight advantage by mounting the heavy experiments near the launch vehicle interface. Also, this approach helps ensure against unforeseen vibrational problems and helps reduce the need for a heavy structure for launch. Follow-on design should consider all the possible means of reducing the weight penalty imposed by deflection requirements.

14-5

Since the baseline structural weight was determined by deflection limits rather than by stress, there is a possibility that a concept having a slightly smaller diameter (approximately 1 inch smaller) would permit a greater allowable deflection and consequently a less rigid, lighter structure. The possible structural weight saving is on the order of 800 pounds. A modification of the baseline structural concept to include enclosed box beams instead of truss beams may yield a lighter structure.

10. Data Handling and Communications. The baseline system can record data at a rate of 27.5 kilobits per second (25 kilobits per second of experiment data and 2.5 kilobits of housekeeping data) and can store up to 1728 megabits. The system is state-of-the-art, and many of the components are available as catalog items from the vendor; those requiring design are straightforward engineering problems. Although the tape recorders are probably the least reliable components in this system, there are several high performance models now undergoing qualification testing for other programs whose specifications are within HEAO design requirements, and which are expected to be available for selection.

Although the baseline system has not been optimized from the standpoint of data handling efficiency, its performance in most areas exceeds the requirements. A possible marginal condition may exist when as many as 35 to 50 spacecraft could be competing for time at the same STADAN station. This condition cannot be altered by increasing data storage, since over the long term the satellite cannot be allowed to produce data faster than the ground stations can accept it. There are several alternatives. One is to increase the down-link data rate standard above the present 200 kilobits per second. Another would be to decrease the data generated by the experiments. A third alternative would be to explore the use of higher orbits and different orbital inclinations to achieve greater station contact time. Another method of resolving the problem would be to refrain from gathering data from some experiments at selected times, such as when the experiment field of view was occulted by the earth, when the spacecraft was in the South Atlantic Anomaly, when opposing experiments were pointed at selected targets, or at other times when the data from an experiment was deemed to be not essential to the success of the mission. For maximum efficiency during such operations, the data format should be variable, which would increase complexity, weight, and power requirements. Still another approach would be to utilize a geosynchronous data relay satellite (if available) for greater ground station contact time. Power requirements and weight would increase as a result of this approach.

The two approaches mentioned above which increase ground station contact time are also attractive for reasons other than the resolution of the onboard data storage problem. It is desirable to have one tracking station handle all the communication with the spacecraft. It is also desirable to have two orbits per day of near-real-time data from the spacecraft at this station and it is desirable to have no more than three consecutive orbits without a station contact of at least 5 minutes. The nature and locations of the STADAN network stations indicate that Rosman, N. C., should be the prime station and Santiago, Chile, the backup station. Hence, any change from the baseline mission which allows greater contact time with these stations will increase the flexibility of the mission as well as decrease the data storage requirements.

The 25 000 bits per second experiment data rate requirement may be relaxed somewhat as a more detailed analysis of experiment requirements is made, and as the impact of such a data rate on ground facilities is assessed. Because of the strong interest by experimenters in high data rates for at least part of the mission, and because the extent of program support from STADAN and possibly other ground networks cannot be fully assessed at this time, the full capability has been carried through the conceptual design. Another special study, now underway, will analyze the onboard system as a part of the pre-Phase B study effort.

11. Ground Data Storage. The cumulative data generated by the HEAO will create ground handling and storage problems caused by its sheer volume. A master tape of the raw (unprocessed) data must be recorded at the receiver and must be kept in storage for a considerable period of time as a permanent record. The data on this tape will be processed through a computer and recorded on separate tapes for each experimenter. Using a standard-type ground station 14-inch-diameter tape reel with tape 1 inch wide, 1.5 mils thick, and 2400 feet long, and recording 9 tracks simultaneously at a rate of 800 bits per inch per track on the tape, more than 4000 of the 2400-foot reels would be used per year for the master tape alone.

Onboard data compression techniques were not baselined during this study, because the data are apparently not redundant enough to warrant implementing such techniques, even if the associated increase in systems complexity could be tolerated. However, because of the above described data handling and storage problems, more efficient methods of handling the data should be investigated in Phase B.

12. Reliability. It is anticipated that selected redundancy will have to be added to increase the spacecraft reliability. The increase in power required for this increased reliability would be extremely low, since most of the redundancy could be "standby." It is estimated that six items of hardware account for over 70 percent of the reliability problems of the baseline spacecraft. These are the solar panel and CBR assemblies, tape recorders, signal processor, flywheel, power converter, and gyros. Therefore, future efforts should be concentrated in these areas. When the flight experiments are defined, their reliability should be established at a level commensurate with the desired mission reliability, and an overall reliability analysis should be performed.

13. Future Missions. The HEAO-A spacecraft concept was determined largely by the baseline experiment payload. The spacecraft concepts for HEAO-B, HEAO-C, and HEAO-D will also be highly dependent on the experiments. One attractive possibility is that there will be sufficient interest in the survey class experiments to warrant a second spacecraft very similar in design to HEAO-A. In this case, HEAO-B could take maximum advantage of the commonality of subsystems. It should also be possible to improve the capability, particularly in the area of pointing, so that greater emphasis could be placed on studying selected targets in greater detail than would be possible in HEAO-A.

The control system changes required would involve the use of more accurate attitude sensors as well as some type of momentum exchange device such as variable speed inertia wheels or a control moment gyro system. The substitution of such components for the HEAO-A sensors and flywheel would increase the spacecraft costs somewhat, but would increase the pointing capability from the present ±1 degree to possibly somewhere in the range of 1 to 10 arc-minutes. The magnetic coils would then serve primarily as momentum desaturation devices for the control moment gyros and as coarse attitude maneuver actuators. Since momentum desaturation can be accomplished whenever the geomagnetic field is favorable, the unfavorable orientations would no longer limit pointing accuracy and durations. The duration, as well as the pointing direction, would still be limited by the solar power available which, in the case of fixed arrays, means a 2- to 4-week band (or its equivalent in celestial coordinates) centered on the spacecraft sunline.

If the HEAO-B mission concept involves experiments with significantly different objectives, the spacecraft may take a different evolutionary

14-8

path. One example of interest is a mission which is devoted exclusively to cosmic-ray physics. For cosmic-ray experiment designs, such as the ionization calorimeter and the cosmic ray electron detector included in the HEAO-A reference payload, there is not expected to be any coupling between these experiments and the attitude control system. For a more advanced experiment, such as one which employes a high intensity magnetic field to increase scientific yield, the expected interaction is much more severe. It should be noted that no analysis of the coupling between the baseline systems was made during the Phase A study, and hence the foregoing statements are speculative.

Fortunately, however, spacecraft pointing is of secondary importance for cosmic-ray physics because of the generally isotropic nature of the incoming radiation. The result is that the impact of the experiments on the attitude control system is minor. Other problems which arise from the use of high intensity magnetic fields, such as their interaction with other cosmic-ray experiments and with spacecraft electronics, would have to be analyzed. Based on a very cursory analysis, however, such an experiment along with several other cosmic-ray devices could be accommodated in the HEAO baseline design without significant impact, provided that the technology associated with the magnetic device itself, in areas such as power requirements and cryogenic equipment, are developed to the point of flight readiness.

For advanced mission concepts along other evolutionary paths, such as in the area of precisely pointed X-ray and gamma-ray instrumentation, the control system may require continued improvement. Some experiments which have been proposed, such as the grazing incidence X-ray telescope, will require long-duration pointing to at least 1 arc minute accuracy. The pointing, electrical power, and thermal control requirements may necessitate significant changes from the current concept, particularly if all-sky observational capability regardless of sun orientation is required. Such concepts will be conceptually developed and analyzed in future programs.

B. Recommendations

The Phase A study has indicated that the HEAO is feasible, and sufficient techniques exist to allow design of hardware and implementation of a program which will satisfy the mission requirements. It is therefore recommended that the Phase B effort be initiated.

VOLUME II — APPENDICES

APPENDIX A. HEAO BASELINE EXPERIMENTS

TABLE OF CONTENTS

LIST OF ILLUSTRATIONS

1. The High Energy Astronomy Program

Astronomical observations involving high energy quanta and particles (X-rays, gamma-rays, cosmic-rays) remained insignificant, or at least severely limited, as long as the observing instruments were restrained to the surface of the earth. With the advent of rockets and satellites, possibilities of observing X-rays and gamma-rays from extraterrestrial sources began to develop. The first definite observations of X-rays from the sun were made by Friedman and co-workers (NRL) in 1959; Kraushaar, with Explorer II, recorded gamma-rays from space in 1961; and Giaconni and his co-workers (AS&E) observed X-rays from sources outside the solar system for the first time in 1962.

During the first decade of high-energy astronomy, a number of unexpected and very exciting discoveries were made. In particular, space observations of X-rays and of stellar and galactic emissions in the UV and extreme UV, together with ground observations of such phenomena as quasi-stellar objects, pulsars, Wolf-Rayet stars, and Seyfert galaxies, have increased our astronomical knowledge in an entirely unprecedented way. The X-ray source of Scorpius, Sco X-1, emits about 10^5 times as much energy per second in the 1 to 10 Å region as our sun emits over the entire spectrum. The galaxy M-87 in Virgo A emits about 10^{10} times the total solar output in the 1 to 10 Å region alone. The Crab Nebula, remnant of the 1054 Supernova, emits X-rays from almost the entire area which is visible to the eye. Its small central star, which has now been recognized as a pulsar with a light modulation of about 30 Hertz, emits X-rays which are modulated at the same frequency. It is believed that the central star is currently on its way to becoming a neutron star. The sun is a prolific emitter of X-rays. X-rays emanate from plage areas and from the corona; solar flares are bright sources of X-rays.

X-rays are being generated in a number of different ways. The excitation levels of highly ionized medium and heavy elements fall into the X-ray region; fast electrons, colliding with atoms, produce X-ray bremsstrahlung; solid bodies at elevated temperatures emit X-rays as part of their black-body radiation; fast electrons, traveling on spiral paths through magnetic

fields, generate synchrotron radiation which is distinguished by a high degree or polarization. Finally, X-rays are produced by the inverse Compton effect when fast particles interact with photons of the visible, infrared, and radio-wave regions.

About 40 discrete sources of X-rays have been found so far, most of them in our own galaxy, and they differ in intensity, spectral distribution, and polarization. The weakest source detected so far is about 300 times weaker than the strongest (Sco X-1). X-ray studies are aiming in two directions; first, a careful, thorough survey of the sky for X-ray sources, hopefully down to about one-millionth the intensity of Sco X-1; and second, an investigation of the shapes and structures of X-ray sources with high-resolution instruments. It is expected that thousands of sources will be found during forthcoming years, and that the aspect of the sky in X-ray light will be quite different from its aspect in visible light. Probably an X-ray atlas of the sky will also show point sources, nebulae, galaxies, and other objects, but their intensities and distributions will be very different from those of the visible stars. It is also expected that the X-ray observation program will reveal a uniform, low-intensity background X-radiation throughout the universe, created by the interaction of fast cosmic-ray particles with the low-energy photons of the 3° K background radiation.

Currently envisioned in the High Energy Astronomy program are survey-type instruments with high-sensitivity and moderate-angular resolution, and grazing incidence telescope systems for high-resolution images, but lesser sensitivity. The results of this program will be continuously compared and coordinated with the results of the UV astronomy program. It is quite possible that these two programs will reveal that the energy content of the universe in the X-ray and UV regions far exceeds the energy content in the regions of conventional astronomy. Recent results with rockets and with OSO and OAO satellites have already forced us to revise some of our older astronomical concepts. They show that energetic processes in the universe are more energetic than previously thought and that our calculations of distances may have to be revised.

Gamma-rays can be detected with scintillation counters, lithium-drifted germanium detectors, Cerenkov counters, and spark chambers. Intensities will always be low; for this reason, large area detectors and long observing times are mandatory. High angular resolution will be difficult to obtain. The newly developed drifted germanium detectors provide a remarkably high proportionality between gamma-ray energy and pulse height. The High Energy Astronomy program will contain several gamma-ray detectors of the types mentioned above.

A-2

Several cosmological processes are known which produce gamma-rays; nuclear transitions, generating line spectra from about 5 Kev to about 5 Mev; bremsstrahlung, covering a wide spectrum of energies up to very energetic gamma-rays; matter-antimatter annihilation radiation with a 0.511 Mev line for electron-positron, and up to thousands of Mev for heavier particle annihilation; the decay of neutral pi-mesons with a 70-Mev peak; the inverse Compton effect with a broad energy spectrum; and the possible "cosmological peak" around 20 Mev.

Of particular interest is the search for gamma-ray lines from decaying radioactive nuclei produced in novae and supernovae. Old super-novae, such as the Crab Nebula, may still emit gamma-rays from the decay series of very heavy transuranic elements. Young supernovae in other galaxies, when caught during the first seconds or minutes of their explosions, may show gamma-ray lines of rapid-process elements, such as nickel. OSO III gave indications of a strong gamma-ray source near the center of our galaxy. Emphasis in high-energy experiments will be placed upon sensitivity, angular resolution, and energy resolution. Observations will concentrate on a broad, but sensitive, survey of the sky; and on a less sensitive, but high-resolution, study of individual sources.

The third member of the high energy family, cosmic-rays, consists of particle radiations. Although a considerable portion of the total cosmic-ray energy impinging upon the earth's atmosphere reaches the surface of the earth, this portion consists mainly of secondary and tertiary radiations such as electrons, mesons, and gammas from interactions between primaries and the atmosphere. It is known that the primary cosmic radiation contains mainly protons; helium nuclei and heavier atomic nuclei are much rarer. Iron nuclei seem to be more frequent than neighboring elements. Very few events caused by transiron nuclei have been recorded, and some may even be because of transuranic nuclei. A survey of cosmic-ray particles with statistically meaningful numbers even for the heaviest elements will be of utmost interest.

Cosmic-ray detectors include proportional counters, scintillation counters, spark chambers, and photographic emulsions. Again, large detector areas and long observation times are mandatory. High angular resolution is not very important, simply because cosmic-ray particles are subject to magnetic deflection during their travel through the universe, and therefore lose their original directionality. A proton of 10^{15} ev evergy will be subject to a curvature with a radius of about 1 light year within our galaxy. Even protons with 10^{18} or 10^{20} ev energy, in traversing our galaxy (120 000 light years), will deviate considerably from their original directions. Although

the search for well-defined cosmic-ray sources, for this reason, is not very promising, cosmic-ray observations would still include at least a coarse angular resolution for particles of around 10^{20} ev energy per nucleon. It is believed that particles of this energy, and most cosmic-ray particles, are accelerated by processes which involve the rapid collapse of stars, and hence a fast increase of the stars' magnetic field intensities. Such processes occur when a star undergoes the transition from red giant to supernova to neutron star.

Cosmic-ray experiments with large detector areas, and for particle energies upward from about 10^{10} ev, are planned for the High Energy Astronomy program[1].

2. Baseline Experiments

High energy astronomy observations (HEAO) of the "survey" category have several features in common: they need large, heavy instrumentation; they do not need very accurate pointing; they can be operated automatically over long periods of time; and the experiments can be ready for flight in about 3 years. Experience as well as scientific results gained from these survey-type observations will be very useful in the planning of more sophisticated and more demanding astronomy experiments which will be designed for operation possibly beginning in 1975 and 1976, in conjunction with a manned space station or shuttle.

To accomplish the conceptual designs required for the feasibility assessment of the HEAO Mission "A," a group of six baseline experiments was selected as representative of this initial "survey" category. A brief technical description of these reference experiments is included in the following paragraphs for completeness. Inclusion of data and descriptions in no way represents a preferred status in the official HEAO-A payload which will be selected on the basis of experiments prepared in response to an AFO.

---

1. The information presented in the above paragraphs was extracted from Reference A-1.

a. Large Area X-Ray Detector

(1) Scientific objective. The principal objective of the X-ray detector system is to detect and classify X-ray "point" sources on the celestial sphere. Since this detector is highly sensitive in defining X-ray sources, measurement of extragalactic sources is of primary interest. In addition, this experiment has the capability of high-resolution spectral analysis of the stronger sources, as well as precise source-position determination when modulation collimators and Bragg crystal spectrometers are used.

(2) Physical description of equipment. This experiment consists of three types of modules or detectors: the basic modules, the modulation collimator modules, and the Bragg crystal spectrometer modules. Furthermore, the equipment has been separated into two groupings which are designated as Part 1 and Part 2. Part 1 consists of six basic modules, three modulation collimator modules and two Bragg crystal spectrometer modules. Part 2 consists of six basic modules. This grouping will permit internal variation of the Part 2 modules, if desired, without major change in the module size or location on the spacecraft. The individual modules are described in the following paragraphs.

(a) Basic module. The basic counter module, as shown schematically in Figure A-1, is a combined proportional-scintillation counter which is used as a 16-channel pulse-amplitude spectrometer covering a pulse-amplitude range of 10^2 to 6×10^4 ev. In the module, the proportional counter serves as a transmission window for the scintillation counter set. The proportional counter gas consists of equal parts of argon and xenon with a small proportion of CO_2 added as a quenching agent and will detect soft X-radiation in the 10^2 to 1.5×10^4 ev region.

A set of 18 thallium-doped sodium-iodide crystals will measure the hard component (1.5×10^4 to 6×10^4 ev) of the X-ray flux. Photomultiplier tubes attached to the crystals record scintillations which will be sorted in a 7-channel pulse-height analyzer.

X-radiation will enter the proportional counter through metal collimating vanes which act as a cellular collimator and will restrict the field of view to 1 by 4 degrees. The vanes are arranged to provide the 4-degree width of scan about the spacecraft spin axis. An aluminum honeycomb plus strongback will hold a thin (approximately 1/8 mil) plastic window which will contain the gas within the body of the proportional counter. The gas pressure within the counter will be held at 0.2 atmosphere; however,
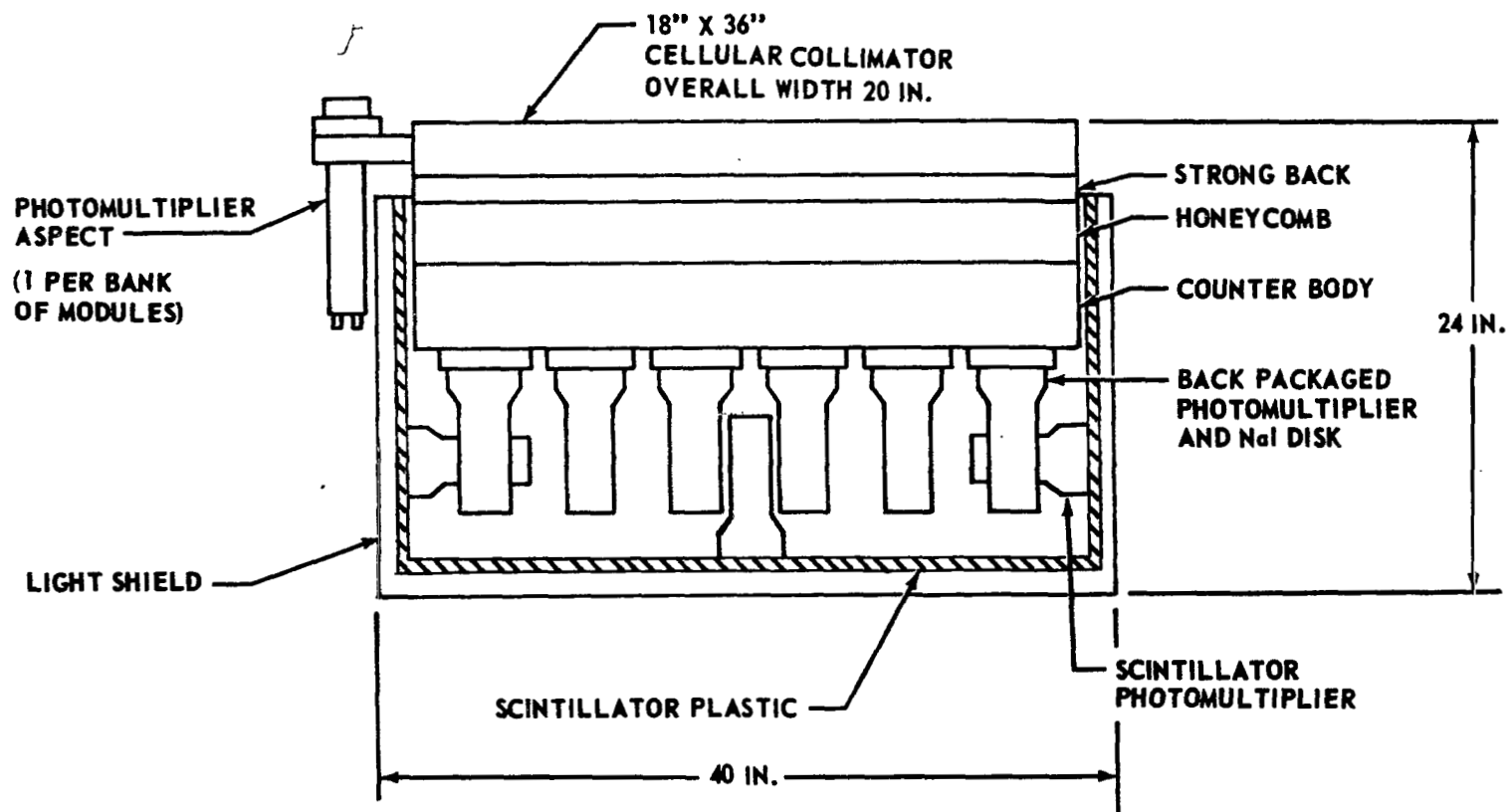
Figure A-1. Large area X-ray detector (basic module).

the gas will diffuse through the window at the rate of 0.1 ft³/day/module. Local gas resupply will be required.

The active elements of the module are surrounded by a plastic scintillator anticoincidence shield and a beryllium outer casing which will offer both active and passive protection from radiation entering from random directions.

(b) Modulation collimators. The modulation collimators will give more precise positions and define the extent of X-ray sources to a higher degree than the basic module counter. A collimator of this type, as illustrated schematically in Figure A-2, combines high resolution with wide field of view. It consists essentially of two-plane grids of parallel wires placed one in front of the other at a suitable distance. The minimum angular size of a source that can be resolved depends on the mechanical precision achieved in the construction of the collimator, on the statistics of the data, and on the noise level.

(c) Bragg crystal spectrometer. The Bragg crystal spectrometer will provide a more detailed spectral analysis of the X-radiation. It differs from the basic module in that the 18 scintillation counters and the standard collimators have been removed; however, a hinged door, essentially a flat plate has been added on which a continuous array of lithium fluoride crystal plates are mounted. The angular position of the door relative to the detector plane is changed to selected fixed positions by a motorized drive contained within the module. Actual spectral scanning is accomplished by the spin of the spacecraft. This module is illustrated schematically in Figure A-3.

(3) Spacecraft mounting requirements. Integration of these modules into the spacecraft structure will require consideration of the following special mounting requirements to obtain the proper "look" directions:

● All modules must be mounted to look in a plane perpendicular to the spin axis.

● The six basic modules and the three modulation collimators in Part 1 of the experiment preferably should be mounted to look in the same direction, but may look in not more than two directions.

● The three modulation collimators must look in the same direction.

18" X 36"
WIRE GRID COLLIMATORS
(OVERALL WIDTH 20")

21 IN.

PHOTOMULTIPLIER
ASPECT

(1 PER BANK OF MODULES)

STRONG BACK

HONEYCOMB

45 IN.

COUNTER BODY

24 IN.

BACK PACKAGED
PHOTOMULTIPLIER
AND NaI DISK

LIGHT SHIELD

SCINTILLATOR PLASTIC

SCINTILLATOR
PHOTOMULTIPLIER

40 IN.
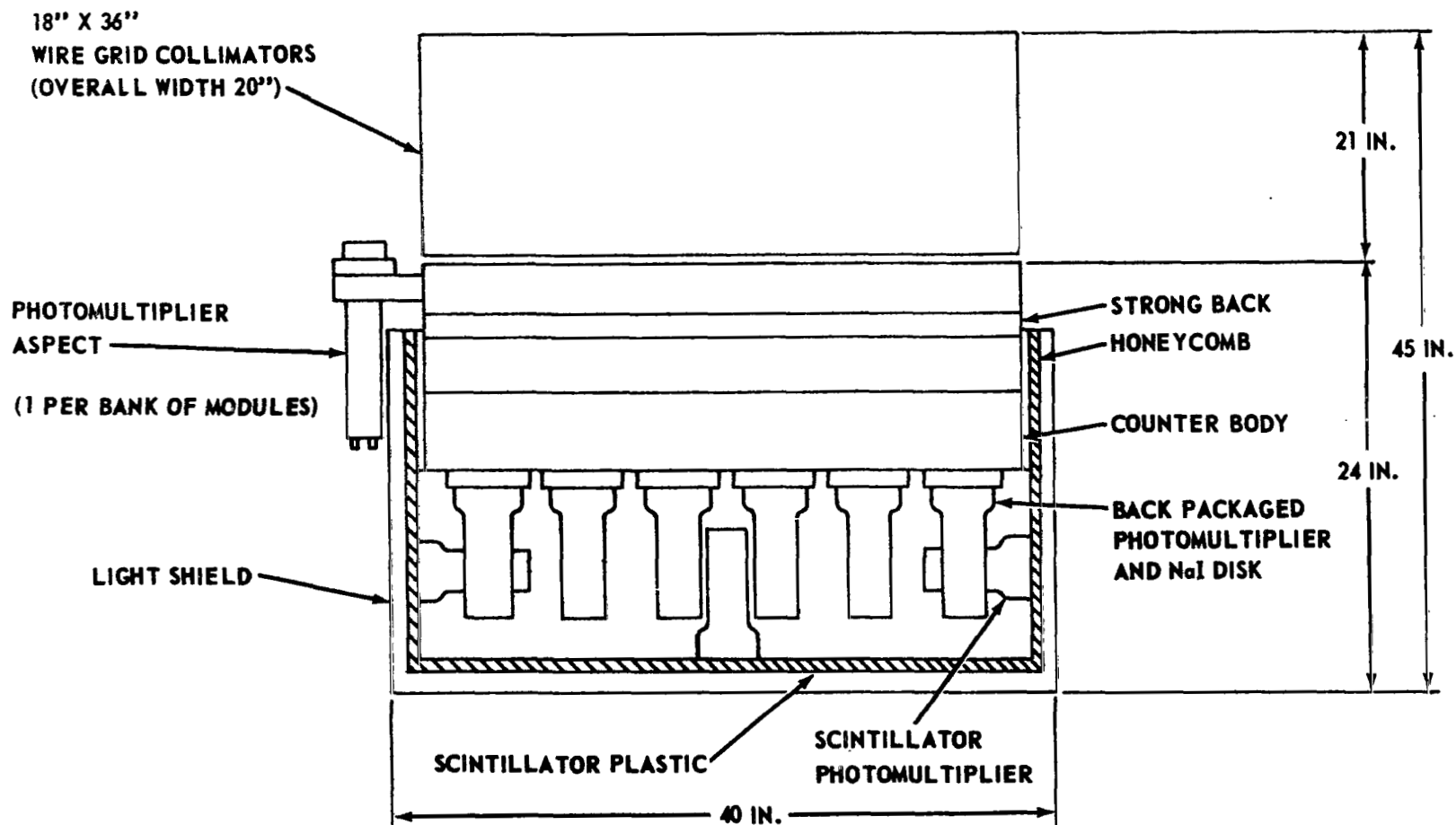
Figure A-2.   Large area X-ray detector (modulation collimators).

LITHIUM FLUORIDE
CRYSTAL ARRAY
ON HINGED DOOR

20° - 90°

12 IN.

BASIC MODULE
(LESS COLLIMATOR
AND SCINTILLATION
ARRAY)

48 IN.

20 IN.

38 IN.
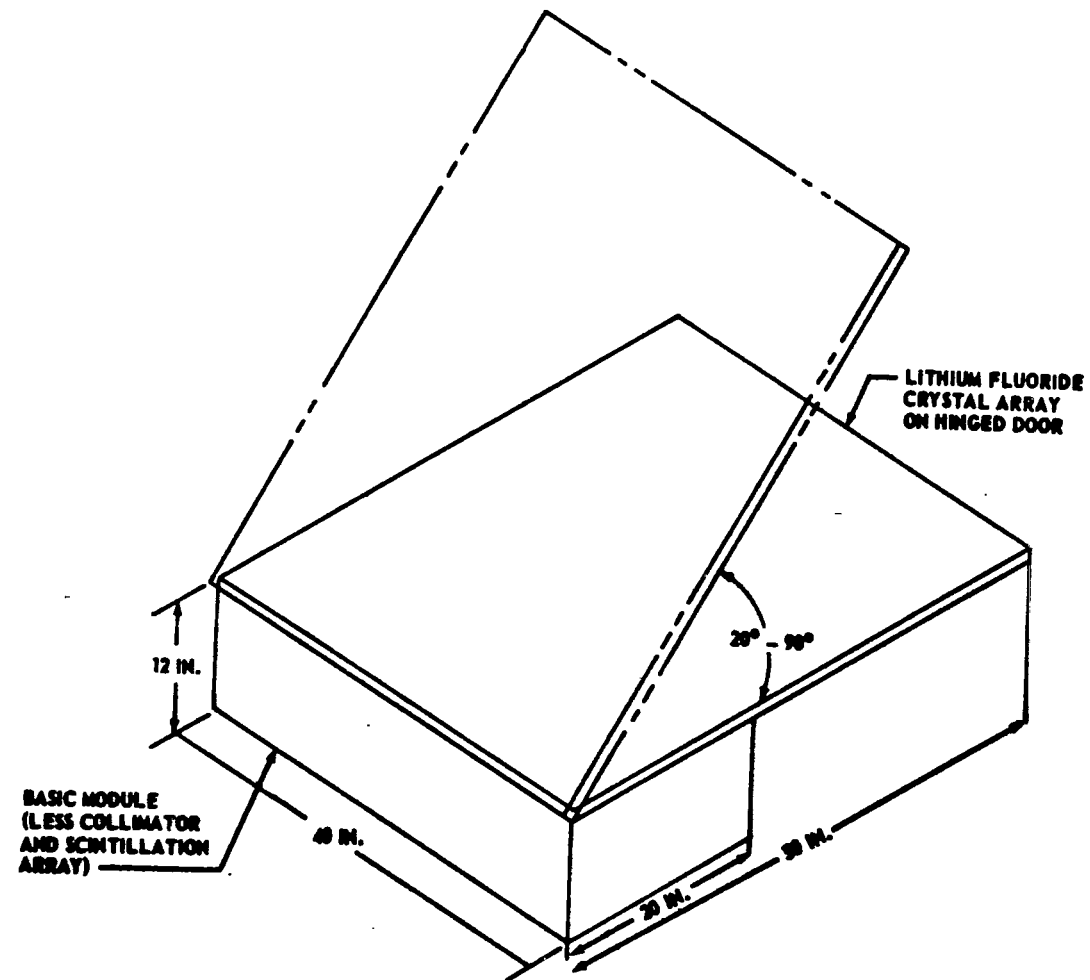
Figure A-3.   Large area X-ray detector (Bragg crystal spectrometer).

● The two Bragg crystal modules must look in the same direction, but this direction may be different from that of all other modules. Also, the Bragg crystal modules must have an almost clear view of space over the range of view angles corresponding to specular reflection of radiation from the door, i.e., about 20 to 90 degrees from the normal to the detector plane as measured in a plane perpendicular to the door hinge as illustrated in Figure A-3.

● The six basic modules in Part 2 of the experiment should be mounted to look in the same direction, but may look in not more than two directions.

b. Low-Energy Gamma-Ray Detector

(1) Scientific objective. The objective of this experiment is to conduct a general survey of the celestial sphere to measure the flux and spectra of photons in the 10^4 to > 5×10^5 ev range. Any source of flux will be localized and its position measured with respect to the celestial sphere.

(2) Physical description of equipment. The current design for the detector is illustrated in Figure A-4. A cesium iodide crystal serves as the basic detector; another cesium iodide crystal encloses the first crystal and serves as the anticoincidence system. The gamma-ray flux enters the detector through 61 collimating holes which effectively reduce the field of view to 4 degrees. Photomultipliers view the reactions of the crystals with photons and charged particles. The logic circuitry then directs the gamma-ray-induced pulses into the proper channel of the 128-channel pulse-height analyzer.

c. Medium-Energy Gamma-Ray Detector

(1) Scientific objective. The objective of this experiment is to conduct a general survey of the celestial sphere to determine the position and spectrum of possible gamma-ray sources in the energy range from 2×10^5 to 10^7 ev. Any source of flux will be localized and its position measured with respect to the celestial sphere.

(2) Physical description of equipment. This experiment uses a crystal scintillator technique for measuring gamma-rays. The NaI (Tℓ) crystal which serves as the detector is shown in Figure A-5. The NaI crystal and its amplifying electronics are surrounded by an anticoincidence CsI (Na) crystal. This CsI(Na) crystal acts as an active collimating device which will

61 COLLIMATING HOLES.
4° FIELD OF VIEW

COLLIMATOR [CsI (Na)]

CRYSTAL DETECTOR [CsI (Na)]

PHOTOMULTIPLIER ASSEMBLY

10.62 IN.

6.00 IN.

ANTICOINCIDENCE SHIELD [CsI (Na)]

11.25 IN.

21.25 IN.
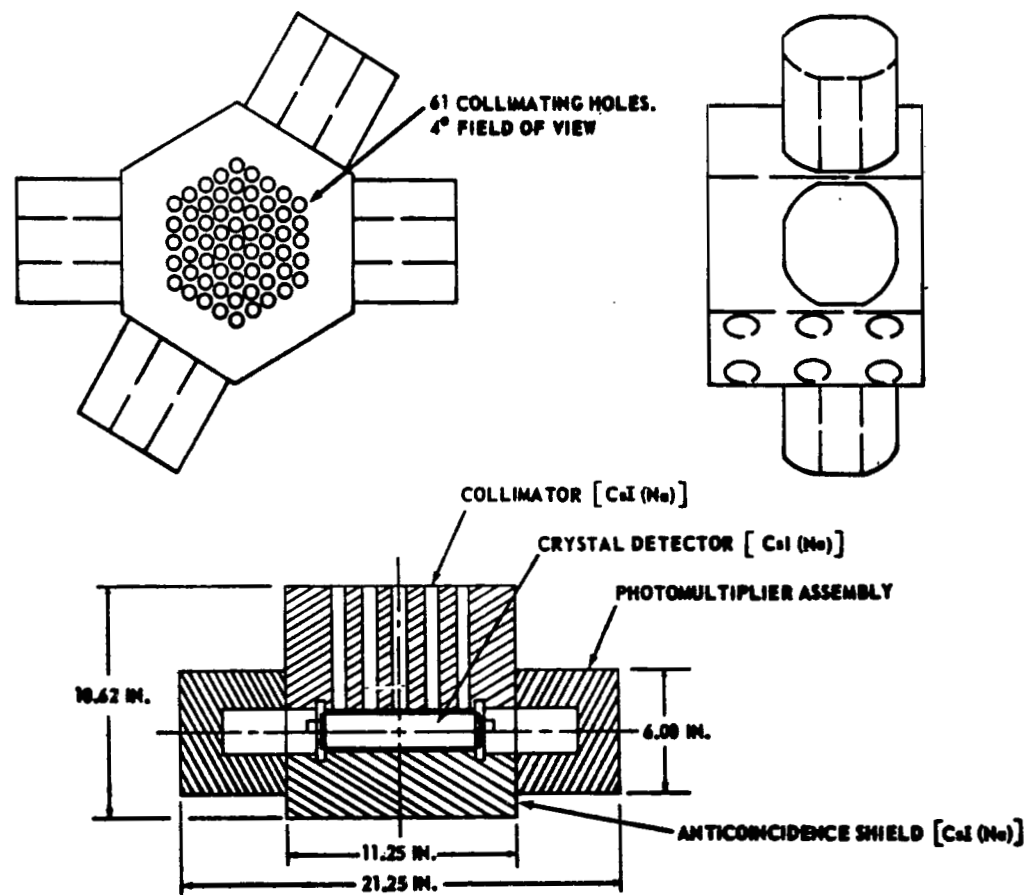
Figure A-4. Low-energy gamma-ray detector.
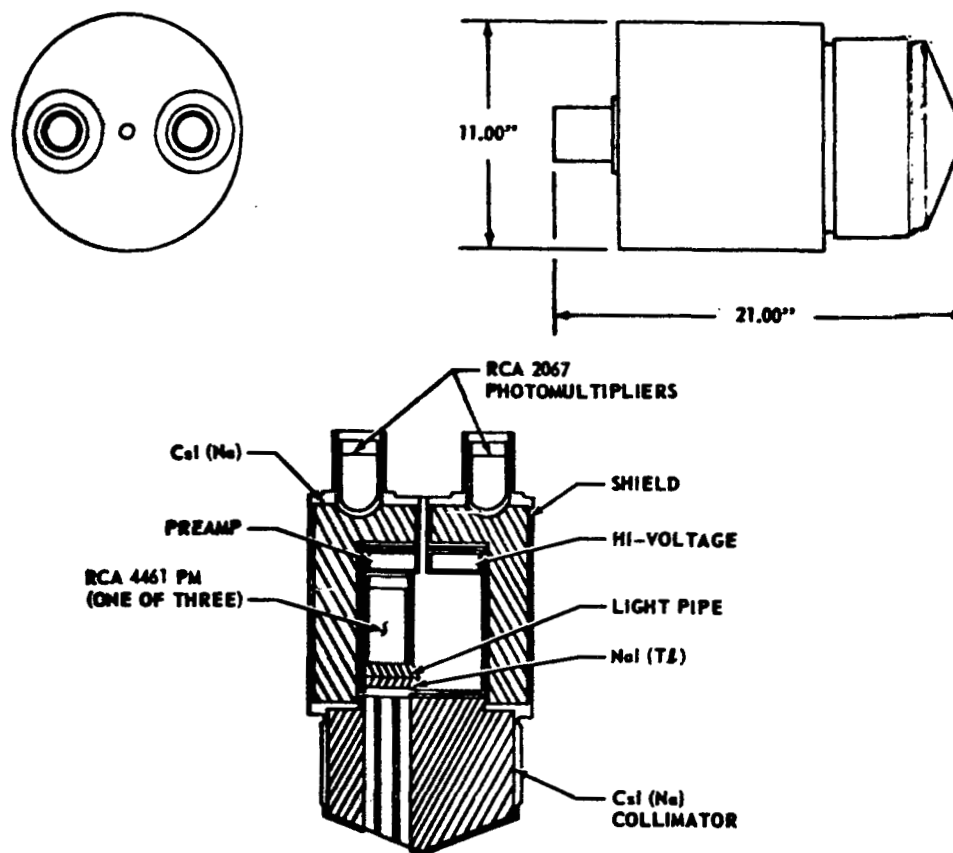
Figure A-5. Medium-energy gamma-ray detector.

allow gamma radiation to enter the detector from a desired direction through the collimating holes. The RCA 2067 photomultipliers amplify the anticoincidence signal produced in the CsI(Na) shield.

The scintillations produced by the central NaI(Tℓ) crystal will be converted by photomultiplier tubes into electrical pulses which will be slotted into a 216-channel pulse-height analyzer.

d. Gamma-Ray Telescope

(1) Scientific objective. The objective of this experiment is to study high-energy astrophysics of our galaxy. On a recent OSO-III flight, a flux of gamma-rays above 5×10^7 ev emitting primarily from the galactic plane was detected. The primary aim of this experiment is to scan the entire celestial sphere to determine the extent of gamma radiation and its origin. A further goal is to conduct measurements of the energy spectrum of possible discrete sources to aid in determination of the mechanisms or processes that produce the gamma radiation. Since known sources lie within the galactic plane, primary interest is in this area of the celestial sphere.

(2) Physical description of equipment. The basic unit shown in Figure A-6 consists of a plastic scintillator dome used as an anticoincidence device; a pair of spark chambers interlaid with thin plates to convert gamma-rays and provide pictorial representation of each event; a group of central plastic scintillators; Cerenkov detectors used as triggering devices; and a total-energy measuring device. The trajectory obtained in the spark chambers provides information on the arrival direction of the gamma-ray and its energy. The threshold energy is about 2.5×10^7 ev, and the energy measurement provided by the Coulomb scattering of the electrons in the thin plates between the spark chamber modules will permit accurate determination of the gamma-ray energy up to a few hundred million ev. Above that level, the total-energy detector will give a measurement of the energy.

The use of two basic units is being considered at the present time. It is envisioned that the two telescope units would not be exactly the same, although each unit would be built around a digitized spark chamber and would have essentially the same dimensions. The two units would be mounted back-to-back to look in opposite directions. The internal variations would permit measuring of different properties of the gamma radiation while still achieving results of high statistical validity.
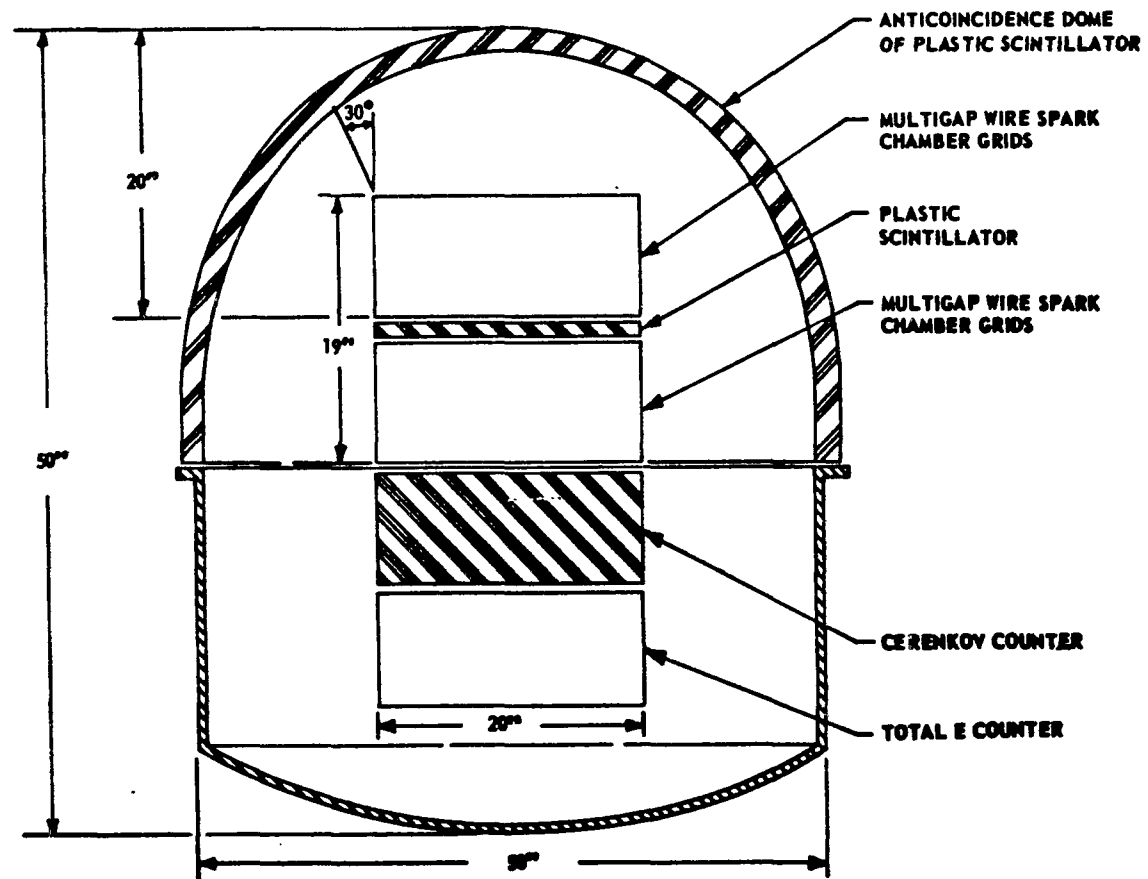
Figure A-6. Gamma-ray telescope.

e. Primary Cosmic-Ray Electron Detector

(1) **Scientific objective.** The objective of this experiment is to make a detailed study of the energy spectrum of the cosmic-ray electrons. A study of the shape of this spectrum above 5×10^9 ev can be used to determine the production mechanism of the electrons and, hence, energies will be measured from 5×10^8 ev to at least 10^{12} ev.

(2) **Physical description of equipment.** Pulse height will be measured directly from eight detectors in a tungsten-scintillator "sandwich" as shown in Figure A-7. These pulse heights are proportional to the numbers of relativistic particles passing through each scintillator and, therefore, sample the development of the electron-photon shower produced by an electron incident on the top of the tungsten stack. From the distribution of shower particle density as a function of depth in the stack, the energy of the incident electron is obtained. The distribution of the number of incident electrons as a function of energy will yield the desired energy spectrum.

The ratio of positive-to-negative electrons will be determined by measuring relative fluxes of electrons arriving from angles inclined toward the east and toward the west from the zenith. This is possible because the geomagnetic cutoffs are, in general, different for positive and negative particles arriving from a given direction.

f. Cosmic-Ray Calorimeter

(1) **Scientific objectives.** This experiment has two primary goals. The first is to study the properties of the cosmic radiation itself, and the second is to utilize the cosmic-rays as a source of highly relativistic particles to study high-energy interaction. The cosmic-ray study includes the following:

● Measurements of the charge composition of cosmic-rays as a function of energy in the range of 10^{10} to 10^{15} ev.

● Measurement of the electron spectrum in the range of 10^{10} to 10^{14} ev.

● The detection of any anisotropy in the arrival direction of the incident particles.

These measurements will lead to an increased understanding of the processes which produce high-energy cosmic-rays and act as a probe of the interstellar medium. They will yield information about the nucleosynthesis of elements in stellar interiors.
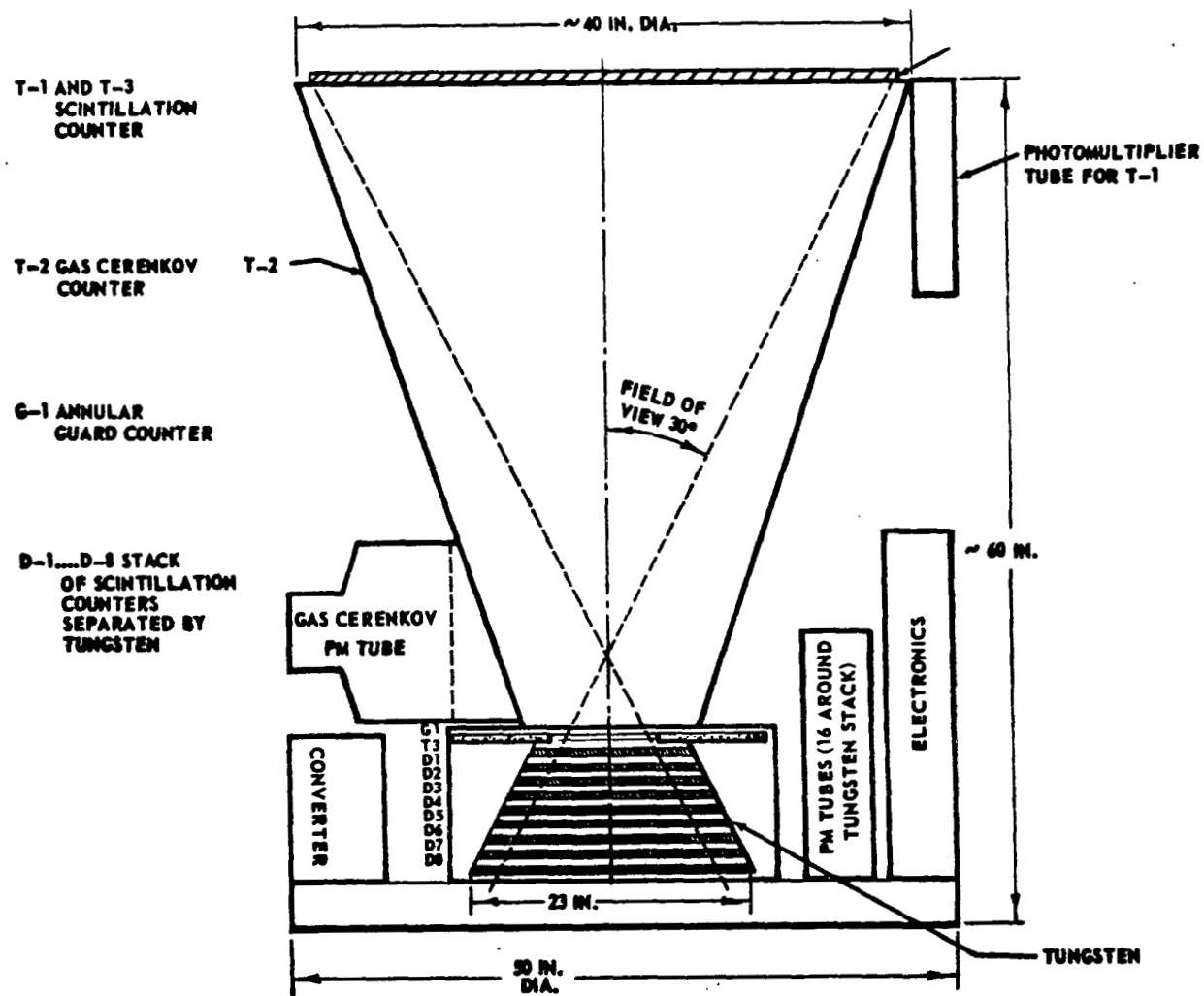
Figure A-7. Primary cosmic-ray electron detector.

The nuclear interaction experiment will determine interaction probabilities and multiplicities as a function of energy at high energy. The interaction studies will yield information about the nature of strong interactions and probe the structure of nuclear matter.

(2) Physical description of equipment. The cosmic-ray calorimeter consists of three major components:

- An ionization calorimeter.

- A cosmic-ray charge identification unit.

- A high-energy nuclear-interactions unit.

The detector is built around a calorimeter (total-absorption ionization spectrometer). The final configuration will depend on the exact weight and volume available. A double-ended unit, as illustrated in Figure A-8, is the most probable design.

(a) Ionization calorimeter. The double-ended calorimeter shown is constructed of iron (copper can be used if its magnetic properties are more desirable). This calorimeter is viewed by photomultiplier tubes from two sides. The two photomultiplier tube pulses from the scintillators, viewing opposite ends, will be added. These photomultiplier tubes provide redundancy as well as improved resolution.

(b) Cosmic-ray charge identification unit. This unit consists of an electron section, a charge identification section, and a trajectory section placed upon one end of the calorimeter. These would determine the trajectory and charge of the incident particles and separate electrons from protons.

(c) Nuclear interaction unit. The other end of the calorimeter will contain systems to identify nuclear active particles, measure their trajectories, study their interactions, and count the interaction products.

Each of the experiments selected for the reference baseline package is currently receiving intensive scientific investigation. The foregoing descriptions are based on the efforts of the scientists and their referenced work [A-2, A-3, A-4, A-5, A-6, A-7, A-8].
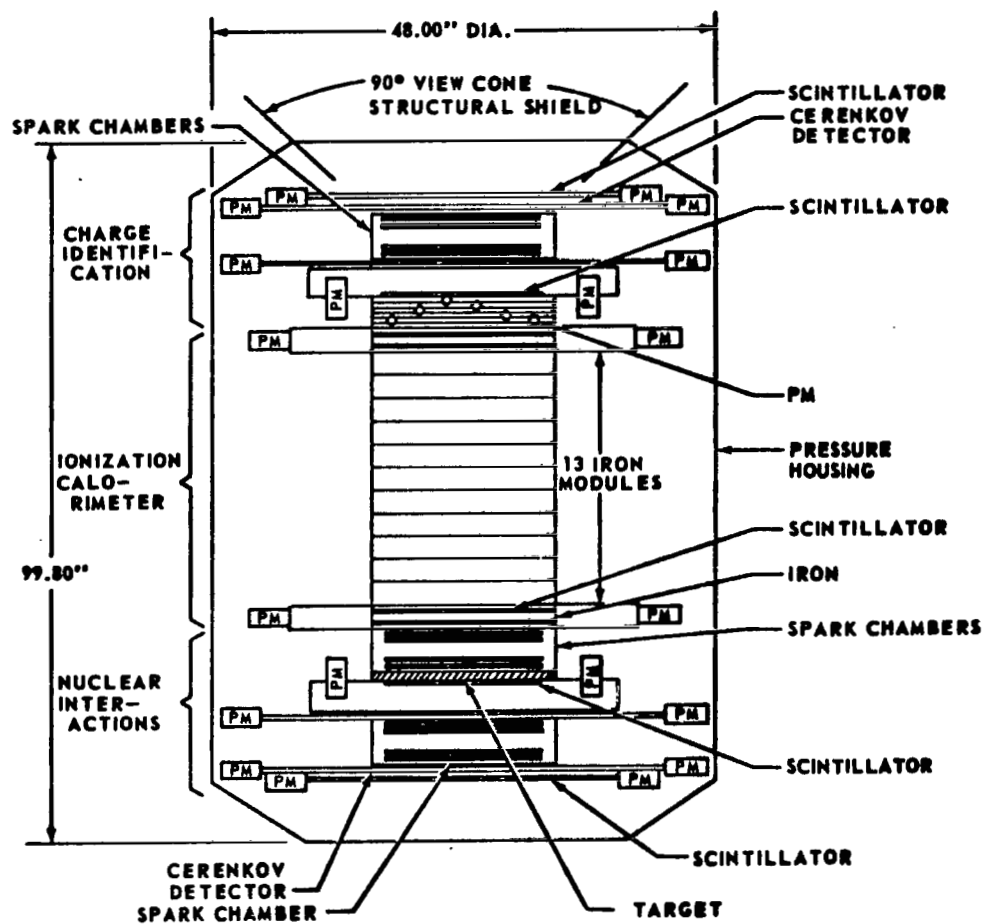
Figure A-8.   Cosmic-ray calorimeter.

3. Experiment Scan-Rate Considerations

The primary objective of the HEAO is to scan the entire celestial sphere and provide complete coverage by all experiments. This coverage can be accomplished by slowly rotating the entire spacecraft about the scan axis so that the instruments sweep out circular bands on the celestial sphere. During a large portion of the mission (celestial scan period), the spacecraft scan axis will be pointing along the solar vector, so as to obtain maximum solar panel illumination. In addition, the sun is used as an attitude reference, and, therefore, the pointing direction of the scan axis will move around the celestial sphere along the ecliptic at the same rate as the sun, approximately 1 degree per day.

The experiments will be hard-mounted to the spacecraft and will point in directions perpendicular to the longitudinal axis and the scan axis of the spacecraft. Rotating the spacecraft about its scan axis while maintaining the axis in alignment with the solar vector will result in sweeping out the entire celestial sphere in the time required for the earth to move half-way around the sun, i. e. , 6 months.

A high scan rate would spin-stabilize the spacecraft, helping to minimize the effects of disturbance torques on the spacecraft motion; however, the scientific instruments require a slow scan for proper resolution of the celestial sources, and, hence, the maximum scan-rate requirement for the baseline spacecraft was set at 0. 1 rpm. The minimum scan rate is the rate which will permit complete coverage of the celestial sphere by the instruments having the narrowest field of view.

The large area X-ray detectors have the smallest fields of view (1 by 4 degrees each) of any of the experiments. The 1-degree dimension lies in the X-Y plane, and the 4-degree dimension is the Y-Z plane. Neglecting the earth occultation and the experiment saturation periods while in the South Atlantic Anomaly, the minimum scan rate would be the rate which would allow the viewing bands to be swept out on the celestial sphere to be exactly adjacent to each other along the ecliptic plane. Using the 4-degree angle, this rate would be 1 revolution in 4 days, or 1/5760 rpm.

If this scan rate were selected, the 1- by 4-degree field-of-view instruments would view the points on the celestial sphere which are near the ecliptic plane during only one pass, since on the next revolution, these points would have passed out of view. Since only one opportunity would exist to view

these points, those points which are blocked from view by the earth during each revolution would not be viewed until mapping of the entire sphere were repeated, and perhaps not even then. In addition, during those periods when the spacecraft was in the South Atlantic Anomaly, no meaningful data could be measured by the instruments. Hence, certain areas of the celestial sphere would not be mapped. The likelihood of missing points further away from the ecliptic plane would be less, since some of these points would be scanned during more than one pass, because the bands swept out on the celestial sphere begin to overlap as the sweep moves away from the ecliptic plane.

Figure A-9 shows the time that a point would be within the field of view of an instrument during one revolution for various scan rates as a function of the width of the field of view. This figure does not include the effects of occultation and the South Atlantic Anomaly passage. These effects would produce gaps in the coverage of the celestial sphere. Hence, the theoretical minimum scan rate must be at some higher value, if such gaps in the celestial sphere are to be avoided.

Consideration was also not given in this analysis to the effects of pointing errors. Since a 1-degree pointing error is allowed, there could possibly be a 1-degree gap between the sweep bands previously described at the locations where they intersect the ecliptic plane, or there could likewise be a 1-degree overlap at these locations.

No further analysis was performed to determine a more accurate value of the theoretical minimum scan rate, since this rough analysis indicated no particular advantage in going to the lower values of scan rate, and the inclusion of the factors mentioned above which were not considered in the studies all seem to force the scan rate upward. The 0.1 rpm scan rate was selected for the baseline. This spin rate is so low that stability is not greatly enhanced by choosing it rather than a lower value.

Further analysis should be performed to evaluate the total integrated viewing time for various scan rates, including effects of occultation and the South Atlantic Anomaly.
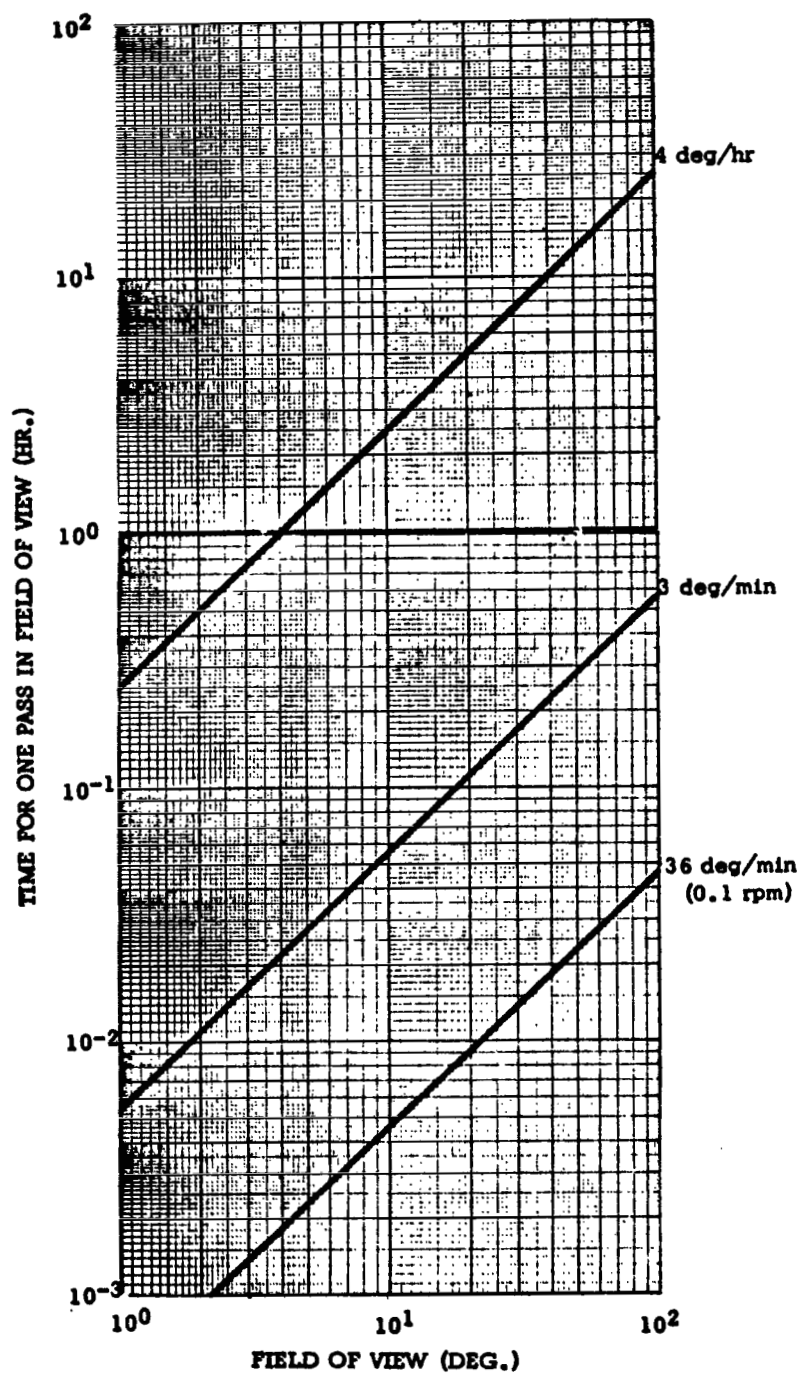
Figure A-9. Time in the field of view during each revolution.

REFERENCES

1. Project Plan for High Energy Astronomy Observatory. George C. Marshall Space Flight Center, October 1969.

2. Friedman, Dr. Herbert: June 1969 Version of '100-Square-Feet' X-Ray Panels for Superexplorers. Proposal submitted to NASA by Naval Research Laboratory.

3. Frost, Dr. H. J.: Low Energy Gamma-Ray Sky Survey. Proposal submitted to NASA by Goddard Space Flight Center, October 1967.

4. Frost, K. J.; and Dennis, B. R.: High Energy Celestial X-Rays — A Proposal for OSO-1. Goddard Space Flight Center, May 1969.

5. Peterson, Dr. L. E.: Proposal for Gamma-Ray and X-Ray Spectroscopy from an Earth Orbiting Manned Laboratory. Proposal submitted to NASA by University of California at San Diego, March 1966.

6. Fichtel, Dr. C. E.: Proposal for Apollo Experiment to Map the Galactic High Energy Gamma Radiation Using a Digitized Spark Chamber. Proposal submitted to NASA by Goddard Space Flight Center, September 1966.

7. Meyer, Dr. Peter: Cosmic Ray Electron. Proposal submitted to NASA by the University of Chicago, July 1966.

8. McDonald, Dr. F. B.: High Energy Facility for Super Explorer. Goddard Space Flight Center Memoranda for MSFC In-House Studies, May 1969.

APPENDIX B. LAUNCH VEHICLE ALTERNATIVES

TABLE OF CONTENTS

LIST OF ILLUSTRATIONS

LIST OF TABLES

v

APPENDIX B. LAUNCH VEHICLE ALTERNATIVES

1. Introduction

Although some consideration was given very early in the Phase A studies to the possible use of the Atlas Centaur (SLV3-C), the Titan IIIB, and the Saturn IB launch vehicles for the HEAO mission, all of these vehicles were very quickly eliminated from further consideration. The Atlas Centaur and Titan IIIB were eliminated because of lack of payload capability to deliver the entire HEAO payload on a single launch. It was found that these vehicles would not compete on a cost effectiveness comparison even if the single launch requirement were waived and the HEAO payload divided into multiple payload packages small enough to fit on these vehicles. The possible use of existing Saturn IB launch vehicles was eliminated from consideration early in the study since these vehicles are currently scheduled for manned launches in the Apollo Applications Program, and because other unmanned programs during the time frame of HEAO are currently planning to use Titan vehicles.

These considerations determined that the launch vehicle selection should be between the Titan IIID and Titan IIIC. Although modifications to the Titan IIID guidance system are required to adapt the Titan IIID to ETR, it was selected as the baseline launch vehicle from an overall cost effectiveness standpoint. The Titan IIIC, therefore, becomes the primary alternate to the Titan IIID launch vehicle for the HEAO missions. Either of two possible situations could develop which would make the Titan IIIC launch vehicle more attractive, but neither of these situations is anticipated at the time: (1) problems arise in adapting Titan IIID to ETR which cause its cost to exceed Titan IIIC cost; and (2) growth of the HEAO payload which would preclude the use of Titan IIID.

A brief description of the Titan IIIC and comparative launch vehicle performance capability data for the Titan IIID and Titan IIIC are presented in this appendix.

2. Titan IIIC Launch Vehicle

The Titan IIIC consists of a three-stage liquid propellant core vehicle supplemented by two SRM strap-ons, as shown in Figure B-1. The complete

Figure B-1.   Titan IIIC launch vehicle.

Text visible in the figure:

Payload
Interface

STG II/III Sep

STG I/II Sep

6.2 ft
29.0 ft
72.9 ft
108.1 ft

HARDPOINTS - 8
UNEQUALLY SPACED
GUIDANCE - ALL INERTIAL

STAGE III (TRANSTAGE)
PROPELLANTS LOADED 23,470 lb
I_{sp} NOM 302 (vac) sec
THRUST 16,000 (vac) lb
LOADED WEIGHT 27,477 lb

STAGE II
PROPELLANTS LOADED 67,299 lb
I_{sp} NOM 316.9 (vac) sec
THRUST 101,890 (vac) lb
LOADED WEIGHT 73,171 lb

STAGE I
PROPELLANTS LOADED 258,996 lb
I_{sp} NOM 299 (vac) sec
THRUST 523,000 (vac) lb
LOADED WEIGHT 274,398 lb

STAGE 0
PROPELLANT WEIGHT 848,494 lb
TVC (N_2O_4) LOADED 16,848 lb
I_{sp} NOM 231.8 sec
THRUST 2,340,000 lb
LOADED WEIGHT 1,016,050 lb

LIFTOFF
   FOUR STAGES WITHOUT PAY-
   LOAD OR PAYLOAD FAIRING
WEIGHT 1,390,340 lb
THRUST 2,327,430 lb

four-stage launch vehicle (less payload and fairing) has an overall length of approximately 110 feet and a lift-off weight of approximately 1.4 million pounds.

The Titan IIIC space launch vehicle uses the ITL complex at the ETR.

a. <u>Airframe</u>. Stage 0 consists of two identical SRM's mounted 180 degrees apart on the core vehicle. Each is approximately 10 feet in diameter and 85 feet long, weighs about 0.5 million pounds, and produces an initial thrust of 1.2 million pounds. The TVC is provided by liquid injection of pressurized liquid N_2O_4.

Stage I is 10 feet in diameter and approximately 71.5 feet long, is of aluminum skin-stringer construction, and consists of two liquid propellant tanks with the necessary skirts and two gimbaled engine assemblies.

Stage II is 10 feet in diameter and approximately 31 feet long, is of the same type of construction as Stage I, and consists of two liquid propellant tandem tanks with skirts, between-tank truss, and one gimbaled engine assembly.

The Transtage (Stage III) is 10 feet in diameter and approximately 14.5 feet long, is of aluminum skin-stringer construction, and consists of two liquid propellant titanium tandum tanks, two equipment trusses, and two gimbaled engine assemblies. Payload and fairing interfaces are provided at the forward end of the Transtage.

b. <u>Core Propulsion</u>. The Stage I propulsion system uses an Aerojet YLR87-AJ-11 engine assembly comprising two gimbaled engines and related equipment. The engines are pump fed and combined regenerative and ablative cooled. The normal vacuum thrust is approximately 520 000 pounds. Propellants are aerozine-50 and N_2O_4.

The Stage II propulsion system uses an Aerojet YLR91-AJ-9 engine assembly consisting of a single-gimbaled engine and related equipment and a gimbaled gas generator exhaust nozzle for roll control. It is pump fed and ablative cooled. Normal vacuum thrust is approximately 100 000 pounds. Propellants are identical to those of Stage I.

The Transtage main propulsion system uses an Aerojet AJ10-138 engine assembly consisting of two 8000-pound nominal vacuum thrust engines. These engines are ablative cooled and pressure fed, using helium as pressurant. Propellants are identical to those used for Stages I and II. Multiple start capability is provided.

The Transtage multipurpose ACS uses a monopropellant blowdown hydrazine system and fixed thruster assemblies to provide attitude control; propellant settling; orbit adjust, maneuvering, and vernier control; and multipayload deployment and controlled dispersion.

c. Electrical. All electrical power required for the Transtage payload fairing and payload is derived from Transtage-mounted silver-zinc storage batteries. Power is a nominal 28 vdc on five different buses and is available from lift-off until approximately 6.75 hours.

d. Tracking and Flight Safety. Engine shutdown and destruct commands are supplied by two redundant independent UHF systems. Tracking is provided by C-band pulse transponder and related equipment.

e. Hydraulics. The hydraulics system is used in each of the three liquid propellant stages to gimbal the thrust chambers of the respective stage. In Stage II, the gas generator exhaust nozzle is also gimbaled for roll control. Electric valves are included in Stage 0 for TVC injectant and require no hydraulics.

f. Guidance. The Titan IIIC inertial guidance system (IGS) consists of an IMU that is a gimbaled platform with three pendulous integrating gyro accelerometers; an MGC, which is a random access, thin film core memory, parallel, binary, digital computer; a TCU that provides liquid coolant circulated in the IMU and MGC; and an SC.

g. Flight Controls. The flight control system stabilizes the attitude of the vehicle in all phases of flight from launch through payload separation. This system establishes the flight path of the vehicle by implementing all steering commands issued by the IGS. It consists of software in the MGC, Stage I and II attitude rate sensors, LASS, TVC for the SRM's, and hydraulic actuators in the three core stages.

h. Instrumentation. The instrumentation system, a PCM/FM system, operates in the S-band frequency. Data signals are sampled and encoded by two RMIS's, each of which includes a group of RMU's, and a single central converter. The RMU samples, amplifies, and holds the signals to provide a serial PAM output train to the central converter.

B-4

3. Launch Vehicle Capabilities

Performance data on the Titan IIID and the Titan IIIC launch vehicles required for HEAO-A mission planning are presented in this section. These data are presented in a general fashion and are therefore applicable to missions other than HEAO-A. Trajectory and performance assumptions, vehicle characteristics, payload capabilities, trajectory profiles, time histories for the inertial velocity, flight path angle, longitudinal acceleration, Mach number, dynamic pressure, and altitude are presented for the Titan IIID and/or the Titan IIIC launch vehicles.

While these data are sufficient for planning purposes and preliminary studies, additional performance studies will be required when more definitive weights data and mission parameters are available. It should be noted that slightly different weights assumptions were used in developing the performance charts in this paragraph from those used and documented in Paragraph 4 and which are based on recent data from the Lewis Research Center. In addition, the payload fairing is assumed to be dropped at 283 seconds, which is approximately 100 seconds later than shown in Paragraph 4. However, these discrepancies in assumptions should not impair the comparative quality of the data presented since the magnitude of the performance numbers differ only slightly.

a. <u>Assumptions and Data Sources</u>. Assumptions and data sources used in the Titan IIID and Titan IIIC trajectory calculations are as follow:

● Vehicle weight and propulsion data from SMSD-PVEL-191, "Titan III Vehicle Description," Brown Engineering Company, August 1968, Unclassified.

● Payload shroud and payload adapter weights from BMI-NLVP-ICM-69-92, "Titan IIIC, Titan IIID, and Titan IIID/Centaur Performance (to 200 n.mi. orbits)," July 17,1969, Unclassified.

● Aerodynamic data from SSD-CR-66-103, "Titan III Data Book for Performance Calculations (V), AF04 (695) - 997," August 1967, Confidential.

● Launch from KSC on an azimuth of 90 degrees measured from north to south over east.

● The two 5-segment 120-inch SRM's ignited on the pad.

● Vertical ascent for 10 seconds, initiation and execution of a constant pitch rate program until 30 seconds' flight, after which a zero angle-of-attack was flown until SRM burnout. At that point atmospheric effects were neglected since the dynamic pressure was less than 13 lb/ft^2. The altitude achieved was 188 370 feet (Titan IIID to a 200-n. mi. orbit).

● The 271-pound heat shield and the 242-pound starter propellant jettisoned 107 seconds after lift-off.

● The main stage engines (Core Stages I and II ignited at 110 and 253.682 seconds after lift-off. The transtage, Titan IIIC only, was ignited at 457.906 seconds after lift-off.

● The SRM cases, the Core Stage I, and the Core Stage II for Titan IIID were jettisoned at 121, 253.682, and 453.297 seconds after lift-off (stage cutoff). Titan IIIC was the same as Titan IIID, except Core Stage II and the transtage were jettisoned at 457.906 and 859.850 seconds, respectively, after lift-off.

● Vacuum flight thrust angles optimized via steepest ascent method.

● The 2310-pound payload shroud jettisoned at 283.682 seconds after lift-off.

● Payload is defined for Titan IIID as weight above the Core Stage II at stage injection. The Titan IIIC payload is defined as weight above the transtage at stage injection.

b. Trajectory Profile. The Titan IIID trajectory profile is three stages (0, Core I, and Core II) direct-ascent to orbit. The Titan IIIC trajectory profile is four stages (0, Core I, Core II, and transtage) direct-ascent to orbit. The following typical Titan IIID launch-to-orbit profile is illustrated in Figure B-2.

● Start SRM's and lift-off at 0.0 second.

● Core Stage I ignition at 110 seconds.

● Solid rocket motors jettisoned at 121 seconds.

● Core Stage I staged and Core Stage II ignited at 253.682 seconds.

ORBIT ALTITUDE

SECQUENCE OF EVENTS (ORBIT ALTITUDE 200 N. MI.)

1 START SOLID ROCKET MOTORS AND LIFT OFF
2 CORE STAGE 1 IGNITION
3 SOLID ROCKET MOTORS JETTISIONED
4 CORE STAGE 1 STAGED AND CORE STAGE 2
  IGNITION
5 SHROUD JETTISIONED
6 CORE STAGE 2 SHUTDOWN, STAGED, AND
  PAYLOAD INJECTED INTO ORBIT
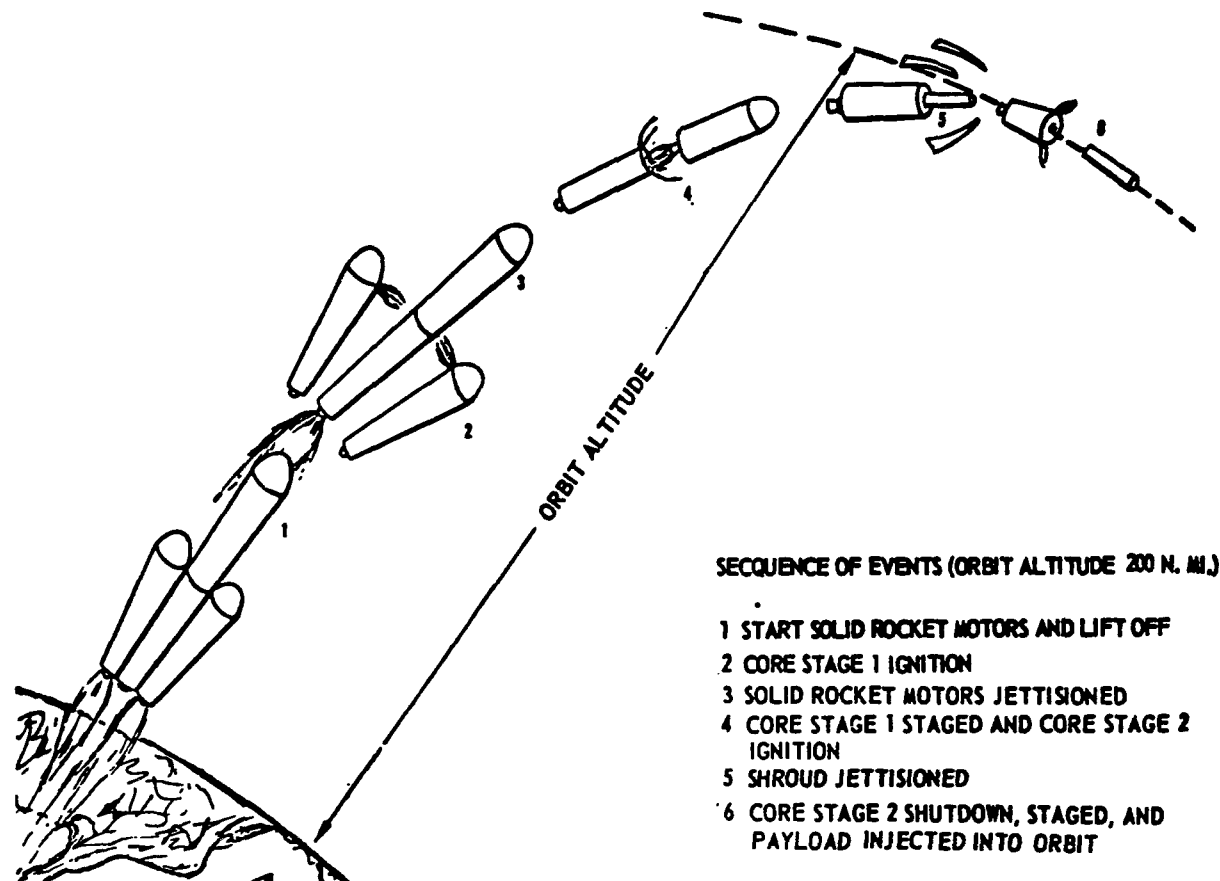
Figure B-2.   Typical Titan IIID launch-to-orbit profile.

● The 2310-pound shroud jettisoned at 283.682 seconds.

● For Titan IIID, Core Stage II cutoff, staged, and payload injected into orbit at 453.297 seconds.

● For Titan IIIC, Core Stage II staged and the transtage ignited at 457.906 seconds.

● For Titan IIIC, transtage cutoff, staged, and payload injected into orbit at 859.85 seconds.

c. Payloads and Trajectory Data. Graphs and tables of payloads and trajectory data for the Titan IIID and Titan IIIC launch vehicles are presented and explained as follows:

● Figure B-3 is a graph showing net payload as a function of orbital altitude for the Titan IIIC and Titan IIID launch vehicles. For these missions the trajectories were direct ascent to circular orbit with an orbital inclination of 28.5 degrees.

● Figure B-4 is a graph of net payload versus apogee altitude for the Titan IIIC and Titan IIID launch vehicles'. For these missions the trajectories were direct ascent to an elliptical orbit with an orbital inclination of 28.5 degrees and a perigee injection at 90 n.mi.

● Figure B-5 is a graph of net payload versus perigee altitude for the Titan IIID launch vehicle. For these missions the trajectories were direct ascent to an elliptical orbit with an orbital inclination of 28.5 degrees, with a 1-year orbital lifetime, associated with a plus two-sigma solar activity.

● Figure B-6 is a graph of apogee altitude versus perigee altitude for the HEAO having a 1-year orbital lifetime associated with a plus two-sigma solar activity. This graph is to be used in conjunction with data presented in Figure B-5 in determining payload, apogee, or perigee when two of of the three parameters are specified.

● Figure B-7 is a graph of inertial velocity, inertial flight path angle, and longitudinal acceleration versus flight time for the Titan IIID launch vehicle. For this mission, the trajectory was a direct ascent to a 200-n.mi. circular orbit with an orbital inclination of 28.5 degrees.

B-8
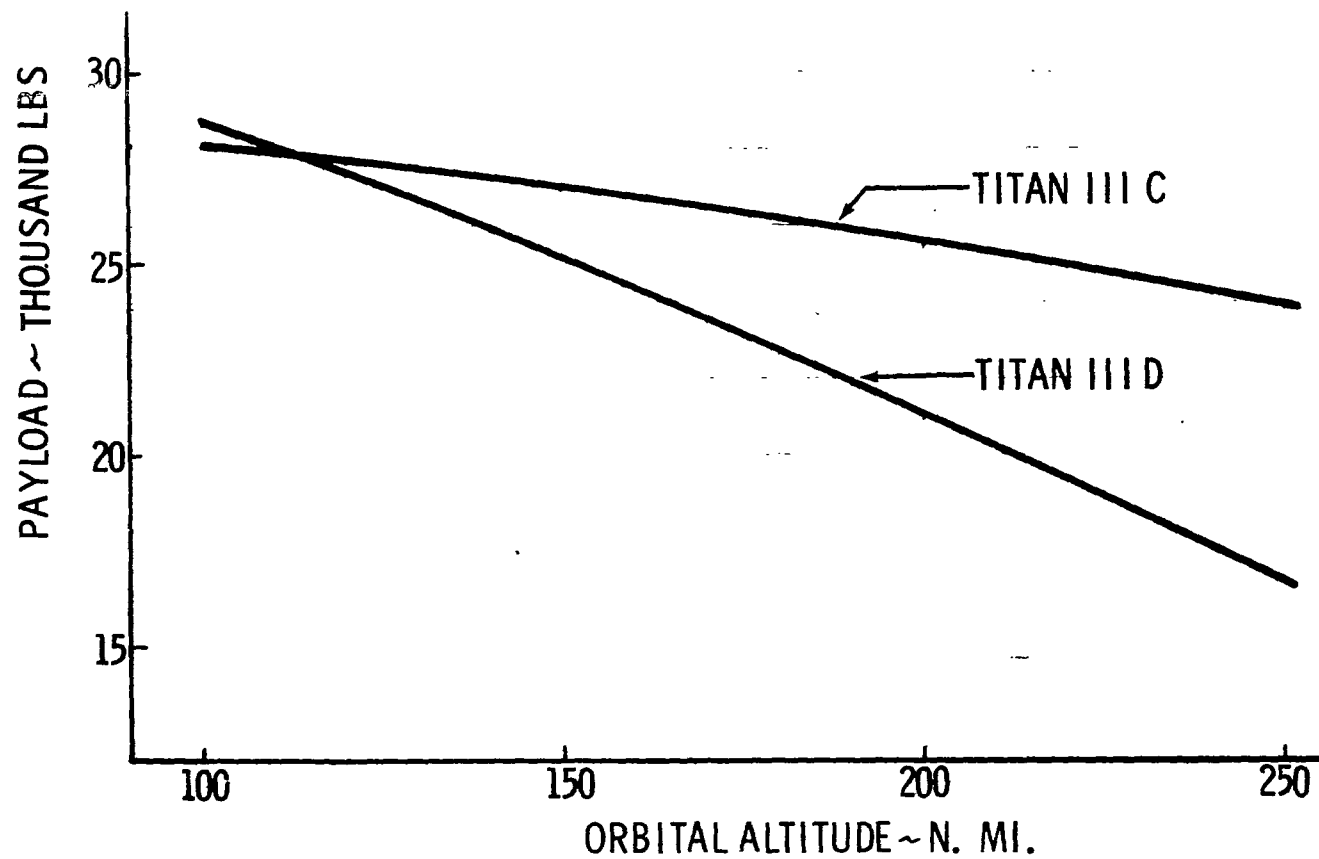
Figure B-3. Titan IIID and IIIC performance to circular
orbit inclination 28.5 degrees.
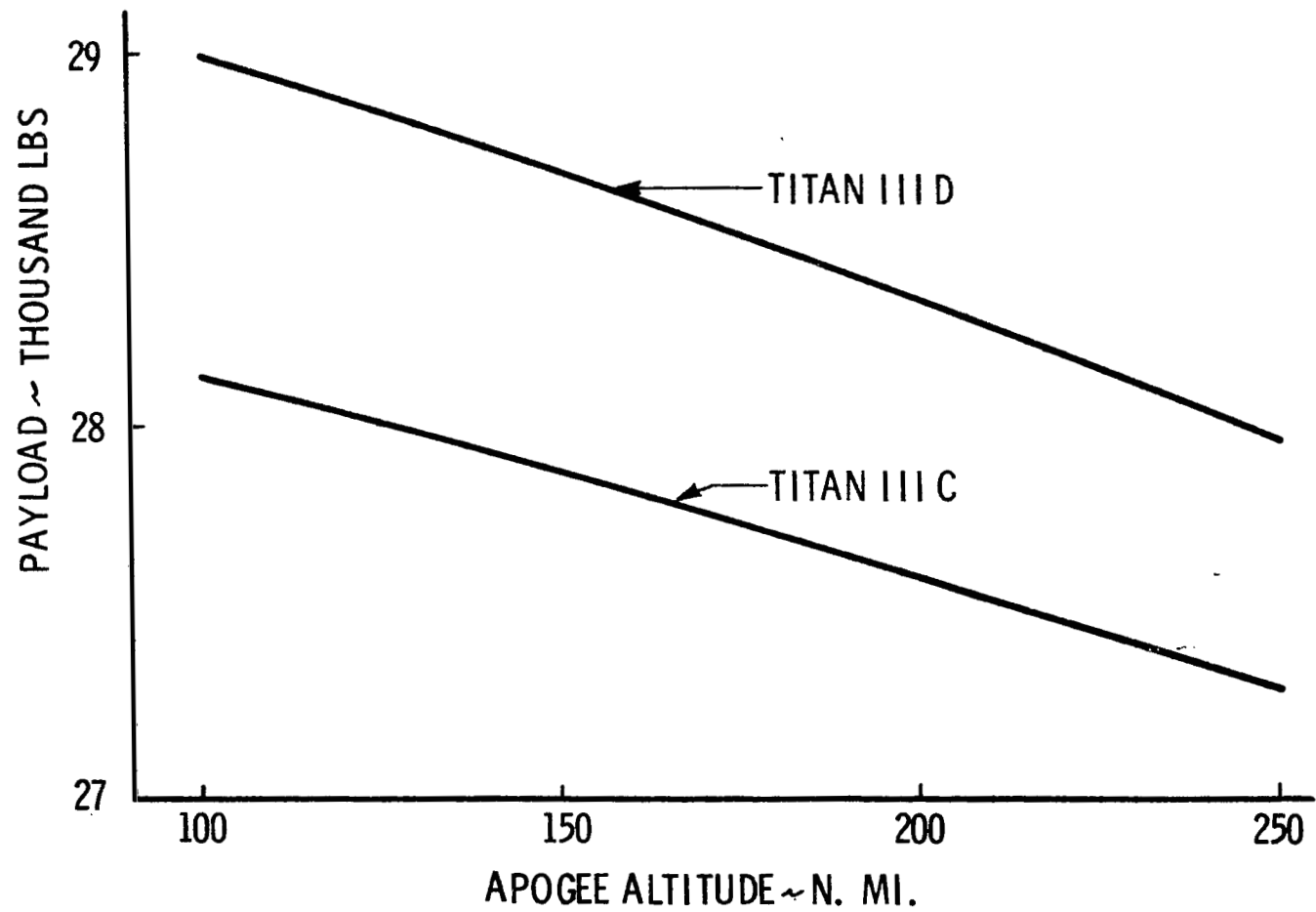
Figure B-4. Titan IIID and IIIC performance-to-perigee
injection at 90 n. mi. versus apogee altitude.
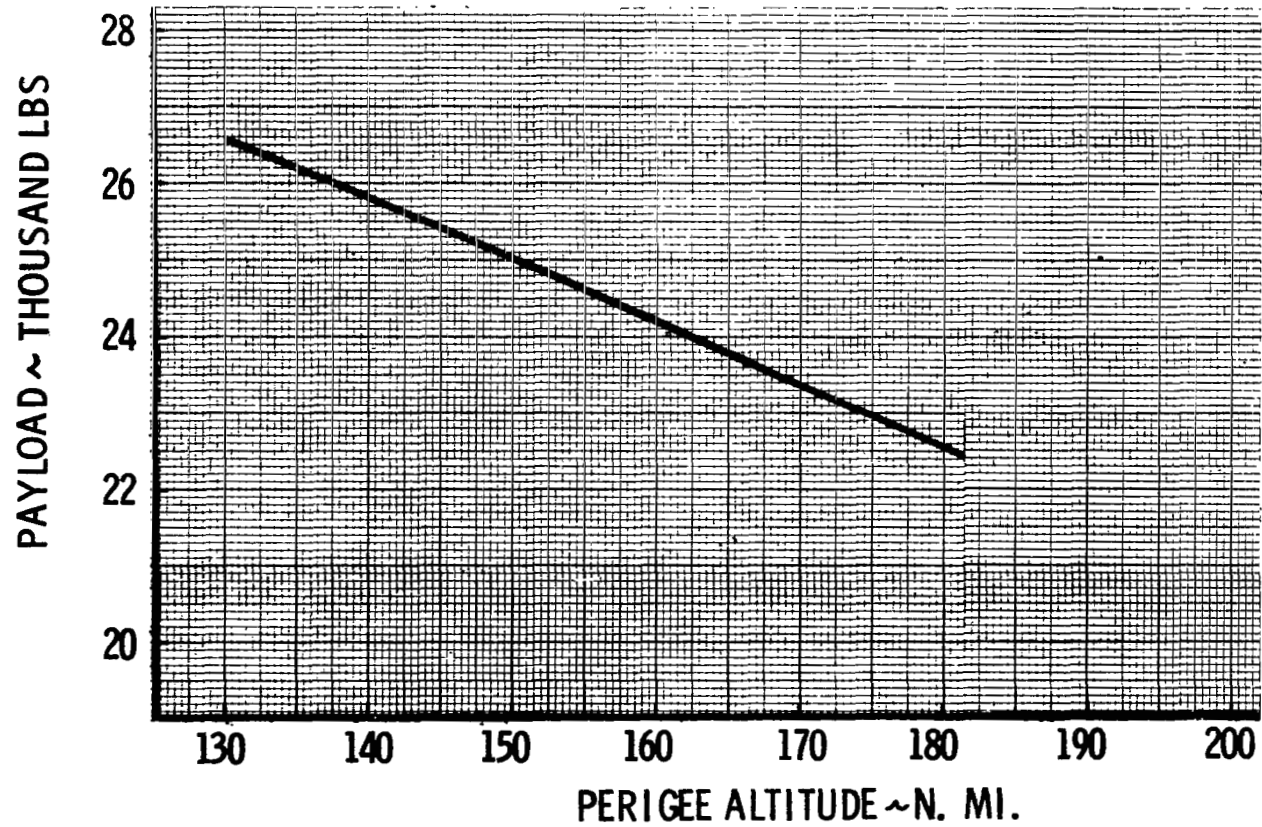
Figure B-5. Titan IIID payload capability for elliptical orbit injection with
1 year minimum orbital lifetime for +2σ solar activity.
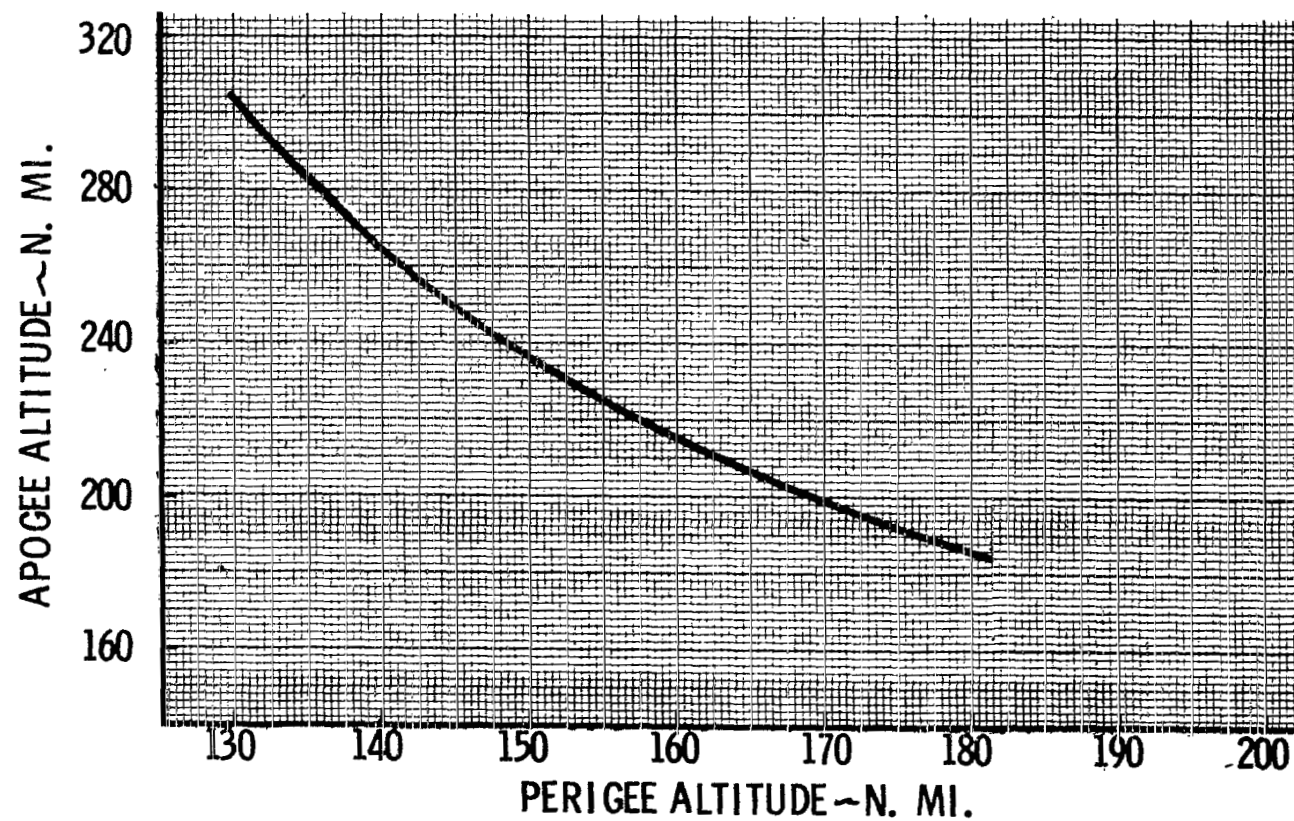
Figure B-6. Apogee versus perigee altitude of HEAO spacecraft with
1 year orbital lifetime and +2σ solar activity.
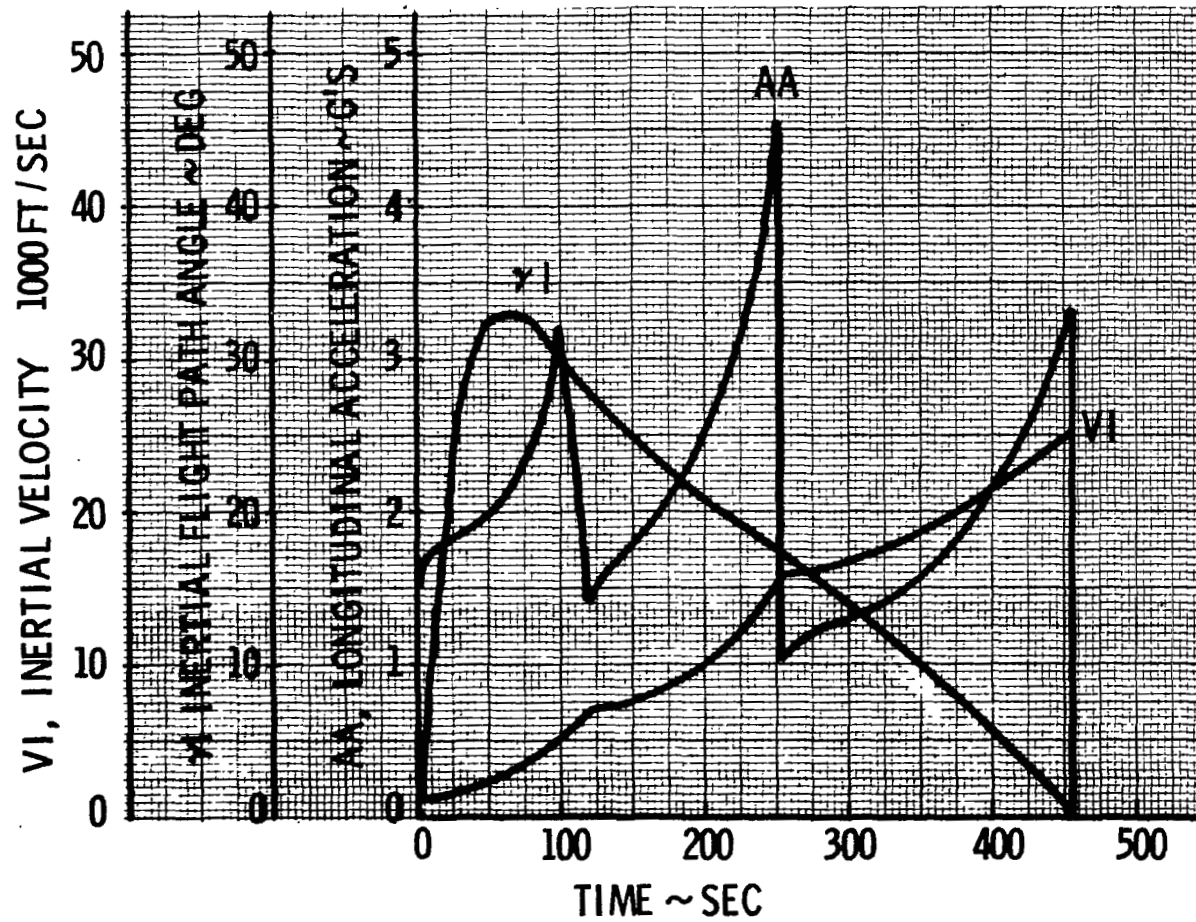
Figure B-7. Titan IIID trajectory parameters direct injection into a
200-n. mi. circular orbit, 28.5-degree inclination.

- Figure B-8 is a graph of Mach numbers and dynamic pressure versus flight time for the Titan IIID launch vehicle. For this mission the trajectory was a direct ascent to a 200-n. mi. circular orbit and an orbital inclination of 28.5 degrees.

- Figure B-9 is a graph of altitude versus flight time for the Titan IIID launch vehicle. For this mission the trajectory was a direct ascent to a 200-n. mi. circular orbit with an orbital inclination of 28.5 degrees.

- Figure B-10 is a graph of net payload versus orbital inclination for the Titan IIID launch vehicle. For these missions the trajectories were direct ascent to 100-, 200-, and 300-n. mi. circular orbits with and without yaw steering. For the northerly launch, the vehicle was launched with a 45-degree launch azimuth, and yaw steering was initiated at 90 seconds after lift-off.

- Table B-1 contains payload capabilities for the Titan IIIC and Titan IIID launch vehicles to a 200-n. mi. circular orbit with an orbital inclination of 28.5 degrees. This table gives the payload capabilities to a 200-n. mi. circular orbit by direct ascent and by Hohmann transfer. To achieve a 200-n. mi. circular orbit by Hohmann transfer, the vehicle was assumed to go direct-ascent to a 90- by 200-n. mi. elliptical parking orbit, inject at perigee and circularize at apogee.

The Titan IIIC transtage is restarted to circularize at apogee. To circularize at apogee, 695 pounds of transtage propellant was required.

The Titan IIID Core Stage II has no restart capabilities. To do a Hohmann transfer, a kick stage was added to the payload. This stage was composed of four SRM's. To circularize at apogee, 620 pounds of solid rocket propellant was required (see Appendix G).

- Table B-2 contains Titan IIIC and Titan IIID performance data to a 200-n. mi. circular orbit with orbital inclinations of 28.5 degrees, 20 degrees, 15 degrees, and 10 degrees. Titan IIID performance below 28.5 degrees inclination is not shown. The Core Stage II on the Titan IIIC or IIID is not restartable. This fact causes a yaw maneuver to be performed at off optimum position in the trajectory to effect lower inclination orbit; the lowest inclination which can be achieved by the Titan IIID is 23 degrees with a payload of zero. The payload drops off linearly from 20 920 pounds at 28.5 degrees to zero at 23 degrees. The performance was calculated assuming the following mission profile:
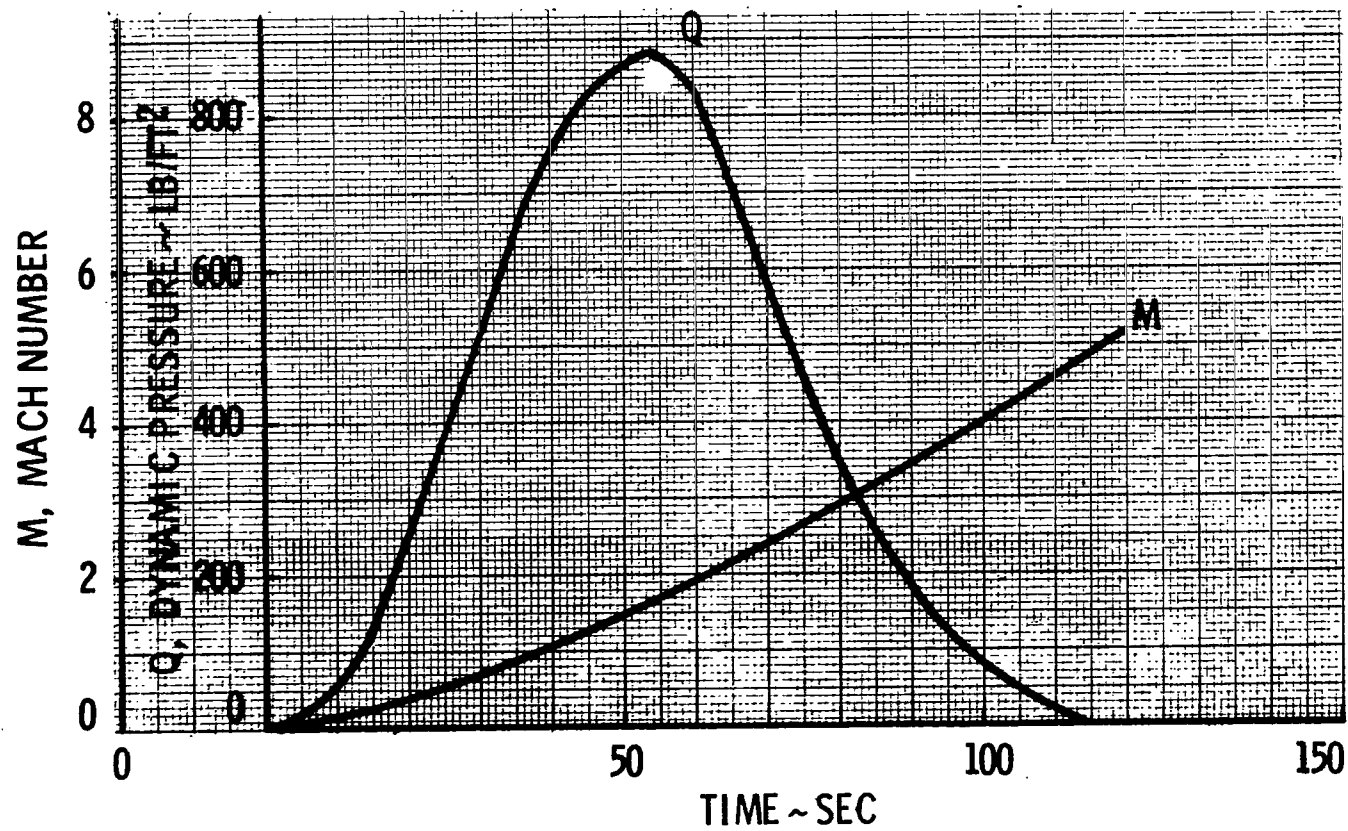
Figure B-8. Titan IIID trajectory parameter direct injection into a
200-n. mi. circular orbit, 28.5-degree inclination.
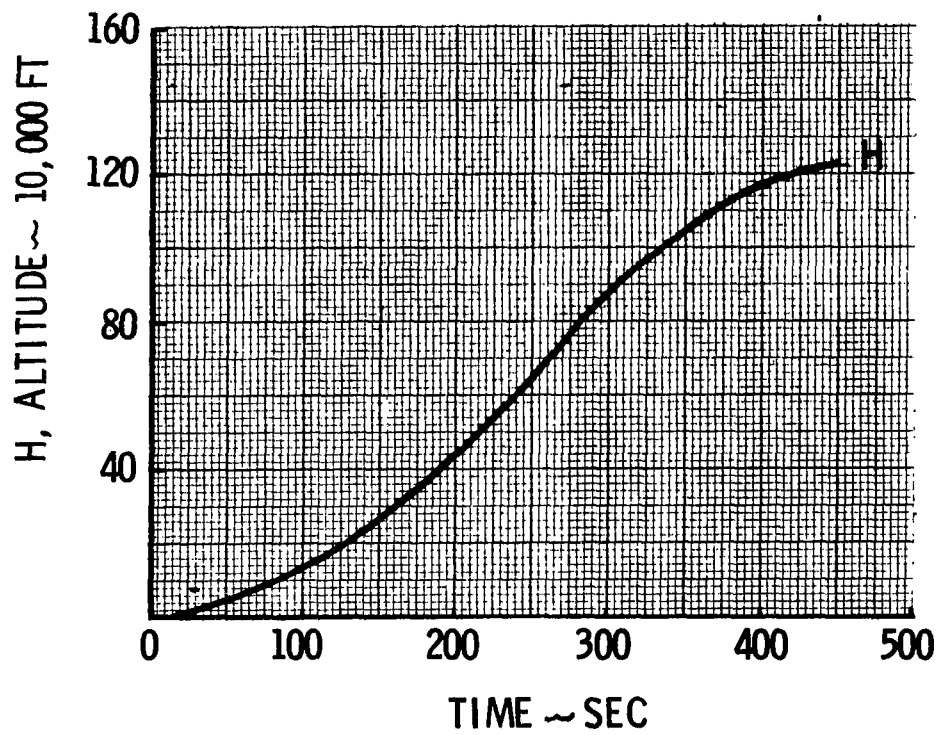
Figure B-9. Titan IIID direct ascent, 200-n.mi. orbit, 28.5-degree inclination.
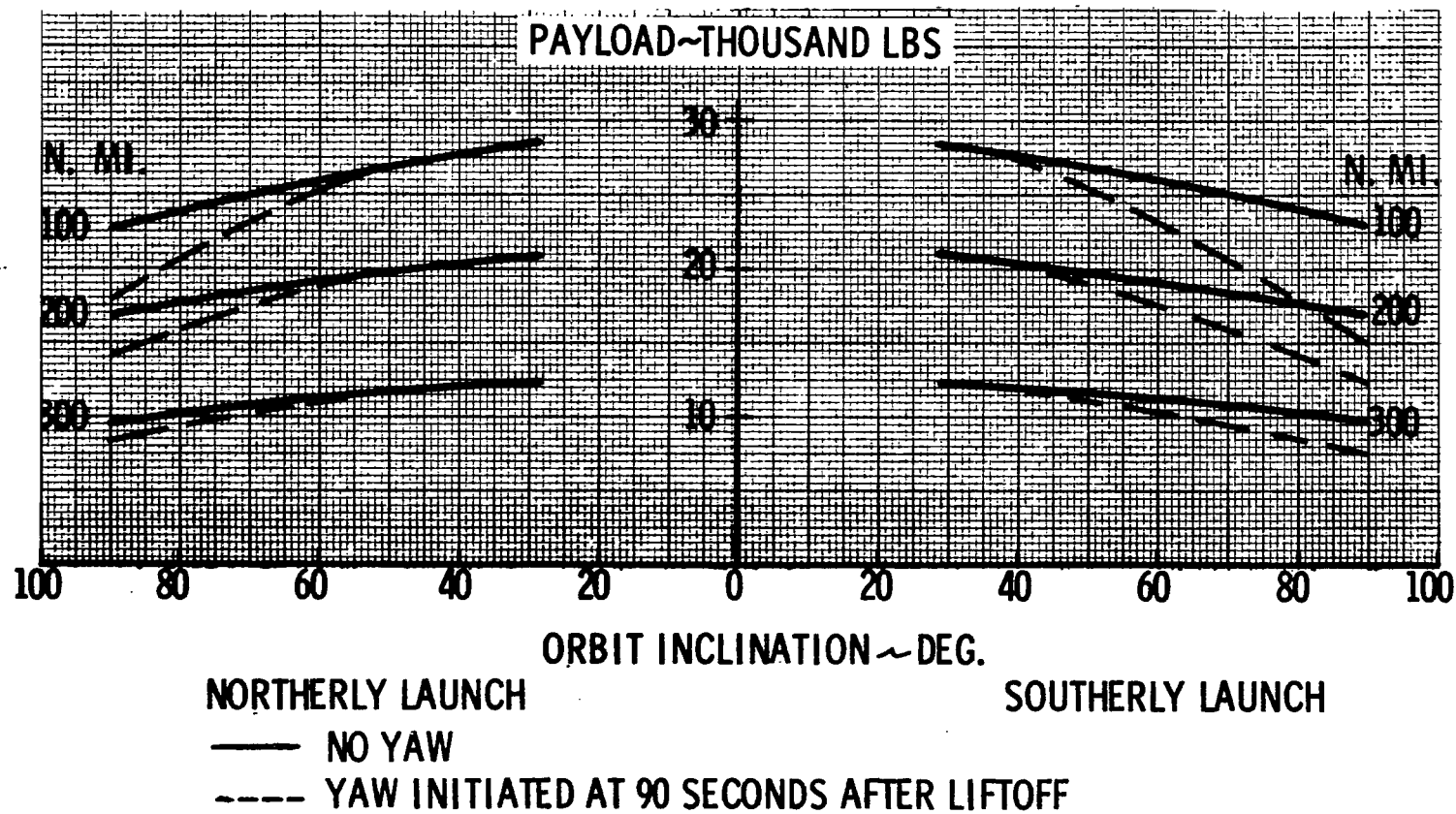
Figure B-10. Titan IIID payload capability to circular orbit.

TABLE B-1. TITAN IIIC AND TITAN IIID PAYLOAD CAPABILITY TO 200-N. MI. CIRCULAR ORBIT WITH 28.5-DEGREE INCLINATION

Direct Ascent

Vehicle	Payload (lb)
Titan IIIC	25 424
Titan IIID	20 922

Hohmann Transfer[a]

Vehicle	Payload (lb)
Titan IIIC	26 898
Titan IIID[b]	27 582

a. The vehicle was assumed to go direct-ascent to a 90-n. mi. perigee and circularize at a 200-n. mi. apogee.

b. Hohmann transfer was accomplished by adding a kick stage to the payload.

TABLE B-2. TITAN IIIC AND TITAN IIID PAYLOAD CAPABILITIES TO A 200-N. MI. CIRCULAR ORBIT WITH 28.5-, 20-, 15-, AND 10-DEGREE INCLINATIONS

Direct Ascent

Vehicle	28.5 deg. incl.			
Titan IIIC	25 424 lb			
Titan IIID	20 922 lb			

Hohmann Transfer[a]

Vehicle	28.5 deg. incl.	20 deg. incl.	15 deg. incl.	10 deg. incl.
Titan IIIC	26 304 lb	16 148 lb	11 069 lb	6816 lb
Titan IIID[b]	20 922 lb	-	-	-

a.   The vehicle was assumed to go direct-ascent to a 100-n. mi. circular parking orbit with a 28.5-degree inclination and then a two-burn Hohmann transfer with necessary plane changes to a 200-n. mi. circular orbit.

b.   Direct ascent (Core Stage II not restartable).

(1) The vehicle achieved a 100-n. mi. parking orbit.

(2) The 100-n. mi. parking orbit had a 28. 5-degree orbital inclination.

(3) Hohmann transfer to a 200-n. mi. circular orbit.

(4) Necessary plane changes are made during Hohmann transfer to achieve desired orbital inclination.

4. Titan IIID Performance Capability

Based on recent data from Lewis Research Center, the preliminary estimate of Titan IIID spacecraft system weight (separated spacecraft, adapter, etc.) capability for the HEAO Mission is 20 641 pounds. A tabulation of vehicle weights and event times for selected flight events is given in Table B-3.

The ground rules for this performance analysis were as follows:

1.   Launch azimuth — 93 degrees.

2.   Direct injection into a 200-n. mi. circular orbit.

3.   Orbital inclination — 28. 5 degrees.

4.   Shroud weight (40 feet long, 10 feet in diameter) — 2877 pounds.

5.   Shroud jettison — T + 182 seconds (360 000 feet).

6.   No spacecraft adapter nor any special spacecraft support equipment.

7.   Titan Stage II modifications — 76 pounds.

8.   Titan Stage II specific impulse — 313 seconds (vac).

9.   Improved Centaur Guidance System substituted for BTL Radio Guidance System.

10.   Flight performance reserves — 1800 pounds.

11.   No launch vehicle contingency.

TABLE B-3. FLIGHT EVENTS AND WEIGHTS
(HEAO-A MISSION)

Event	Time (sec)	Vehicle Weight (lb)
Lift-off	0.0	1 381 382
Solid motor burnout Stage I ignition	110.45	527 779
Solid motor jettison	121.45	346 375
Shroud jettison	182.00	237 338
Stage I burnout	253.92	111 238
Stage II ignition	254.92	93 998
Stage II burnout	458.63	29 261
Stage II jetison weight		8 620

Basic Stage II jettison weight	6444	
Stage II modifications	76	
Centaur guidance system	300	
FPR	1800	

Spacecraft system weight capability		20 641

It should be recognized that this performance analysis includes several uncertainties. Among these are the identification of the hardware penalties for modifications to the Titan IIID vehicle to accommodate the HEAO Mission and the determination of the trajectory simulation and the flight performance reserves. In addition to these performance aspects, it should also be recognized that a detailed evaluation of the interface of the Centaur Guidance System with the Titan IIID, including environmental considerations associated with guidance equipment relocation, will be required.

BIBLIOGRAPHY

MCR-68-62 Titan IIIC Payload Users' Guide, Revision 1. Martin Marietta Corporation, Denver Division, Systems Engineering, April 17, 1969.

T-IIID Launch Vehicle at ETR for High Energy Astronomical Observatory, Revision 1. Martin/Denver, September 19, 1969.

APPENDIX C.   SOUTH ATLANTIC ANOMALY
AND ORBIT OCCULTATION

TABLE OF CONTENTS

LIST OF ILLUSTRATIONS

LIST OF ILLUSTRATIONS (Concluded)

APPENDIX C. SOUTH ATLANTIC ANOMALY AND ORBIT OCCULTATION

1. Location and Intensity of Flux

Figure C-1 shows the electron flux counting rate over the South Atlantic Anomaly in 1966 at an altitude of approximately 400 km (216 n. mi.) [1]. It is seen that the counting rate above 0.5 MeV at the center of the anomaly exceeds 10^6 electrons/cm^2-sec at a relatively low altitude of 400 km (216 n. mi.). To obtain the total flux count received by a satellite, it is necessary to integrate over successive passes in the anomaly. The proton flux intensity is approximately three orders of magnitude less than the electron flux intensity in this region. Figure C-2 shows proton isointensity contours above 50 MeV at 400-km (216-n. mi.) altitude [2].

2. Energy Spectrum of the Trapped Flux

Recent models of the omnidirectional proton and electron fluxes have been proposed by Vette, et al. [3,4]. Figures C-3 and C-4 show the average omnidirectional electron and proton flux as a function of altitude accumulated by an orbiting spacecraft over a 24-hour period at various energy levels as predicted by the Vette models.

It is evident from looking at Figure C-5 that the electron flux is concentrated mainly in energies below 1.5 MeV. Figure C-6 shows the integral proton flux in the same approximate energy range. The integral flux-rate above zero energy is two orders of magnitude greater for electrons than protons. Both curves of Figures C-5 and C-6 are for a 200-n. mi. altitude, 30-degree inclination orbit.

From previous figures it was observed that the anomaly is centered near 30-degree South latitude. This observation implies that a 30-degree-inclination orbit can pass near the center of the anomaly. Figures C-7 and C-8 show the variation of electron and proton dose rate per day as a function of orbital inclination for four altitudes (after [2]).

3. Temporal Variations of Flux

The anomaly region is relatively constant in size and shape with time. Variations in particle flux and energy levels encountered by the spacecraft, and hence variations in experiment dead time, are due mainly to precession of the spacecraft orbit. This precession (approximately 0.5 degree per revolution for the baseline HEAO orbit) causes the spacecraft to follow different paths through the anomaly on successive revolutions. The net effect in terms of flux encountered by the spacecraft is illustrated in Figure C-9 for proton flux above 15 MeV. Although not directly applicable to the HEAO orbit due to difference in particle, energy level, and altitude, the figure illustrates qualitatively the wide variations in flux between successive orbits and the long periods of time during which no significant flux is encountered. Peak-to-average fluxes in the figure vary as much as 3 orders of magnitude, and approximately half the orbits do not encounter any significant flux.

Although the particle fluxes at about 200-n. mi. altitude are fairly stable, the count rate may vary by a factor of 2 to 3 with time, following solar disturbances. One of the largest factors that influenced electron flux at low altitudes was the thermonuclear (Starfish) explosion in the upper atmosphere. This detonation produced energetic electrons in the MeV range which will affect particle-counting rates for years. The electron data described above are based on 1966 to 1968 predicted fluxes. Actual fluxes expected beyond 1970 may be somewhat smaller [5].

4. Occultation Analysis

a. <u>Occultation of the Sun.</u> When planning a space mission which depends upon power derived from solar rays, a consideration of how much the vehicle will be occulted from the sun is imperitive. Also, since in the case of the HEAO satellite the sun is used as an attitude reference during much of the mission, it must rely upon a backup mode of attitude sensing when it is occulted. For these reasons, it is necessary to consider factors influencing occultation. In the following four sections is a brief description of the effects on occultation by the right ascension of the ascending node of the satellite orbit, altitude of the orbit, time of year, and inclination of the spacecraft orbit to the earth equatorial plane. It is assumed that two-body conic approximations describe the spacecraft motion. The nominal orbit is taken to be a 200-n. mi. circular orbit at an inclination of 28.5 degrees to the equatorial plane and right ascension of ascending node of 0.0 degrees. The sun is at its location for June 1, 1973, which is in the plane of the ecliptic at an angle of 70.1 degrees measured counterclockwise from the vernal equinox. In each of the following four sections, only one parameter is varied at a time (from the nominal) and the resulting effect upon occultation is observed. See Figure C-10 for identification of parameters.

C-2

1.   Variation with regression of the nodes.   Occultation is quite dependent upon right ascension of the ascending node of the spacecraft orbit as can be seen from Figure C-11.   As the right ascension increases from 0 degree, the orbital plane moves from a minimum angle from the ecliptic of 5 degrees to a maximum angle of 23. 5 + 28. 5 = 52. 0 degrees when the node has moved through an angle of 180 degrees from its nominal position.   From Figure C-11, it is observed that the time during each orbit that the spacecraft is in the dark decreases from a maximum at the nominal position of the node to a relative minimum value at the half revolution point.   As the ascending node is positioned at angles larger than 180 degrees to the vernal equinox the portion of each orbit that is occulted increases until the node has moved through a total of 360 degrees from the nominal.   The total difference in time occulted during each orbit is 6 minutes.

2.   Variation with altitude.   In Figure C-12, altitude was allowed to vary from 200-n. mi. to 150-n. mi. simulating orbital decay.   As the altitude decreases, the percent of the orbital period occulted increases from about 41. 4 percent at 200-n. mi. to about 42. 4 percent at 150-n. mi. , a difference of about 1 minute.   The occultation would approach 50 percent as a limit if altitude were allowed to approach zero.

3.   Variation with time of year.   The portion of each period that is occulted is plotted in Figure C-13 versus month of the year for the period June 1973 to May 1974.   Longitude of the sun is the physical quantity that varies with the date and causes the occultation time to decrease from about 38 minutes per orbit in June to about 37 minutes per orbit in November and increase to about 38 minutes per orbit again in May.

4.   Variation with inclination.   Figure C-14 shows how occultation time during each orbital period varies with inclination of the orbit to the equatorial plane.   Time occulted increases from about 37 minutes when the inclination is 0 degree to a relative maximum of about 38 minutes when the inclination is about 28 degrees and decreases to 27. 5 minutes when the inclination of the orbit reaches 90 degrees.   The maximum time occulted corresponds to an inclination of about the same as the angle between the ecliptic and equatorial planes.

5.   Summary.   Of the four factors considered, inclination of the orbit appears to be the most significant if it is allowed to vary from 0 to 90 degrees changing occultation time by more than 11 minutes.   In the consideration of the 90-degree orbit, a spherical earth model was used with a radius equal to the equatorial radius.   Since the polar radius is smaller than the equatorial radius by about 22 km, the time occulted for a polar orbit would be less than the figures in this study indicate.

Another significant factor in the determination of time occulted is right ascension of the orbital node, which varies the occultation from 32 to 38 minutes. The time of year and altitude of the orbit do not appear to be major factors affecting occultation as far as this preliminary investigation can determine.

It should be kept in mind that this preliminary study was made on the basis of estimating the behavior of physical quantities with a few data points and should not be construed to represent a thorough analysis of the problem.

b. Occultation of Specific Stars

1. General. It is desirable to know during what portion of each revolution that visible contact will not be possible with a given star. This discussion is concerned with determining what portion of time the line of sight between the satellite and a given star or constellation in the galactic plane is occulted by the earth. In the following sections is a brief discussion of the effects on occultation by the right ascension of the ascending node of the spacecraft orbit, altitude of the orbit, inclination of the orbit to the earth equatorial plane, and star location in the galactic plane. It is assumed that two-body conic approximations describe the motion of the spacecraft. Since an analysis of occultation for all stars in the galactic plane would not be feasible, two constellations were selected for study; an estimate of the effects of different star locations is made. The constellations selected for study are Monoceros (Unicorn) with right ascension of 105 degrees and declination of -5 degrees and Vela (Sail of Ship) with right ascension of 135 degrees and declination of -50 degrees. Of the constellations considered, Monoceros experiences relatively large occultation time and Vela undergoes the minimum occultation time for the particular nominal satellite orbit used. The nominal orbit is taken to be a 200-n. mi. circular orbit at an inclination of 28.5 degrees to the equatorial plane and a right ascension of the ascending node of 0 degree. A significant factor affecting occultation is the angle θ between the earth-star line and the orbital plane. The range of θ is from 0 to 90 degrees. Occultation time decreases from a relative maximum at $\theta = 0$ degree (when the star is in the orbital plane) to a relative minimum of zero at $\theta = 90$ degrees (when the star is at its maximum distance from the orbital plane). The angle θ is the quantity affecting occultation time that varies when any of the following parameters are varied: (1)right ascension of the node of the orbit, (2)inclination of the orbit, and (3)star location.

Launch time on a rotating body such as the earth significantly affects the orbital plane orientation; therefore, since launch time is not known

C-4

precisely prior to liftoff, it is necessary to consider various orbital plane orientations. The effect of delaying launch time is an increase in the right ascension of the node. Hence, analyzing the effects of varying the nodal location corresponds to analyzing effects of varying launch time.

In each of the following paragraphs, one parameter is varied at a time (from the nominal) and the resulting effects upon occultation are observed.

2. Variation with right ascension of the node. Occultation time for the constellations Monoceros (Unicorn) and Vela (Sail of Ship) varies with right ascension of the ascending node of the satellite orbit as exhibited by Figures C-15 and C-16, respectively. Orbital inclination and altitude are fixed at 28.5 degrees and 200-n.mi., respectively.

Monoceros, being located at right ascension = 105 degrees and declination = -5 degrees, is near its maximum distance from the orbital plane when the right ascension of the ascending node is zero. This orbital orientation corresponds approximately to a relative minimum occultation time per orbit. (The angle θ is near its maximum of 28.5 + 5 = 33.5 degrees.) As the right ascension of the node is increased, the orbit revolves about the earth's North Pole-South Pole axis; the constellation Monoceros is in the orbital plane when the line of nodes has rotated approximately 110 degrees producing a relative maximum occultation time of about 36.5 minutes as seen in Figure C-15. (The angle θ is zero.) As the right ascension increases from 110 degrees, the orbital plane moves away from Monoceros and is again at a relative maximum occultation time of about 35.5 minutes. The curve in Figure C-15 is periodic of period 260 degrees and is symmetric about approximately 200 degrees. (If the star were in the equatorial plane, the curve would be periodic with a period of 180 degrees and symmetric about 180 degrees.) The total variation in occultation time when the node is rotated through a complete revolution is about 2 minutes, a relatively minor effect for this particular constellation and satellite orbit.

Figure C-16 displays results of occultation time using the constellation Vela (Sail of Ship) and a satellite orbit having an altitude of 200-n. mi. and an inclination of 28.5 degrees. As in Figure C-15, right ascension of the ascending node is allowed to vary from 0 to 360 degrees. It is evident from the comparison of Figures C-15 and C-16 that star location or more specifically, the angle θ between the earth-star line and the orbital plane, is a significant factor affecting occultation time. Vela is located at a right ascension of 135 degrees and a declination of -50 degrees. When the

right ascension of the satellite orbit's ascending node increases from zero, the angle θ increases to a relative maximum of $28.5 + 50 = 78.5$ degrees; therefore, occultation time decreases to its minimum of zero, indicating that the line of sight is not blocked by the earth. This situation occurs when the node has moved through the positive angle of 20 degrees from its nominal position. For values of right ascension of the ascending node between 20 and 50 degrees, the line of sight is not occulted by the earth. For values larger than 50 degrees, occultation time increases rapidly to a relative maximum of approximately 35 minutes. The curve is periodic of period 360 degrees and is symmetric about approximately 215 degrees. The maximum and minimum occultation times occur at 180 degrees apart for stars having declinations greater in magnitude than the orbital inclination since the angle θ is a relative minimum 180 degrees after it is a relative maximum.

For stars having negative declinations smaller in magnitude than the orbital inclination, occultation time will be a minimum when the right ascension of the ascending node is 90 degrees less than the right ascension of the star. Maximum occultation time will occur at two locations where the orbital node has rotated between 90 to 180 degrees and 180 to 270 degrees from the position of minimum occultation. For stars having positive declinations smaller than the orbital inclinations, occultation time will be a minimum when the right ascension of the ascending node is 90 degrees greater than the right ascension of the star. Maximum occultation time will again occur at two locations where the orbital node has rotated between 90 to 180 degrees and 180 to 270 degrees from the position of minimum occultation.

For stars having a declination of 0 degrees maximum occultation will occur when the star is collinear with the line of nodes. Minimum occultation occurs when the line of nodes has rotated 90 degrees from its position of maximum occultation.

For stars having a declination greater than the orbital inclination, minimum occultation will occur when the right ascension of the ascending node is 90 degrees greater than the right ascension of the star. Maximum occultation will occur when the right ascension of the star is 90 degrees greater than the right ascension of the ascending node. If the star declination is negative, but greater in magnitude than the orbital inclination, maximum occultation time will occur when the right ascension of the ascending node is 90 degrees greater than the right ascension of the star.

3. Variation with altitude. If a space vehicle is allowed to coast in near-earth orbit for an extended period of time, its altitude will gradually

decay. In Figure C-17, altitude was allowed to vary from 200 to 150-n. mi. simulating orbital decay, and the results upon occultation were observed. Orbital inclination and right ascension of the ascending node are fixed at 28.5 and 0 degrees, respectively. As the altitude decreases, the percent of the orbital period occulted increases approximately linearly. For the constellation Monoceros (Unicorn), occultation varies from 37.5 percent at an altitude of 200-n. mi. to about 39.5 percent at an altitude of 150-n. mi. , representing a time difference of about 1 minute. Percent of orbital period occulted for the constellation Vela (Sail of Ship) varies from about 25 percent for a 200-n. mi. altitude orbit to about 32 percent for a 150-n. mi. altitude orbit. The constellation Vela is visible more than the constellation Monoceros for each altitude because the angle θ between the earth-constellation line and the orbital plane is greater for the constellation Vela.

4. Variation with inclination. Occultation time can be quite dependent upon inclination as indicated in Figure C-18. The effect of variation in inclination is easily visualized if we investigate the effects upon θ, the angle between the earth-star line and the orbital plane. The orbit which is initially in the equatorial plane (inclination = 0 degrees) rotates about the line of nodes to an inclination of 90 degrees. At an inclination of 0 degree, Monoceros is nearest the orbital plane and the angle θ is a minimum; therefore, occultation time is greatest. As the inclination increases, the orbital plane moves further from Monoceros, the angle θ increases and, hence, occultation time decreases. It decreases to zero at an inclination of approximately 75 degrees allowing complete visibility.

The constellation Monoceros is not occulted by the earth for the orbit with the 200-n. mi. altitude and 0 degree right ascension of the ascending node for inclinations greater than 75 degrees. The total variation of occultation time with inclination is about 36 minutes.

Included in Figure C-18 is the occultation time per orbit for the constellation Vela. Initially, as the orbital inclination is increased, the angle θ increases also (the orbital plane is rotating away from Vela), causing occultation time to decrease. The angle θ reaches its maximum at an inclination of 30 degrees and, hence, occultation time is minimum. Because Vela is located at a right ascension of 135 degrees and a declination of -50 degrees, the angle θ does not become large enough for complete visibility. As orbital inclination is increased from 30 degrees, occultation time gradually increases from its minimum of 23 to 35 minutes at 90 degrees.

5. Variation with star location. Figure C-19 displays the occultation time per orbit for seven stars or constellations selected from the

galactic plane. The stars are arranged in order of increasing occultation. The constellation Vela (Sail of Ship) at a right ascension of 135 degrees and a declination of -50 degrees allows line-of-sight contact more of the time than any other star or constellation considered.

The occultation times shown in Figure C-19 represent values obtained using the nominal earth orbit with altitude = 200 n. mi., inclination = 28.5 degrees, and right ascension of the ascending node = 0 degree. It is obvious that the location of the star in the galactic plane significantly affects occultation.

c. <u>Summary.</u> It is difficult to predict the occultation time for stars selected at random from the galactic plane. As indicated in this study, the two factors which influence occultation are the angle θ between the earth-star line and the orbital plane and the orbital altitude. For a fixed altitude, the angle θ may be varied by altering orbital inclination or location of the node. For all stars for which the angle θ is approximately 0 degree, there is a long occultation time. For all stars for which the angle θ is greater than approximately 72 degrees, there is no occultation.
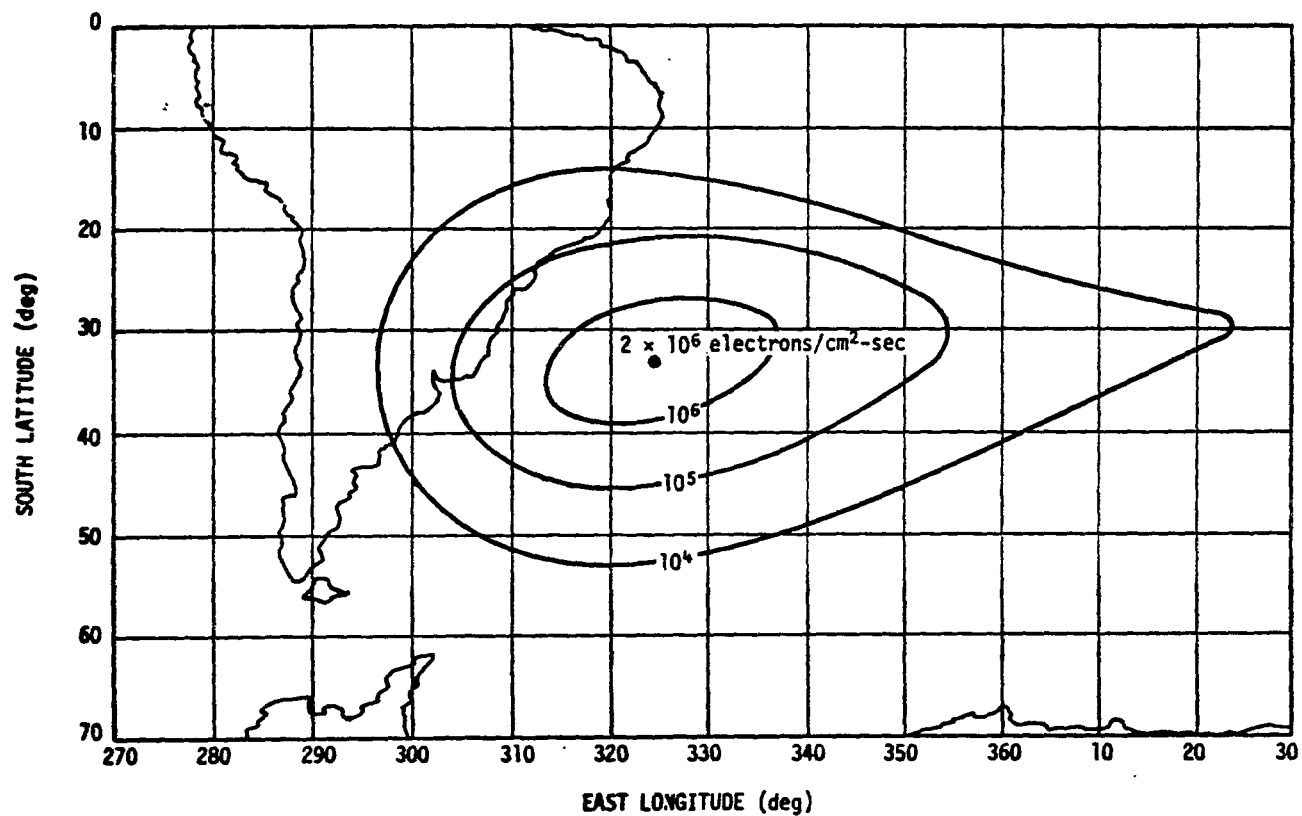
Figure C-1. Electron isointensity contours at 400 km in 1966 for E > 0. 5 MeV [1].
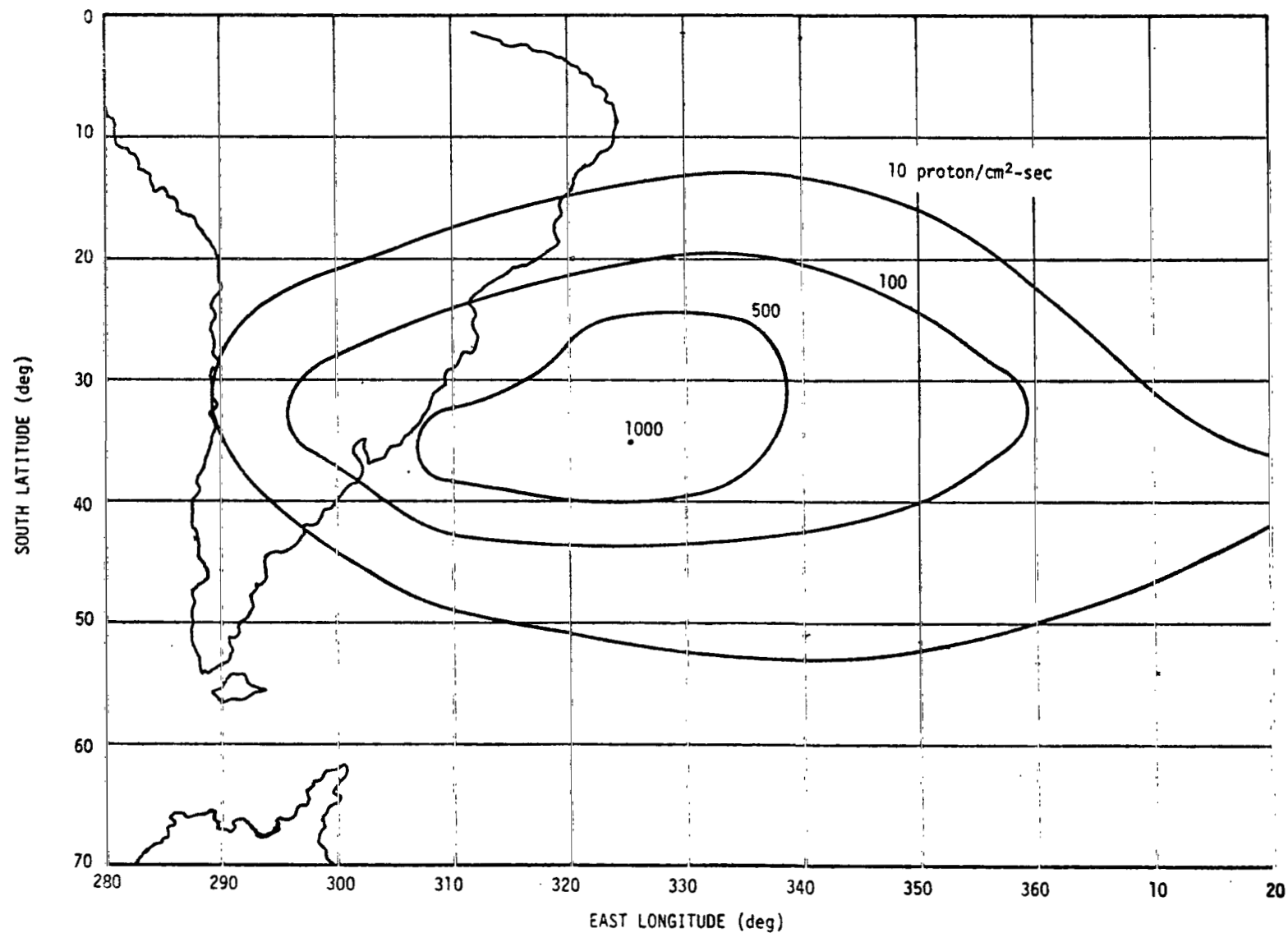
Figure C-2. Proton isointensity contours in the South Atlantic Anomaly at 400 km [2].
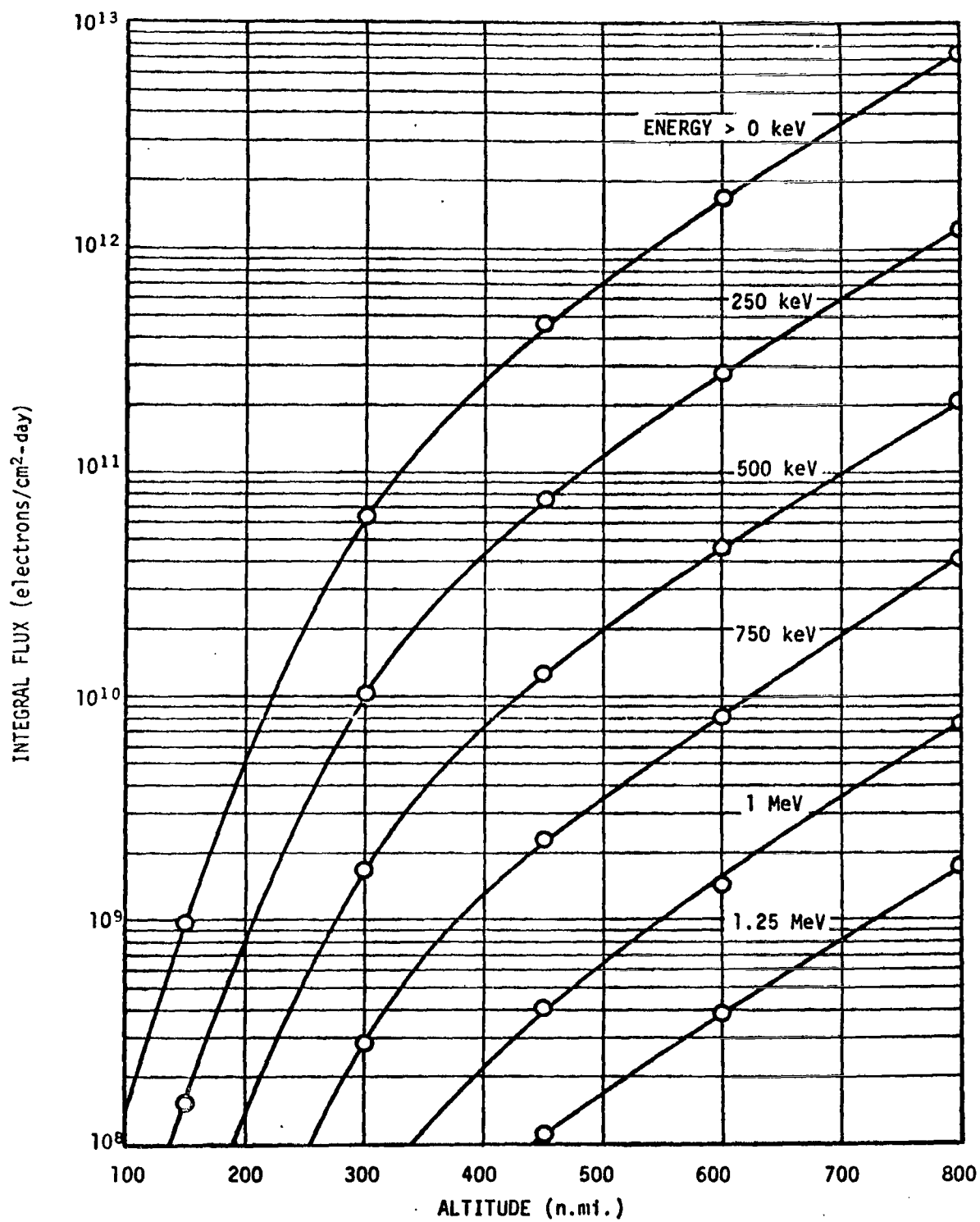
Figure C-3.   1968 electron data for 30-degree inclination orbit [3].
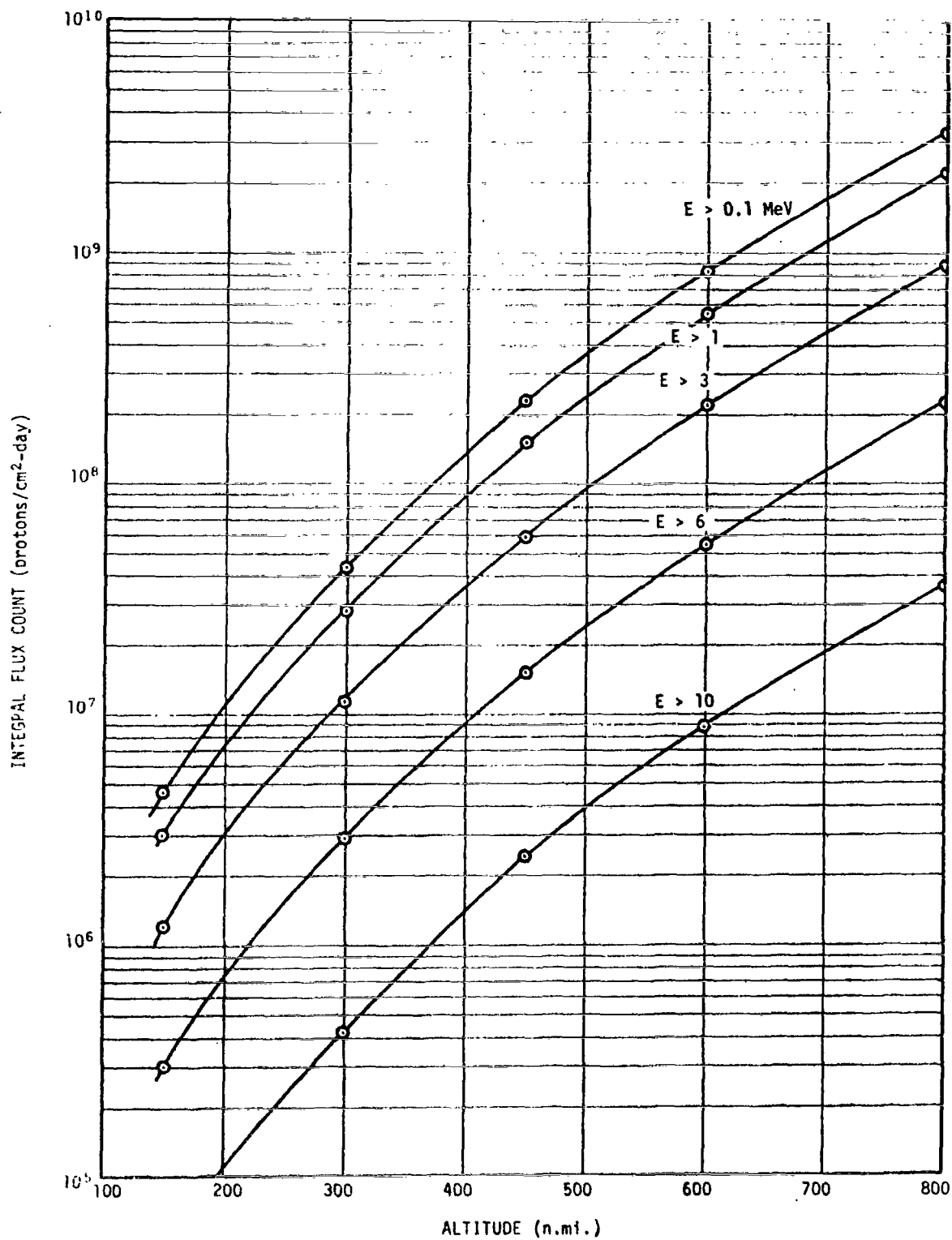
Figure C-4. 1966 model integral proton flux for 30-degree inclination orbit [4].
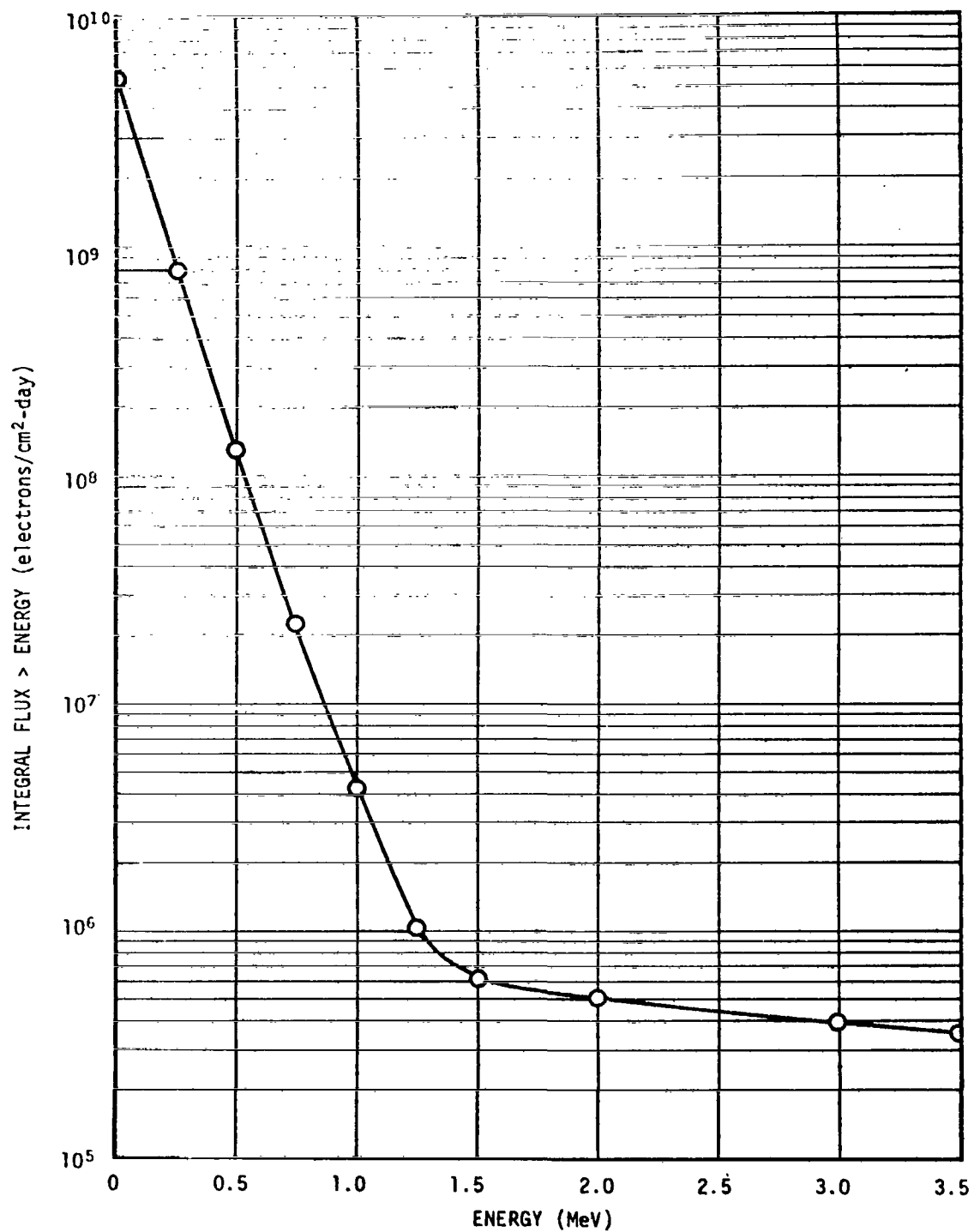
Figure C-5. 1968 projected data on electron integral flux for
30-degree inclination orbit (200 n. mi.) [3].
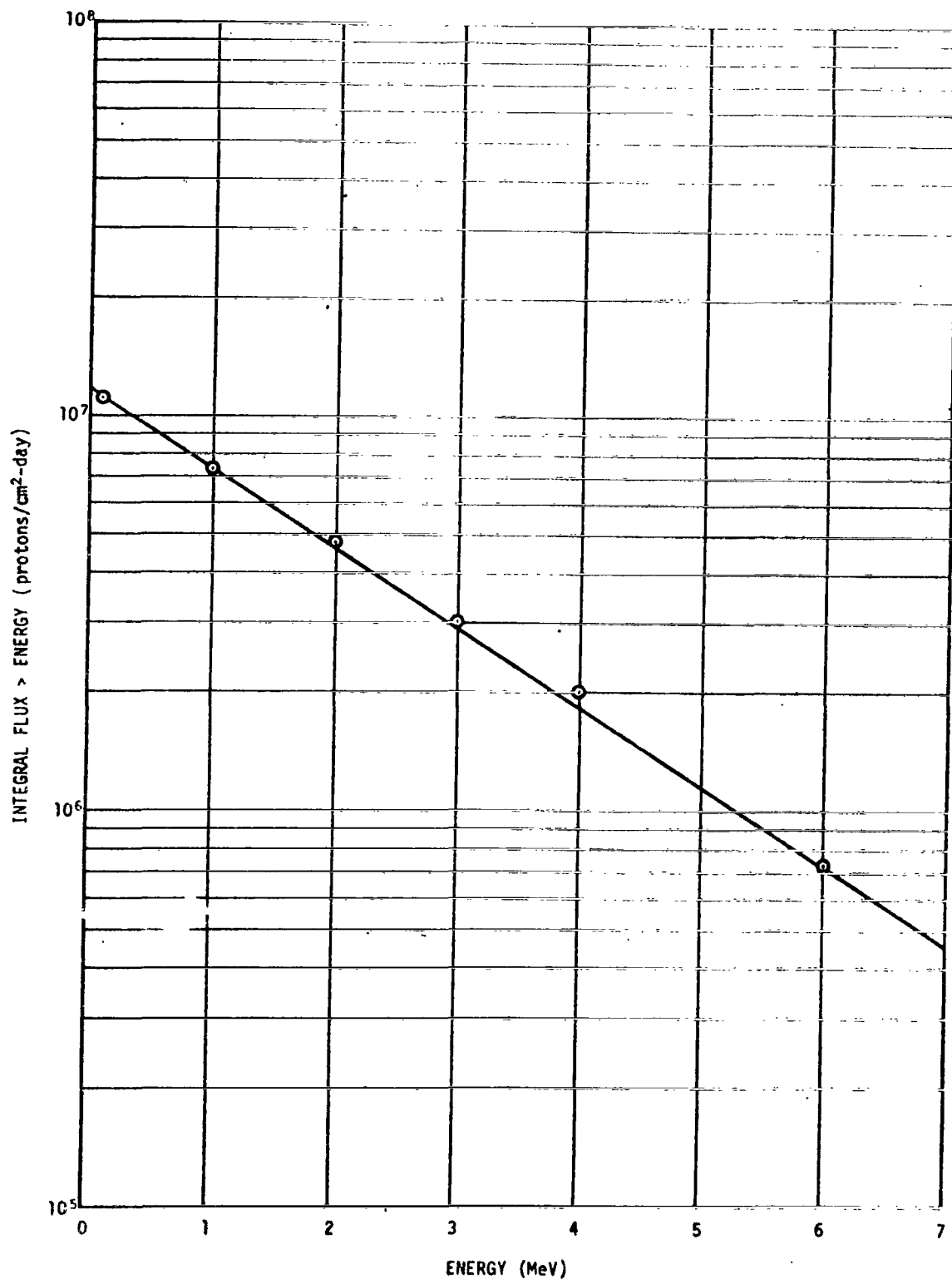
Figure C-6. 1968 projected data on proton integral flux for
30-degree inclination orbit (200 n. mi.) [4].
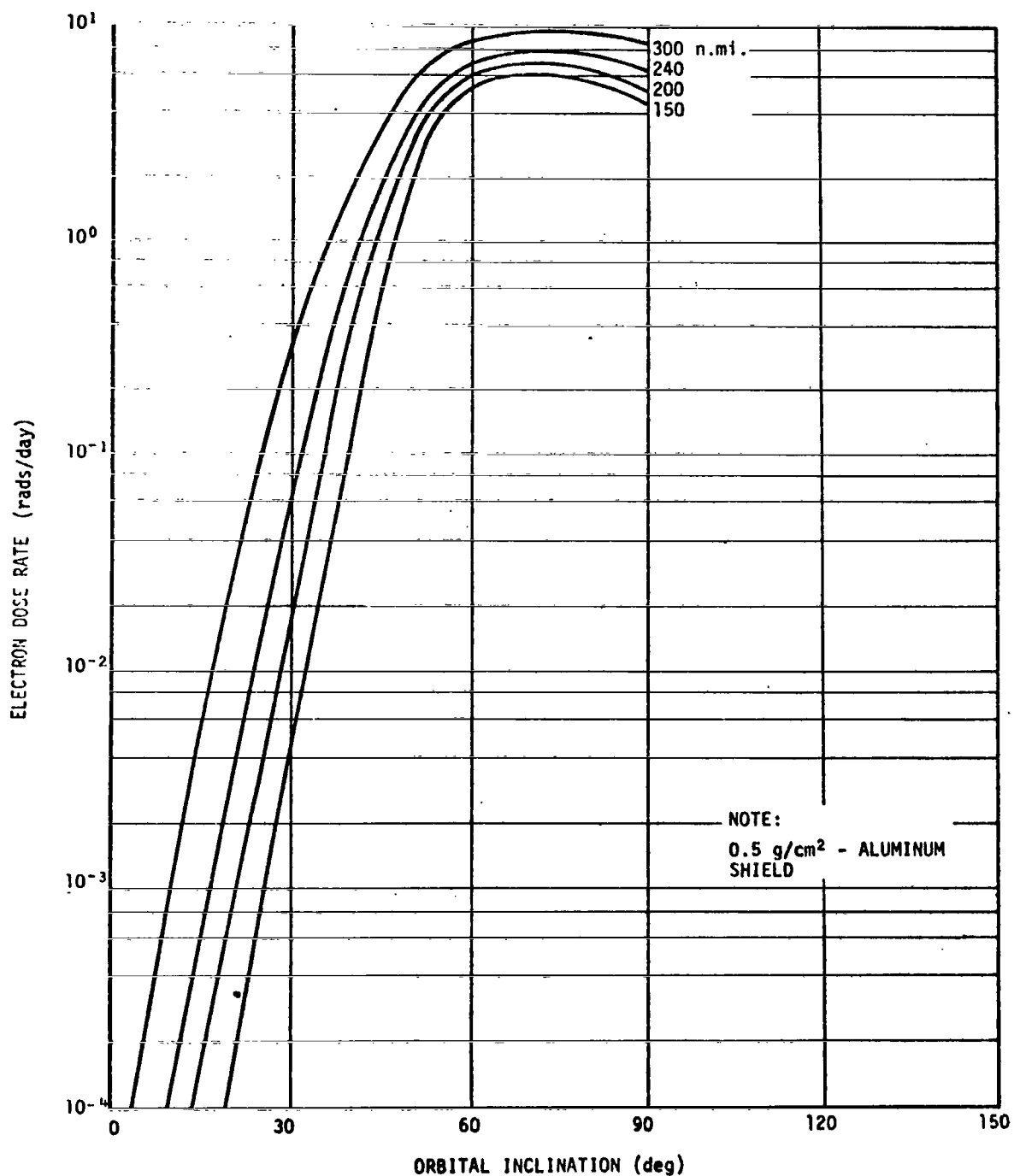
Figure C-7. Electron dose rate as a function of
orbital inclination (after [2]).
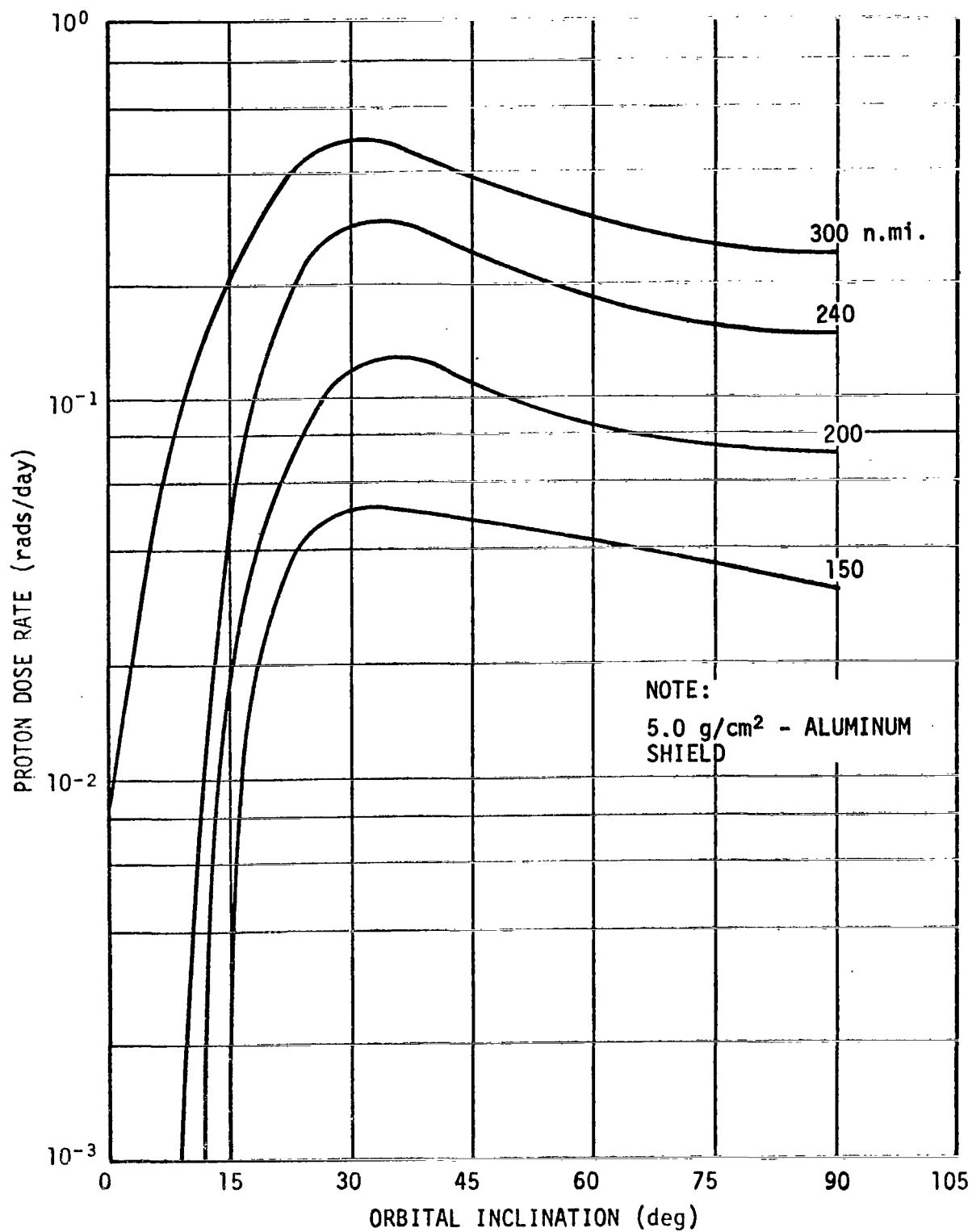
Figure C-8.   Proton dose rate as a function of
orbital inclination (after [2]).
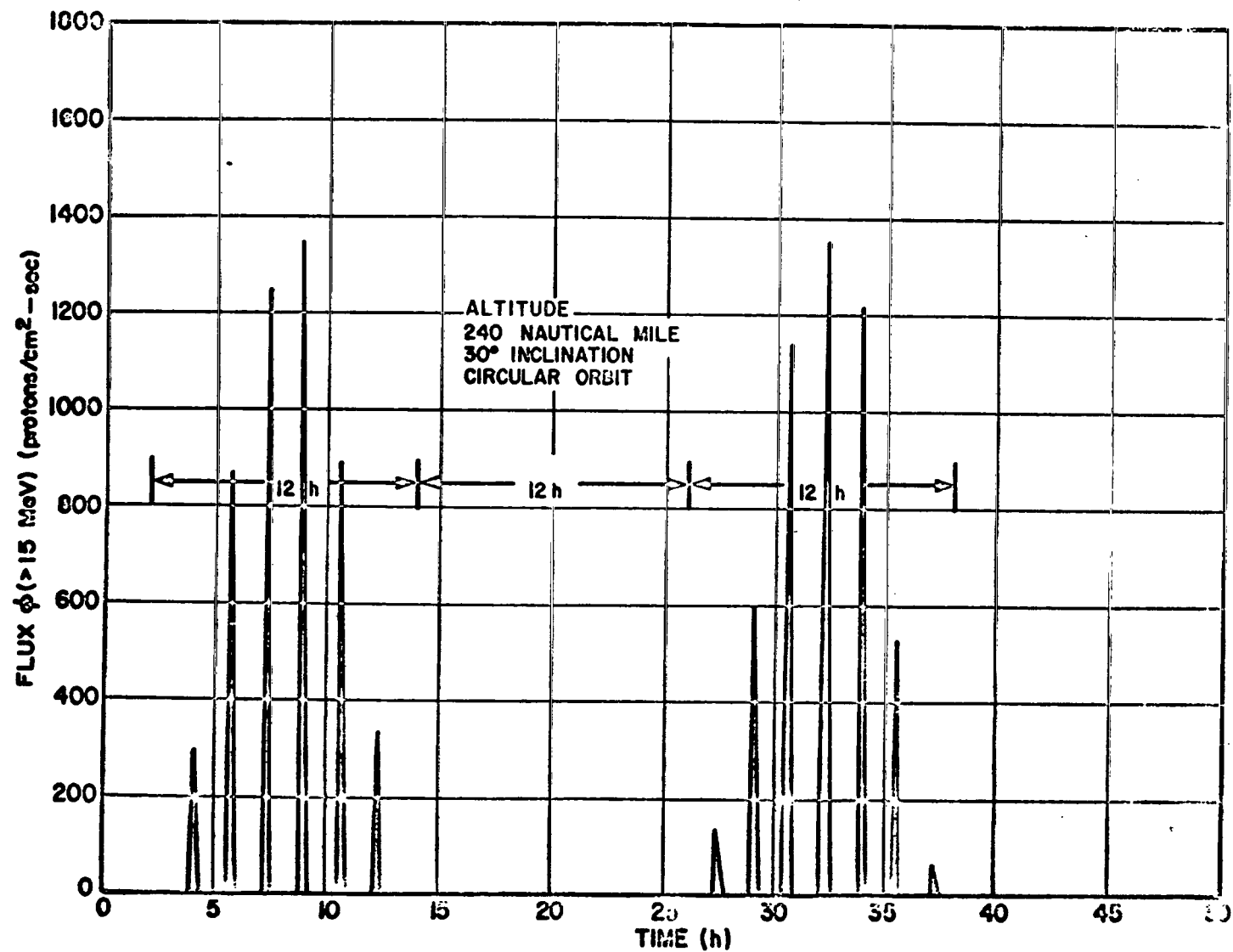
Figure C-9. Integral proton flux versus time [2].

X,γ — vector toward vernal equinox $i \triangleq$ — inclination

Y   — vector parallel to equator plane $\Omega \triangleq$ — longitude of ascending
      and 90 deg from X   node

Z   — completes right-hand system $\omega \triangleq$ — argument of perigee

$\overline{P}$ — vector toward perifocus

$\overline{Q}$ — vector in orbit plane 90 deg
      from $\overline{P}$

$\overline{W}$ — vector perpendicular to
      orbit plane

$\overline{N}$ — vector directed toward
      ascending node
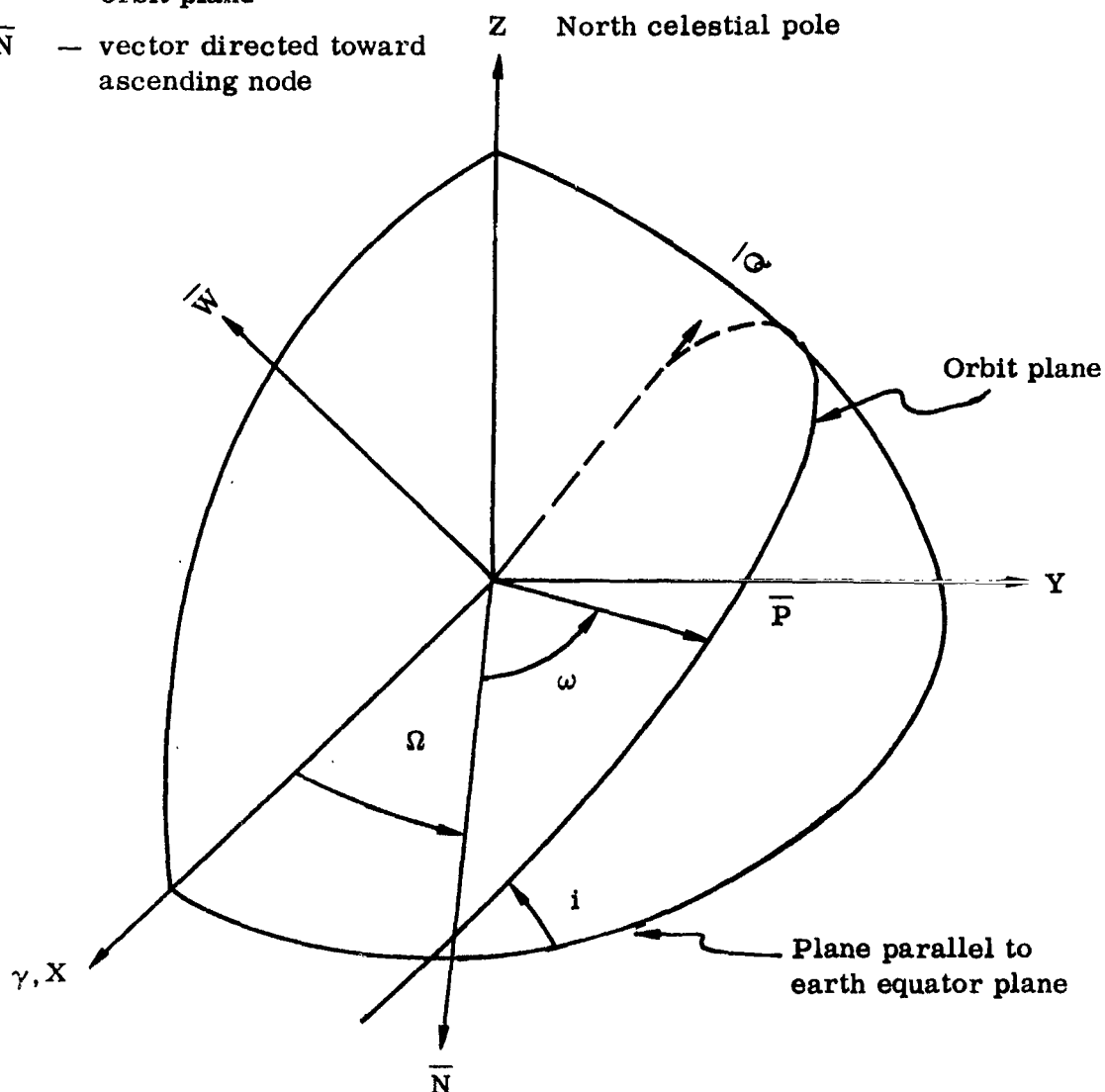
Figure C-10. Inertial and orbital (reference) coordinate system.

C-18
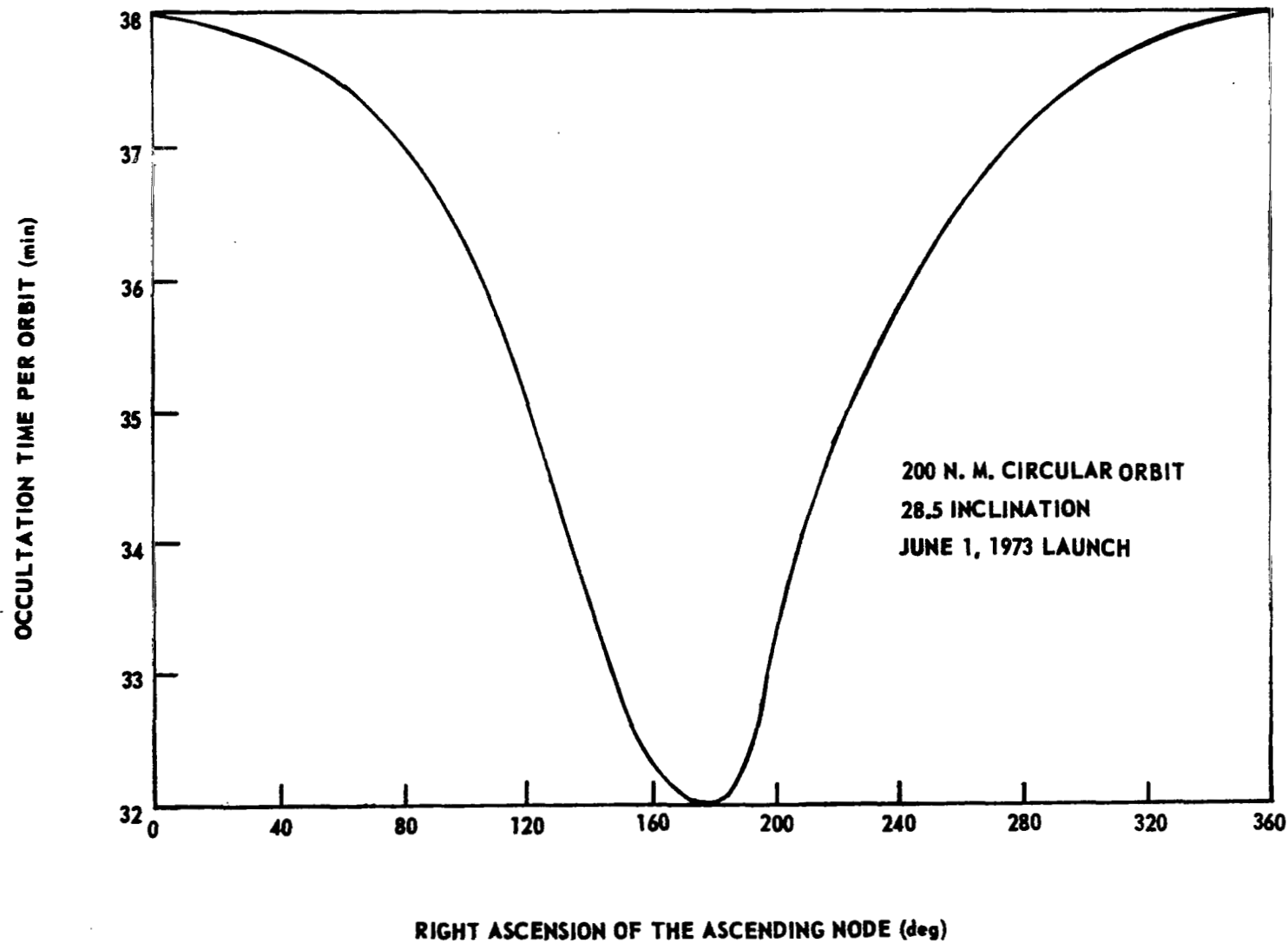
Figure C-11. Variation with nodal regression.
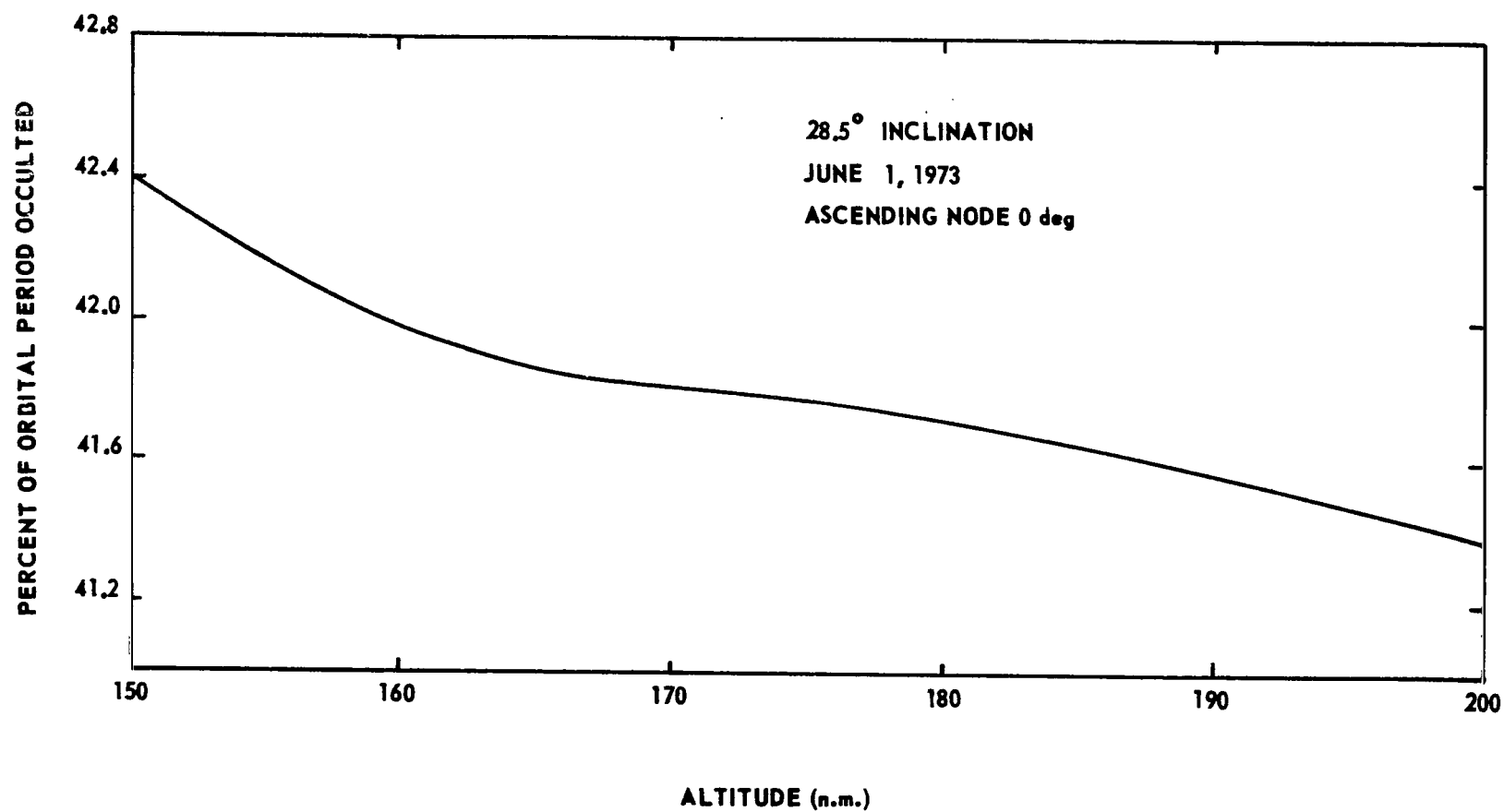
Figure C-12. Variation with altitude.
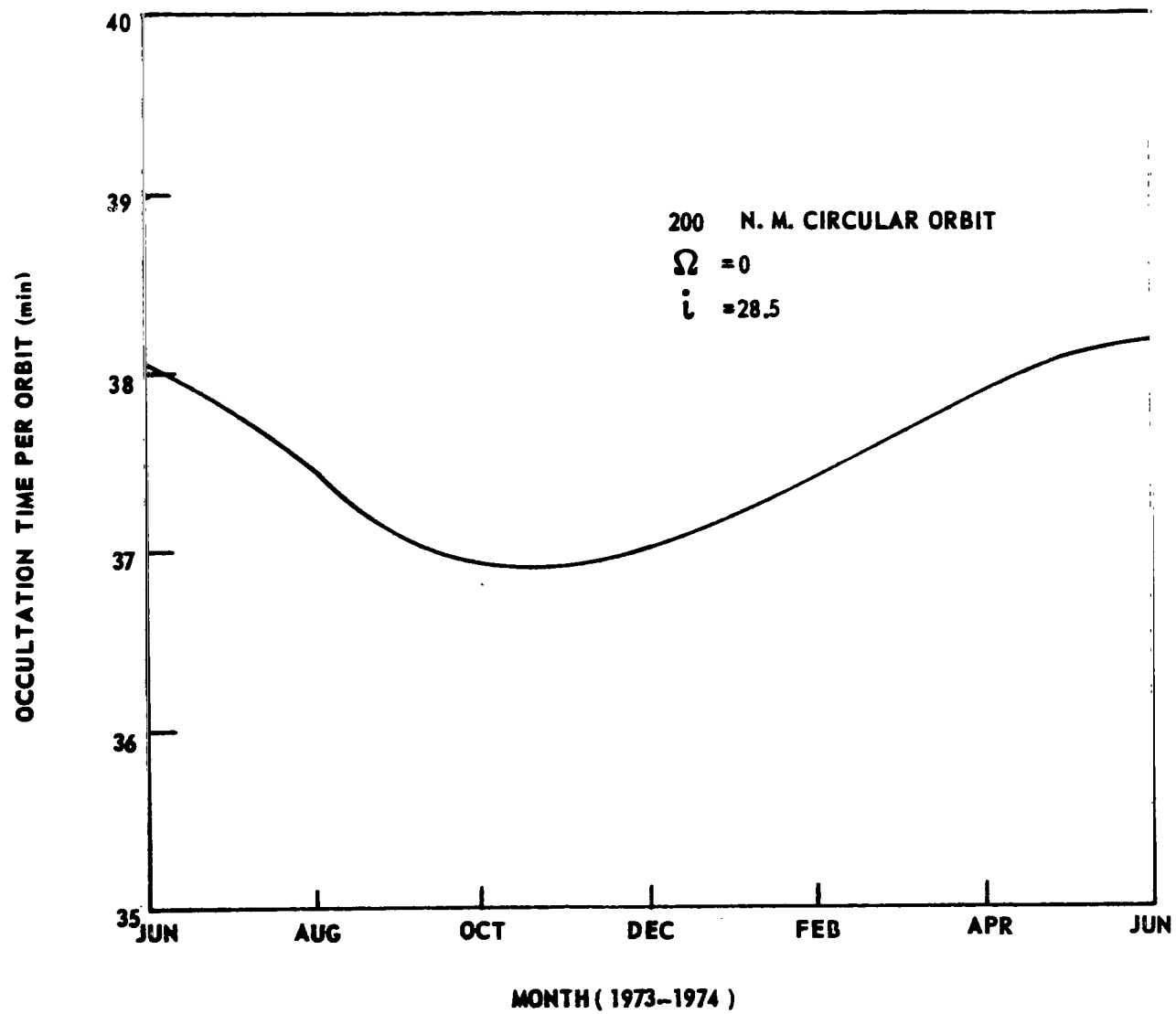
Figure C-13. Variation with time of year.
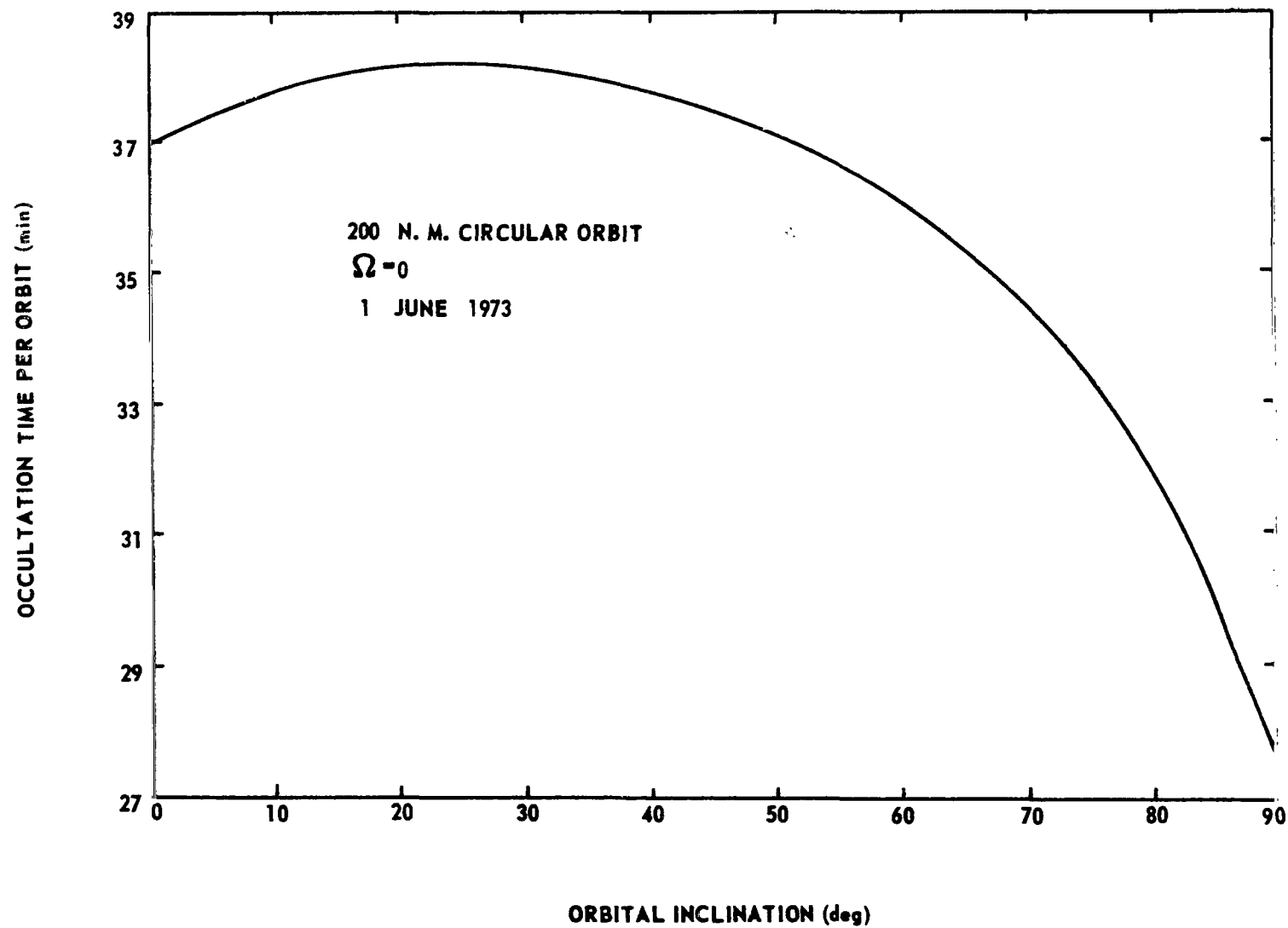
Figure C-14.   Variation with inclination.
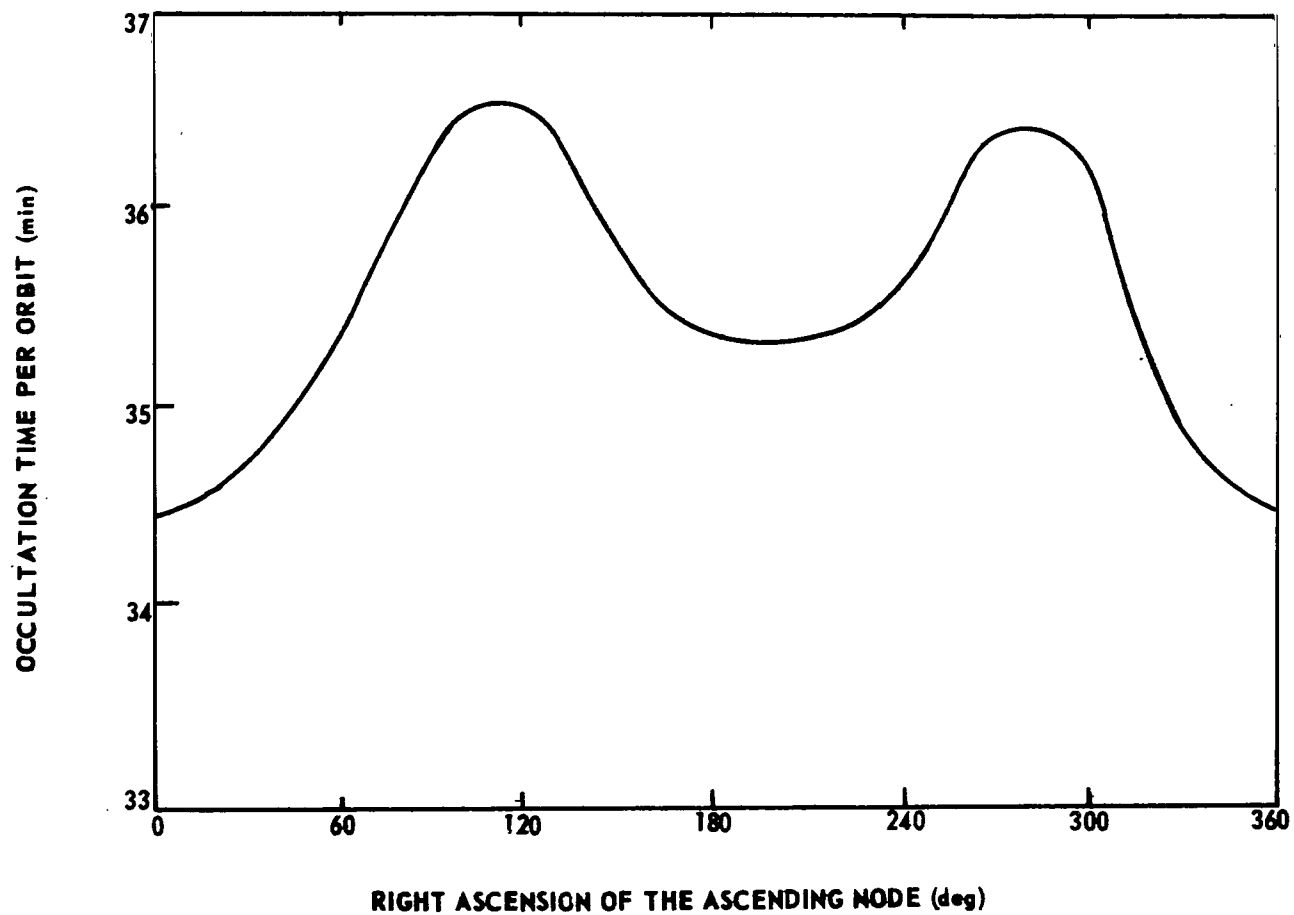
Figure C-15. Variation with nodal position
for the constellation Monoceros (Unicorn).
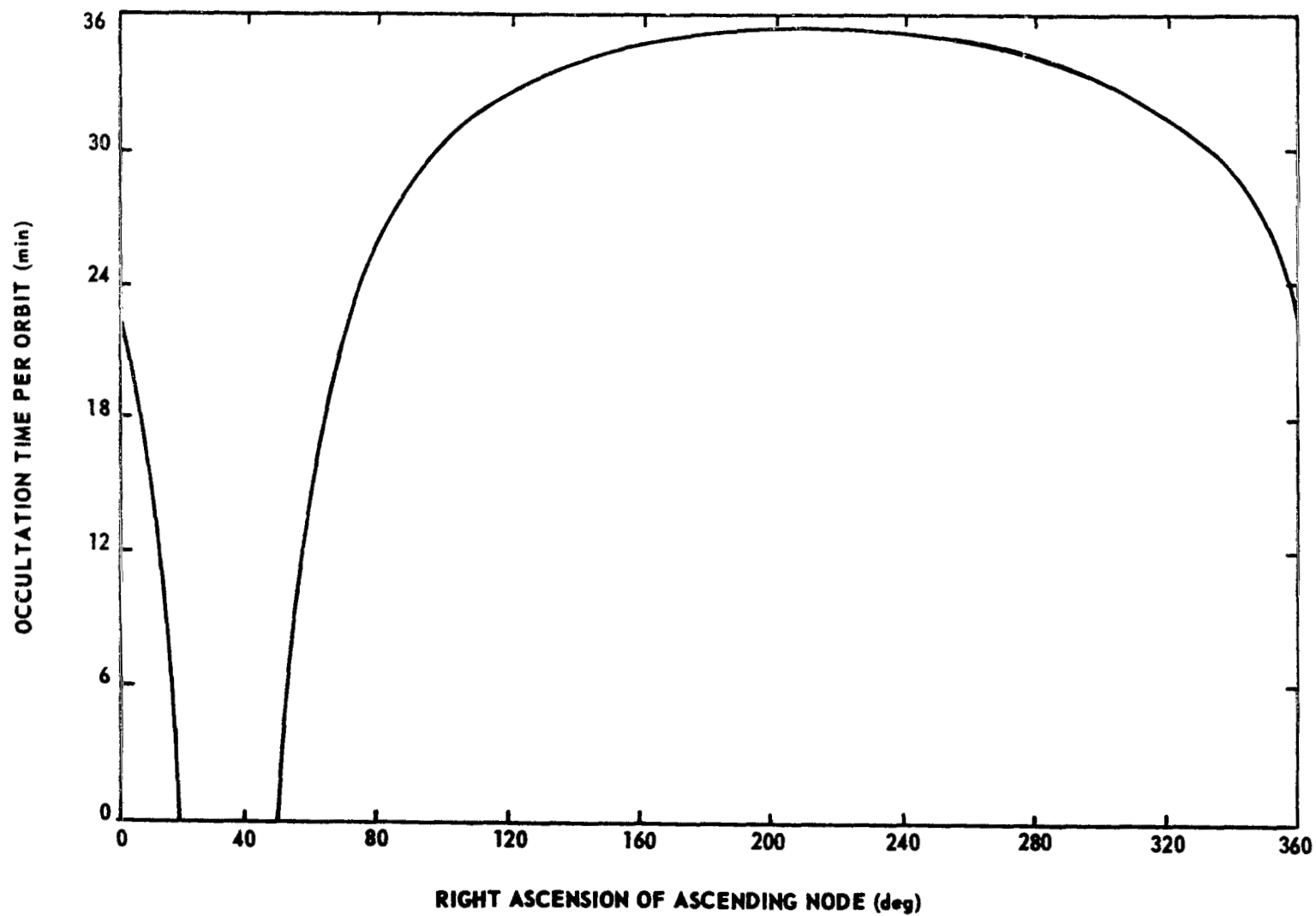
Figure C-16. Variation with nodal position for the
constellation Vela (Sail of Ship).
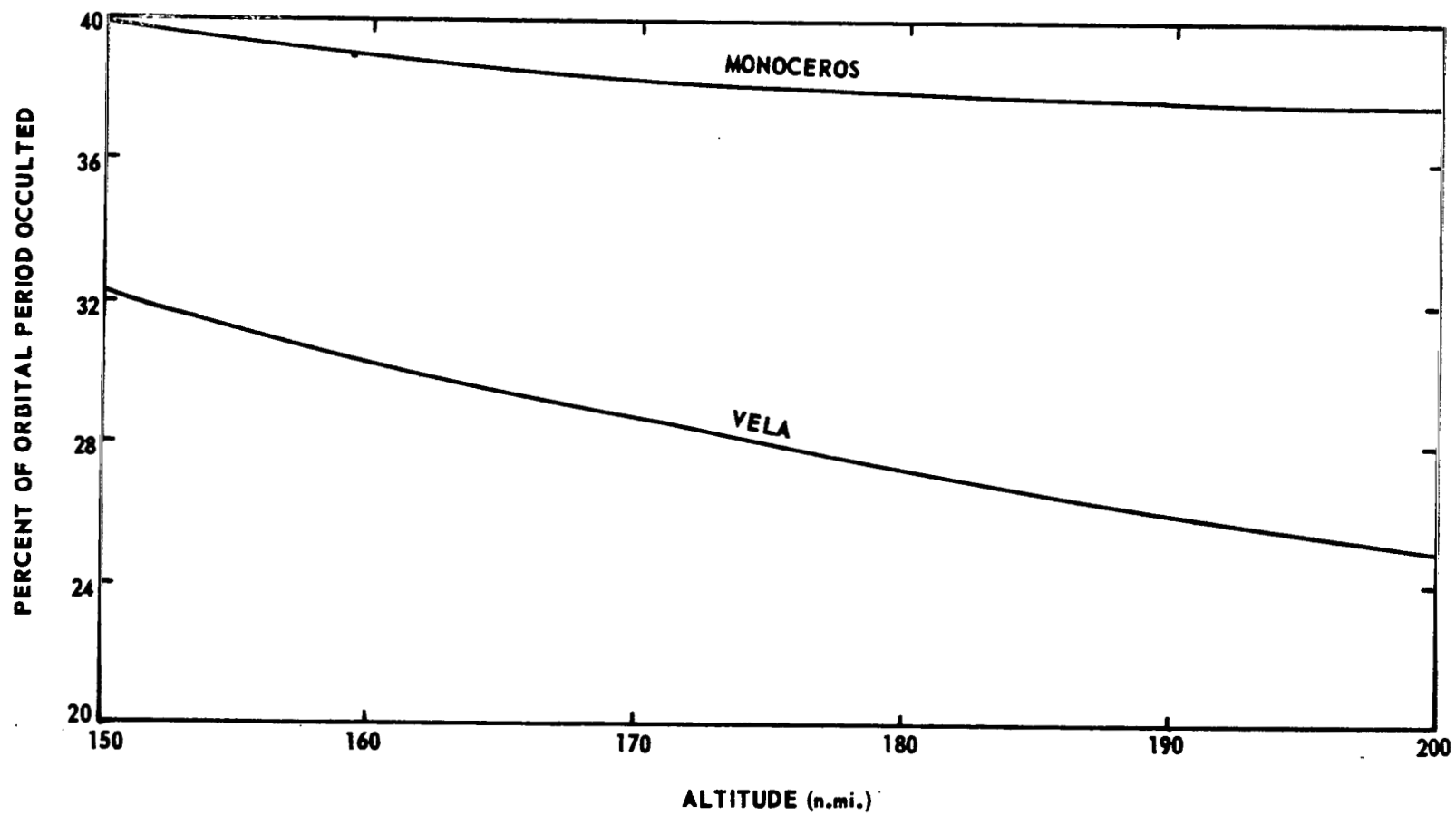
Figure C-17. Variation with altitude.
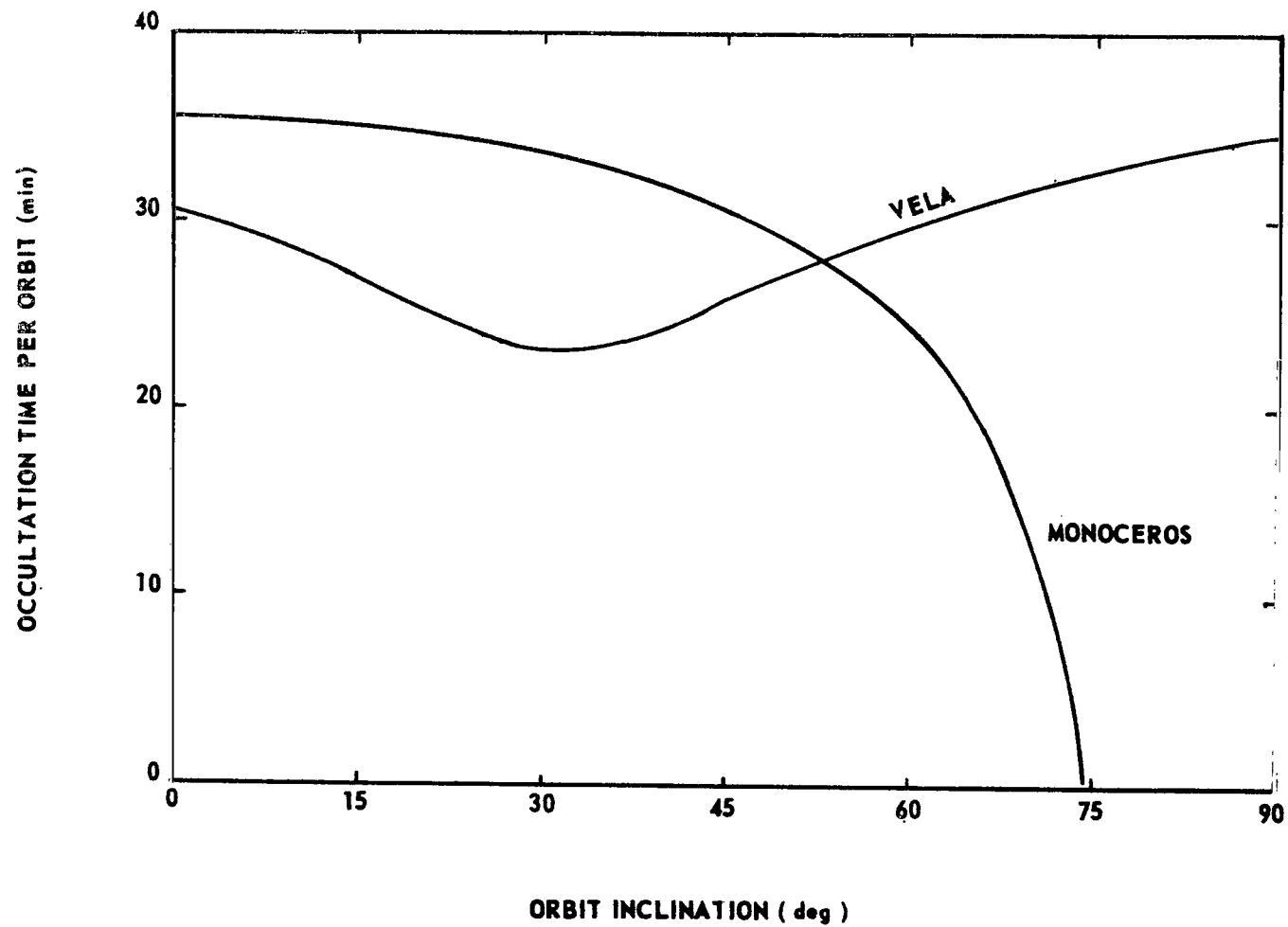
Figure C-18.   Variation with inclination.
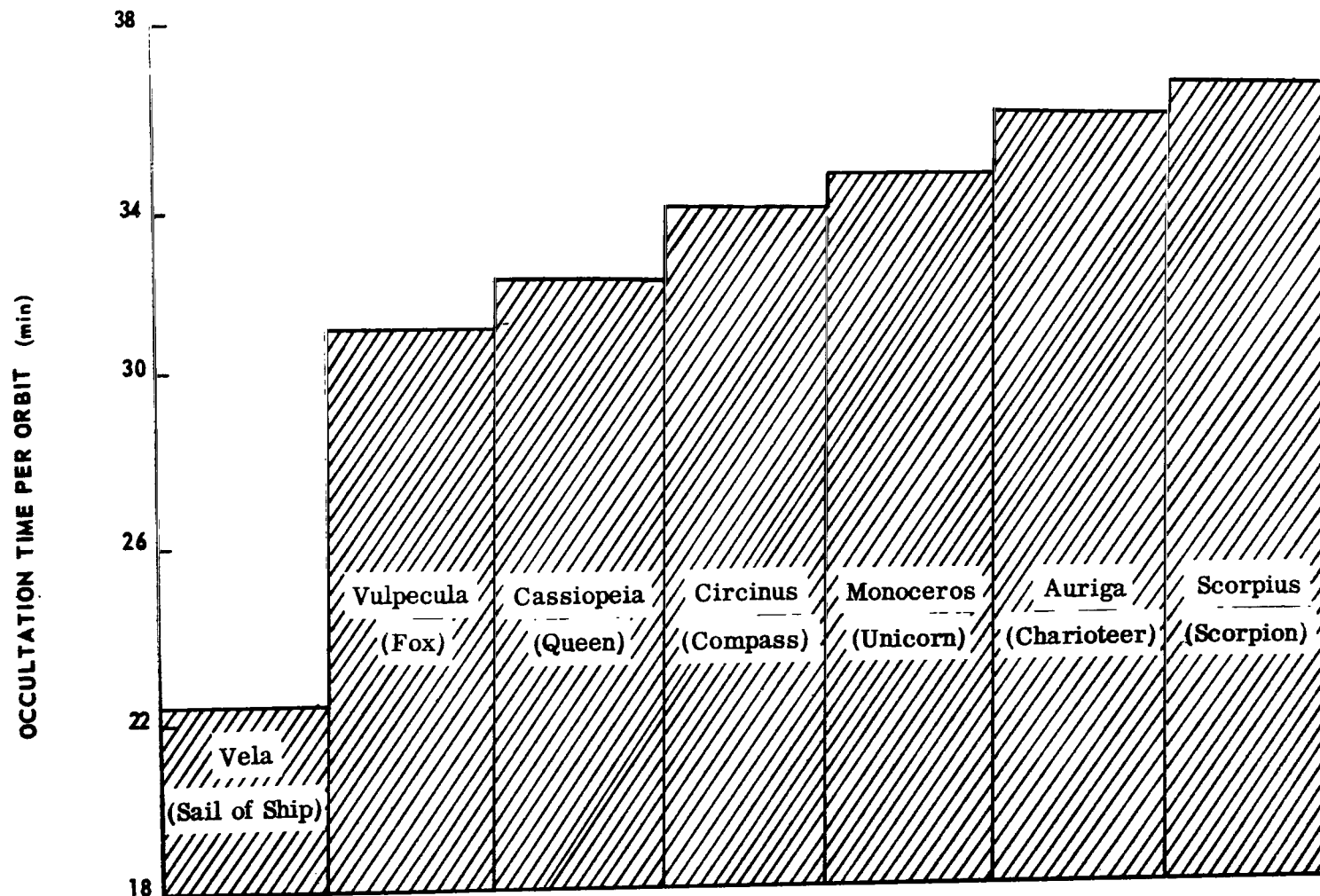
Figure C-19. Variation with star location.

REFERENCES

1. Smalley, V. G.; Smart, D. F.; and Filz, R. C.: Corpuscular Radiation Environment of a Low-Altitude, Polar-Orbiting Earth Satellite — A Brief Summary. Air Force Report Number CRL-66-540, 1966.

2. Burrell, M. O.; Wright, J. J.; and Watts, J. W.: An Analysis of Energetic Space Radiation and Dose Rates. NASA Report No. TN D-4404, February 1968.

3. King, J. H.: Models of the Trapped Radiation Environment, Volume IV. Low Energy Protons, NASA Report No. SP-3024, 1967.

4. Vette, J. I.; Lucero, A. B.; and Wright, J. A.: Models of the Trapped Radiation Environment. Volume II: Inner and Outer Zone Electrons. NASA Report Number SP-3024, 1966.

5. Haffner, J. W.: Radiation and Shielding in Space. Academic Press, New York, 1967.

APPENDIX D. ALTERNATE CONFIGURATIONS

TABLE OF CONTENTS

LIST OF ILLUSTRATIONS

APPENDIX D. ALTERNATE CONFIGURATIONS

Because of potential problems associated with the baseline configuration, several alternate spacecraft configurations were studied. A primary consideration in the study of the alternates was the ability of each to provide power growth capability. Other goals were to reduce spacecraft length, weight, deflection during launch, and to examine different packaging arrangements. All of the configurations were divided into three classes on the basis of the solar array design. Definition of each class is given as follows:

Class I   — Fixed solar array, side oriented toward sun.

Class II   — Deployable solar arrays, side oriented toward sun.

Class III   — Deployable solar arrays, end oriented toward sun.

Class I includes the baseline which is discussed in Volume I and one variation which is considered here. In Class II, three alternates are discussed. One configuration is discussed in Class III. These configurations are considered in the following paragraphs. Each configuration is designated by the figure number in which it appears.

Several of the configurations are 31 feet long, rather than 30 feet long, to take advantage of the additional volume available in the 1-foot cylindrical portion of the shroud conical section. This extra 1-foot length would provide a slightly larger internal volume, if needed, and a slightly greater area for body-mounted solar arrays.

Access to the experiments and equipment mounted internally is an important design consideration and can be obtained in a similar fashion for all configurations. Removable skin panels located along the sides of the spacecraft at strategic places will be provided, and internal and external access platforms will be provided. This approach should allow easy access to all equipment while the spacecraft is in either the vertical (launch) or horizontal position.

Several types of deployable solar arrays are shown, all of which are within the present state-of-the-art and should offer no great concern about

reliable deployment and operation. Similar types of arrays have been flown on other spacecraft, and much data are available from the design and test efforts thus far on the ATM and Saturn V Workshop arrays. Two types of arrays other than those shown which might be considered as good candidates for future study are (1) arrays mounted flat on each end of the spacecraft, which swing out 90 degrees to face the sun in a side-oriented spacecraft configuration, and (2) an end-mounted deployable array which could be folded up and packaged in the almost empty volume of the shroud nosecone, for use with an end-oriented spacecraft configuration. The aerodynamic drag and thermal aspects of each configuration will have to be assessed, and the temperatures and degree of orbital lifetime degradation determined. The large deployable arrays will exhibit some mechanical flexing and will tend to store and release mechanical energy as they flex, thus causing some effect on the spacecraft motion. Since the large dimensions of the deployable arrays lie in the plane perpendicular to the spin axis, their moment of inertia will increase the moment about the spin axis; this feature of the arrays will tend to add stability to the spacecraft motion.

No detailed assessment was made of the alternate configurations; however, a rough assessment is provided herein for the purpose of comparison. The calculations used for power estimates are based on utilization of an 89-percent packing factor of the cells on the spacecraft with no allowance made for a packing factor associated with fitting modules on the available surface area of each configuration. The power estimates will be slightly optimistic from this standpoint. All power calculations on alternate configurations are based on cell temperatures of 30° C. The power values are probably some-what optimistic, since the average temperature on most arrays are expected to be hotter than 30° C. Power values at the end of 1 year are based on a 5-percent yearly degradation of the array. Power values at off-sun tilt angles of the spin axis are based on a simple cosine function.

1. Configuration Class I

This class includes the baseline which was discussed in the main volume. One variation of this has been developed and is illustrated in Figure D-1. It is characterized by the fixed solar arrays mounted on one side which is entirely flat. The three largest experiments are located in the center of the spacecraft, and the X-ray detectors extend from there to each end. The experiments are mounted to a box-beam-type main structure which provides a stable support for the experiments. The experiment layout is the same as the baseline configuration, although the systems layout would be different. The main structure is connected to the beams that attach to the
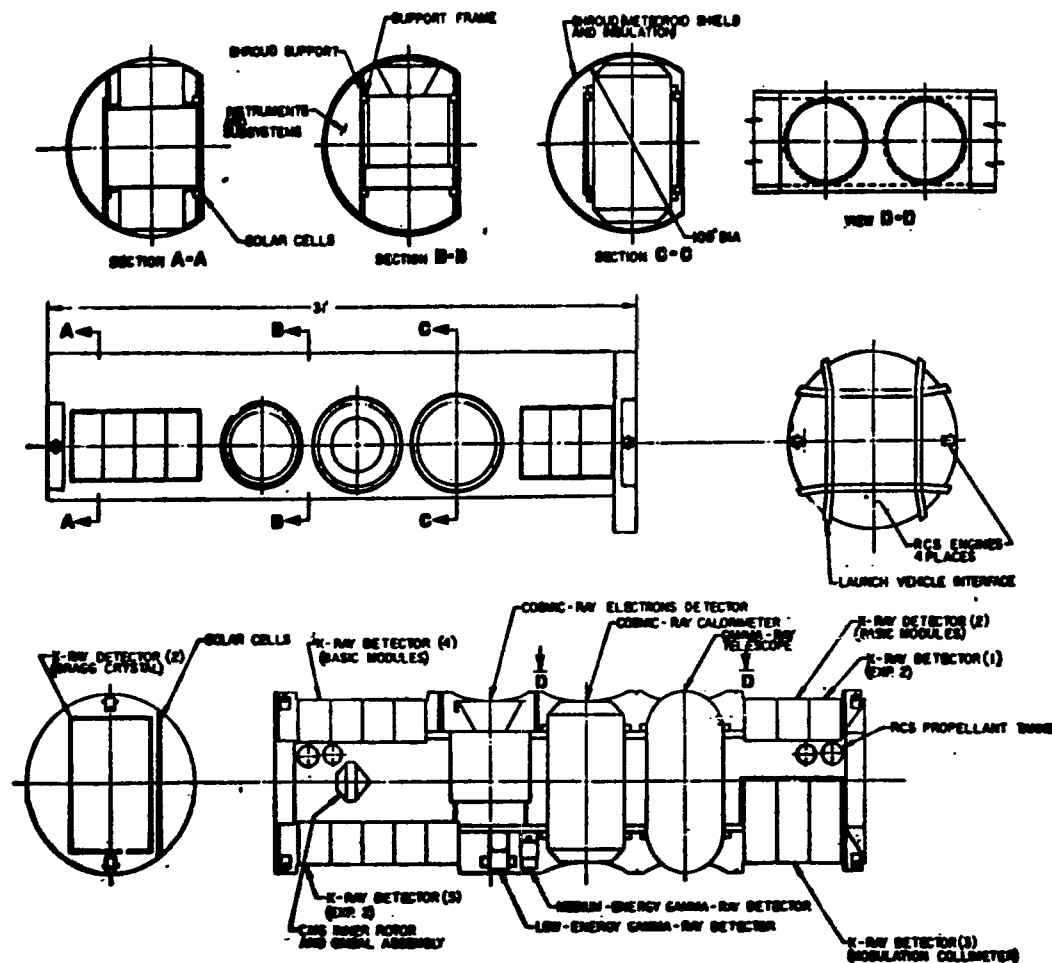
Figure D-1.   Class I configuration with flat side.

payload truss. The skin is a non-load-carrying structure that is supported by the main structure and provides micrometeoroid and thermal protection for the experiments and instruments. The subsystems and experiments are located inside the main structure and between the main structure and the skin.

This configuration was included for consideration primarily for its different array shape and different packaging arrangement, rather than for its available solar power which is less than the baseline spacecraft (compare with the data on cross-sectional shapes given in Appendix H). The advantages of this configuration include a rigid experiment mounting structure, good experiment access, and sufficient enclosed volume for subsystems. Also, the maximum projected available solar panel area (207 square feet), with the spin axis pointed at the sun, is the same as the actual available area for mounting solar panels. On the baseline, the maximum projected available area (240 square feet) is less than the surface area of the three sides (300 square feet) because of the 45-degree side surfaces. Hence, a more effective utilization of the spacecraft area is achieved for mounting solar cells, and fewer solar cells are required. Solar array power output can be roughly estimated by multiplying the available solar panel area (207 square feet) by the same cell per module packing density factor (89 percent) used for baseline panels and the same watts per square foot factor (13 watts per square foot) used for the baseline center panel at 30° C. This figure turns out to be 935 watts at the load, including a 2.57 performance factor, as in the baseline, but not solar panel degradation; the inclusion of a 5-percent degradation factor yields 890 watts at the load at the end of 1 year.

For the case where the spacecraft spin axis is tilted 45 degrees off-sun, the initial power at the load is 660 watts, and the power at the end of 1 year is 625 watts. Problems arise in trying to fit existing solar array modules (such as ATM modules) on this surface efficiently, since the surface area was not sized for any particular module dimensions. Other potential problems are that the internal temperatures may be too high because the solar array is close to the experiments and equipment and the internal volume is somewhat reduced from that of the baseline configuration. The main disadvantage of this configuration appears to be the limited power growth capability.

2. Configuration Class II

Three variations of this class were studied and are shown in Figures D-2, D-3, and D-4. All variations have deployable arrays. The variations shown in Figures D-2 and D-3 have the same cross-sectional shape as the baseline and are sized for effective utilization of ATM solar panel modules. The solar panel deployment scheme for Concepts D-2 and D-3 is very simple and reliable; the mechanism could be a system which requires no power (spring-damper-latch devices) except for the initiation mechanism. The configurations in Figures D-3 and D-4 have experiment layouts which are the same, although the systems layouts would be different.

The approach shown in Figure D-2 is 5 feet shorter than the baseline. This was accomplished by relocating the X-ray detector experiments along each side, pointing in opposite directions. The cosmic-ray calorimeter (6000 pounds) was relocated to shift the center of gravity toward the launch vehicle interface. This experiment relocation along with the compact arrangement provides a configuration with minimum deflection during launch. A rough estimate of the spacecraft structural weight savings possible in this concept can be obtained by subtracting the weight of a 5-foot section of the baseline spacecraft (400 pounds). Also, a complete 5-foot (standard length) section of the payload shroud can be eliminated. A non-load-carrying skin of octagonal or circular cross section can be used. There is some question as to whether this approach provides the volume required for the subsystems. Further investigation must be made in this area. There are potential thermal problems associated with this configuration, because of the packaging density and the proximity of some of the X-ray detectors to the solar array and to the back surface. Electromagnetic interference (EMI) problems may be intensified by the dense packaging arrangement.

The field of view of the X-ray detector is 1 by 4 degrees, and on the baseline HEAO, these experiments are located so that a 4-degree wide band is scanned as the spacecraft rotates. On the approach shown in Figure D-2, the X-ray detectors are rotated 90 degrees with respect to their orientation on the baseline configuration, and hence, only a 1-degree wide band would be scanned. An apparent solution to this problem is to rearrange the collimators inside each X-ray detector experiment box so that the 1- by 4-degree field of view is rotated 90 degrees, and the full 4-degree wide band can be scanned as the spacecraft rotates. There appear to be adequate field-of-view clearances for all experiments in this compact configuration. However, one-half of the X-ray detectors' fields of view would be blocked if the solar array panels failed to deploy properly in the approach shown in Figure D-2.

D-5

Figure D-2. Class II configuration with fold-out arrays and bottom-mounted experiments.
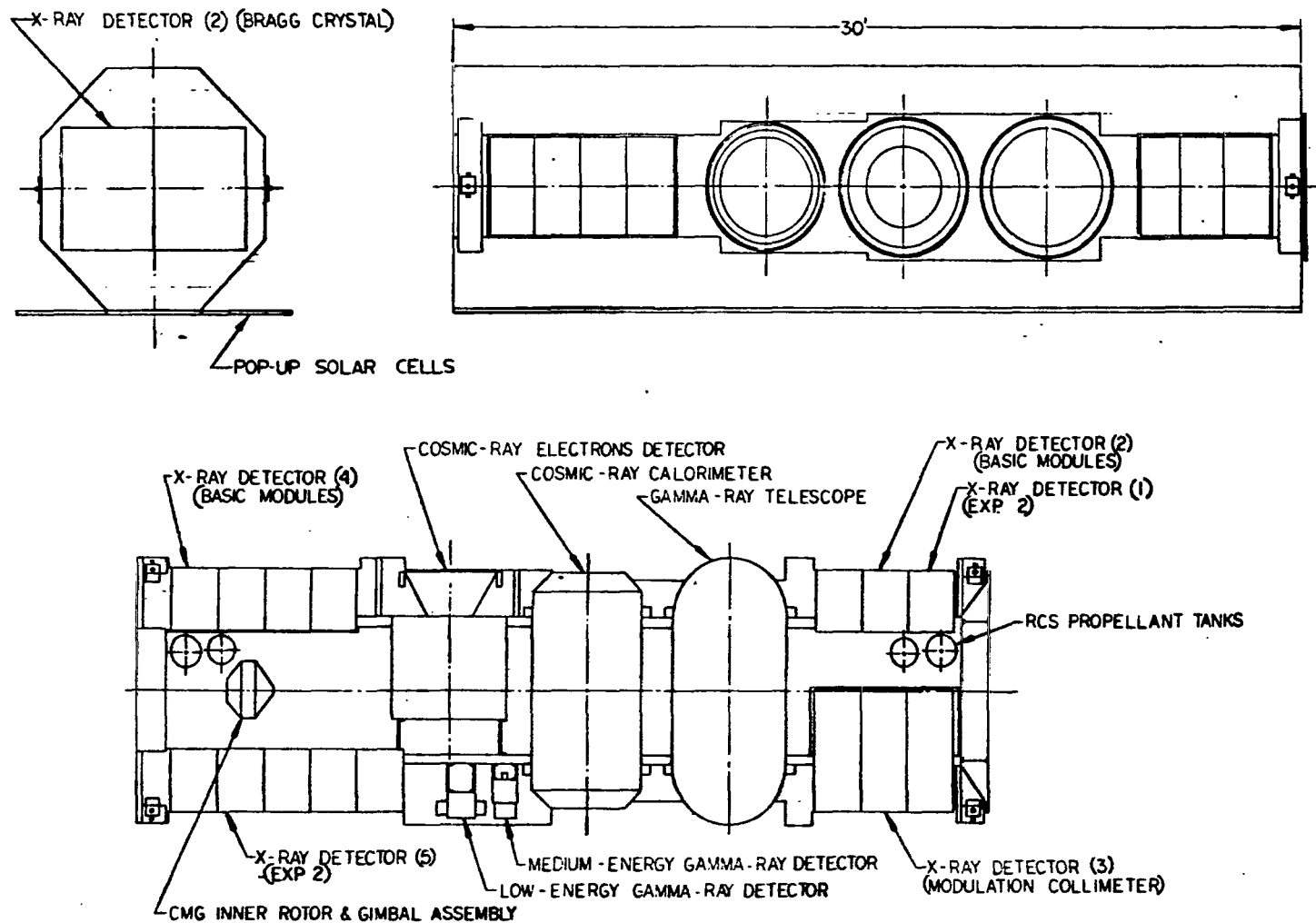
Figure D-3. Class II configuration with fold-out solar array and center-mounted experiments.
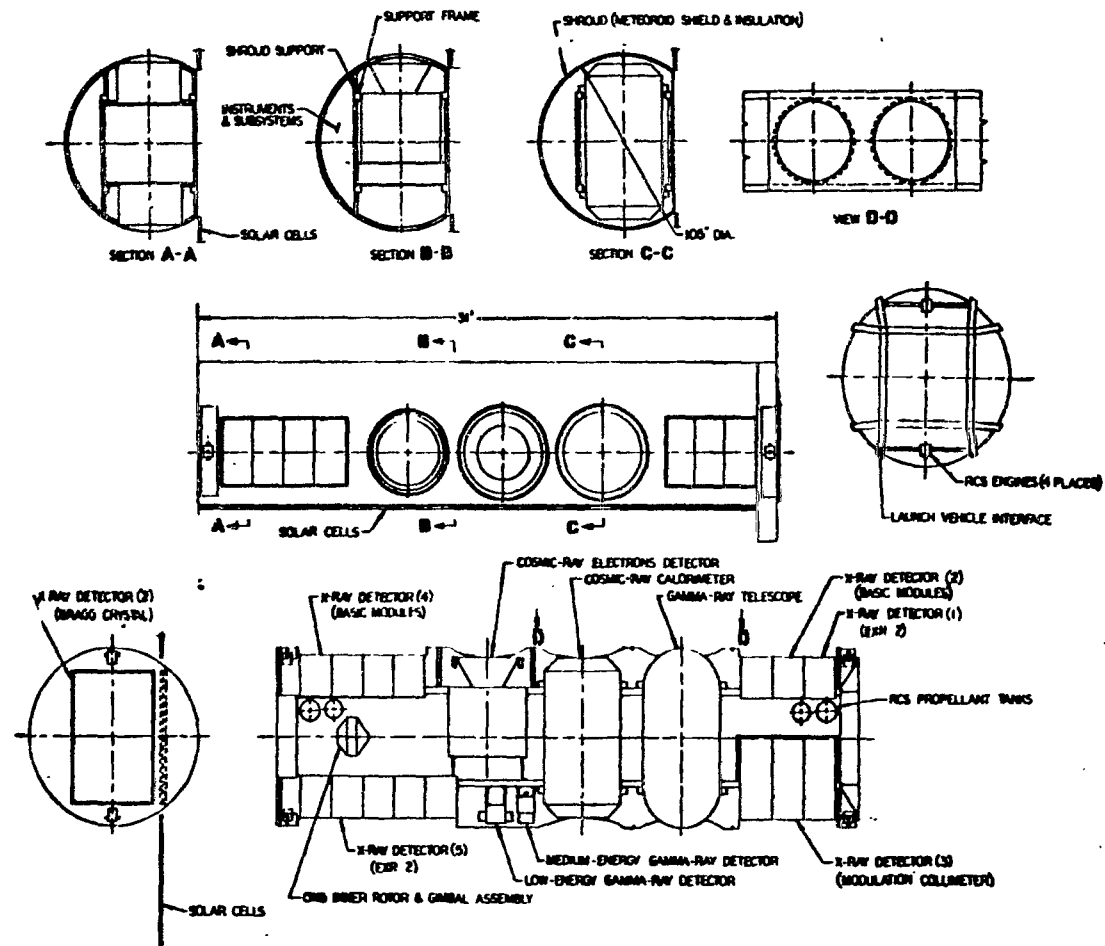
Figure D-4.   Class II configuration with fold-out arrays and center-mounted experiments.

No orbital lifetime calculations were performed for this configuration (Fig. D-2). The maximum projected solar panel area available in this configuration is approximately five-sixths of the surface area of the baseline configuration (300 square feet), or 250 square feet. A rough estimate of the initial power available in this configuration at 0-degree tilt angle off-sun can be obtained by multiplying the 250 square feet by the 89-percent cell-packing factor, and by the 13 watts per square foot and dividing by the 2.57 performance factor used for Concept D-1. This gives 1120 watts at the load for initial operation, and 1064 watts at the end of 1 year.

For the case where the spin axis is tilted 45 degrees off-sun, the initial power available at the load is 792 watts, and the power at the end of 1 year is 752 watts. Further study will be required to verify the adequacy of this configuration. The advantages of this configuration include a lower structural weight and less deflection during launch.

The configuration shown in Figure D-3 has greater power capability than that in Figure D-2 or the baseline. In effect, the D-3 configuration is the baseline configuration with the two 45-degree solar panels designed to deploy. The maximum projected solar array area available is 300 square feet. The maximum initial power is approximately 1350 watts, and the power at the end of 1 year is approximately 1280 watts. For the case where the spin axis is tilted 45 degrees off-sun, the initial power available at the load is 955 watts, and the power at the end of 1 year is 900 watts. Because of increased aerodynamic drag associated with the pop-out panels, the nominal orbital lifetime would be shortened to 681 days at the +2σ solar activity point. The main advantage of this configuration is the easy power-growth capability over the baseline at very low risk; the experiment fields of view are not affected by the solar array in either the deployed or undeployed mode, and if the panels should fail to deploy, the configuration reverts back to that of the baseline. The solar-array-to-CBR connection could be designed for the situation where the array fails to deploy, to have maximum efficiency in the event that the nonplanar array must be utilized.

The configuration shown in Figure D-4 is essentially the same as the Class I configuration shown in Figure D-1, except for the addition of deployable panels on each side of the body-fixed panel. The width of these deployable panels can vary, with the primary limitation being determined by the point at which they intersect with the fields of view of the experiments. If two 31-foot-long rectangular side panels are used, the maximum panel width which can be used is 18 inches, since beyond that point they intersect with the field of view of the Cosmic Ray Calorimeter. This would give a maximum projected area increase of 93 square feet over the concept shown in Figure D-1,

for a total of 300 square feet. A rough estimate of the power increase over that from the configuration shown in Figure D-1 can be obtained by taking 93/207 of the power given in this configuration. This gives 1350 watts at the load initially and 1280 watts at the end of 1 year. For the case where the spin axis is tilted off-sun 45 degrees, the initial power is 955 watts, and the power at the end of 1 year is 900 watts.

Rather than restricting the deployable panels to a rectangular configuration, they could be designed for the full size (80 inches by 31 feet each) of the flat side of the spacecraft, with a cutout of approximately 77 square feet in each, in the shape of a trapezoid, for the experiment fields of view. (The Cosmic Ray Electrons experiment field of view intersects the side panel at 28 inches away from the center panel and the Gamma Ray Telescope at 42 inches away from the center panel.) This would yield a maximum effective available projected solar array area of 130 square feet for each side panel and a maximum initial load power of 2100 watts.

Still another approach would be to deploy each side panel through some angle less than 180 degrees so that it does not intersect with the experiment field of view.

Orbital lifetime would be decreased somewhat because of the deployed arrays, but no values for this were calculated.

3. Configuration Class III

One concept of this class is illustrated in Figure D-5. This class is a radical departure from the baseline; however, it allows greater than 100 percent solar arry area growth over the baseline. Although the configuration in this class is dynamically stable, Configuration Classes I and II provide better stability since the scan axis for each of those configurations rotates about the axis of maximum moment of inertia. There is also some question about the thermal control problem associated with the end located away from the sun, and heaters would probably be required for the equipment located there. Since the back side of the solar panels face cold space, their surface temperature should be cooler than that experienced with the baseline configuration, and the power available per unit area is therefore greater. The power growth potential is manifested in the optional length of the panels. Theoretically, they can be lengthened to 31 feet. The spacecraft end toward the sun is covered with an aluminum skin panel to prevent direct impingement of sunlight on the internal equipment. No solar cells are mounted on the end panel, since
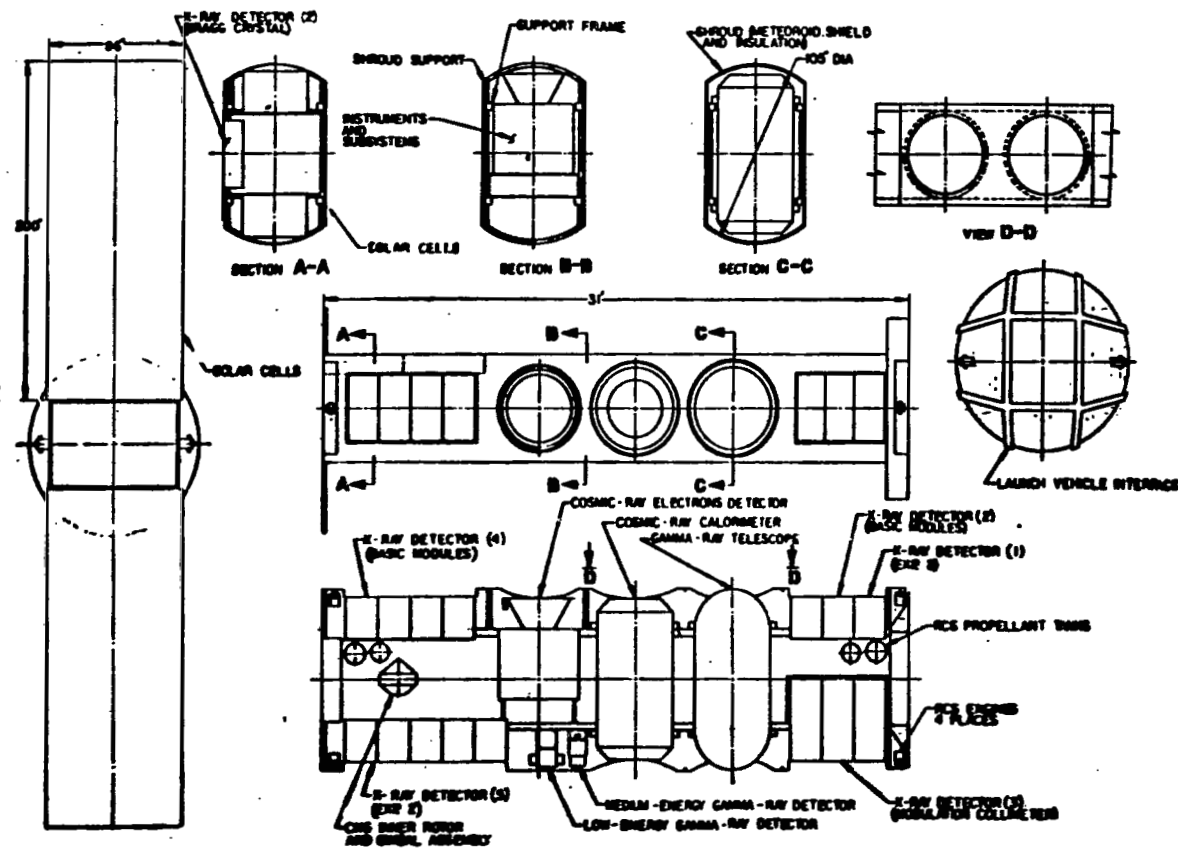
Figure D-5. Class III configuration with end oriented large fold-out solar array.

cell efficiency would be reduced because of high temperatures, and the equivalent power is available from the cooler, more efficient foldout panels with very little increase in weight and aerodynamic drag area for this addition. However, the spacecraft end provides an additional growth potential for this configuration. For the solar panel dimensions shown (16.7 by 7.15 feet), the maximum projected available solar panel area is 240 square feet, and a rough estimate of the maximum initial power available at the load is 1080 watts (using the 89-percent cell density factor, the 13 watts per square foot and 2.57 performance factor used in the calculations for Configuration D-1. (It should be noted that although the baseline configuration is also 240 square feet, this power figure is higher than that shown for the baseline in Figure D-6, because of the omission of the module-to-surface area packing factor consideration.) The power available at the end of 1 year is 1030 watts. For the maximum solar panel dimensions of 31 by 7.15 feet, the maximum projected available solar panel area is 444 square feet. The power available at the load is 2000 watts initially and 1900 watts at the end of 1 year. This configuration presents a large surface area which increases aerodynamic drag above that of the baseline. The estimated lifetime of this configuration with 240 square feet of solar panel area is 558 days for the $+2\sigma$ solar activity case. The structural weight increase for the deployable panels is estimated to be 120 pounds for the 7.15-foot-long panels. If cells are mounted to the end (60 square feet), the additional power available would be approximately 270 watts. Thus, the maximum total power available from this configuration is estimated to be 2270 watts.

It should be noted that in the thermal and aerodynamic drag considerations (Appendix F and Section IV), the configurations of the solar arrays differ somewhat from the configuration shown in Figure D-5. However, for the purposes of this report, these differences are not expected to be significant.

Figure D-6 is a tabulated comparison of the three configuration classes, and it summarizes the major characteristics of each class. One of the major differences between the configuration classes is the potential power available or power growth potential. The sensitivity of weight-to-power growth was investigated using the baseline as a point of reference.

The growth capability of each configuration class is illustrated in Figure D-7. For Class I, growth can be accomplished by lengthening the spacecraft. As the spacecraft length is increased, additional Titan III-C shroud segments must be added in 5-foot sections. As a rough estimate of the additional spacecraft structural weight is required for small increases in spacecraft length, the weight per linear foot of the baseline can be used. The estimated

Comparison Items		Configuration Class		
		I	II	III
Control Factors		All Configurations are Stable (I and II are Preferred)		
Available Power (Initial Load Wattage at 30°C)	45 Deg to Sun	688 (Baseline) 660 (D-1)	792 (D-2) 955 (D-3) 955 (D-4, 300 ft²) 1480 (D-4, 467 ft²)	1600 (504 ft², D-5) 1410 (444 ft², D-5) 765 (240 ft², D-5)
	0 Deg to Sun	974 (Baseline) 935 (D-1)	1120 (D-2) 1350 (D-3) 1350 (D-4, 300 ft²) 2100 (D-4, 467 ft²)	2270 (504 ft², D-5) 2000 (444 ft², D-5) 1080 (240 ft², D-5)
Power Growth Potential		0 Percent (Baseline) 16.7 Percent (Ext Length)	15 Percent (D-2) 38.6 Percent (D-3) 38.6 Percent (D-4, 300 ft²) 116 Percent (D-4, 467 ft²)	133 Percent (504 ft², D-5) 105 Percent (444 ft², D-5) 10.9 Percent (240 ft², D-5)
Structure (lb)	EC[a]	3670	3670	3870
	EB[b]	3295	3295	3495
Orbit Lifetime (Days) (at +2σ Solar Activity)		833	681	540

a. EC = Experiments Center-Mounted

b. EB = Experiments Bottom-Mounted

Figure D-6. Performance comparison.
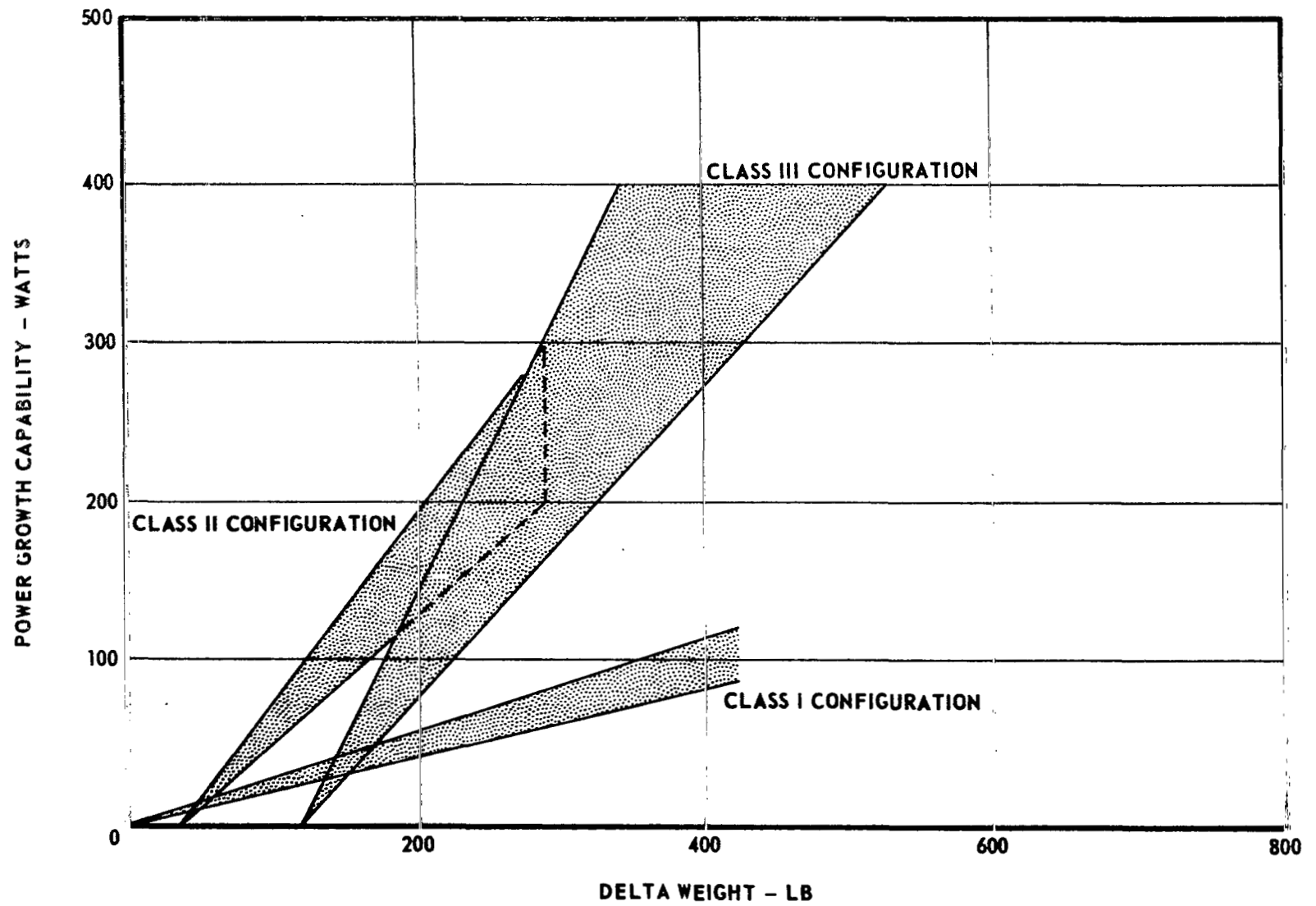
Figure D-7. Growth capability of each configuration class.

weight increase caused by the addition of a 5-foot length would be about 400 pounds using this approach, in addition to the weight of a 5-foot shroud section. The power increase would be approximately 10 percent. Power growth through additional spacecraft length thus can be seen to have large weight penalties. Of course, even if an additional payload shroud section must be added, the spacecraft length need not necessarily be increased by the same amount. For structural reasons, it is believed that the weight penalties associated with spacecraft lengths greater than 35 feet probably cannot be tolerated.
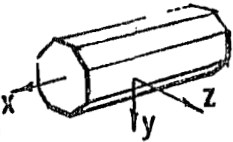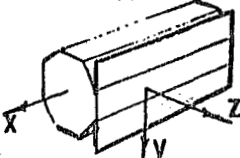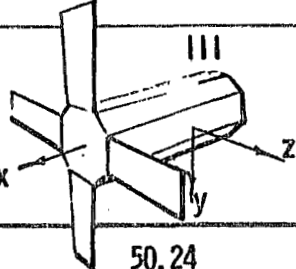
Class II configurations provide a rather easy method to increase the power capability without a major structural weight increase. Each side panel folds out 45 degrees in the case of Figures D-2 and D-3. As shown in Figure D-4, each panel folds out 180 degrees. Power growth is measured from the level provided by the baseline, 0 degree off the sunline. The initial weight penalty associated with foldout side-oriented arrays is 40 pounds. The limit of the delta power is about 200 watts at a cost of 250 pounds.

The weight penalty associated with the end-oriented approach (Class III) is 120 pounds; however, a much greater capability exists to increase the power level. This approach would be valuable if the experiment package or systems were radically changed such that the power requirements increased greatly.

A summary of the mass characteristics of the three configuration classes studied is given in Figure D-8. The associated center of gravity locations are given in Figure D-9. For a given experiment package arrangement, it was found that the inertias varied very little between configuration Classes I and II. For this reason, the inertias were not computed for configuration II with the experiments mounted near the bottom.
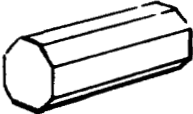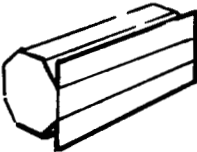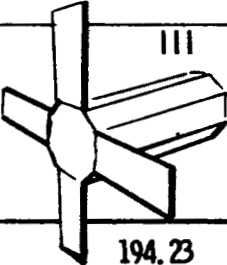
4. Conclusions

The alternate configurations presented herein indicate several different approaches to resolving potential problems associated with the baseline. However, each of the alternates contributes its own disadvantages in the process of providing solutions to the baseline problems. The alternates were not examined to the depth of detail to which the baseline was examined, and consequently, the assessments and comparisons of the alternates cannot be expected to be as accurate as the assessment of the baseline. It can be readily seen that the experiments are very strong configuration drivers in all
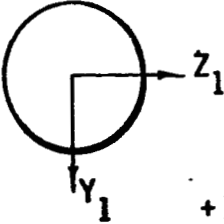
INERTIA lb-in²	CONFIGURATION CLASS			
	I	II	III	
Ix	18.51	18.92	50.24	Experiments Center
Iy'	163.15	163.56	183.24	
Iz	171.18	171.18	191.81	
Px	18.40	18.40	50.14	
Py	163.26	163.26	183.35	
Pz	171.18	171.18	191.81	
Ix	17.12	—	41.75	Experiments Bottom
Iy	237.39	—	268.81	
Iz	242.96	—	267.96	
Px	17.10	—	41.74	
Py	237.40	—	268.80	
Pz	242.97	—	267.96	

Figure D-8. Summary of mass characteristics.

C. G. LOCATION (Inches)	CONFIGURATION CLASS			
	I	II	III	
X	188.98	188.98	194.23	EXP. CENTER
Y	- .68	- .68	- .68	EXP. CENTER
Z	1.18	1.418	0	EXP. CENTER
X	168.45	-	173.70	EXP. BOTTOM
Y	- .17	-	- .17	EXP. BOTTOM
Z	1.18	-	0	EXP. BOTTOM

+ X_1 LAUNCH DIRECTION
- Z_1 SUN (Except for III)
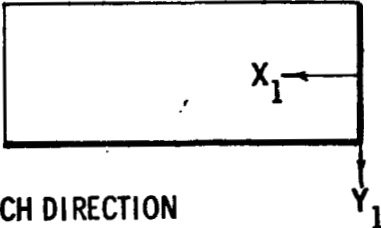
Figure D-9. Center of gravity locations.

configurations studied. When the actual flight experiment package is defined, it may very well be that one of the configurations shown (or a completely different concept) may stand out as obviously superior in every respect. Certainly, no firm selection of a configuration can be made until the experiment package is defined, and even after then, it should be delayed sufficiently long to allow study of particular problem areas and different configurations to an adequate depth before making the decisions.

The major advantages and disadvantages of each configuration class have been discussed herein. Class I configurations have some advantages in solar array simplicity (no deployable solar arrays) and in orbital lifetime. However, it appears that the power growth limitations of this class may ultimately result in an unacceptable approach. Class III configurations have the greatest power growth potential, although solar array complexity is increased somewhat, lifetime is decreased considerably, and thermal control problems are aggravated. This class might be the choice if power require- ments become excessive enough to outweigh the associated disadvantages of the configuration. Considering the baseline experiment package and the growth in power requirements normally expected in similar programs, it would seem that the Class II configurations offer the best power growth potential for the least penalty. The simple types of deployable solar panels used are fairly common on space flight hardware, and deployment mechanisms requiring no power except for the initiating mechanisms can be achieved. For example, a spring-damper-latch deployment scheme with an explosive-nut release mechanism could be designed using flight-proven hardware. Probably the greatest selling point for this approach is that the failure of the panels to deploy properly would still allow the spacecraft to operate at a reduced power level. In fact, failure to deploy would merely transform this configuration to the baseline array configuration in the case of the configuration shown in Figure D-3. The array-to-CBR connection could be designed for worst-case, nonplanar array operation, for maximum efficiency in the event the arrays failed to deploy. Thus, there appears to be much to gain and little to lose by such an approach. Orbital lifetime would decrease slightly, but would still be within the design limits and could be increased, if desired, by going to a higher orbital altitude.

On all configurations, packaging of the systems and thermal and attitude control considerations may become stronger drivers as more details of these considerations become available.

D-18

APPENDIX E. ALTERNATE STRUCTURAL CONFIGURATION

TABLE OF CONTENTS

LIST OF ILLUSTRATIONS

LIST OF TABLES

ALTERNATE STRUCTURAL CONFIGURATION

Introduction and Design Approach

The baseline structural design was developed to minimize the disturbing gravity gradient torque by locating the spacecraft center of gravity near the geometric center. To accomplish this, the heavy experiments were located near the geometric center of the spacecraft. This constraint caused the primary load paths to become long, thereby decreasing the structural efficiency of the spacecraft.

An alternate structural design which places the heavier experiments in the aft portion of the structure was developed to minimize this penalty and is shown in Figure E-1.

The shortened load paths and reduced bending moments acting on the structure will result in smaller member sizes, thereby lower weight, and in smaller deflections.

The design approach taken for the alternate structural system of the spacecraft is an open truss assembly similar to the baseline. The primary structural load paths are through two opposing box truss sections which are parallel to the spacecraft longitudinal axis. Secondary and equipment support members are attached to the box truss to complete the structure.

The cross section of the box truss is changed where necessary to accommodate the various experiments and particularly at the aft attach plane where the spacecraft structure will be attached to the adapter at the eight attach points.

The same advantages of flexibility and accessibility that the baseline configuration has are also present in the alternate design.

Flight
Direction

Scan Axis
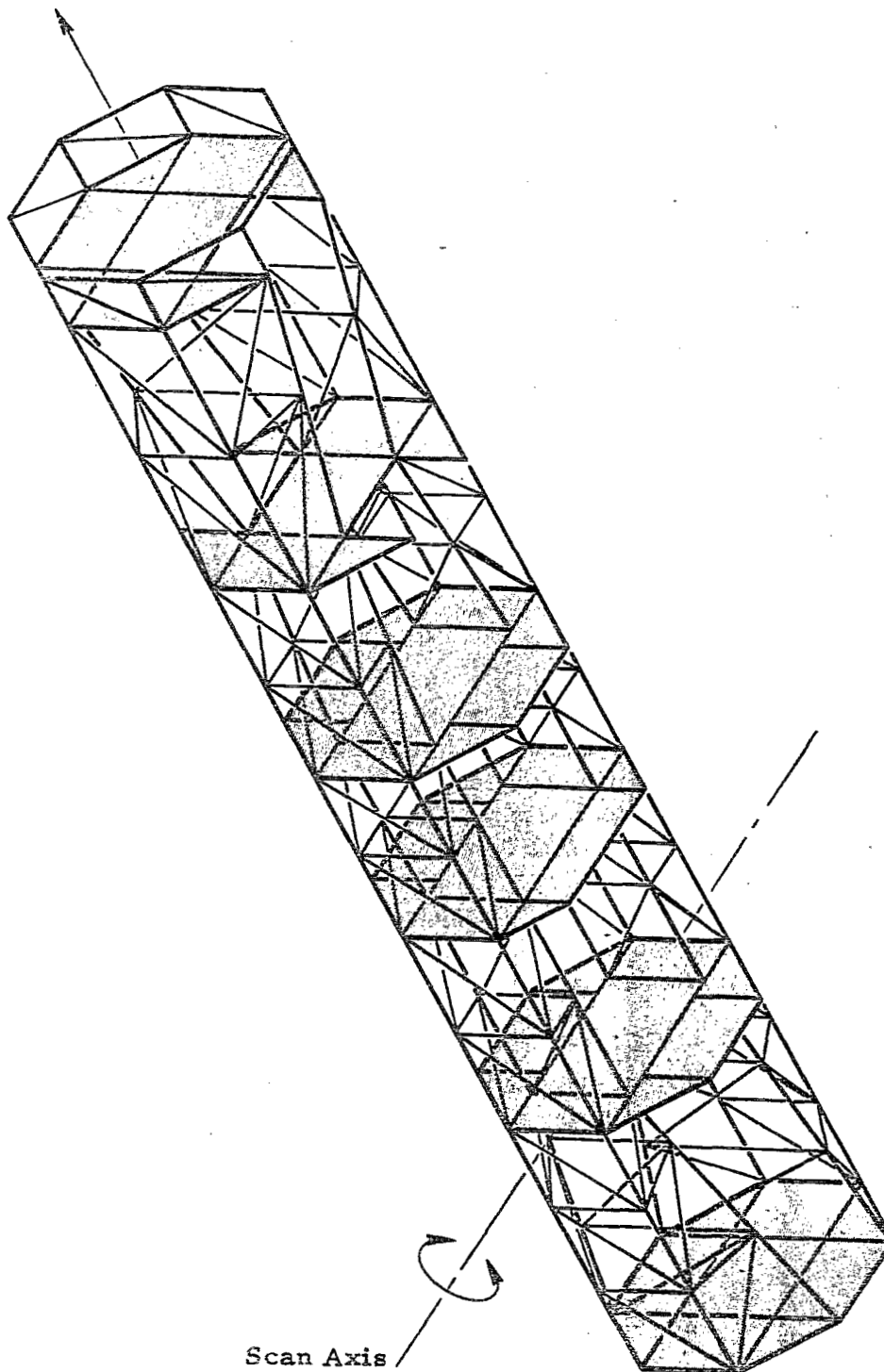
Figure E-1. Alternate spacecraft structural concept.

Structural Design Requirements

The alternate structural configuration will have to meet the same structural design requirements as the baseline structure, which are discussed in Section VI, Paragraph B of Volume I.

Structural System Description

The alternate structural design developed for the spacecraft is shown in Figure E-2.

The major load paths are through eight longerons which serve as chord members for the two parallel longitudinal box truss sections. Two angles are used to form T-sections for these longerons. Struts and diagonals are angle sections, and cross beams used between the two truss assemblies at various levels are I-sections. Specific sizes for these members are shown in Figure E-2; all members are aluminum.

The other structural characteristics are similar to those of the baseline configuration, as discussed in Section VI, Paragraph C of Volume I.

Weight Analysis

The weight breakdown and deflection of the structure designed for loads only, and for loads and deflections, are shown in Table E-1.

Assumptions made for the purpose of conducting the weight analysis are the same as for the baseline which were discussed in Section VI, Paragraph D of Volume I. However, because of the analytical complexity presented by the structural arrangement, only one iteration of member sizing for deflection was made within the scope of this study, and, consequently, the structural weight given is for a structure which had considerably less than the allowable deflection.

As can be seen from Tables E-1 and from VI-2 in Section VI, Paragraph D of Volume I, the alternate design for loads and deflections is 375 pounds less than the baseline and has approximately one half as much deflection.
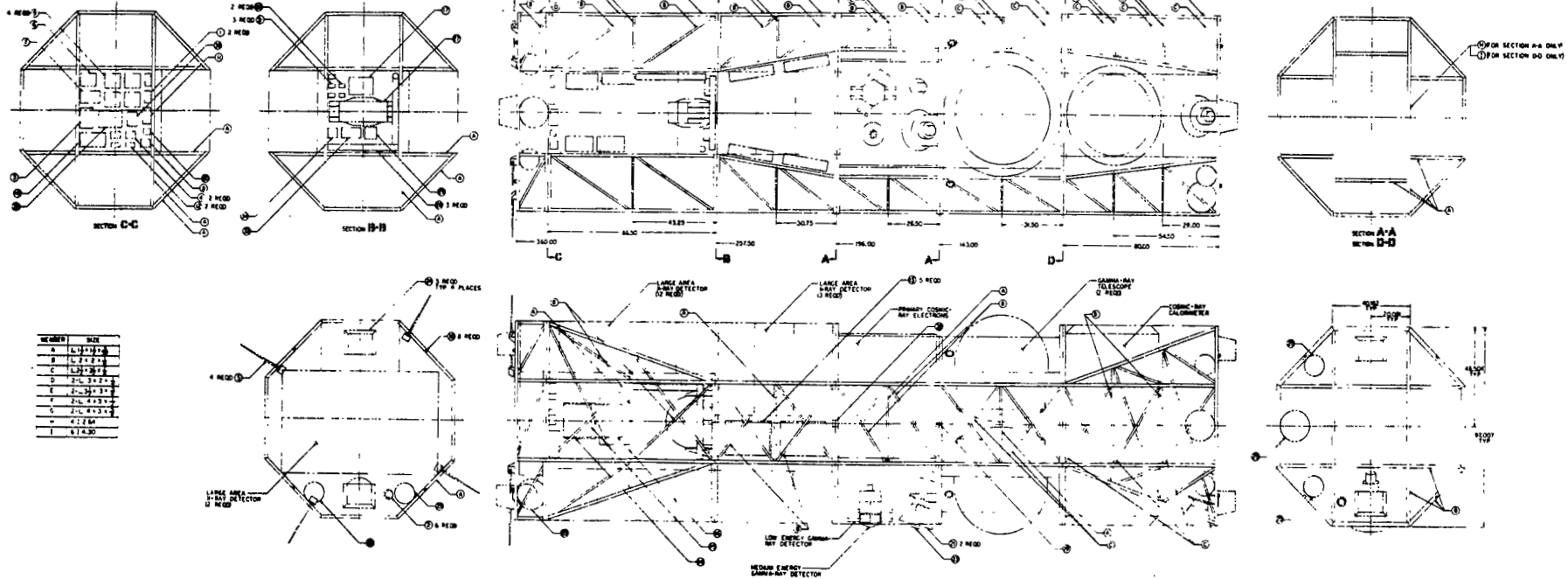
Figure E-2. Alternate structural design.

TABLE E-1. COMPARATIVE WEIGHT AND DEFLECTION

Component	Designed for Loads and Deflections	Designed for Loads Only
Basic structure (trusses, bulkheads), lb.	2395	1407
Skin (0.025-inch aluminum), lb.	300	300
Internal equipment mounting panel (estimated), lb.	600	600
Total weight, lb.	3295	2307
Maximum deflection, in.	0.44	1.76

With an optimization study of the alternate structure, the deflection can be made closer to the limiting 1.0 inch and a larger weight savings than the 375 pounds should be realized.

APPENDIX F. THERMAL ANALYSIS

TABLE OF CONTENTS

LIST OF ILLUSTRATIONS

LIST OF ILLUSTRATIONS (Concluded)

LIST OF TABLES

APPENDIX F. THERMAL ANALYSIS

A chronological sequence of studies was made on various configurations, using a very cursory thermal analysis. These studies allowed some of the configurations to be eliminated because they were not considered feasible from a thermal viewpoint.

After some of the configurations were selected as candidates a preliminary thermal analysis was made using a more sophisticated thermal model and the latest information available at that time. These data and information are presented here.

Six different cases were analyzed using the vehicle structure and layouts shown in Figures F-1 and F-2. These were a combination of vehicle orientation with respect to the sun and vehicle configuration.

1. Guidelines and Assumptions

Guidelines and assumptions followed in performing this analysis are:

● Alternate structure, panels, and experiment layout as shown in Figures F-1, F-2, and Table F-1 are used in the analysis.

● All external, internal, and backing panels for solar cells are 1-inch aluminum honeycomb.

● Solar absorptivity and emissivity values used are:

	α	ϵ
X-ray detectors	0.34	0.04
Solar panels	0.7	0.8
All other surfaces	0.3	0.8

● The spacecraft is in a 200-n. mi. circular orbit which is at an inclination angle of 28.5 degrees with respect to the equatorial plane.

- Heat dissipated by each component is presented in Table F-2.

- All subsystem components have good metal-to-metal contact with the mounting panels.

- Heat source constants used are:

  Solar constant — 447 Btu/hr-ft^2

  Earth albedo — 43 percent

  Earth IR — 68.2 Btu/hr-ft^2

Figure F-3 is a sketch of each case ccndition as viewed from the earth's north ecliptic pole. Cases A and B represent the spacecraft with the scan axis pointed to the sun. The difference is that Case B represents a vehicle orientation rotated 90 degrees on the scan axis from the position shown in Case A. Cases C and D represent the vehicle rotated on its longitudinal axis so that the scan axis is off the sunline 35 and 45 degrees, respectively. Case E represents the vehicle oriented the same as in Case A with the side solar panels swung out so that they are perpendicular to the sunline.

In Case F the spacecraft has the same sun orientation as in Case A. However, in Case F additional heat paths were included in the thermal model to simulate a network of conductors to transfer heat from the solar panels to the three panels on the opposite side of the vehicle. The heat transfer capability of the conductors chosen for this case analysis totaled 1200 Btu/hr-° F. Theoretically this amount of heat could be transported by heat pipes.

Heat pipe investigation has pointed out the fact that, although heat pipes are excellent devices to use in thermal control problems, they are quite difficult to manufacture in the size range that would be required for this application. Use of an active type thermal control system where a fluid must be transported to move heat from one side of the spacecraft to the other would decrease the overall spacecraft reliability and require considerable power to perform the pumping operation.

2. Results

a. Component Temperatures. Table F-3 presents the resulting component temperature ranges throughout the orbit for each case. It is noted

that there is very little difference in any temperatures between Cases A and B. These two cases, which represent the vehicle with the scan axis parallel to the sunline, show that the thermal effect of vehicle scan in this orientation is negligible.

There are two columns under each of the two cases labeled Case C spin axis 35 degrees off sunline and Case D spin axis 45 degrees off sunline. The first column presents the resulting temperature ranges as if the spacecraft were pointing in these orientations. The second column presents the average temperature ranges resulting from the scan motion of the spacecraft.

The opposing experiment face panels, which are facing 90 degrees to the scan axis, exchange position with respect to the sun every 5 minutes (due to the scan rate of 0.1 rpm). All of the experiments are massive and have considerable heat capacity. This condition produces a thermal lag that resists rapid temperature changes. Therefore with the 0.1-rpm scan rate, the varying heat flux will result in temperatures averaging between the extremes for experiments located on the opposing face panels. For example, in the 45-degree-off-sunline cases the cosmic ray calorimeter 1 and 2 covers show temperatures of 35° to 48° F and 3° to 13° F, respectively. Because of the change in position with respect to the sun, every 5 minutes the temperature will average halfway between these extremes or from 19 to 30° F.

The same situation occurs for the subsystem components on the inside. Most of the components stay essentially at the same temperature as the panels on which they are mounted. So the average temperatures for the components are based on the average temperatures of the panel pairs (1 and 3), (2 and 4), (6 and 8), and (7 and 9).

b. **Solar Panel Temperatures.** Figures F-4 through F-9 present curves representing the solar panel temperatures for the six cases. Numbers 21, 22, and 23 mean that the associated curve is a plot of the temperature in the center of panels 21, 22, and 23 as shown in Figure F-1. Time zero is the instant that the spacecraft goes into the earth's shadow. At 0.5 hour from this time it comes out of the shadow and is again exposed to the sun. At 1.53 hours the cycle begins to repeat.

Cases A and B (Figs. F-4 and F-5), which are the same except for spacecraft orientation, show no significant difference in the solar panel temperatures.

The vast temperature differences that occur in Panels 21 and 23 in Cases C and D (Figs. F-6 and F-7) are due to the fact that no scanning action

of the spacecraft was considered. Thus, in the analysis, Panel 23 receives very little (Case C) or no (Case D) solar radiation while Panel 21 is constantly exposed during the daylight portion of the orbit. The panel temperatures shown in Figures F-6 and F-7 apply to a pointing (nonscanning) mode of spacecraft operation with the spacecraft oriented to the earth and sun previously explained. In fact, the spacecraft is spinning at 0.1 rpm about its scan axis and Panels 21 and 23 pass from total illumination to very little (Case C) or no (Case D) illumination every 5 minutes, while the spacecraft is in daylight. For this reason the average temperatures of Panels 21 and 23 are considered to be an accurate estimate of the side panel temperatures for Cases C and D. This average curve is plotted for these two cases.

Figure F-8 presents the solar panel temperature curves representing Case E in which the two side solar panels are folded out 45 degrees so that they are perpendicular to the sunline as is the center panel. It is noted that the center panel temperature is a few degrees cooler than in Case A. This is caused by a larger temperature difference between the center panel and the associated spacecraft hardware to which it conducts and radiates. This hardware is cooler because the side panels are no longer in direct contact with it. The side panel temperature curves show very little difference from Case A while exposed to the sun. This can be explained by the fact that although the panels can radiate approximately 49 percent more heat to space because of panel backside exposure, they are picking up 40 percent more heat from solar radiation and have lost some of their conduction paths to the spacecraft. These paths conducted away approximately 9 percent of the panel heat in Case A. All panels in Case E are somewhat cooler than Case A while the spacecraft is in the earth's shadow caused by the added surface exposure to space.

With conductors incorporated into the thermal model as in Case F, additional heat is conducted away from the solar panels to the panels on the opposite side of the spacecraft. The result, of course, is a decrease in solar panel temperatures as shown in Figure F-9. Table VII-3 indicates that the temperature distribution is more nearly even throughout the spacecraft in Case F than in Case A.

Another thermal analysis was done to determine the most favorable vehicle configuration. Figure F-10 shows the orientation for these calculations. Figure F-11 indicates the two other configurations considered. Configuration 1 was the baseline. Configuration 2 had fold-out panels all arranged normal to the sunline, and Configuration 3 had end-mounted fold-out panels. In this

F-4

analysis the worst case was assumed using $\alpha = 0.7$, $\epsilon = 0.8$ for the solar panels and $\alpha = 0.8$, $\epsilon = 0.9$ for the nonsolar panels.

Figures F-12 through F-17 show the surface temperature for one orbit after equilibrium conditions have been obtained.

From this very cursory analysis, the large ΔT from the front of the vehicle to the rear was excessive in Configuration 3 and it would create a thermal stress problem as well as a thermal distribution problem. The solar panels operate cooler, but because of the other problem created it was dropped. Configurations 1 and 2 were the two picked for further study as discussed earlier.

TABLE F-1. ASSUMED COMPONENT LOCATIONS FOR THERMAL ANALYSIS I

Panel Number	Component
1	Power supply Transmitters Recorders Beacon transmitter Diplexer Command receiver PCM multiplexers
2	Switch selector Power distributor Measuring distributor Control distributor Master measuring voltage supply
3	Signal processor
5	Magnetic coils Magnetometer Attitude control electronics Rate gyros Flywheel
11	Propellant valves and plumbing No. 1 Propellant and tank No. 1 Charger-battery regulators
14	Propellant Valves and plumbing No. 2 Propellant and tank No. 2

TABLE F-2. ASSUMED HEAT DISSIPATED BY EACH EXPERIMENT AND COMPONENT — THERMAL ANALYSIS I

Component	Number of Components	Heat Dissipated by Each Unit (w)
Large area X-ray detector	4	16.2
Primary cosmic-ray electron experiment	1	20
Cosmic-ray calorimeter experiment	1	54
Gamma-ray telescope	2	13
Medium energy gamma-ray detector	1	20
Low energy gama-ray detector	1	3
136 MHz Beacon transmitter	1	3
Diplexer	1	2
S-band transmitter	2	15
Command receiver	1	2
Power supply	1	10
PCM multiplexer	1	5
Magnetic tape recorders	4	9
Charger-battery regulators	4	250
Power distributor	1	10
Switch selector	1	20
Measuring distributor	1	10
Control distributor	1	10
Magnetic coils	3	3
Rate gyros	3	3.5
Flywheel	1	55
Magnetometers	1	2
Attitude control electronics	–	10
Signal processor computer	1	10

TABLE F-3. COMPONENT TEMPERATURE VARIATIONS DURING ORBIT

Component Experiments	Case A Center Solar Panel 90° to Sun Line	Case B Center Solar Panel 90° to Sun Line With Vehicle Rotated 90° on Spin Axis	Case C Spin Axis 35° Off Sun Line Average Due to Scan	Case D Spin Axis 45° Off Sun Line Average Due to Scan	Case E Center Solar Panel 90° to Sun Line With Side Solar Panels Folded Out In Line With Center Panels	Case F Center Solar Panel 90° to Sun Line With Conductors Connecting Solar Panels to Panels on Shade Side
X-ray detector 1	63 to 65	64 to 66	65 to 67	65 to 67	53 to 55	65 to 67
X-ray detector 2	61 to 63	61 to 63	60 to 63	60 to 62	50 to 53	62 to 63
X-ray detector 3	61 to 63	62 to 65	60 to 63	59 to 62	53 to 56	64 to 66
X-ray detector 4	62 to 64	62 to 64	59 to 61	59 to 61	58 to 61	62 to 64
Cosmic ray electron detector case	39 to 43	36 to 46	48 to 57	39 to 46	25 to 29	43 to 48
Cosmic ray electron detector core	48 to 50	48 to 50	59 to 60	48 to 50	35 to 38	53 to 55
Cosmic ray calorimeter 1 cover	25 to 30	17 to 31	40 to 51	35 to 48	3 to 8	26 to 34
Cosmic ray calorimeter 1 core	68 to 69	67 to 68	70	68 to 69	65 to 67	68 to 69
Cosmic ray calorimeter 2 cover	23 to 28	15 to 24	3 to 4	3 to 13	-5 to 8	21 to 37
Cosmic ray calorimeter 2 core	67 to 68	67 to 68	65 to 67	66 to 67	65 to 66	68 to 69
Gamma ray telescope 1 case	20 to 30	19 to 32	56 to 66	37 to 47	13 to 23	21 to 30
Gamma ray telescope 1 core	66 to 67	66 to 67	70 to 71	70 to 71	65 to 66	66 to 67
Gamma ray telescope 2 case	18 to 29	18 to 24	18 to 27	17 to 25	10 to 19	21 to 34
Gamma ray telescope 2 core	66 to 67	66 to 67	66 to 67	66 to 67	65 to 66	67 to 68
Low energy gamma ray detector	24 to 29	22 to 29	21 to 24	22 to 27	20 to 23	23 to 28
Medium energy gamma ray detector	20 to 25	18 to 23	17 to 19	20 to 25	16 to 18	19 to 24
SUBSYSTEMS						
Beacon	44 to 45	45 to 48	43 to 44	41 to 43	31 to 32	62 to 68
Multiplexer	44 to 45	45 to 48	43 to 45	41 to 43	31 to 32	62 to 68
Transmitters	44 to 45	45 to 48	43 to 44	41 to 43	31 to 32	62 to 68
Command receiver	44 to 45	45 to 48	43 to 44	41 to 43	31 to 32	62 to 68
Power supply	44 to 45	45 to 48	43 to 44	41 to 43	31 to 32	62 to 68
PCM multiplexer	44 to 45	45 to 48	43 to 44	41 to 43	31 to 32	62 to 68
Recorders	44 to 46	45 to 48	43 to 44	41 to 43	31 to 32	62 to 68
CBR units	32 to 46	33 to 47	25 to 34	21 to 35	37 to 47	41 to 54
Power distributor	78 to 88	78 to 90	75 to 87	71 to 79	60 to 64	65 to 74
Switch selector	78 to 88	78 to 90	76 to 87	71 to 79	60 to 64	65 to 74
Measuring distributor	78 to 88	78 to 90	75 to 87	71 to 79	60 to 64	65 to 74
Control distributor	78 to 88	78 to 90	75 to 87	71 to 79	60 to 64	65 to 74
Equipment panel 1	44 to 45	44 to 48	42 to 44	41 to 43	30 to 32	62 to 68
Equipment panel 2	78 to 88	78 to 90	75 to 85	71 to 81	59 to 64	65 to 74
Equipment panel 3	34 to 48	35 to 48	31 to 34	29 to 32	20 to 36	51 to 64
Equipment panel 4	67 to 92	67 to 98	57 to 74	53 to 65	53 to 73	54 to 76
Equipment panel 5	68 to 71	69 to 73	66 to 69	62 to 66	58 to 60	70 to 73
Equipment panel 6	34 to 41	34 to 41	30 to 36	31 to 34	26 to 34	41 to 50
Equipment panel 7	61 to 88	50 to 88	55 to 79	49 to 71	39 to 50	45 to 66
Equipment panel 8	25 to 36	27 to 36	22 to 27	18 to 23	15 to 27	40 to 56
Equipment panel 9	58 to 83	58 to 83	47 to 62	52 to 72	38 to 53	45 to 67
Equipment panel 10	52 to 61	52 to 62	46 to 53	42 to 50	49 to 57	51 to 59
Octagonal end 11	32 to 46	33 to 47	25 to 39	20 to 43	36 to 46	41 to 53
Octagonal interface 12	43 to 48	48 to 51	50 to 58	44 to 58	30 to 34	46 to 53
Octagonal interface 13	53 to 63	53 to 63	50 to 56	51 to 59	40 to 44	52 to 62
Octagonal end 14	-14 to 5	-14 to 14	-13 to 7	-14 to 6	-30 to -19	-15 to 5
Vehicle side panel 15	-23 to 3	-25 to 8	-25 to 2	-24 to 5	-47 to -15	25 to 66
Vehicle side panel 16	-37 to -11	-34 to -9	-38 to -5	-36 to -3	-52 to -24	7 to 52
Vehicle side panel 17	-27 to 7	-17 to -8	-27 to -2	-26 to -3	-49 to -11	17 to 74
Solar panel 18	65 to 143	62 to 152	72 to 175	69 to 174	36 to 109	32 to 109
Solar panel 19	72 to 170	72 to 170	64 to 150	64 to 150	68 to 174	38 to 142
Solar panel 20	66 to 151	70 to 138	26 to 50	8 to 43	50 to 166	35 to 123
Solar panel 21	63 to 150	56 to 156	60 to 163	61 to 131	41 to 159	23 to 111
Solar panel 22	75 to 191	68 to 188	63 to 173	63 to 173	53 to 174	30 to 143
Solar panel 23	66 to 161	67 to 146	21 to 79	41 to 131	45 to 163	26 to 122
Solar panel 24	54 to 131	58 to 141	58 to 161	38 to 115	51 to 161	32 to 108
Solar panel 25	66 to 172	65 to 172	57 to 151	49 to 134	60 to 166	36 to 140
Solar panel 26	61 to 146	64 to 134	17 to 68	38 to 115	55 to 162	34 to 122
Magnetic coils	69 to 71	69 to 73	66 to 69	68 to 72	57 to 60	70 to 74
Rate gyros	69 to 71	69 to 73	66 to 69	68 to 72	57 to 60	70 to 74
Inertial wheel	69 to 71	69 to 73	66 to 69	68 to 72	57 to 60	70 to 74
Master measuring voltage supply	78 to 88	78 to 88	78 to 86	76 to 86	60 to 64	65 to 74
Propellant and tank No. 1	55 to 57	55 to 59	31 to 33	43 to 46	56 to 59	60 to 64
Propellant valves and plumbing No. 1	36 to 46	32 to 48	28 to 36	30 to 42	23 to 32	43 to 52
Propellant and tank No. 2	34 to 38	36 to 43	10 to 12	22 to 26	28 to 30	0 to 5	10 to 15
Propellant valves and plumbing No. 2	-14 to 5	-11 to 16	-13 to 6	-14 to 6	-30 to -19	-16 to 5
Magnetometers	69 to 71	69 to 73	66 to 67	67 to 70	62 to 66	70 to 74
Attitude control electronics	69 to 71	69 to 73	66 to 67	67 to 70	62 to 66	70 to 74
Signal processor	34 to 48	35 to 48	31 to 35	33 to 37	29 to 32	51 to 64

Note: All of the above temperatures are degrees Fahrenheit.

EQUIPMENT MOUTING PANEL ASSY. (AFT)

SHROUD PANEL ASSY

EQUIPMENT TRUSS

EQUIPMENT MOUNTING
PANEL ASSY.(FORWARD)

SHROUD PANEL ASSY

BULKHEAD (4 PLACES)

SHROUD PANEL ASSY.

SHROUD PANEL ASSY. ON WHICH
SOLAR PANELS ARE MOUNTED
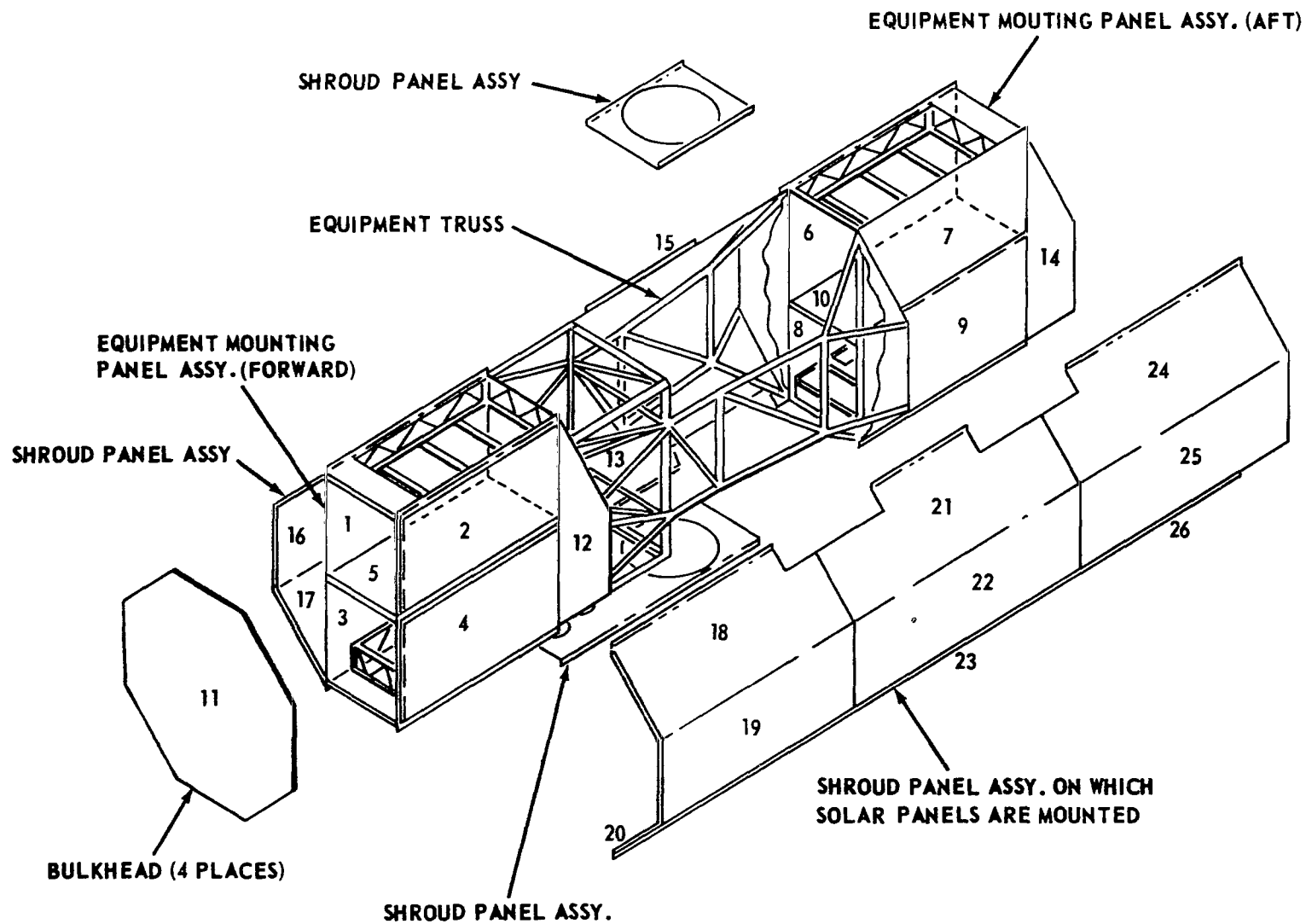
Figure F-1.   Vehicle structure, equipment panel, and solar panel
layout used in thermal analysis 1.

LARGE AREA X-RAY DETECTORS

PRIMARY COSMIC-RAY ELECTRONS

GAMMA-RAY TELESCOPE

MEDIUM ENERGY GAMMA-
RAY DETECTOR

COSMIC-RAY CALORIMETER

LOW ENERGY GAMMA- RAY DETECTOR
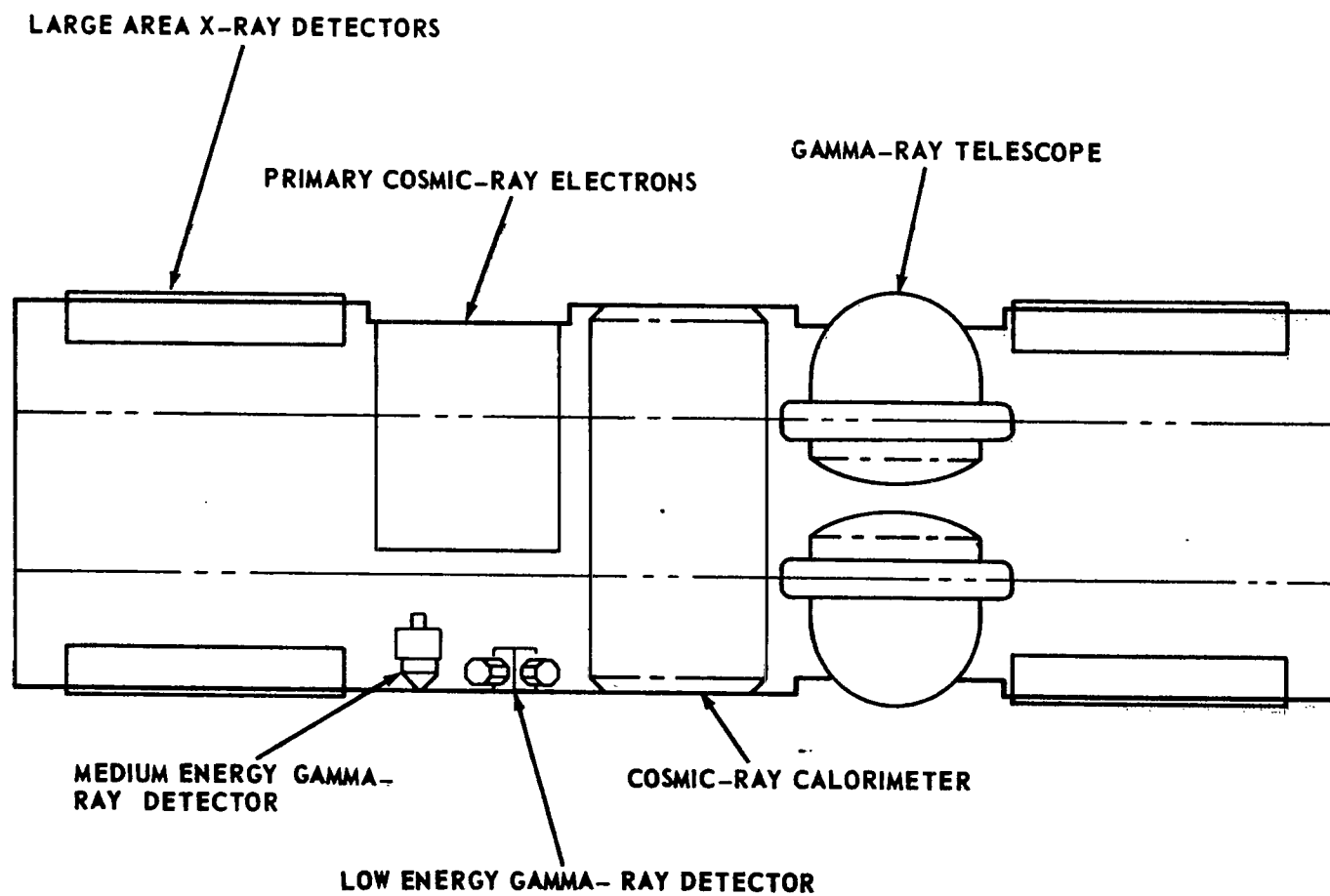
Figure F-2. Experiment layout used in thermal analysis 1.
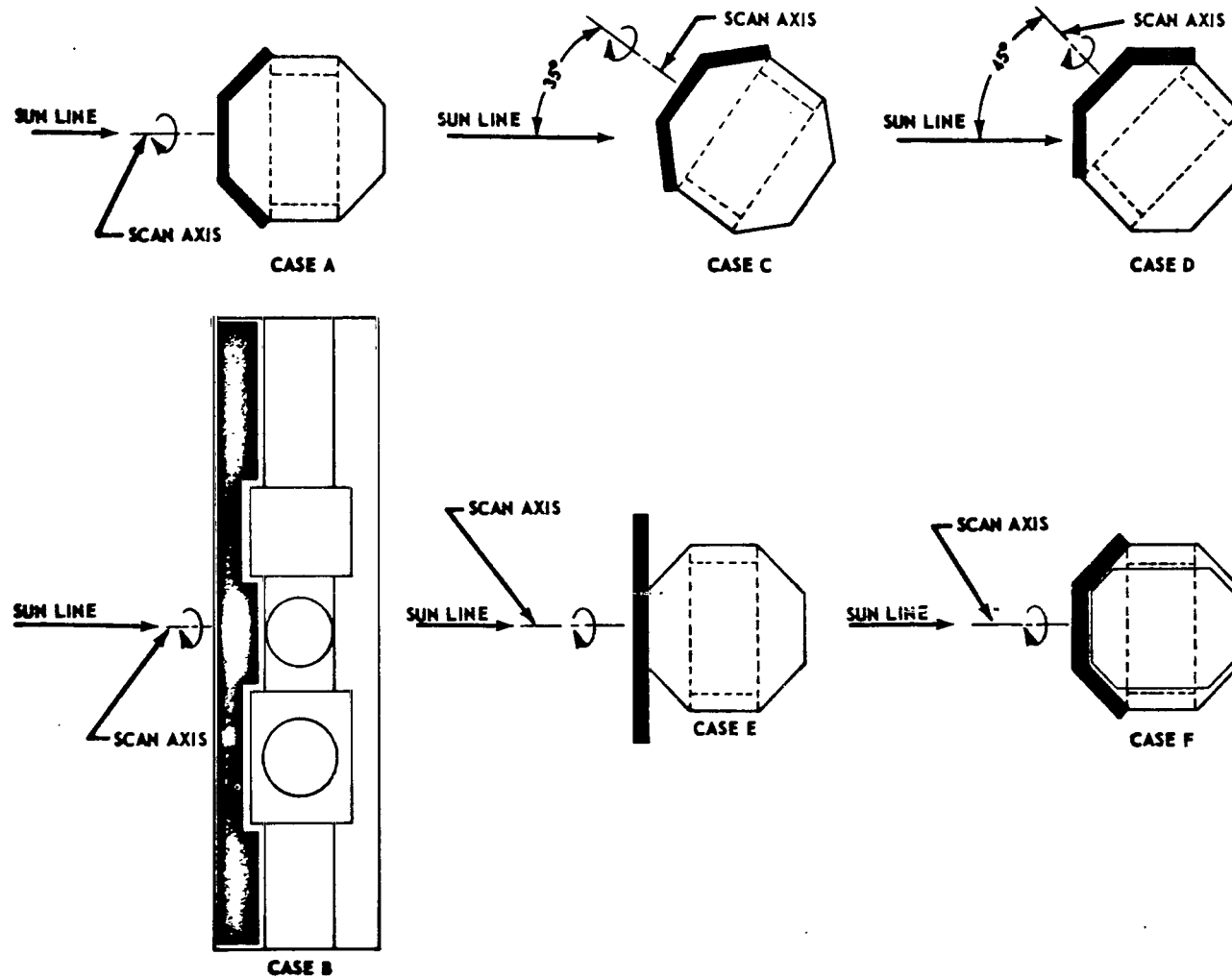
Figure F-3. Cases analyzed.
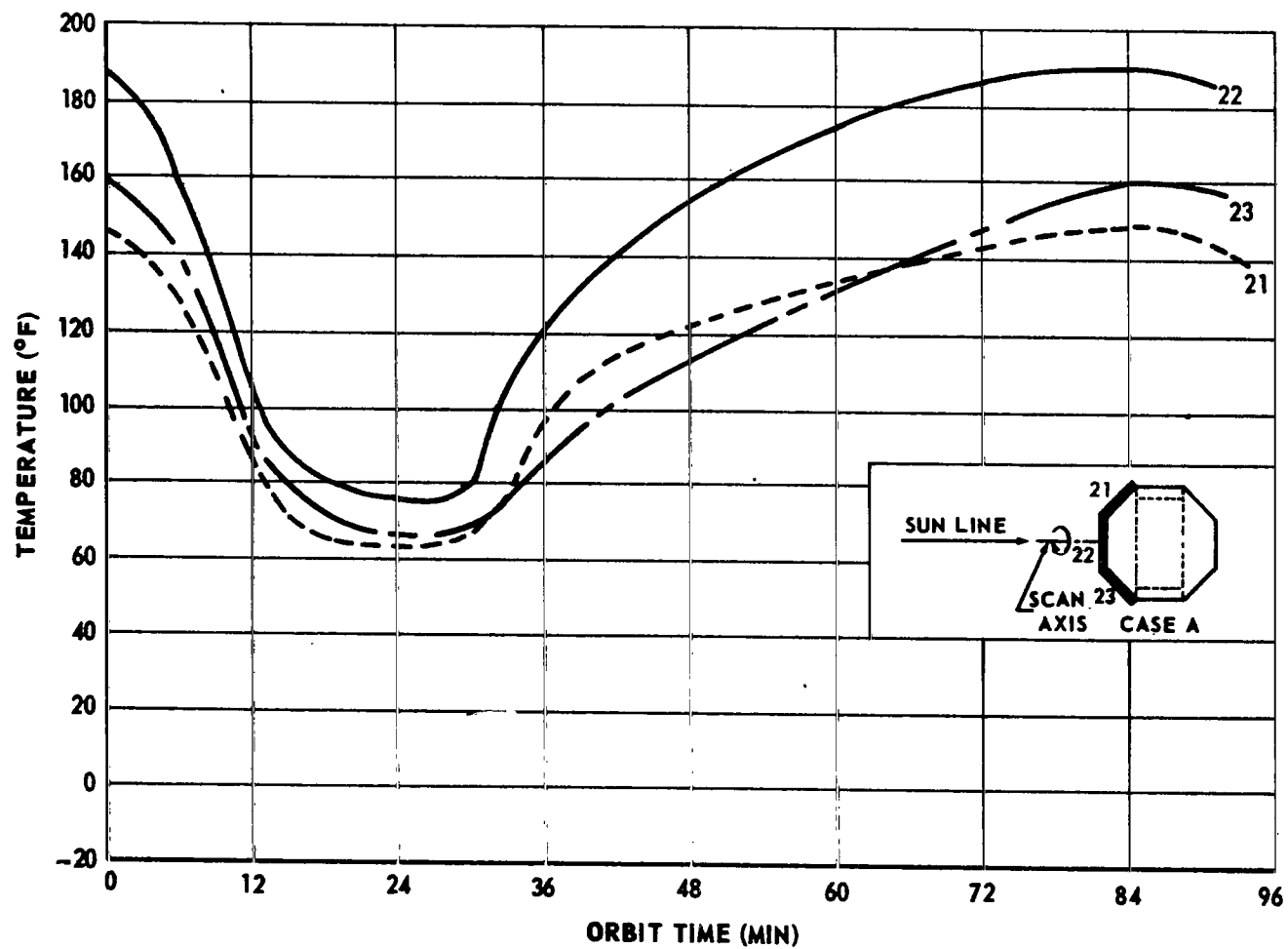
Figure F-4. Solar panel temperature variations during one orbit
for Case A thermal analysis 1.
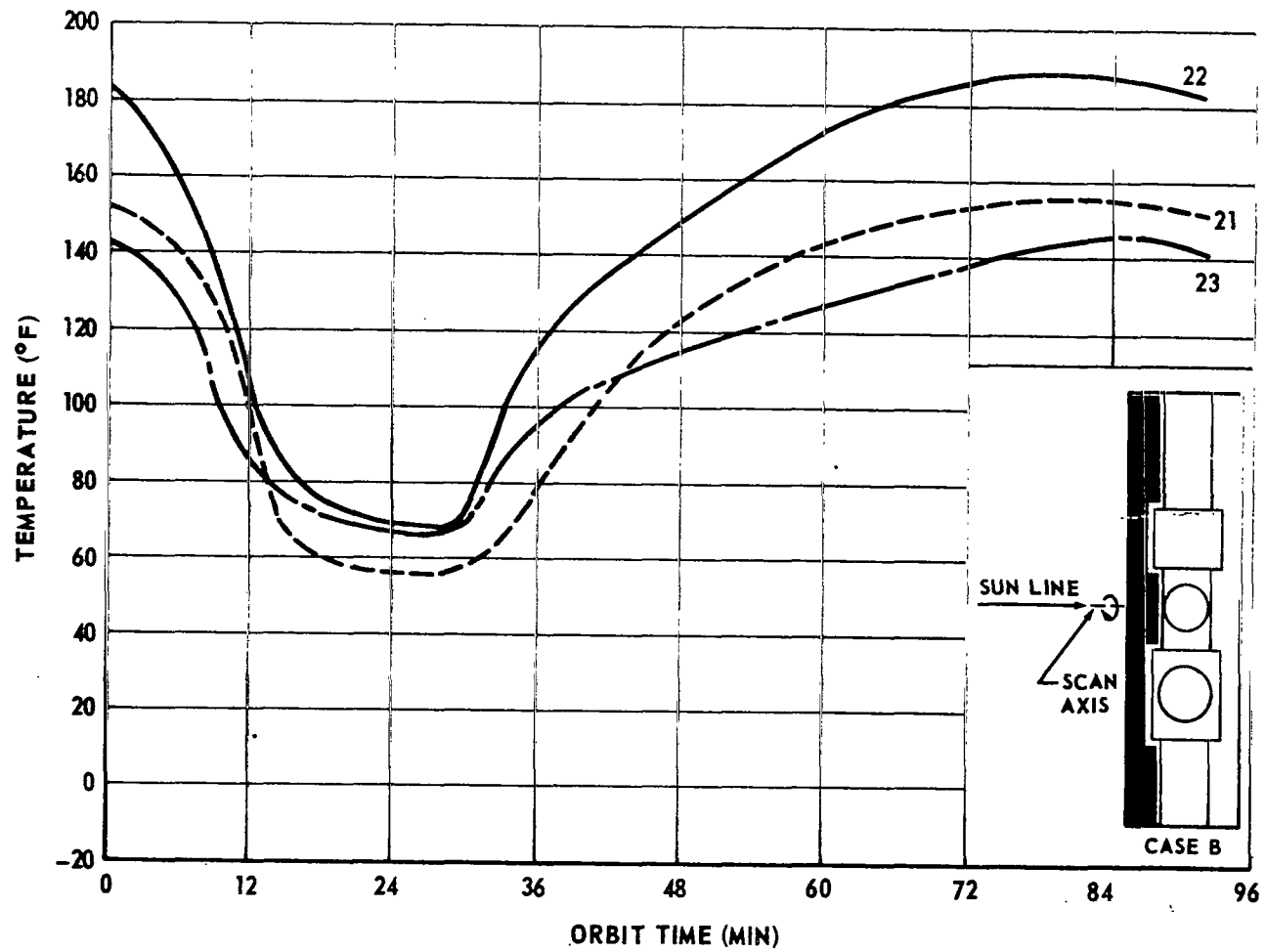
Figure F-5. Solar panel temperature variations during one orbit for
Case B thermal analysis 1.
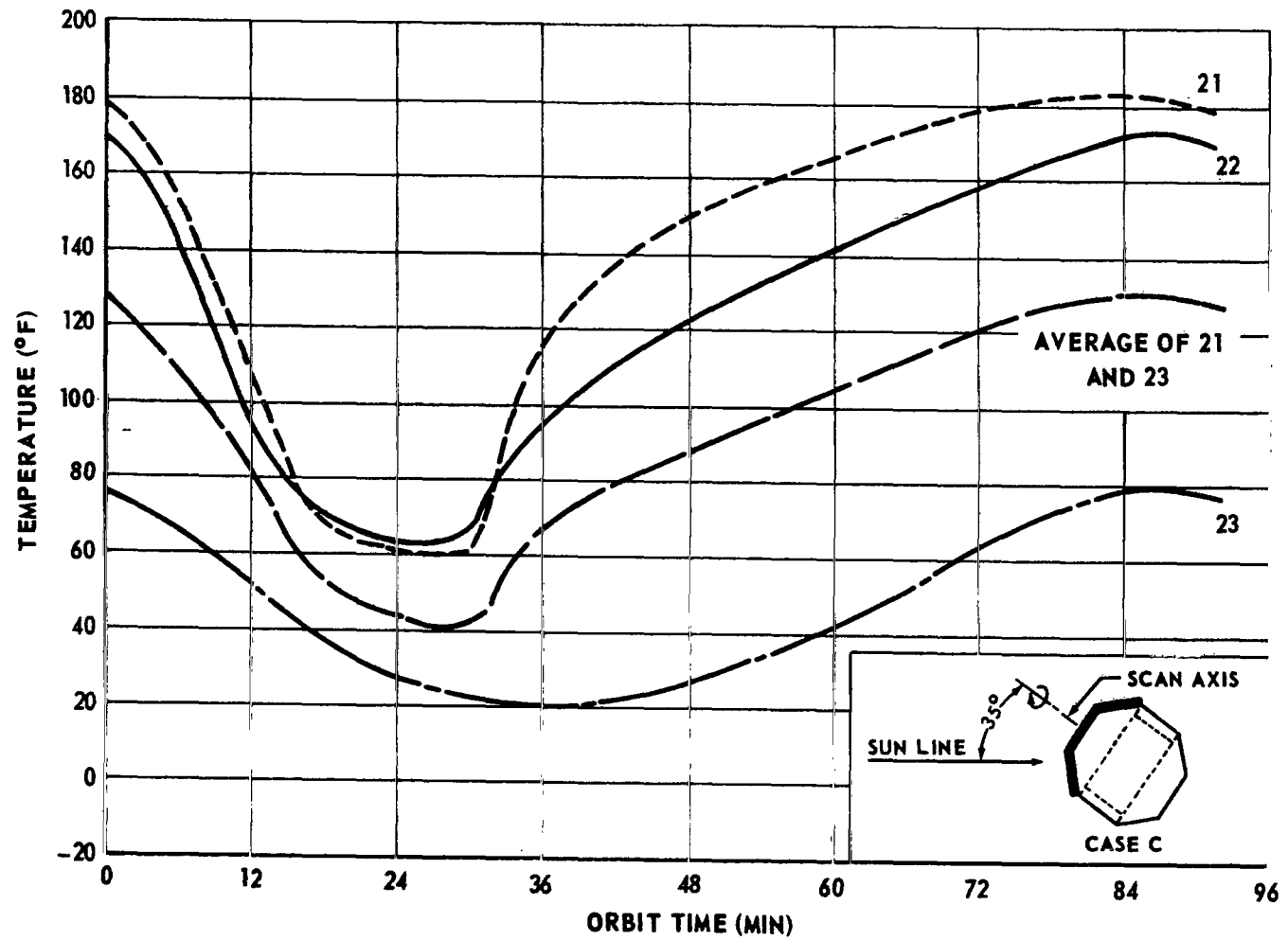
Figure F-6. Solar panel temperature variations during one orbit for Case C thermal analysis 1.
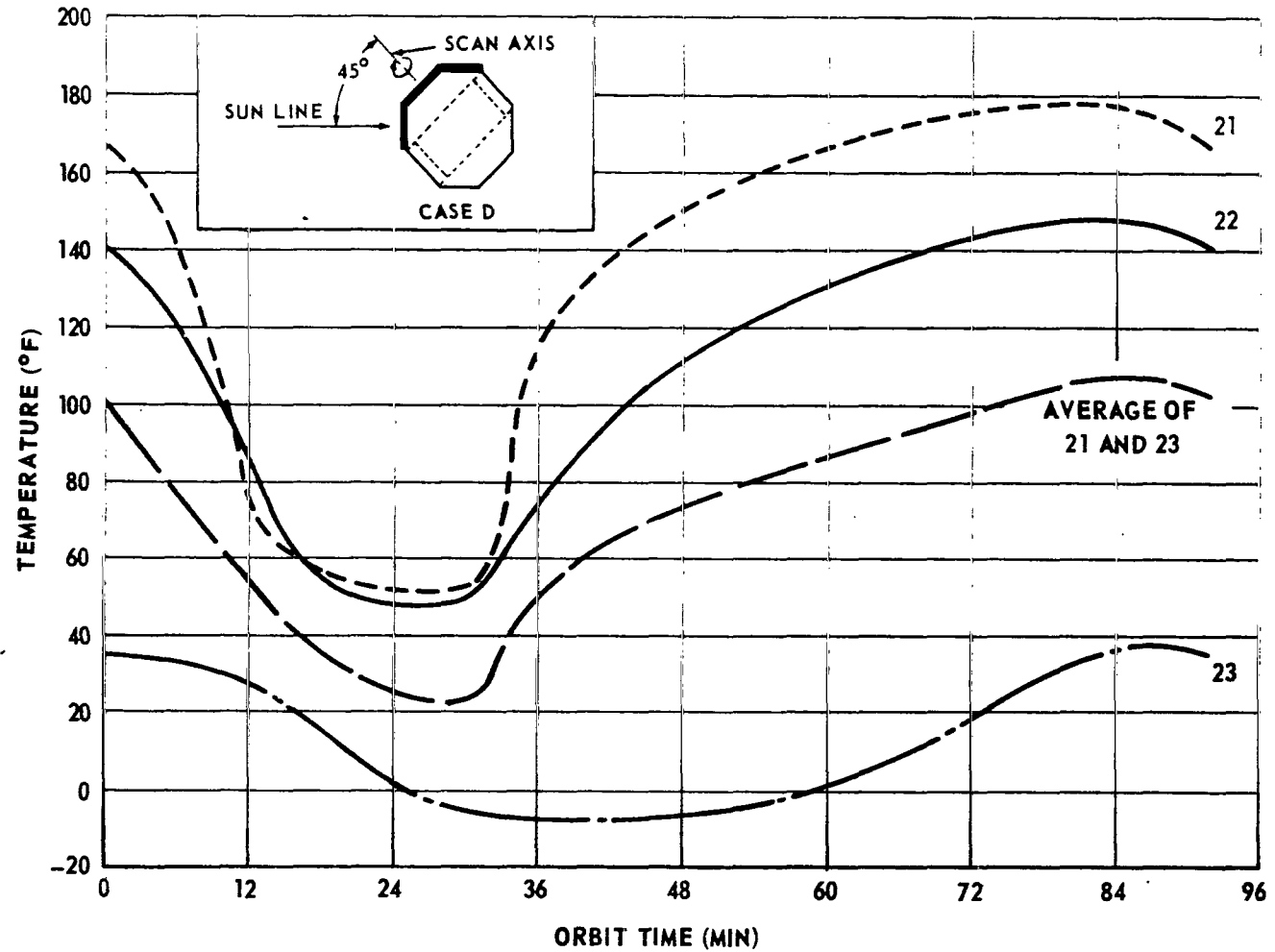
Figure F-7. Solar panel temperature variations during one orbit for Case D thermal analysis 1.
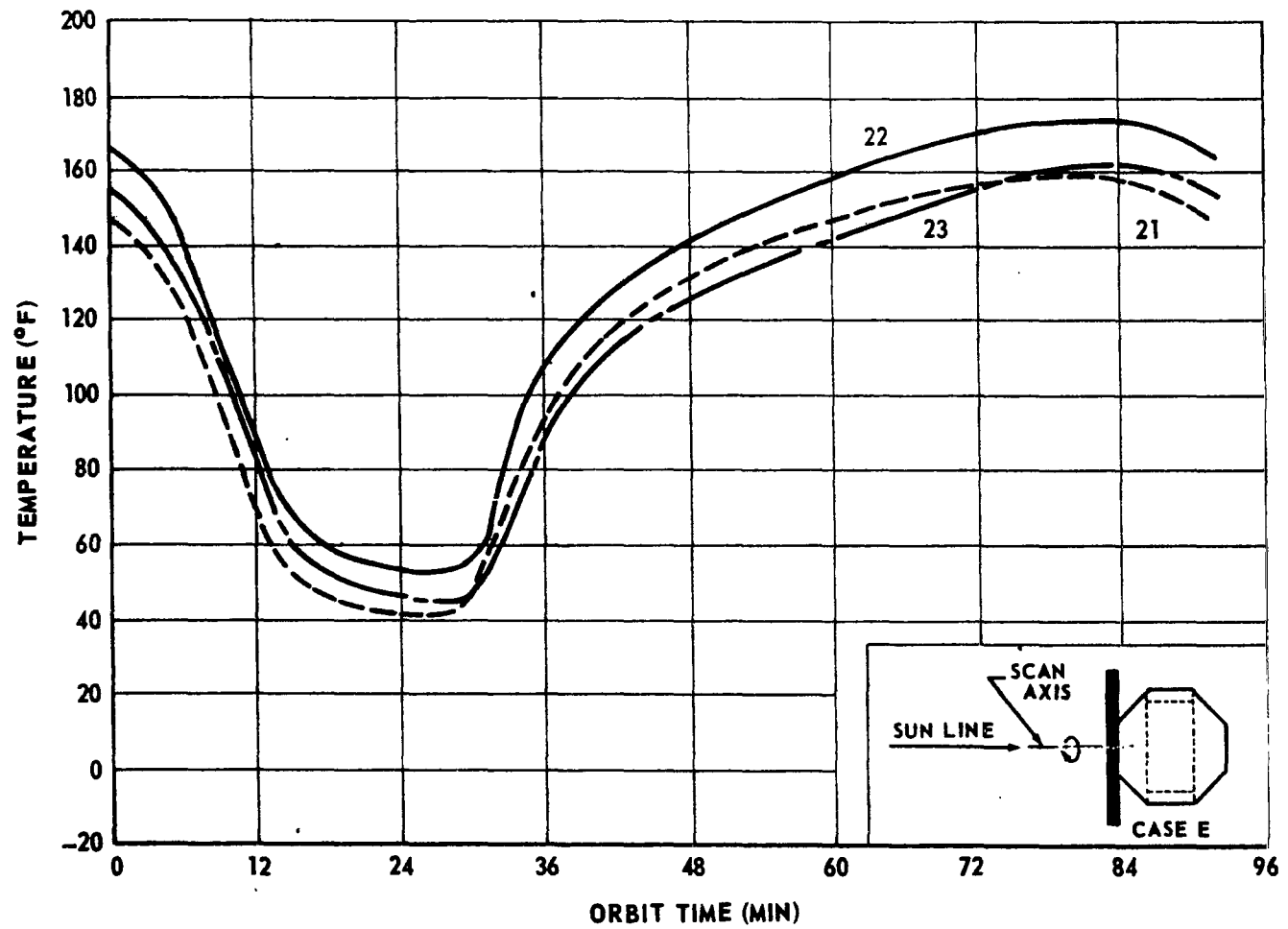
Figure F-8. Solar panel temperature variations during one orbit for
Case E thermal analysis 1.
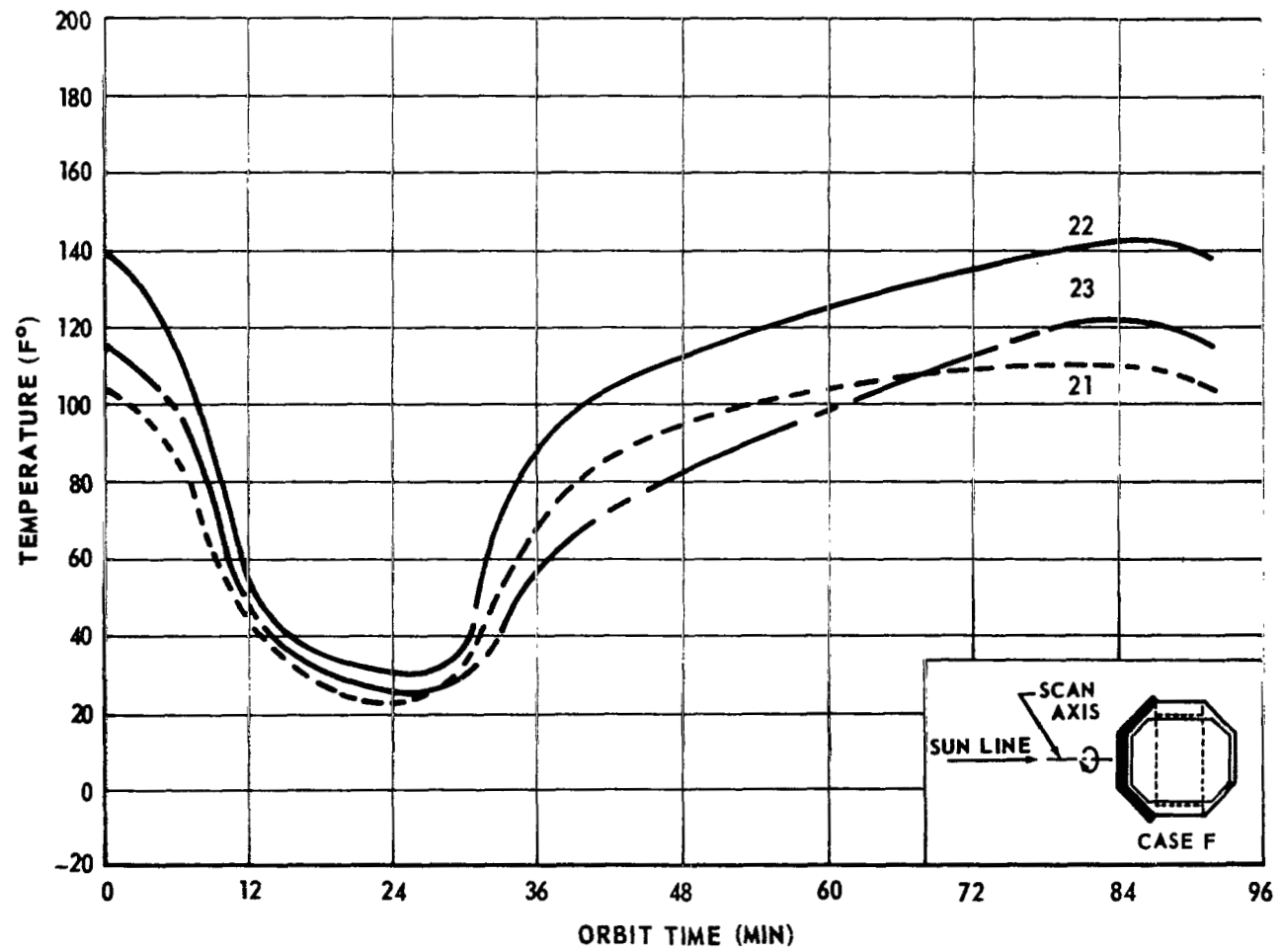
Figure F-9. Solar panel temperature variations during one orbit for Case F thermal analysis 1.
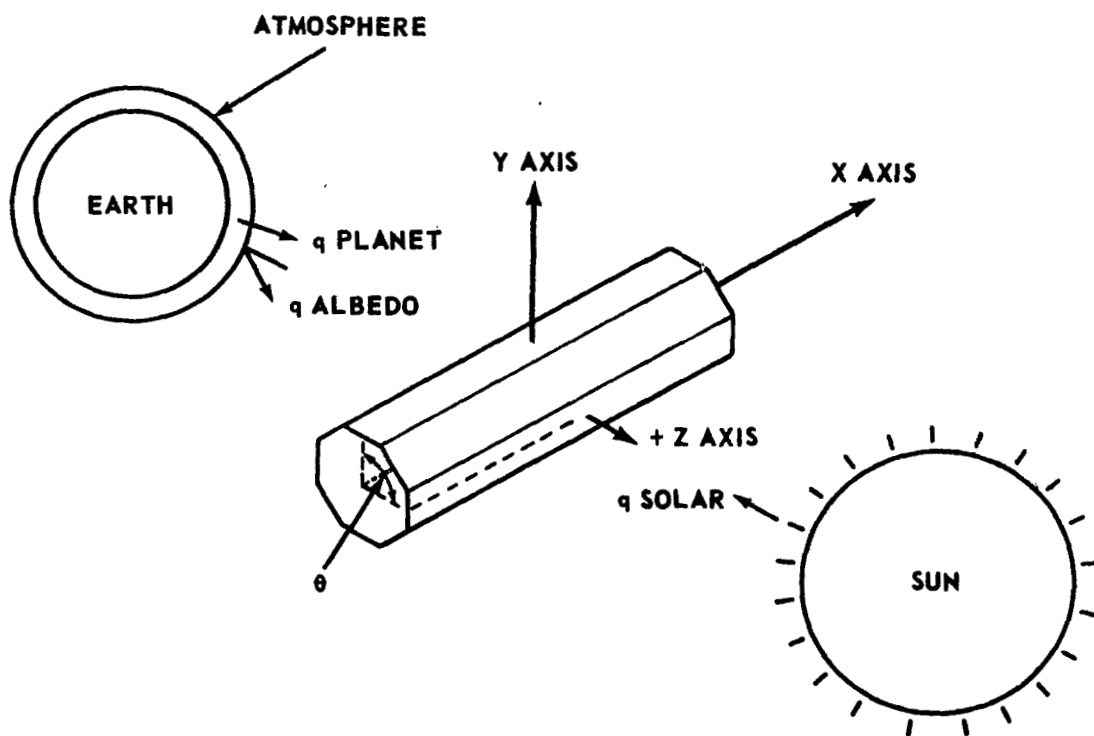
Figure F-10. Vehicle orientation (Configuration 1).

CONFIGURATION II
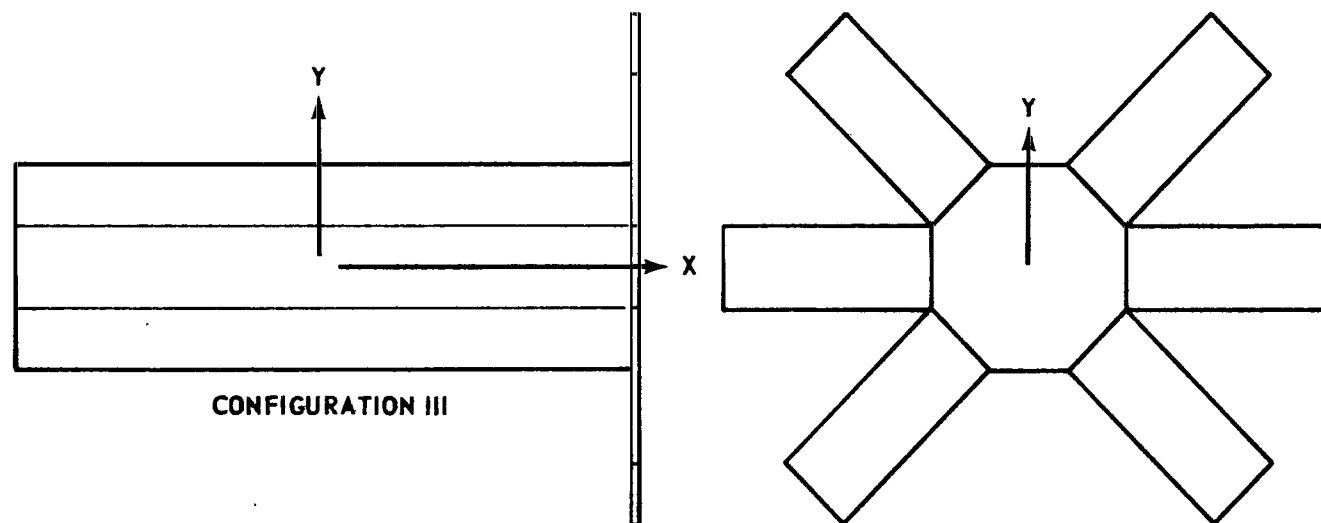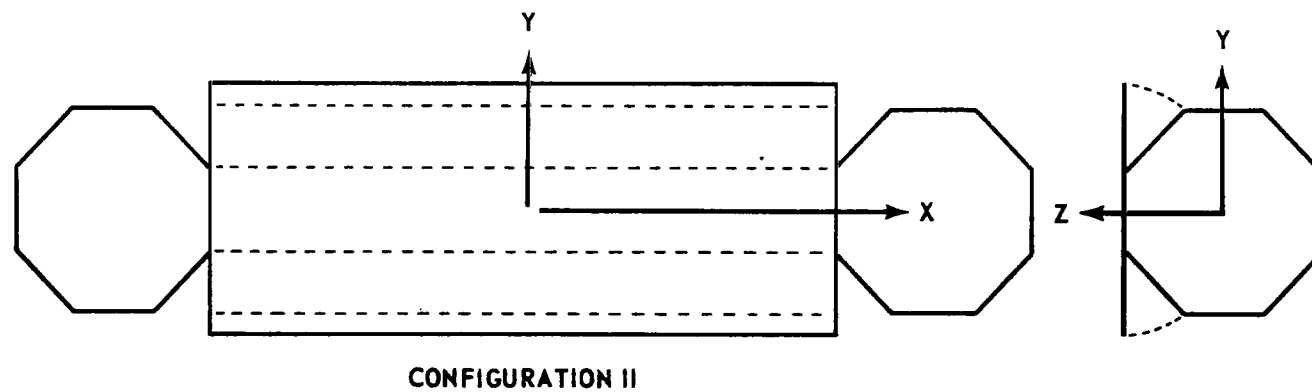
CONFIGURATION III

Figure F-11.   Alternate configurations.
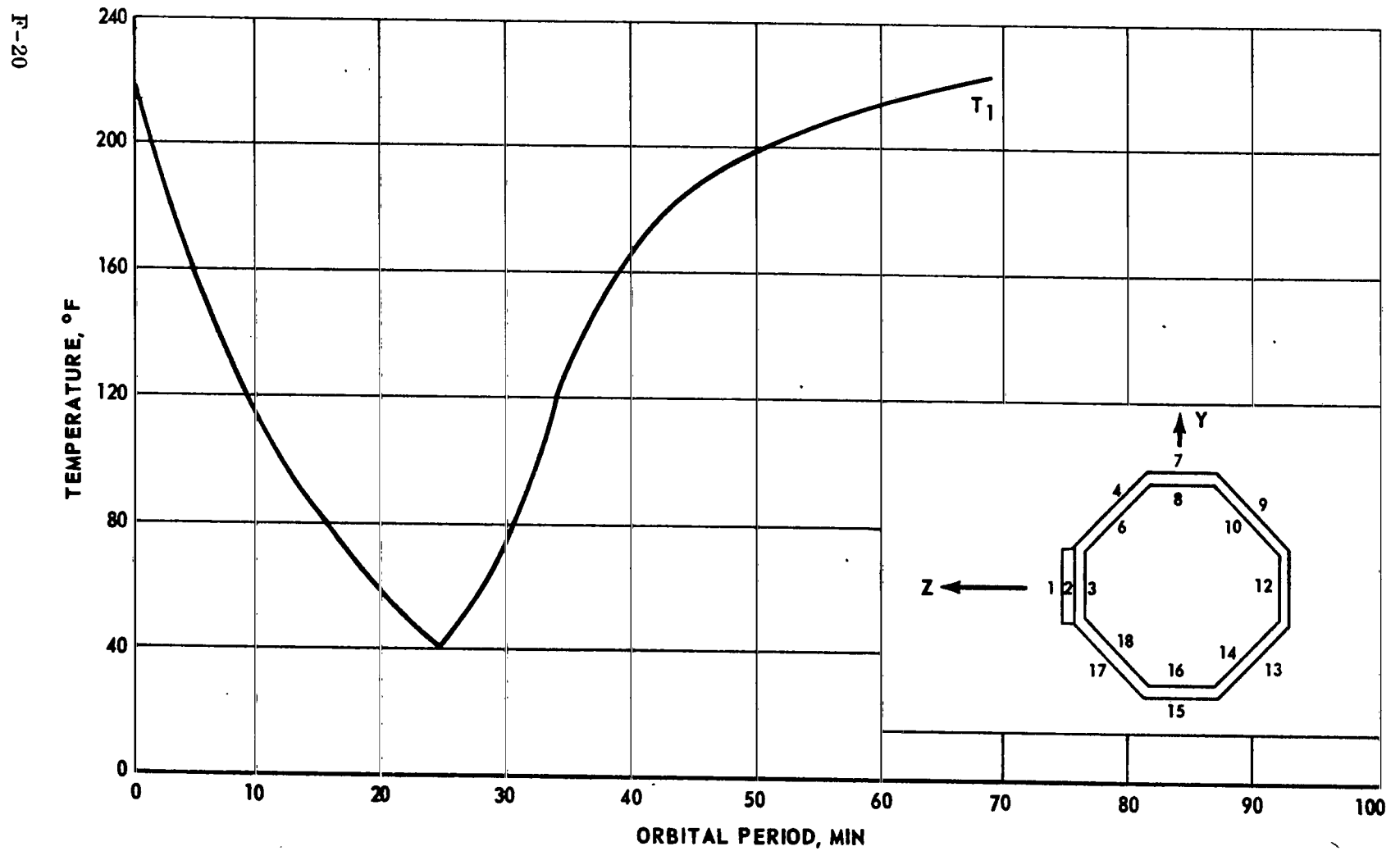
Figure F-12.   Front face High Energy Astronomy Observatory
(Configuration 1).
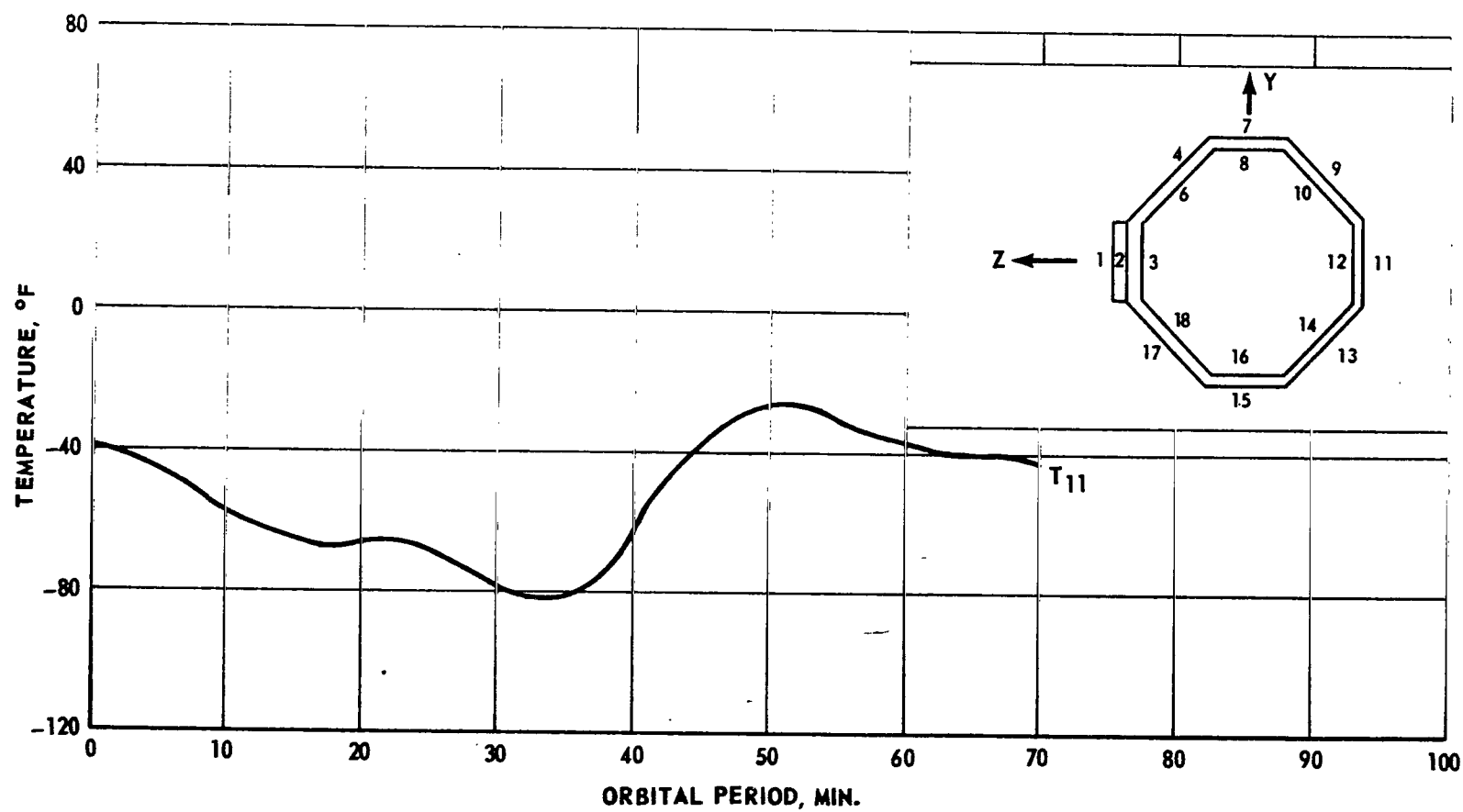
Figure F-13. Back face High Energy Astronomy Observatory (Configuration 1).
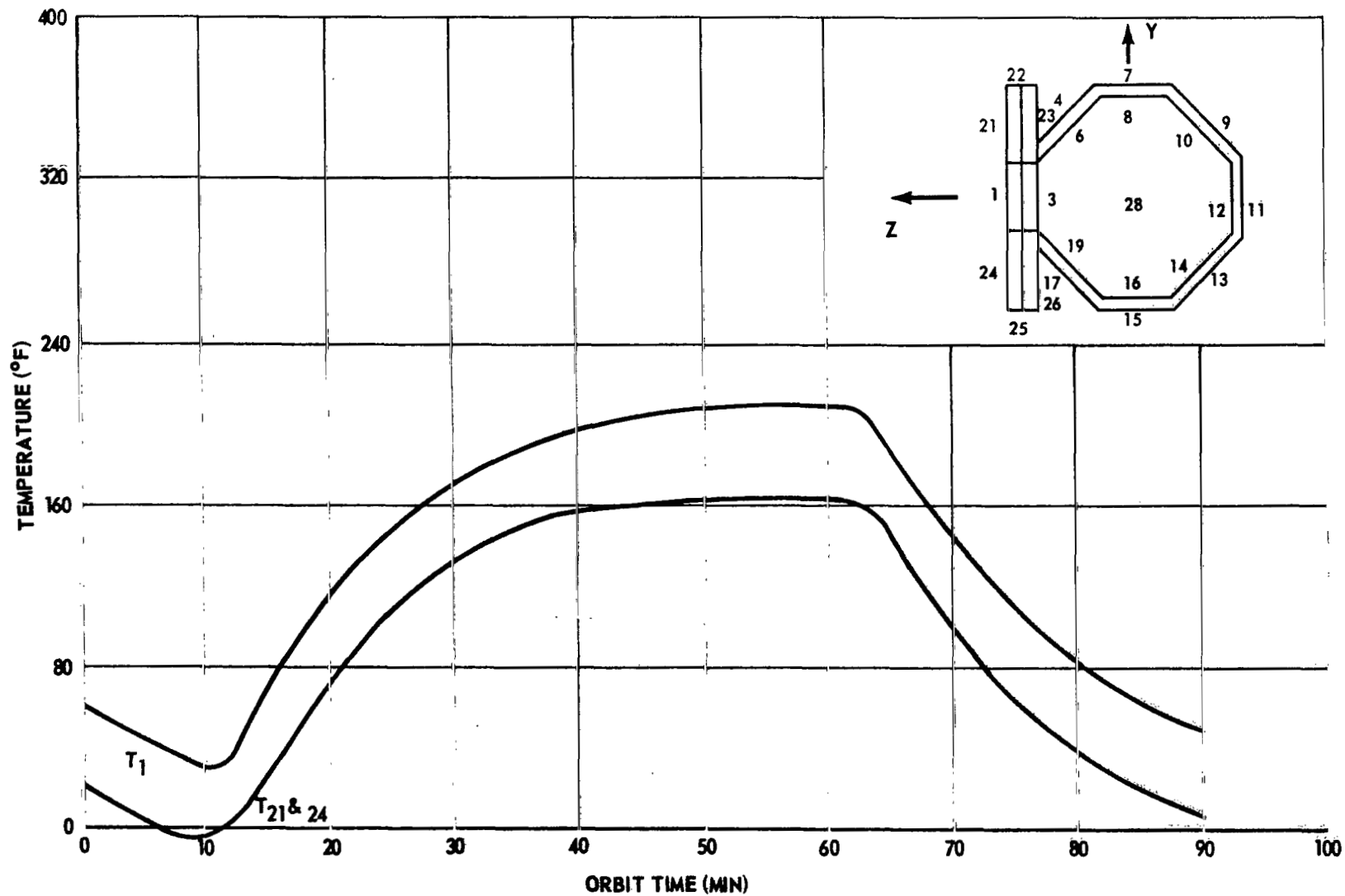
Figure F-14. High Energy Astronomy Observatory (Configuration 2).
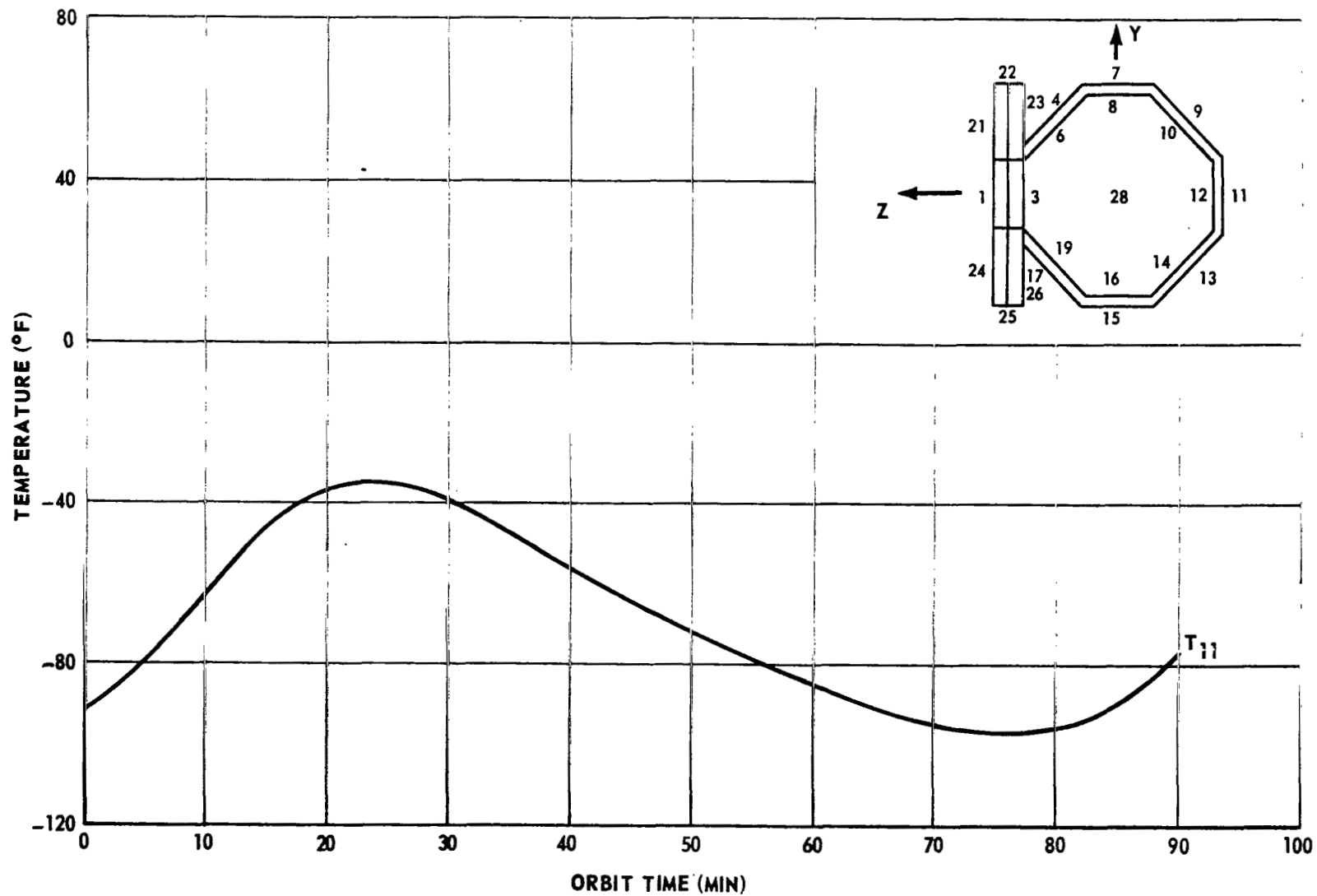
Figure F-15. High Energy Astronomy Observatory (Configuration 2).
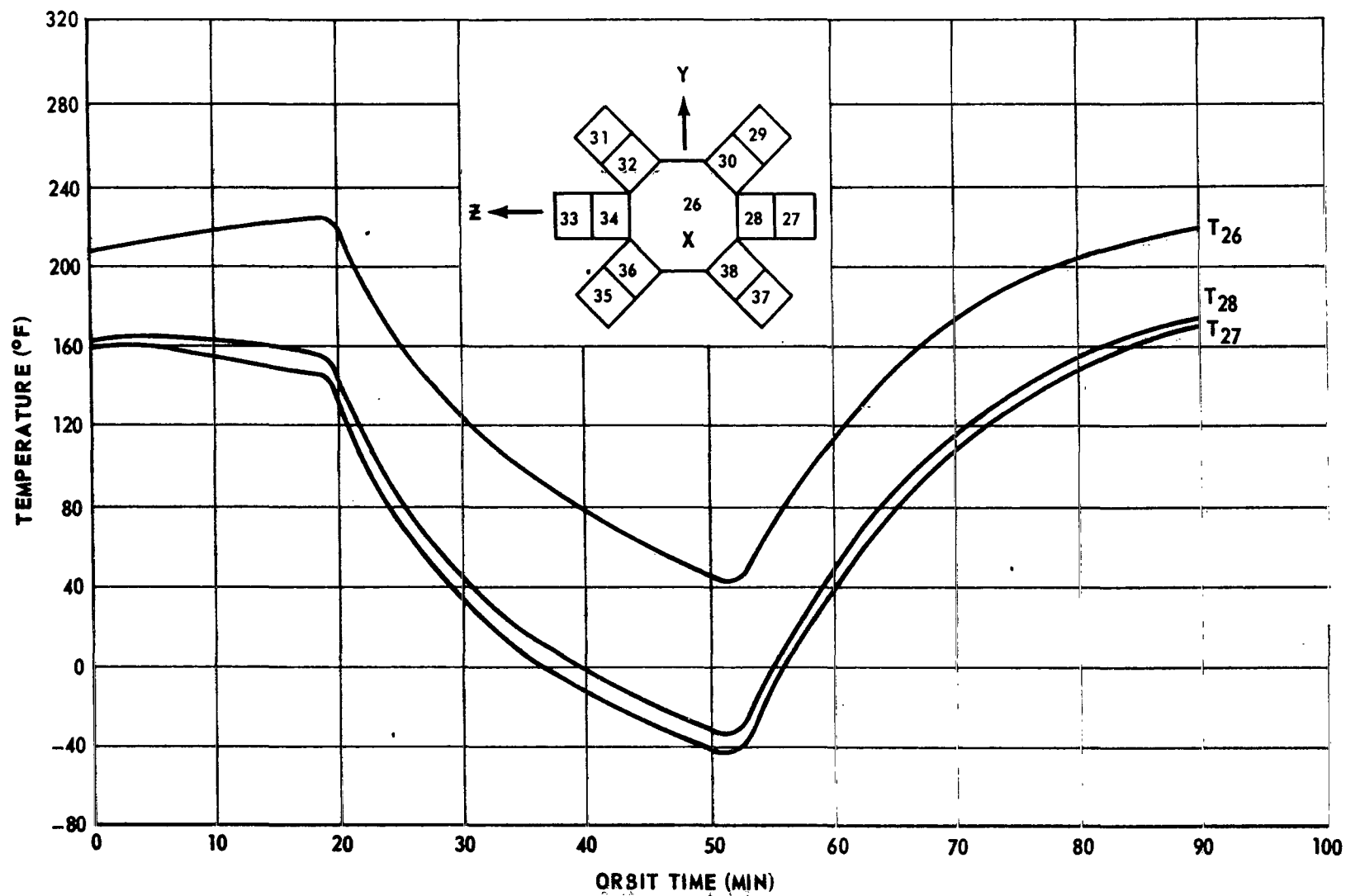
Figure F-16. High Energy Astronomy Observatory (Configuration 3).
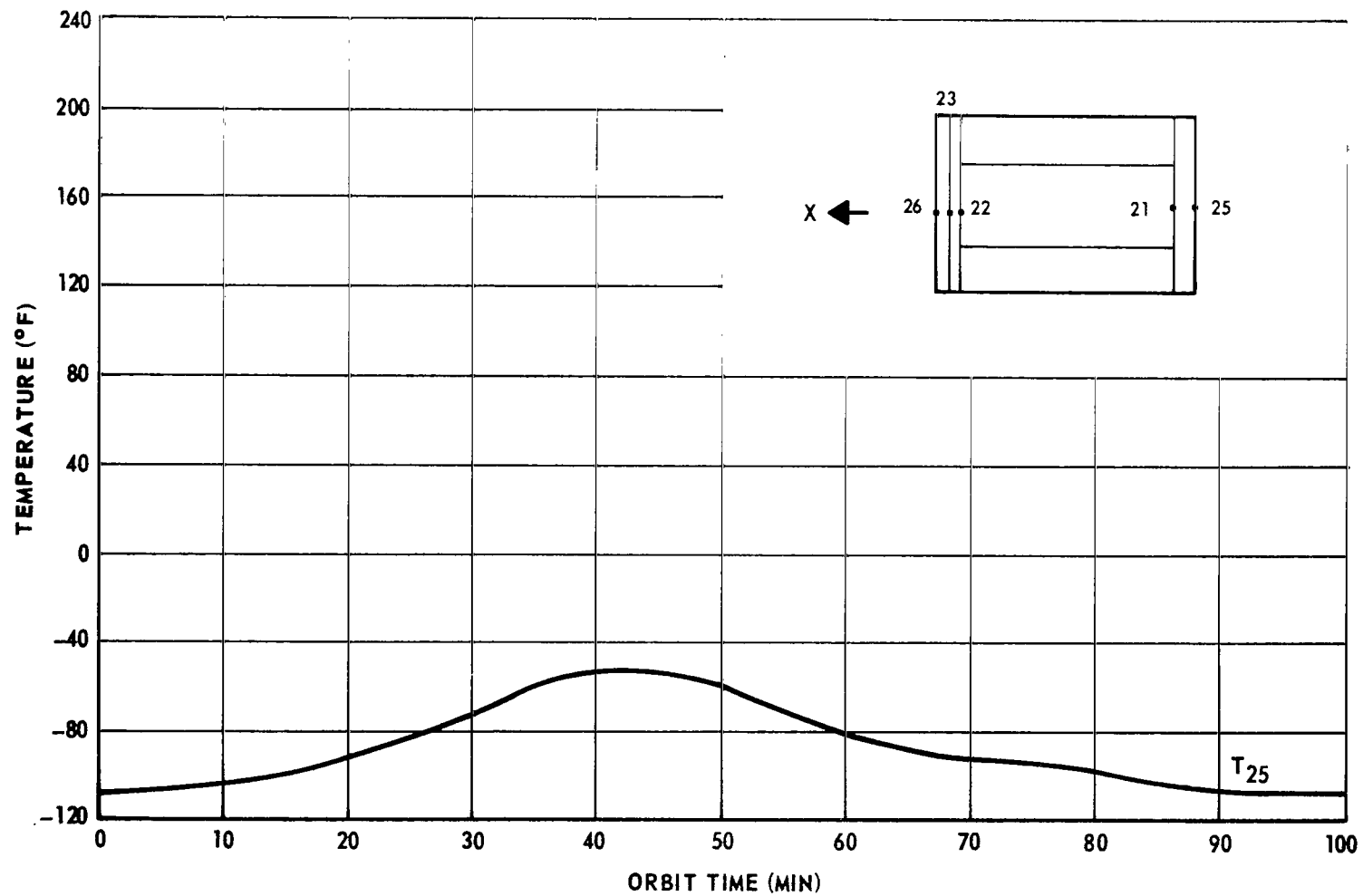
Figure F-17. High Energy Astronomy Observatory (Configuration 3).

APPENDIX G. REACTION CONTROL SYSTEMS
AND KICK STAGE ANALYSES

TABLE OF CONTENTS

LIST OF ILLUSTRATIONS

LIST OF TABLES

v

This appendix presents a discussion and a comparison of two alternate attitude control systems considered for the baseline HEAO. A summary and comparison of all alternate RCS concepts considered for the baseline HEAO are also included.

A detailed analysis of an Apogee Kick Stage for use on the HEAO to increase the Titan IIID launch vehicle payload is also presented in this appendix.

Alternate Concepts

1. Alternate Attitude Control Systems. The following alternative methods of attitude control were considered for the HEAO: RCS used in conjunction with a flywheel — no magnetic torquers, and RCS only.

● RCS/Flywheel — The RCS flywheel system, with gyroscopic stability, has the ability to resist disturbing torques for some time without active control.

With the absence of magnetic torquers, the total impulse required of the RCS was calculated to be about 75 000 lb_f-sec. This value is based on an estimated average propellant consumption of 0.5 pound per day over a 2-year period. The average specific impulse was assumed to be 200 seconds because of thruster pulsing. An N_2H_4 monopropellant system was chosen for the RCS, and the RCS total system weight is approximately 400 pounds (Fig. G-1). The flywheel weighs approximately 240 pounds; thus the total system would weigh 640 pounds. Even though a bipropellant system would weigh approximately 100 pounds less, the simplicity and reliability of the monopropellant system are considered to off set the weight penalty. A schematic drawing of such an N_2H_4 monopropellant system is shown in Figure G-2.

● RCS only — If reaction jets are required to perform all of the control functions of the HEAO, calculations show that the required total
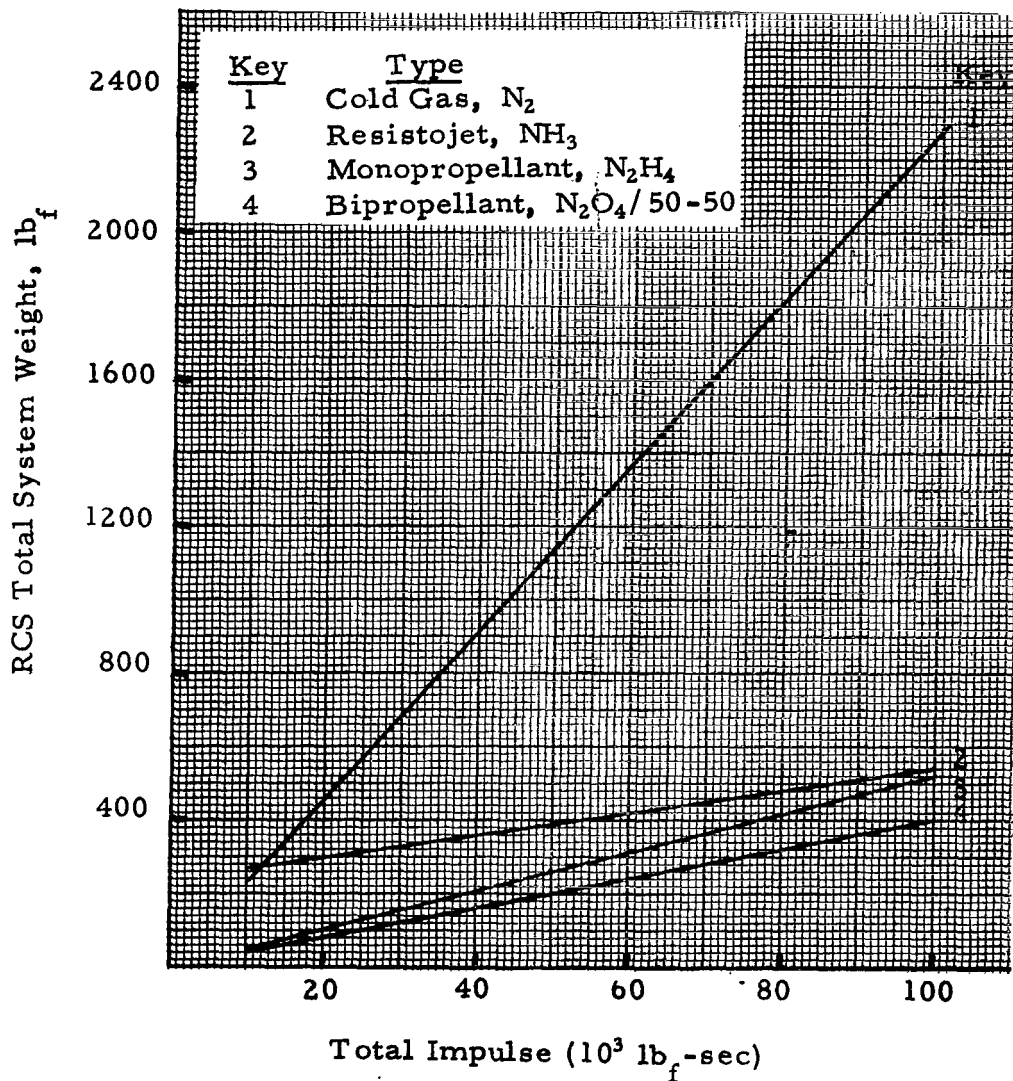
Figure G-1. RCS total system weight versus total impulse.

impulse will be approximately 150 000 lb_f-sec. This value is based on an estimated average propellant consumption of 1 pound per day over a 2-year period. The average specific impulse was assumed to be 260 seconds because of thruster pulsing. An N_2O_4/50-50 bipropellant system was chosen for the RCS because of its lower total system weight. The RCS total weight is approximately 600 pounds. An N_2H_4 monopropellant system would weigh approximately 800 pounds.
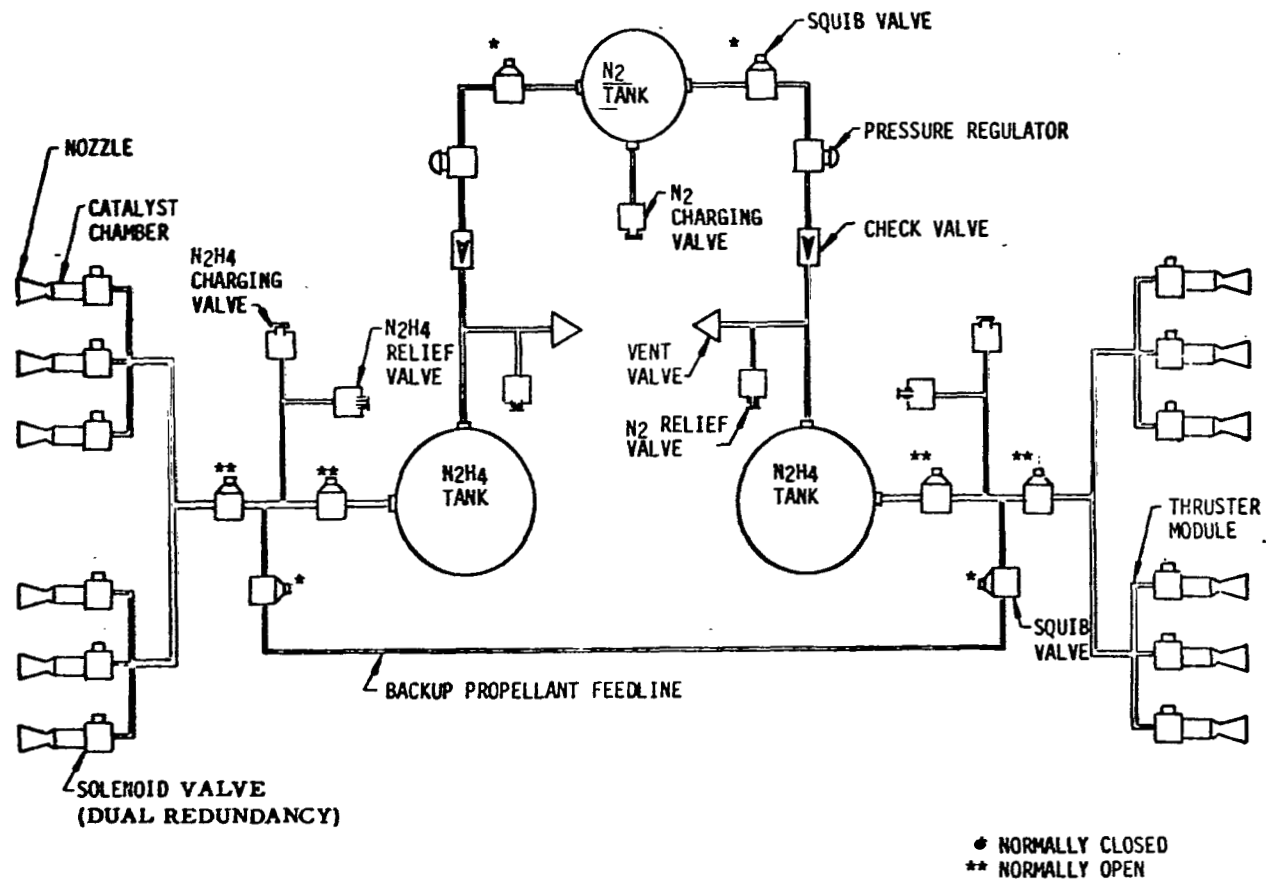
Figure G-2. System schematic of an N_2H_4 monopropellant RCS.

From a weight point of view, bipropellant systems are very attractive for large total impulses, and the savings in weight is considered to more than off set the lack of simplicity and reliability characteristics of a bipropellant system. Values of theoretical specific impulse above 325 seconds are readily obtainable with bipropellant systems and are much greater that the 260 seconds assumed in this case; thus, the weight of the system can be lowered. A schematic drawing of such a bipropellant RCS is shown in Figure G-3.

2. Alternate RCS. Three alternate RCS's were considered for use on the baseline HEAO: a cold N_2 gas system, a resistojet system, and a bipropellant system. A detailed discussion and comparison of these systems are presented in the following paragraph.

Concept Comparisons (RCS)

Figure G-1 presents a plot of RCS total system weight versus total impulse for the three alternate RCS concepts considered for the HEAO, as well as the baseline N_2H_4 monopropellant system. It should be noted that the weights derived from Figure G-1 do not reflect any leakage.

The three alternate RCS concepts considered for the HEAO will now be discussed in detail.

1. Cold Nitrogen Gas. As shown in Figure G-1, the weight of the N_2 cold gas system becomes prohibitive as the total impulse increases. For total impulses of about 300 to 400 lb_f-sec., the cold gas and monopropellant systems weigh about the same. But, the cold gas system is used for higher total impulses rather than the monopropellant or bipropellant system because of its simplicity, higher reliability, shorter lead time, more advanced state-of-the-art, and lower cost. Direct expansion of compressed gas produces the reactive thrust. This simple approach appeals to the designer since it requires the least cost for reliable hardware and no large system development costs.

The cold gas thrust motor consists of a control valve and expansion nozzle. No combustion or decomposition chamber, required in a bipropellant or monopropellant system, is needed between the valve and nozzle.
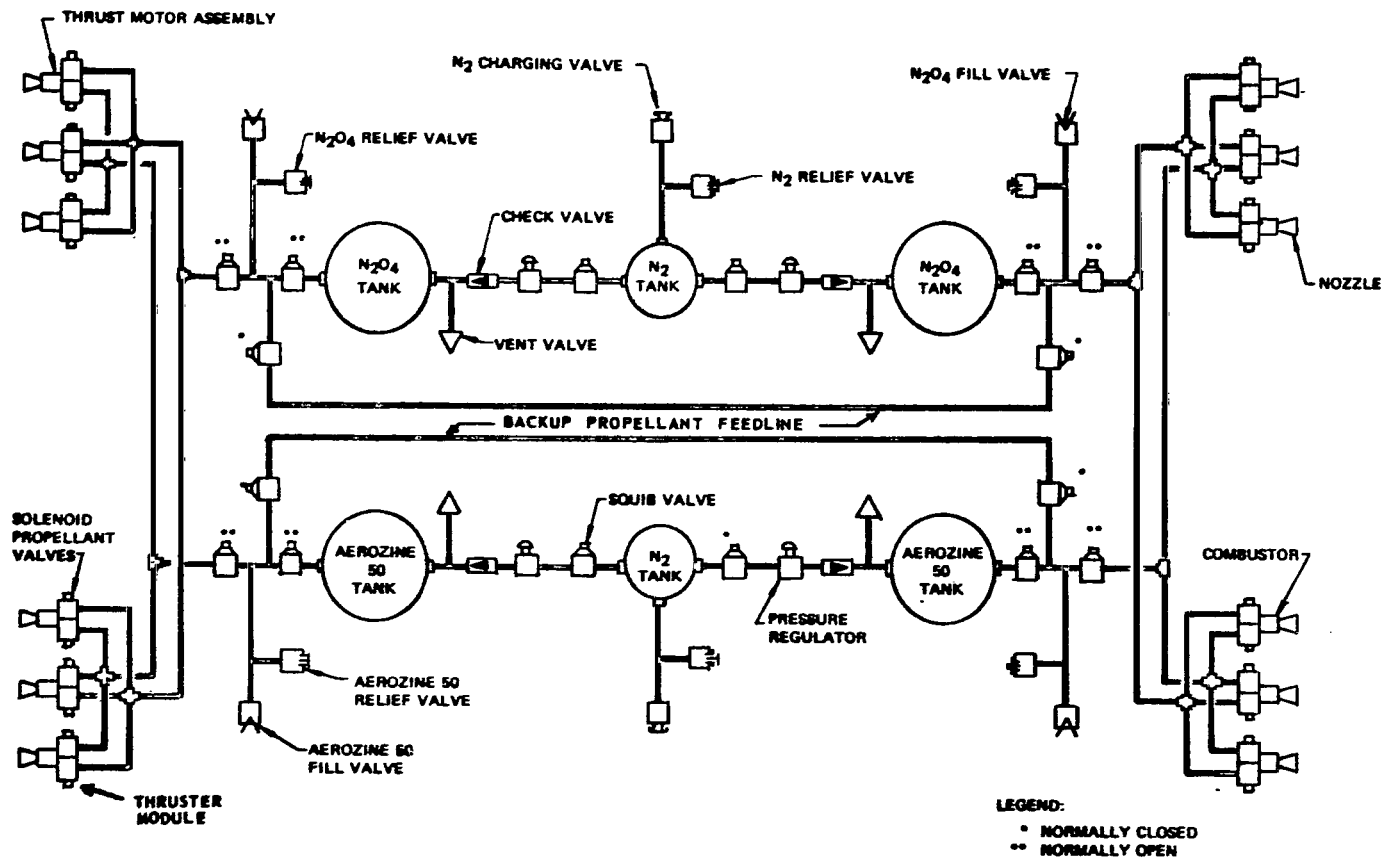
G-4

Figure G-3. System schematic of an N_2O_4/50-50 bipropellant RCS.

Therefore, response time is equal to or better than that of other systems, since it is primarily the time required to operate the valve. Available standard valves operate in 5 to 10 milliseconds. Shorter response time designs can be made for low thrust.

At first glance, the cold gas system would seem overwhelmingly attractive compared to alternate methods. However, consideration of primary parameters — total impulse, thrust level, and envelope — reveals serious limitations of system applications.

The specific impulses of cold gases appear comparable to those of liquid monopropellants and even bipropellants. For example, the specific impulse of H_2 is 290 seconds; for helium, 168 seconds. These values compare favorably with those for other propellants. The disadvantage appears in the density impulse; i. e., the impulse available per unit volume of storage system. The density impulse for gases is low, even when they are stored at high pressures. N_2 has a specific impulse of only 71 seconds, low compared to H_2 and helium. Despite this low impulse, an N_2 system would be the lightest of the three for the same total impulse because N_2 has a higher density. Weight comparison reveals that N_2 competes well against any other gas. The vast experience with nitrogen, low cost, availability, and its handling ease, make it more attractive than other gases that may offer only a few percent weight saving. Thus, N_2 is considered the basic medium for stored gas control systems [G-1].

Since the density impulse for gases is low, stored gas systems are limited to low total impulse applications. But where extremely high reliability is essential, the increased weight of a cold gas system may be tolerable. Thrust levels of 0.5 to 1 pound are obtainable with available N_2 gas RCS's. The envelope of a cold N_2 gas RCS is not considered a problem on the HEAO. Figure G-4 is a schematic of a cold N_2 gas RCS for use on the baseline HEAO. Table G-1 presents a weight summary of this system. Of the 115 pounds of N_2 gas loading, about 100 pounds are required of the RCS to perform the required HEAO maneuvers. The remaining 15 pounds is the expected leakage over the 2-year operating period.
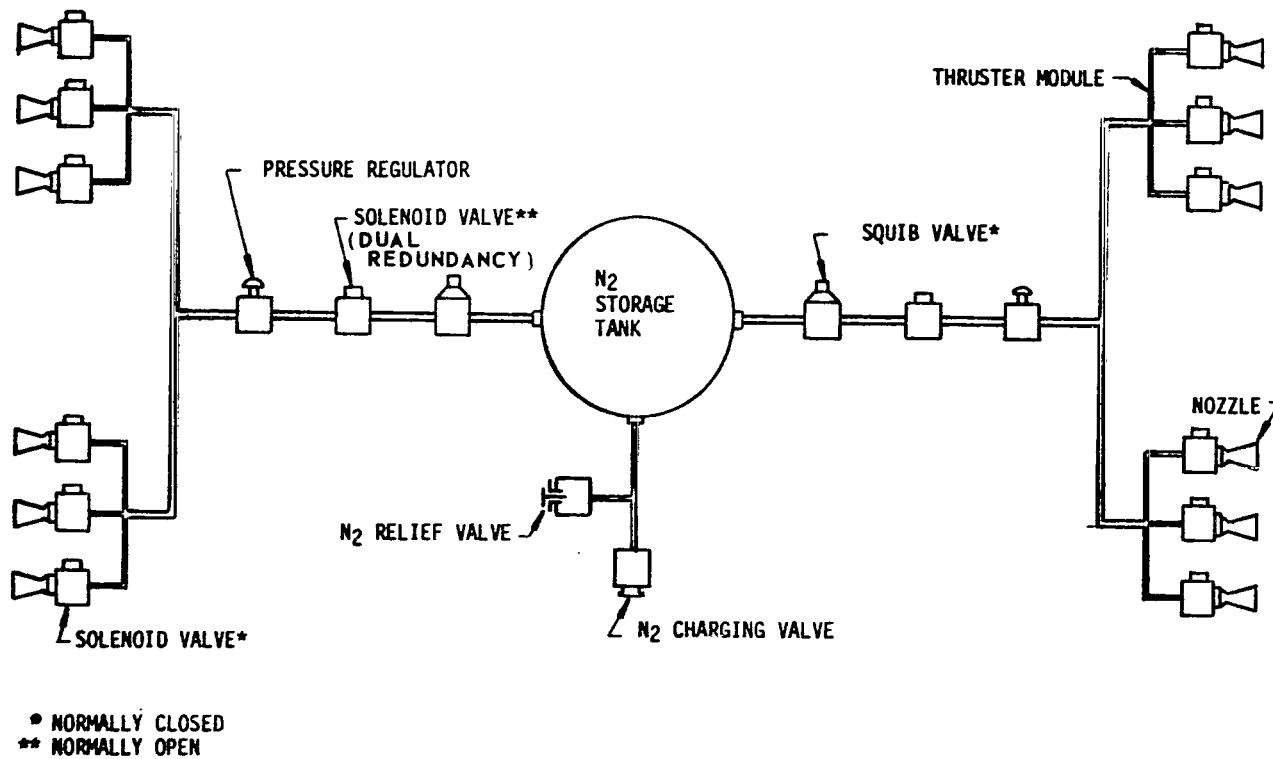
PRESSURE REGULATOR

SOLENOID VALVE**
(DUAL
REDUNDANCY)

N2
STORAGE
TANK

THRUSTER MODULE

SQUIB VALVE*

NOZZLE

N2 RELIEF VALVE

N2 CHARGING VALVE

SOLENOID VALVE*

* NORMALLY CLOSED
** NORMALLY OPEN

Figure G-4.   System schematic of a cold N_2 gas RCS.

TABLE G-1. COLD N_2 GAS RCS WEIGHT SUMMARY

Item	Component Weight, lb (total impulse $\approx$ 7000 lb_f-sec)
N_2 storage tank (titanium)	143.00
N_2 charging valve	0.12
N_2 relief valve	0.26
Pressure regulator (2)	0.60
Squib valve (2)	0.70
Solenoid valve (14)	4.20
Nozzle (12)	0.60
Miscellaneous (lines, etc.)	3.00
Dry system weight	152.48
N_2 charged (15-lb leakage)	115.00
Total system weight	267.48

The RCS is not activated until the HEAO is placed into orbit. Activation is achieved by opening a squib valve which leads to each RCS unit. The N_2 gas then passes through a pressure regulator to reduce the pressure to operating conditions. Control is maintained by opening and closing appropriate solenoid valves at each thruster. Should control of the spacecraft become critical because of thruster failure or valve malfunction at one end of the spacecraft, a solenoid valve can be activated to close down that entire RCS unit. Control can then be maintained by operating the other RCS unit.

The cold N_2 gas RCS was rejected for use on the baseline HEAO because the weight of the system was considered excessive when compared to the N_2H_4 monopropellant system.

2. **Resistojets.** A resistojet RCS that uses NH_3 as a propellant was considered for use on the baseline HEAO. Resistojets have never been test-flown, but have been tested extensively on the ground. Potential resistojet applications range from earth-satellite orbit changes to station-keeping and attitude control. The low thrust of a resistojet is ideally suited for the required accuracy of in-orbit astronomical and earth resources experiments. A recent study of the Manned Orbital Research Laboratory by McDonnell-Douglas [G-2, G-3] shows the attractiveness of 10-millipound-thrust resistojets operating in conjunction with control moment gyros for attitude control and simultaneous drag makeup.

As shown in Figure G-1, the weight of the resistojet RCS becomes more attractive as the total impulse increases. This resistojet curve reflects the added weight caused by power requirements, but it does not reflect the weight caused by leakage.

The resistojet is an electrically heated rocket. The propellant is passed over a resistance-heated heat exchanger and through a nozzle to produce thrust. The evacuated, concentric, tubular design for the resistojet is shown schematically in Figure G-5. The two primary inputs to the resistojet are the electric power and the propellant flow which are supplied simultaneously. The electrical path is through the outer pressure case, the case end, the nozzle, and the inner and outer heating elements. A strut connector joins the inner and outer heating elements electrically and permits a gas passage between them. The current passes along the outer heating element and the inner pressure case, completing the circuit at the power source. The ohmic heating takes place primarily in the inner heating element ($\approx$ 80 percent) and, to a lesser degree, in the outer heating element ($\approx$ 15 percent). A small percentage is developed in the pressure cases. The gas flow is introduced into the annulus between the inner and outer pressure cases and flows down the passage, through the transition area, and back between the inner and outer heating elements, where a significant amount of gas heating occurs. The flow passes through the strut connector and down the center heating element, where it approaches the wall temperature before expulsion out the nozzle. Heat loss is minimized, and electrical efficiency is maximized by use of the vacuum jacket, the regenerative passage between the inner and outer pressure case, and the thermal insulation. The thermal and gas pressure loads are minimized by a bellows expansion compensator at the rear of the resistojet.
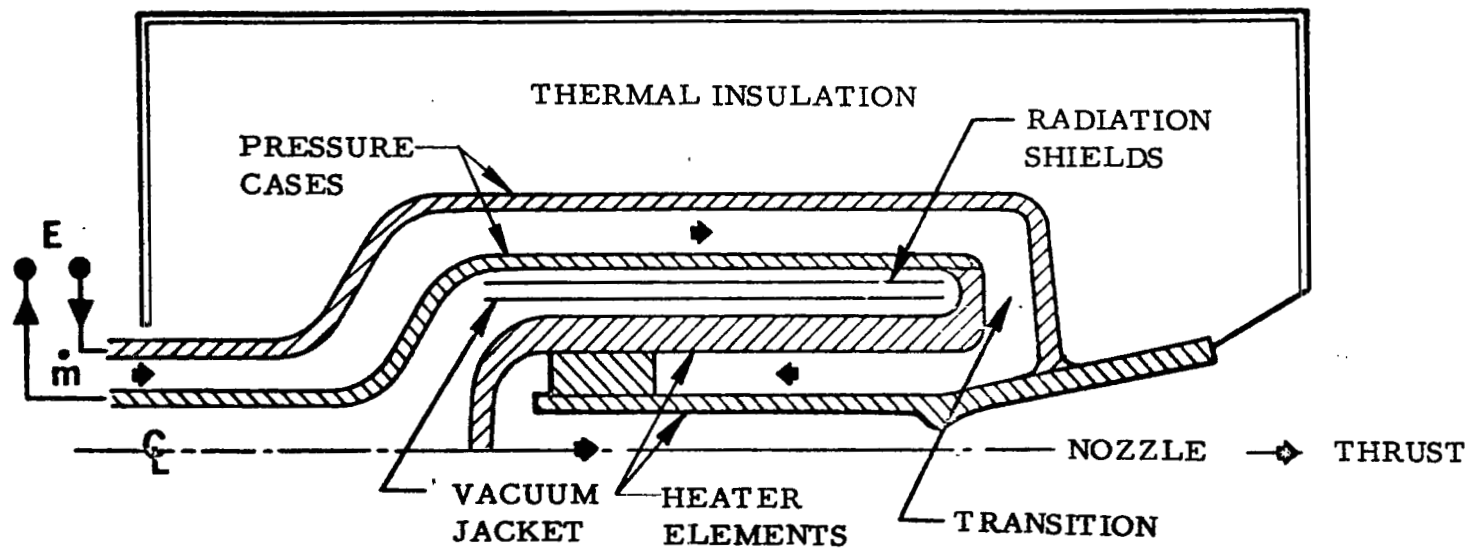
Figure G-5. Evacuated–concentric tubular resistojet [G-3].

H_2 has also been used as a propellant for the resistojet with better performance, but NH_3 is more easily stored. The expulsion of N_2 and H_2 from an NH_3 resistojet and the low rate of expelled propellant results in a clean exhaust.

The resistojet engine has a backup "cold-flow" operating mode which can be used in the event spacecraft power is not available for the propulsive function or if there is a control electronics failure. In the cold flow mode, the resistojet thrust is almost identical to the normal operating mode thrust (because of the constant supply pressure design feature). Conventional chemical engines have no backup operating mode of this type.

High reliability has been predicted for resistojet systems and is based on the inherent long-life system design. The previously described evacuated concentric tubular resistojet is somewhat analogous to a light bulb, in that its operating life is dictated by sublimation rate of the heater element. The resistojet has an operating life of more than 20 000 hours (or a 50-percent duty cycle over a 5-year mission). This life is predicted for operations at design thrust and specific impulse within allowable tolerances.

The control electronics of the resistojet system have already been flown on the NASA ATS with an operational low-performance resistojet system. The control electronics consist of inverters, transformers, and control logic/signal conditioning assemblies of the type used by many other spacecraft subsystems with long operating life requirements.

The resistojet systems reliability is enhanced by the simple propellant tankage and feed system design. NH_3 and H_2 propellant tanks require no positive expulsion system as the propellant is expelled by its own vapor pressure. An NH_3 propellant storage and feed system has already flown on ATS vehicles.

An NH_3 resistojet RCS will result in lower RCS total system weight for high impulse requirements (500 000 to 1 000 000 lb_f-sec) than a monopropellant or bipropellant system. The delivered performance of an NH_3 resistojet is about 25 percent higher than a bipropellant engine and some

40 percent higher than a monopropellant engine (pulse mode performance). Chemical systems also require a pressurant and pressurization system, which further increases their weight.

The NH_3 resistojet RCS must pay a weight penalty for electrical power of about 500 pounds per kilowatt for a rollout solar panel [G-2].

Table G-2 presents a performance summary for an NH_3 resistojet thruster.

A schematic drawing of the proposed NH_3 resistojet RCS considered for the baseline HEAO is presented in Figure G-6. Table G-3 presents a weight summary for this system.

The resistojet RCS is not activated until the HEAO is placed into orbit. Activation is achieved by opening a squib valve which leads to each RCS unit. NH_3 is charged and stored in the liquid phase and flows to a heat exchanger where it is changed to a gaseous state for use in the pressure regulator. The heat energy for the heat exchanger is derived from the spacecraft's electric power source and/or by dissipation of the spacecraft's heat load. Once the pressure has been regulated for operating conditions, control of the spacecraft is maintained by opening and closing the thruster solenoid valve. Should control of the spacecraft become critical because of thruster failure or valve malfunction at one end of the spacecraft, a solenoid valve can be activated to close down that entire RCS unit. Control can then be maintained by operating the other RCS unit.

The leakage rate for NH_3 was assumed to be the same as for N_2 gas, i.e., two standard cubic centimeters per minute per valve. The NH_3 leakage over a 2-year period was calculated to be about 10 pounds. Twenty-five pounds of NH_3 are required by the RCS for the entire mission. This is based on an assumed pulsing specific impulse of 280 seconds.

The resistojet RCS was rejected for consideration on the baseline HEAO for two reasons. First, the weight of the system is considered excessive over the N_2H_4 monopropellant system. Second, the electrical power requirements (159 watts) for one thruster are considerably greater than the baseline spacecraft can supply to the RCS. An additional 150 square feet of solar panels would have to be placed aboard the spacecraft if only two thrusters were to fire simultaneously.

TABLE G-2. NH$_3$ RESISTOJET THRUSTER PERFORMANCE [G-3]

Element	Performance
Chamber pressure	35 psia
Thrust	10 mlbf
Expansion ratio	35:1
Thrust coefficient	1.42
Chamber temperature	4356° R
I_{sp} (delivered)	364 sec
Required thruster power	159 watts
Heat efficiency	81%
Power efficiency	87%
Propellant tank pressure	325 psia
Propellant tank temperature	585° R
Throat diameter	0.016 in.
Mass flow rate, per thruster	2.75 x 10^{-5} lb$_m$/sec
Total flow rate, maximum	11 x 10^{-5} lb$_m$/sec
Total flow rate, minimum	5.5 x 10^{-5} lb$_m$/sec
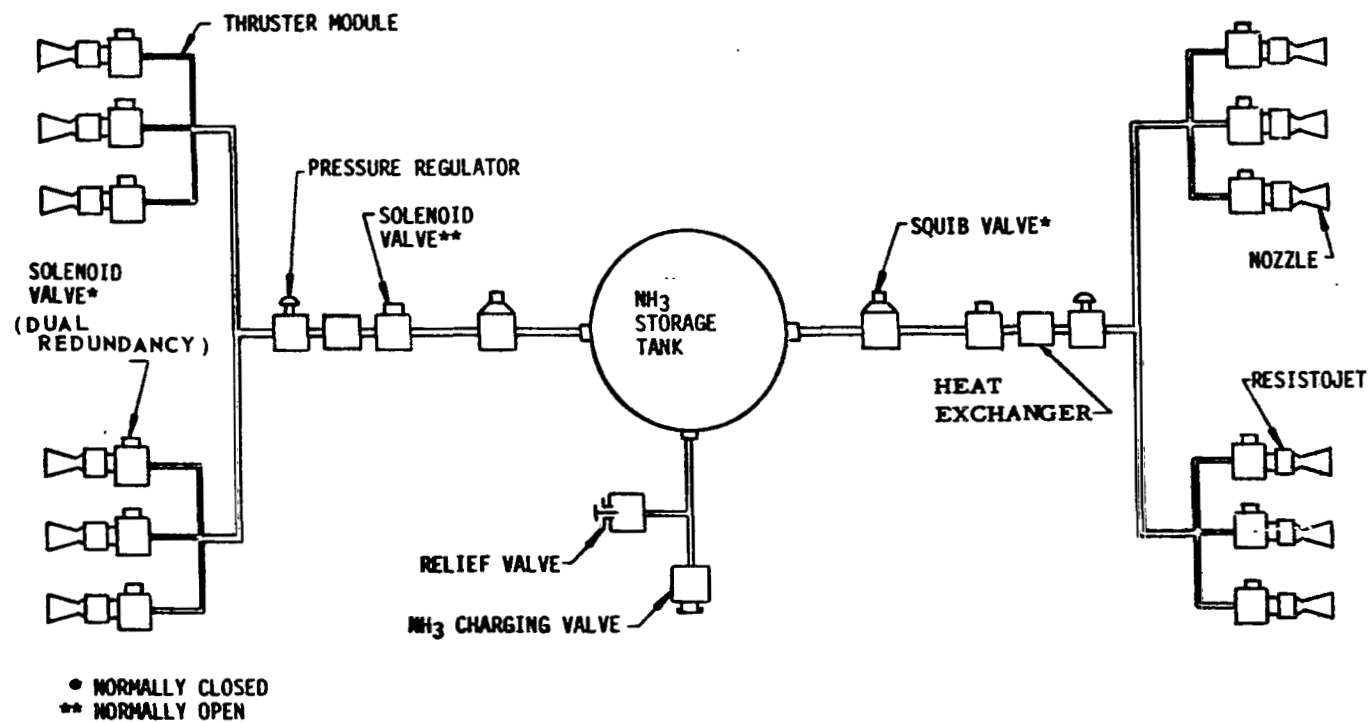
Figure G-6. System schematic of an NH$_3$ resistojet RCS.

TABLE G-3. NH$_3$ RESISTOJET RCS WEIGHT SUMMARY

Item	Component Weight, lb (total impulse $\approx$ 7000 lb$_f$-sec)
NH$_3$ storage tank (6-Al-4V-Ti)	5.00
NH$_3$ charging valve	0.12
NH$_3$ relief valve	0.26
Pressure regulator (2)	7.00
Squib valve (2)	0.70
Solenoid valve (14)	5.00
Thruster module (4)	30.00
Power control module	36.00
Heat exchanger (2)	3.00
Weight assessment for electrical power (additional solar panel area required 150 ft^2)[a]	151.00
Brackets, lines, and miscellaneous	23.00
Dry system weight	261.08
NH$_3$ charged (10-pound leakage)	35.00
Total system weight	296.08

a. Based on a required 159 watts for each thruster with two fired simultaneously.

3. <u>Bipropellant.</u> A bipropellant RCS that uses N_2O_4/50-50 as propellant was considered for use on the baseline HEAO. As shown in Figure G-1, the weight of the bipropellant system is the lightest of all the other systems for a given high total impulse requirement. But it is also the most complex, and an increase in design complexity has a tendency to lower reliability and increase costs.

The weight advantage of bipropellant systems for large total impulse requirements results from the high specific impulse available. Values of theoretical specific impulse above 325 seconds are readily obtainable with bipropellant systems. The maximum specific impulse provided by the bipropellant concept considered for the HEAO is 260 seconds because of thruster pulsing. The thrust level per engine is 1 pound. Bipropellant thrusters show good response characteristics, an important factor for pulse-type operation. The pulse characteristic is affected by such factors as propellant feed pressure, equilibrium chamber pressure, combustion gas effective characteristic velocity, chamber characteristic length, ignition delay characteristics of propellants, and the injector valve opening and closing characteristics. One of the most important of these items is that of the valve response time. Fast-acting injector valves are necessary and must be closely coupled to the thruster.

The engine design of a bipropellant system must represent a compromise between developed impulse and other factors including size, response, and operating pressures. The selection of a large nozzle expansion ratio yields improved performance, but may result in nozzle sizes too large for compact vehicle installation. High velocity injectors using large pressure differentials give good results, but the time to build up pressure slows down response. The characteristic chamber length (L^*) can be increased to improve performance, but the larger chamber volumes slow down both pressure rise and decay times.

The high energy release of bipropellants occurs with high chamber temperature. Chamber cooling becomes necessary, and radiation cooling depends on the emission of heat from the very hot chamber wall at a rate sufficient to maintain the necessary minimum temperature drop across the gas side film. The advantage of radiation cooling is chamber simplicity. Radiation cooling is most effective at low chamber pressure and, as a result, leads to larger chambers for steady-state operation. For low thrust levels the resulting chamber sizes are acceptable although as thrust level increases, the penalty may become excessive. It is necessary to mount the thrust chambers so that they have viewing space for radiative purposes; furthermore,

G-16

mounting must be carefully designed so that local heating of the spacecraft structure in the area of the radiation-cooled chamber is not possible. These disadvantages are generally met through the use of reflectors and radiation shields installed as part of the chamber. Heat-sink cooling is a possible technique for low-duty cycles [G-4].

Table G-4 presents a data and performance summary for a bipropellant RCS thruster for use on the baseline HEAO.

A schematic of the proposed bipropellant RCS considered for the baseline HEAO is presented in Figure G-3. Table G-5 presents a weight summary for this system.

The RCS is not activated until the HEAO is placed into orbit. Activation is achieved by opening squib valves which lead from the N_2 pressurization tanks to the oxidizer and fuel tanks at each end of the spacecraft. The N_2 gas then passes through a regulator to be conditioned for pressurizing the bladders in the fuel and oxidizer tanks. The fuel and oxidizer are then expulsed to the thrusters where spacecraft control is maintained by opening and closing a fuel and oxidizer solenoid valve. $N_2O_4/50$-50 are hypergolic propellants. Should control of the spacecraft become critical because of thruster failure or valve malfunction, a squib valve can be activated to stop the flow of oxidizer and fuel to that RCS unit. Control can be maintained by the other RCS unit until depletion of its propellant. Then, activation of other squib valves allows the fuel and oxidizer to flow through their respective backup feedlines from the inoperable end so the thrusters at the operable end can continue to function.

For total impulse requirements greater than 75 000 lb_f-sec, the bipropellant RCS is considered to be best. In this range, its low weight is considered to off set its lack of reliability, simplicity, and higher costs. But for the baseline HEAO, the bipropellant RCS was rejected because it was considered more complex and less reliable. The storage of oxidizers for up to 2 years is not now considered practical (tankage materials compatibility).

Kick Stage

The Titan IIID is assumed capable of placing 20 920 pounds into a direct 200-n. mi. circular earth orbit and 28 320 pounds into a 90- by 200-n. mi.

TABLE G-4. RCS BIPROPELLANT ENGINE FOR USE ON HEAO [G-5]

Item	Data
Manufacturer	Bell Aerosystems Company
Designation	Model 8360
Type	Liquid bipropellant
Propellant	N_2O_4/50-50
Thrust, lb_f	1.0
Chamber pressure, lb_f/in^2	50.0
Specific impulse, sec	260
Mixture ratio, O/F	1.4
Flow rates, lb_m/sec	
Oxidizer	0.00224
Fuel	0.00160
Expansion area ratio (ϵ)	60:1
Engine weight, lb	1.1
Chamber temperature, °F	2800
Cooling technique	Radiation chamber and nozzle

TABLE G-5. BIPROPELLANT RCS WEIGHT SUMMARY

Item	Component Weight, lb (total impulse ≈ 7000 lb_f-sec)
Fuel pressurization system	
N_2 tank	15.00
Squib valve (2)	0.70
Pressure regulator (2)	0.60
N_2 relief valve	0.52
Check valve (2)	0.22
Vent valve (2)	0.24
Oxidizer pressurization system	
N_2 tank	21.00
Squib valve (2)	0.70
Pressure regulator (2)	0.60
N_2 relief valve	0.52
Check valve (2)	0.22
Vent valve (2)	0.24
Fuel tank (2)	9.20
Fuel charging valve (2)	0.24
Fuel relief valve (2)	0.52
Fuel squib valve (6)	2.10
Oxidizer tank (2)	14.60
Oxidizer charging valve (2)	0.24
Oxidizer relief valve (2)	0.52
Oxidizer squib valve (6)	2.10
Thruster modules (4)	16.00
Miscellaneous	6.00
System dry weight	92.08
Nitrogen charged (27.9-lb leakage)	30.00
Fuel (aerozine-50) charged	11.25
Oxidizer (N_2O_4) charged	15.75
Total system weight	149.08

elliptical orbit. A study was performed to determine how much additional usable HEAO payload could be gained by circularizing the HEAO with a kick stage into the 200-n.mi. orbit from the 90- by 200-n.mi. elliptical orbit.

The change in velocity required to perform this maneuver was calculated to be 62.25 meters per second. The burn will occur at apogee, and the burn time (t) is less than 5 minutes to avoid ΔV losses. Simplicity is desired in such a kick stage system to perform this maneuver.

By use of Figures G-7 through G-11, a kick stage can be sized and a delta payload determined. Figures G-7 through G-10 are used primarily if the characteristics of a kick stage are not known and one has to be sized.

Figure G-7 is a plot of kick stage burn time versus thrust-to-weight ratio for a specific impulse range of 100 to 400 seconds. Assuming or knowing a thrust-to-weight ratio of the kick stage-HEAO package delivered to the 90- by 200-n.mi. elliptical orbit, the burn time required to circularize into a 200-n.mi. orbit can be determined.

Figure G-8 is the same plot as Figure G-7 except this curve is plotted for higher thrust-to-weight ratio values.

Figure G-9 is a plot of the propellant to initial gross weight ratio versus specific impulse of the kick stage engine. If the specific impulse of the kick stage is assumed or known, the propellant weight required to circularize the kick stage-HEAO package into the 200-n.mi. orbit from the initial 90- by 200-n.mi. elliptical orbit can be determined, provided the payload weight injected into the elliptical orbit is known.

Figure G-10 is a plot of the weight of the kick stage versus the propellant weight determined in Figure G-9 for various kick stage mass fractions. After determining the propellant weight required to perform the circularization maneuver and assuming or knowing the mass fraction of the kick stage, the total weight of the kick stage can be determined. By knowing the payload weight that can be injected directly into the 200-n.mi. circular orbit, the payload weight that can be injected into the 90- by 200-n.mi. elliptical orbit, and the kick stage weight, the gain in useful HEAO payload can be determined or Figure G-11 may be used.

Figure G-11 is a plot of payload gain versus the kick stage specific impulse for various kick stage mass fractions. If the specific impulse of the kick stage is known, the gain in payload can be determined provided the kick stage mass fraction is known and the direct injected payload weight and the elliptical injected payload weight do not vary.

G-20
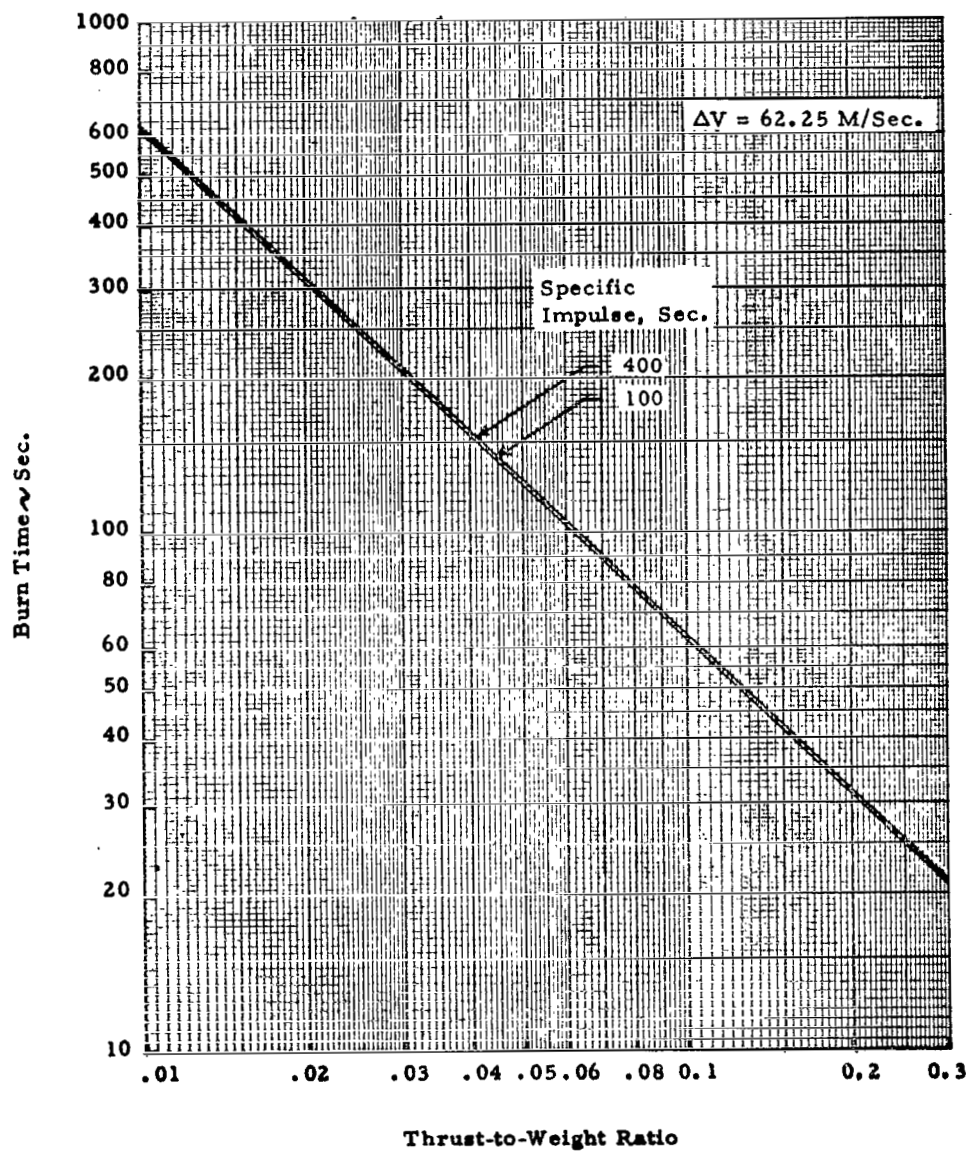
Figure G-7. Burn time versus thrust-to-weight ratio.
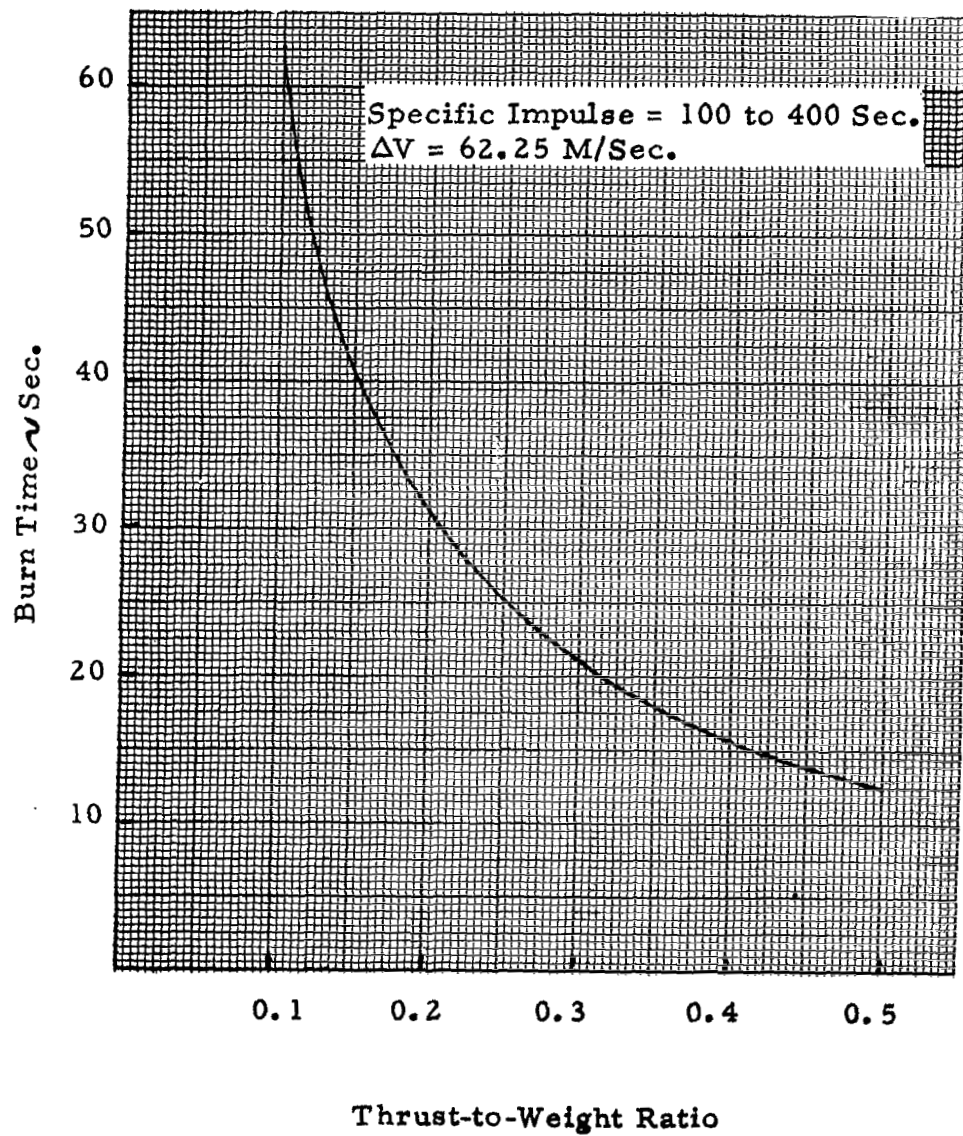
Figure G-8. Burn time versus thrust-to-weight ratio.
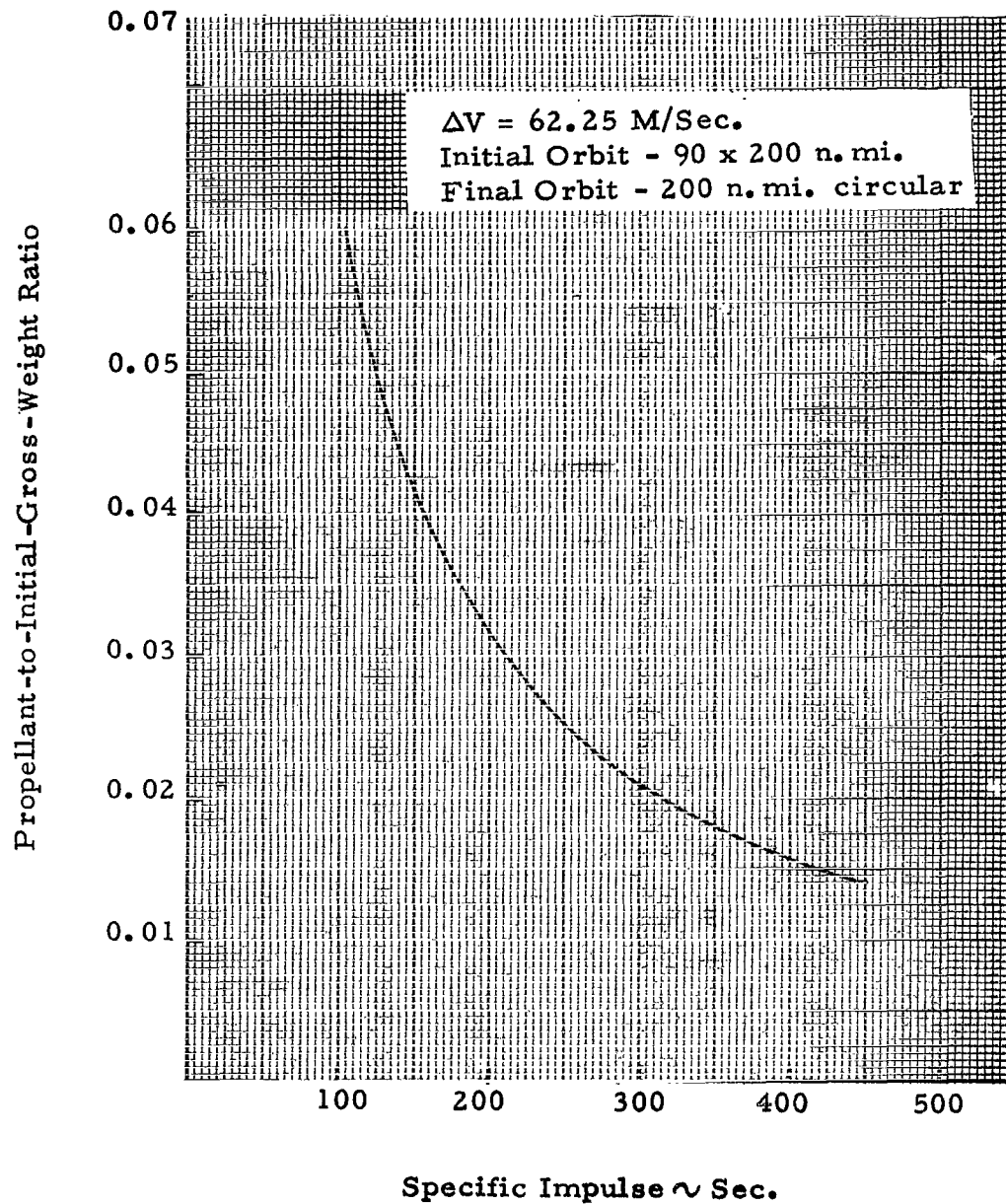
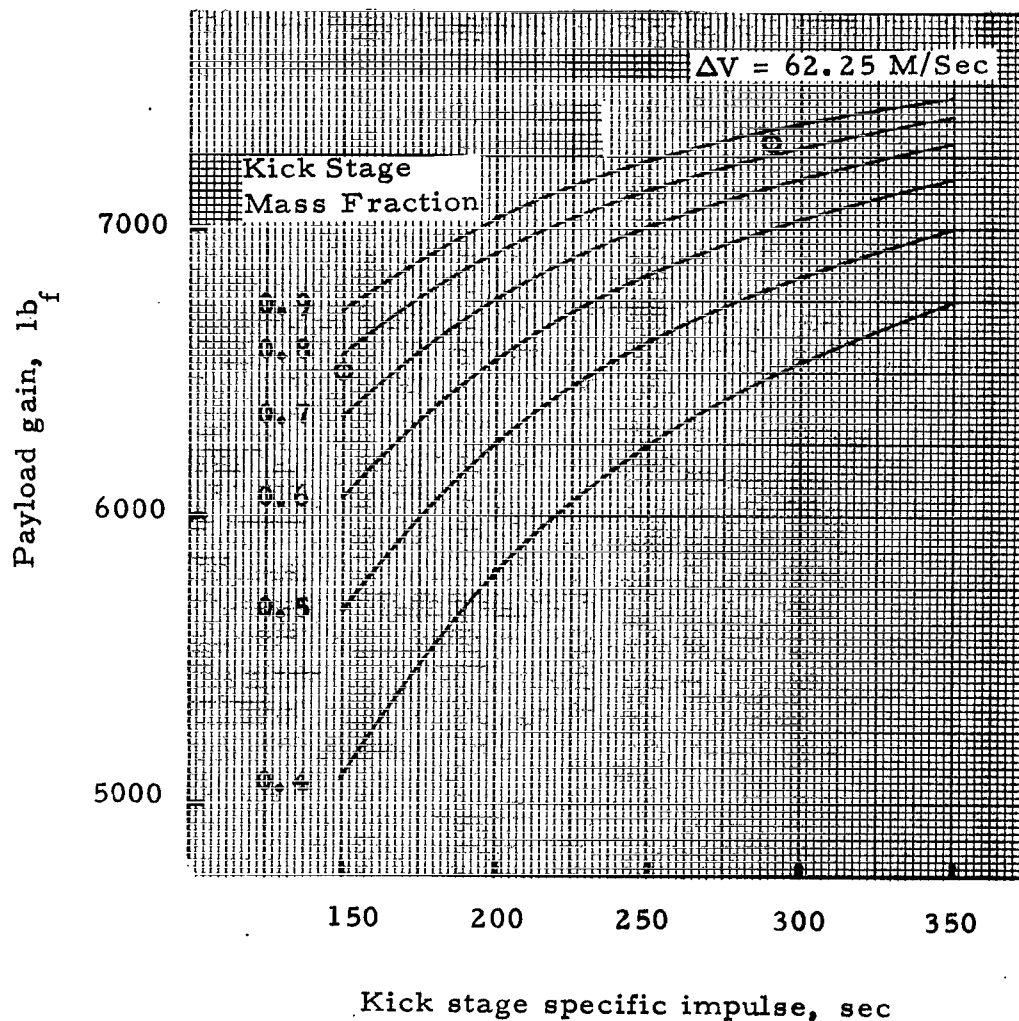Figure G-9. Propellant-to-initial-gross weight ratio
versus specific impulse.
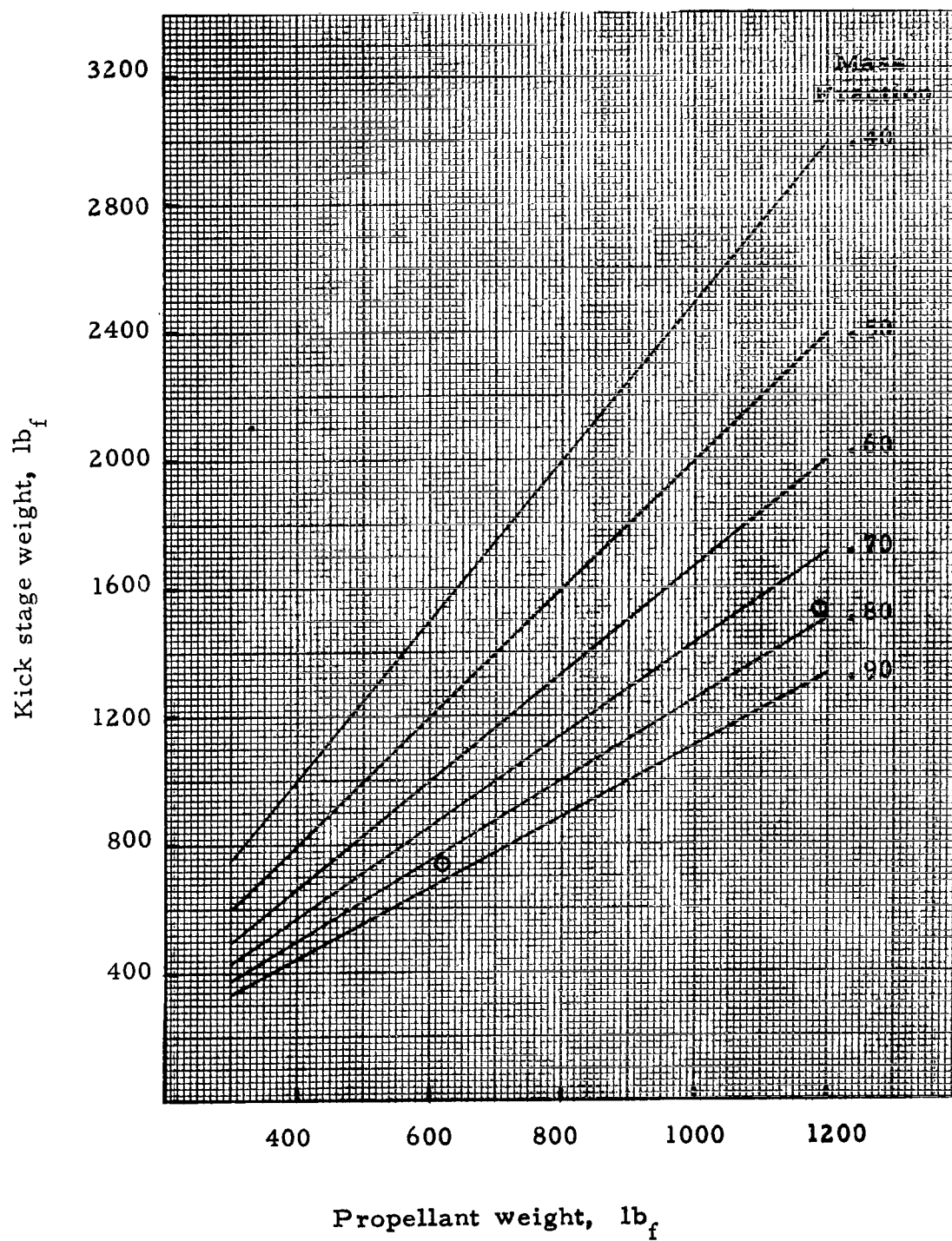
Figure G-10. Kick stage weight versus propellant weight.

Direct Injection Payload = 20, 300 lb$_f$ *
Elliptical Injection Weight = 28, 320 lb$_f$

Kick stage specific impulse, sec

*Since this plot was made based on this direct
injection payload, 620 pounds should be sub-
tracted for each payload gain value obtained
because the direct injection payload has been
increased to 20, 920 pounds.

Figure G-11. Payload gained by using a kick stage
to circularize HEAO.

It should be noted that in Figure G-11, 620 pounds should be subtracted from the payload gain value obtained because the direct injection payload has been increased from 20 300 to 20 920 pounds.

A liquid and a solid existing propulsion system was considered for use as a candidate kick stage propulsion system. The liquid system is an H_2O_2 monopropellant APS used on the second stage of the Scout launch vehicle and is operational. The solid propellant system consists of a cluster of four spherical solid propellant motors. One of these spherical motors has flown on the RAES, managed by the Goddard Space Flight Center. The motor is used as an apogee kick motor for the RAES and is operational.

Table G-6 presents a data and performance comparison of the two systems. As shown, the monopropellant peroxide system has a low thrust, and hence a low thrust-to-weight ratio which results in about 5 minutes of burn time required to perform the circularization maneuver. For a 5-minute burn, attitude control of the spacecraft could become critical. The solid system has a high thrust and thrust-to-weight ratio which results in a few seconds of burn time. For spacecraft control, a low burn time is desirable.

Table G-7 presents a weight summary statement comparing the liquid and solid systems. As shown, the total weight of the solid propellant kick stage required to perform the circularization maneuver is much less than the liquid system. The mass fraction of the solid kick stage is higher than the liquid. The circles shown on Figures G-10 and G-11 represent where these two existing systems appear.

A payload gain of 5865 pounds is obtained by using the liquid kick stage, and a payload gain of 6660 pounds is obtained by using the solid kick stage.

The solid propellant kick stage system was chosen to circularize the HEAO into a 200-n. mi. orbit from the initial elliptical orbit. This system was chosen over the liquid system because of its low total weight, higher mass fraction, and shorter burn time. The solid system is also much simpler, and provides a larger increase in payload.

The solid propellant motor is manufactured by the Thiokol Chemical Corporation and is designated as TE-M-479. The reliability of this motor is 0.999 at 90-percent confidence level; i.e., there has never been a failure of this motor. There is a 10- to 12-month lead time for purchasing this motor. The price per motor is approximately 25 thousand dollars.

G-26

TABLE G-6. CIRCULARIZATION CANDIDATE PROPULSION SYSTEMS DATA AND PERFORMANCE

Type	Liquid Propellant	Solid Propellant
Propellant	H_2O_2	Composite
Number required	1	4
Performance (vacuum)		
Thrust, F-lb_f	500	10 000 (2500)[a]
Specific impulse, $I_{sp} - \dfrac{lb_f - sec}{lb_m}$	150	290
Burn time, t - sec	352	18
Chamber Pressure, P_c - psia	256	800
Total impulse, I_t - lb_f - sec	176 000	178 000 (44 500)[a]
Dimensions:		
Overall length, in.	$\approx$ 36 (tankage)	30
Diameter, in.	36 (tankage)	17
Usages (engine/motor)	Scout 2nd stage APS	Apogee kick motor
Current status	Operational	Operational

a. Numbers in parenthesis indicate single unit values.

TABLE G-7. CIRCULARIZATION CANDIDATE PROPULSION SYSTEMS WEIGHTS

Propellant Type	Monopropellant (H_2O_2)		Composite Solid		
Weights, lb					
Propellant	1175		620 (155)[a]		
Inert (total)	360		80 (20)[a]		
	Pressurant gas	40	Case	C	(9)[a]
	Propellant tanks, bladder, etc.	140	Nozzle	N	(7)[a]
	Pressurant tanks	160	Misc.		(4)[a]
	Engine	20	--		
Structural attachment	--		40		
Total	1535		740		
Stage mass fraction	0.77		0.84		
ΔPayload (Reference payload weight 20 920 lb)	5865		6660		

a. Numbers in parenthesis indicate single unit values.

This study was performed to show an alternate approach that could be taken to place the HEAO into a 200-n. mi. circular orbit using a Titan IIID launch vehicle. This alternate approach should be taken only if the weight of the HEAO increases to the point that a direct injection would be marginal.

REFERENCES

G-1.   Traynelis, K. A.; and Rzan, D. L.: Using Reaction to Control
        Vehicle Attitude. Hot Gas Control Systems — III. Walter Kidde &
        Company, Inc., McGraw-Hill, Reprinted from Control Engineering,
        January, May, July, 1961.

G-2.   Greco, R. V.; and Charhut, D. E.: Resistojet Systems Manned
        Spacecraft Applications. McDonnell Douglas Astronautics Company,
        Western Division, Huntington Beach, California, Douglas Paper 5252,
        Contract No. NAS1-6702 to Langley Research Center, March 1969.

G-3.   Pisciotta, A.; and Eusanio, E. N., et al: Definition of a Resistojet
        Control Systems for the Manned Orbital Research Laboratory Final
        Report. Volume II Resistojet Control Systems Analysis. Douglas
        Aircraft Company, Missile and Space Division, Huntington Beach,
        California, NASA CR-66601, DAC-58131, May 1968.

G-4.   Anonymous: Spacecraft Flight Control Systems. Walter Kidde &
        Company, Inc. Belleville, New Jersey, Report Number A-48-2M-10-
        63-NP.

G-5.   Anonymous: Data Sheet on Bell Aerosystems Company Model 8360,
        Liquid Propellant Engine Manual. Chemical Propulsion Information
        Agency, Unit No. 2, December 1967.

APPENDIX H. POWER SYSTEM DESIGN

Page

LIST OF ILLUSTRATIONS

LIST OF TABLES

v

1. Solar array

    ● Cell type — For a pre-1975 application, only silicon N-ON-P cells need be considered.[1]

    ● Base resistivity — 7 to 14 ohm-cm.

    ● Cell size — Indicate size used (less than 2 by 8 cm) and the ratio of active area to cell area used.[2]

    ● Cell efficiency — Use 10.5 percent for the average uncovered cell under initial, standard condition of 28° C, 140 mw per cm^2.

    ● Cell thickness — To be consistent with efficiency. Indicate thickness used between 8 to 16 mils.

    ● Cell spacing factors — The cell-to-cell, cell-to-slide, or slide-to-slide spacings are the following: (a) cell in series — 15 mils, (b) cells in parallel — 5 mils, (c) submodule, group, or row spacing — 90 mils.

    ● Module packing factor — Indicate factor used between 0.82 and 0.92. Factor is ratio of total cell area (not active area) to module area and includes cell spacing factors, connector area, and edge and attachment areas.[3]

    ● Array packing factor — Ratio of module area to array or array section area (to be determined by design).

---

1. A cursory assessment of Lithium-doped, radiation-hardened cells is desired (i.e., compare standard cell with Li-doped cell for output versus temperature and life and for cost per kw).

2. ATM thermal cycling indicates 2 by 6 cm as maximum size practicable. Today's standard is 2 by 3 cm, but it appears 2 by 4 cm may become the most economical. For all final comparison data, show results in terms of a 2 by 2 cm cell equivalent.

3. A module is the largest assembly of cells to be fabricated at one time.

II-2

- Absorption/emissivity (α/ϵ) is as follows:

    1. Covered cells: $\dfrac{\alpha \text{ nom}}{\epsilon \text{ nom}} = \dfrac{0.71}{0.82}$

    2. Thermal point, S-13G: Use 0.24/0.89.

Beginning of life range for today's 0.22 to 0.26/0.90 to 0.85.

- Temperature coefficient — Indicate value used for efficiency and maximum voltage. ATM cells range from 0.46 to 0.50 percent per degree C; use 0.5 percent per degree C.

- Substrate of module and array sections — To be determined. Identify materials and applicable criteria such as weight, volume, strength, rigidity, and coatings if needed.

- Assembly and connection technique — Use Orbital Work Shop solar cell module specification as guidelines [H-1, H-2].

- Degradation — Controversial subject, dependent on electron and proton doses, UV deterioration, temperature, cover slides, etc. Justify the values selected. Sensitivity of design to probable range of degradation factors should be given. Use a minimum of 4 percent per year for overall effects [H-3].

- Aspect ratio — Applicable to deployed arrays. Length to width ratio of array should be limited to 5 to 1. A 4 to 1 ratio may be more realistic.

b. Specific Energy Storage Criteria

    1. Batteries. Use Reference H-4 for general background and undesignated battery criteria.

- Primary batteries (nonrechargeable) — Consider only Ag-Zn type and determine the realistic active life for the type and date of cells as follows:

    1. Medium and low rate change — 3 to 6 months

    2. High rate — 30 days maximum

3. Energy density — indicate value used within following limits:

    a. **High rate** — 50 watt-hours/lb (maximum)

    b. **Medium rate** — 90 watt-hours/lb (maximum)

    c. **Low rate** — 110 watt-hours/lb (maximum).

● Secondary batteries (rechargeable) — Type: (a) For low altitude orbit and continuous duty with solar-array consider only Ni-Cd batteries, and (b) for occasional, low-cycle duty consider trade-off Ag-Cd type with Ni-Cd type.[1]

● Energy density — Today's cells at standard initial conditions give 12 watt-hours/lb for Ni-Cd and 24 watt-hours/lb for Ag-Cd. Use 12 watt-hours/lb for Ni-Cd assemblies and 24 watt-hour/lb for Ag-Cd assemblies of 1975. (Above values relate to installed capacity; depth of discharge not included.)

● Cell size — Based on present availability, a cell size between 20 and 40 ampere-hours should be selected as a baseline.

● Energy efficiency — Not to exceed 85 percent for Ni-Cd batteries. Indicate value selected or use 80 percent. A value of 70 percent is suggested for Ag-Cd batteries.

● Electrode style — Justify selection of 2, 3, or 4 electrode type cells.

● Depth of discharge — Because of life requirement, design should limit discharge depth to 30 percent. Peak discharges over 60 percent should be prohibited and such duty should be permitted only a very few times while the battery is in service on the bus.

---

1. Where thermal constraints exist, remember that the watt-hour recharge efficiency is poorer for Ag-Cd than for Ni-Cd.

● Temperature range — Without innovation in cell technology, system design should provide temperature control between 0° and 20° C. Maximum temperature range should not exceed -20° to +40° C for a short time.

● Recharge

Rate — (a) Limit maximum rate to "C" value or less when undercharged, especially at low temperatures, and (b) in over-charge region, rate should be limited to continuous allowable for the temperature or to trickle charge level.

Overcharge voltage — Temperature dependent. Except for special controls, use 1.5 volts per cell maximum.[1]

c.   Points Emphasized in Design

1.   Preliminary solar array layout.   The first designs of the solar array assumed the use of ATM solar cell modules.   As the study progressed, it became evident that these were not suitable for reasons of physical size, availability, and packing factor.   Accordingly, a new solar cell module was designed.   The characteristics are discussed in detail in Section IX.

2.   Preliminary power system design.   The power system design assumed, where possible, the use of ATM equipment.   The following specific items were used:

Equipment	Drawing Number
Switch selector	50M67846
Control distributor	D40M37383
Power distributor	D40M37381
CBRM	40M26200

3.   Operational analysis.   The conditions under which the power system would operate were used in an analysis to determine how orbital

_____   _ _ _____

1.   Excessive overcharge is to be avoided.

parameters, attitude with respect to the sun, and thermal conditions impacted the design.

4. Battery problems. The rechargeable Ni-Cd battery and its charger were studied. Methods of charging and charge control, effects of high and low temperature on battery life, and cell arrangement were considered.

5. Load sharing. The use of six CBR modules required a study of possible problems incurred in matching inputs and outputs. The ATM CBRM is matched to the solar array output at a point where maximum power can be utilized without resorting to power tracking methods. This matching was possible on ATM because the solar array output was constant and predictable. However, the baseline HEAO is rotating during much of the mission, and does not have a flat solar array. This means that different portions of the solar array have different current-voltage characteristics. To get most efficient utilization of the solar array, the CBR modules for HEAO will have to be modified to accept the solar array output at a fixed voltage and variable current rather than constant current as in the standard ATM unit.

An additional problem was the distribution of power and load isolation. An analysis of the problem indicated that this is not a major source of loss; care will have to be taken to ensure that the power system is adequately protected from short circuits within experiments and spacecraft systems.

2. Concepts for Deploying the Outer Panels of the HEAO Solar Array

Reasons for a Deployable or Foldout Solar Array. The baseline HEAO solar array is a fixed, body mounted system. The HEAO has a regular, octagonal cross-section; the solar array is composed of three adjacent sides. Since the two side panels are at an angle of 45 degrees to the center panel, the output of each of the side panels is only about 70 percent of their capability, at the best (excluding temperature effects). Actually, when the offset angle of the spacecraft causes the light incident angle on the surface to exceed 60 degrees, surface reflections reduce the output more rapidly than does the decrease in the projected area. Thus, at angles of more than about 75 degrees, the solar array output is negligible. By folding out the two side panels to form a flat array, it will be possible to avoid these adverse conditions. The output from a foldout array is at least 23 percent more than the fixed array, or 1000 watts total, for those conditions most favorable to the fixed array. As the power margin (contingency) for the baseline is not large at the end of 1 year, it was believed

H-6

that the Phase A work should include some definition of a foldout solar array for HEAO. The study performed is summarized here.

The objective of the study was to investigate several methods of deploying the outer two panels so that they assume a position in the same plane as the third or center panel. Schematically, the HEAO is a structure 360 inches long whose cross section is octagonal in shape. The solar panels occupy three adjacent sides along the full length of the spacecraft. The original and final positions are shown in Figure H-1. (This figure indicates one method of fitting the deployable arrays into the existing 105-inch envelope, using an irregular octagonal spacecraft cross-section.) In the final position, the panels would be latched and remain in that position.

The criteria used in the investigation were as follows:

      a.   28 modules required per panel; wired in groups of four and two-thirds.

      b.   Each module is 25 by 19.75 inches; weight is approximately 3.5 pounds exclusive of mounting frame.

      c.   Solar cells mounted to within 0.187 inch of module edge; substrate of 0.375-inch honeycomb.

      d.   Spacecraft mounting surface; 40.2 inches wide by 360 inches long.

      e.   Deployed during first orbit — time not a factor.

      f.   Final position tolerance ±5 degrees.

      g.   Spacecraft rotates about axis perpendicular to solar array plane at 0.1 rpm.

      h.   No retraction after deployment.

      i.   Environmental conditions; launch acceleration and vibration.

With the above criteria it was desired to investigate a concept for each of the following items:

a. Framework for mounting solar panels.

b. Pivots or hinges for the sections.

c. Tiedowns or cinching of sections to spacecraft.

d. Release mechanisms.

e. Latching devices.

Several concepts for each of these were considered with the results shown in the following paragraphs.

a. <u>Framework</u>. Before the framework could be designed it was necessary to determine the size of a section which could be deployed practically. Although the modules were to be wired in groups of four and two-thirds, it was decided to consider mounting in sections of four modules each. The possibilities are shown in Figure H-2. At the most there would be 7 sections of 4 panels each and at the least 1 section of all 28 panels. Case 2 (Fig. H-2) seemed to be the most practical approach and was selected for the rest of the study. This consists of two outer sections of 8 panels each with a center section of 12 panels. This avoids having an excessive number of pieces of hardware and also the necessity of deploying the full 30-foot section. The layout of the panels is shown in Figure H-3. It should be noted that two modules side by side need almost the full 40.2-inch-width allowable for the panel.

The framing is shown in Figure H-3. It consists of aluminum square tubing: 1.75 inches square with 0.083-inch wall. The modules would be attached to the framing as shown in Figure H-4. The weight for the frames for a 30-foot side was estimated at 75 pounds with 25 pounds of fittings. The modules weigh 98 pounds for each side. The total panel weight was then 198 pounds.

A problem arose when the framework with modules installed was considered for mounting on the spacecraft structure. The envelope given was for an octagon-shaped spacecraft with the largest cross-sectional dimension being 105 inches. Each side measures 40.2 inches. The maximum occurred at the corners, and here the tolerance between the spacecraft and the shroud was of the order of 1 inch. As noted above, the panel layout requires all but about 0.5 inch of the 40.2 inches allowed for the array on the spacecraft. If it is now assumed that the thickness of the module and their mounting frames is on the order of 2.25 inches, it becomes apparent that the envelope will not

accommodate them, if the baseline spacecraft structure is utilized without modification. The impact of violation of the payload envelope, or other possible solutions to this problem, must be investigated in Phase B.

b. Deployment Mechanisms. Generally, two types of mechanisms were considered: powered and spring actuated. Those requiring power are shown in Figure H-5 and H-6 and those requiring no power are shown in Figure H-7. Some of the advantages and disadvantages of each are given in Table H-1.

TABLE H-1. DEPLOYMENT MECHANISMS

System	Advantages	Disadvantages
Direct drive	Compact Controlled deployment	2 systems required Power required Beefy torque tube required
Direct drive with linkages	Positive control Tandem operation	Bulky, heavy Power required Retractions not required Poor mechanical advantage
Direct drive with cable	Positive control Tandem operation, Light	Power required Poor mechanical advantage
Linear extender	Positive control Good mechanical advantage	Expensive Retraction not required Power required

Torsion springs	Compact, light
	Simple
	Reliable
	No power required
		System continues to accelerate
		  when activated unless damper
		  is used

Tension springs	Light
	Reliable
	No power required
		System continues to accelerate
		  when activated unless damper
		  is used

Under the criteria given, there is no reason why any one of these would not perform the required function. The motor-driven systems require power but with time not being a factor the motors could be small and of low power. The motion is under better control than that of pure spring devices which suffer from the necessity of absorbing the initial energy given the sectional structure by the springs; however, a simple damper device could be utilized with the springs to smooth the motion. Knowledge of ambient temperature of the devices is an important factor in the design of such devices; however, they require no power and have other advantages. It is recommended that a concept for each be selected and more design attention be given to them during Phase B. Testing should be performed before a final decision is made.

The power required for the drive motors is approximately 2.5 watts. If necessary, the motor operation could be sequenced — the motor on each section starting after deployment of the previous section. The weight of each motor is approximately 0.75 pound.

c. Cinching and Release Mechanisms. Five concepts for this were investigated. Three of the devices require powered drives and two are spring actuated as shown; however, the motion required is over small displacements, and it is conceivable that spring-force actuators could be applied to most cases. It is assumed that the cinch and release device is required to carry only the lateral and not the longitudinal loads during launch.

Figures H-8, H-9, and H-10 are conceptual drawings of the powered devices while Figures H-11 and H-12 show those requiring spring or similar forces. In the former, the release is accomplished by application of power to the motor and in the latter a squib initiated spring release is used. Power requirements in all cases are small. A motor for this purpose would use about 2.5 watts and weigh approximately 0.75 pounds. It could be made redundant in operation and sequenced in use. For six sections, the total power required for deployment would be only 15 watts.

d. Latching Devices. Once the section is in final position it must be latched and held in place. The type device used depends somewhat on the deployment mechanism employed. For those deployment mechanisms using a spring force, it is necessary to provide for some type of damping to absorb the energy given the panel by the spring force. Figures H-13, H-14, and H-15 show concepts for such a device. Temperature condition must be predictable for a suitable design. It is possible to design the deployment mechanism and latching device in one system if it is decided to approach the problem with spring devices.

3. Power System Performance Characteristics

<u>Solar Array Tradeoff Study</u>

Array tradeoff study. A review of possible cross-sectional shapes that might be used for the HEAO spacecraft was made to determine the one which would provide a maximum usable solar panel area. Usable area is defined as the area which can be covered by HEAO solar cell modules.

The spacecraft diameter considered was 105 inches. Since viewing surfaces on opposite sides of the spacecraft are required for several of the experiments, only shapes having opposing faces were considered. Seven of the cross-sectional shapes which were reviewed for HEAO application are shown in Figure H-16. The angle between the sun and the solar-panel surfaces is given for the celestial scan mode of spacecraft operation. With the sun position shown in the figures, the electrical power generation is maximum.
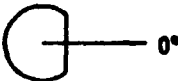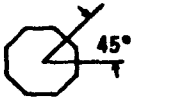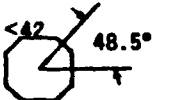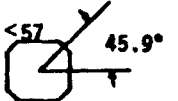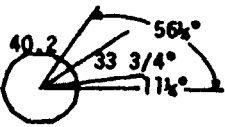
Table H-2 gives the number of HEAO solar cell modules which can be located on the panels for each cross-sectional shape. The equivalent number of modules projected toward the sun and the raw power output at 86° F for each shape are also given in Table H-2. .For the body-mounted concepts, the shape which will accommodate both the maximum number and maximum projected equivalent number of HEAO modules is the regular octagon. Thus, the shape which will provide the maximum electrical power from the body-mounted panels when the spacecraft is in the celestial scan mode of operation is the regular octagon. A 23-percent increase can be obtained from this configuration by folding out the two side panels.

As an indication of the power which could be expected during the galactic scan mode of spacecraft operation, the outputs from the various configurations have been plotted for angles up to 50 degrees. The curves in Figure H-17 indicate that the relative power outputs in the galactic scan mode.

These curves include the effect of the scanning spacecraft. The effect of reduced solar panel temperature for off solar viewing angles has not been considered. All panels are assumed to be at 86° F, the same temperature which was used for the celestial scan mode output calculations of Table H-2.

On the basis of these data, the regular octagon having three solar panels, each 40.2 inches wide, is the preferred cross-sectional shape for the HEAO spacecraft. Figure IX-4 shows the module layout for the solar panels on this baseline configuration. The alternative of deployable side panels is proposed as a desirable feature for contingency purposes.

TABLE H-2. COMPARISON OF CROSS-SECTION SHAPES

Shape		Number of Panels	Number of Modules	Equivalent Number of Modules	Raw Power at 86° F (Watts)[a]
Regular hexagon		2	72	62.5	2313
Cylinder with flat face		1	56	56.0	2072
Regular octagon		3	84	67.6	2501
Irregular octagon 1		3	78	65.8	2435
Irregular octagon 2		3	70	61.5	2276
Modified octagon		6	84	66.2	2449
Regular octagon with foldouts		3	84	84.0	3108

a. Based on module output of 37 watts
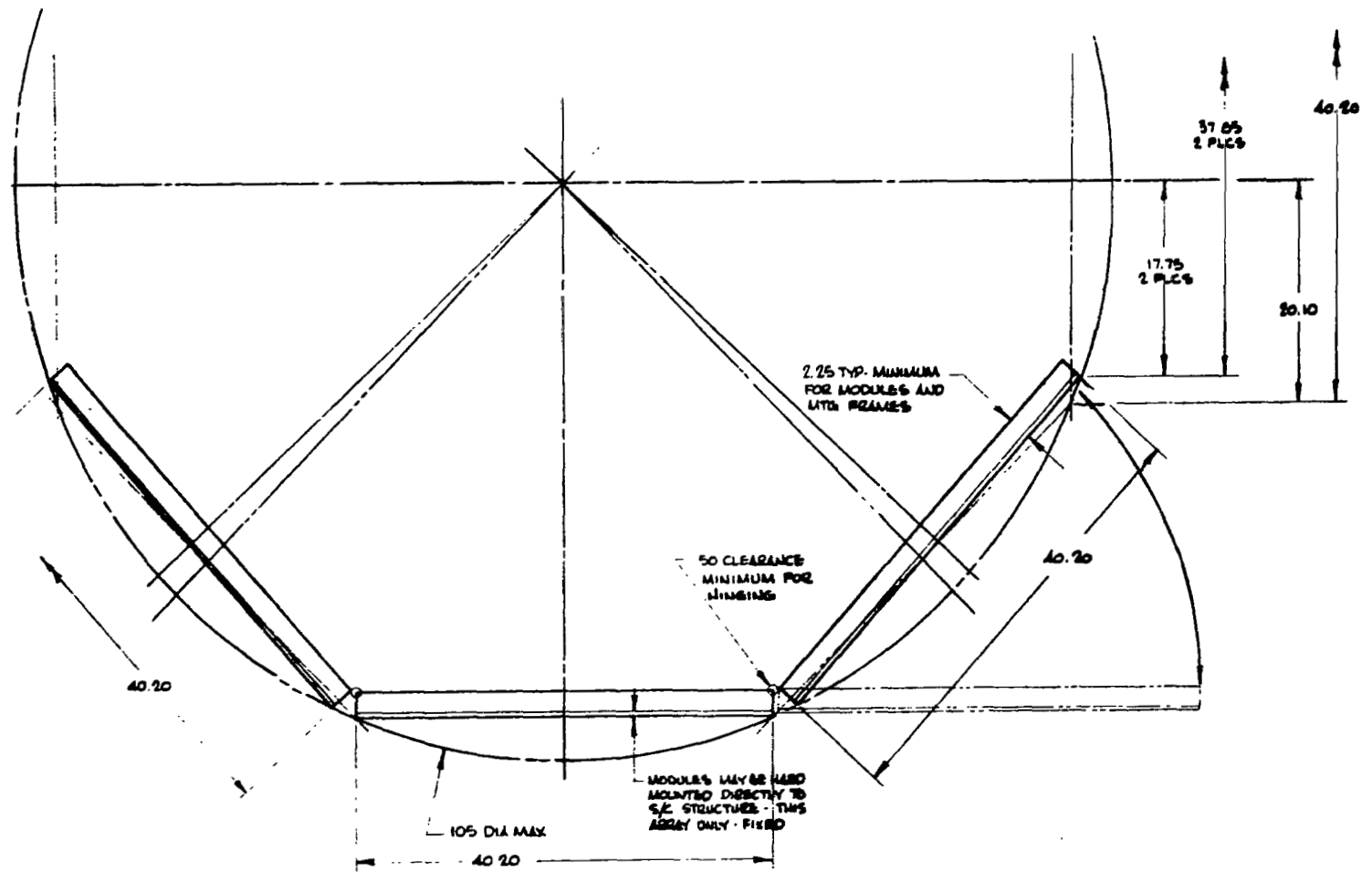
Figure H-1. Solar array mounting.
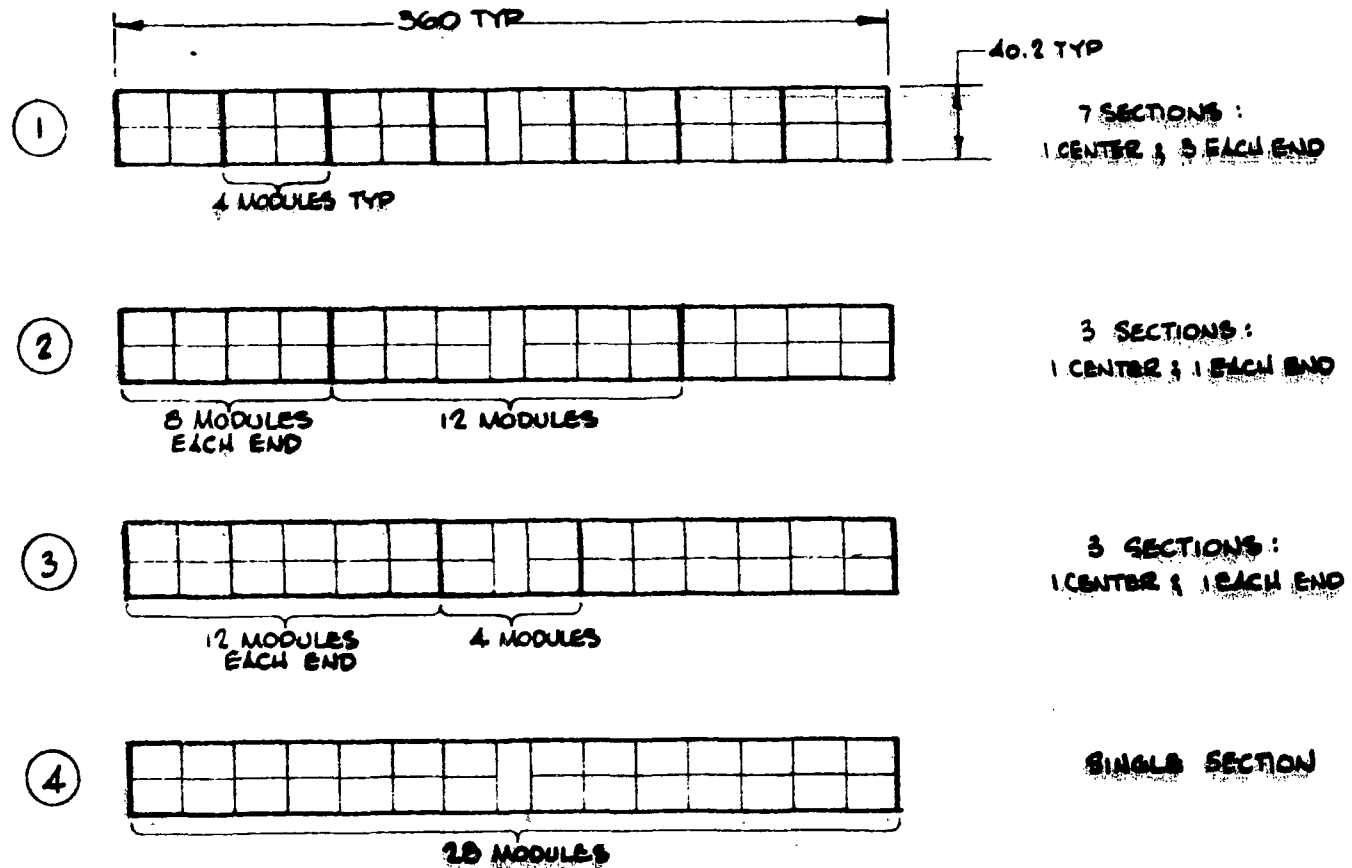
Figure H-2. Possible configurations.

FRAMING - ALUMINUM 1.75 SQ x .083 WALL
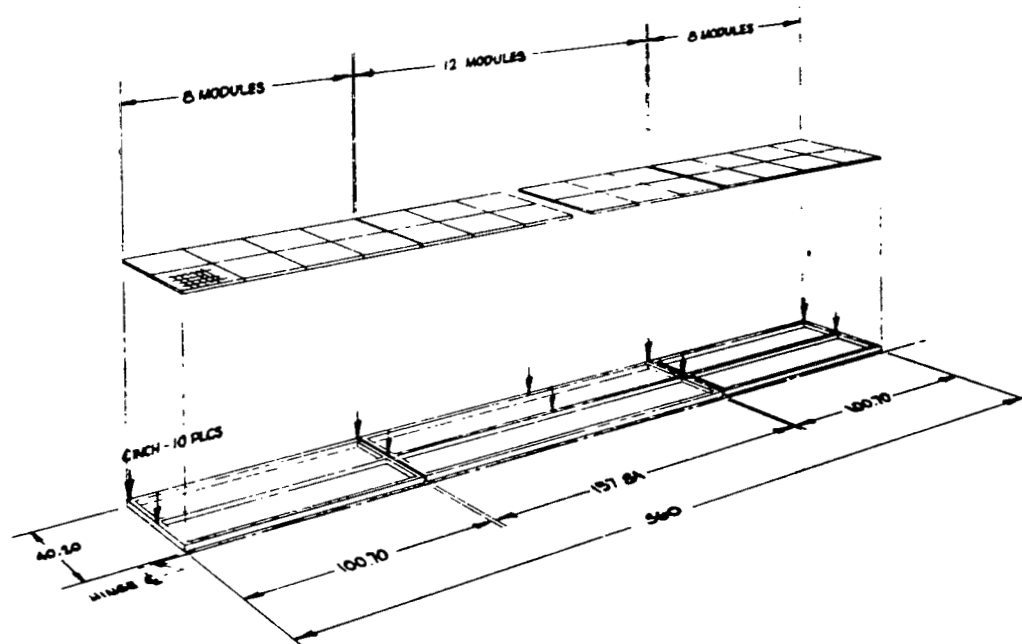
Figure H-3. Solar array concept.
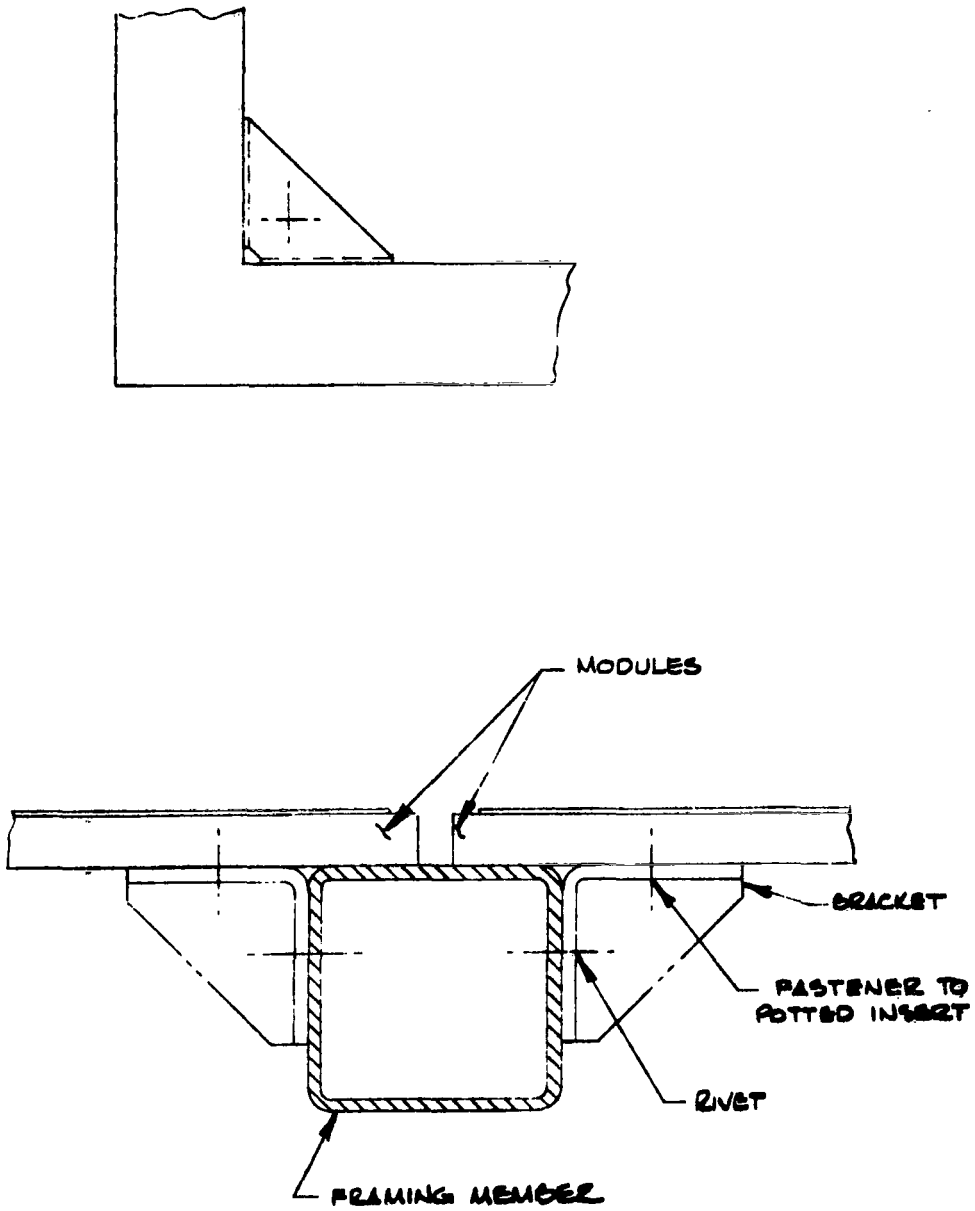
Figure H-4. Typical mounting to center member.
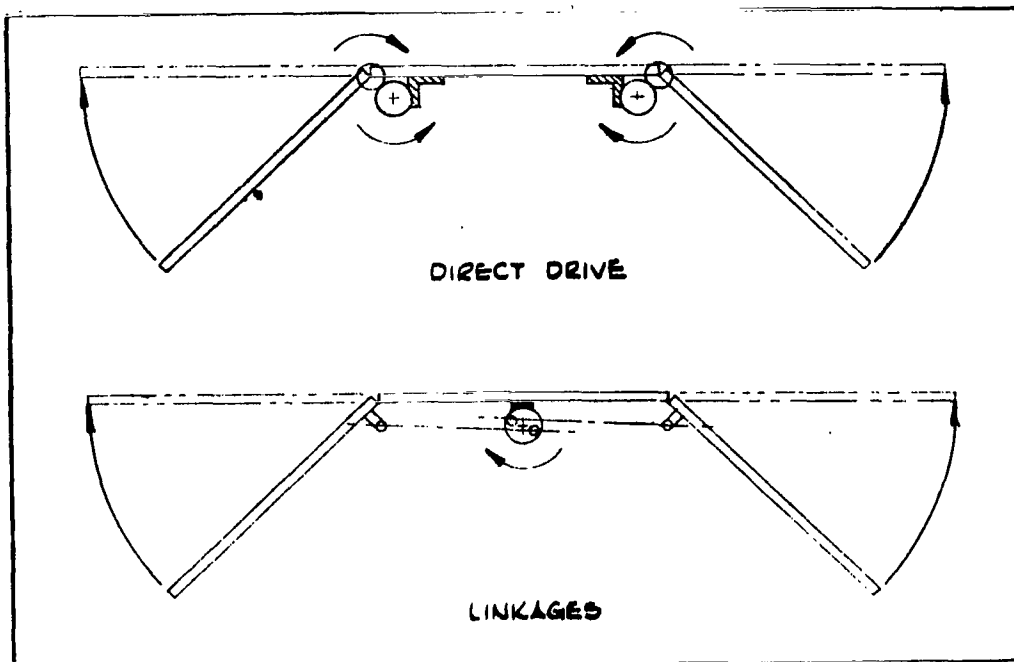
Figure H-5. Deployment concepts — direct drive and linkages.
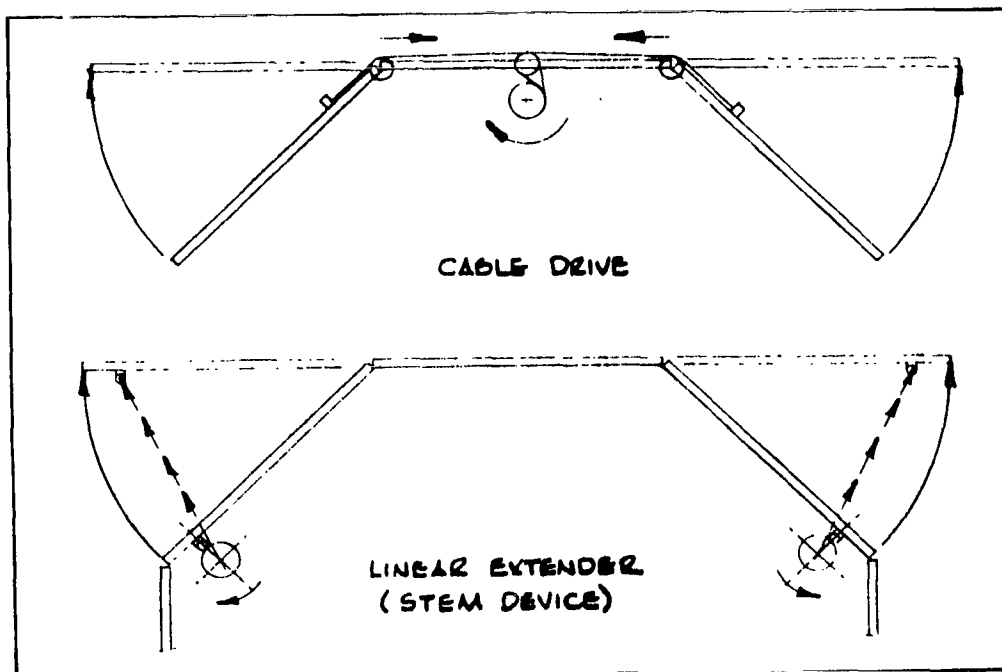
Figure H-6. Deployment concepts — cable drive and linear extender.

H-17

TENSION SPRINGS

TORSION SPRINGS
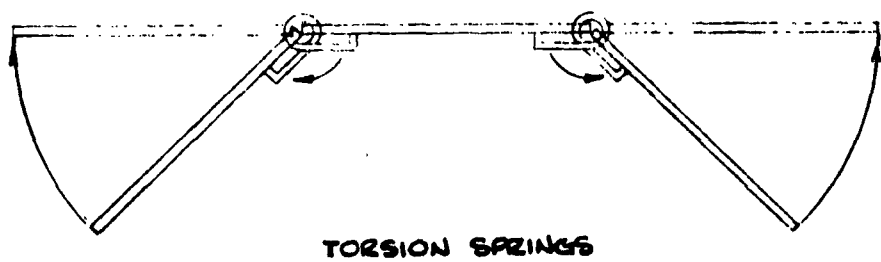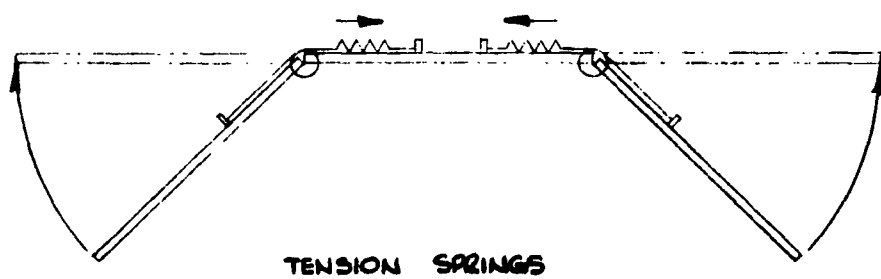
Figure H-7. Deployment concepts.

HINGED

SOLAR ARRAY.

MOUNTED TO
S/C
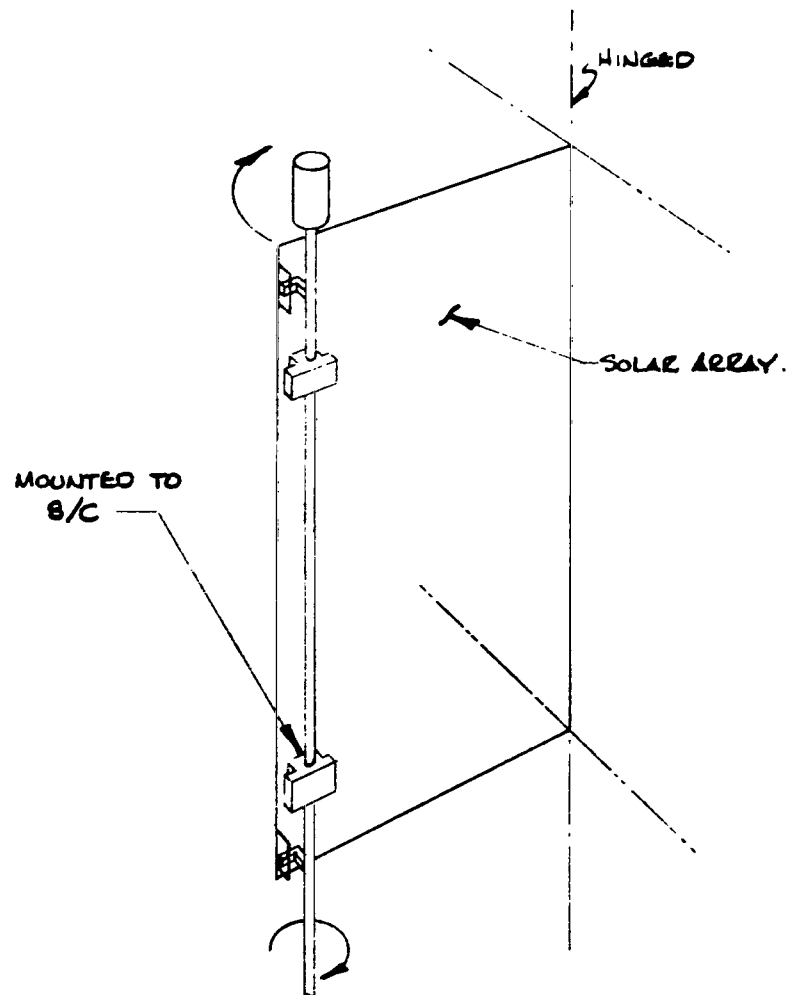
Figure H-8. Cinching — torque tube release.

HINGED FRAME W/MODULES

PIVOT MOUNTED TO
S/C STRUCTURE

SWAGED BALL TO CABLE

OR

DIRECT LINK
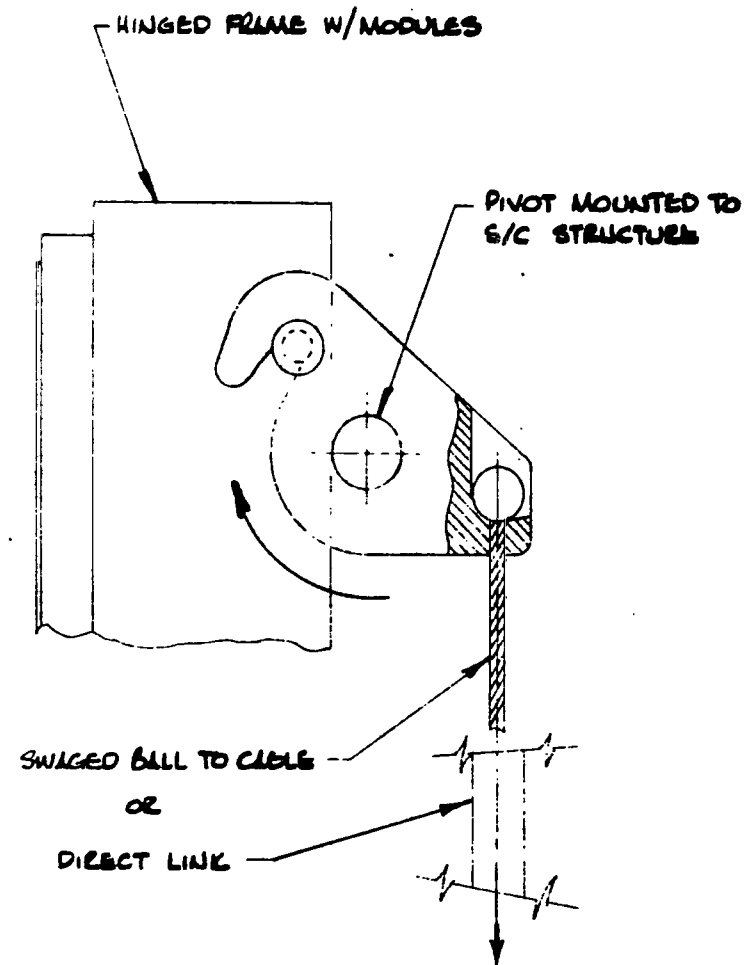
Figure H-9. Cinching — cammed catch.
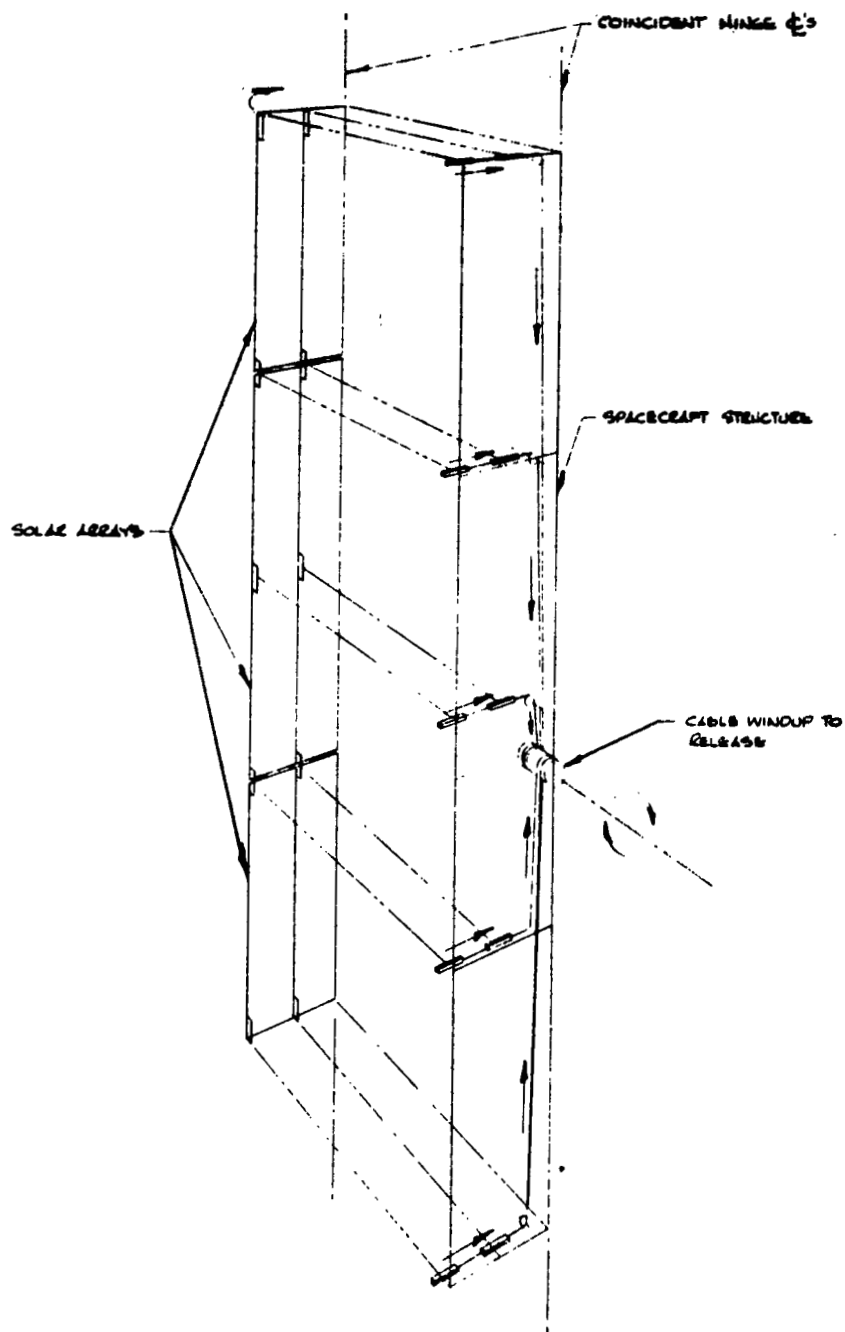
Figure H-10. Cinching — bayonet latch.

WITHDRAWAL

OUTBOARD
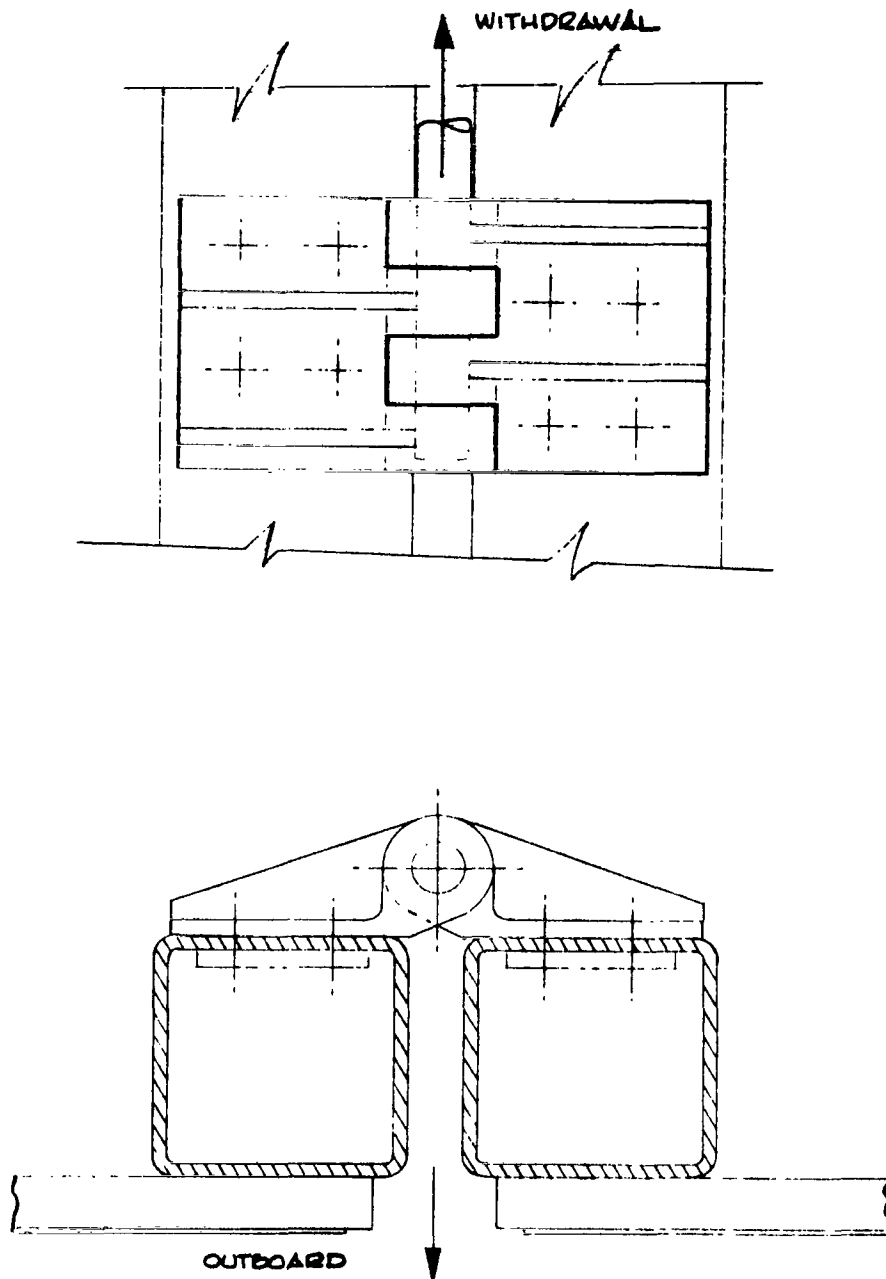
Figure H-11. Bayonet latch for cinching — common four places.

SOLAR ARRAYS

HINGE ℄
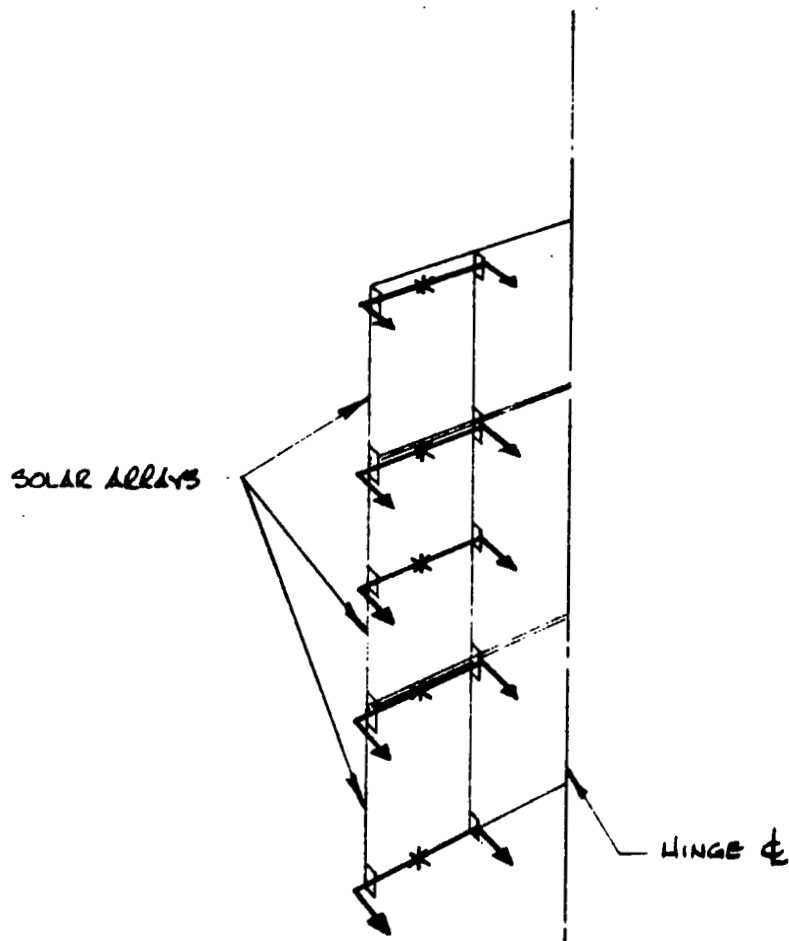
Figure H-12. Arrays banded and cinched at arrowheads; cut
to release at star.

SOLAR ARRAYS

HINGE ℄

STRIKER ℞ ATTACHED TO S/C STRUCTURE
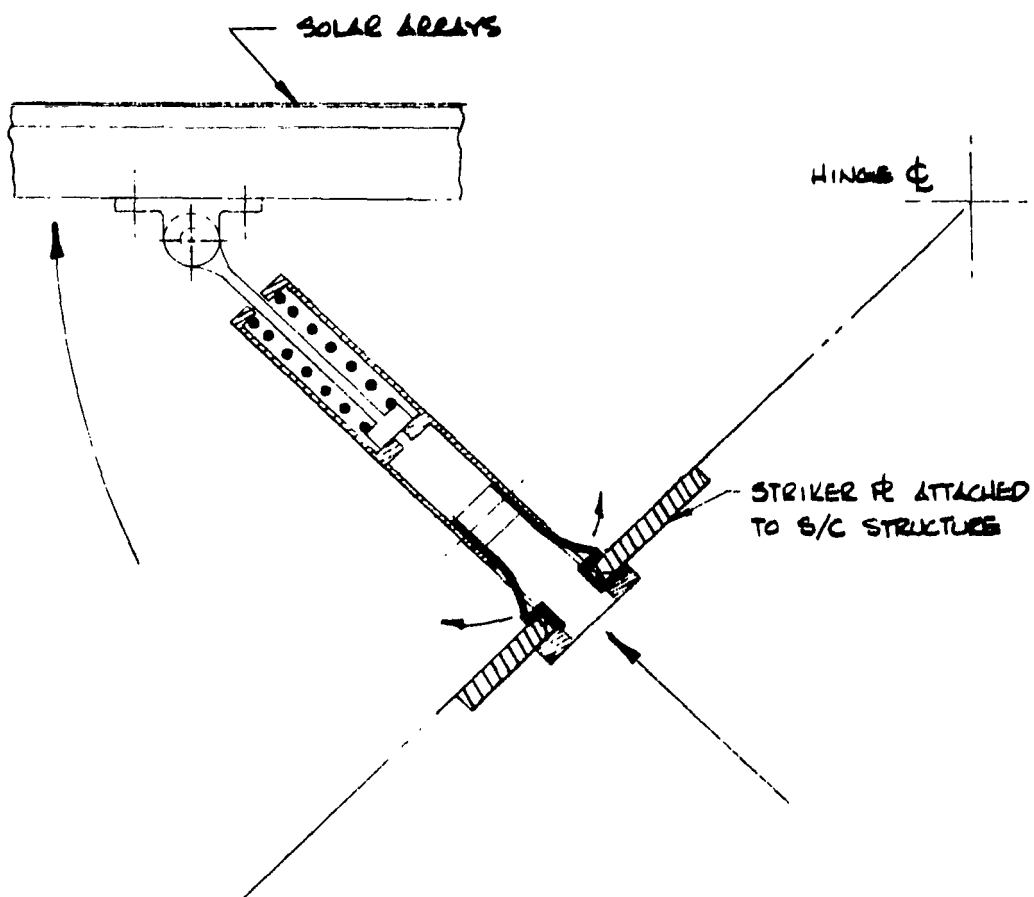
Figure H-13. Energy absorbing drag link deployed and locked.

STATIONARY

AT LAUNCH

STATIONARY

DEPLOYED AND LOCKED
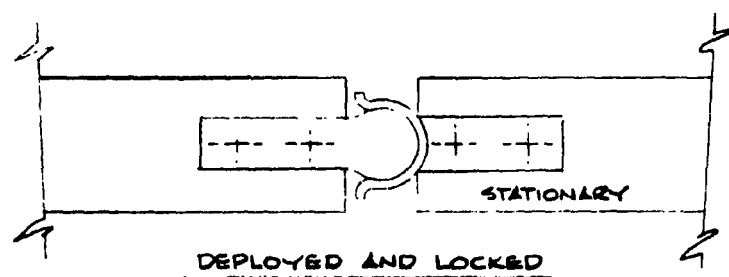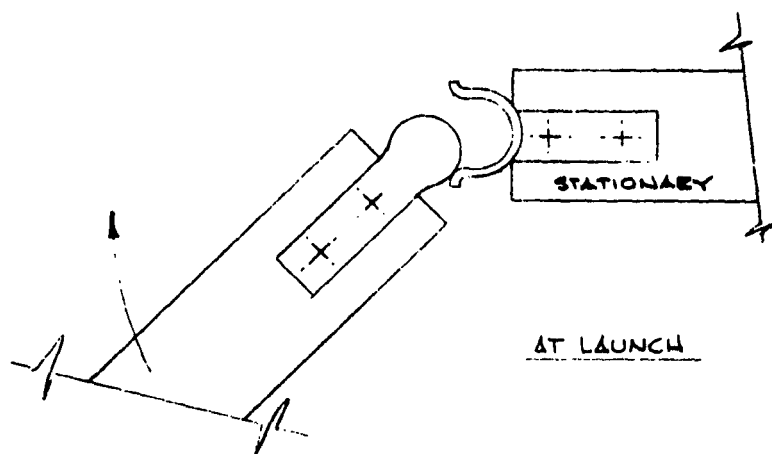
Figure H-14.   Locking: energy absorbing spring catch.

STATIONARY

AT LAUNCH

STATIONARY

DEPLOYED AND LOCKED
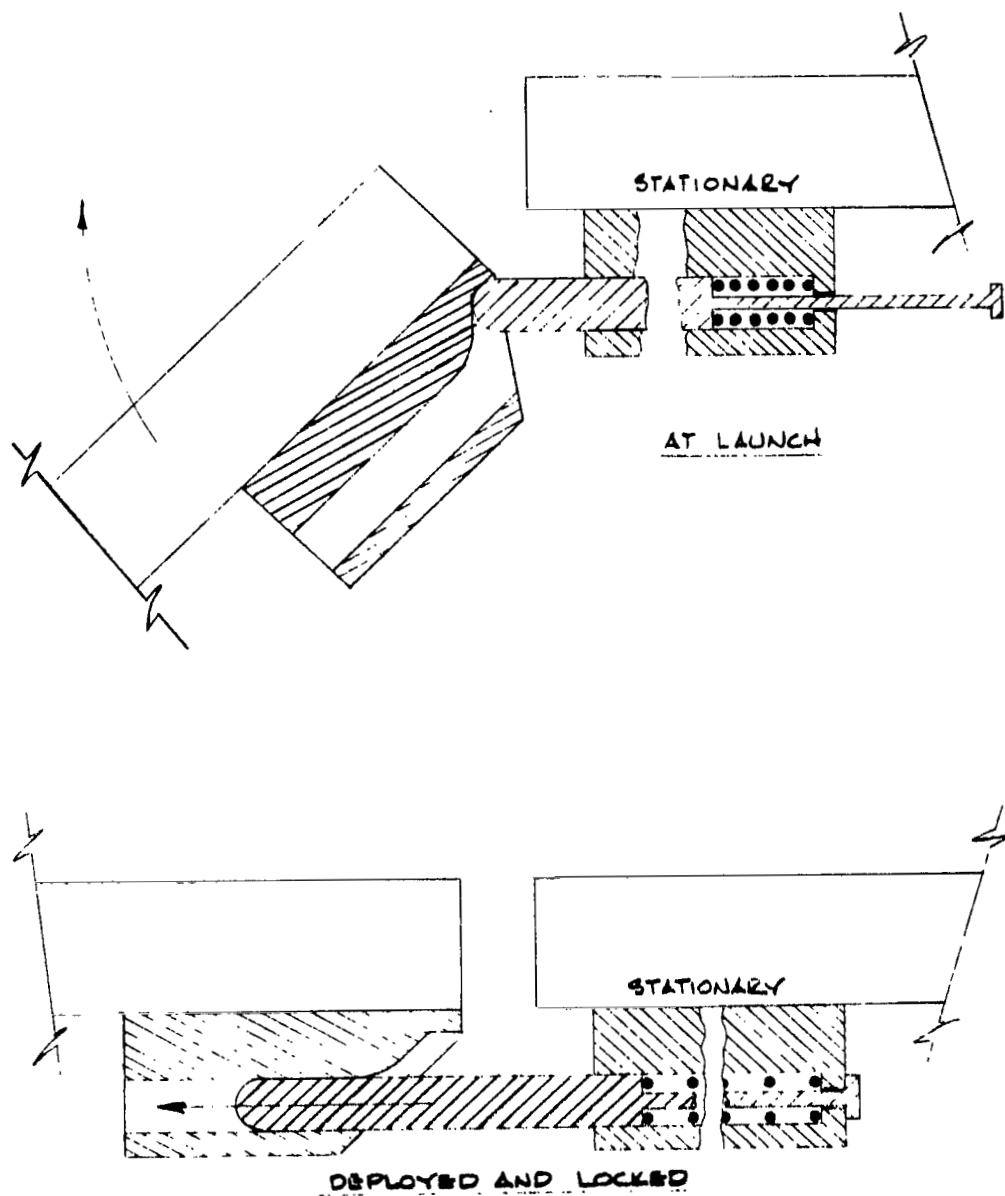
Figure H-15. Locking: spring loaded barrel bolts.
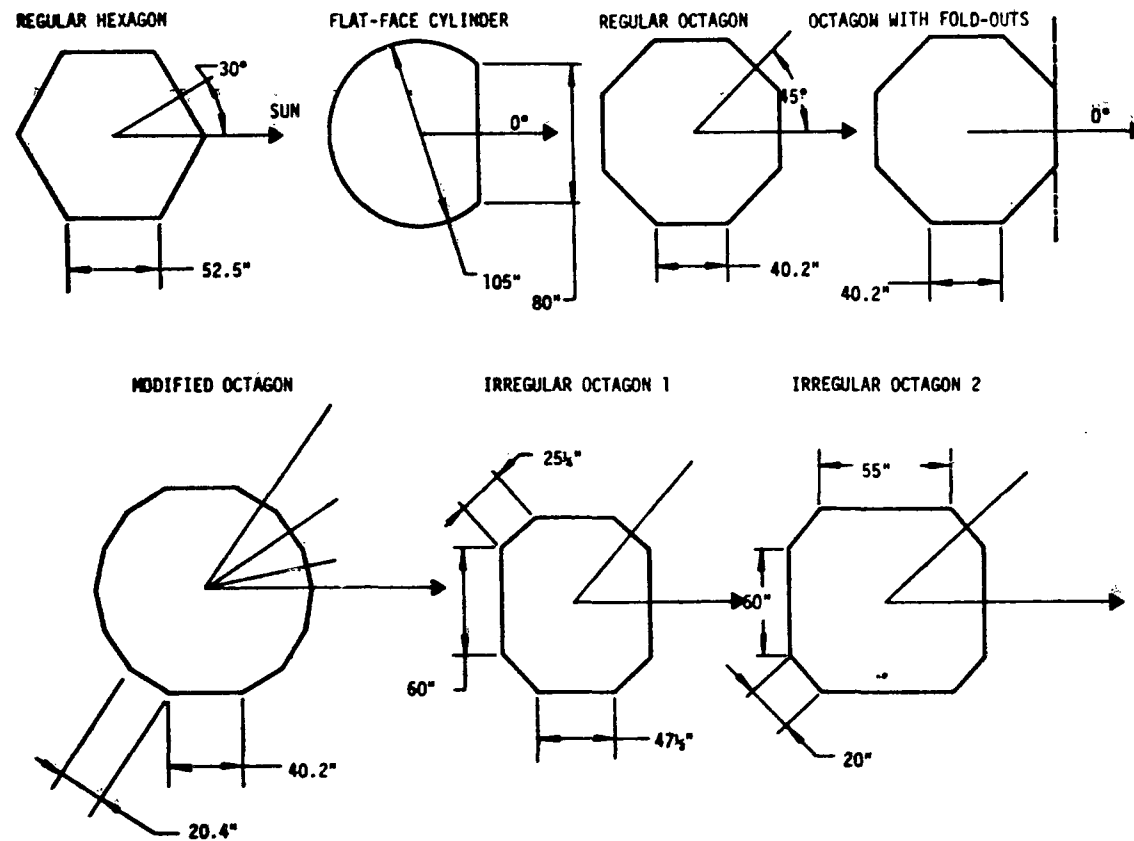
Figure H-16. HEAO cross-sectional shapes.
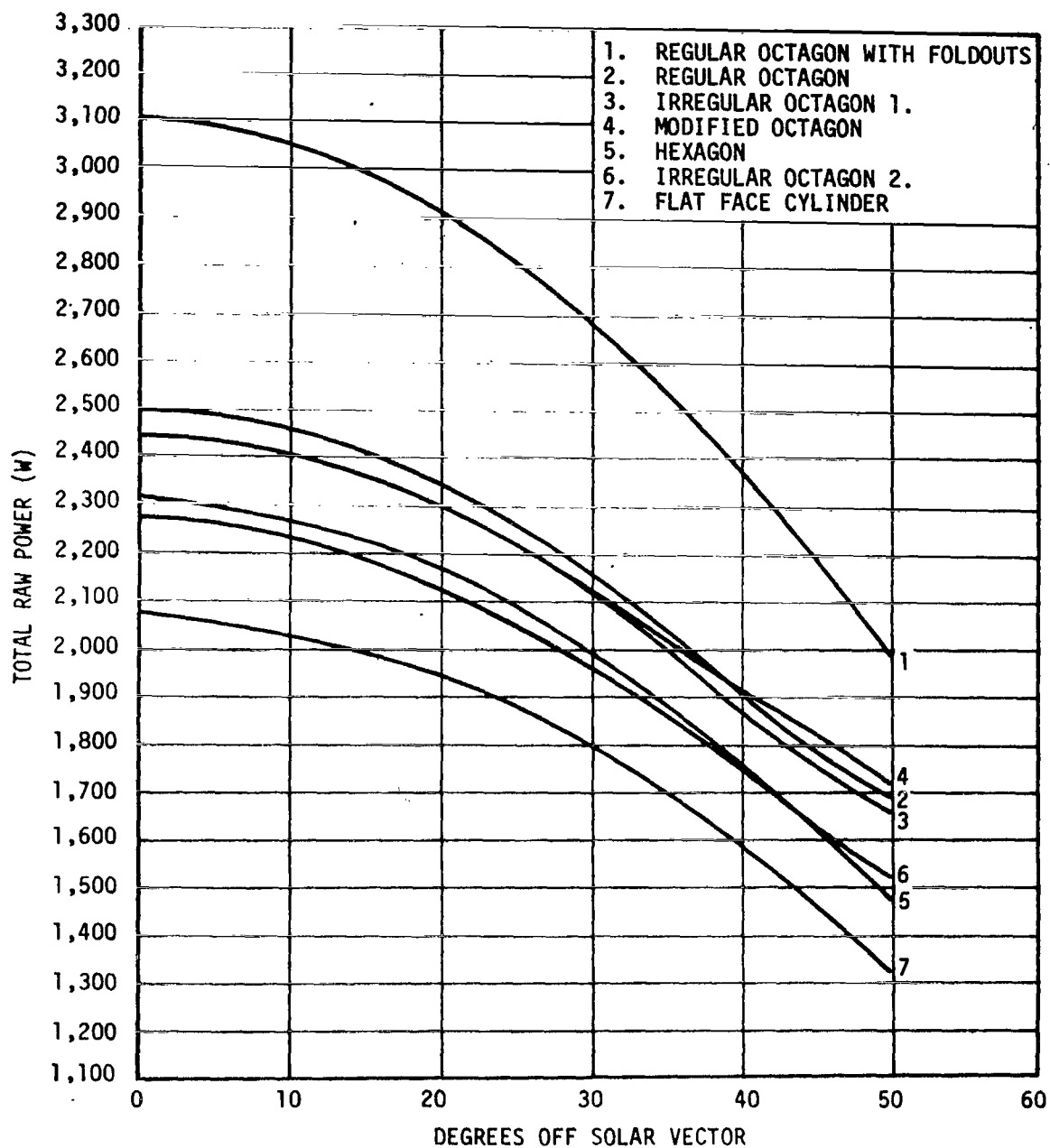
Figure H-17. Total raw power as a function of degrees off solar
vector for 86° F temperature.

REFERENCES

H-1.   Solar Cell Module Specification for AAP Orbital Workshop.
       MSFC-40M-26424.

H-2.   Engineering Evaluation Test Report Investigation of Solder Joint
       Failures on ATM Solar Cell Modules.   Electrical Systems Integration
       Division, Astrionics Laboratory, Test Report, December 20, 1968.

H-3.   Apollo Applications Program Payload Integration Technical Reports
       (Electrical and Power System Task Report).   Contracts NAS8-24000
       and NAS8-21004.

H-4.   Batteries for Space Power Systems.   NASA-SP-172.

BIBLIOGRAPHY

Concepts for Deployable Solar Array for HEAO.   S&E-ASTR-M-70-106.

APPENDIX I. COMMUNICATIONS AND DATA SYSTEMS

TABLE OF CONTENTS

LIST OF ILLUSTRATIONS

LIST OF TABLES

APPENDIX I. COMMUNICATIONS AND DATA SYSTEMS

1. Communications/Data System Alternatives

The purpose of this appendix is to briefly review several communication and data system configurations that were considered in the Phase A study and to present the rationale that eliminated them from consideration in the baseline system design.

a. <u>Antennas.</u> Spinning satellites require either a despun or omnidirectional antenna system. Antennas may be despun mechanically by switching the antenna feed to the element in an array that points toward the ground station at a given time.

Mechanically despun antennas are relatively complicated and require a drive motor. The space environment is hostile to mechanical drive and lubrication systems, resulting in relatively low reliability.

Electrically despun antennas require a switching matrix, an input from an earth sensor network, and control logic to select the proper antenna, or a system that senses signal strength at each antenna location when the spacecraft is illuminated by a signal from the ground, and automatically selects the proper transmitting antenna.

The size, shape, and motion of the spacecraft coupled with the wavelength at S-band presents a formidable problem in obtaining omnidirectional antenna coverage. The four methods commonly used to approximate an isotropic pattern are the following:

(1) Array of elements.

(2) Frequency diversity.

(3) Polarization diversity.

(4) Adaptive antenna.

Spacecraft that are not too large in diameter have used continuous arrays around the largest diameter. Telestar is a good example of this technique; however, Telestar was only about 2 feet in diameter. The HEAO

is approximately 9 to 10 feet in diameter and would require over 100 radiating elements to completely encircle the spacecraft. A boom was used on the relay satellite to support a broadbeam antenna. This minimized the effect of the vehicle on the pattern. An approach was considered which utilized two conical spiral elements: one on a fixed boom extending into the nose cone area and the other mounted on the opposite end of the spacecraft. This would result in a null or interference around the spacecraft center.

The use of the frequency diversity technique requires at least two transmitters and two carrier frequencies per down link. The ground-station antenna would have to be wideband enough to cover all the carrier frequencies used. A receiver for each carrier frequency would be diplexed onto the antenna. The output of each receiver would be weighted and combined with the outputs of all the other receivers to form a composite which would be a stronger signal than that from any of the receivers alone.

In the case of HEAO, two down links are involved and four space-craft surfaces, thus requiring 8 wideband channels. If alternate sides of the spacecraft used the same frequency, this could possibly reduce the number of channels to 4.

Polarization diversity is very similar, except only one transmitter is required. The transmitter output power is divided between the antennas of different polarization. The output power of the single transmitter must there-fore be larger than the output of each of the individual units of the frequency diversity system. In the case of solid-state transmitters this could amount to a slight saving in primary power by increasing the DC to RF conversion efficiency. Polarization diversity is usually selected over frequency diversity on the basis of conservation of the RF spectrum.

Consideration was given to an adaptive antenna system where the radiating elements would be driven through switches activated either by earth sensors or received signal strength of the ground-based command system. Only the antenna coplaner with the receive antenna providing the best signal would be driven. This would reduce the output power required from the trans-mitter, but would require a separate receiver for each receiver antenna on the spacecraft plus a decision and switching logic network. The adaptive antenna scheme would no doubt require less power than the baseline, but in the end it would be less reliable.

The baseline design that was selected is very conservative. It is based on proven techniques and has the fewest active elements. The baseline

system is an omnidirectional array, consisting of four radiating elements spaced at 90-degree intervals around the spacecraft midsection and alternately polarized. This system will give good coverage except off the ends of the spacecraft. A short duration signal dropout is likely in the event that the spacecraft longitudinal axis trains momentarily on the ground station.

Other configurations are certainly possible, and it is quite likely that detailed design and test will result in improved coverage with fewer radiating elements. Antenna pattern testing will play an important role in the final selection.

b. <u>Multiple Link Operation.</u> Early in the program, consideration was given to provide a separate tape track and RF link for each experiment. This would lead to a large number of data links operating at relatively low data rates.

Since it appears that the STADAN network will be limited to accommodation of two RF links, this concept was discarded.

c. <u>Tape Recorders.</u> The tape recorder chosen for the HEAO communication/data system must be an optimal combination of several desirable characteristics. These include high reliability, high storage efficiency, lightweight, low power drain, and small size.

The search for suitable, space-qualified tape systems is narrowed to two candidate systems.

The first of these is the Leach 2000, which was selected for the baseline system. The Leach 2000 offers small size, reliability, and high density (10 000 bits per inch) recording. This high density mode is particularly attractive for the HEAO application. For a given recorder size, much more data can be stored. For a given data rate, tape speeds are lower, therefore enhancing tape and transport reliability.

Since the high density recording technique is relatively new, it is appropriate to consider alternatives. The most obvious alternative would be to use parallel recording techniques. A digital bit density of 2000 bits per inch per track is easily attainable. If a five-track parallel digital format were used, effective packing densities of 10 000 bits per inch of tape are possible. A serial-to-parallel converter would be necessary at the recorder input and a parallel-to-serial converter would be required at the recorder output.

During the Phase A study, it was assumed that a tape recorder physically and electrically similar to the Leach 2000 series recorder with an effective recording capacity of 10 000 bits per inch would be available by the time final hardware selection was made.

An alternative to the Leach 2000 recorder is the Borg Warner R-310. This machine is now undergoing final qualification for use in the Apollo Telescope Mount Program. Bit densities of 3200 to 4000 thousand bits per inch per track are available. Up to 8 tracks of serial pulse code modulated (PCM) data may be recorded on the tape by reversing the tape direction at tape end. This reversal effectively converts the 350-foot tape reel to 10 800 feet of available recording track. Data storage capability is therefore (10 800) (12) (3200) = 415 megabits or 4 × 415 = 1660 megabits for the four recorder system.

Because of the lower bit density and serial "zig-zag" format, tape movement will be about 313 inches per million bits of data recorded as compared to 50 inches with the Leach 2000. This tends to favor the Leach system for long-term mission reliability.

Additionally, the Leach machine can accept the two channels of digital data simultaneously, resulting in having only one machine at a time on line in either record or playback modes. Since the Borg-Warner machine is a one-channel system, two machines would have to operate simultaneously in record and playback, resulting in less redundancy for the basic four-recorder system and increased power consumption. A functional block diagram of the Borg-Warner system appears in Figure I-1.
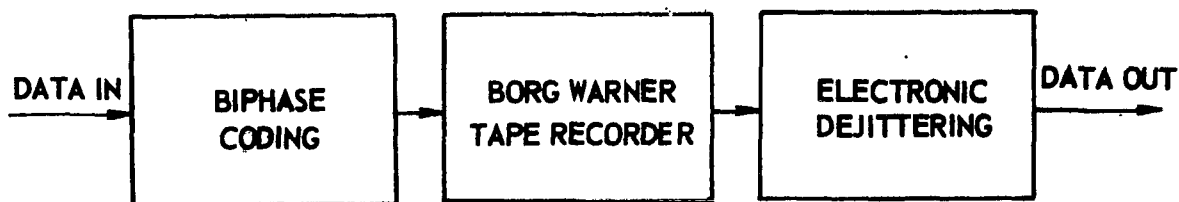

Figure I-1. Borg Warner tape system functional block diagram.

Consideration was given to the use of parallel digital tape recording formats. Such systems are attractive when the storage capability of a multitrack parallel format is considered. However, serial-to-parallel converters would be required between the data multiplexer and the tape recorder input. Additionally, parallel-to-serial conversion would be required before

presentation of the data to the S-band transmitters. These two additional operations add to the complexity of the data-handling system without a significant increase in system performance. Quarter-inch tape machines are limited to 5 to 7 parallel tracks, and larger transports have not been considered because of increased weight, volume, and power demands. Bit density for parallel digital operation is much below that allowable for serial digital operation.

2. Further Considerations

Preliminary analyses were conducted in the areas of communications/ data systems that were not well defined at this time. These areas are recommended for further study during Phase B.

a. <u>Interfaces.</u> The system interface between the experiments and the data-handling subsystem must serve as a data buffer.

Since most experiment outputs are dependent on sensed events, the data generated are asynchronous in time. The data multiplexer samples experiment outputs synchronously, so some memory is required in the interface to store data until the multiplexer samples it. Since the multiplexer sampling rate would be at least equal to the average data generation rate of an experiment, the memory requirement is small. Some form of core solid-state memory is indicated.

Discussions with representatives of potential experimenters indicate that at this time many experimenters favor a separate interface unit for each experiment, integral with experiment electronics. This approach would require that great care be taken in the area of system compatibility. The present state of development of the experiment data circuitry has been for interface with telemetry for a balloon flight. The experiment outputs are not presently suitable for incorporation into a system where telemetry links must be shared with other experiment and systems data.

A great deal of coordination will be required to fit the various data sources into a coherent system. Data compression possibilities and elimination of redundant data outputs (such as each experiment generating spacecraft attitude or timing data) should be a major Phase B effort.

In the long run, a central data buffer and interface which is part of the spacecraft communications/data system may prove to be the only interface method flexible enough to cope with changes in experiments or mission

objectives. If this concept is used, the experimenters must be given clear specifications for data outputs, and the experiment data circuitry must be designed to interface with the spacecraft system, rather than vice versa. Only in this way can a flexible and universal spacecraft data-handling system be developed.

b. Reliability. Preliminary estimates indicate that the communications/data system is inherently one of the least reliable spacecraft systems because of the records. To achieve a system design lifetime of 2 years, maximum use must be made of available techniques for enhancing system reliability.

The most useful techniques for systems of this sort include parts and components screening, careful "burn-in," and system redundancy. The baseline system has a considerable amount of redundancy built in at this stage of design. The ability of the system to tolerate individual equipment failures and still achieve a large portion of mission goals is illustrated in part by the discussion on tape recorder operation in Paragraph B of Section X.

In actual operation, the "standby redundancy" concept described in the reliability section of this report will be the most important single method of meeting system reliability goals.

c. Variable Data Formatting. Variable data formatting improves the ability of the spacecraft communications/data system to adjust efficiently to changes in spacecraft mission or to experiment failures or shifts in emphasis.

If, for example, an experiment that generated 8000 bits per second should fail, almost 30 percent of the total data capacity would be lost. A variable format could either reallocate the available information bandwidth to other experiments, or reduce the overall data rate, which would simplify ground data acquisition and data reduction operations.

Two basic methods for accomplishing reformatting are available. The first would involve use of an on-board computer and would be completely flexible, as in the Small Scientific Satellite (S³) program. The other alternative is to "hardwire" a small number of fixed data sampling formats designed to take care of major contingencies, such as a high data rate experiment failure.

This second method appears to be simpler to implement, and offers most of the advantages of the first. Further study will be required after experiments are defined to arrive at a final solution to this problem.

d. Data Relay Satellite Alternative. The baseline system in the 200-n.mi. 28.5-degree inclination orbit will not provide two orbits of data per day with an interval of 12 hours between contacts to a mission control center in the USA. This was evident in the station contact analysis. There are several alternatives that could be explored that would satisfy this mission requirement, if it should continue to receive consideration in program planning. A satellite dedicated to data relay will not be available until 1975 or later, but present plans indicate that the ATS-F spacecraft should be in orbit contemporary with the HEAO. The geosynchronous orbit and the large aperture antenna that will be a part of the ATS-F make it a candidate for possible data relay activities. A satellite in geosynchronous orbit will be able to contact a satellite at lower orbit for slightly over half an orbit. Therefore, the data taken by the HEAO when it is behind the earth and the data currently being gathered would be transmitted to the relay satellite. These could be equal data rates since the playback period of the tape recorder could be the same as the write period. In the case of the baseline design, the data rate would be reduced to 27.5 instead of 200 kilobits per second; however, the range is increased to 22 400 n.mi. The link considerations are shown in Table I-1.

TABLE I-1. HEAO TO ATS-F/G LINK CALCULATIONS

HEAO Transmitter	43	dbm (20 watts)
Antenna	-2	db
Polarization Loss	-0.3	db
Space loss (22 400 n.mi.)	-191	db
ATS-F Antenna Gain	37	db
Received Power	-113.3	dbm
ATS-F Noise Power	-169.8	dbm/Hz
ATS-F IF BW (12 MHz)	55.7	db
Degrees N	-114.1	db
S/N in IF BW	0.8	db

This adverse margin could only be increased by a directional antenna and a pointing system on the HEAO or increased transmitter power. The present NASA policy with regard to the use of ATS-F precludes its use for operational data relay. If this policy should change, then consideration may be given to this alternative although it appears of limited attraction.

e. <u>Orbital Plane Inclination.</u> In an effort to improve the tracking station contact time, in particular the duration of the contacts and the frequency of the conacts at Rosman, consideration was given to those parameters that determine these characteristics, primarily altitude and inclination. The maximun north and south latitude that the subsatellite point reaches is always equal to orbital inclination. The latitude of Rosman is 35 degrees 12 minutes north; therefore, all the passes for a 28.5-degree inclination orbit would be low in the southern sky and of short duration. Increasing the inclination to equal the latitude of the station raises the spacecraft higher in the sky and thus results in zenith passes which are slightly longer. To examine this situation in more detail, GSFC furnished a computer run of STADAN station contacts. This run is summarized in Table I-2 and compared with the 28.5-degree case.

TABLE I-2. SUMMARY OF TRACKING STATIONS AVAILABILITY

200 n. mi.	i = 28.5 deg	i = 35 deg
Orbits examined	100	100
Orbits with contacts ≥ 6 min.	37	58
Orbits with contacts ≥ 5 min.	71	90
Orbits without a contact	7	5
Consecutive orbits without a contact ≥ 5 min.	3	2

To further examine the impact of increased inclination on the data in the storage system, several curves were generated. Data in storage at the beginning (just prior to Rosman contact) of each orbit for both the 28.5- and 35-degree inclinations were computed using only those contacts that exceed 5 minutes and using a dump rate of 400 kilobits per second during contact. The curves are shown in Figure I-2. At first, the 35-degree case appears to give a significant gain; however, closer scrutiny indicates that a reduction from 800 to 500 megabits peak storage is still beyond the capability of a single base-line design tape recorder; an additional 300 feet of tape is therefore needed in a second recorder, which would also be required for redundancy and for down time of the tracking stations. The reduction from four recorders to two does not significantly impact the weight and power of the overall spacecraft but it simplifies and improves the reliability of the data system somewhat. This improvement would have to be weighed against launch vehicle performance, scientific instrumentation saturation and other factors during the Phase B study before a final orbit selection could be made.
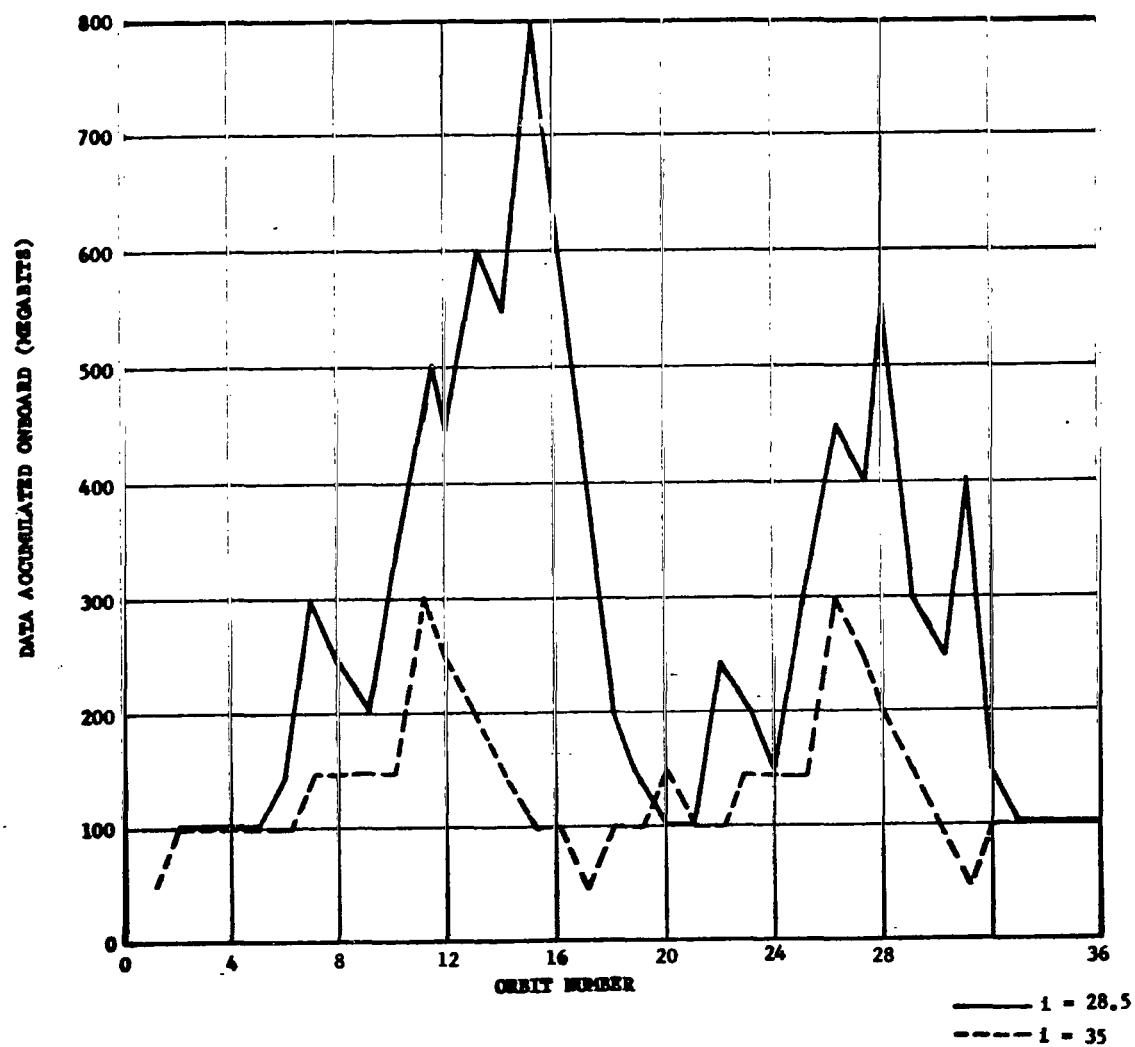
I-8

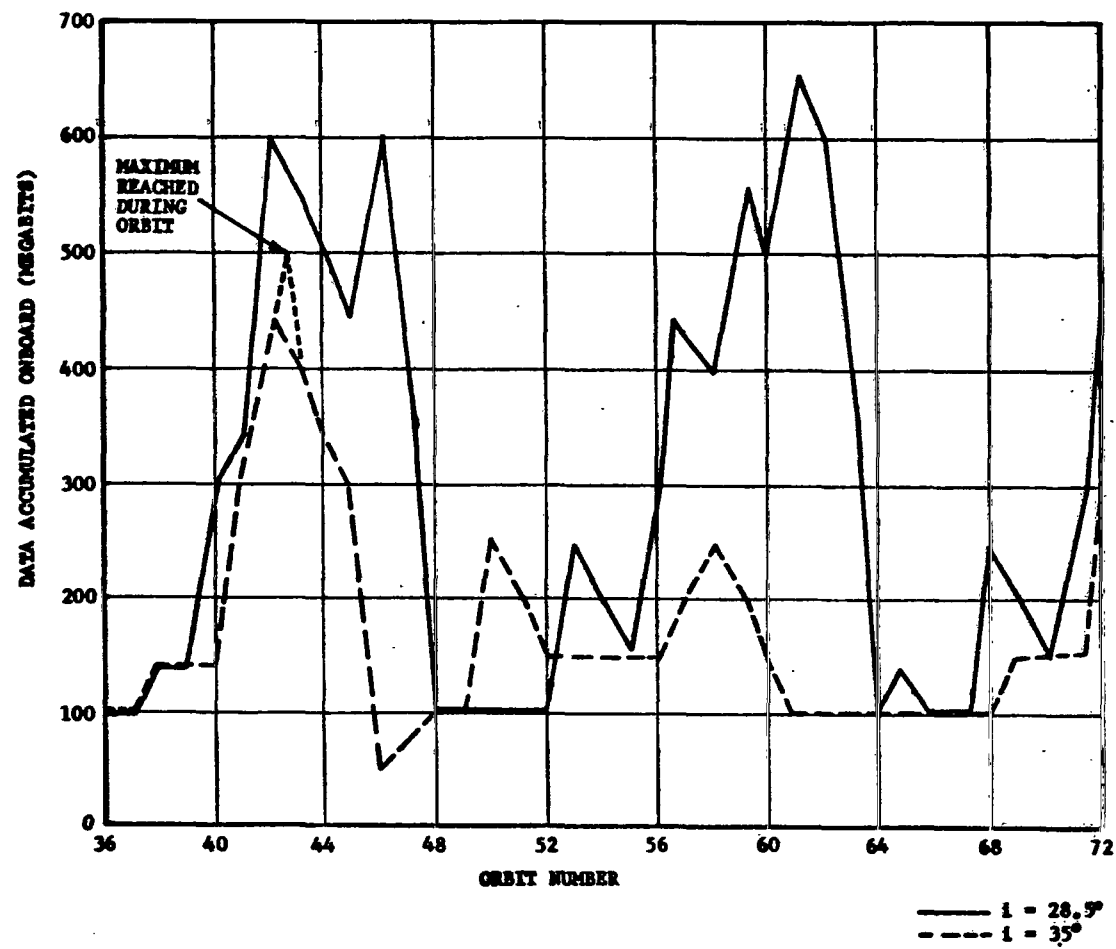Figure I-2. Comparison of data storage as a function of inclination angle.

Figure I-2.   (Concluded).

It was stated early in the study that it would be desirable to have one prime tracking station that would handle all the communication with the spacecraft. In addition, it would be desirable to have two orbits of near real time data per day at the control center. If these two requirements were met, this would dictate that Rosman be the prime tracking station and that some other station whose contacts occur on the orbits when the spacecraft trajectory remains below the horizon at Rosman be the backup station. Santiago contacts usually occur about midway of the time interval when Rosman is out of contact. For a 28.5-degree inclination orbit, there would be 5 orbits between the last Rosman contact and the first Santiago contact. The gap would be 7 orbits between the last Santiago contact and the first 5 minute contact with Rosman. In each instance, the contacts at both Rosman and Santiago are for only two consecutive orbits. The data rates on the down link must be capable of dumping 7 orbits ($\approx$ 1050 megabits) of data in two 5-minute contacts. This amounts to 1.75 megabits per second. If two links are used, as in the baseline design, the individual link capacity could be reduced to 875 kilobits per second. This is 4 times the present GSFC standard for the STADAN network.

The 35-degree inclination orbit shows some reduction in out of contact time. The interval between Santiago and Rosman is 5 orbits ($\approx$750 megabits) and both Rosman and Santiago have 3 consecutive orbits of at least 5 minutes duration. The data dump rate would be reduced to approximately 400 kilobits per second per link. Data rates as high as this are possible with the present ground station hardware. The standards for the ground stations will very likely be updated in the near future to allow higher rates. It should be noted that the maximum data storage capability of the baseline design system is compatible with this scheme.

APPENDIX J. ATTITUDE SENSING
AND CONTROL SYSTEM

TABLE OF CONTENTS

TABLE OF CONTENTS (Concluded)

LIST OF ILLUSTRATIONS

LIST OF ILLUSTRATIONS (Continued)

LIST OF ILLUSTRATIONS (Concluded)

LIST OF TABLES

DEFINITION OF SYMBOLS

<u>Symbol</u>	<u>Definition</u>
A_{ab}	Transformational matrix between "a" and "b" coordinates
A_{mn}	Directional cosine (m, n = 1, 2, 3) element of A_{ab}
C	Cosine
CM	Center of mass
K	Control system feedback gains
e = 23.5 deg	Angle between ecliptic and equatorial planes
δ	Scan axis solar offset angle
H	Momentum (subscripts denote components)
$\tilde{I}$	Inertia matrix (dyadic)
I_{xy}, I_{xz}, I_{yz}	Products of inertia
I_x, I_y, I_z	Moments of inertia
i, j, k	Unit vectors (subscripts denote coordinate system)
L	Lever arm

DEFINITION OF SYMBOLS (Continued)

$\overline{R}_o$ — Unit vector along R

R_e — Radius of the earth

R — Distance from earth center to body CM (R_e + altitude)

R_x, $\overline{R}_y$, R_z — Vector components of $\overline{R}_o$ in body coordinates

γ, μ — Angles of longitude and inclination

S — Sine

T — Torque (subscripts denote components)

t — Time in seconds

t' — Time in days

W_o — Orbital angular rate

X_b, Y_b, Z_b — Body principal axes

X, Y, Z — Body fixed coordinates (structural)

X_e, Y_e, Z_e — Earth-equatorial coordinates

X_g, Y_g, Z_g — Geocentric inertial coordinates

X_o, Y_o, Z_o — Orbit fixed coordinates

X_1, Y_1, Z_1 — Inertial coordinates

DEFINITION OF SYMBOLS (Continued)

X_p, Y_p, Z_p	Local vertical (plumb line) coordinates
X_r, Y_r, Z_r	Body reference coordinates
X_s, Y_s, Z_s	Solar fixed coordinates
$\overline{X}$	Vector (subscripts denote coordinate system)
$\widetilde{X}$	Vector transpose of vector components
α_{mn}	Directional cosine angle, $\cos(\alpha_{mn}) = A_{mn}$
e_r, e_γ, e_μ	Unit vectors in spherical coordinates
X_m, Y_m, Z_m	Geomagnetic coordinates
X_n, Y_n, Z_n	Geographic coordinates
ψ, Θ, ϕ	Euler angles for body-reference axes misalignment
ξ	Declination (11 deg.) of the Earth's magnetic dipole
Ω_m	Longitude of the Earth's magnetic dipole
ι	Angle of orbital inclination (between orbital and equatorial planes)
Λ	Angle between sun-Aries and the sun-earth lines
λ	Earth's seasonal position (angle between Υ and earth-sun lines)

DEFINITION OF SYMBOLS (Continued)

Symbol	Definition
$\mu = GM$	Gravitational constant
Υ	Earth-sun-Aries inertial reference
Θ_o	Angle of orbital rotation (between ascending node and spacecraft)
Ψ_o	Angle between ecliptic and orbital planes ($\Psi = \alpha_{33}$)
Ω	Angle or orbital regression (between Υ and orbital ascending node)
$\overline{\omega}$	Spacecraft angular velocity vector (body coordinates)
$*$	Superscript denoting matrix transpose
$\cdot$	Superscript to indicate time derivative
$\overline{B}$	Earth's magnetic field in vector form
B_x, B_y, B_z	Vector components of $\overline{B}$
M_e	Earth's magnetic dipole moment (8.1×10^{25} emu)
C_x, C_y, C_z	Eigen vector components ($\overline{C}$)
α_e	Angle of rotation about $\overline{C}$
$\overline{M}$	Magnetic moment vector (coil dipole)
M_x, M_y, M_z	Vector components of $\overline{M}$

DEFINITION OF SYMBOLS (Continued)

<u>Symbol</u>	<u>Definition</u>
$h_f = I_f W_f$	Flywheel momentum
I_f	Flywheel inertia
W_f	Flywheel spin rate
W_s	Vehicle scan rate
$\overline{H}$	Momentum vector
h_x, h_y, h_z	Vector components of $\overline{H}$
$\overline{T}$	Torque vector
T_x, T_y, T_z	Vector components of $\overline{T}$
σ	Coil resistivity
ρ	Coil density
D	Coil diameter
V_c	Coil volume
WP	Coil mass-power product
L	Length
A_{ref}	Reference area
C_A	Axial force coefficient, $\dfrac{F_A}{q\,A_{ref}}$

DEFINITION OF SYMBOLS (Continued)

Symbol	Definition

C_L — Rolling moment coefficient, $\dfrac{M_X}{q\,A_{ref}\,D_{ref}}$

C_m — Pitching moment coefficient, $\dfrac{M_Y}{q\,A_{ref}\,D_{ref}}$

C_N — Normal force coefficient, $\dfrac{F_N}{q\,A_{ref}}$

C_n — Yawing moment coefficient, $\dfrac{M_Z}{q\,A_{ref}\,D_{ref}}$

C_Y — Side force coefficient, $\dfrac{F_Y}{q\,A_{ref}}$

D_{ref} — Reference diameter

F_A — Axial force (positive in the negative direction of X)

F_N — Normal force (positive in the negative direction of Z)

F_Y — Side force (positive in the positive direction of Y)

M_X — Rolling moment; i.e., moment about the X-axis (a positive rolling moment tends to rotate the positive Y axis toward the positive Z axis)

DEFINITION OF SYMBOLS (Concluded)

Symbol	Definition
M_Y	Pitching moment; i.e., moment about the Y axis (a positive pitching moment tends to rotate the positive Z axis toward the positive X axis),
M_Z	Yawing moment; i.e., moment about the Z axis (a positive yawing moment tends to rotate the positive X axis toward the positive Y axis)
q	Dynamic pressure, $\frac{1}{2} \rho V^2$
$\overline{V}$	Velocity of the body relative to the surrounding atmosphere
V	Speed of the body relative to the surrounding atmosphere, $V = |\overline{V}|$
V_X, V_Y, V_Z	Components of the velocity in the direction of the respective X, Y, Z axes (positive in the positive direction of the coordinate denoted by the subscript)
X, Y, Z	Longitudinal, lateral and normal axes, respectively
α	Angle of attack (angle between the plane formed by the X and Y and the plane formed by the Y axis and $\overline{V}$)
α_T	Total angle of attack (angle between $\overline{V}$ and the positive X axis)
β	Yaw angle (angle between the plane formed by the X and Z axes and $\overline{V}$)
ϕ	Roll angle (this is the angle between the plane formed by the velocity vector and the X axis and the plane formed by the X and Z axes)

APPENDIX J. ATTITUDE SENSING
## AND CONTROL SYSTEM

1. Alternate System Considerations (Sensors)

a.   Star Mapper Alternate.   An alternate to the slitted reticle star
mapper discussed in the baseline configuration is an instrument which generates
a star map through an electronic scanning technique.   The beam scanning type
mapper has two modes of operation: acquisition and tracking.   If this type of
instrument is used to provide a star map while the spacecraft is operating in
one of the scanning modes, it will be operated in the acquisition mode only.
In the acquisition mode, a small field of view (FOV) is electronically swept
through the larger instrument FOV.   The smaller FOV scans the larger FOV
from left to right in steps until the entire field is covered; the scan is then
repeated.   If there is a star image in the instrument FOV, its coordinates with
respect to the optical axis will be measured as it is scanned by the smaller
FOV; thus, a star map is provided.   Operation of the beam scanning tracker in
both acquisition and track modes is illustrated in Figure XI-19.

Both the instrument FOV and the scan rate determine the accuracy
of star positions.   It appears that instrument FOV and scan rate can be designed
to meet the ±0.1-degree accuracy requirement in the attitude determination
solution; however, this has not been verified.

b.   Digital Sun Sensor Alternate.   An alternate to using the digital sun
sensor for solar offset tracking in the galactic scan mode is to locate a guide
star tracker on the spacecraft Z-axis to track guide stars at some angle, δ,
from the solar vector, which lies in the ecliptic plane.   Figure J-1 illustrates
this scheme.   The star image is focused in the tracker FOV by the imaging
optics.   The position of the image with respect to the optic's cross axis is given
as a two-component error signal which represents scan-axis deviations from
the star.   The errors generated by the star tracker are processed by the atti-
tude sensing and control system (ASCS) computer and result in the production
of control torques which tend to align the scan axis on the guide star.   This
procedure is termed "nulling" on target.

Using the tracker in this manner causes the attitude of the scan axis
of the spacecraft to be fixed in space; this results in the same area of the galactic
plane region being repeatedly scanned.   Reorientation of the scan axis to another
star permits scanning of a different portion of the galactic plane region.   The
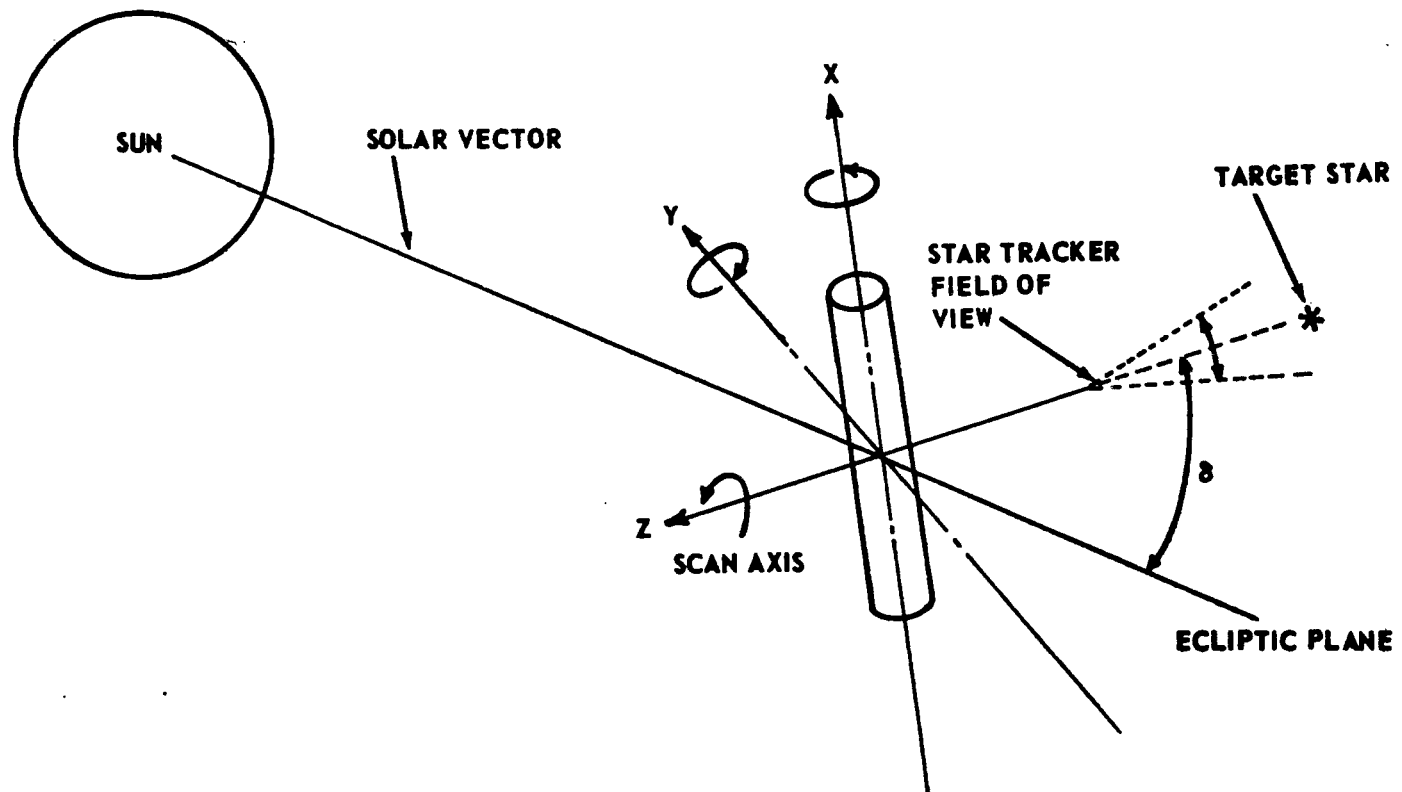
NOTE: δ – SOLAR OFFSET ANGLE REQUIRED
FOR GALACTIC ACQUISITION

Figure J-1. Solar offset guiding stellar tracking.

disadvantage of this technique is its dependence on the availability of suitably located guide stars since the guide star must be located almost exactly on the azimuth of the desired scan-axis orientation. After completing the desired scan of one portion of the galaxy, it is necessary to reorient the scan axis to a second suitably located guide star. If the angle to the second guide star is greater than the narrowest scanning experiment FOV, some portion of the area of interest will not be scanned.

If guide stars are not suitably located to permit complete coverage of the area of interest by the method just described, it may be possible to use a somewhat different technique. In this technique, either a fixed star tracker having a wider FOV or a gimbaled star tracker is used to track a guide star located at some angle off the desired scan-axis orientation.

The strapdown trackers with off-axis tracking capability necessarily must have a larger FOV than those designed to track on-axis. The larger FOV creates some potential target identification problems; however, this can be minimized by adding automatic threshold adjust circuitry. If the known maneuver will put two stars of the same magnitude in the FOV, then the next higher or lower magnitude star within the tracker's FOV may serve as the target source. A beam scanning type tracker would be a suitable instrument for this off-axis tracking function. The operation of this type of instrument has been previously discussed for use as a star mapper. In the present application, when the target star is detected by the scanning FOV the track mode is automatically switched in. The null position of the tracker is electronically shifted from the optic cross axis to the desired offset position of the guide star. Two-axis error signals are generated giving scan-axis deviations from this offset position. Data from the star tracker located in the spacecraft X-axis would be utilized to measure any scan-axis drift around the cone of half angle equal to the off-axis angle.

Using a gimbaled star tracker permits the use of a smaller FOV for the instrument, thereby reducing ambiguity in target identification. However, the low reliability associated with gimbaled systems may not prove suitable for the 2-year HEAO mission. Using a gimbaled star tracker does require a second reference to prevent scan-axis drift around the offset angle cone and to provide the additional reference to give two-axis error signals. The use of a gimbaled star tracker requires a more complex implementation scheme than the strapdown design tracking either "on" or "off" axis.

c.   Earth Horizon Scanner. To control scan-axis drift around the offset angle cone using the stellar offset tracking technique discussed previously, the earth may be used to provide a second reference for holding spacecraft position. There are several types of earth sensors available for use; however, the conical scan type appears to be the most suitable for consideration in this scheme. Figure J-2 illustrates the use of this sensor. The conical scanner rotates at a rate to scan across the horizon at a frequency of approximately 6 times per second. Each time the scanner cross axis is aligned with the spacecraft axis, a reference time pulse is generated. At the instant of earth intercept, another time pulse is generated. The difference between these two pulses together with the spacecraft scan rate gives the instantaneous position of the spacecraft X-axis with respect to the local vertical. In addition, the scan-axis (Z-axis) position with respect to the local vertical may be calculated using horizon scanner outputs and orbital parameter information. The sensor does not provide this angle directly. A coordinate system transformation is required which transfers the spacecraft position in earth coordinates to the inertial system.

To utilize horizon scanners to provide a second reference for offset star tracking, an onboard computation will be required to determine the space-craft attitude. Continuous attitude determination is difficult to implement, since compensation for orbital nodal precession must be made. However, it can be implemented by sensing the scan-axis drift motion using the star tracker and triggering on a 1.0-degree deadband. Scan-axis drift motion can be detected by measuring the period of a signal generated by the star tracker. Because of the spacecraft rotation, the star tracker two-axis output is a time varying signal. The period of the tracker output signals must equal the scan-rate signal period if no scan-axis drift exists. If scan-axis drift occurs, the period of the star tracker output signal changes relative to the scan-rate signal period. By gating the zero crossing of the star tracker outputs to a high-frequency counter and doing the same with the scan rate signal, frequency measurement differences can be detected. The amount of difference would be proportional to the amount of drift. Corrective action is taken to maintain a 1-degree drift maximum.

The earth horizon sensors can be used in lieu of the star tracker located on the spacecraft Z-axis to provide a second reference source. The horizon sensors would be used with the digital sun sensor in the galactic scan mode.
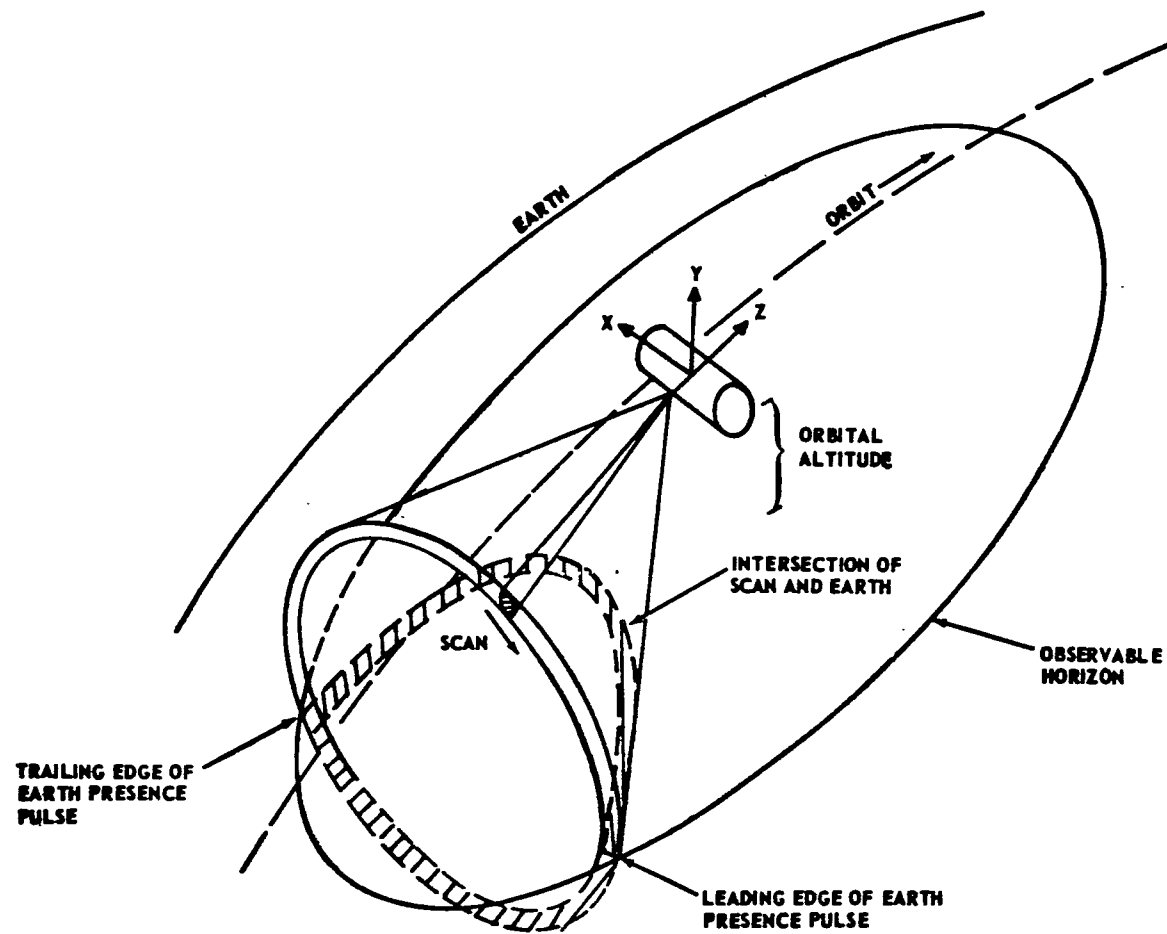
J-4

Figure J-2. Horizon scanner.

Using the conical scan-type horizon sensor will be expensive. Two scanning sensors would be required in the spacecraft to allow continuous earth coverage. To assure continuous earth coverage during the orbital period, the sensor's location on the spacecraft may require canting of the sensor axis with respect to the spacecraft body axis.

2. Magnetic Torquer Sizing

The sizes of the magnetic torquers required for the HEAO spacecraft were determined as described below. Magnetic torquers may be either empty coils or coils with core material; the sizing of both types is discussed below. Magnetic torquers will perform two functions on the HEAO spacecraft; scan-axis attitude orientation control- and scan-rate control.

a. Scan-Axis Attitude Control Coil. The coil located on (parallel to) the scan axis of the spacecraft should be capable of producing a control torque equal to the maximum value of the disturbance torque which acts in the plane normal to the scan axis. The maximum value of this disturbance torque was calculated to be 0.0727 ft-lbf. The minimum value of the component of the earth's magnetic field that is effective for scan-axis attitude control is expected to be not less than 0.10 gauss. The magnetic moment (M) required to produce a control torque (T) of 0.0727 ft-lbf in a field of 0.10 gauss is

$$M = \frac{T}{B} = \frac{0.0727}{0.10} = 0.727 \text{ ft-lbf/gauss}$$

or

$$M = 9858.1 \text{ amp-m}^2 \qquad .$$

1. Coil with no core material. The windings of this coil would be placed around the inside surface of the spacecraft to obtain the maximum possible coil area and hence the maximum magnetic moment. In this arrangement, most of the space inside the coil is occupied by materials of low permeability and the coils can be regarded as air cored.

J-6

The mass power product in watt-kilograms for a circular coil is given by Reference J-1 as

$$WP = \frac{16 \, \sigma \, \rho \, M^2}{D^2} \quad ,$$

where

σ — resistivity of the coil (2.82×10^{-8} ohm-m for aluminum)

ρ — density of the coil (2.7×10^3 kg/m^3 for aluminum)

M — magnetic moment required (9858.1 amp-m^2)

D — diameter of the coil (7 ft $\equiv$ 2.133 m)

Solving this equation gives

$$\frac{16 \times 2.82 \times 10^{-8} \times 2.7 \times 10^3 \times (9858.1)^2}{(2.133)^2} = 26 \, 021 \text{ watt-kg} \quad .$$

If the power available for use by the scan-axis attitude control coil is limited to 100 watts, the weight of the coil is 260.21 kg or 573.79 lb. This coil weight can be reduced by using coils having a suitable core material.

2. Coil with core material. Selection of core material is based on a desire for low coercive force and low permeability to provide ease in magnetization and high dipole moment per unit weight. If Permendur is used for the core material, then it is possible to provide a saturated field strength (B_s) of 2.33 webers/m^2 with a field (H) of 3940 amp-turns/m [J-2].

The volume of core material (V_c) needed to produce a magnetic moment (M) of 9858.1 amp-m^2 is given by

$$V_c = \frac{\mu_0 \, M}{B_s}$$

where μ_0 = the permeability of Permendur, = 4π by 10^{-7}. Solving this equation gives

$$V_c = \frac{4\pi \times 10^{-7} \times 9858.1}{2.33} = 5.317 \times 10^{-3} \text{ m}^3 \quad .$$

The density of Permendur is 8.32 by 10^3 kg/m^3. Therefore, the mass of Permendur required is

$$M_p = 5.317 \times 10^{-3} \times 8.32 \times 10^3 = 44.24 \text{ kg} \ (97.55 \text{ lb})$$

A length-to-diameter ratio of 20 was chosen as convenient for the size of the core material.

Then the core length L = 20 D and the volume of a cylindrical-shaped core is given by

$$V = \frac{\pi}{4} D^2 L$$

or

$$V = 5\pi D^3 \quad .$$

Therefore, the core diameter is

$$D = \left(\frac{V_c}{5\pi}\right)^{1/3} = \left(\frac{5.317 \times 10^{-3}}{5\pi}\right)^{1/3} = 0.070 \text{ m} \ (2.76 \text{ in.})$$

and the length is

$$L = 20 D = 1.40 \text{ m} \ (4.59 \text{ ft}) \quad .$$

J-8

The mass power product in watt-kilograms for the coil, excluding the core, is given by

$$WP = 4 \pi H^2 L \sigma \rho V_c$$

where

L – length of the core = 1.40 m

V_c – volume of the rods = 5.317×10^{-3} m^3

H – field strength = 3940 amp-turns/m

Solving this equation gives

$$WP = 4 \pi (3940)^2 \times 1.40 \times 2.82 \times 10^{-8} \times 2.7 \times 10^3 \times 5.317 \times 10^{-3}$$

$$= 110.56 \text{ watt-kg}$$

If the power is limited to 100 watts, the mass of the windings is 1.11 kilograms (2.45 pounds).

Therefore, total weight of the core material plus windings is

$$44.24 \text{ kg} + 1.11 \text{ kg} = 45.35 \text{ kg} (100.00 \text{ lb}) \qquad .$$

The length of the coil windings (L) is given by

$$L = \left(\frac{R\,W}{\rho\,\sigma} \right)^{1/2}$$

where R is the resistance of coil and W, ρ, σ, are as previously defined. For a maximum power available of 100 watts, a coil of 10 ohms resistance will have a maximum current of 3.17 amps, which is low enough for transistor circuitry. For a coil resistance of 10 ohms, the winding length L is

$$L = \left(\frac{10 \times 1.11}{2.7 \times 10^3 \times 2.82 \times 10^{-8}} \right)^{1/2} = 381.8 \text{ m} \quad .$$

The perimeter p of the circular coil windings is given by

$$p = \pi \text{ diameter} \quad .$$

Thus,

$$p = \pi \times 0.07 \text{ m} = 0.2199 \text{ m} \quad .$$

The number of turns of coil winding is

$$N = \frac{L}{p}$$

or

$$N = \frac{381.8}{0.2199} = 1736 \text{ turns} \quad .$$

b. **Scan Rate Control Coils.** Preliminary results of spacecraft motion simulation indicate a variation of about 1 percent in the scan rate during one orbit of the spacecraft. Therefore, a control torque which is capable of changing the scan rate by 1.1 percent during a 60-second period would appear to be adequate. On this basis, the coils located on the axes normal to the scan axis were sized to produce a change in the scan rate of 0.0067 deg/sec in a

60-second period. The torque required to change the scan rate of the spacecraft by 0.0067 deg/sec in a 60-second period is

$$T = I\dot{\omega}$$

where

T — torque, ft-lb

I — mass moments of inertia about the spacecraft scan axis, 36 900 ft-lb-sec^2

$\dot{\omega}$ — angular acceleration of the spacecraft about the scan axis, radians/sec^2.

Solving this equation gives

$$T = \frac{36\ 900}{60} \times \frac{0.0067}{57.3} = 0.072 \text{ ft-lbf} \qquad .$$

Scan-rate control is carried out whenever the earth's magnetic field component along the scan axis is as small as possible to minimize the cross-coupling effect of rate control torques on the scan axis. For this condition the total earth's field, which varies from 0.263 to 0.372 gauss, lies in the plane normal to the scan axis. Therefore, the lower value of 0.263 gauss was used as the strength of the earth's field for sizing the scan-rate control coils. The magnetic moment of each coil is

$$M = \frac{T}{B} = \frac{0.072}{0.26} = 0.277 \frac{\text{ft-lb}}{\text{gauss}}$$

or

$$M = 3756 \text{ amp-m}^2 \qquad .$$

1.   Coils with no core material.   The mass power product in watt-kilograms for a circular air coil is

$$WP = \frac{16\,\sigma\,\rho\,M^2}{D^2}$$

or

$$WP = \frac{16 \times 2.82 \times 10^{-8} \times 2.7 \times 10^3\,(3756)^2}{(2.133)^2} = 3778 \text{ watt-kg} \quad .$$

For 20 watts of power available for scan-rate control the mass of coil is 188.9 kg or 415.6 lb.   Total weight for two coils is about $2 \times 416 = 832$ lb and total power required is 40 watts.

2.   Coils with core material.   If Permendur is used for the magnetic rods (core material), the volume of rods required is

$$V_c = \frac{\mu_0\,M}{B_s}$$

or

$$V_c = \frac{4\pi \times 10^{-7} \times 3756}{2.33} = 2.026 \times 10^{-3}\ m^3 \quad .$$

The mass of the rods is

$$2.026 \times 10^3 \times 8.32 \times 10^3 = 16.86 \text{ kg } (37.12 \text{ lb}) \quad .$$

For rods, a length-to-diameter ratio of 20 is taken, then the rod diameter is given by

J-12

$$D = \left(\frac{V_c}{5\pi}\right)^{1/3}$$

or

$$D = \left(\frac{2.026 \times 10^{-3}}{5\pi}\right)^{1/3}$$

where $D = 0.0114$ m and rod length $L = 20D = 0.228$ m.

The mass power product for the windings of the electromagnet is

$$WP = 4\pi H^2 L \sigma \rho V_c \qquad .$$

Substituting the values gives

$$WP = 4 (3940)^2 \times 0.228 \times 2.82 \times 10^{-8} \times 2.7 \times 10^3 \times 2.026 \times 10^{-3}$$

$$= 6.86 \text{ watt-kg} \qquad .$$

For 20 watts of power available for scan-rate control, the mass of windings required is 0.34 kg (0.75 lb). The weight of the rods plus windings is

16.86 kg + 0.34 kg = 17.20 kg (37.87 lb)

From this analysis it appears that it is better to use electro-magnets rather than empty coils. In this analysis no attempt has been made to optimize the magnetic moment producing devices for mass and power.

In the celestial pointing mode of spacecraft operation, any one of the three axes of the spacecraft may be required to point in some inertial direction and its attitude held within ± 1 degree. This will require a three-axis attitude control system. Since the roll angle on the pointing axis is not required to be precisely controlled, and can vary as much as ● 37 degrees, a two- or three-coil system can be used for pointing mode operation. The coil located parallel to either the X· or Y spacecraft axis should be the same size as the coil located on the scan (Z) axis. The third coil may be smaller than the other two because its primary use will be scan rate control.

Therefore, the total weight of the three coils is (100 + 100 + 37. 87) = 237. 87 lb, and requires a maximum of 100 watts of power. Providing 24 lb for insulation cover, mounting, connection, etc. , the total weight of the three coils becomes (237. 87 + 24) = 262 lb.

3. Celestial Pointing Mode

The baseline concept assumed early in this study for this mode assumes that the spacecraft Z-axis is kept aligned with the solar vector at all times. This concept reduces flexibility in choice of targets since the target will be in a favorable position for viewing only twice per year. By carefully programming the sequence of target sightings, the baseline concept can be implemented using a simple attitude control system.

An alternate approach to performing this mode is possible without using any additional sensors or actuators other than the ones specified for the baseline system. The primary constraint for this alternate is that the Z-axis offset from the solar vector must not exceed approximately 37 degrees; however, this limiting offset angle can possibly be increased by turning off the electrical power to experiments that have no interest in gathering data during this particular time of operation. The scheme requires that the Z-axis be offset from the sunline and that the spacecraft be rolled about the Z-axis until the experiment line of sight is aimed at the point of interest. The two-axis digital sun sensor is used to measure the commanded solar vector offset angles about the X and Y axes. By the acquisition and recognition of a selected star, the star tracker, which has its line of sight along the X-axis, provides update information on the angle ϕ that is used to resolve the digital sun sensor measured angles into the θ, Ψ, and ϕ coordinates. Therefore, by obtaining ground-computed pointing information and by using the digital sun sensor to measure solar offset angles and the star tracker to supply information for the angle ϕ complete three-axis positioning of the spacecraft is possible.

The rate gyro package is again used to provide rate and position outputs for stabilization and for use in attitude holds during planned star and sun occultation periods.

In summary, the basic mechanization of this alternate approach is almost identical to that used for the galactic scan except for a change in control caused by the vehicle being nonrotating.

4. HEAO Coordinate Systems

It is necessary to select several reference coordinate systems and relate the selected system in physically meaningful geophysical terms so that the vehicles attitude (angular position) can be described at any instant of time. Furthermore, the environmental forces which act on an orbiting spacecraft are usually known or calculated with respect to a local vertical reference frame. Since the HEAO will have its principal body axes solar oriented, the local vertical must be transformed into solar coordinates to evaluate the environmental forces and estimate their impact on control system design. For example, evaluation of gravity gradient torques in body axes requires that the components of the unit local radius vector, $\overline{R}_O$, directed from the earth's center to the spacecraft center of mass, be obtained in body axes components. Since orbital parameters such as altitude, inclination, ascending line of nodes, and time of year are usually specified, $\overline{R}_O$ will be known or can be calculated in terms of a local vertical coordinate system. But for use in the gravity gradient torque equations, the components of $\overline{R}_O$ must be derived in terms of the body fixed frame.

Such a derivation will require the definition and use of several coordinate systems and transformations between systems. The actual number of transformations depends upon the specific mission of the orbiting vehicle and its desirable attitude orientation, and upon the accuracy in evaluating the torque components and the time interval over which the evaluation is to be made. For practical design purposes it can be assumed that the earth's orbit about the sun is circular instead of elliptical, the earth-moon barycenter is identical with earth center, and the spacecraft orbit is circular. These assumptions result in considerable simplifications in geocentric earth-sun inertial reference coordinates and orbital dynamics. The earth moves about the sun at a constant angular rate (Fig. J-3) of approximately 1 degree per day, the earth's solstices and equinoxes occur at even 90-degree intervals measured from Aires (an inertial reference denoted by ϒ), the moon's gravitational effects are ignored, and ephemeris tables or calculations are not necessary to specify the earth's seasonal position.
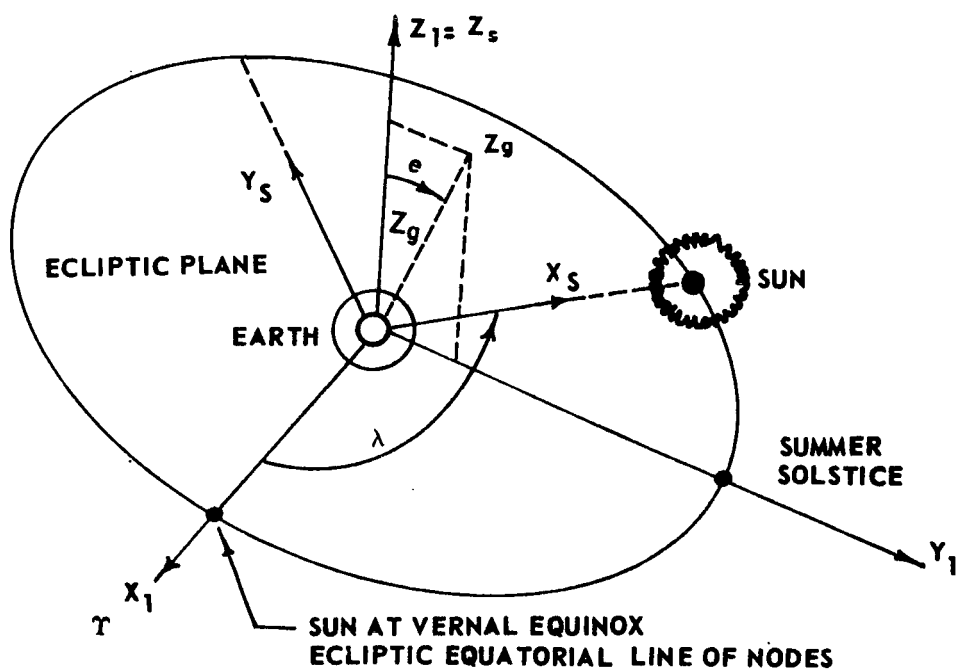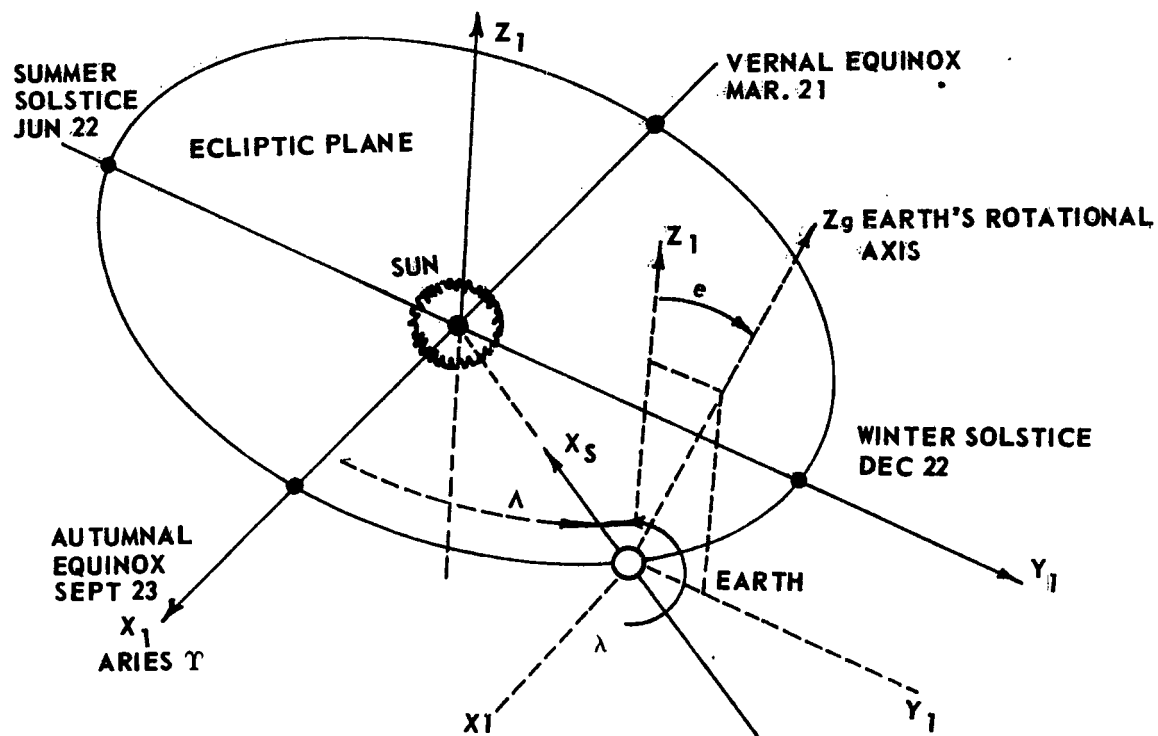
Figure J-3. Earth-sun inertially referenced to Aries.

Three planes relative to the celestial sphere provide the basic references for development of the coordinate systems necessary to describe the HEAO's attitude reference at any time: the orbital plane, equatorial plane, and ecliptic plane. In defining reference systems for the HEAO, standard coordinates, as given in Reference J-3, will be utilized when applicable. When defining axes relative to a plane, the following philosophy should be observed: the X-axis is utilized as a pointing axis in the plane (as examples, along an ascending line of nodes, the sunline vector, Aries inertial direction, etc.), directed from the geocenter or spacecraft to the object being located; the Z-axis is always perpendicular to the plane directed in a northerly direction (as examples, perpendicular to the orbital plane (POP), the ecliptic plane (PEP), etc.); and the Y-axis completes a right-hand triad in the plane. Angles are always defined in a positive sense by the right-hand rule being applied to the (X, Y, Z) triad. Unit vectors along the reference axis are denoted by the (I, J, K) triad. A subscript on the triads indicates a specific coordinate system. Reference J-4 provides a basis for the HEAO coordinate reference definition. In addition, a standard Euler angle sequence, References J-5 and J-6, Type 3, 2, 1, is necessary to express attitude errors from the desired reference frame. Since HEAO must be oriented toward the sun to receive the proper amount of solar energy for power conversion, solar coordinates are selected as the body reference frame and the Euler angles (Ψ, θ, ϕ) are used to express the vehicles attitude relative to the solar reference frame.

Figure J-4 indicates the earth-orbit-ecliptic plane geometry and the angular relations necessary to relate the spacecraft's orbital position to either inertial or solar coordinates. The subscripts on angles indicate the sequence in which the rotations must occur. The count may be either forward or backwards, but the arrows indicate a forward count rotation that brings the solar into the orbital coordinate system. The angles and coordinates between the three planes are shown in more detail in Figure J-5.

In performing transformations between coordinates, vector matrix notation is used for simplification whenever practical. For example, $\tilde{X}_s$ denotes the transpose of the triad (X_s, Y_s, Z_s) and the subscript "s" indicates solar coordinates. Capital letters are used to indicate matrices or transformations between coordinates with a double subscript to indicate the coordinates being related by the transformation. For example, A_{ab} denotes a matrix operation which carries the "b" into the "a" coordinate frame and is written algebraically as $\tilde{X}_a = A_{ab} \tilde{X}_b$. The elements of A_{ab} are identified by double numerical subscripts which indicate the row and column, respectively.
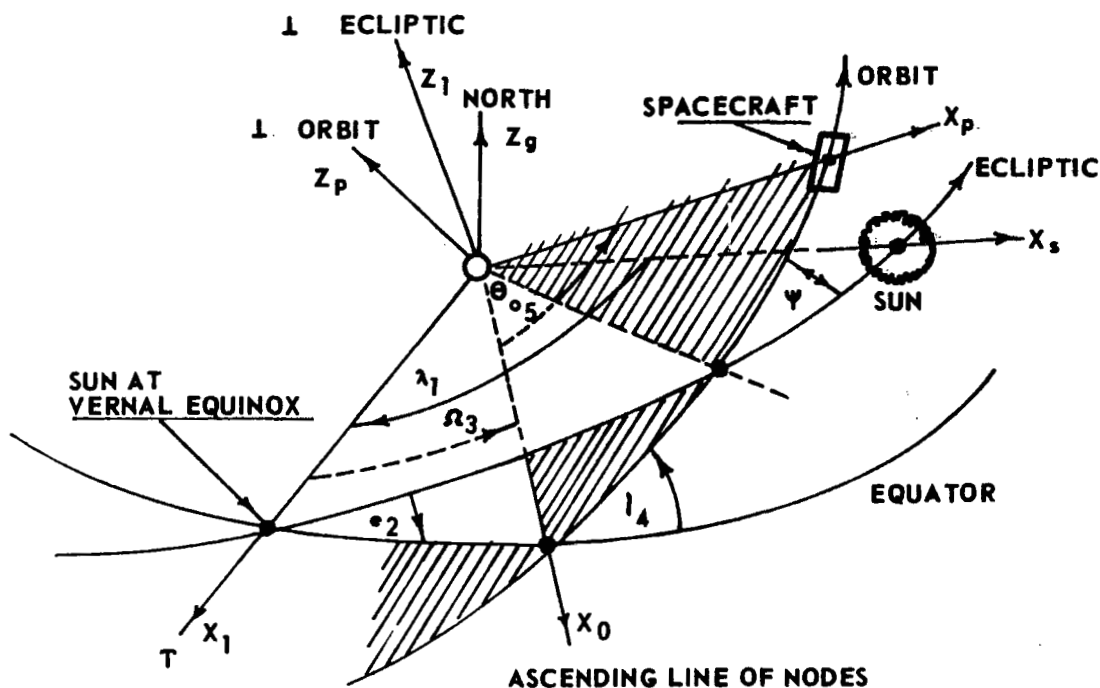
Figure J-4. Earth-orbit-ecliptic geometry.

Since the matrices used in the transformations are orthogonal, the reciprocal (inverse) matrix is identical to the transposed matrix which is denoted by a superscript "asterisk." Hence, $A_{ab} A_{ab}^* = I = A_{ab}^* A_{ab}$ where I is the identity matrix and A_{ab}^* is the inverse of A_{ab}. The specific reference frames, Reference J-4, are defined in the following paragraphs.

X_s, Y_s, Z_s are solar fixed coordinates (the HEAO body reference coordinates) with X_s directed from the earth to the sun in the ecliptic plane, Z_s is PEP (perpendicular to the ecliptic plane) directed northward, and Y_s completes the right-hand triad.

X_1, Y_1, Z_1 are inertial coordinates referenced to the ecliptic plane with X_1 directed toward Aries, $Z_1 = Z_s$ is PEP, and Y_1 completes the triad in the ecliptic plane. The inertial is transformed into solar coordinates by rotating about Z_1 by the angle λ, $\tilde{X}_s = A_{sl} \tilde{X}_1$. The angle λ represents the apparent rotation of the earth about the sun as measured from the vernal equinox and indicates the seasonal time of the year.

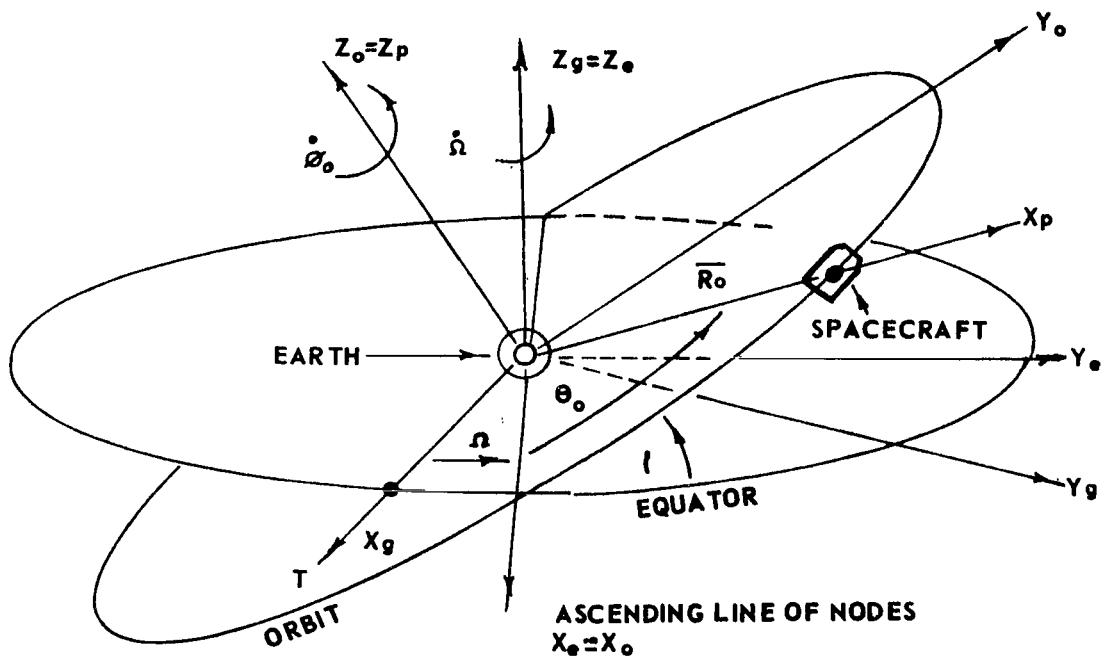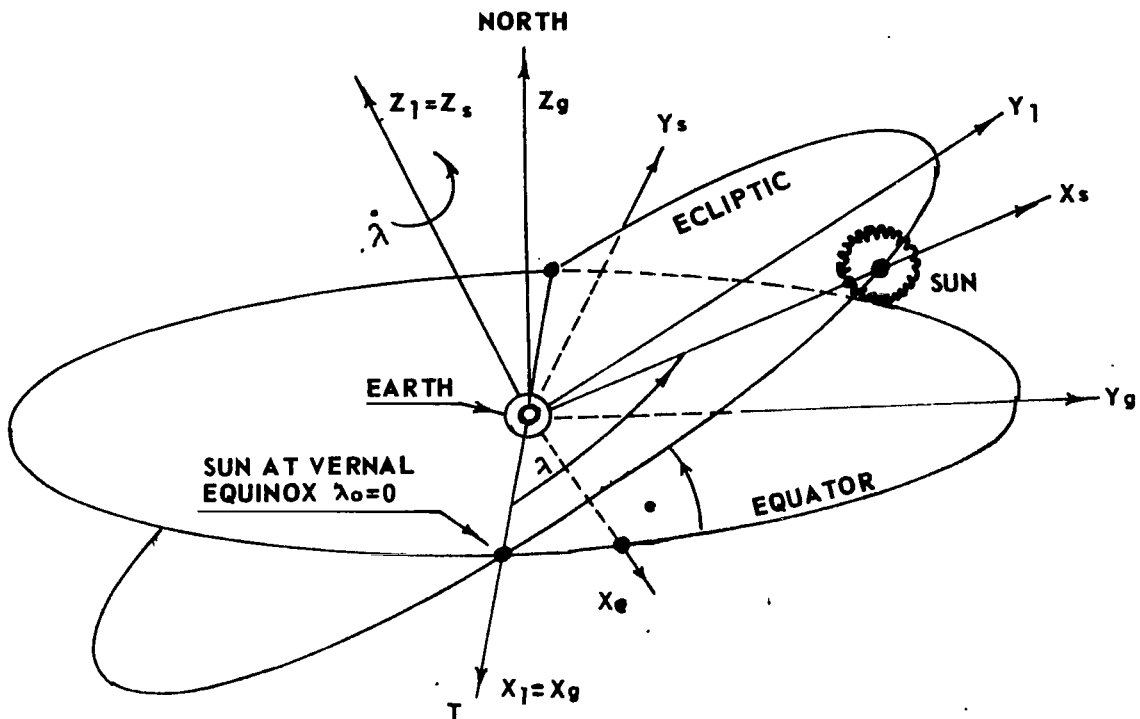Figure J-5. Geocentric coordinate systems.

X_g, Y_g, Z_g are geocentric inertial coordinates referenced to the equatorial plane with $X_g = X_1$ pointing toward Aries, Z_g is perpendicular to the equatorial plane directed northwardly, and Y_g completes the triad. The geocentric is transformed into inertial rotating about X_g by the angle e = 23.5 degrees, $\tilde{X}_1 = A_{1g} \tilde{X}_g$. The angle e, between the ecliptic and equatorial planes, is always constant and X_g is always on the ascending line of nodes between the two planes.

X_e, Y_e, Z_e is an earth-equatorial system referenced to the equatorial plane with X_e on the ascending line of nodes between the equatorial and orbit planes, $Z_e = Z_g$ is perpendicular to the equatorial directed northward, and Y_e completes the triad. The geocentric is carried into the earth-equatorial by a rotation about Z_g by the angle Ω between the ecliptic-equatorial and equatorial-orbital lines of nodes (LON). The angle Ω is known as the orbital regression angle and its time derivative as the orbital regression rate. The rate is always negative for orbital inclinations less than 90 degrees. The initial angle value may be related to orbital injection conditions necessary to produce the LON. The transformation is $\tilde{X}_g = A_{ge} \tilde{X}_e$.

X_o, Y_o, Z_o is an orbit-fixed system referenced to the orbital plane with $X_o = X_e$ on the ascending LON, Z_o is POP in a northerly direction, and Y_o completes the triad. The earth-equatorial system is transformed into the orbital system by a rotation about X_e by the orbital inclination angle ι, and $\tilde{X}_e = A_{eo} \tilde{X}_o$. The angle of inclination is measured positively at the ascending LON when the spacecraft crosses the equator going from southern to northern hemisphere.

X_p, Y_p, Z_p is a local vertical (plumb line) system referenced to the orbital plane and the vehicles position in orbit. The X_p-axis is directed from the earth's center to the spacecraft in orbit (opposite the local gravity vector), $Z_p = Z_o$ is POP, and Y_p completes the triad (aligned with the orbital velocity vector). The orbital plane is carried into local vertical coordinates by a

positive rotation about Z_o by the orbital position angle θ_o, $\tilde{X}_o = A_{op} \tilde{X}_p$. The orbital angle is measured from the ascending LON, to the spacecraft in orbit, and defined for circular orbits by $\theta_o = W_o t$, where W_o is the orbital rate and t the orbital time from the LON.

The individual transformational matrices between local vertical and solar (reference) axes are combined to give $\tilde{X}_s = A_{sp} \tilde{X}_p$. The elements of A_{sp} are defined in Reference J-4 with $\varphi \equiv \theta_o$.

X_r, Y_r, Z_r are mission-dependent reference coordinates on which the spacecraft body axes are to be oriented. HEAO is referenced to solar coordinates because of the use of hard mounted solar ponnels. Therefore, $\tilde{X}_r \equiv \tilde{X}_s$.

X_b, Y_b, Z_b are body fixed coordinates which are usually chosen so that the cross products of inertia are zero. The HEAO principal axes have been assumed to be identical to the body control axes. Since several configurations are being studied, confusion between relating structural axes to control axes and reference axes can be avoided by defining a consistent reference of body fixed coordinates for attitude control purposes. It is suggested that the following axes definitions be utilized for the HEAO: let the X_b be directed toward the sun and be the axis about which the vehicle rotates to scan either the galactic belt or celestial sphere, let Z_b be the prime experimental pointing axis, as such the experiments must view in the general direction of Z_b, and let Y_b complete the triad. In a solar-oriented mode without spin, the body axes are ideally aligned with the solar axis, $\tilde{X}_s = \tilde{X}_b$ without perturbations; however, if the spacecraft is perturbed from the desired reference or if a solar offset angle is commanded, as in the galactic scan mode, then a three-angle modified Euler transformation (type 3, 2, 1) is utilized to relate the two systems. Reference J-5 contains a standard derivation of the modified Euler angle transformation which is commonly used for aircraft simulations and is valid for small-angle approximations.

Initially the solar and body axes are assumed to be misaligned and the solar axes are carried into the misaligned body axes by first rotating about the Z_s-axis by the angle ψ. This is followed by a positive rotation about the once-transformed Y_{s1}-axis by the angle θ, and finally by a positive rotation about

the twice-transformed X_{s2}-axis by the angle ϕ. At the end of the sequence, the solar (reference) frame is coincident with the body principal frame. The Euler angle sequence is shown in Figure J-6. The angle Ψ is measured in the ecliptic from the sunline to the perpendicular projection of the scan axis on the ecliptic plane. The angle θ is measured normal to the ecliptic plane along the perpendicular projection of the scan axis, and the angle ϕ is the scan angle. In aircraft nomenclature, the Euler angles Ψ, θ, ϕ correspond to yaw, pitch, and roll, respectively.

The transformation from reference (solar) to body axes is given by $\tilde{X}_b = B_{bs} \tilde{X}_s$ where the elements of B_{bs} are defined in Reference J-5 and J-6.

The Euler angles are related to the rotational equations (Euler equations) of motion by kinematic relations which express the body rates as functions of the Euler angles and rates. These relations are commonly derived by transforming each angular rate into body coordinates and then summing components to produce the body rates (W_x, W_y, W_z). The kinematic relations for the (3, 2, 1) type transformation are

$$W_x = \dot{\phi} - \dot{\Psi}\, S\theta$$

$$W_y = \dot{\theta}\, C\phi + \dot{\Psi}\, S\phi\, C\theta \qquad\qquad (1)$$

$$W_z = \dot{\Psi}\, C\phi\, C\theta - \dot{\theta}\, S\phi \qquad .$$

The Euler kinematic relations may be solved for $\dot{\Psi}$, $\dot{\theta}$, $\dot{\phi}$:

$$\dot{\Psi} \quad (W_y\, S\phi + W_z\, C\phi)/C\theta$$

$$\dot{\theta} \quad W_y\, C\phi - W_z\, S\phi \qquad\qquad (2)$$
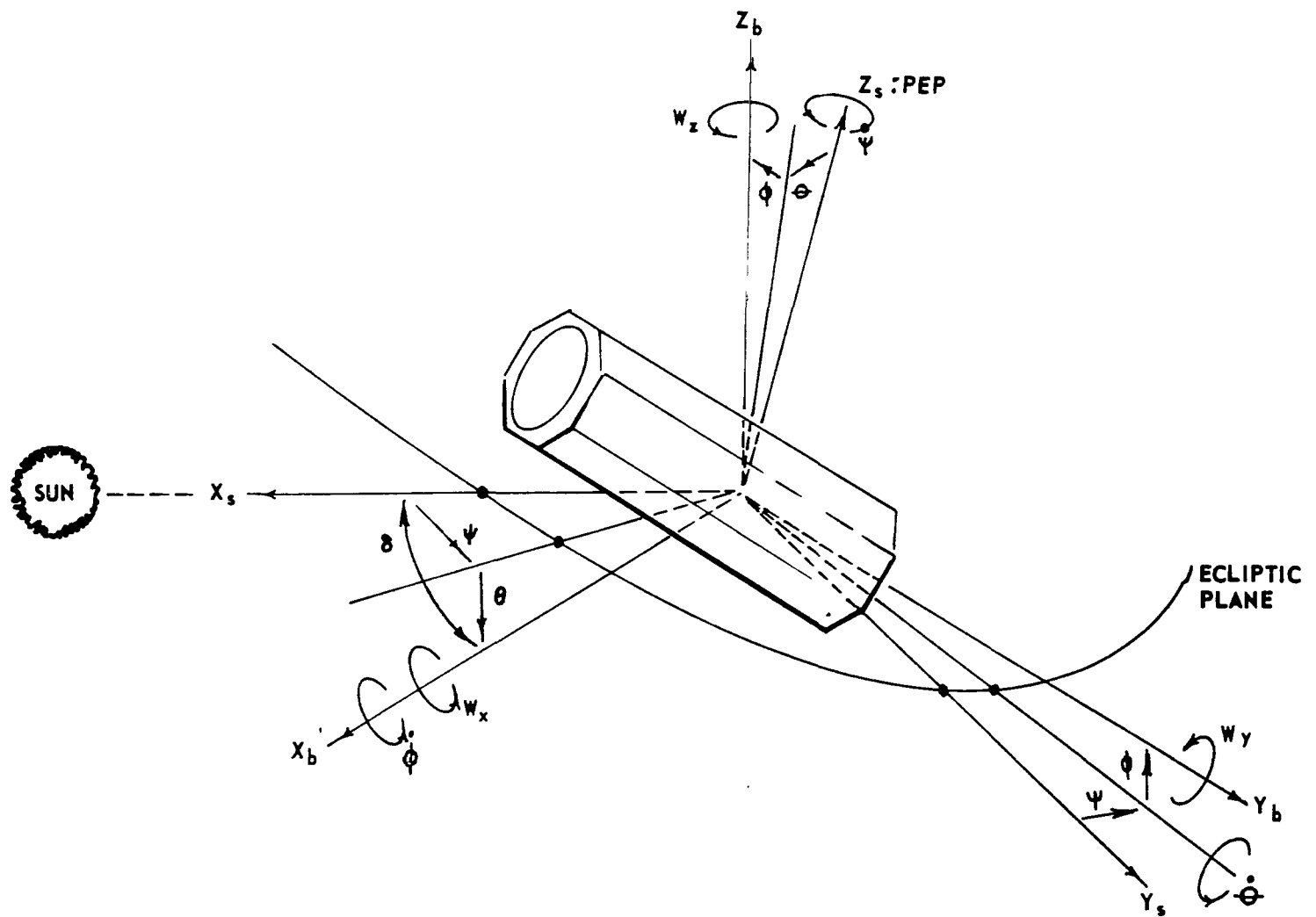
$$\dot{\phi} \quad W_x + \dot{\Psi}\, S\theta$$

J-22

Figure J-6. Orientation of body relative to solar axis and the Euler angle sequence.

As defined, the kinematic relations are valid for angles Ψ, θ, and ϕ bounded by

$$0 \leq \Psi \leq 2\pi$$

$$-\pi/2 < \theta < \pi/2 \qquad (3)$$

$$0 \leq \phi \leq 2\pi \qquad .$$

Note that there are no restrictions on Ψ and ϕ, and that gimbal lock (nonlinearity) occurs whenever $\theta = \pm 90$ degrees. For HEAO, the Euler angles are the heading angle Ψ measured in the ecliptic plane, the attitude angle θ measured perpendicular to the ecliptic plane, and the bank (spin) angle ϕ measured about the solar pointing body axis (Ψ, θ, and ϕ corresponds to yaw, pitch, and roll, respectively). Since HEAO is restricted to point in a sunwardly direction to receive the proper amount of solar energy and since $\theta = \pm 90$ degrees corresponds to pointing the spin axis perpendicular to the ecliptic plane (either north or south), gimbal lock will not occur during an operational mode. Hence, it is recommended that the 3, 2, 1 type Euler angles be used for all HEAO simulations. Furthermore, during a solar-oriented spin mode the solar offset angle is expected to be less than 2 degrees uncontrolled and 1 degree controlled per orbit, hence small-angle approximations may, in some cases, be used for Ψ and θ to gain insight to the expected rotational motion and stability characteristics. However, since ϕ is the spin angle, it can attain all possible values.

Combining the transformations from local vertical to solar and from solar to body produces

$$\widetilde{X}_b = B_{bs} A_{sp} \widetilde{X}_p = C_{bp} \widetilde{X}_p \qquad . \qquad (4)$$

The elements of C_{bp} are

$$C_{11} = B_{11} A_{11} + B_{12} A_{21} + B_{13} A_{31}$$

$$C_{12} = B_{11} A_{12} + B_{12} A_{22} + B_{13} A_{32}$$

$$C_{13} = B_{11} A_{13} + B_{12} A_{23} + B_{13} A_{33}$$

$$C_{21} = B_{21} A_{11} + B_{22} A_{21} + B_{23} A_{31}$$

$$C_{22} = B_{21} A_{12} + B_{22} A_{22} + B_{23} A_{32} \tag{5}$$

$$C_{23} = B_{21} A_{13} + B_{22} A_{23} + B_{23} A_{33}$$

$$C_{31} = B_{31} A_{11} + B_{32} A_{21} + B_{33} A_{31}$$

$$C_{32} = B_{31} A_{12} + B_{32} A_{22} + B_{33} A_{32}$$

$$C_{34} = B_{31} A_{13} + B_{32} A_{23} + B_{33} A_{33}$$

The transformation given by equation (4) is utilized to project the local radius vector (known in local vertical coordinates as $\overline{R}_o - i_p$) into body coordinates

$$\overline{R}_o = i_p = C_{11} i_b + C_{21} j_b + C_{31} k_b \tag{6}$$

after which, the gravity gradient torque equations in body principal axes may be evaluated by using $R_x = C_{11}$, $R_y = C_{21}$, and $R_z = C_{31}$. The gravity gradient torque components acting on the HEAO in the celestial scan mode are given in a forthcoming section.

Furthermore, an evaluation of the aerodynamic torques acting on the HEAO also requires that equation (4) be utilized to project the orbital velocity vector, $\overline{V}$ $V j_p$, into body axes components; after which, the angle of attack and the side slip angle are calculated, drag and lift coefficients are obtained, and then the aerodynamic torques can be algebraically obtained about each spacecraft axis.

Additional coordinate systems (Fig. J-7) must be defined to relate the earth's magnetic field to the HEAO body axes. The number of additional systems depends upon the desired accuracy as well as the assumed model of the field. For preliminary design purposes, a tilted-centered dipole model of the earth's field will probably be adequate. The declination of the magnetic dipole is assumed to be 11 degrees from the geocentric north (79 degrees north latitude). The magnetic environment field measured at the spacecraft is generally denoted by the vector $\overline{B}$. The magnitude and direction of $\overline{B}$ depends upon both the motion of the spacecraft and the earth. The field is assumed to be known in geomagnetic coordinates which must be transformed into the spacecraft body axes. A tilted dipole model of the Earth's magnetic field is contained in Reference J-9.
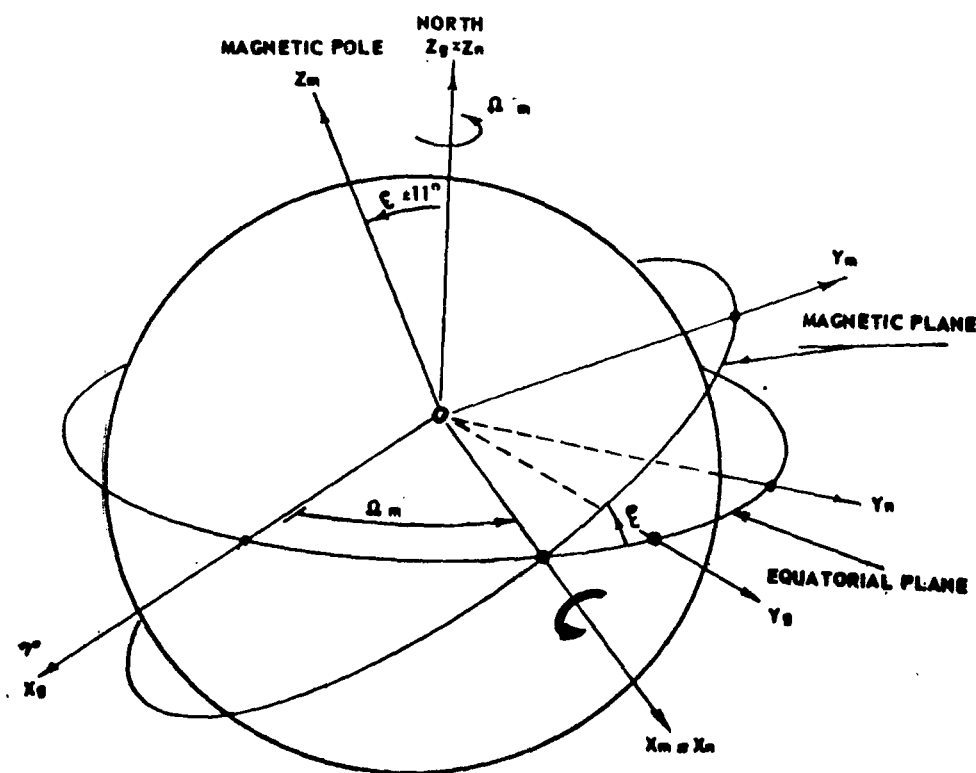

Figure J-7. Geomagnetic coordinates relative to the geocentric
inertial system.

X_m, Y_m, Z_m are geomagnetic coordinates referenced to the magnetic plane. The X_m-axis is on the ascending LON between the equatorial and geomagnetic planes, the Z_m-axis is perpendicular to the geomagnetic plane directed northward, and the Y_m-axis completes a triad in the geomagnetic plane.

X_n, Y_n, Z_n are geographic coordinates referenced to the equatorial plane with $X_n \equiv X_m$. The Z_n-axis is perpendicular to the equatorial plane directed northward, hence, $Z_n \equiv Z_g$, and the Y_n-axis completes a triad in the equatorial plane. The $\tilde{X}_n$ axes are carried into the $\tilde{X}_m$ system by a positive rotation about the X_n-axis by the angle $\xi = 11$ degrees. In vector matrix form, $\tilde{X}_n = A_{nm} \tilde{X}_m$.

The $\tilde{X}_n$ triad is related to the previously defined geocentric $\tilde{X}_g$ system by a positive rotation about the Z_g-axis by the angle $\Omega_m = \Omega_{om} + W_e t$. The angle Ω_{om} is an initial value used to position the longitude of the magnetic pole relative to the orbital plane LON at time zero, and the earth's angular rate is denoted by W_e. Algebraically, $\tilde{X}_g = A_{gn} \tilde{X}_n = A_{gn} A_{nm} \tilde{X}_m$.

Combining previously defined transformations, the geocentric is related to the solar (body reference) coordinates by $\tilde{X}_s - A_{s1} A_{1g} \tilde{X}_g$. Therefore, the geomagnetic to solar transformation is

$$\tilde{X}_s \cdot A_{s1} A_{1g} A_{gn} A_{nm} \tilde{X}_m \equiv D_{sm} \tilde{X}_m \qquad (7)$$

Equation (7) is operated upon by the Euler angle transformation B_{bs} to obtain the final transformation which relates the geomagnetic to the HEAO body axes.

$$\tilde{X}_b = B_{bs} \tilde{X}_s = B_{bs} D_{sm} \tilde{X}_m = M_{bm} \tilde{X}_m \qquad (8)$$

Utilizing equation (8), the components of the earth's magnetic field, known in geomagnetic axes, are obtained in the HEAO body principal (control) axes. The elements of D_{sm}, which are listed in Table J-1, may be used in a simpler form by assuming a fixed angle for λ and Ω_m, in which case the elements become constants. The elements of M_{bm} are of the same form as those shown in equation (5), with A_{ij}'s replaced by D_{ij}'s and C_{ij}'s replaced by M_{ij}'s. Paragraph 7 of this appendix utilizes the M_{bm} transformation to obtain the earth's magnetic field in body fixed coordinates.

For completeness, the elements of A_{sp} are given in Table J-2 as functions of five physically meaningful angles: once specified, ι and e are constant, λ and Ω vary slowly with time, and θ_o varies rapidly with time. Assuming a winter solstice launch ($\lambda = 270$ degrees) with the ascending LON perpendicular to the sunline ($\Omega = 180$ degrees) and defining $\Psi_o = \iota + e$ as the angle between the orbit and ecliptic planes, the simplified directional cosines of A_{sp} are given in Table J-3 as functions of the orbital position angle θ_o. The gravity gradient torque can be maximized by selecting $\Psi_o = 45$ degrees. The elements of the Euler angle transformational matrix B_{bs} are given in Table J-4. Without misalignments from the solar reference, B_{bs} becomes the identity matrix.

5. Euler's Equations for HEAO

The dynamic equations which govern the rotational motion of a space-craft with a flywheel aligned with its spin (scan) axes are derived by first obtaining the angular momentum in body coordinates and then substituting the momentum into Euler's equations. However, before deriving the equations, an alternate body principal axes system will be defined which is identical with the reference (solar) coordinates at time zero. Using such a body axes system alternate configurations can be compared without rewriting the equations of motion.

TABLE J-1. ELEMENTS OF THE TRANSFORMATION, D_{sm}, FROM GEOMAGNETIC TO SOLAR INERTIAL

$$D_{11} = C\lambda\, C\Omega_m + S\lambda\, S\Omega_m\, Ce$$

$$D_{12} = -C\lambda\, S\Omega_m\, C\xi + S\lambda\, C\Omega_m\, Ce\, C\xi + S\lambda\, Se\, S\xi$$

$$D_{13} = C\lambda\, S\Omega_m\, S\xi - S\lambda\, C\Omega_m\, Ce\, S\xi + S\lambda\, Se\, C\xi$$

$$D_{21} = -S\lambda\, C\Omega_m + C\lambda\, S\Omega_m\, Ce$$

$$D_{22} = S\lambda\, S\Omega_m\, C\xi + C\lambda\, C\Omega_m\, Ce\, C\xi + C\lambda\, Se\, S\xi$$

$$D_{23} = -S\lambda\, S\Omega_m\, S\xi - C\lambda\, C\Omega_m\, Ce\, S\xi + C\lambda\, Se\, C\xi$$

$$D_{31} = -S\Omega_m\, Se$$

$$D_{32} = -C\Omega_m\, Se\, C\xi + Ce\, S\xi$$

$$D_{33} = C\Omega_m\, Se\, S\xi + Ce\, C\xi$$

TABLE J-2. ELEMENTS OF A_{sp}

$$A_{11} = C\theta_o[C\lambda\, C\Omega + S\lambda\, S\Omega\, Ce] + S\theta_o[-C\lambda\, S\Omega\, C\iota + S\lambda\, C\Omega\, Ce\, C\iota + S\lambda\, Se\, S\iota]$$

$$A_{12} = -S\theta_o[C\lambda\, C\Omega + S\lambda\, S\Omega\, Ce] + C\theta_o[-C\lambda\, S\Omega\, C\iota + S\lambda\, C\Omega\, Ce\, C\iota + S\lambda\, Se\, S\iota]$$

$$A_{13} = S\iota[C\lambda\, S\Omega - S\lambda\, C\Omega\, Ce] + C\iota\, S\lambda\, Se$$

$$A_{21} = -C\theta_o[S\lambda\, C\Omega - C\lambda\, S\Omega\, Ce] + S\theta_o[S\lambda\, S\Omega\, C\iota + C\lambda\, C\Omega\, Ce\, C\iota + C\lambda\, Se\, S\iota]$$

$$A_{22} = S\theta_o[S\lambda\, C\Omega - C\lambda\, S\Omega\, Ce] + C\theta_o[S\lambda\, S\Omega\, C\iota + C\lambda\, C\Omega\, Ce\, C\iota + C\lambda\, Se\, S\iota]$$

$$A_{23} = -S\iota[S\lambda\, S\Omega + C\lambda\, C\Omega\, Ce] + C\iota\, C\lambda\, Se$$

$$A_{31} = -C\theta_o\, S\Omega\, Se - S\theta_o[C\Omega\, Se\, C\iota - Ce\, S\iota]$$

$$A_{32} = S\theta_o\, S\Omega\, Se - C\theta_o[C\Omega\, Se\, C\iota - Ce\, S\iota]$$

$$A_{33} = C\Omega\, Se\, S\iota + Ce\, C\iota$$

TABLE J-3. SIMPLIFIED ELEMENTS OF A_{sp}
$[\lambda = 270 \text{ deg}, \Omega = 180 \text{ deg}]$

$$A_{11} = S\theta_o \, C\Psi_o \quad , \quad A_{23} = 0$$

$$A_{12} = C\theta_o \, C\Psi_o \quad , \quad A_{31} = S\theta_o \, S\Psi_o$$

$$A_{13} = -S\Psi_o \quad , \quad A_{32} = C\theta_o \, S\Psi_o$$

$$A_{21} = -C\theta_o \quad , \quad A_{33} = C\Psi_o$$

$$A_{22} = S\theta_o \quad , \quad \Psi_o \equiv \iota + e$$

TABLE J-4. ELEMENTS OF THE EULER TRANSFORMATION, B_{bs}

$$B_{11} = C\theta \, C\Psi$$

$$B_{12} = C\theta \, S\Psi$$

$$B_{13} = -S\theta$$

$$B_{21} = S\phi \, S\theta \, C\Psi - C\phi \, S\Psi$$

$$B_{22} = S\phi \, S\theta \, S\Psi + C\phi \, C\Psi$$

$$B_{23} = S\phi \, C\theta$$

$$B_{31} = C\phi \, S\theta \, C\Psi + S\phi \, S\Psi$$

$$B_{32} = C\phi \, S\theta \, S\Psi - S\phi \, C\Psi$$

$$B_{33} = C\phi \, C\theta$$

Let X_b, Y_b, Z_b be a body principal axes triad such that the X_b-axis is the scan (spin) axis and must be solar oriented. The majority of the experiments which view the celestial sphere are aligned with the Z_b-axis which is perpendicular to the X_b-axis, and the Y_b-axis completes a right-hand triad. In a solar inertial mode, $\tilde{X}_s \equiv \tilde{X}_b$. Figure J-8 shows the baseline HEAO (Configuration I) and a possible alternate (Configuration III) with the axis of minimum inertia as the scan axis. The body structural coordinates are shown for each configuration and the redefine $\tilde{X}_b$ system is shown superimposed on solar coordinates referenced to the ecliptic plane. Eulers equations are derived relative to the $\tilde{X}_b$ body principal coordinates.

The angular momentum of the flywheel aligned with the X_b-axis is

$$\bar{h}_f = I_f W_f i_b \equiv h_f i_b \tag{9}$$

where I_f is the inertia, W_f is the angular rate, and h_f is the momentum of the flywheel. The flywheel inertia is also included in the X_b-axis body inertia. The vehicle angular momentum vector in body axes is

$$\bar{H} = h_x i_b + h_y j_b + h_z k_b \tag{10}$$

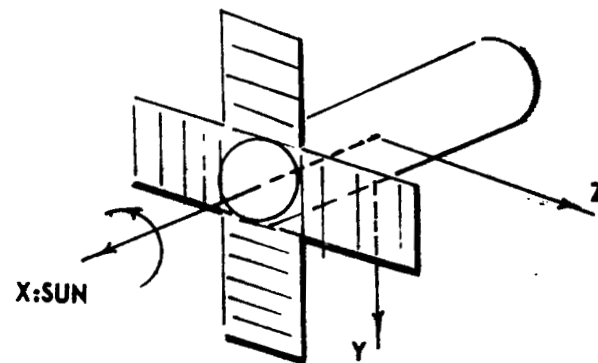The components of $\bar{H}$ for the HEAO body principal axes are
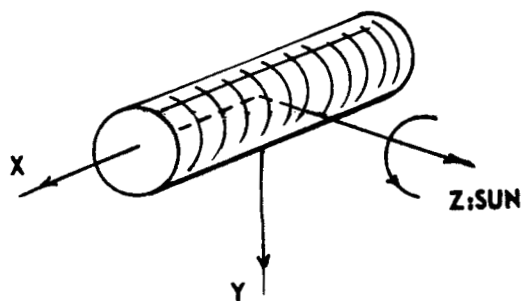
$$h_x = I_x \dot{W}_x + h_f$$

$$h_y = I_y W_y \tag{11}$$

$$h_z = I_z W_z$$

CONF. I (BASELINE)

$ly\,b = lx = 3,979$ (SL-FT^2)

$lzb = ly = 35,210$

$lxb = lz = 36,900$

CONF. III

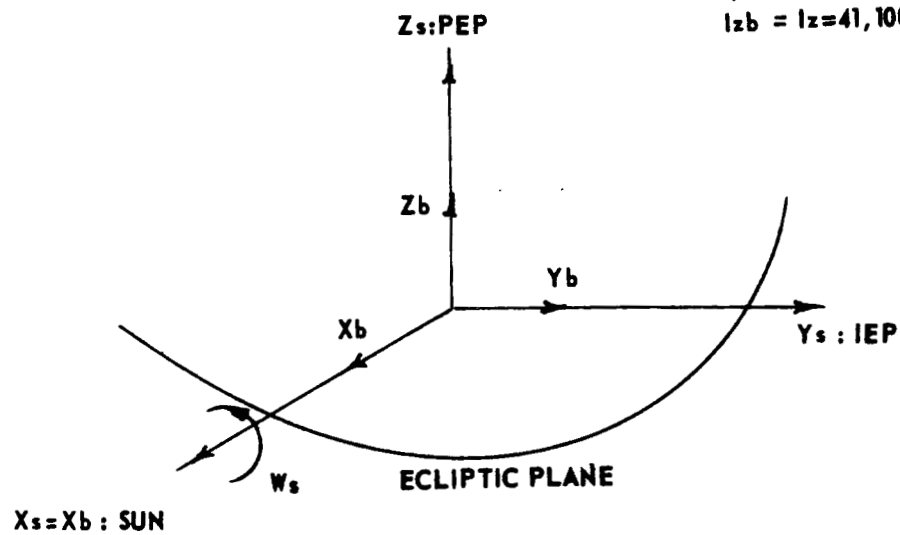$lxb = lx = 10,800$ (SL-FT^2)

$lyb = ly = 39,120$

$lzb = lz = 41,100$

Figure J-8. HEAO axes definition.

where W_x, W_y, W_z are the angular rates and I_x, I_y, I_z are the principal moments of inertia about the X_b, Y_b, and Z_b axes. In vector form, Euler's equation is

$$\overline{T} = \dot{\overline{H}} + \overline{W} \times \overline{H} \quad . \tag{12}$$

Expanding equation (12) and equating components produces

$$T_x = \dot{h}_x + h_z W_y - h_y W_z$$

$$T_y = \dot{h}_y + h_y W_z - h_z W_x \tag{13}$$

$$T_z = \dot{h}_z + h_y W_x - h_x W_y$$

Substituting equation (11) into equation (13) produces the HEAO Euler equations which govern its rotational motion about its center of mass.

$$I_x \dot{W}_x + (I_z - I_y) W_z W_y + I_f \dot{W}_f = T_x$$

$$I_y \dot{W}_y + (I_x - I_z) W_x W_z + h_f W_z = T_y \tag{14}$$

$$I_z \dot{W}_z + (I_y - I_x) W_y W_x - h_f W_y = T_z \quad .$$

The right-hand side of equation (14) represents the applied torques (T_x, T_y, T_z) which are assumed to originate from both environmental and active attitude control actuators. For a stability analysis, the applied torque components are set equal to zero. For vehicle time response studies, the applied torques are set equal to either the environmental torques as gravity gradient (or aerodynamic) or the control torques from reaction jets (or magnetic coils) or possibly

a combination of all torque sources as the simulation complexity increases. For active control system sizing, the dominant environmental torque is used as a basis for determinimg the energy requirements (impulse) that is necessary for attitude hold. For the HEAO, the gravity gradient torque is the dominant environmental torque. Orbital conditions, time of year, and time of day of launch are selected such that the gravitational effects are maximized and the active attitude control system is sized proportionally.

It is well known that the gravity gradient torques are maximized whenever the longitudinal body axis makes an angle of 45 degrees with respect to the local vertical. For the HEAO, the maximizing conditions are shown in Figure J-9. A winter solstice launch has been selected (λ = 270 degrees) with the ascending orbital equatoral plane LON perpendicular to the sunline (Ω = 180 degrees). For a 28.5-degree orbital inclination, the angle between the orbit and ecliptic planes is 52 degrees. By selecting the inclination at 21.5 degrees, the angle Ψ_o between the orbit and ecliptic plane is 45 degrees, as well as the angle between the longitudinal body axis and the local vertical, $\bar{R}_o$. In all of the HEAO time response simulations, which includes gravitational effects, the parameters have been selected to produce worse-case environmental torques.

The Euler equations (14) are solved for the body rates ($\tilde{W}$) which are then used in the Euler kinematic relations;

$$\dot{\Psi} = (W_z C\phi + W_y S\phi)/C\theta \qquad (15)$$

$$\dot{\theta} = W_y C\phi - W_z S\phi$$

$$\dot{\phi} = W_x + \dot{\Psi} S\theta \qquad .$$

The kinematic relations are integrated to obtain the Euler angles (Ψ, θ, ϕ) that relate the vehicles attitude to the reference coordinates (solar). Then, the Euler angles along with updated orbital parameters are utilized to re-evaluate the transformational matrices and the simulation cycle is repeated for the next time step. For small Euler angles, the solar offset angle is given by

Figure J-9. Solar orientations.

$$\delta = (\Psi^2 + \theta^2)^{\frac{1}{2}} \tag{16}$$

The gravity gradient torque components acting along the principal body axes of the spacecraft are

$$T_{gx} = 3 W_o^2 (I_z - I_y) R_z R_y$$

$$T_{gy} = 3 W_o^2 (I_x - I_z) R_x R_z \tag{17}$$

$$T_{gz} = 3 W_o^2 (I_y - I_x) R_y R_x$$

where R_x, R_y, R_z are the body axes components of a unit vector along the radius vector directed from the earth's center to the spacecraft center of mass. In local vertical axes, $\overline{R}_o = i_p$. The transformation from local vertical to body principal coordinates, $\tilde{X}_b = C_{bp} \tilde{X}_p$, is utilized to obtain

$$\overline{R}_o = C_{11} i_b + C_{21} j_b + C_{31} k_b \tag{18}$$

hence,

$$R_x \equiv C_{11}, \quad R_y \equiv C_{21}, \quad \text{and} \quad R_z \equiv C_{31}.$$

As previously defined in Paragraph 4 of this Appendix,

$$C_{bp} = B_{bs} A_{sp} \tag{19}$$

The matrix B containing the Euler angles becomes the unity matrix without misalignments from the solar reference, such is the case assuming ideal attitude hold control. Figure J-10 illustrates the gravity gradient torque components plotted as a function of the orbital position angle θ_o for the spinning baseline vehicle. The traces have the general appearance of an amplitude modulated carrier wave: the scan (spin) frequency represents the carrier wave and the orbital frequency the modulated waveform. The amplitude is about 0.06 ft-lb on both the X (scan) and Z (experiment) axes and about 0.003 ft-lb on the Y-axis of minimum inertia. When the components are projected back into solar axes, $T_x \equiv T_{sx}$, but the T_{sy} and T_{sz} components are linear combinations of T_y and T_z. The T_{sy} component is shown to illustrate the bias on the solar Y_s-axis. This torque bias results in a secular momentum component that tends to rotate the vehicle about the Z_b-axis in the direction of the apparent sun's movement about the earth. The attitude control system must be sized to provide a torque magnitude slightly larger than the maximum gravity gradient torque magnitude.

The time integral of the gravity torques taken in a positive sense gives a measure of the energy (impulse) requirements necessary to attitude hold over an orbital time period. The accumulated momentum over an orbital time period is shown in Figure J-11 for both the baseline and alternate configurations. Assuming ideal control, the baseline requires 230 ft-lb-sec momentum per orbit, assuming a lever arm of 10 ft, 23 lb-sec impulse per orbit, or assuming a specific fuel impulse of 230 sec., 0.1 lb fuel per orbit. These numbers must be multiplied by the number of orbits per day (about 16) and the number of days in the mission to evaluate the total energy requirements. However, since worse-case conditions only exist at discrete time intervals, the actual energy requirements will be less than those obtained.

Insight into the basic control and stability problems may be obtained by conducting a simplified analysis of the Euler equations (14). Assume that all the applied torques are zero except a rate proportional feedback on the Y- and Z-axis; i.e., $T_x = 0$, $T_y = -K_y W_y$ and $T_z = -K_z W_z$ where K_y and K_z are to be selected to give the desired damping. Furthermore, assume that the scan rate, W_x, will be much larger than either W_y or W_z. Under these conditions, $W_y W_z \simeq 0$ so that X-axis equation produces a constant angular rate $W_x = W_s$ (scan rate) about the scan axis. Substituting $W_x = W_s$ into the Y and Z equation produces

$$I_y \dot{W}_y + \left[h_f + (I_x - I_z) W_s \right] W_z + K_y W_y = 0 \qquad (20)$$

$$I_z \dot{W}_z - \left[h_f + (I_x - I_y) W_s \right] W_y + K_z W_z = 0 \qquad \bullet$$

Notice that the flywheel, which is about 80 percent or more of the total angular momentum, introduces very strong cross coupling between the Y- and Z-axes. Hence, the gyroscopic effect is expected to show up when the forced solution of the equations is simulated. Furthermore, a damping feedback on either the Y- or Z-axes should introduce damping on the other axis also. By dividing each equation (20) by its principal moment of inertia, taking the Laplace transform with zero initial conditions, and using the definitions

$$\bar{K}_y = K_y / I_y$$

$$\bar{K}_z = K_z / I_z$$

$$D_y = \left[h_f + (I_x - I_z) W_s \right] / I_y \qquad (21)$$

$$D_z = \left[h_f + (I_x - I_y) W_s \right] / I_z$$

$$B = \bar{K}_y + \bar{K}_z$$

$$C = \bar{K}_y \bar{K}_z + D_y D_z \qquad \bullet$$

J-38
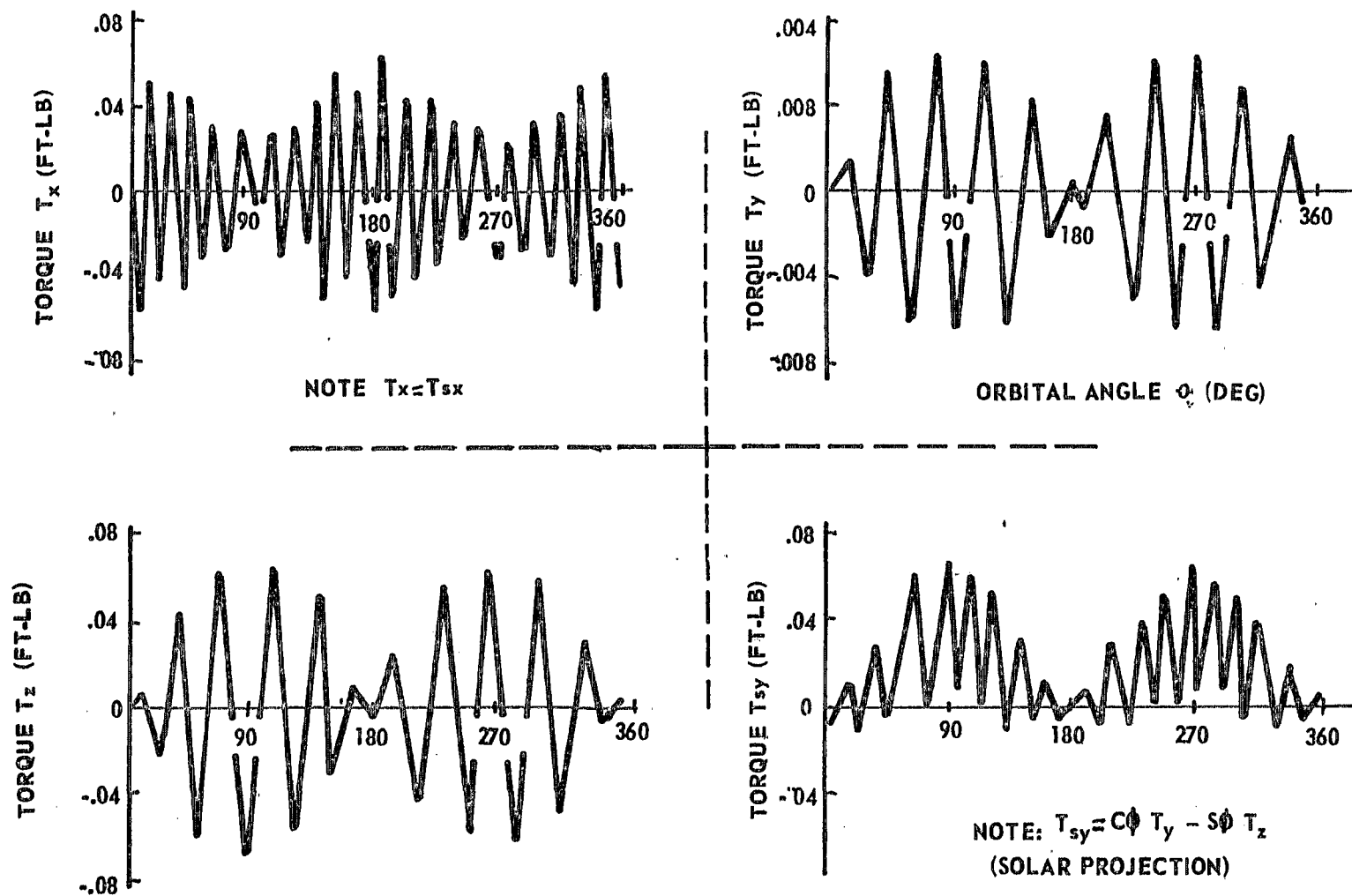
Figure J-10. Gravity gradient torques, ideal solar spin pointing.
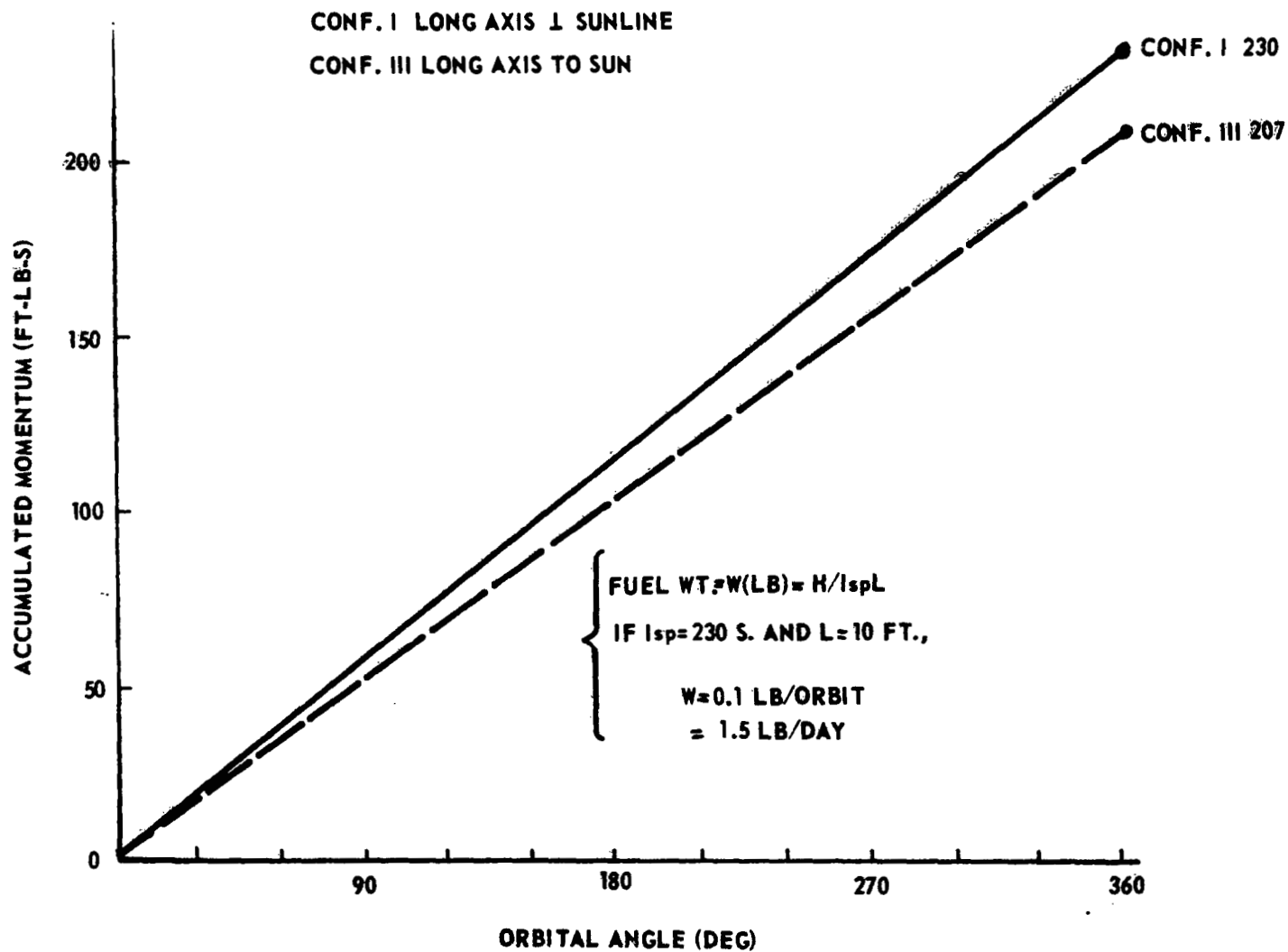
Figure J-11. HEAO momentum caused by gravity torques.

Equations (20) are rewritten as

$$\dot{W}_y + \overline{K}_y W_y + D_y W_z = 0$$

$$\dot{W}_z + \overline{K}_z W_z - D_z W_y = 0 \quad , \qquad (22)$$

and after taking the Laplace transform and arranging in vector-matrix form, equation (22) becomes

$$\begin{bmatrix} S + \overline{K}_y & D_y \\ -D_z & S + \overline{K}_z \end{bmatrix} \begin{bmatrix} W_y \\ W_z \end{bmatrix} = 0 \qquad . \qquad (23)$$

The characteristic equation for equations (23) is

$$S^2 + B S + C = 0 \qquad . \qquad (24)$$

The roots of equation (24) are obtained by using the quadratic equation and are plotted in root locus form in Figure J-12 for both the baseline HEAO and the alternate configuration. The loci have been plotted as a function of the flywheel momentum and rate feedback gains. The roots for the baseline without flywheel or rate damping are ¡ 0.0066 on the imaginary axis. As the flywheel momentum is added, the roots move outward from the origin along the imaginary axis, attaining a natural frequency of 0.155 at h_f = 2000 ft-lb-sec. If both $\overline{K}_y$ and $\overline{K}_z$ are introduced, the roots move from the marginally stable imaginary axis into the stable left-half complex plane, the natural frequency as well as damping increases as the gains are increased. If either $\overline{K}_y$ or $\overline{K}_z$ is introduced, the roots move in a circular arc at constant frequency in the stable left-half plane until the real axis is intercepted. Further gain increase causes the roots to split; one approaches the origin and the other infinity as the gain becomes very large. The numbers in parenthesis are the gain values. Similar trends occur when rate feedback is added to Configuration III, but the natural
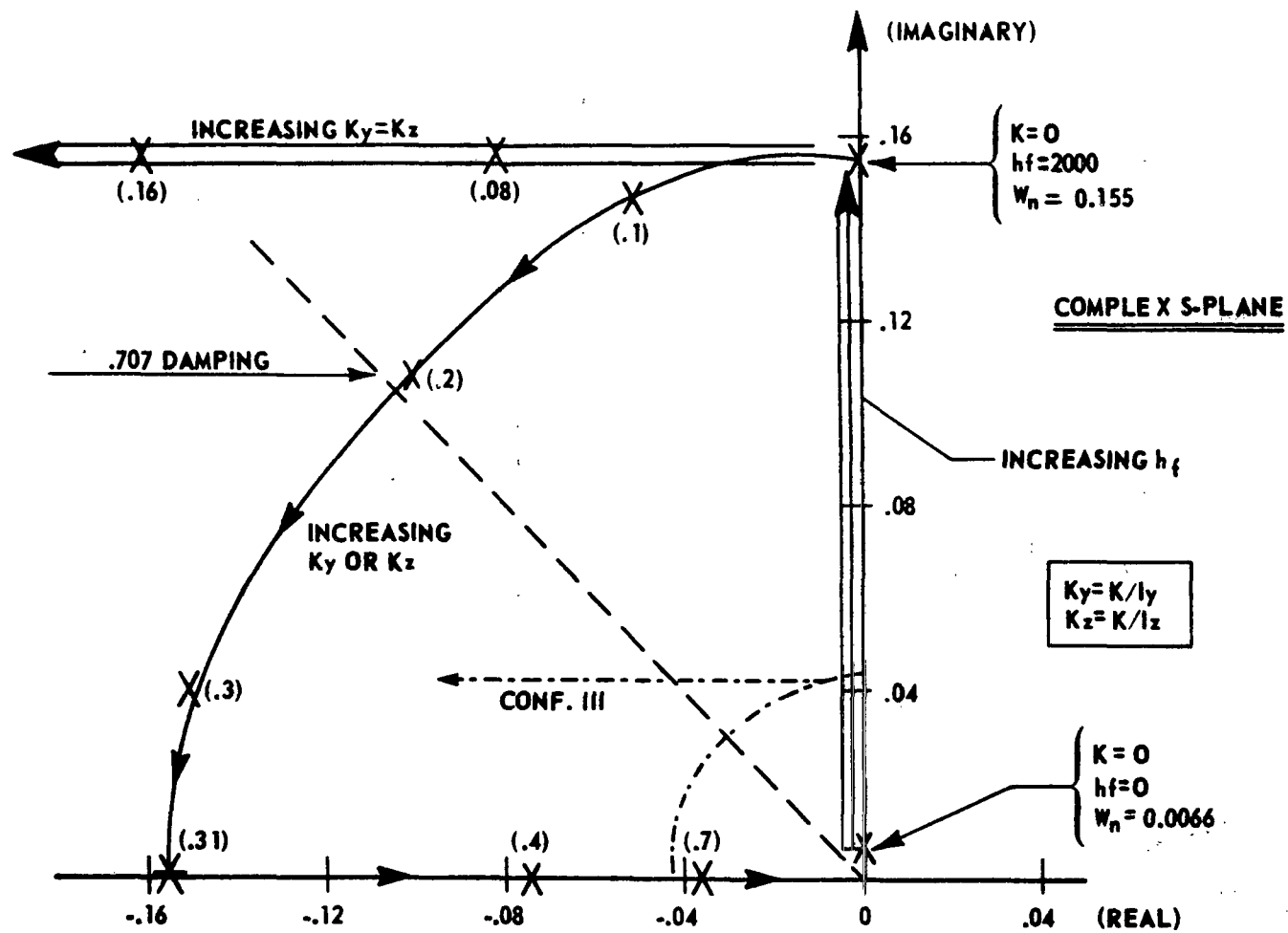
Figure J-12. HEAO root locus with rate feedback.

frequency is about four times less than the baseline. Since the system roots are indicative of the vehicles time response, the baseline is expected to respond more quickly to commands, and for a given disturbance the magnitude of precession should be less than that of the alternate configuration.

The time response of the baseline to a constant applied torque of 1 ft-lb about the Z_b - axis is shown in Figure J-13. At one spin period ($T_s = 2\pi/W_s$), about 600 seconds, δ approaches zero before starting another coning cycle. The structural natural frequency ($W_n = 0.155$) appears as oscillations (wobble) superimposed on the cone. A $\Psi - \theta$ phase plane plot of δ is shown in Figure J-14 with time tick marks along the curve for a 600- second coning interval. Without the cross coupling and gyroscopic action produced by the flywheel and vehicle scan rate, a torque about the Z_b-axis would have produced a rotation only in the angle Ψ .

6. Summary of Control Laws for Attitude and Scan-Rate Control of the Spacecraft

The spacecraft mission has three distinct normal operational modes. These modes are:

- Celestial scan mode.

- Galactic scan mode.

- Celestial pointing mode.

Magnetic torques are used to maintain spacecraft attitude in each of these modes. For maneuvers in going from one mode to another, magnetic torques are used if possible; otherwise jets are used. In this section, a control scheme for the application of control torques as a function of sensor output for different maneuvers and normal operational modes is given.

a. Initial Stabilization After Booster Separation. The control torques to be applied in the spacecraft body axes using either magnetic torquers or jets for damping of body rates are proportional to the body rates

Conf I

T_Z = 1 Ft-Lb (Experiment Axis)

W_S = 0.1 RPM → T_S = 600 Sec

W_n = 0.155 Rad/s → T_η = 40.5 Sec

$\delta = (\psi^2 + \theta^2)^{1/2}$
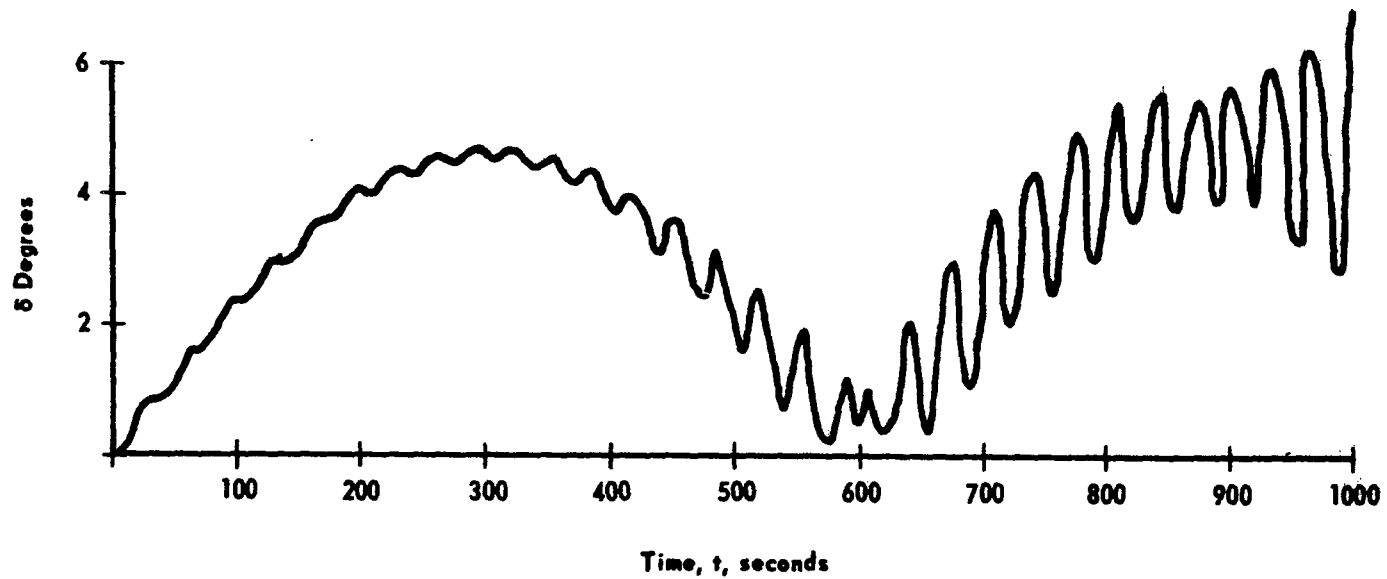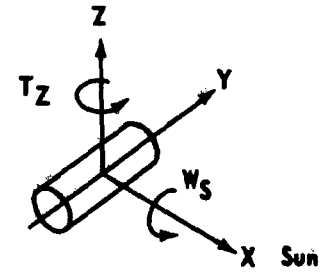
Figure J-13.   Baseline time response to a constant torque.
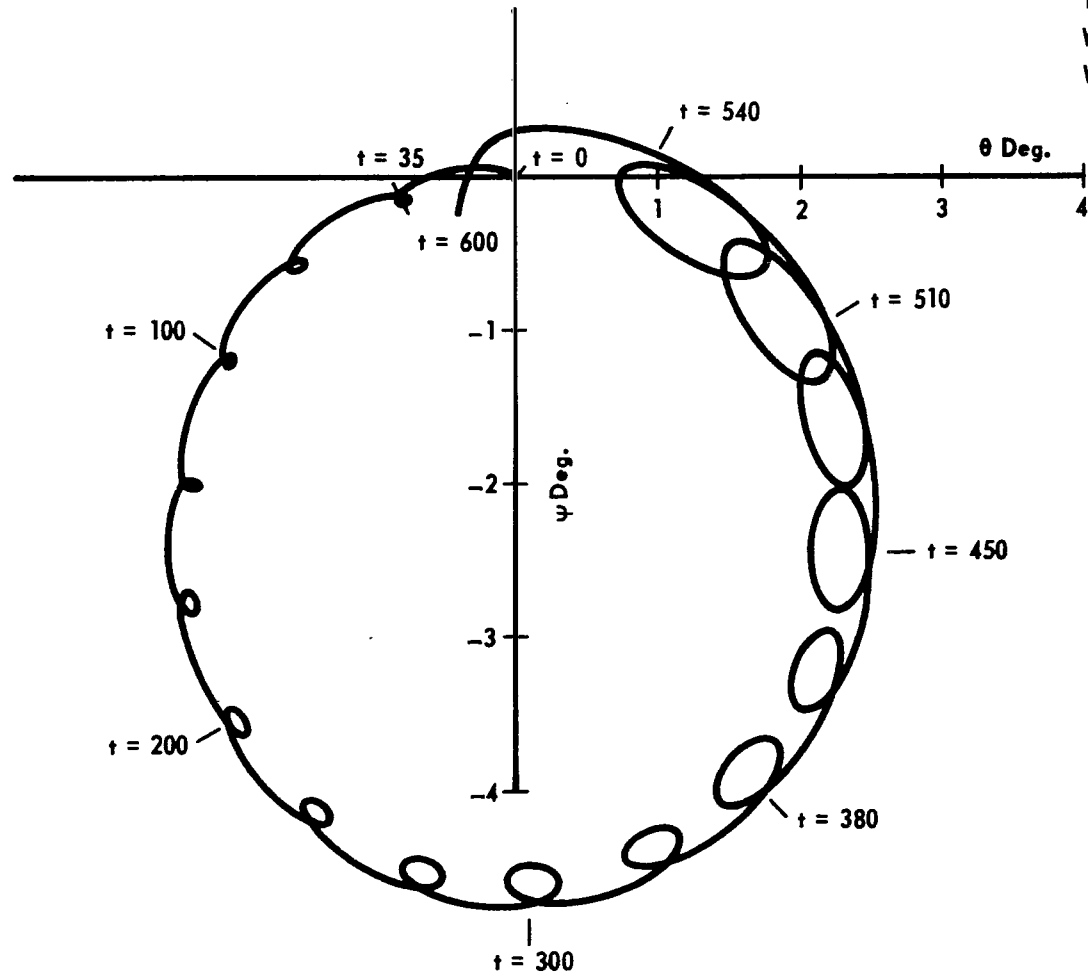
Figure J-14.   Baseline phase plane time response.

$$T_x = -K_{x_1} \dot{\omega}_x$$

$$T_y = -K_{y_1} \omega_y \qquad\qquad (25)$$

$$T_z = -K_{z_1} \dot{\omega}_z$$

where

T_x, T_y, T_z — control torques in X, Y, Z body axes

ω_x, ω_y, ω_z — body rates in X, Y, Z axes

K_{x_1}, K_{y_1}, K_{z_1} — some positive constants selected on the basis of speed of response and damping desired.

The jet thrusters are driven by pulse-frequency, pulse-width modulators.

b. <u>Solar Acquisition.</u> For this maneuver, either of the two following methods for the application of control torque can be used:

● Three single-axis slews (conventional technique).

● Three-axis slew (optimum scheme).

In the latter scheme, the time required for large angle maneuvers can be reduced by minimizing the angular distance traversed by the spacecraft in changing its attitude. In the former scheme, the slew maneuvers are performed on each axis step by step. The three-axis slew scheme requires more computation onboard but it requires fewer ground commands. The three single-axis slews are simpler in operation but the slew time is greater than for the three-axis slew.

In the three single-axis slew schemes, the torques in the body axes are applied proportional to the attitude and attitude rate as

$$T_x = - \left[K_{x_1} \omega_x + K_{x_2} \int \omega_x \, dt \right]$$

$$T_y = - \left[K_{y_1} \omega_y + K_{y_2} \int \omega_y \, dt \right] \tag{26}$$

$$T_z = - \left[k_{z_1} \omega_z + K_{z_2} \int \omega_z \, dt \right] \qquad .$$

In the three-axis slew scheme, the control torques are applied proportional to attitude and attitude rate as [J-7, J-8]:

$$T_x = - \left[K_{x1} \omega_x + \frac{K_{x2} \, (2 \sin \alpha_e)}{(1 + \cos \alpha_e)^2} \, C_x \right]$$

$$T_y = - \left[K_{y1} \omega_y + \frac{K_{y2} \, (2 \sin \alpha_e)}{(1 + \cos \alpha_e)^2} \, C_y \right] \tag{27}$$

$$T_z = - \left[K_{z1} \omega_z + \frac{K_{z2} \, (2 \sin \alpha_e)}{(1 + \cos \alpha_e)^2} \, C_z \right]$$

where

C_x, C_y, C_z — real unit eigencolumn of R corresponding to eigenvalue + 1 where R is an error matrix defined as

$$R = A_a A_d^T$$

and

A_a — the direction cosine matrix defining the actual orientation of the body relative to inertial reference frame (solar)

A_d^T — transpose of the direction cosine matrix for the desired attitude of the body relative to inertial reference frame.

The control law forces A_a to be aligned with A_d. For this, R is the identity matrix

$$R = I = \begin{vmatrix} 1 & 0 & 0 \\ 0 & 1 & 0 \\ 0 & 0 & 1 \end{vmatrix}$$

The angle α_e is defined as the difference between actual body orientation and desired orientation and is given by

$$\alpha_e = \cos^{-1}\left\{ \frac{1}{2}\left[t_r(R) - 1 \right] \right\} \tag{28}$$

where

$$\text{tr}(R) = \sum_{i=1}^{3} R_{ii} \qquad .$$

For the maneuver of solar acquisition

$$A_d = \begin{vmatrix} 1 & 0 & 0 \\ 0 & 1 & 0 \\ 0 & 0 & 1 \end{vmatrix} \qquad . \tag{29}$$

The angle α_e and norm, defined as

$$\text{norm} = (\omega_x^2 + \omega_y^2 + \omega_z^2)^{1/2} \qquad , \tag{30}$$

can be assigned some minimum value after which solar acquisition operation is considered complete.

J-48

c. **Celestial Scan Mode.** During this operational mode, magnetic torquers will be used. The torquers must provide both attitude control of the scan axis and scan-rate control.

1. Scan-axis attitude control. For attitude orientation control, a single electromagnet aligned along the scan axis can be used. The magnetic moment produced caused by this electromagnet reacts with the earth's magnetic field to produce a control torque normal to the scan axis. The torque (T) is given by

$$\overline{T} = \overline{M} \times \overline{B} \tag{31}$$

where

$\overline{M}$ — magnetic moment produced due to electromagnet

$\overline{B}$ — earth's magnetic field vector.

Since only an electromagnet aligned with the scan axis is used for attitude orientation control, $M_y = M_z = 0$. Therefore, equation (31) becomes

$$T_x = 0$$

$$T_y = -M_x B_z \tag{32}$$

$$T_z = M_x B_y \qquad .$$

The value of M_x is obtained from equation (32) as

$$M_x = \left(\frac{T_y^2 + T_z^2}{B_y^2 + B_z^2} \right)^{1/2} \qquad .$$

Figure J-15 shows the deviation of scan axis X from inertial axes X_s, Y_s and Z_s. The torque required to control (decrease) the angle ψ is given by
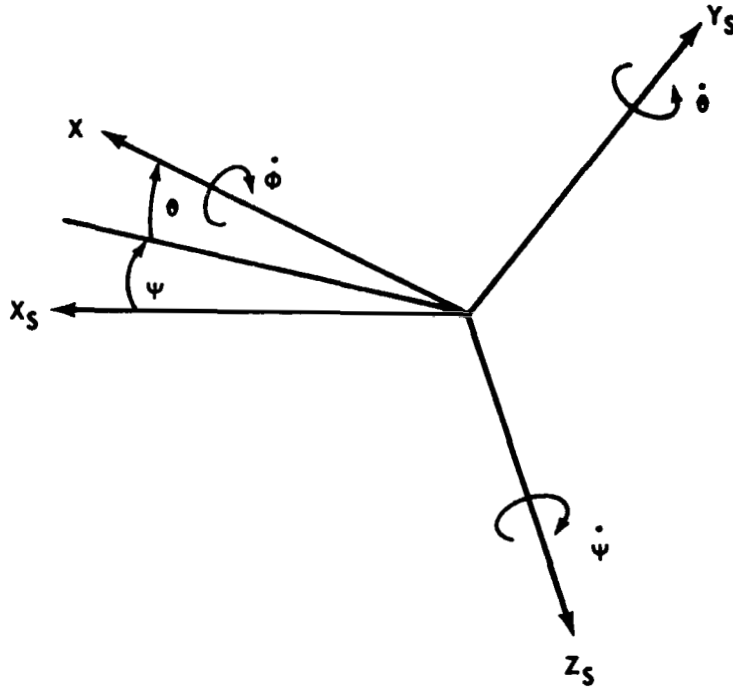

Figure J-15. Scan-axis deviation from inertial axes.

$$T_{ys} = - \left| \dot{\overline{\psi}} \times \overline{H} \right| = - \dot{\psi} H \tag{33}$$

where

T_{ys} — torque along Y_s - axis

$\dot{\psi}$ — angular velocity along z_s-axis

H — spacecraft angular momentum (assumed to be along X_s-axis).

θ — angular velocity along the Y_s - axis

Torque required to control (decrease) angle θ is

$$T_{z_s} = |\dot{\overline{\theta}} \times \overline{H}| = \dot{\theta} H \tag{34}$$

The components of the torque T_{y_s} and T_{z_s} in body axes are

$$T_y = T_{y_s} \cos \phi + T_{z_s} \sin \phi$$

$$T_z = T_{z_s} \cos \phi - T_{y_s} \sin \phi \tag{35}$$

where

ϕ — rotation angle on X-axis.

Substituting equations (33) and (34) into equation (35) gives

$$T_y = -\dot{\Psi} H \cos \phi + \dot{\theta} H \sin \phi$$

$$T_z = \dot{\theta} H \cos \phi + \dot{\Psi} H \sin \phi \qquad .$$

Introducing some damping torque expressions for damping of body rates in the above equations, we have the modified torques in the body axes as

$$T_{y'} = -\dot{\Psi} H \cos \phi + \dot{\theta} H \sin \phi - K_{y_1} \omega_y$$

$$T_{z'} = \dot{\theta} H \cos \phi + \dot{\Psi} H \sin \phi - K_{z_1} \omega_z \qquad . \tag{36}$$

In vector form the required control torque in body axes is

$$\overline{T} = T_{y'} j_b + T_{z'} k_b \qquad .$$

For the modified torques in the body axes given by equation (36), the inertial torque components are

$$T_{y_s} = T_{y'} \cos \phi - T_{z'} \sin \phi$$

$$T_{z_s} = T_{y'} \sin \phi + T_{z'} \cos \phi$$

The resultant of T_{y_s} and T_{z_s} is T_{yz}, a torque lying in the $Y_s - Z_s$ plane. The magnitude of T_{yz} is

$$T_{yz} = \left(T_{y_s}^2 + T_{z_s}^2 \right)^{1/2} \quad . \tag{37}$$

The angle α_T shown in Figure J-16 depicts the position of T_{yz} in the $Y_s - Z_s$ plane.

From Figure J-16,

$$\tan \alpha_T = \frac{T_{z_s}}{T_{y_s}} \quad . \tag{38}$$
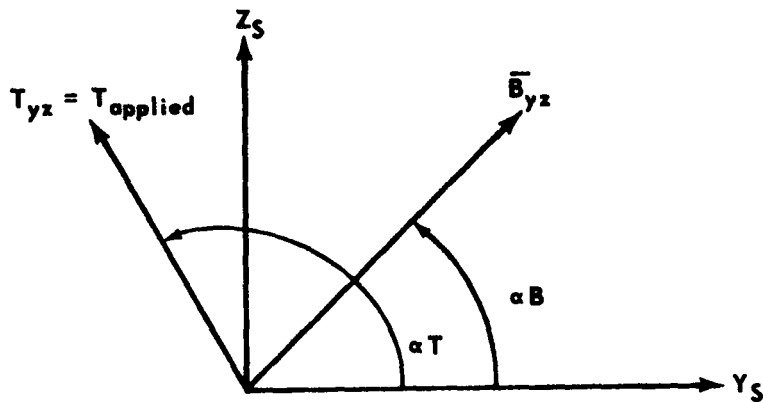
Figure J-16. $Y_s - Z_s$ plane showing angles α_B, α_T with respect to inertial axis, Y_s, Z_s.

The components B_{y_s} and B_{z_s} of the earth's magnetic field $\overline{B}$ are

$$B_{y_s} = B_y \cos \phi - B_z \sin \phi$$
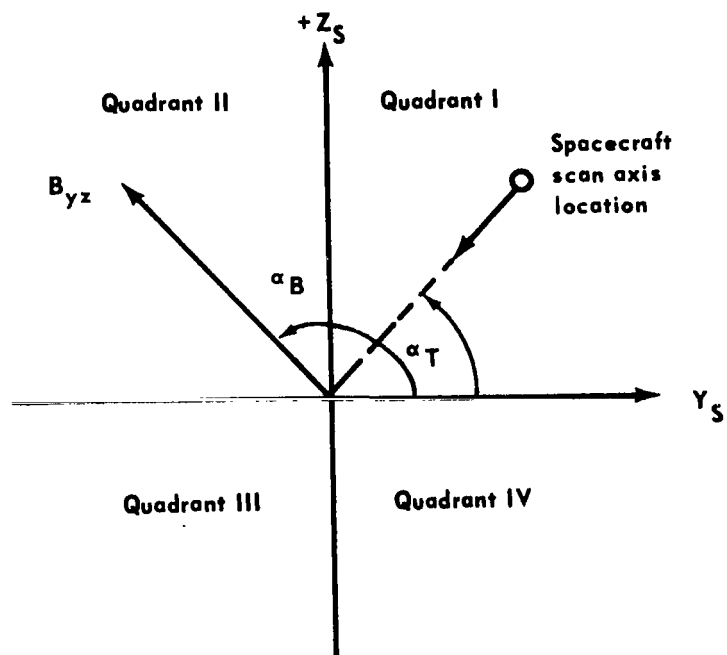
$$B_{z_s} = B_y \sin \phi + B_z \cos \phi$$

(39)

Figure J-17. Location of the spacecraft scan axis and orientation of field B_{yz} in $Y_s - Z_s$ plane.

where B_y and B_z are body axes components of $\overline{B}$ which are measured by the magnetometer. The magnitude of the component of $\overline{B}$ normal to the scan axis is

$$B_{yz} = \left(B_{y_s}^2 + B_{z_s}^2\right)^{1/2} = \left(B_y^2 + B_z^2\right)^{1/2} \quad . \tag{40}$$

From Figure J-16, the orientation of B_{yz} is given by

$$\tan \alpha_B = \frac{B_{z_s}}{B_{y_s}} \quad . \tag{41}$$

Substituting equation (39)

$$\tan \alpha_B = \frac{B_y \sin \phi + B_z \cos \phi}{B_y \cos \phi - B_z \sin \phi} \quad . \tag{42}$$

From equation (31), it is clear that the torque produced by the electromagnet located on the spacecraft X_b-axis (scan axis) will be normal to $\overline{B}_{yz}$. For optimum control, the control torque produced should coincide with $\overline{T}_{yz}$ as defined in equations (37) and (38).

In this event

$$\alpha_T = \alpha_{T'}$$

where $\alpha_{T'}$ is the angle to the applied torque vector, and

$$\alpha_T - \alpha_B = \pm 90 \text{ deg} \quad . \tag{43}$$

Whenever the condition expressed by equation (43) is satisfied and control torques given by equation (36) are applied, then both θ and Ψ angles will be reduced simultaneously. This is the optimum control law as minimum torquer on time is required. Because of variations in α_T and α_B with time, the opportunities when equation (43) is satisfied and the durations of these opportunities are limited. Therefore, the requirement for the condition defined in equation (43) is modified and the following control philosophy is used:

"Magnetic control torque will be used whenever it is possible to decrease either θ or Ψ, or both, without increasing either θ or Ψ."

Table J-5 gives the required orientation of the earth's magnetic field vector $\overline{B}_{yz}$ in the $Y_s - Z_s$ plane for attitude control of the scan axis. If $\overline{B}_{yz}$ is not in the required orientation, no control torques may be applied. Application of the constraints defined in Table J-5 is illustrated in Figure J-17. The scan-axis orientation is shown in Quadrant I; the direction of the desired control torque is shown as T. If a torque can be applied along this vector, the angles θ and Ψ will be reduced in the most efficient manner. However, to produce a torque in exactly this direction, the magnetic field vector $\overline{B}_{yz}$ must be perpendicular to T. Applying the previously stated control philosophy to the situation depicted in Figure J-17, a correction may be made whenever the $\overline{B}_{yz}$ vector lies in either Quadrant II or Quadrant IV. If $\overline{B}_{yz}$ lies in Quadrant II, as shown, the electromagnet parallel to the scan axis will be energized to produce a magnetic moment in the positive direction $(+M_x)$. If $\overline{B}_{yz}$ lies in Quadrant IV, a negative magnetic moment $(-M_x)$ is required and the scan-axis control electromagnet will be energized to produce this moment. The direction of the moment is determined by the direction of the current flow in the coils. Application of control torques under these restrictions will cause both θ and Ψ to be reduced, but not necessarily in the most efficient manner. If $\overline{B}_{yz}$ does not lie in a favorable quadrant, control of the scan axis must be deferred until it does. The angles α_T and α_B are calculated using equations (38) and (42), respectively. Whenever the conditions described in Table J-5 are satisfied, the control torques given by equation (36) are applied to the spacecraft until the scan-axis drift is less than some preset value.

TABLE J-5. REQUIRED ORIENTATION OF THE EARTH'S MAGNETIC FIELD VECTOR $\bar{\bar{B}}_{yz}$ FOR SCAN-AXIS ATTITUDE CONTROL

Position of Spacecraft Scan Axis in $Y_s - Z_s$ Plane	Angles in the $Y_s - Z_s$ Plane Measured from Y_s		Magnetic Moment (M_x) Direction
	α_T	α_B	
$\theta+$; $\Psi+$ (Quadrant I)	$0 < \alpha_T < \pi/2$	$\pi/2 < \alpha_B < \pi$	$+M_x$
		$3\pi/2 < \alpha_B < 2\pi$	$-M_x$
$\theta+$; $\Psi-$ (Quadrant II)	$\pi/2 < \alpha_T < \pi$	$\pi < \alpha_B < 3\pi/2$	$+M_x$
		$0 < \alpha_B < \pi/2$	$-M_x$
$\theta-$; $\Psi-$ (Quadrant III)	$\pi < \alpha_T < 3\pi/2$	$3\pi/2 < \alpha_B < 2\pi$	$+M_x$
		$\pi/2 < \alpha_B < \pi$	$-M_x$
$\theta-$; $\Psi+$ (Quadrant IV)	$3\pi/2 < \alpha_T < 2\pi$	$0 < \alpha_B < \pi/2$	$+M_x$
		$\pi < \alpha_B < 3\pi/2$	$-M_x$
$\theta = 0$; $\Psi+$	$\alpha_T = 0$	$\alpha_B = \pi/2$	$+M_x$
		$\alpha_B = 3\pi/2$	$-M_x$
$\theta = 0$; $\Psi-$	$\alpha_T = \pi$	$\alpha_B = 3\pi/2$	$+M_x$
		$\alpha_B = \pi/2$	$-M_x$
$\theta+$; $\Psi = 0$	$\alpha_T = \pi/2$	$\alpha_B = \pi$	$+M_x$
		$\alpha_B = 2\pi$	$-M_x$
$\theta-$; $\Psi = 0$	$\alpha_T = 3\pi/2$	$\alpha_B = 0$	$+M_x$
		$\alpha_B = \pi$	$-M_x$

2. Scan-rate control. Scan-rate control can be effectively carried out using two electromagnets or coils aligned along the two spacecraft axes Y and Z normal to the scan axis. The current applied to the Y-axis coil is directly proportional to the value of the Z-axis magnetometer reading, and the Z-axis coil current is similarly directly proportional to the Y-axis magnetometer reading. The two electromagnets, together with the earth's magnetic field, function as an electric motor to apply a control torque about the scan axis. The torque produced is given by equation (31). Since the electromagnet parallel to the scan axis X is not energized, $M_x = 0$ and the torques produced along the spacecraft axis are

$$T_x = M_y B_z - M_z B_y$$

$$T_y = M_z B_x \qquad\qquad\qquad (44)$$

$$T_z = -M_y B_x \qquad .$$

For scan-rate control, only torque about the spacecraft X-axis is desired. Unless the earth's magnetic field is exactly perpendicular to the scan axis $(B_x = 0)$ when the Y- and Z-axes' electromagnets are energized, a disturbing torque is produced on the attitude of the scan axis. Therefore, scan-rate corrections are made only when B_x is as small as possible. If B_x is large, control is deferred to a more favorable time.
favorable time.

Assume

$$M_y = K B_z \qquad\qquad\qquad (45)$$

and

$$M_z = -K B_y \qquad\qquad\qquad (46)$$

where K is some positive constant to be determined. Substituting equations (45) and (46) into equation (44) gives

$$K = \frac{T_x}{B_y^2 + B_z^2} \qquad .$$

(47)

Torque T_x can be expressed as

$$T_x = \frac{I_x}{t} \Delta\omega_x$$

(48)

where

I_x — spacecraft moment of inertia about the X-axis

t — time that magnetic torquers are energized

$\Delta\omega_x$ — change in spin rate desired.

d. Galactic Scan Mode. In this mode, magnetic torquers are used for attitude control. The principal of operation is the same as discussed in the celestial scan mode; however, in this case the inertial reference axis is the solar offset axis instead of solar axis. The angles θ and Ψ are measured relative to this new inertial reference axis. The scan-axis attitude control and scan-rate control equations are the same as for the celestial scan mode.

e. Celestial Pointing Mode. In this mode the spacecraft is not rotating, but the flywheel is spinning. Attitude is controlled using a magnetic coil or electromagnet located on each of the spacecraft body axes. In the HEAO baseline configuration, the viewing direction of the major experiments is aligned with the spacecraft Y-axis. To point these experiments at a target, it is necessary to align the spacecraft Y-axis on this target. Furthermore, it is necessary to control the spacecraft attitude to ±1.0 degree about the spacecraft X- and Z-axes during the pointing period. Control about the spacecraft Y-axis (line-of-sight of the experiments) is not required by the experiments, but control to within a few degrees is necessary to maintain the proper solar panel orientation to the solar vector. The control required about the Y-axis is a function of the electrical power requirement and the orientation of the solar vector relative to the target, rather than an experiment pointing requirement.

The pointing mode control requirements are illustrated in Figure J-18. The inertial axis system X_s, Y_s, Z_s is spacecraft centered. The P-axis is along the vector from the spacecraft to the viewing target. The X_s-axis is normal to Y_s and is parallel to the ecliptic plane. The Z_s-axis forms a right-hand orthogonal system with X_s and Y_s. To bring the Y-axis back onto the target, a torque $\overline{T}_d$ in the direction shown is desired. This torque is produced by energizing coils on all three spacecraft axes. The control torque $\overline{T}$ produced by the coils is given equation (21), which is repeated as follows:

$$\overline{T} = \overline{M} \times \overline{B}$$

where $\overline{M}$ is the magnetic moment produced by the coils and $\overline{B}$ is the earth's magnetic field. To get an expression of the value of M, each side of equation (31) is multiplied by the vector $\overline{B}$

$$\overline{B} \times \overline{T} = \overline{B} \times (\overline{M} \times \overline{B}) \qquad (49)$$
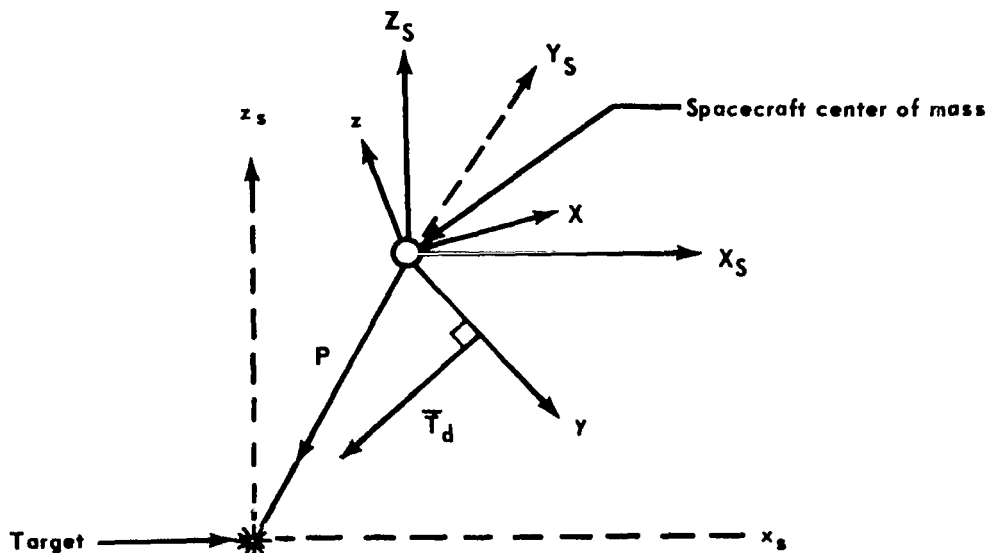
Figure J-18. Spacecraft Y-axis position relative to desired target position in the celestial pointing mode.

To produce maximum torque using minimum power, the vector $\overline{M}$ should be perpendicular to the magnetic field vector $\overline{B}$. In this case,

$$\overline{M} \cdot \overline{B} = 0 \tag{50}$$

and equation (49) becomes

$$\overline{B} \times \overline{T} = B^2 \overline{M} \tag{51}$$

or

$$\overline{M} = \frac{\overline{B} \times \overline{T}}{B^2} \quad . \tag{52}$$

Expansion of equation (52) gives the magnetic moments required for each coil.

$$M_x = \frac{1}{B^2} (B_y T_z - B_z T_y)$$

$$M_y = \frac{1}{B^2} (B_z T_x - B_x T_z) \tag{53}$$

$$M_z = \frac{1}{B^2} (B_x T_y - B_y T_x)$$

where B_x, B_y, B_z are the components of the earth's magnetic field along spacecraft body axes X, Y, and Z, respectively and T_x, T_y, T_z are torques about the spacecraft body axes X, Y, and Z, respectively.

J-60

Since the produced torque $\overline{T}$ is normal to the magnetic field vector $\overline{B}$,

$$\overline{T} \cdot \overline{B} = 0 \tag{54}$$

and

$$T_x B_x + T_y B_y + T_z B_z = 0 \tag{55}$$

or

$$T_y = - \left(\frac{T_x B_x + T_z B_z}{B_y} \right) \ . \tag{56}$$

Thus, even though no torque is desired about the line-of-sight axis Y, a torque is produced about this axis because of vector cross products. The magnitudes and directions of the required magnetic moments for each coil are obtained by substituting the values of T_x and T_z from equation (27) and the value of T_y from equation (56) into equation (53). The values of B_x, B_y, and B_z are measured directly by the magnetometer on the spacecraft. The amount of current required for each coil is determined from equation (57) (for a coil with no core).

$$M = NIA \tag{57}$$

where

N — the number of turns in the coil

A — the cross sectional area of the coil

I — the current in the coil, amperes.

For a coil with a core (electromagnet), the required power is given by equation (58) [J-1].

$$p = 4\pi \frac{\mu_0 H^2 L \sigma \rho}{W} \frac{M}{B_s} \tag{58}$$

where

p — power, watts

W — weight of the winding of the electromagnet, kg

H — field strength produced by the winding of the electromagnet, amp turns/m

L — length of the core, m

σ — coil resistivity, ohms/m

ρ — density of the coil, kg/m^3

μ_0 — constant = $4\pi \times 10^{-7}$

M — magnetic moment required, amp turns

B_s — induced field strength, weber/m^2 .

A disadvantage of magnetic coil attitude control in the celestial pointing mode is the presence of the undesirable torque, T_y. Whenever B_y is very small, T_y tends to be very large, as indicated by equation (56). In addition, the small value of B_y and large value of T_y result in the requirement of large magnetic moments about the X and Z spacecraft axes, as indicated in equation (53). The requirement for large magnetic moments imposes a requirement for large currents in these coils. Therefore, attitude control corrections cannot be made using this control scheme when B_y is very small. Whenever B_y is too small, attitude control about the X- and Z-axes may be performed using the single coil on the Y-axis, as in the

celestial scan mode, providing the field orientation is favorable for the desired correction. If neither of these conditions is satisfied, attitude control must be postponed until one condition becomes favorable. The spinning flywheel will provide a measure of stability about the spacecraft Y- and Z-axes, but not about the X-axis.

7. Transformation of the Earth's Magnetic Field Into Spacecraft Coordinates

The analysis of a control system making use of the earth's magnetic field requires knowledge of the field in vehicle coordinates as a function of the satellites' position in orbit. Accordingly, the equations of the earth's magnetic field in body principal (control) axes must be derived as functions of geophysical and orbital parameters. Several models of the earth's field are available, but all are expressed in terms of geomagnetic or spherical coordinates referenced to the geomagnetic axes. For preliminary design purposes, a magnetic field model with a magnetic dipole set along the earth's geomagnetic axis will provide sufficient accuracy for control system design and simulation. The declination of the dipole with the geometric north is assumed to be 11 degrees with the positive end towards the geographic South pole. Such a model has been utilized in the HEAO control system simulations using magnetic torquers.

A tilted dipole model of the earth's magnetic field [J-9] is given in vector form in polar coordinates by

$$\bar{B} = \frac{Me}{R^3} \left(c\mu \, \bar{e}_\mu - 2 \, s\mu \, \bar{e}_r \right) \tag{59}$$

where

M_e — Earth's magnetic dipole moment (8.1×10^{25} emu)

$\bar{e}_r$ — Unit vector along $\bar{R}$

$\bar{e}_\mu$ — Unit vector normal to $\bar{R}$, and directed northward (tangent to a meridian)

$\bar{e}_\gamma$ — Unit vector such that $(\bar{e}_r, \bar{e}_\gamma, \bar{e}_\mu)$ form a right-hand triad

Figure J-19 illustrates the spherical relative to the geomagnetic coordinate system. The transformation necessary to relate the geomagnetic coordinates to the body principal axes, and the elements of the transformation matrices, have been listed in Paragraph 4 of this appendix. The spherical can be related to the geomagnetic coordinates by either projecting the

components of $\overline{e}_r$, $\overline{e}_\gamma$, and $\overline{e}_\mu$ on to the geomagnetic axes to obtain

$$\overline{e}_r = C\mu C\gamma \, i_m + C\mu S\gamma \, j_m + S\mu \, k_m \qquad (60)$$

$$\overline{e}_\gamma = -S\gamma \, i_m + C\gamma \, j_m$$

$$\overline{e}_\mu = -S\mu C\gamma \, i_m - S\mu S\gamma \, j_m + C\mu \, k_m$$

or by rotating about the $\overline{e}_\gamma$ axis by the angle μ and then about the once-transformed $\overline{e}_\mu$ axis by the angle $-\gamma$. In vector matrix form, the result is

$$
\begin{vmatrix} \overline{e}_r \\ \overline{e}_\gamma \\ \overline{e}_\mu \end{vmatrix} \equiv \tilde{e} = \begin{vmatrix} C\mu C\gamma & C\mu S\gamma & S\mu \\ -S\gamma & C\gamma & 0 \\ -S\mu C\gamma & -S\mu S\gamma & C\mu \end{vmatrix} \tilde{X}_m \qquad . \qquad (61)
$$

Notice that the first of equations (60) is a unit vector directed from the earth's center to the spacecraft in orbit and may be identified with equation (6) of Paragraph 4 which is repeated below:

$$\overline{R}_o = i_p = C_{11} \, i_b + C_{21} \, j_b + C_{31} \, k_b \qquad . \qquad (62)$$
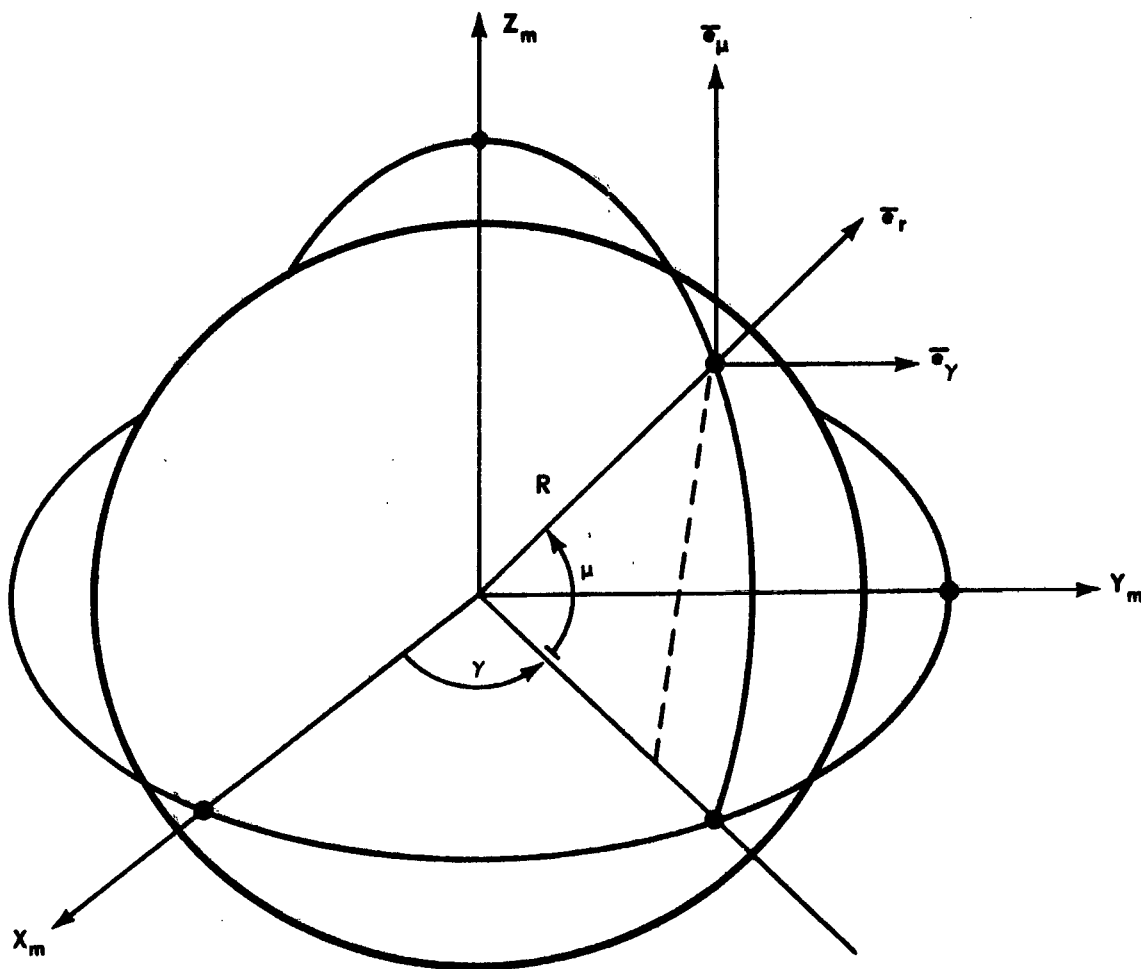
Figure J-19. Spherical components of earth's magnetic field relative to
geomagnetic coordinates.

Hence, $\bar{R}_o \equiv \bar{e}_r$, but the two are expressed relative to different coordinate frames. The first of equations (60) can be rewritten as

$$\bar{e}_r = \bar{R}_o = R_{xm}\, i_m + R_{ym}\, j_m + R_{zm}\, k_m \tag{63}$$

where R_{xm}, R_{ym}, and R_{zm} are the components of $\bar{e}_r$ in geomagnetic coordinates as given in equation (60).

Substituting equation (60) into equation (59) gives $\bar{B}$ in the geomagnetic reference frame.

$$\bar{B} = \frac{-M_e}{R^3}\left[3\, C\mu\, S\mu\, C\gamma\, i_m + 3\, C\mu\, S\mu\, S\gamma\, j_m + (3\, S^2\mu - 1)\, k_m \right] \quad . \tag{64}$$

Equation (64) is sometimes expressed in terms of the components of $\bar{e}_r$, given in equation (5), as

$$\bar{B} = \frac{-M_e}{R^3}\left[3\, R_{xm}\, R_{zm}\, i_m + 3\, R_{ym}\, R_{zm}\, j_m + (3\, R^2_{zm} - 1)\, k_m \right] \tag{65}$$

The vector components of $\bar{B}$ are now known in the geomagnetic reference frame, but for control studies must be projected into body principal axes by using the transformation matrix

$$\tilde{X}_b = M_{bm}\, \tilde{X}_m \tag{66}$$

whose elements are given in this appendix. The components R_{xm}, R_{ym}, and R_{zm} which form the elements of $\bar{B}$ are known functions of the sperical parammeters μ and γ. However, to avoid introducing additional unknown parameters into the system simulation, R_{xm}, R_{ym}, and R_{zm} can be replaced as functions of previously defined direction cosines [J-4].

$$\widetilde{X}_g = A_{gn} A_{nm} \widetilde{X}_m = L_{gm} \widetilde{X}_m \tag{67}$$

where the elements of L_{gm} are

$$L_{11} = C\Omega_m \qquad , \qquad L_{23} = -C\Omega_m S\xi \tag{68}$$

$$L_{12} = -S\Omega_m C\xi \qquad , \qquad L_{31} = 0$$

$$L_{13} = S\Omega_m S\xi \qquad , \qquad L_{32} = S\xi$$

$$L_{21} = S\Omega_m \qquad , \qquad L_{33} = C\xi$$

$$L_{22} = C\Omega_m C\xi$$

and

$$\widetilde{X}_g = A_{ge} A_{eo} A_{op} \widetilde{X}_p \equiv E_{gp} \widetilde{X}_p \tag{69}$$

where the elements of E_{gp} are

$$E_{11} = C\theta_o C\Omega - S\theta_o S\Omega C\iota \qquad , \qquad E_{31} = S\theta_o S\iota$$

$$E_{12} = -S\theta_o C\Omega - C\theta_o S\Omega C\iota \qquad , \qquad E_{32} = C\theta_o S\iota \tag{70}$$

$$E_{13} = S\Omega S\iota \qquad , \qquad E_{33} = C\iota$$

$$E_{21} = C\theta_o S\Omega + S\theta_o C\Omega C\iota$$

$$E_{22} = -S\theta_o S\Omega + C\theta_o C\Omega C\iota$$

$$E_{23} = -C\Omega S\iota$$

J-68

Combining equations (67) and (69) produces

$$\tilde{X}_m = L^*_{gm} \, E_{gp} \, \tilde{X}_p \equiv F_{mp} \, \tilde{X}_p \qquad (71)$$

Using equation (71) to convert the local vertical to geomagnetic coordinates, the local vertical unit vector in equation (62) is

$$\overline{R}_o = i_p = F_{11} \, i_m + F_{21} \, j_m + F_{31} \, k_m \qquad . \qquad (72)$$

Equating components of equations (63) and (72) produces

$$R_{xm} \equiv F_{11} \equiv E_{11} L_{11} + E_{21} L_{21} + E_{31} L_{31} \qquad (73)$$

$$R_{ym} \equiv F_{21} \equiv E_{11} L_{12} + E_{21} L_{22} + E_{31} L_{32}$$

$$R_{zm} \equiv F_{31} \equiv E_{11} L_{13} + E_{21} L_{23} + E_{31} L_{33} \qquad \qquad .$$

Utilizing equation (73) permits rewriting equation (65) in terms of known direction cosine values:

$$\overline{B} = B_{xm} \, i_m + B_{ym} \, j_m + B_{zm} \, k_m \qquad (74)$$

where

$$B_{xm} = (3 - M_e/R^3) \, F_{11} \, F_{31} \qquad (75)$$

$$B_{ym} = (3 - M_e/R^3) \, F_{21} \, F_{31}$$

$$B_{zm} = (3 - M_e/R^3) \, (F_{31}^2 - 1/3) \qquad \qquad .$$

The components of the earth's magnetic field, $\overline{B}$, in body principal (control) axes are obtained by operating on the components of equation (74) by the matrix transformation given in equation (66). The resultant is

$$\overline{B} = B_x \, \mathbf{i}_b + B_y \, \mathbf{j}_b + B_z \, \mathbf{k}_b \qquad (76)$$

where

$$B_x = B_{xm} \, M_{11} + B_{ym} \, M_{12} + B_{zm} \, M_{13} \quad , \qquad (77)$$

$$B_y = B_{xm} \, M_{21} + B_{ym} \, M_{22} + B_{zm} \, M_{23} \quad ,$$

and

$$B_z = B_{xm} \, M_{31} + B_{ym} \, M_{32} + B_{zm} \, M_{33} \quad .$$

Although the procedure used to obtain the earth's magnetic field vector in body principal axes is complicated by the number of necessary transformations, these matrix transformations and their elements are greatly simplified by assuming constant values for those angles which vary slowly with time. In the HEAO computer simulations, the angular constants were selected such that worst case time response data were obtained.

8. Aerodynamic Coefficients for the HEAO Satellite

Aerodynamic force and moment coefficients were calculated for the HEAO satellite depicted in Figure J-20. The axial and normal force coefficients and the pitching moment coefficients (Figs. J-21, J-22, J-23) were calculated assuming free molecular flow and diffuse reflection. Data were obtained for a circular orbit altitude of 200 n. mi. and total angles of attack, α_T, ranging from 0 to 180 degrees and a roll angle, ϕ, of 0 degree. For an axisymmetric body and ϕ equal to 0 degree, the side force and the yawing and rolling moments are zero. The HEAO coefficients were obtained through Reference J-10.
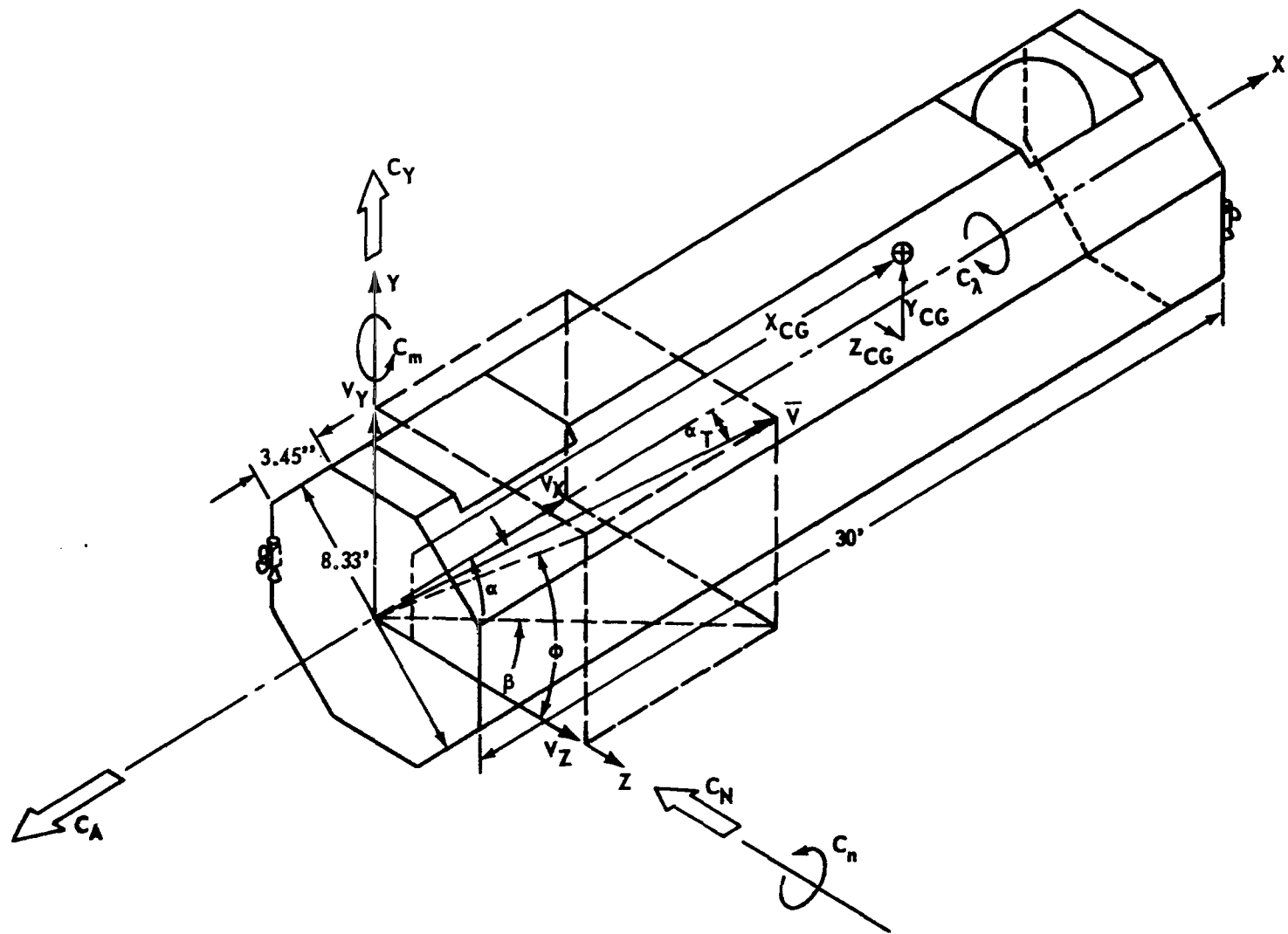
Figure J-20.   HEAO satellite.
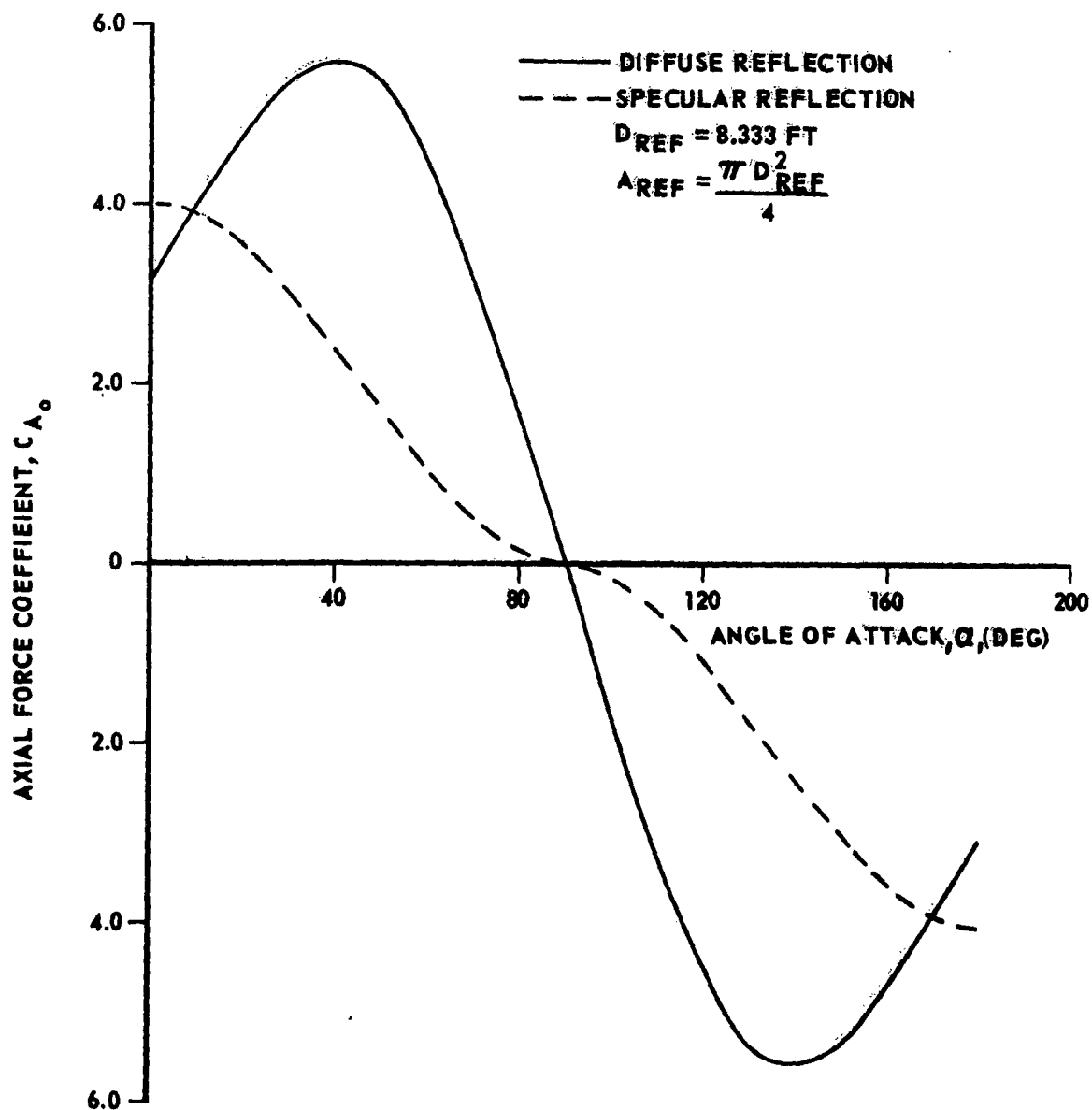
Figure J-21. Axial force coefficient versus angle of attack.
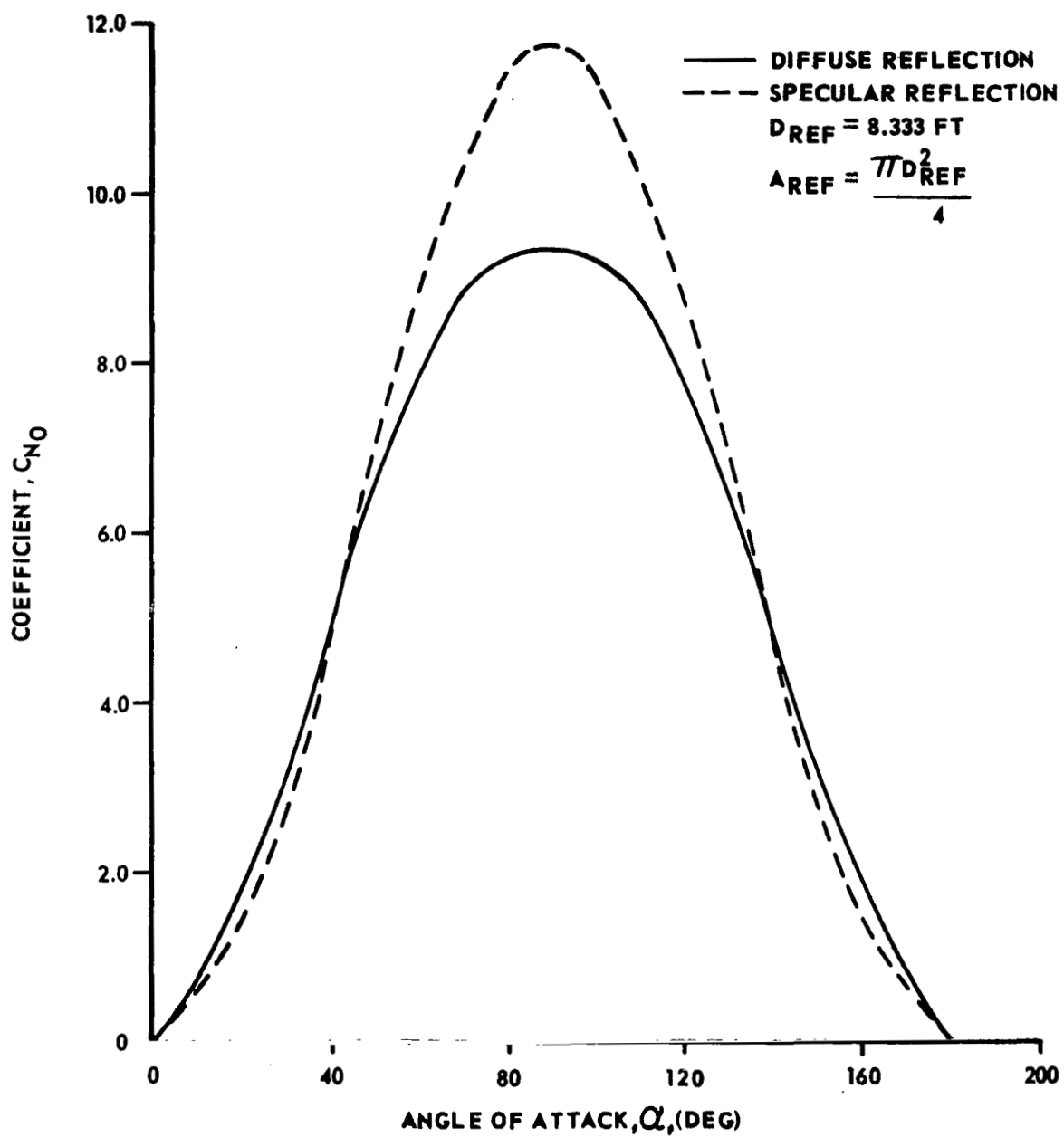
Figure J-22. Axial normal force coefficient versus angle of attack.

Figure J-23.   Moment coefficient versus angle of attack.

A Fourier series curve fit of the resulting data was made using the truncated Fourier series

$$C(\alpha_T) = \frac{A_o}{2} + \sum_{i=1}^{m} \left[A_i \cos (i \, \alpha_T) + B_i \sin (i \, \alpha_T)\right] \tag{78}$$

where m is the number of terms required to achieve the desired degree of accuracy. A_i and B_i are calculated using the relations

$$A_i = \frac{1}{\pi} \int_0^{2\pi} C(\alpha_T) \cos (i \, \alpha_T) \, d\alpha_T \tag{79}$$

$$B_i = \frac{1}{\pi} \int_0^{2\pi} C(\alpha_T) \sin (i \, \alpha_T) \, d\alpha_T \tag{80}$$

where $C(\alpha_T)$ is the aerodynamic coefficient being curve fitted.

Curve-fit coefficients were obtained for the axial and normal force coefficients, C_{A_o} and C_{N_o}, respectively, and the pitching moment coefficient, C_{m_o}. The resulting expressions as a function of α_T are as follows:

$$C_{A_o} = 5.77121 \cos (\alpha_T) - 1.75706 \cos (3\alpha_T) - 0.40363 \cos (5\alpha_T)$$
$$-0.08961 \cos (7\alpha_T) + 0.04889 \cos (9\alpha_T) \tag{81}$$

$$C_{N_o} = 8.77165 \sin (\alpha_T) - 0.96271 \sin (3\alpha_T) - 0.34303 \sin (5\alpha_T)$$
$$+ 0.02238 \sin (7\alpha_T) + 0.00889 \sin (9\alpha_T) \tag{82}$$

$$C_{m_o} = 14.88051 \sin (\alpha_T) - 1.60280 \sin (3\alpha_T) - 0.54178 \sin (5\alpha_T)$$
$$+ 0.00297 \sin (7\alpha_T) - 0.01482 \sin (9\alpha_T) \tag{83}$$

Equations (81), (82), and (83) will yield the axial and normal force coefficients and the pitching moment coefficients, respectively, for ϕ equal to zero and for any given α_T.

To determine the aerodynamic coefficients for an arbitrary ϕ, substitute the values of C_{A_o}, C_{N_o}, and C_{m_o} for a given α_T along with the chosen value of ϕ into the following equations:

$$C_A = C_{A_o} \tag{84}$$

$$C_N = C_{N_o} \cos\phi \tag{85}$$

$$C_Y = -C_{N_o} \sin\phi \tag{86}$$

$$C_L = C_{L_o} = 0 \tag{87}$$

$$C_m = C_{m_o} \cos\phi \tag{88}$$

$$C_n = -C_{m_o} \sin\phi \tag{89}$$

If α and β (Fig. J-20) are known instead of α_T and ϕ, the following equations can be used to determine α_T and ϕ as a function of α and β.

$$\phi = \tan^{-1}\left[\frac{\tan\beta}{\sin\alpha}\right] = \tan^{-1}\left[\frac{V_y}{V_z}\right] \tag{90}$$

$$\alpha_T = \cos^{-1}\left[\frac{\sin\beta}{\tan\alpha \, \tan\phi}\right] = \cos^{-1}\left[\frac{V_x}{|V|}\right] \tag{91}$$

Where V_x, V_y, V_z are components of the velocity vector expressed in body coordinates.

For convenience the origin of the body axis system (moment reference point) was located at one end of the vehicle (Fig. J-20). For dynamic studies, the axis origin is usually located at the center of gravity (CG) of the orbiting vehicle. To determine the moment coefficients about the CG location, the following moment transfer equations should be used:

$$C_{m_{CG}} = C_m + C_A \frac{Z_{CG}}{D_{ref}} - C_N \frac{X_{CG}}{D_{ref}} \qquad (92)$$

$$C_{n_{CG}} = C_n - C_Y \frac{X_{CG}}{D_{ref}} - C_A \frac{Y_{CG}}{D_{ref}} \qquad (93)$$

$$C_{L_{CG}} = C_L + C_Y \frac{Z_{CG}}{D_{ref}} + C_N \frac{Y_{CG}}{D_{ref}} \qquad (94)$$

In these equations, X_{CG}, Y_{CG}, and Z_{CG} are the coordinates of the CG location expressed in terms of the aerodynamic body axis system defined in Figure J-20.

Aerodynamic moments about the CG can then be calculated with the following equations:

$$M_{X_{CG}} = q A_{ref} D_{ref} C_{L_{CG}} \qquad (95)$$

$$M_{Y_{CG}} = q A_{ref} D_{ref} C_{M_{CG}} \qquad (96)$$

$$M_{Z_{CG}} = q A_{ref} D_{ref} C_{n_{CG}} \qquad (97)$$

9. Alternate Spacecraft Concept
Performance Simulations

In Section XI, computer simulated performance data for the baseline configuration with a spinning flywheel were given for the following two cases:

- Uncontrolled spacecraft gravity torques acting as disturbance torques.

- Spacecraft controlled with magnetic torquers. A three-coil control scheme was used for attitude control. Gravity torques were acting as disturbance torques.

In addition to the above cases, computer simulation data were also obtained for the following cases of Configurations I and III (Fig. J-8) for the same orbital parameters:

- Configuration I (baseline)

    - Baseline configuration with a flywheel and with attitude control (one-coil control scheme).

    - Baseline configuration without a spinning flywheel and without attitude control

    - Baseline configuration without a spinning flywheel and with attitude control (three-coil control scheme).

- Configuration III

    - Configuration III with a flywheel and without attitude control

    - Configuration III without a flywheel and without attitude control.

Performance results for each of the above cases are given in the following Paragraphs.

a. Configuration I (Baseline)

1. With flywheel and control. The case simulated was the baseline configuration with a spinning flywheel and with attitude control. The

difference between this case and the one reported in Section XI is that in this case a single-coil control scheme was used to control scan-axis drift, whereas in the previously reported case a three-coil control scheme was used.

In the one-coil control scheme, only one coil is used for scan-axis attitude control in the scan mode; this coil is aligned along the scan axis. The other two coils, which are mounted normal to the scan axis, are used primarily for scan-rate control in the scanning mode. In the three-coil control scheme, three coils aligned along the three body axes of the spacecraft are used simultaneously to produce a magnetic moment vector normal to the instantaneous earth's magnetic field vector. The disadvantages of the three-coil control scheme are that an undesirable torque about the scan axis is produced and it is more difficult to apply than the one-coil control scheme. The advantages of the three-coil control scheme, compared with the one-coil control scheme, are that it requires less power and provides continuous control torque except when the earth's magnetic field vector is in the direction of desired control torque.

The control laws used for applying magnetic control torquers in the body axes are given in Paragraph 6 of this appendix as

$$T_{y'} = -\dot{\Psi} H \cos \phi + \dot{\theta} H \sin \phi - k_{y_1} w_y$$

$$T_{z'} = \dot{\theta} H \cos \phi + \dot{\Psi} H \sin \phi - k_{z_1} w_z \qquad .$$

These equations can be modified and expressed as

$$T_{y'} = -k_{y_2} \Psi \cos \phi + k_{y_3} \theta \sin \phi - k_{y_1} w_y$$

$$T_{z'} = k_{z_2} \Psi \sin \phi + k_{z_3} \theta \cos \phi - k_{z_1} w_z$$

where k_{y_2}, k_{y_3}, k_{z_2}, k_{z_3} are some positive constants selected on the basis of speed of response desired. For the computer simulation of the baseline with single-coil control logic, the values of gain constants selected are as follows:

$$k_{y_1} = k_{z_1} = 110 \ \delta > 0. \ 2 \text{ degree}$$

$$k_{y_1} = k_{z_1} = 130 \text{ for } \delta \leq 0. \ 2 \text{ degree}$$

$$k_{y_2} = k_{y_3} = k_{z_2} = k_{z_3} = 20 \qquad .$$

The performance results for this case are given by Figures J-24, J-25, and J-26. Figure J-24 shows the scan-axis drift angle δ in one orbit time for the controlled spacecraft. The value of δ does not become greater than 0. 29 degree. The value of δ starts increasing at a faster rate at about 800 sec and goes to its peak value of 0. 29 degree at about 1600 seconds and then starts decreasing at a faster rate to less than 0. 067 degree in the next 500 sec, at which time the magnetic torquers are shut off. The same cycle is repeated during the 3500- to 4500- second interval. There are two reasons for this rapid buildup of δ during the 800 to 1600 second and the 3600 to 4300-second periods. Firstly a one coil system can utilize only half of the faborable Earth's field for the production of sufficient control torques at these times, and secondly gravity disturbance torques in the Y_s and Z_s axes are nearly maximums at these times.

Figure J-25 is the plot of the trace of the scan axis in $\Psi - \theta$ plane for the controlled spacecraft. Figure J-26 shows the power profile for the magnetic torquers in X, Y, Z body axes. The maximum allowed power of 100 watts is utilized during 800-to 1400- and 3600- to 4100- second intervals due to the unfavorable control opportunities of a one coil system.-

In the actuator subsection, it was shown that the effective component of the earth's magnetic field for scan axis attitude control is the component of the field which lies in the plane $Y_s - Z_S$; this component is normal to the scan axis X_s. From Figures XI-21 and XI-22 it is seen that the component of the earth's magnetic field in the $Y_s - Z_s$ plane is very small in the 800- to 1300- second and 3500- to 4000- second intervals of the orbit time and that most of the field lies along the axis Z_s (Fig. XI-20) during this period. At these times, the production of control torques for scan-axis attitude control cannot be optimally produced by the scan axis coil, M_x, as indicated by the large power usage shown in Figure J-26.
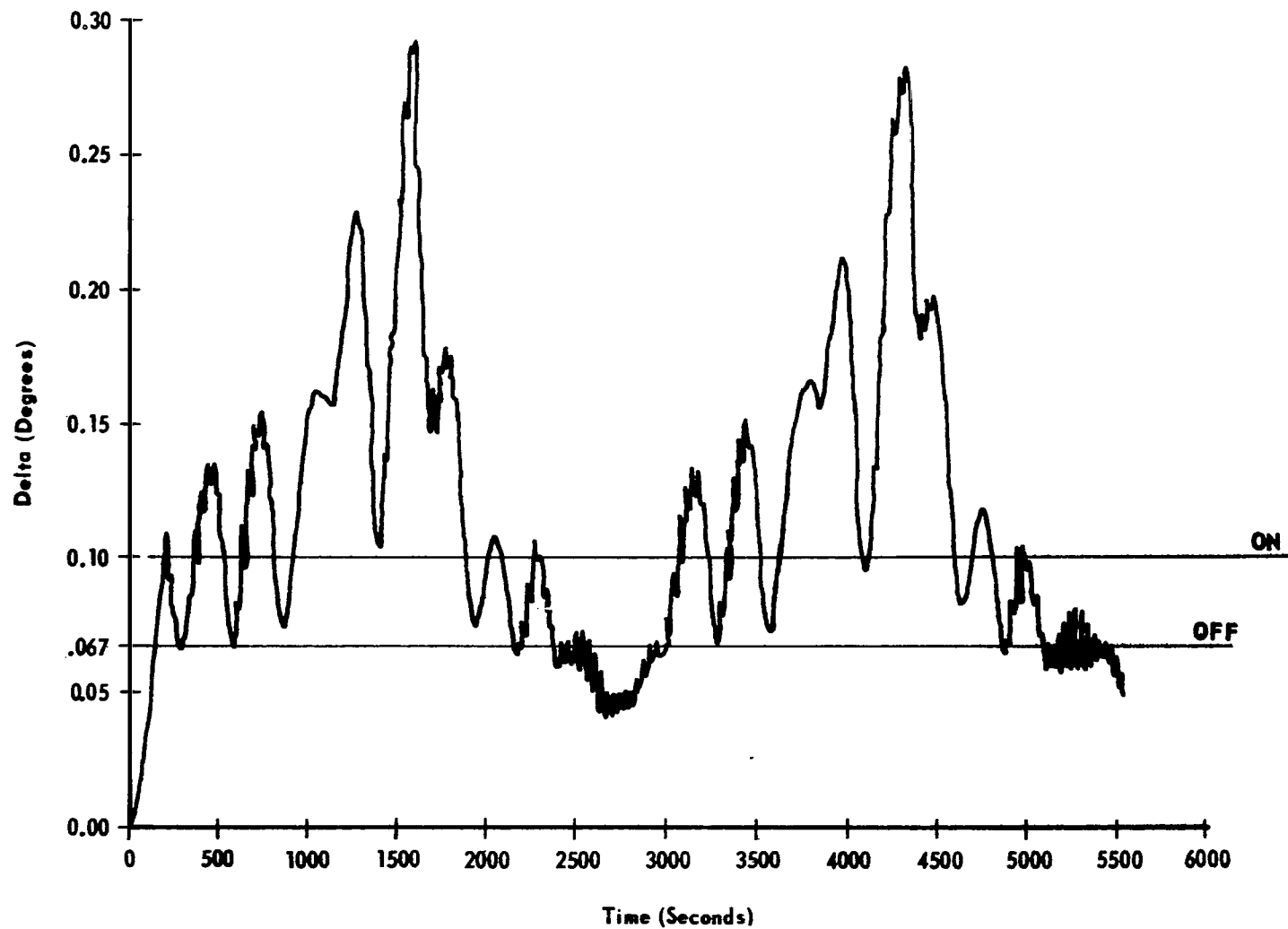
Figure J-24. Baseline configuration with flywheel and single-coil control scheme deviation angle δ as a function of time.
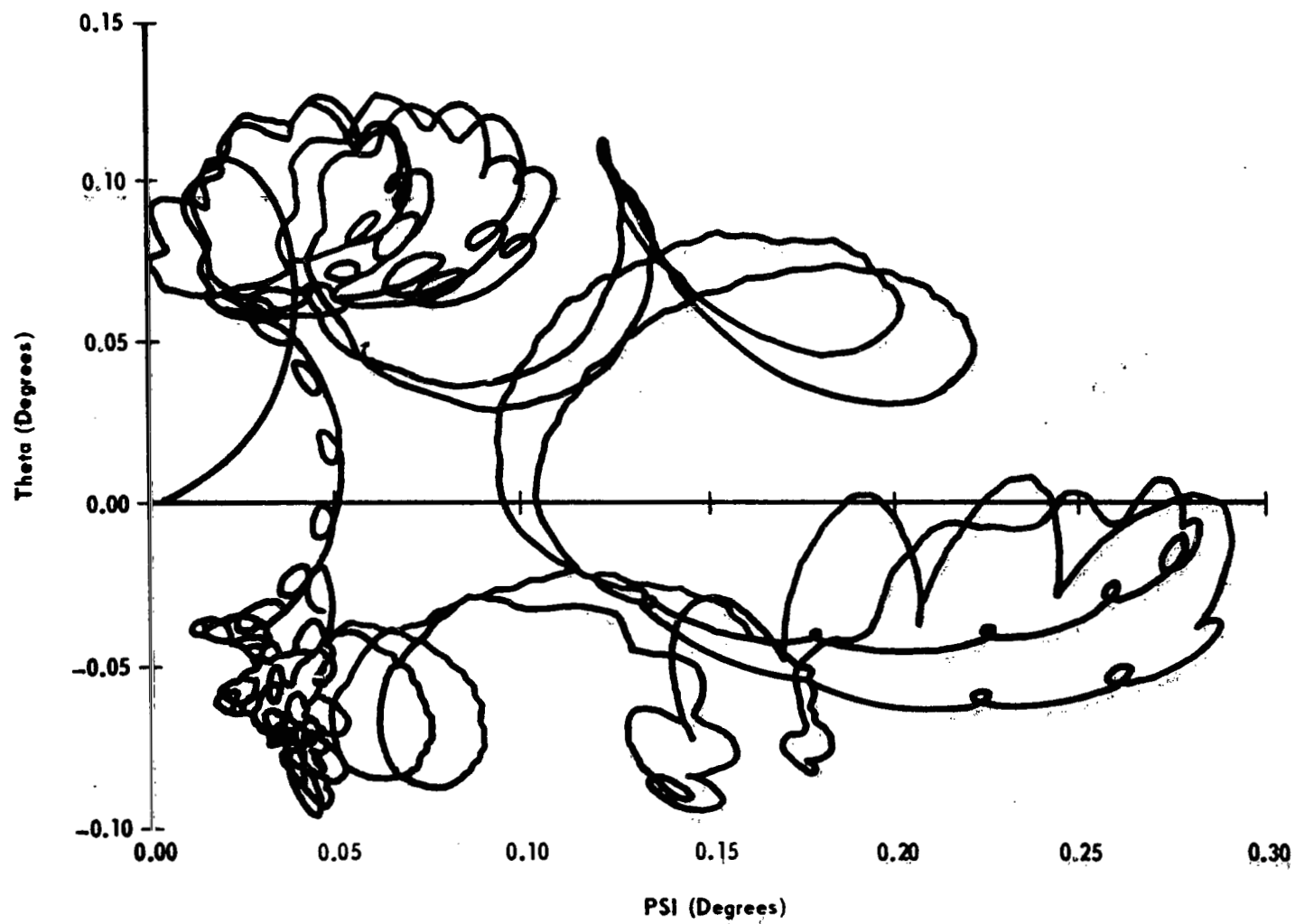
Figure J-25. Baseline configuration with flywheel and single-coil control scheme.
Trace of scan axis in the $\theta - \Psi$ plane.
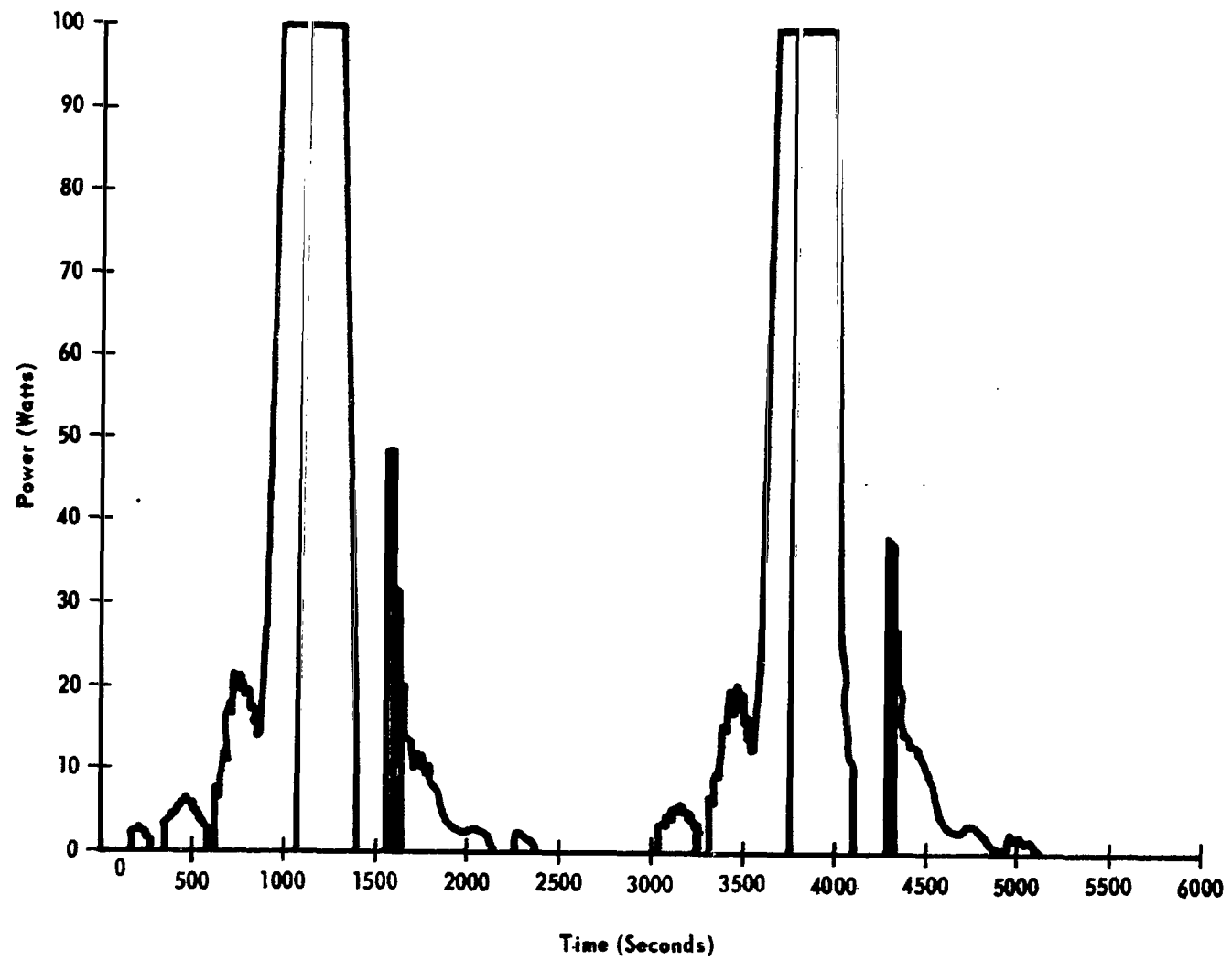
Figure J-26. Baseline configuration with flywheel and single-coil control scheme. Power required for control torques.

It was also pointed out in the actuator subsection that scan rate adjustments would be carried out only when the earth's magnetic field component along the scan axis is very small ($B_{x_s} \leq 0.001$ gauss). However from Figure XI-20 it is seen that B_{x_s} maintains a value of 0.15 during most orbital periods. In this situation, scan-rate adjustments can be made, but this will cause a perturbation in the attitude of the scan axis caused by undesirable components of the torque produced in the plane normal to the scan axis.

2. Without flywheel and control. In this case the flywheel is not spinning. Since the angular momentum of the spacecraft caused by spacecraft rotation alone is much smaller than the baseline concept having a spinning flywheel, a large drift of the scan axis for the same value of gravity disturbance torque is expected. Figure J-27 shows the variations in the scan-axis drift angle δ with orbit time. The scan axis drifts continuously and reaches a value of 14.1 degrees in one orbit time period. Figure J-28 shows the trace of the scan axis in the $\Psi - \theta$ plane in one orbit period. It is noted in Figure J-28 that Ψ increases continuously and reaches a value of about 14.1 degrees, whereas the variations in θ are cyclic with a secular component of -0.55 degree at the end of the orbit time. In this case, the value of θ at the end of the orbit is negative (-0.55 degree), whereas in the baseline concept with a spinning flywheel and without control it was positive (+0.25 degree, Fig. XI-37). This difference caused by the variations in the values of gravity disturbance torques (Figs. J-29, J-30, and J-31) as the values of Ψ and θ angles get larger.

3. Without flywheel and with control. For this case the three-coil control scheme was used. The values of the gain constants used in the control laws were arbitrarily selected as:

$$k_{y_1} = k_{z_1} = 1.0$$

$$k_{y_2} = k_{y_3} = k_{z_2} = k_{z_3} = 0.3$$

Performance results are given by Figures J-32, J-33, and J-34. With the above gain constants, the system appears to be unstable. However, the system can be made stable by the proper selection of gain constants. High body rates can be damped out by increasing the values of k_{y_1} and k_{z_1}. It is apparent from the power profile, Figure J-34, that the coils are not being properly utilized.

J-84
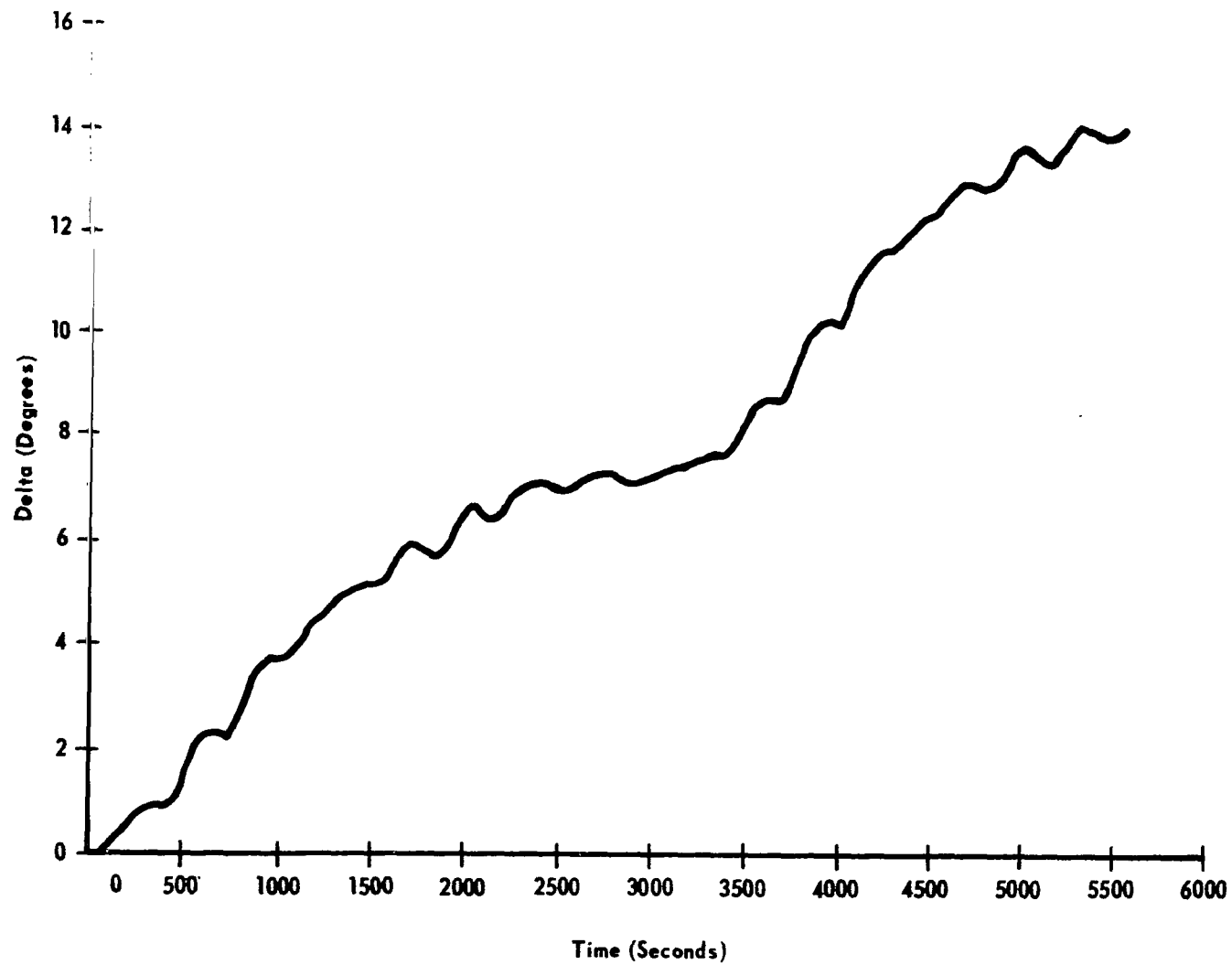
Figure J-27. Scan axis drift angle δ with orbit time for the uncontrolled baseline without flywheel.
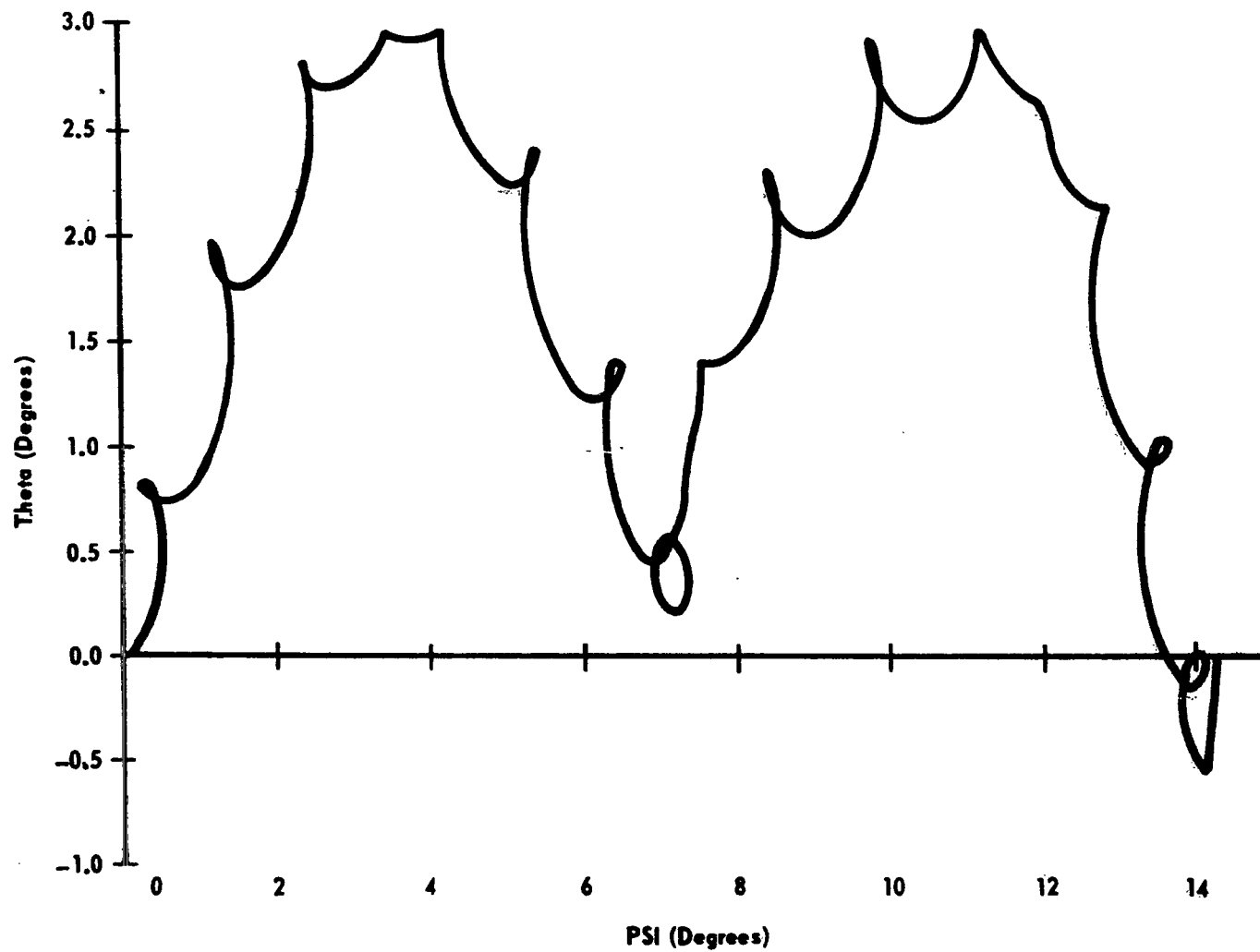
Figure J-28.   Motion of the scan axis in $\Psi - \theta$ plane for the uncontrolled baseline without flywheel.
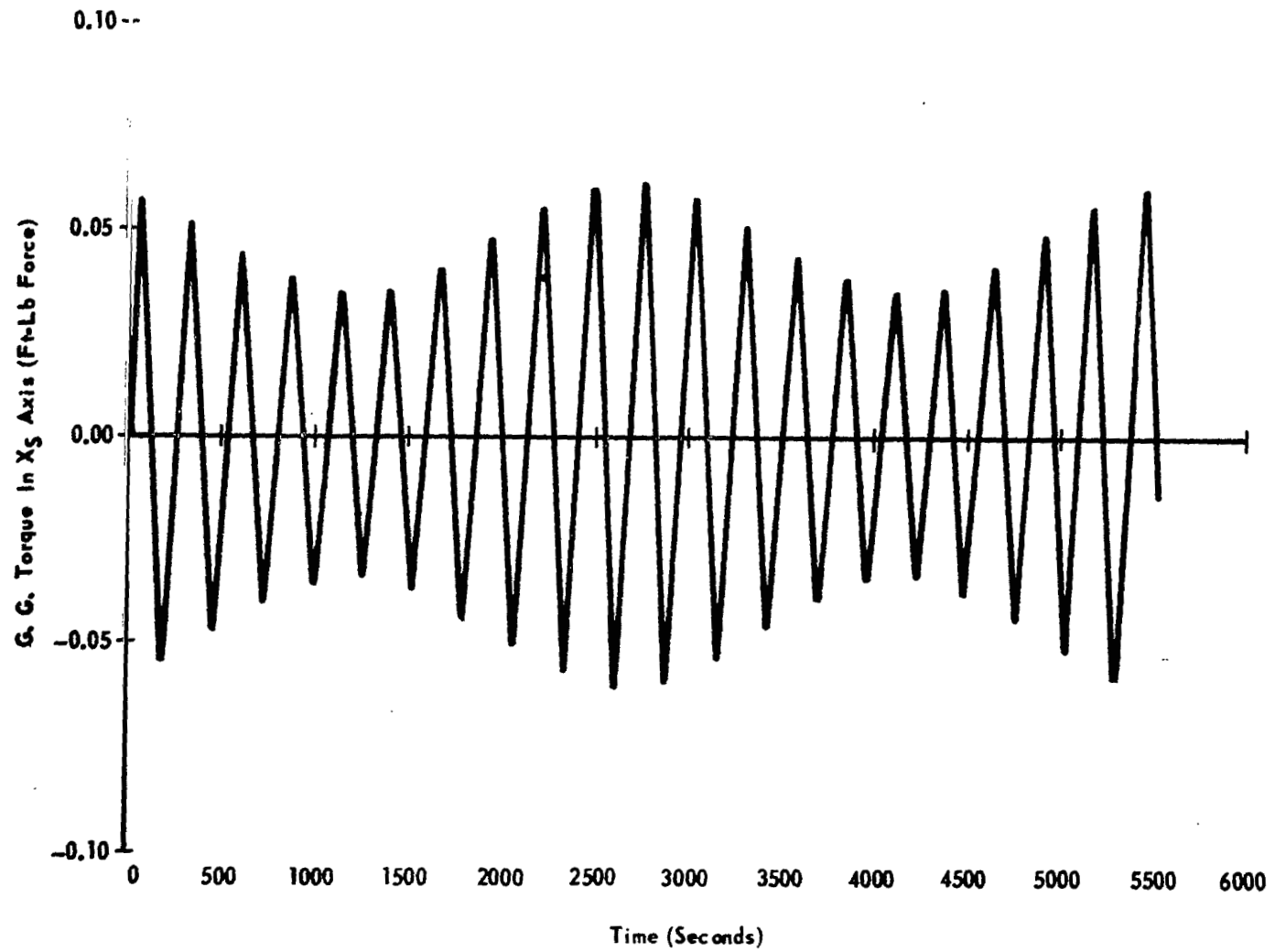
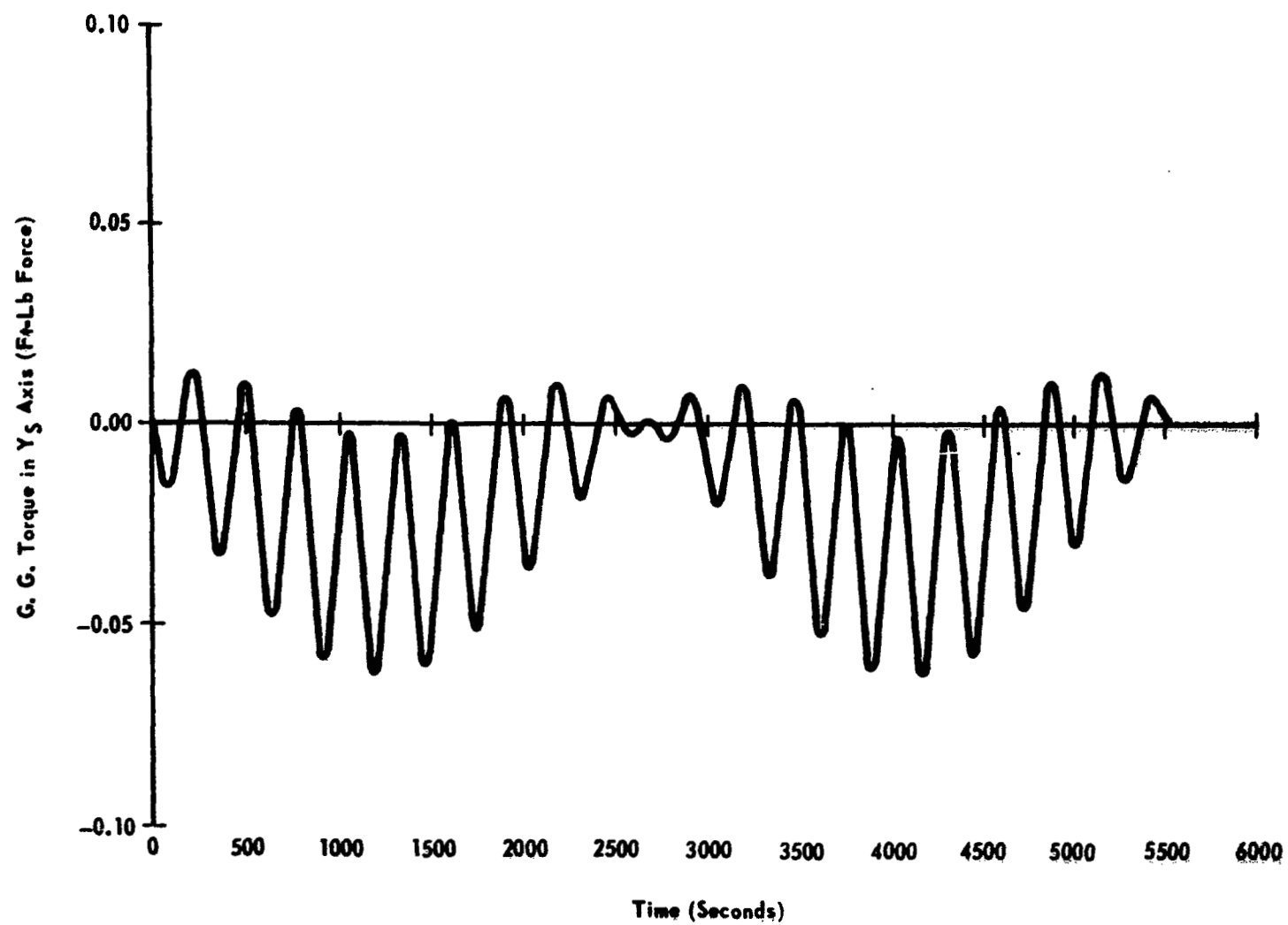Figure J-29. Gravity gradient torque in X_s axis.
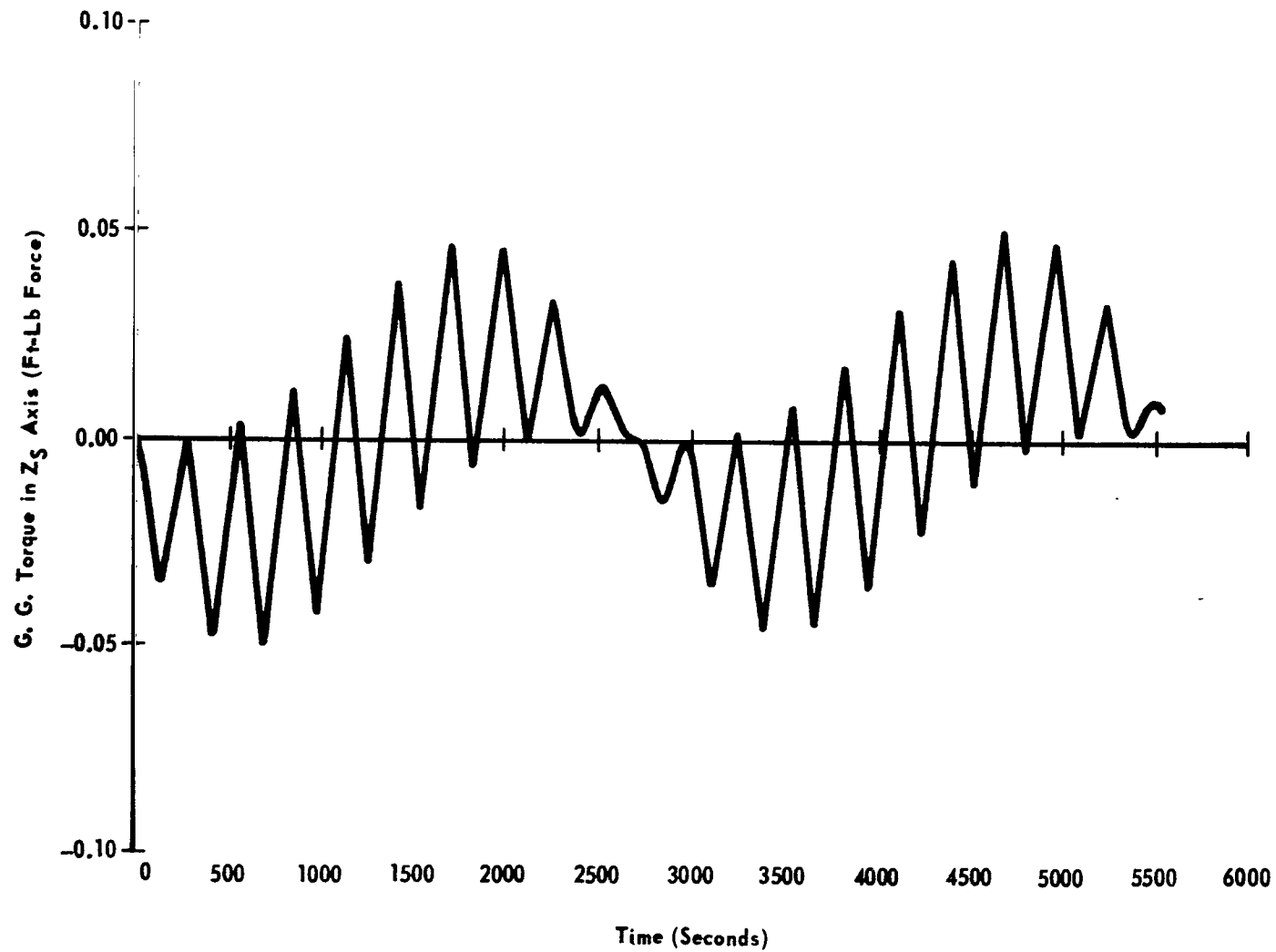
Figure J-30. Gravity gradient torque in Y_s axis.
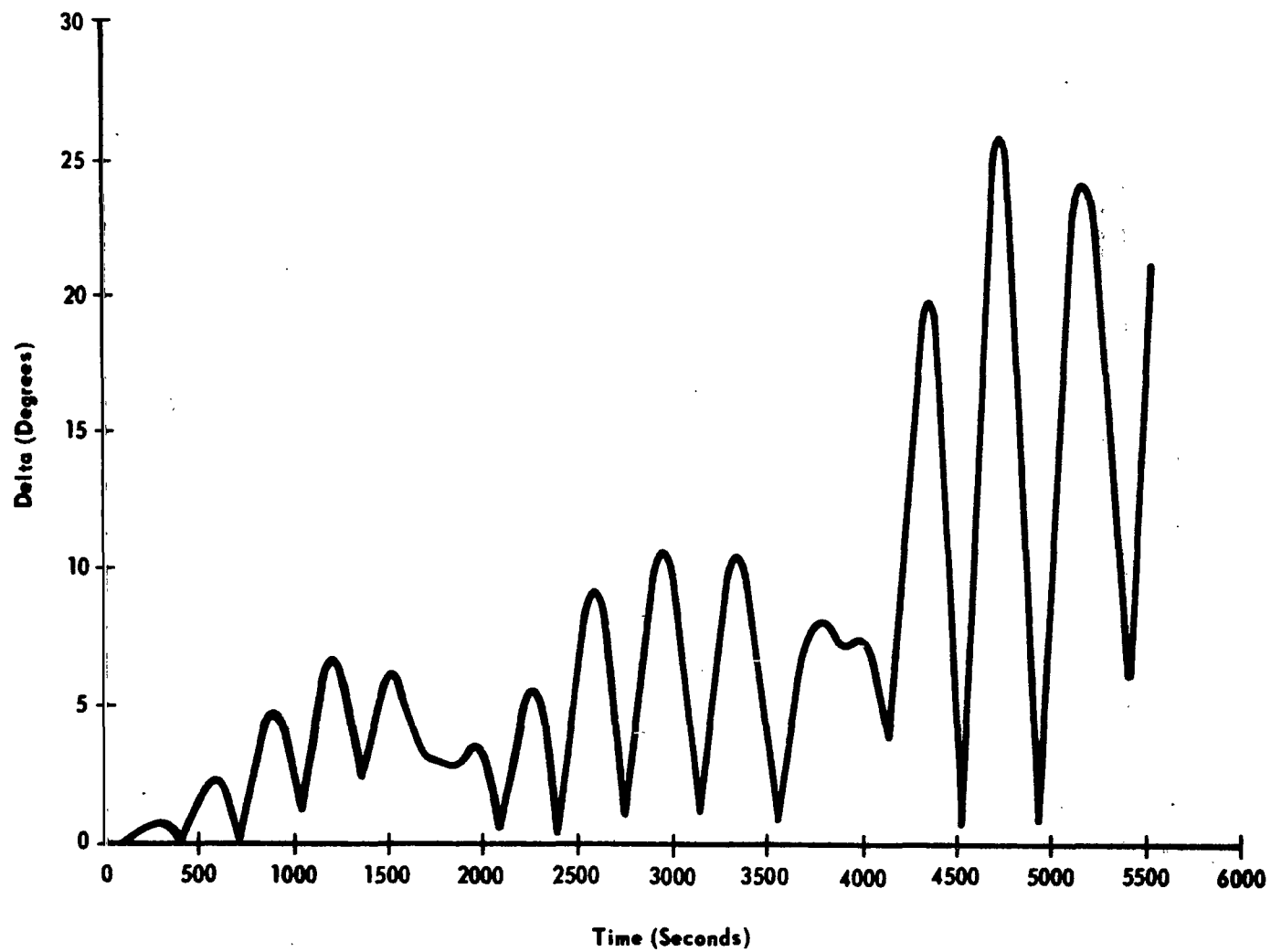
Figure J-31. Gravity gradient torque in Z_s axis.

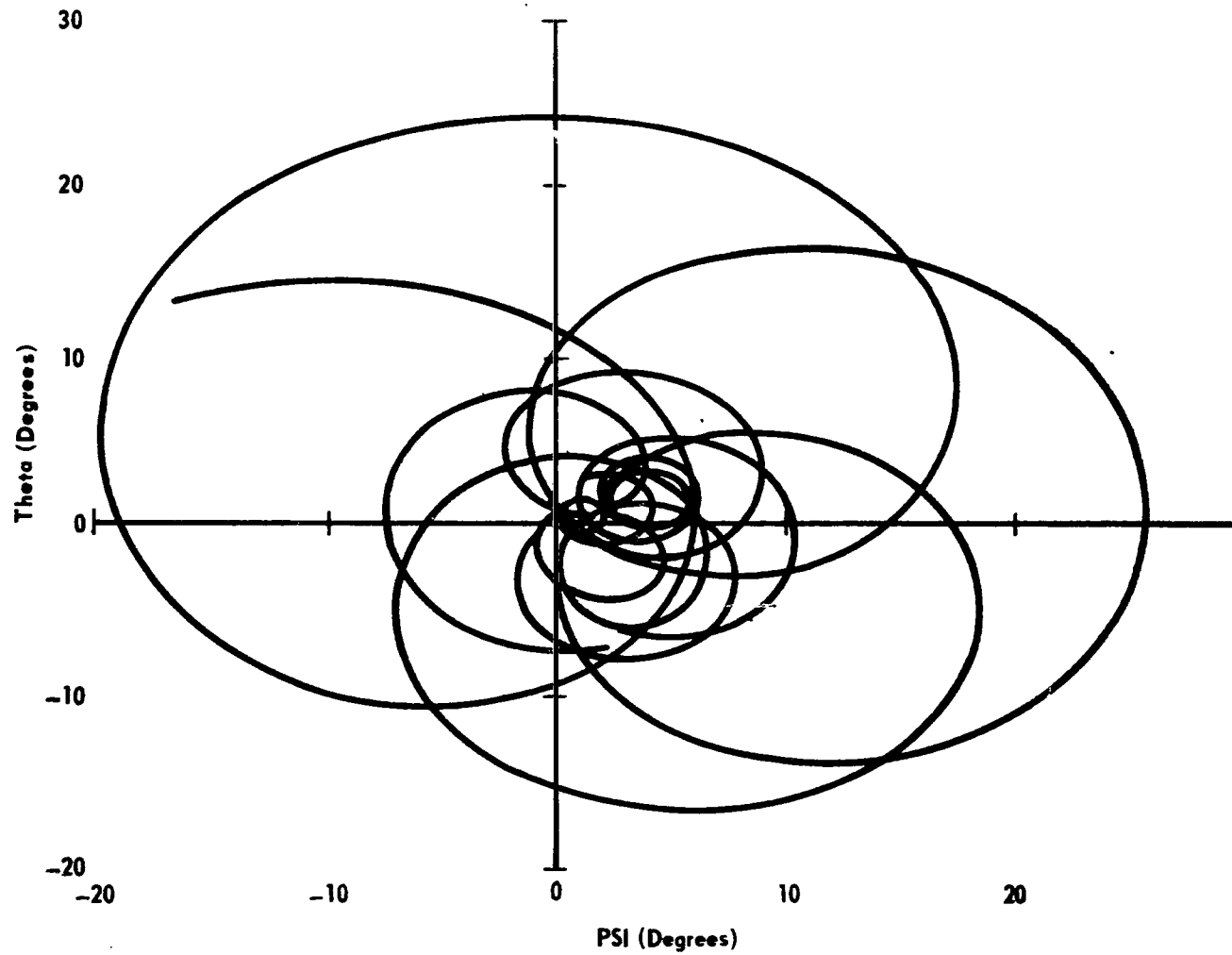Figure J-32. Baseline scan-axis drift angle δ with orbit time for controlled
spacecraft without flywheel.

Figure J-33. Motion of the baseline scan axis in $\Psi - \theta$ plane in one orbit time for controlled spacecraft without flywheel.
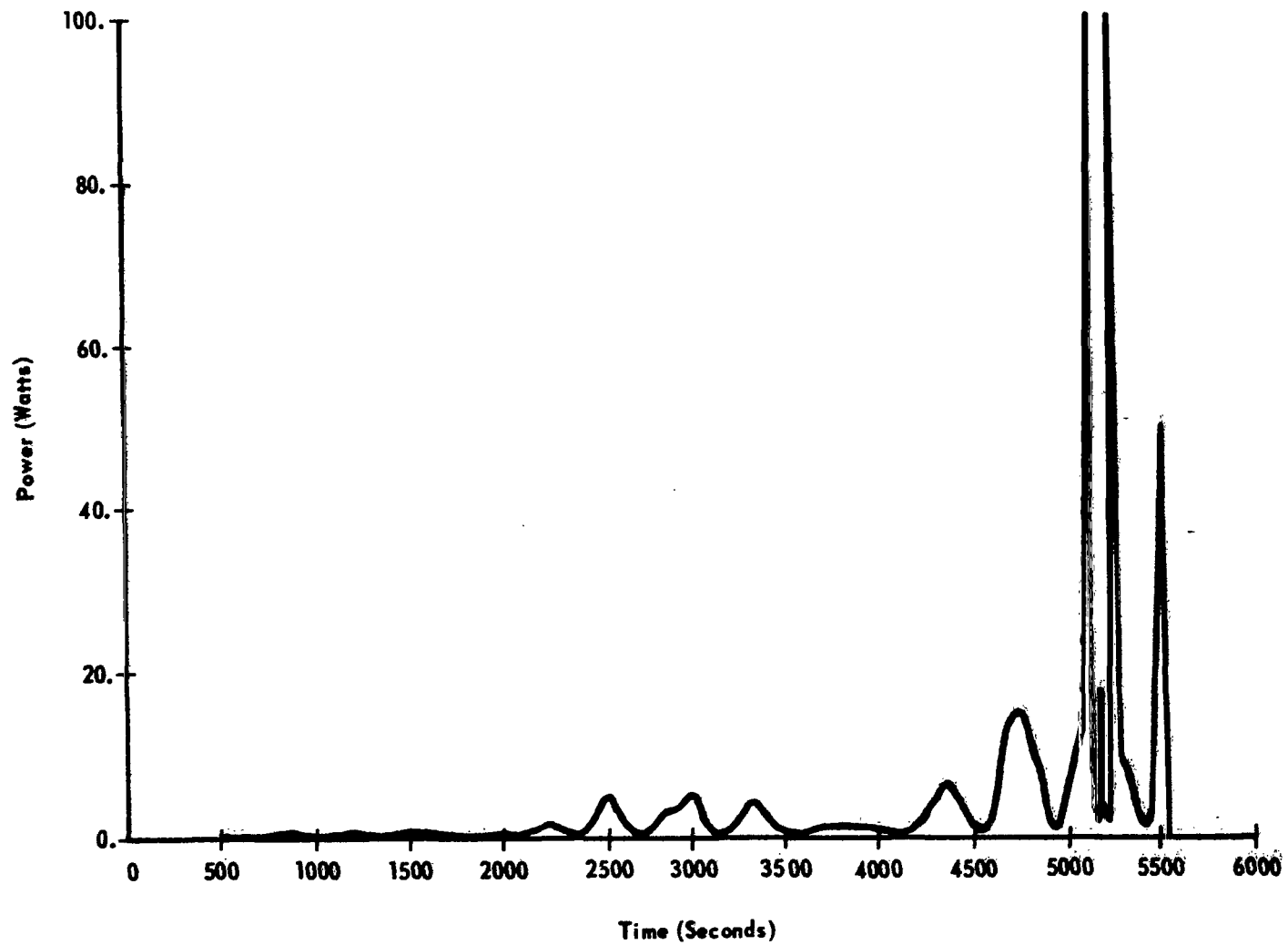
Figure J-34. Baseline without flywheel power profile for the magnetic torquers.

b. **Configuration III.** The moments of inertia for Configuration III are:

$$I_x = 10\ 850 \text{ slug ft}^2$$

$$I_y = 39\ 100 \text{ slug ft}^2$$

$$I_z = 41\ 100 \text{ slug ft}^2$$

1. With flywheel and without control. Figures J-35 through J-39 show the performance data plots for this case. Figure J-35 shows that δ increases continuously and reaches a value of 4.1 degrees in one orbit time. Figure J-36 shows the trace of the scan axis in the Ψ - θ plane. It is noted that Ψ and θ are negative. This is a contrast to the baseline case in which Ψ and θ are positive (Fig. XI-37). In the present case, the spacecraft moves in the ecliptic plane in the opposite direction to the motion of the sun, which is a disadvantage over the baseline concept.

Figure J-37 is a plot of the variation of the gravity gradient torque in the X_s-axis. The maximum value of the torque is 0.0037 ft-lbf and the torque varies at a frequency of twice the spin frequency of the spacecraft. Figures J-38 and J-39 are the plots for gravity torque in the Y_s- and Z_s-axes, respectively.

2. Without flywheel and control. In this case the spacecraft is rotating at 0.1 rpm on the minimum moment-of-inertia axis. The spacecraft has a very small angular momentum compared to the baseline concept; therefore, the scan axis drifts at a very rapid rate. Figure J-40 shows the trace of the scan axis in the Ψ - θ plane in one orbit period. The angle Ψ goes to a maximum of 47 degrees and then starts decreasing; the angle θ increases continuously and goes to a value of 65 degrees. The nature of the trace of the scan axis is different from Figure J-36 because of the difference in gravity gradient torques (Figs. J-41, J-42, and J-43) because of the large values Ψ and θ angles.

c. **Conclusions.** Performance results show that Configuration I is better than Configuration III from the standpoint of attitude control because firstly the scan-axis drift in Configuration I is less than Configuration II under
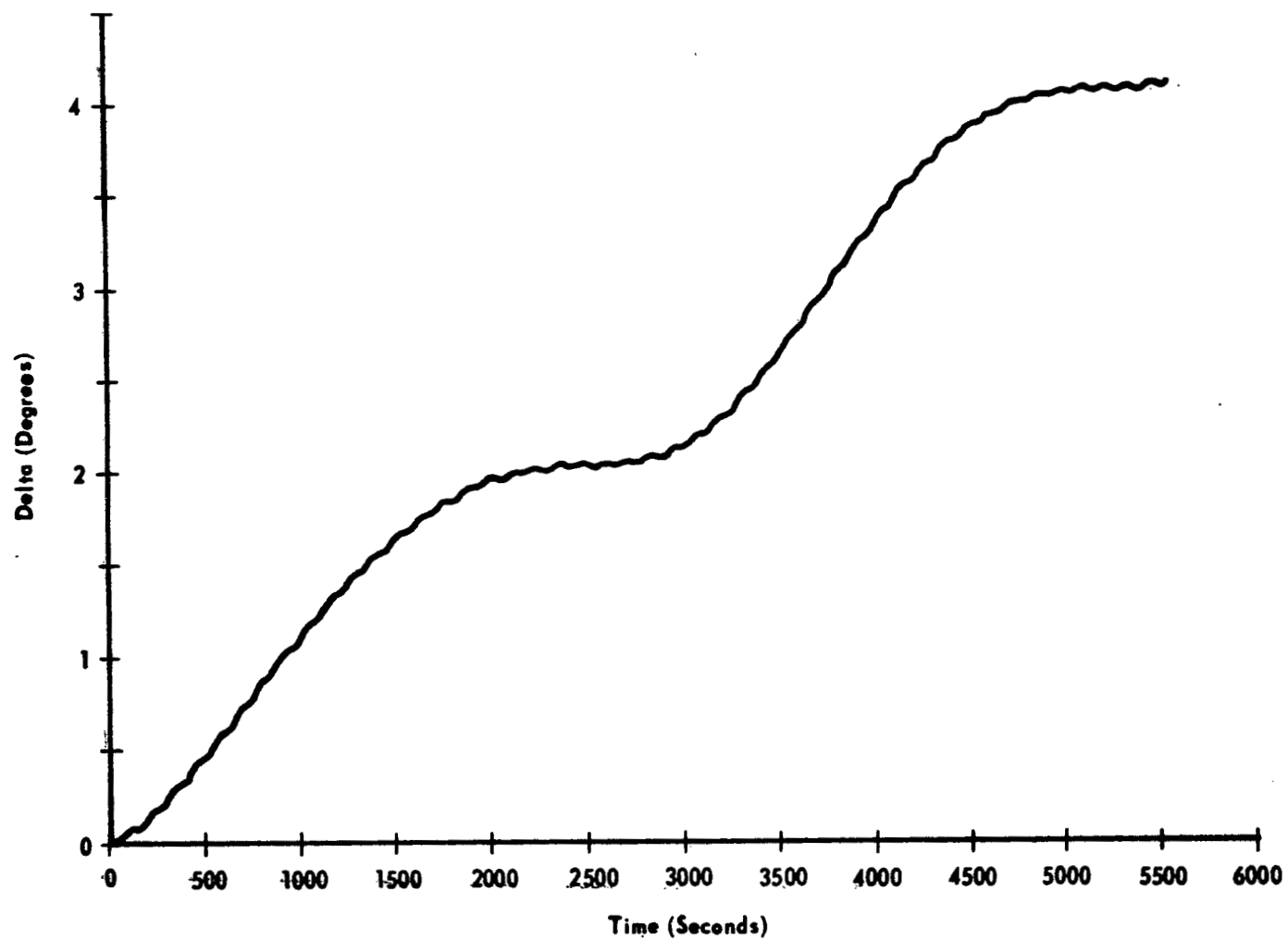
Figure J-35. Configuration III scan-axis drift angle δ with orbit time for uncontrolled spacecraft.
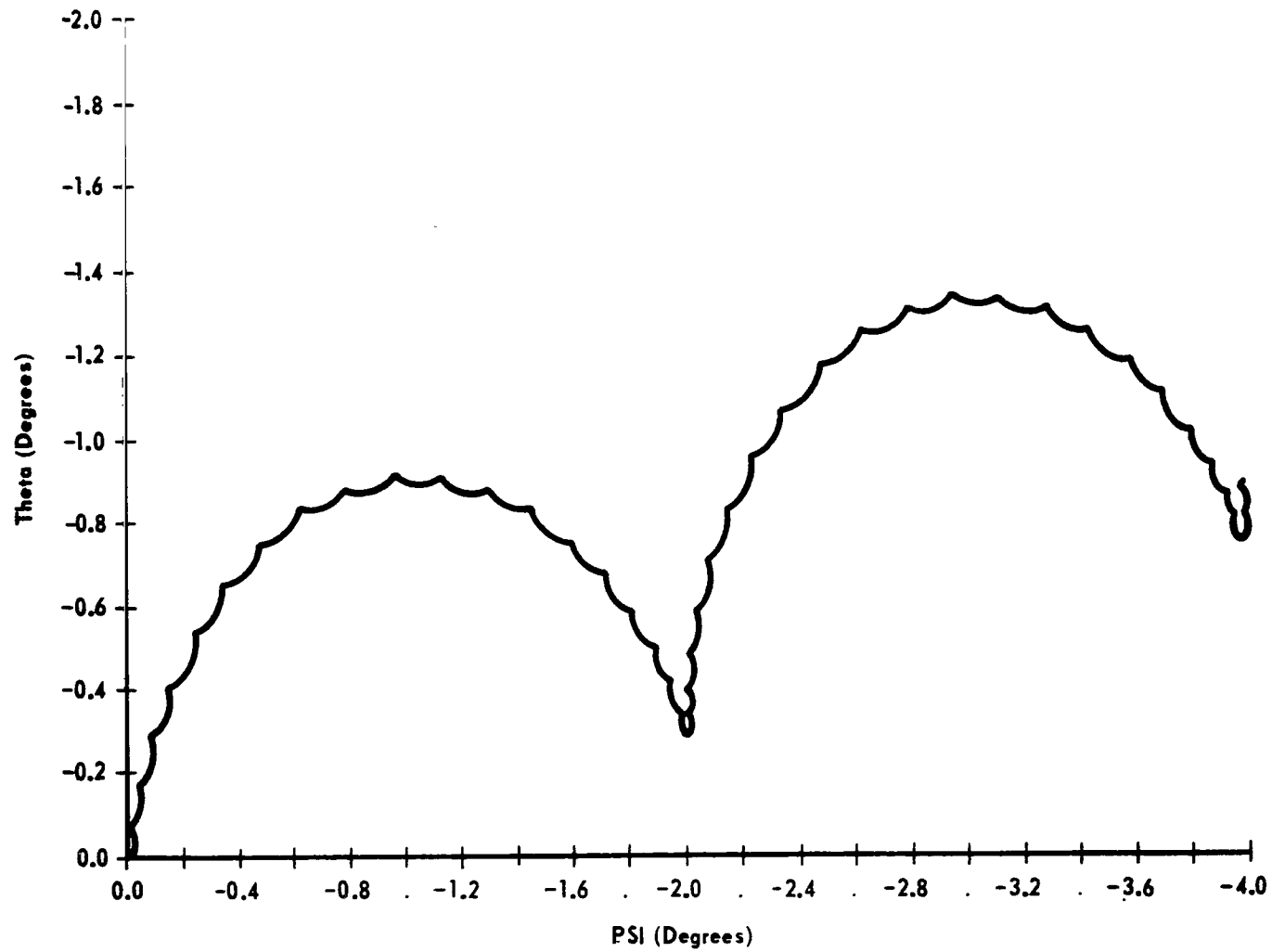
Figure J-36. Configuration III motion of the scan axis in $\Psi - \theta$ plane for uncontrolled spacecraft.
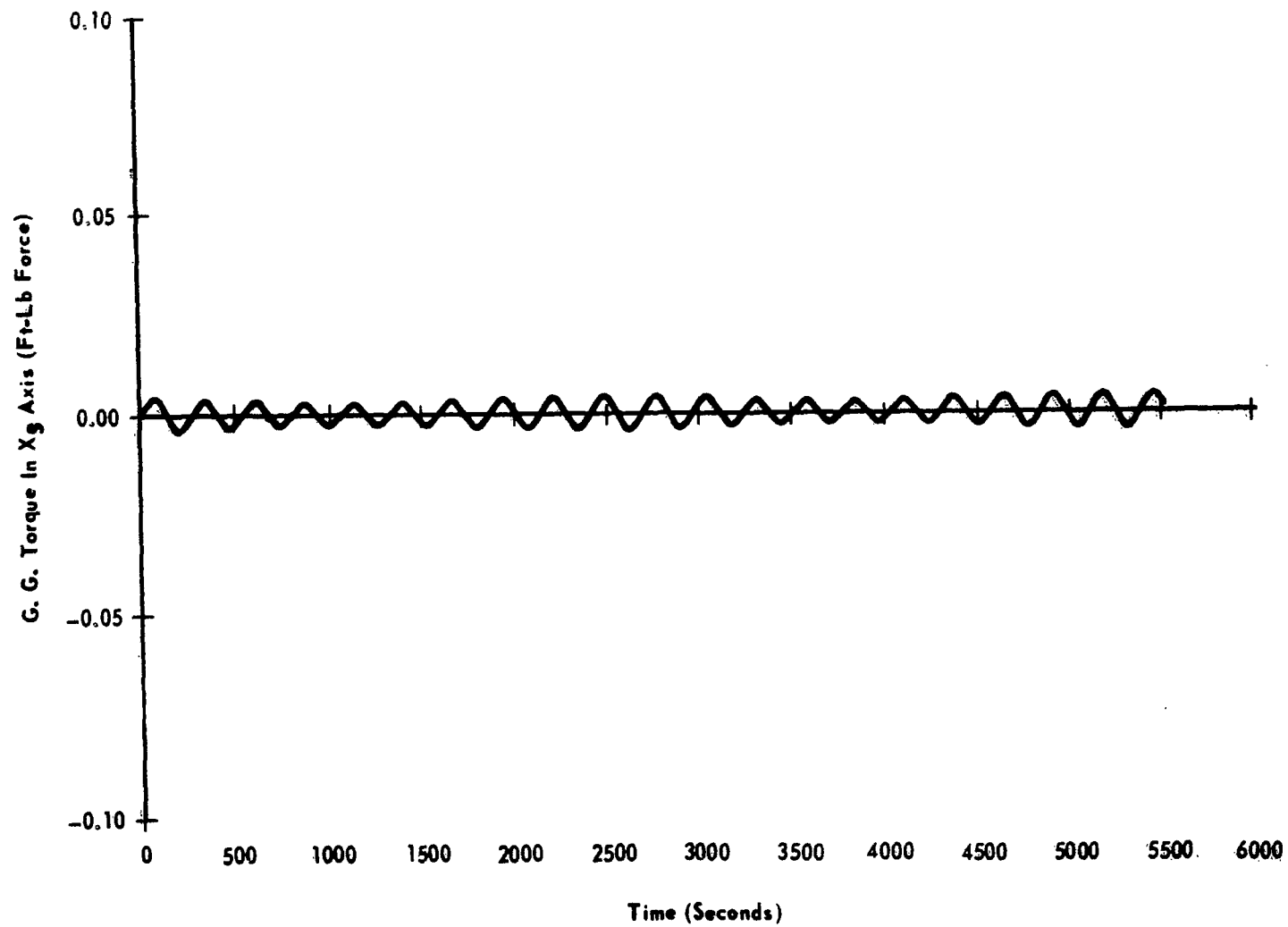
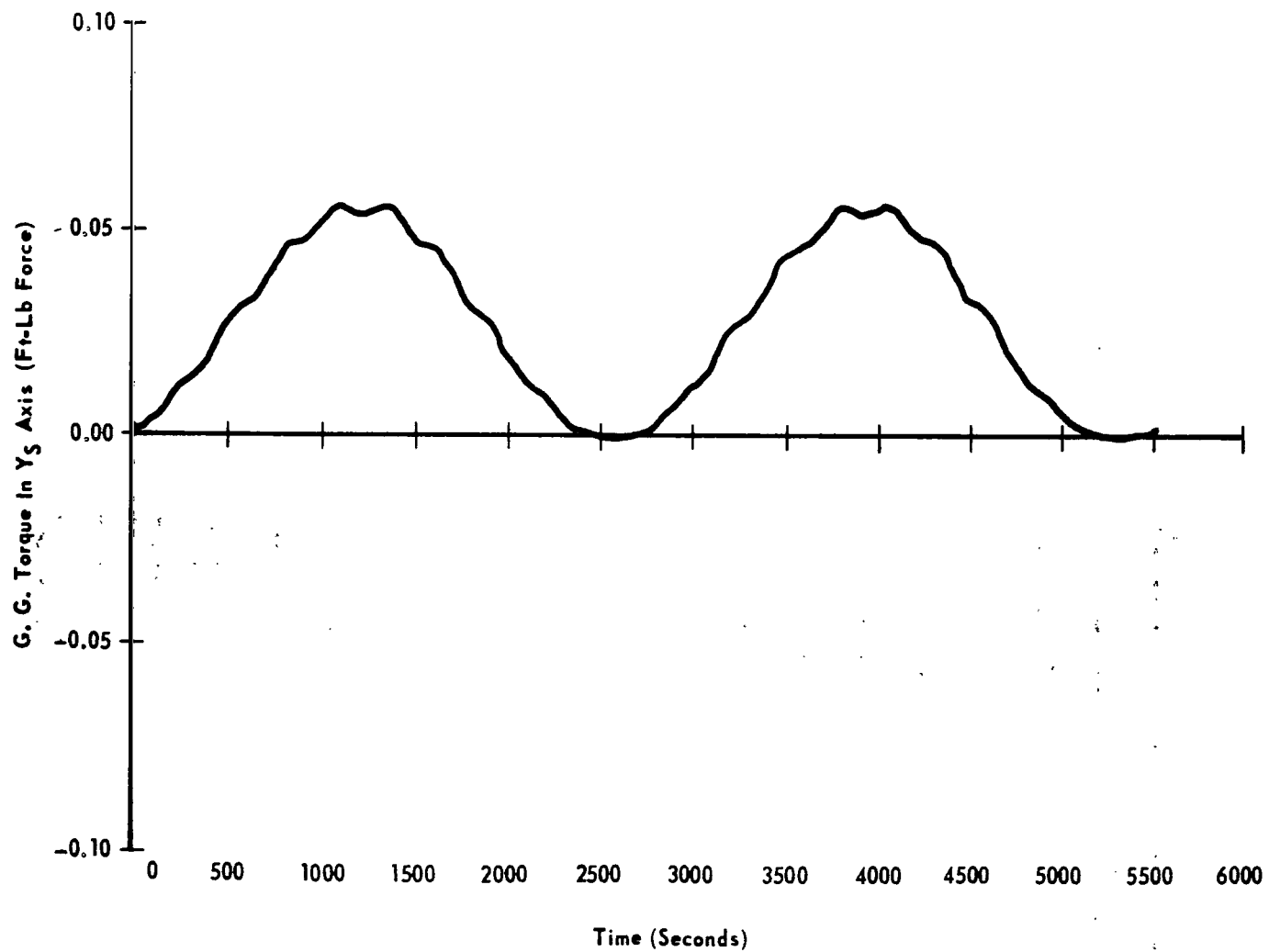Figure J-37. Configuration III gravity gradient torque in X_s axis.

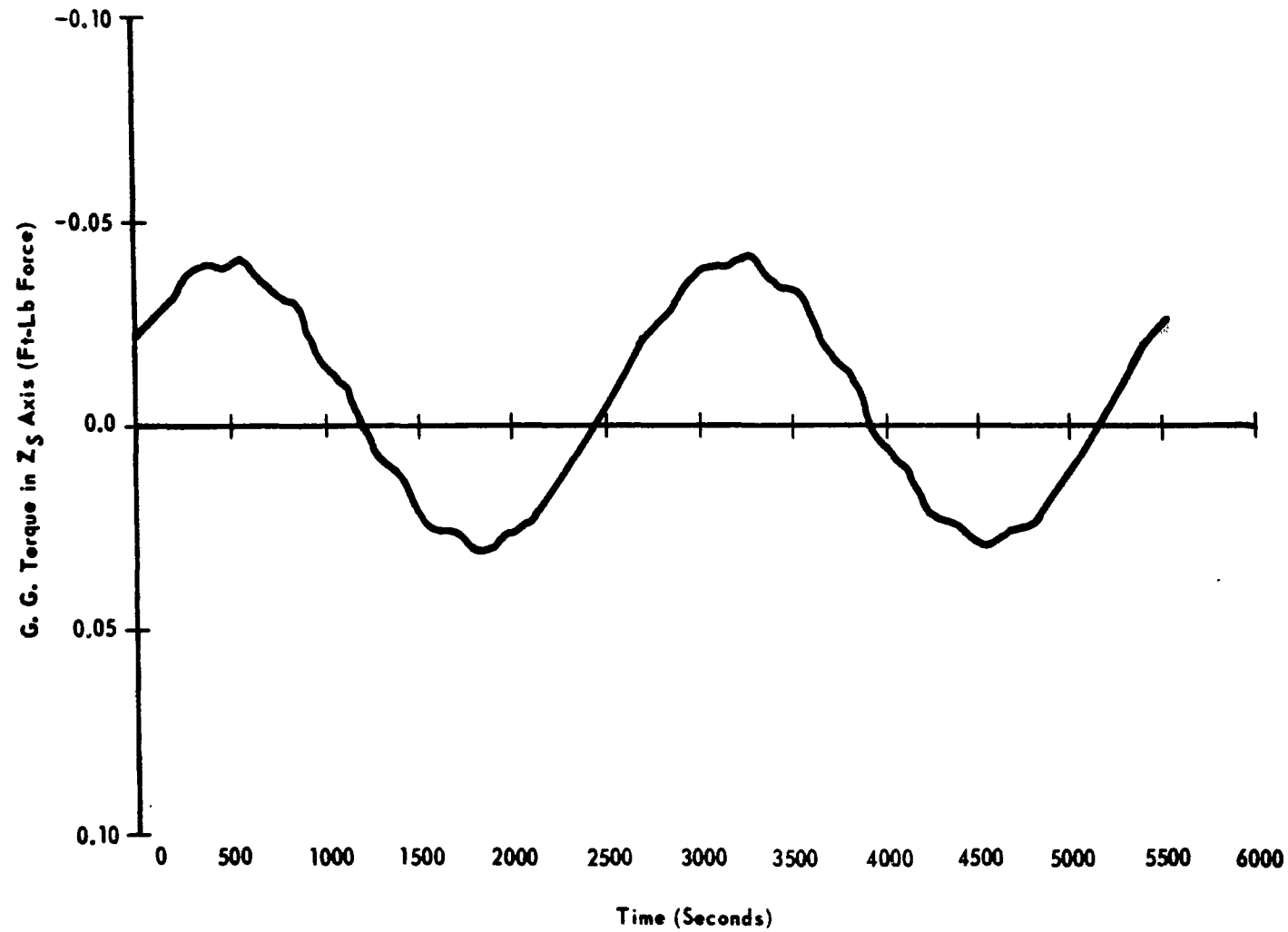Figure J-38. Configuration III gravity gradient torque in Y_s axis.

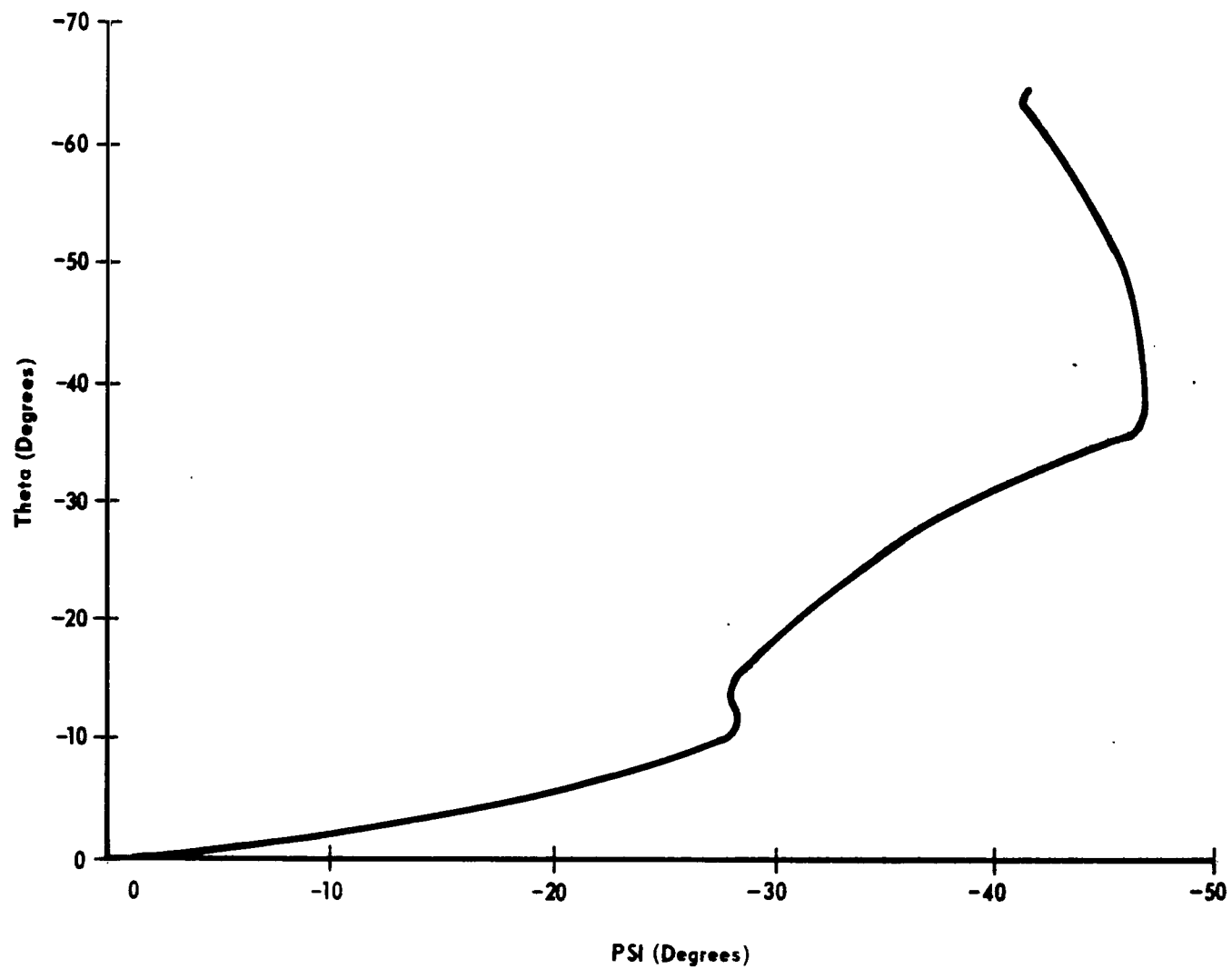Figure J-39. Configuration III gravity gradient torque in Z_s axis.

Figure J-40. Configuration III without flywheel, uncontrolled motion of the scan axis in $\Psi - \theta$ plane.
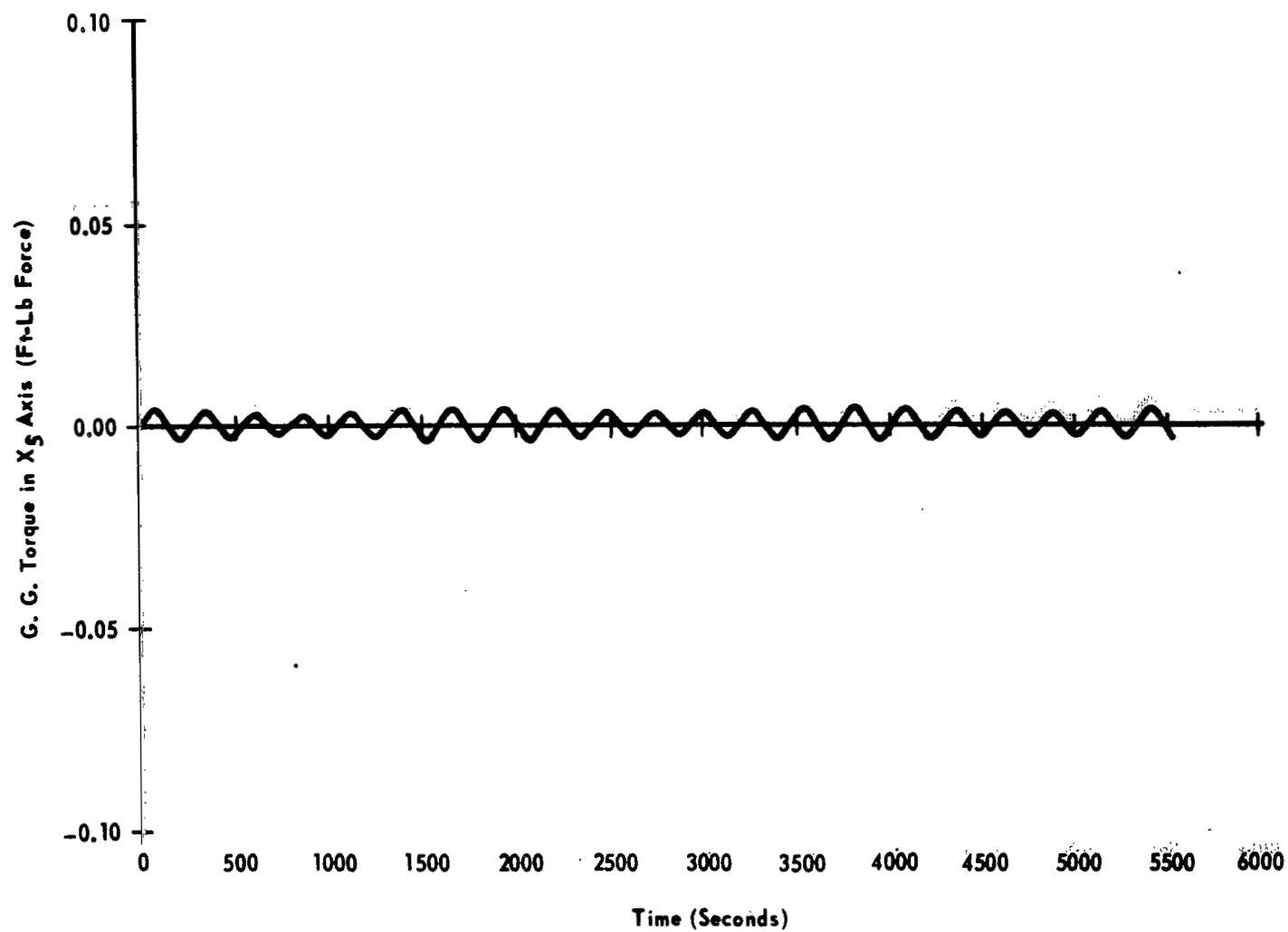
Figure J-41.   Configuration III without flywheel or control, gravity gradient torque in X_s axis.
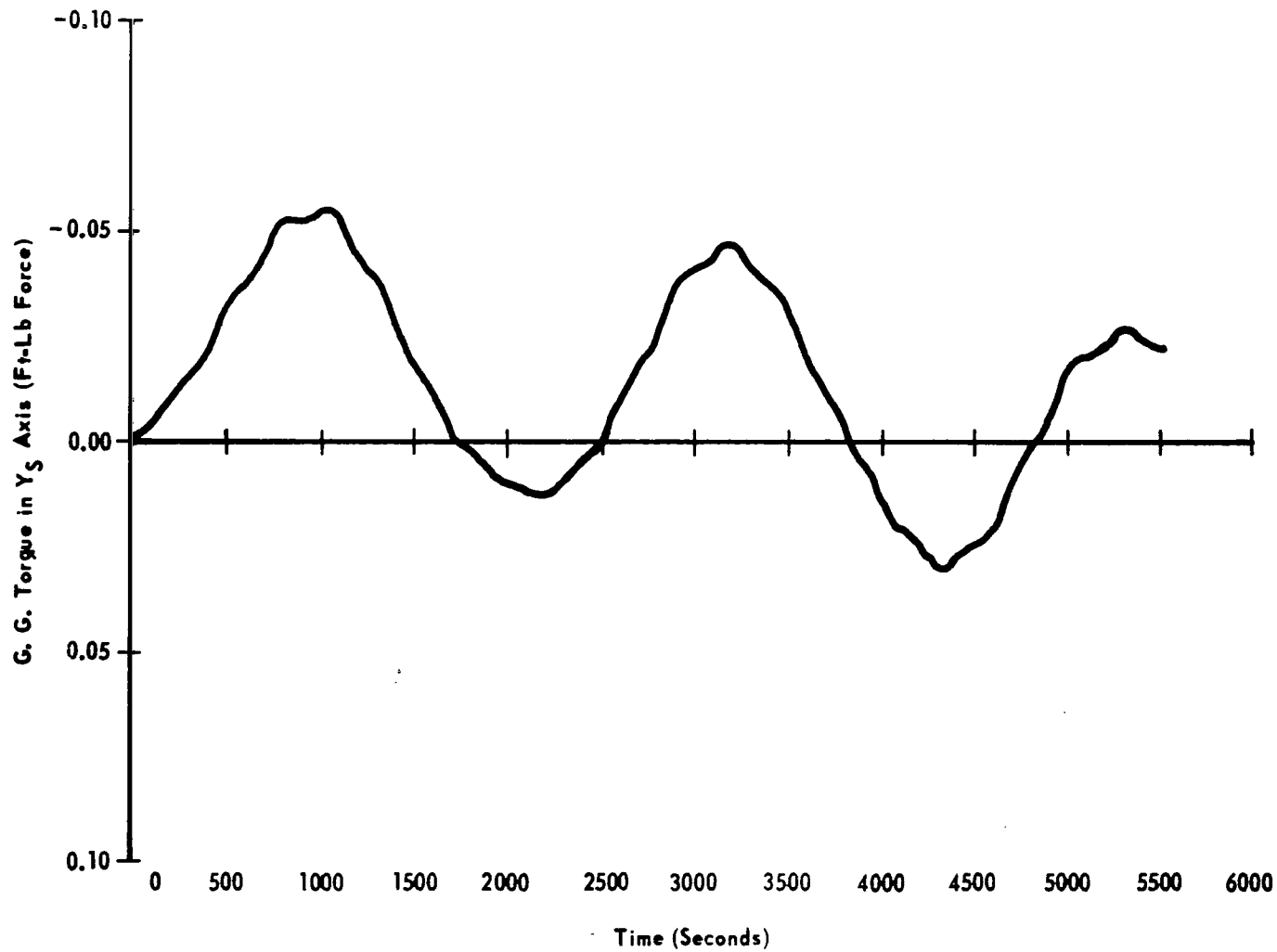
Figure J-42. Configuration III without flywheel or control, gravity gradient torque in Y_s axis.
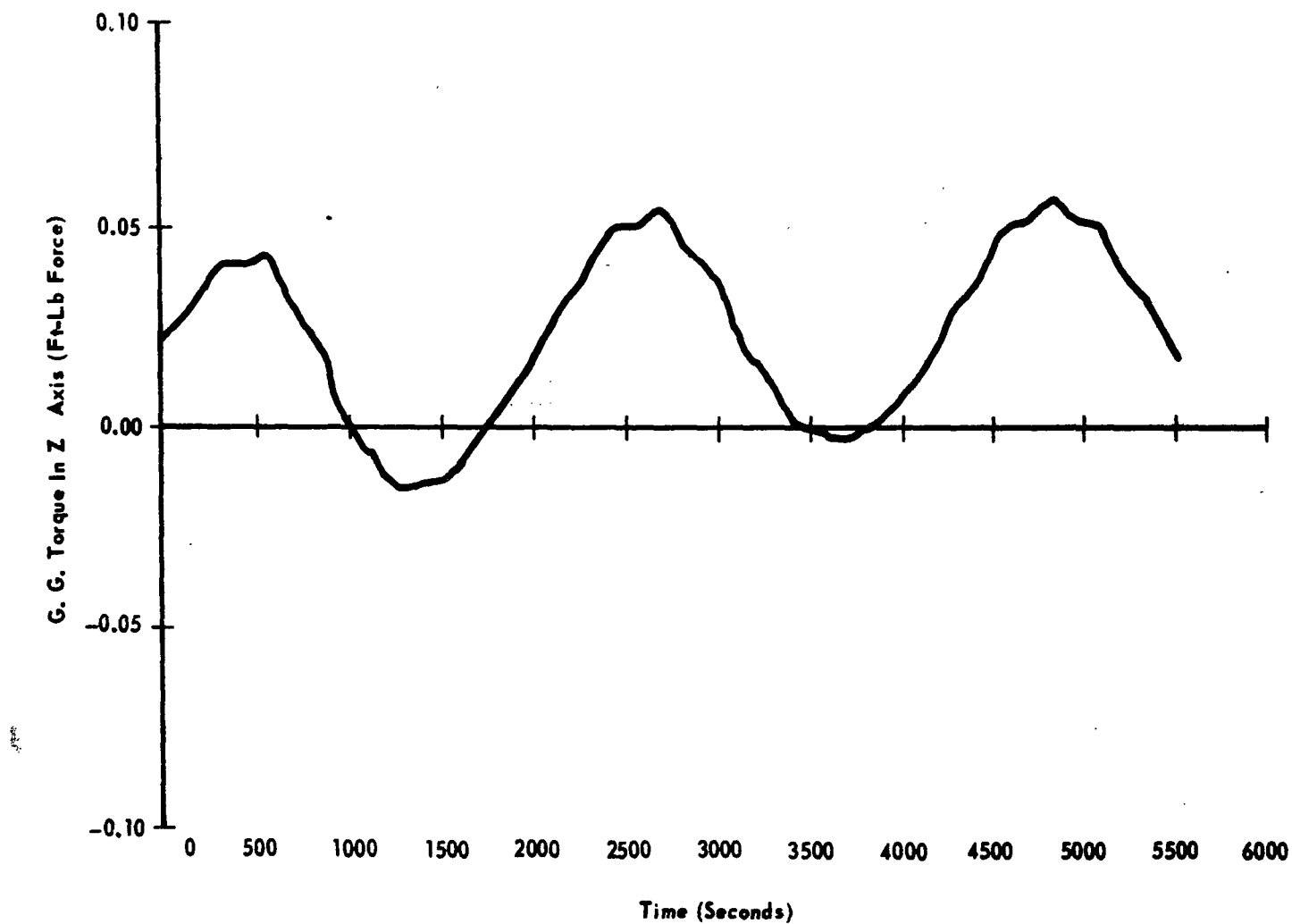
Figure J-43. Configuration III without flywheel or control, gravity
gradient torque in Z_s axis.

the conditions of gravity disturbance torques. Secondly, the scan axis of Configuration I drifts in the same direction as the sunline moves, whereas the scan axis of Configuration III drifts in the opposite direction to that of sunline.

A comparison of the performance of both Configurations I and III shows that the spinning flywheel provides directional stability for the scan axis. Without control under the disturbance of gravity, the flywheel reduced the solar offset angle per orbit by about a factor of 5. The performance data indicate that Configuration I has better response and pointing characteristics than Configuration III. However, this result was expected since Configuration I is spinning about its axis of major inertia, whereas Configuration III is spinning about its minimum axis of inertia. Performance results utilizing magnetic control torques show that it is possible to have almost continuous control of the scan axis with three coil control schemes. The possibility of near continuous control indicates that a flywheel may not be required for providing stability against disturbance torques. However, additional computer simulations are required to confirm this and to define those periods where magnetic torque cannot be generated to counteract gravity gradient torque. Later response data for the baseline without a flywheel indicate that acceptable performance is attained by increasing the control system gains by a factor of 100 over those used to generate the response shown in Figure J-32, but within the scope of this study effort the gains could not be optimized. With optimized control logic and feedback gains vehicle performance should show great improvement over that shown in this report.

REFERENCES

J-1. Kamm, L. J.: Magneto-Orques — A Satellite Orientation Device. ARS Journal, June 1961.

J-2. Memorandum SD-762-69 to Carroll Daily from Chan Crocker. June 18, 1969.

J-3. Phillips, Samual C.: Project Apollo Coordinate System Standards. OMSF SE 008-001-1, June 1965.

J-4. Davis, Billy G.: A Discussion of Orbital Orientation and Gravity Gradient Effects. NASA TM X-53829, May 1969.

J-5. Greensite, Arthur L.: Attitude Control in Space. NAS8-11494, GDC-DDE67-001, February 1967, p. 12.

J-6. Greenwood, Donald T.: Principles of Dynamics. Prentice-Hall, p. 335.

J-7. Goddard Space Flight Center and Grumman Aircraft Engineering Corp.: Feasibility Study of a Man-Attended OAO. Vol. II Appendices, Greenbelt, Maryland and Bethpage, New York, July 1967.

J-8. Meyer, George: On the Use of Euler's Theorem on Rotations for the Synthesis of Attitude Control Systems. NASA TN D-3643, Ames Research Center, Moffett Field, California, September 1966.

J-9. Spacecraft Magnetic Torques. NASA Space Vehicle Design Criteria, SP-8018, March 1969.

J-10. Memorandum S& E-AERO-AA-54 to Archie C. Young from Josh D. Johnson, Dec. 14, 1969.

BIBLIOGRAPHY

Goldstien, Herbert: Classical Mechanics. Addison-Wesley.

APPROVAL

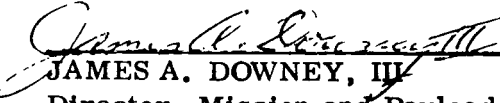## CONCEPTUAL DESIGN OF A HIGH ENERGY ASTRONOMY OBSERVATORY
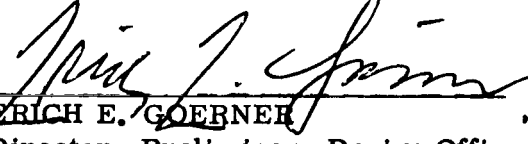
By Program Development

The information in this report has been reviewed for security classification. Review of any information concerning Department of Defense or Atomic Energy Commission programs has been made by the MSFC Security Classification Officer. This report, in its entirety, has been determined to be unclassified.
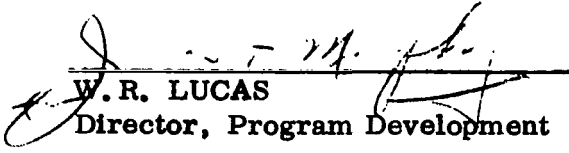
This document has also been reviewed and approved for technical accuracy.

CARROLL C. DAILEY
Chief, Space Physics Group
HEAO PHASE A PROGRAM
MANAGER

JAMES W. HEYER
Assistant Director, Preliminary
Design Office

JAMES A. DOWNEY, III
Director, Mission and Payload
Planning Office

ERICH E. GOERNER
Director, Preliminary Design Office

W. R. LUCAS
Director, Program Development

J-105